MCEER
EARTHQUAKE ENGINEERING TO EXTREME EVENTS

ISSN 1520-295X

Blast and Seismic Resistant Concrete-Filled Double Skin Tubes and Modified Steel Jacketed Bridge Columns

by

Pierre P. Fouché and Michel Bruneau

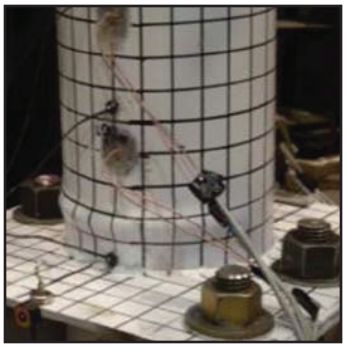
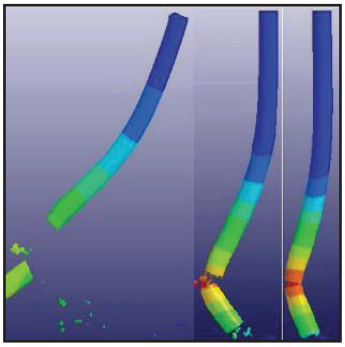

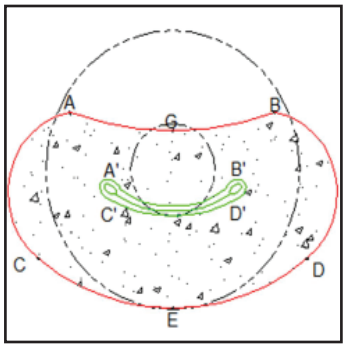

Technical Report MCEER-14-0004

June 30, 2015

This research was conducted at the University of Buffalo, State University of New York, and was supported primarily by MCEER, the Federal Highway Administration and the Infrastructure Protection and Disaster Management Division, Science and Technology Directorate, Department of Homeland Security Security under a cooperative agreement with the Engineer Research Development Center of the U.S. Army Corps of Engineers.

NOTICE

This report was prepared by the University at Buffalo, State University of New York, as a result of research sponsored by the Federal Highway Administration and the Infrastructure Protection and Disaster Management Division, Science and Technology Directorate, U.S. Department of Homeland Security under a cooperative agreement with the Engineer Research Development Center of the U.S. Army Corps of Engineers. Neither MCEER, associates of MCEER, its sponsors, the University at Buffalo, State University of New York, nor any person acting on their behalf:

a. makes any warranty, express or implied, with respect to the use of any information, apparatus, method, or process disclosed in this report or that such use may not infringe upon privately owned rights; or

b. assumes any liabilities of whatsoever kind with respect to the use of, or the damage resulting from the use of, any information, apparatus, method, or process disclosed in this report.

Any opinions, findings, and conclusions or recommendations expressed in this publication are those of the author(s) and do not necessarily reflect the views of MCEER or other sponsors.

MCEER
EARTHQUAKE ENGINEERING TO EXTREME EVENTS

Blast and Seismic Resistant Concrete-Filled Double Skin Tubes and Modified Steel Jacketed Bridge Columns

by

Pierre P. Fouché[1] and Michel Bruneau[2]

Publication Date: June 30, 2015
Submittal Date: May 30, 2014

Technical Report MCEER-14-0004

MCEER Thrust Area 1, Infrastructure and Public Policy

Federal Highway Administration, contract number DTFH61-07-C-00020

Infrastructure Protection and Disaster Management Division, Science and Technology Directorate, U.S. Department of Homeland Security cooperative agreement with the Engineer Research Development Center of the U.S. Army Corps of Engineers, contract number W912HZ-11-2-0001

1 Graduate Student, Department of Civil, Structural and Environmental Engineering, University at Buffalo, State University of New York
2 Professor, Department of Civil, Structural and Environmental Engineering, University at Buffalo, State University of New York

MCEER
University at Buffalo, State University of New York
212 Ketter Hall, Buffalo, NY 14260
E-mail: *mceer@buffalo.edu*; Website: *http://mceer.buffalo.edu*

Preface

MCEER is a national center of excellence dedicated to the discovery and development of new knowledge, tools and technologies that equip communities to become more disaster resilient in the face of earthquakes and other extreme events. MCEER accomplishes this through a system of multidisciplinary, multi-hazard research, in tandem with complimentary education and outreach initiatives.

Headquartered at the University at Buffalo, The State University of New York, MCEER was originally established by the National Science Foundation in 1986, as the first National Center for Earthquake Engineering Research (NCEER). In 1998, it became known as the Multidisciplinary Center for Earthquake Engineering Research (MCEER), from which the current name, MCEER, evolved.

Comprising a consortium of researchers and industry partners from numerous disciplines and institutions throughout the United States, MCEER's mission has expanded from its original focus on earthquake engineering to one which addresses the technical and socio-economic impacts of a variety of hazards, both natural and man-made, on critical infrastructure, facilities, and society.

The Center derives support from several Federal agencies, including the National Science Foundation, Federal Highway Administration, National Institute of Standards and Technology, Department of Homeland Security/Federal Emergency Management Agency, and the State of New York, other state governments, academic institutions, foreign governments and private industry.

This report presents the results of an analytical and experimental study on the use of Concrete-Filled Double Skin Tubes (CFDST) and Modified Steel Jacketed Bridge Columns (MSJBC) to provide blast and seismic resistance (from a multi-hazard perspective). First, the ability of CFDST columns to provide satisfactory seismic performance is verified by cyclic inelastic testing of quarter scaled specimens. Then, their blast resistance is investigated through two series of tests, respectively conducted at the MCEER ECLIPSE testing facility in Buffalo and at the U.S. Army Corps of Engineers Research and Development Center's Facility in Vicksburg, Mississippi. Closed-form equations are also presented for the design of CFDST and MSJFC and to predict their response (lateral deflection and extent of denting) during blast scenarios.

“

ABSTRACT

A proposed paradigm in engineering of bridges prone to the effects of multiple hazards calls for designing and detailing new bridges, as well as retrofitting existing bridges, so that an integrated structural concept provides protection against all credible hazards. This multi-hazard approach is believed to lead to structural systems that are optimal and offer a more uniform level of safety against various credible relevant hazard scenarios.

Toward this objective, research was conducted to develop and experimentally validate two proposed structural concepts capable of achieving the goal of multiple hazard protection for highway bridges, namely Concrete Filled Double Skin Tube (CFDST) and Modified Steel Jacketed Columns (MSJC). CFDST is proposed as seismic and blast resistant column for new bridge multi-column bent. MSJC, on the other hand, is a “retrofit-of-the-retrofit” concept which adds blast protection to the capability of Steel Jacketed Column (SJC) already known to provide seismic resistance.

Performance of CFDST is investigated both under cyclic pushover and blast tests whereas MSJC is tested under blast loading only using ¼ scale column prototypes. The energy dissipation of CFDST under cyclic loading is found to be excellent. Under credible blast scenario, CFDST deform in bending without significant loss in capacity to carry load. For near-contact explosion, another energy dissipation mechanism is engaged in the form of cross-section deformation. In both credible and near contact blast explosion, MSCJ is found to be able to develop large flexural deformations which are not achievable with non-modified SJC that are usually prone to direct shear failure.

Equations are also presented to help designer predict the behavior of CFDST under blast and earthquake loads. Comparison to the experimental data generated in this research as well to data available in the literature shows that those analytical results are accurate, and in some instances conservative.

ACKNOWLEDGEMENTS

Except as noted in the following paragraph, this research was conducted at the University at Buffalo (The State University of New York) with financial support from the Multidisciplinary Center for Earthquake Engineering Research (MCEER), and the Federal Highway Administration. The Buffalo branch of the Federal Bureau of Investigation is sincerely thanked for its help and assistance for the logistics of the blast experiments conducted at the MCEER Experimental Campus for Large Infrastructure Protection, Sustainability and Enhancement (ECLIPSE Campus). The staff of the Structural Engineering and Earthquake Simulation Laboratory at the University at Buffalo is also thanked for its assistance.

The blast engineering research related to the specimens tested at the blast testing facility of the U.S. Army Engineer Research and Development Center (ERDC) in Vicksburg, Mississippi, (described in parts of Chapter 8 and 9) was conducted in collaboration with Vince Chiarito, ERDC Research Structural Engineer, as part of a cooperative agreement with ERDC. Mr. Chiarito's full participation in this research was most valuable and is sincerely appreciated. This specific research effort was supported by the Science and Technology Directorate of the Department of Homeland Security. Permission to publish was granted by the Department of Homeland Security and the Director of ERDC's Geotechnical and Structures Laboratory.

However, any findings, conclusions, and recommendations presented in this report are those of the authors and do not necessarily reflect the views of the sponsors.

TABLE OF CONTENTS

LIST OF FIGURES

LIST OF TABLES

SECTION 1

INTRODUCTION

1.1 Motivation for Research

Awareness is building about the necessity to engineer bridges not only to perform well in their normal operating conditions but also to withstand and survive, in the worst case with repairable damages, the wide range of hazards that they can see within their lifespan. However, at this time, few guidelines exist on how to incorporate synergistically the risks associated with those hazards in the engineering of structural systems at large and of bridges specifically. This may be attributable to the fact that those hazards are often associated with extreme events, both natural (earthquakes, tsunamis, storm surges) and man-made (terrorist attack, vessel impact, accidental explosions) that, individually or combined, are equally difficult to predict and intricate to model. Other impediments may be that they were not initially considered in design because some were never anticipated or the demands they impose on systems were not understood or not considered severe. Furthermore, the lack of adequate computational tools and databases might have hindered the capacity to do so (Ettouney et al., 2005). As information on system performance in previous hazards or in tests is collected and computational tools are getting more efficient, designers are now more opened to the idea that a better way to guard structures against those hazards is not to consider them in standalone hazard resistant designs but to integrate them in a multi-hazard approach that uses a single optimized design concept to provide sufficient performance for all hazards.

As put forth by FEMA (FEMA, 2004), the concept of multi-hazard design means that designers need to understand the fundamental characteristics of hazards and how they interact, so that design for protection against one hazard becomes integrated with all the other fundamental design demands from the others. While multi-hazard is not revolutionary per se, it represents nonetheless, an evolution in design thinking that is in tune with the increasing complexity of today's structures and takes advantage of developments and innovation in structures technology. A key aspect of multi-hazard design is that it looks at the ways in which design methods used to protect against the hazards reinforce or are in conflict with one another. When those methods reinforce each other, the estimated demands on the structure will be consistent and a more uniform level of safety achievable at reasonable cost. Otherwise, the demands can be conflicting, which may increase the cost.

Hence, to insure that engineering and design of bridge structures within a multi-hazard framework is both reliable and safe, two fundamental aspects must be considered. On one hand, designer ought to seek to become knowledgeable about all hazards to gain a good understanding of how they interact with and affect bridges, and determine how they can be accommodated within the design process. On the other hand, an effort should be made to conceive integrated multi-hazard bridge systems that can be analyzed, designed, detailed, and built at cost comparable to existing systems while performing better under the individual or eventually combined effects of the hazards. At the same time, efforts should be undertaken to upgrade existing bridges so that they can perform better when faced with multiples credible hazards. Both new and upgraded bridge systems should take into account lessons learnt from previous failures and provide a uniform level of safety against collapse in all major hazards considered.

This research is part of a larger effort to develop multi-hazard bridge structure able to resist the effects of earthquakes shaking, blast overpressures, tsunamis waves, vessel impact, and storm surges. For this research, the focus is on bridge substructure and most specifically on the development of a multi-hazard bridge pier system, as well as a solution to retrofit existing bridge piers, in a bi-hazard framework of analysis consisting of earthquake shaking and malevolent blast events. Due to their inherent structural qualities, ranging from higher strength, substantial toughness, and ductility, as well as their benefits in situations requiring accelerated construction or repair, composite steel-concrete-steel constructions are studied as candidates for new bridges. In parallel, for existing ductile or non-ductile reinforced concrete column-piers, as well as non-ductile column already retrofitted with steel jacket, a modified steel jacketed retrofit concept is introduced to provide enhanced protection to bridges in a multi-hazard environment.

1.2 Scope and Objective

Being public structures that are not always closely monitored, highway bridges are more accessible and vulnerable than other landmark bridges. Their function determines their vulnerability as they can be used and hence targeted by terrorists. In many instances, the destruction of a highway bridge can have profound effects on the economic communities those infrastructures support. This makes many of those bridges critical and their protection against natural and manmade hazards an imperative. As a consequence, the multi-hazard structural and retrofit concepts covered in this research are developed for highway bridges.

Moreover, a bridge substructure is the most vulnerable component of a bridge system, and its failure generally coincides with partial or complete failure of the structure itself. Besides the fact

that it is readily accessible, which makes it a likely target in a terrorist attack, the multiple functions that the substructure has to play contribute also to this vulnerability. For instance, bridge piers are relied upon to protect the structure during earthquakes by working as structural fuses that dissipate the seismic energy. Bridge pier systems are also relied upon in vehicle collision or in blast events to locally dissipate the impulses imparted by the impact. To satisfactorily fulfill those multiple roles, the substructure has to offer enough versatility to accommodate and survive different types of loading.

1.3 Organization

Following this introduction, Section 2 starts with a general presentation of the performance of bridge systems in several hazards. In particular, damage to bridges observed during earthquake, blast, storm surge, and tsunami are covered. As part of the bi-hazard framework of analysis considered in this research, a summary of the design philosophies and methods of analysis for earthquake and blast loadings is presented. This section ends with considerations on the similarities and differences in the nature and the effects of blast and earthquake hazards on bridges in an attempt to establish when they will generate consistent actions or conflicting demands on a bridge system.

In Section 3, the potential of steel-concrete-steel (SCS) sections for multi-hazard applications is evaluated. A literature review on steel-concrete-steel "sandwich" construction and previous applications are reviewed, focusing on double skin composite panels (DSCP) and concrete filled double skinned tubes (CFDST). Emphasis is put on system description, previous analytical results, and experimental observations.

In Section 4, DSCP Wall pier and multi DSCP and CFDST column multi-hazard bridge pier prototypes are used in a design example. The conflicting and reinforcing design aspects of each prototype for earthquake and blast events are discussed. Each bridge pier prototype is then sized for a maximum credible earthquake and the most promising prototype, in this instance multi CFDST column pier, subsequently checked for credible blast threat.

Section 5 presents advanced finite element analysis of numerical models used to predict the multi-hazard performance of CFDST columns. First, models to replicate experimental behaviors of CFST, a structural concept parent to CFDST, both under cyclic and blast loading are analyzed using LS-DYNA and validated against previous tests. Then, using the same modeling techniques numerical models of CFDST are analyzed in the same environment to predict their behavior.

Section 6 describes cyclic pushover test performed on five quarter-scale CFDST column specimens built using the results of the analysis done for the selected prototype in Section 4.

In Section 7, design equations to predict the behavior of CFDST sections under static, quasi-static, and inelastic loadings are derived.

Two series of experiments, conducted at the Experimental Campus for Large Infrastructure Protection, Sustainability and Enhancement (ECLIPSE) and the Engineering Research and Development Center (ERDC) of the US Army Corps of Engineers on CFDST columns, are reported in Section 8. A total of 12 CFDST and 4 modified steel jacketed columns were subjected to near contact explosive loadings to simulate the effects of a Vehicle Borne Improvised Explosive Device (VBIED) on bridge piers.

In Section 9, theoretical methods to predict the behavior of CFDST column under blast loading are presented. Finally, a summary of research findings, as well as recommendations for future research, are presented in Section 10.

SECTION 2

VULNERABILITY OF BRIDGE STRUCTURE TO MULTIPLE HAZARDS

2.1 General

In this Section, considerations related to the vulnerability of bridges to multiple hazards and most specifically to blast and earthquake loading are discussed. Because the focus is predominantly on blast and earthquake loadings, a primer on philosophies and methods of analysis generally accepted for design against earthquake and blast loadings is presented. This is provided not only to provide context, so a reader with background in only one of the hazards may focus on the aspect of the discussion most relevant to his/her needs, but also to later help make the case for multi-hazard engineering of bridges. A reader familiar with both earthquake engineering and blast engineering principles can skip those sections altogether.

2.2 Vulnerability of Bridge Structure to Multiple Hazards

2.2.1 Vulnerability of Bridge Systems to Earthquake Ground Motion

Reviews of structural damage suffered by bridges in earthquakes can be found in Priestley et al., (1996), Chen and Duan, (1999) and the FHWA Seismic Retrofit Manual for Highway Structures: Part 1-Bridges (FHWA, 2006). When considering structural damage suffered by bridges in earthquakes, both the global structural damage level and the component structural damage level need be considered. At the global level, the effects of an earthquake on bridges vary with the types of bridges. For instance, a main concern in slab-on-girder bridges is that span may unseat

(Figure 2-1) if adequate support width is not provided to accommodate the possible seismic displacements and if a longitudinal restraint system is not in place. Also, from a system point of view, continuous span bridges have generally perform better in seismic events compared to bridges having multiple simply supported span, the reason being the former is more redundant and ductile.

At the component level, bridge girders have generally suffered moderate structural damage in past earthquakes. More significantly, structural damage in reinforced concrete pier columns has repeatedly been observed, often due to inadequate flexural strength and ductility, or brittle shear failures. For example six of the seven bridge structures that failed in the 1994 Northridge earthquake experienced shear failure due to inadequate transverse reinforcement and lack of seismic detailing. It is worth nothing that, while not a failure per se, spalling of cover concrete in reinforced concrete pier components has also been observed. Spalling is mostly evidence that concrete components have reached stress levels greater than the compressive strength of the concrete.

Other bridge components, such as cap-beams and cap-beam-to-column joints, have also suffered significant structural damage in past earthquakes due to lack of shear capacity under the combined actions of earthquake and gravity loads. Other mechanisms of structural damage to cap-beams include negative moment flexural failure due to premature termination of the cap-beam negative moment reinforcement, and insufficient anchorage of cap beam reinforcement into joint regions.

Few footings failures have been observed in past seismic events, likely because due to shear or flexural failure of the columns framing into them; also, rocking of the footings themselves may

have prevented excessive seismic demand to be placed on those elements. Structural damage to such components (specifically those that have not been capacity designed) may occur in the form of flexural or shear failures, if the connecting columns are able to transfer the seismic load to the footing without failing.

Figure 2-1: Example of Bridge Unseating (Priestley, et al., 1996)

2.2.2 Vulnerability of Bridge Structures to Blast Load

Bridge structural damage from blast load can result both from military actions and from non-military (malevolent or accidental) hazards, such as terrorist actions, vapor cloud explosions, or tanker explosions (following collisions or earthquakes). In all cases however, information on the observed or presumed effects of blast overpressures on bridges is scarce or confined in document

with restricted access. As a consequence, only selected aspects of bridge behavior under blast loading are discussed.

It is generally agreed upon that, when analyzing the effects of blast wave on bridges, two categories of factors need to be considered. On one hand, one must consider the type of bridge, its inherent redundancy, its ductility and its "permeability" to blast wave. The latter parameter is an expression of the capacity of bridge to allow the blast wave to "vent", limiting the risk of pressure built-up which may amplify the effects of the blast. On the other hand, its construction materials (reinforced concrete, steel or prestressed concrete) as well as the size of the charge and its location with respect to the targeted bridge (above or under the deck, in contact or with a stand-off with respect to a bridge component) and the components being loaded are other key determinants to consider.

2.2.2.1 Vulnerability by Types of Bridges

Based on the above-considered factors, it has been suggested that the components of suspension bridges, truss bridges with limited redundancy and cable stayed bridges are particularly vulnerable to contact explosion (Bulson, 2003), although they may have sufficient system redundancy in some cases to survive such component loses. In some cases, if the tower of a cable stayed bridge is successfully targeted, or if enough supporting cables are cut by a blast, partial or complete collapse of the structure may occur. For example, Figure 2-23 shows the collapse of a truss bridge on the Tigris River after the explosion of a Vehicle Borne Improvised Explosive Device (VBIED) over the deck.

For all type of bridges, the length of the span has also an effect on the expected structural damage. It is generally accepted that for span length greater than *60m* (*200ft*), almost 80% of the total loading on the span is due to the dead weight of the deck structure and the stiffening girders (Bulson, 2003). As the length of a span increases, the proportion of the capacity of the components used to support the dead load will also increase. Thus even modest structural damage to a key part of the structure of a long span bridge may jeopardize its capacity to support its own weight.

In the case of slab-on-girders bridges or viaducts, simple-span construction is generally more vulnerable than continuous-span bridges to blast load. Observations from World War II have revealed that in continuous girder bridges, some of the main girders can be severed without concomitant partial or total collapse of the entire structure. The reason is that there is generally enough allowance in design to cover redistribution of forces and moments dues to cuts under dead load conditions only. For blast structural damage to significant affect the load carrying capacity of a girder bridge, a significant number of beams need to be structural damaged.

2.2.2.2 Vulnerability due to Type of Construction Materials

Reinforced concrete components of bridges are generally prone to spalling and breaching even in the event of a moderate explosion. In comparison, steel components, specifically in plate girder bridges, structural damage is more likely in the form of lamellar tearing and distortion/removal of the integrity of web and flange elements when subjected to blast wave; in certain circumstances this can lead to shear failure and possible lateral buckling. For a prestressed

concrete component, when prestressed tendons are cut by an explosion, the total capacity of the component to carry service load could be halved (Bulson, 2003).

2.2.2.3 The Influence of Standoff

Both near contact explosion and explosion occurring with a certain standoff may cause similar level of structural damage to a bridge, depending on the combination of charge weight and standoff. Close range explosions of even modest charges may cause partial collapse of one or several spans of multi-span bridge, or even complete collapse of the bridge itself if enough key supporting elements are severed. For instance, spans or bridge collapse is almost unavoidable if a supporting pier is successfully targeted and brought down in the case of an explosion under the deck, as the bridge mays lose locally its capacity to carry gravity and traffic load.

For the case of small to moderate bombs (hand placed bomb for instance) placed in contact with the deck, the effects will be localized for over or under deck explosion and localized shear or membrane failure of the deck itself may follow. When a large explosion occurs beneath a bridge, the deck may be subjected to large uplift pressures, which may be amplified by a pressure build-up in confined regions between the girders and near the abutments. For slab sitting on steel girders, these uplift forces may cause the deck to separate from the girders in case the shear connectors are incapable of resisting the loads induced by the deck response (Winget, et al., 2005).

Preparation of explosive charges and their geometry also affect loads acting on bridge components as pressure distributions and magnitudes can be changed significantly by tamping – covering and packing – the charges with soil, placing them underwater, cutting holes for placing

them inside a structural member, or when they have an hemispherical shape (Ray et al., 2003; Winget et al., 2005)

2.2.3 Vulnerability of Bridge Structures to Storm Surge

A report on the performance of bridges after Hurricane Katrina (MCEER, 2008) provided important observations with respect to the performance of bridge structure under storm surge. Important structural damage to bridges was observed after hurricane Katrina. Most of the structural damage was concentrated in the superstructure. Water elevations that far exceeded those accounted for in design severely affected several bridge superstructures. Waves from the surge impacted the superstructures of several bridges, causing them to shift laterally. Figure 2-2 shows an example of this type of behavior. In this figure, the corners of the pier caps spalled as anchors attached to the girders pushed through the concrete cover.

Figure 2-2: Shifting of Bridge Superstructure After Hurricane Katrina (MCEER, 2008)

Evidence of longitudinal pounding between spans was also recorded, indicating that the surge waves may have loaded those bridges in multiple directions. Many bridges near the coast were submerged by the rising tide; for certain bridges, air was entrapped between the girders causing an uplift component due to buoyancy. The combination of buoyancy and lateral wave impact on the superstructure contributed in many instances to uplift followed by lateral translation of many unrestrained bridges spans, which failed off their support or were completely washed away or flipped over by the surge. This type of failure was widespread for simple span bridge over the area hit by the hurricane (Figure 2-3).

Failure of many prestressed bridge girders was observed. This failure was attributed to buoyant forces cancelling out the weight of the superstructure and thus of the girders, leading the unbalanced prestressed forces in the girder to crack the beam. Extreme deformation of the

girders once cracked also led to failure of the deck and in some instances of transverse diaphragm (Figure 2-4).

For bridges located further inland, the main cause of structural damage was floating debris, including an oil platform, shipping containers, buildings, appliances, logs, and jams made of intertwined smaller debris (Figure 2-5). Impact on both superstructure and substructure were observed.

Figure 2-3: Span Unseating for Simple Span Bridge (MCEER, 2008)

Figure 2-4: Failure of Prestressed Concrete Girder (Top) Accompanied by Diaphragm Failure (Bottom Left) and Deck Failure (Bottom Right) (MCEER, 2008)

Figure 2-5: Debris Lodged Against a Bridge Bent (MCEER, 2008)

2.2.4 Vulnerability of Bridge Structures to Tsunami

Many similarities exist in the way storm surge and tsunami wave loading interact with bridge structure, as described in the reports on structural damage to bridge structures produced by the Japan Bridge Engineering Center (J_BEC, 2011) and the joint American Society of Civil Engineers and Japanese Society of Civil Engineers survey (ASCE/JSCE, 2011) following the magnitude 9 Tohoku earthquake.

In many instances, wash away of superstructures was observed after the tsunami (Figure 2-8). In bridges fitted with seismic restrainers, failure of the superstructure was also accompanied by fracture of steel bracket restrainer as well as of energy dissipation components such as dampers (Figure 2-6 and Figure 2-7).

Figure 2-6: Deck and Brackets Failure (J_BEC, 2011)

Figure 2-7: Damper Failure (J_BEC, 2011)

Failure of truss bridge was not observed during hurricane Katrina, and it was thought that because truss are essentially open structure, pressure was relieved as water and wind loading was able to flow through the truss members. However, during the Tohoku tsunami, failure of a truss bridge fitted with restrainers was observed.

In rare instances, failure of substructure in the form of pier washing away was also observed. However, this could have been the result of a foundation failure due to scouring. In another mode of substructure damage due to tsunami pressure loading, Figure 2-9 shows crushing at the top of the intersection of a reinforced concrete column pier and its cap beam. It is estimated that the beam part of the pier was inclined toward the upstream side by the force of the tsunami acting on the bridge, and as a result, the upstream side of the pier column was crushed.

Figure 2-8: Washed Away Truss Bridge Span (J_BEC, 2011)

Figure 2-9: Crushing of Concrete at the Column to Cap Beam Connection (J_BEC, 2011)

2.3 Seismic Hazard

This section provides an overview of some trends in seismic resistant design of bridge structures. The information presented in this section will be used later for a comparative study of the effects of earthquake shaking and blasts on bridges.

2.3.1 General Methods of Analysis in Seismic Resistant Bridge Design

This section reviews some of the analysis methods generally used to evaluate the forces applied to a bridge system in an earthquake, and the prevailing philosophy and design methods in seismic resistant design. Readers familiar with earthquake engineering design principles may skip this section.

Seismic hazard assessment is generally the first step in the seismic design of any structure. The next is to evaluate the seismic demands that the maximum considered design earthquake can induce on the structure at the site. In determining seismic demands on bridges, several methods of analysis are available to the designer (see also Table 2-1):

1. Static or Quasi-static procedures use an equivalent static force procedure to distribute the earthquake load to the bridge components particularly when the seismic force distributions or likely modes of deformation of the bridge can be estimated. The estimation of the magnitude of the equivalent static force is determined using code compliant provisions or hazard assessment methods. The uniform load method and the single mode spectral analysis method described in AASHTO LRFD are examples of quasi-static procedures.

Table 2-1: Seismic Bridge Analysis Methods (Priestley, et al., 1996)

Load Simulation	Analysis Type[a]	Objective[b]		Comments
		Demand	Capacity	
Static ⟨S⟩	⟨L⟩	X		Linear elastic frame or finite-element analysis with equivalent lateral loads to determine member forces and equivalent displacements
	⟨N⟩	x	X	Pushover or nonlinear analysis to determine available deformation capacities, equivalent elastic member forces, or plastic deformation demands
	⟨L, P⟩	X		Linear elastic demand analysis for tall bridges or slender piers or members where deformations and axial loads can change member demands
	⟨N, P⟩	x	X	Nonlinear pushover or cyclic analysis for tall bridges or slender piers with reduced capacities reflecting P–Δ effects
Response spectrum ⟨R⟩	⟨L⟩	X		Seismic demand analysis based on maximum modal response and appropriate modal combination techniques; member demands reflecting inelastic structural response can be obtained from reduced or "nonlinear response spectra" but still based on linear modal analyses
Dynamic ⟨D⟩	⟨N⟩	X	X	Nonlinear time-history analysis to determine the complete seismic response with nonlinear member characteristics for specific earthquake records
	⟨N, P⟩	X	X	Nonlinear time-history analysis for tall bridges or bridges with slender members and piers, including P–Δ effects

[a] L, linear materials, N, nonlinear materials; P, P–Δ effects.
[b] X, primary tool; x, secondary tool.

2. Response Spectrum Analysis that determines maximum response quantities from the spectrum of a given ground motion or from smoothed design spectra. This method can be used for bridges that are expected to respond in the elastic range based on cracked or effective stiffness properties, for inelastic response assessment of bridge systems and for substitute structure analysis. It is worth nothing that non-linear behavior can only be estimated in that method by using reduced non-linear spectra.
3. Response History Analysis for a bridge provides a complete time history of various response quantities for a particular earthquake ground motion or sets of ground motion.

Three approaches are generally used to solve the dynamic problem: (1) step-by-step integration in the time domain (2) superposition of normalized modes in the time domain and (3) evaluation of frequency-dependent response contributions with transposition to the time-domain.

2.3.2 Seismic Resistant Design Philosophy and Methods

In the AASHTO LRFD Bridge Design Specification (AASHTO, 2010), seismic design of bridges is for a life safety performance objective considering a seismic hazard corresponding to a probability of exceedance of 7% in 75 years. This requirement is intended to achieve minimal structural damage to the bridge during moderate earthquake ground motions and to prevent collapse during rare and severe event. The current provisions do allow however design for higher performance levels.

Design for a life safety performance criterion implies that the bridge will not collapse, but that it can nonetheless suffer significant structural damage in the form of permanent offsets, cracking,

yielding of reinforcement, spalling of concrete, and extensive yielding and local buckling of steel columns. In all these cases important repairs will be necessary and significant disruption in service (including limited access to the bridge) might occur.

The basis for design in the Specification is a NEHRP-type elastic response spectrum (or a site-specific response spectrum if the bridge is considered critical or essential, if near fault effects could control the response of the bridge, or significant soil disruption could amplify the response of the bridge). The characteristic parameters of this spectrum are determined based on maps developed by the US Geological Survey (USGS) for AASHTO for the aforementioned probability of occurrence. An example of such a spectrum is given in Figure 2-10.

To incorporate soil effects, site factors magnify the ordinates of the spectrum developed to take into account any amplification of the ground motions that could result due to specific soil conditions at a site location. For a definition and characterization of site class, one can refer to the Seismic Provisions. The site modification factors for different types of soil are summarized in Table 2-2.

With a few exceptions, the preferred strategy is to limit inelastic deformation to the columns so that structural damage can be readily inspected and repaired after an earthquake. Capacity design procedures are then used to prevent structural damage from occurring in the rest of the structures, such as in the foundations and cap beams. Figure 2-11 summarizes the design approaches that can be adopted in order to achieve the required performance.

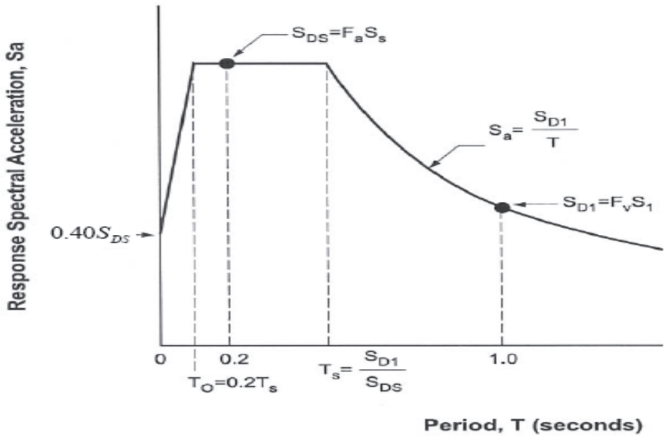

Figure 2-10: Design Spectrum for Bridge Analysis (AASHTO, 2010)

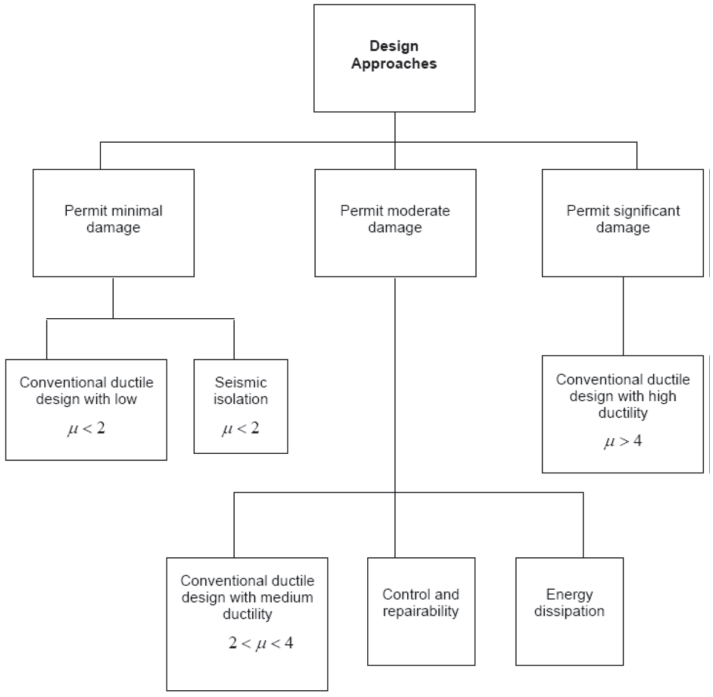

Figure 2-11: Seismic Design Approach (AASHTO, 2010)

Table 2-2: Values of F_a and F_v as a Function of Site Class and Mapped Short and 1 Second Period Spectral Acceleration Respectively

Site Class	Mapped Spectral Response Acceleration at Short Periods				
	$S_s \leq 0.25$ g	$S_s = 0.50$ g	$S_s = 0.75$ g	$S_s = 1.00$ g	$S_s \geq 1.25$ g
A	0.8	0.8	0.8	0.8	0.8
B	1.0	1.0	1.0	1.0	1.0
C	1.2	1.2	1.1	1.0	1.0
D	1.6	1.4	1.2	1.1	1.0
E	2.5	1.7	1.2	0.9	0.9
F	*a*	*a*	*a*	*a*	*a*

Table notes: Use straight line interpolation for intermediate values of S_s, where S_s is the spectral acceleration at 0.2 second obtained from the ground motion maps.

a Site-specific geotechnical investigation and dynamic site response analyses shall be performed (Article 3.4.3).

Site Class	Mapped Spectral Response Acceleration at 1 Second Periods				
	$S_1 \leq 0.1$ g	$S_1 = 0.2$ g	$S_1 = 0.3$ g	$S_1 = 0.4$ g	$S_1 \geq 0.5$ g
A	0.8	0.8	0.8	0.8	0.8
B	1.0	1.0	1.0	1.0	1.0
C	1.7	1.6	1.5	1.4	1.3
D	2.4	2.0	1.8	1.6	1.5
E	3.5	3.2	2.8	2.4	2.4
F	*a*	*a*	*a*	*a*	*a*

Table notes: Use straight line interpolation for intermediate values of S_1, where S_1 is the spectral acceleration at 1.0 second obtained from the ground motion maps.

a Site-specific geotechnical investigation and dynamic site response analyses shall be performed (Article 3.4.3).

2.3.3 The AASHTO Guide Specification for LRFD Seismic Bridge Design

The AASHTO Guide Specification for LRFD Seismic Bridge Design also uses design identical ground motion maps as the LRFD Specifications for a 1000-year return period and also has Life Safety as a basic performance goal. However other higher performance based design objectives linked to specific probability of occurrence of defined earthquake events are allowed as summarize in (Marsh, et al., 2001). Design categories reflect variations in seismic risk across the country and to specify different requirements for methods of analysis, minimum span support lengths, column design details, and foundation and abutment design procedures a in the Specifications. There are 4 Seismic Design Categories (SDC) to differentiate it from the LRFD Specifications although the partitioning is identical.

Permissible Earthquake Resisting System (ERS) and Earthquake Resisting Elements (ERE) are provided in the Guide. The designer chooses between the permissible systems, and elements within the complete load path for that system, as part of his global design strategy. Elastic methods of analysis are still permitted to calculate seismic displacement demands on most bridge structures. However, for bridges located in the highest seismic zone, and if the demands exceed the implicit capacity of the structural elements, a non- linear static analysis ("pushover" analysis) must be used to further define actual demands, and is required for the highest design category. The demand and capacity evaluations are not primarily based on forces on the ductile elements within the structure, but on their deformation, as such the methodology of the Guide is often termed as displacement based.

Figure 2-12 presents the main design categories and some of the salient design strategy for each category.

Table 2-3: Design Earthquakes and Seismic Performance Objectives (Marsh, et al., 2001)

Probability of Exceedance For Design Earthquake Ground Motions		Performance Level	
		Life Safety	Operational
Rare Earthquake (MCE) 3% in 75 years	Service	Significant Disruption	Immediate
	Damage	Significant	Minimal
Expected Earthquake 50% in 75 years	Service	Immediate	Immediate
	Damage	Minimal	Minimal to None

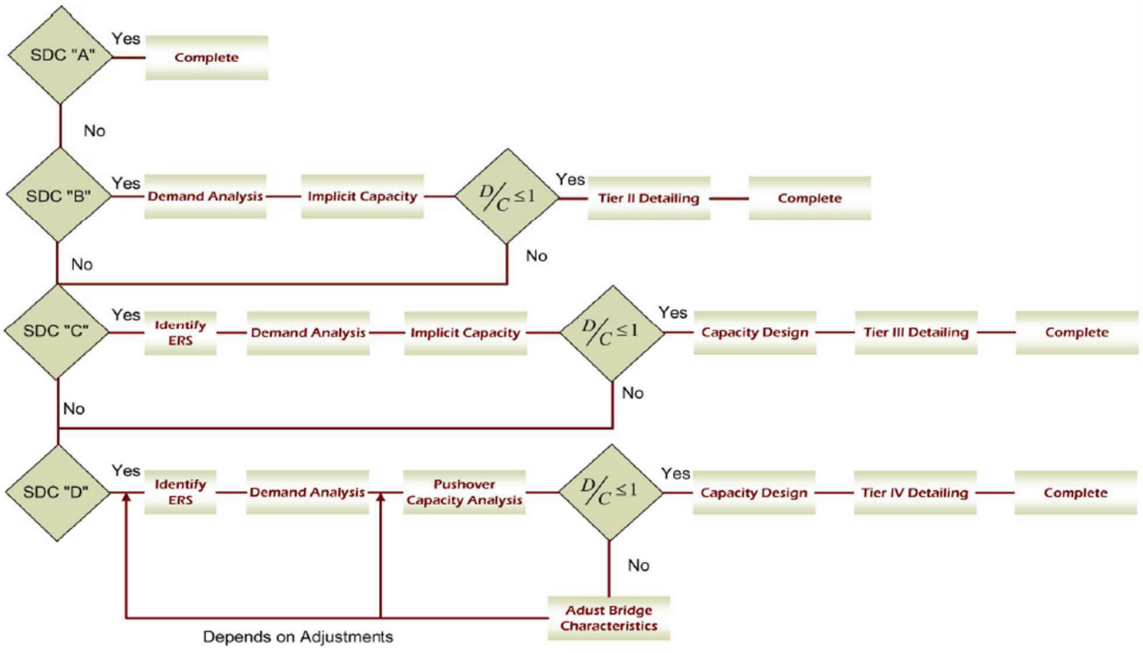

Figure 2-12: Seismic Design Category Core Flowchart (AASHTO, 2007)

2.4 Explosion Hazard

Extensive discussion of blast phenomenology can be found in several references including Baker et al. (1983), the Army Technical Manual TM 5-855-1 (USDA, 1986), the Tri-Service Manual TM 1300 (USDA, 1990), Smith and Hetherington (1994), Mays and Smith (1995), Cormie, et al., (2009), UFC 3-340-02 (DoD, 2008). The following section summarizes information contained in the literature about the blast phenomenon and its effects on bridges. Since the consideration of blast wave overpressures as a design load on bridges is a relatively recent concern in the public domain, this section also includes some insight on data from past military conflicts and declassified experiments so as to draw lessons for design. It also discusses briefly the different methods available to the designer to assess and evaluate the risk of a bridge being exposed to an explosion, presents concisely the different methods used to evaluate the loading due to a blast wave on a structure and discuss briefly the accompanying analysis and design techniques commonly adopted in blast-resistant design.

2.4.1 Nature and Description of the Phenomenon

When a bomb detonates or an explosion occurs in free air (*free airburst*), hot gases at pressure in excess of atmospheric pressure (so the appellation *overpressure*) are suddenly released. Those gases expand due to the heat and force the air in the surrounding space out of the volume it occupies. Almost instantly, a layer of compressed air referred to as the *blast* or *shock wave*, forms in front of those gases and propagates away from the source. The blast wave contains most of the energy released by the explosion. The sudden increase in pressure recorded generally decays from its initial peak value back to atmospheric in a few milliseconds. However, if the

blast wave impinges on a structure that can provide a relative degree of confinement of the wave, it can take several milliseconds more for the wave to clear and the pressure to settle back to atmospheric values.

At some point the gases expand and cool down and their pressure falls below atmospheric value. Because the mass of the moving gas molecules contributes to the momentum of the system and needs some time to come completely to rest, it ensues an over expansion of the gases and a reversal flow is observed toward the source due to the small differential pressure between the source and the wave front. The existence of this under pressure at the wave front gives rise to the so called *negative phase* of the blast by opposition to the phase marked with pressure in excess of the atmospheric pressure which is commonly termed the *positive phase* of the blast (Figure 2-13). However, the effects of the negative phase are negligible compared to the positive phase's and are generally discarded in practical applications.

If the blast wave interacts with a structure, the *incident or side-on overpressure* in the shock front rises almost instantaneously to a peak, as the wave is reflected by the target, before decaying quite rapidly back down to ambient pressure during the positive phase. The pressure measured at the shock front during this interaction is referred to as the *peak overpressure* and the time it takes for the shock to decay is termed the *duration* of the positive phase of the blast (Figure 2-13).

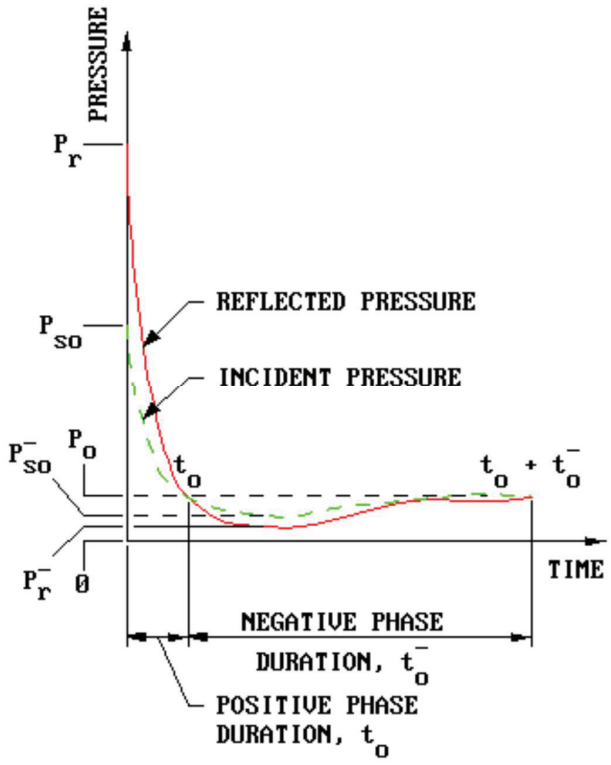

Figure 2-13: Pressure-Time Variation for a Free-Air Burst (DoD, 2008)

The general effects of a blast wave on structures vary with the type and size of structure as well as with the scale of the blast. For instance in the case of a large scale blast wave like that produced by a nuclear explosion, upon arrival of the wave, the target will be engulfed and crushed. In that case, the structure is loaded as a whole and the blast tends to move the target in the direction of the moving wave front. If the target is small relative to the blast wave, it will be submitted instantly to a more or less equal squashing *overpressure* and any resultant translatory pressure will only last for a short time.

If a structure is, otherwise, sizeable compared to the blast scale, the response of individual elements of the structure needs to be evaluated separately because they will likely be loaded in sequence and large reflection of the blast wave may occur. As explained by Mays and Smith, (1995) and Cormie, et al., (2009), when a blast wave is interacting with a solid surface denser than air, it will reflect from it and, depending on its geometry and size, diffract around it. As interaction between the target and the incident blast wave takes place, energy is transferred from the blast to the structure and reflection and amplification of the blast wave follows. This produces a region of further compression of the air in the vicinity of the target. On a molecular level, the surface applies an external force on each air molecule, which is sufficient to impart an equal momentum to each in the opposite direction. By Newton's third law, the air applies the same external force to the surface. This change in momentum of the air particles gives rise locally to increase of the pressure over the incident pressure that would occur at the same location. This pressure in excess of the incident is termed reflected pressure. As for the incident pressure, the reflected pressure will reach a peak, usually at the same time as the incident pressure; this is the *peak reflected pr*essure (p_r in Figure 2-13), which also decays with time. As for the incident pressure, the *peak reflected impulse* is a measure of the energy the reflected wave can deliver and is measured by the surface under the curve of the peak reflected pressure history. In studying the effect of blast loading on structures, it is generally agreed that the following parameters will control structural response (see Figure 2-13):

1. The *peak overpressure*, p_s (ps_o on Figure 2-13), which since Hopkinson (1915) and Cranz (1926) has been recognized to be inversely proportional to some power of the *scaled distance*

Z (ratio of the distance of the charge to the target, R, to the cubic root of the weight of the charge W):

$$Z = \frac{R}{W^{\frac{1}{3}}} \tag{2-1}$$

2. The *duration of the positive phase,* t_d (t_o on Figure 2-13), upon which the effects of the loading are dependent. The longer the exposure and the shorter the scale distance the greater the effects of the blast overpressure on the structure and vice versa.
3. The *impulse* (i_s) a measure of the kinetic energy delivered by the blast to the target structure. Specifically the impulse is the area under the pressure history curve (see Figure 2-13).
4. The *angle of incidence* (α) of the blast wave, which at any point of a target interacting with a blast wave can be measured by the angle formed by the normal at that point and the line that connect said point to the center of the charge.
5. The *peak reflected pressure* (respectively *reflected impulse*) measured at a point of a target loaded by blast loading. It is a function of the angle of incidence. The peak reflected pressure is maximal for an angle of incidence of 0 degree (point on the target facing directly the charge). In such case the reflected pressure can be as high as ten times the incident pressure (Figure 2-14). For an angle of incidence of 90 degrees, no reflection of the incident wave will occur. In the range of 0 up to 40 degrees, reflection of the incident pressure is generally termed normal. For value of the angle of incidence in excess of 40 degrees, the reflection process is complex, giving rise to the so-called Mach reflection process. In air, Mach

reflection is a complex process sometimes described as a "spurt"-type effects (Mays and Smith 2009, Smith and Hetherington, 1994). In this process, the incident wave "skims" off the reflecting surface rather than bouncing off of it as observed for lower values of the angle of incidence. As a result, the reflected wave catches up with the incident wave and fuses with it at some point above the reflecting surface to produce a third wave front called the *Mach stem* (Cormie, et al., 2009). The point at which the three waves coalesce is called the triple point. Behind the Mach stem and reflected waves is a *slip-stream* region where, although pressure is the same, different densities and particle velocities exist. The formation of a Mach stem is important when a conventional device detonates at some height above the ground or inside a structure where the angle of incidence can vary over a wide range. Figure 2-15 illustrates the concept of incident (side-on) pressure, regular reflection and Mach stem reflection.

In design, all the values discussed above are taken to be those of the positive phase of the blast. Corresponding values for the negative phase also exists for some of those parameters, but they are usually of no consequence in blast resistant design.

To put in perspective the different parameters covered in the previous paragraphs, a simple example is presented here. Using the first prediction method of blast load described in Section 2.4.4, it can be estimated that a car bomb containing 1000*lb* of TNT (treated as a spherical charge for convenience) would produce a peak dynamic overpressure and impulse of approximately 1000*psi* and 100 *psi-msec* at a distance of 10 *ft* (scaled distance of $1 ft/lb^{1/3}$) from the geometric center of the charge. At a distance of 100*ft* (scaled distance of $10 ft/lb^{1/3}$), those

peaks will have decayed to overpressure and impulse of approximately 10*psi* and 5*psi-msec* respectively.

However, if the blast wave is interacting with a structure, upon impingement on that structure the values can more than decuple due to reflection of the dynamic overpressure. This simple example shows that the extent of the effects of a blast event on a structure will vary both with the size and the standoff of the charge with respect to that structure. It also gives an idea of the type of overpressure that a blast event can impose on a civilian structure that often times is designed to withstand static pressure of about 1*psi* (Weidlinger, 1994).

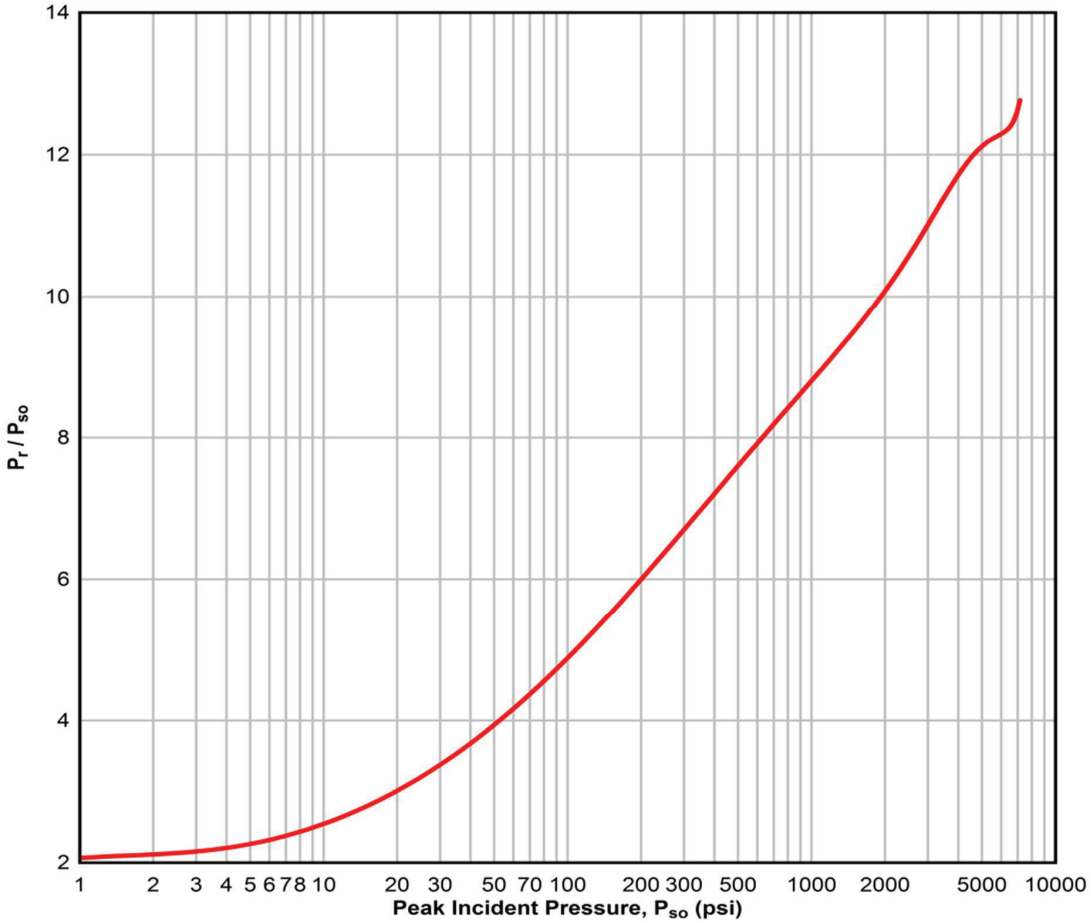

Figure 2-14: Peak Incident Pressure vs. Ratio of Normally Reflected Pressure / Incident Pressure for a Free Air Burst (UFC 3-340-02)

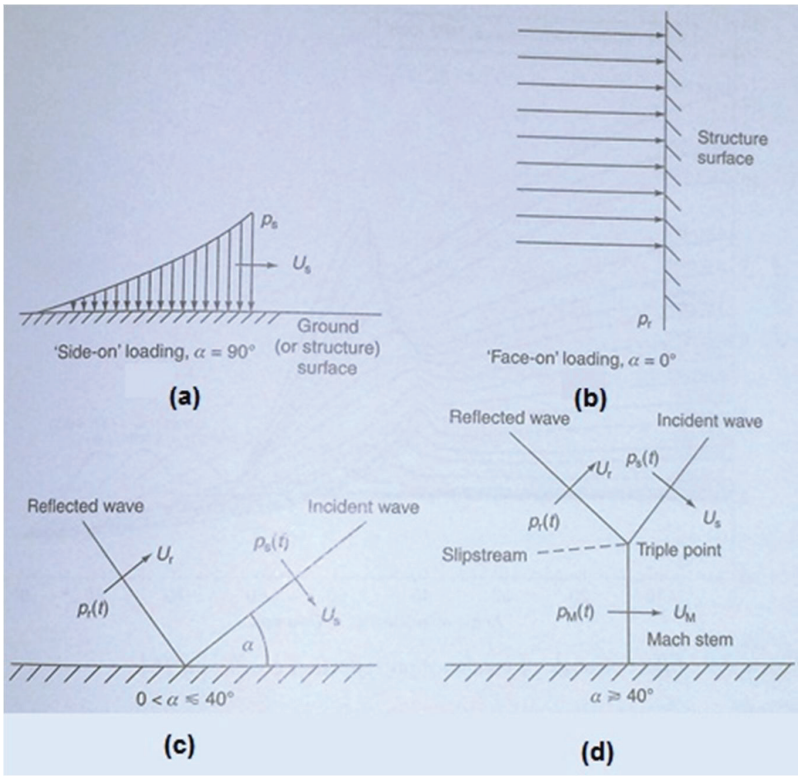

Figure 2-15: Side-on (a) and Face-on (b) Pressure Loading, Regular (c) and Mach Reflection (d) (Cormie et al., 2009)

2.4.2 Threat Assessment in Blast Engineering

As a first step in blast analysis, a threat analysis must be conducted, so a credible blast scenario can be decided on before the loading parameters discussed above can be calculated. This section reviews the commonly adopted practices in the area of blast hazard assessment.

All facilities face a certain level of risk associated with natural events, accidents, or intentional acts to cause harm. Regardless of the nature of the threats, facility owners have a responsibility to limit or manage risks and protect a facility or other asset to the extent possible (Smith, 2003).

However, in the specific realm of hazard resistant design, protection is not an absolute concept and there is a level of protection for which the cost of protection provided with respect to the cost of the potential loss is optimized (Mays and Smith, 1995; Krauthammer, 2008). Also, protection can never offer a complete guarantee of safety. Thus, it is paramount to think of the consequences of loss before deciding what level of protection should be provided. It is important as well to have in mind that some loss is incremental and acceptable, but certain losses, such as human life or critical facilities are not. Some risks will have to be accepted, while others must be deflected at all costs (Mays and Smith, 1995). For these reasons, a hazard assessment should be made to assess the type, the likelihood and the consequences of a given blast scenario.

The literature generally agrees on four (4) fundamental aspects of hazard assessment when dealing with terrorist attack: threat assessment, physical security assessment, vulnerability assessment and risk assessment.

Threat assessment considers a complete spectrum of threats, includes a wide variety of credible scenarios and quantifies the type and/or size of devices that might be used to carry out the attack. *Physical (information) security assessment* usually consists of an evaluation of the existing countermeasures. For bridges, it generally includes suggestions for upgrades to existing countermeasures, as required to meet a desired protection goal. *Vulnerability assessment* quantifies the potential impact from specific threat scenarios based on existing or planned conditions. *Risk assessment* integrates the results of a threat assessment, a physical and/or information security assessment, and a vulnerability assessment to evaluate the potential risks associated with each threat. The objective of risk assessment is to quantify the existing risks and to make recommendations to reduce high and/or moderate risks to the extent possible. For

planned facilities like bridges, a risk assessment can be used to help in the development of design criteria.

A comprehensive discussion of threat analysis in blast resistant design is available in Dusenberry (2010) and ASCE (1999). In the later, a threat determination methodology developed by the Protective Design Center of the US Army Corps of Engineers is reproduced in full extent.

All of the abovementioned assessment types in conjunction with the implementation of assessment recommendations help to provide risk mitigation. Risk mitigation involves reducing risks through lowering the potential impact of loss from a successful event and/or reducing vulnerability to an attack. But they also provide valuable information that can be transformed into design criteria. A good example of the global outcome of a terrorist attack assessment for bridge is offered by Winget, et al., (2005) and is reproduced in Table 2-6. This table includes information relative not only to the threat level to design for, but also to the level of structural damage that is acceptable with respect to the criticality of the bridge.

Table 2-4: Performance Based Standards for Bridges (Winget, et al., 2005)

Category 1 (Very Important Bridges) Concept: Each structural element is designed to withstand 2 separate cases, large loads with repairable damage and smaller loads with negligible damage.[1]

Design Loads – Case 1 (small loads):

"most-likely" threat scenarios using the following at worst possible locations for each structural element being designed:

- mid-size truck bomb [2]
- mid-size hand emplaced explosive scenarios
- mid-size static load for vehicle impact scenarios

Acceptable Damage – Case 1 (small loads):

local deck failure; support system still intact with negligible damage; truss / cables / piers *still capable of supporting design loads when considering structural redundancy*; no unrepairable foundation instabilities and no span loss;
steel girders < 5% max deflection to length ratio, reinforced concrete girders < 4%

Design Loads – Case 2 (large loads):

"most-likely" threat scenarios using the following at worst possible locations for each structural element being designed:

- large truck bomb
- large hand emplaced explosive scenarios
- large static load for vehicle impact scenarios

Acceptable Damage – Case 2 (large loads):

local deck failure; support system still intact with minor damage; *not capable of supporting design loads but easily repairable*; no unrepairable foundation instabilities and no span loss;
steel girders < 12% max deflection to length ratio, reinforced concrete girders < 8%

Category 2 (Important Bridges) Concept: Designed to withstand smaller loads with repairable damage.

Design Loads – Same as category 1, case 1
Acceptable Damage – Same as Category 1, Case 2

Category 3 (Slightly Important Bridges) Concept: Designed to withstand smaller loads with no more than one span loss.

Design Loads – Same as category 1, case 1
Acceptable Damage – no more than one span loss (no progressive collapse)

Category 4 (Insignificant Bridges)
No standard

Notes: 1. Design explosive loads for some Category 1 bridges may need to be increased based on a detailed threat assessment.
2. Exact design charge weights have been omitted for security reasons.

2.4.3 Prediction of Blast Load on Structures

Several equations have been proposed to estimate the blast wave parameters on structures. Discussion of such equations can be found in Smith and Hetherington (1994), Mays and Smith (1995) and Cormie, et al. (2009). These equations are generally based on the scaled distance Z defined earlier. As discussed before, the parameters usually of interest are the peak (static) overpressure (p_s), the dynamic pressure (q_s), the peak reflected pressure (p_r) and impulse (i_r) and the duration of the positive phase (t_d).

Equations to predict blast load parameters are available in the literature for explosion in air (free air burst). They are presented in Table 2-5 along with the source. For explosion that occurs near contact with the ground (surface burst), blast parameters prediction can be done by considering that the strength of the blast can be obtained from an equivalent free air burst coming from a charge 1.8 times bigger than the actual charge (Smith and Hetherington, 1994; Mays and Smith, 1995).

While the equations presented can be used to get an estimate of the blast wave front parameters, they are rarely used in design since they have either been represented on charts or designers prefer more robust methods of prediction that can take into account such parameters as the degree of venting provided by the structure being analyzed, the angle of incidence of the blast with respect to members being designed, and the level of structural damage expected. The following paragraphs discuss some of those methods and their relative merits.

Table 2-5: Blast Load Parameters Equations

Description	Equation	Authors
Peak Incident Overpressure	$p_s = \frac{6.7}{Z^3} + 1 \text{ bar} \quad (p_s > 10bar, \text{near field})$ (2-2)	(Brode, 1955)
	$p_s = \frac{0.975}{Z} + \frac{1.455}{Z^2} + \frac{5.85}{Z^3} - 0.019 \text{ bar}$ $(0.1 < p_s < 10bar, \text{medium to far field})$ (2-3)	
	$p_s = \frac{6784}{Z^3} + \frac{93}{Z^{\frac{3}{2}}} \text{ bar} \quad (\text{high explosive surface blast})$ (2-4)	(Newmark and Hansen, 1961)
	$p_s = \frac{1772}{Z^3} - \frac{114}{Z^2} + \frac{108}{Z} \text{ kPa} \quad (W \text{ in kg})$ (2-5)	(Mills, 1987)
Dynamic Overpressure	$q_s = \frac{5p_s^2}{2(p_s + p_o)} \quad (p_o \text{ is the atmospheric pressure})$ (2-6)	(Glasstone and Dolan, 1977)
Peak Reflected Pressure	$p_r = C_{r\alpha} p_s \quad \begin{pmatrix} C_{r\alpha} \text{ coefficient of reflection,} \\ \text{depends on angle of incidence } \alpha \end{pmatrix}$ (2-7)	(Glasstone and Dolan, 1977)
	$C_{r\alpha} = 2p_s \left(\frac{7p_o + 4p_s}{7p_o + p_s} \right) \text{ for } \alpha = 0^\circ$ (2-8)	
Duration of the positive phase	$t_d = \frac{3S}{U_s} \quad \begin{pmatrix} S\text{: The lesser of the dimensions of} \\ \text{the loaded structure.} \\ U_s\text{: Normal speed of the sound } 340 m/s \end{pmatrix}$ (2-9)	(Baker, et al., 1983)
Peak reflected impulse	$i_r = \frac{1}{2} p_r t_d$ (2-10)	(Baker, et al., 1983)

2.4.4 Prediction Methods and Accuracy

For the structural designer, the most important aspect of blast phenomenology is to be able to translate the complex pressure and impulse histories into loads that can be used for design and structural assessments. The state of the practice for prediction of blast load parameters is based on a deterministic approach where for a given blast scenario equations, charts or specialized software are used to estimate the blast wave parameters. This subsection reviews some of the methods available in blast resistant design for blast wave parameters prediction and their relative quality.

2.4.4.1 Simplified Methods

Simplified methods of prediction of airblast parameters have been developed in documents such as TM-1300, TM-5-855, UFC 3-340-02 or Baker and al. (1983). They generally permit to predict parameters such as peak overpressures and reflected pressures, peak impulses, time of arrival, and others. The evaluation of those parameters is based on curves and equations (such as the one presented in Section 2.4.3) developed for both spherical charges in the air and for hemispherical charges placed at ground level (e.g. Figure 2-16). Curves relating the reflected pressure and impulse to the incident pressure and angle of incidence are also available (Figure 2-17 and Figure 2-18).

Methods to evaluate blast load parameters have been automated in some prediction codes such as the Conventional Weapon Effects Predictions (CONWEP), which is of restricted access, and AT-Blast, which is available in the public domain. Those codes, as the charts, are based on empirical results and equations that have been developed for specific air blast environments. However,

actual structures are generally located in a loading environment that rarely corresponds exactly to these conditions. The accuracy of these methods of prediction diminishes accordingly and the limitations of their use must always be considered on a case by case basis (Ray, et al., 2003). For this reason they are considered low-resolution in terms of accuracy.

2.4.4.2 Advanced Methods

In more complex blast environments, more robust predictions methods are necessary. The empirically based methods mentioned above can give a feel of the magnitude of the blast parameters, but will likely largely underestimate the actual values of some of the parameters. This is the case for instance when the structure targeted contain several reflecting surfaces, in which the blast wave can be trapped and reflected to cause pressure buildups. This is the case for instance in the semi open environment like the underside of a bridge overpass, particularly near the abutment (Winget, et al., 2005). For such an environment, fully empirical methods are not suitable. Ray, et al. (2003) advanced that, in such a case, a semi-empirical model using ray-tracing scheme and nonlinear methods of wave propagation analysis is preferred. Such a method is implemented in a code like BlastX to calculate blast pressures at one point due to reflection off of adjacent surfaces. BlastX was developed to model airblast propagation through openings and inside of structures, but it is applicable in any environment (such as a bridge) where the blast environment should be carefully modeled to accurately predict the corresponding loading. Such considerations are included in companion software to BlastX: Bridge Explosive Loading (BEL) developed specifically to model the blast environment for bridges.

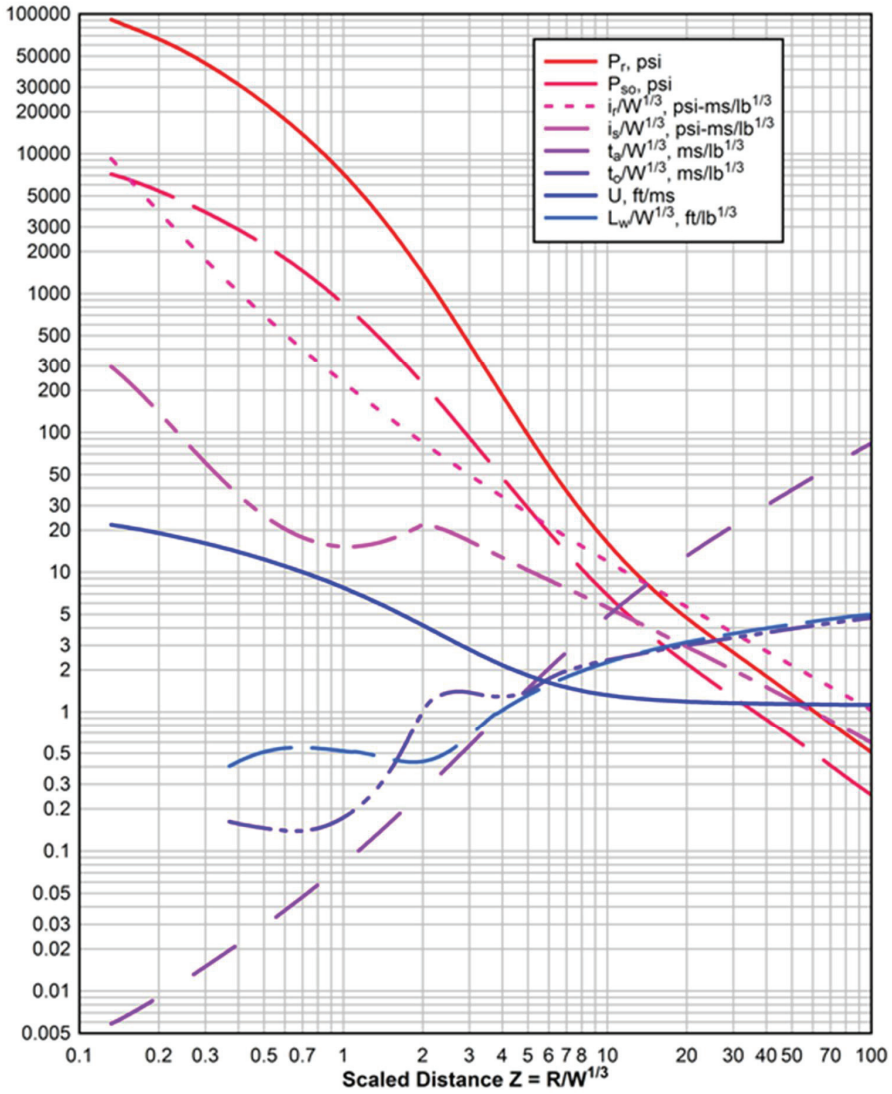

Figure 2-16: Positive Phase Shock Wave Parameters (DoD, 2008)

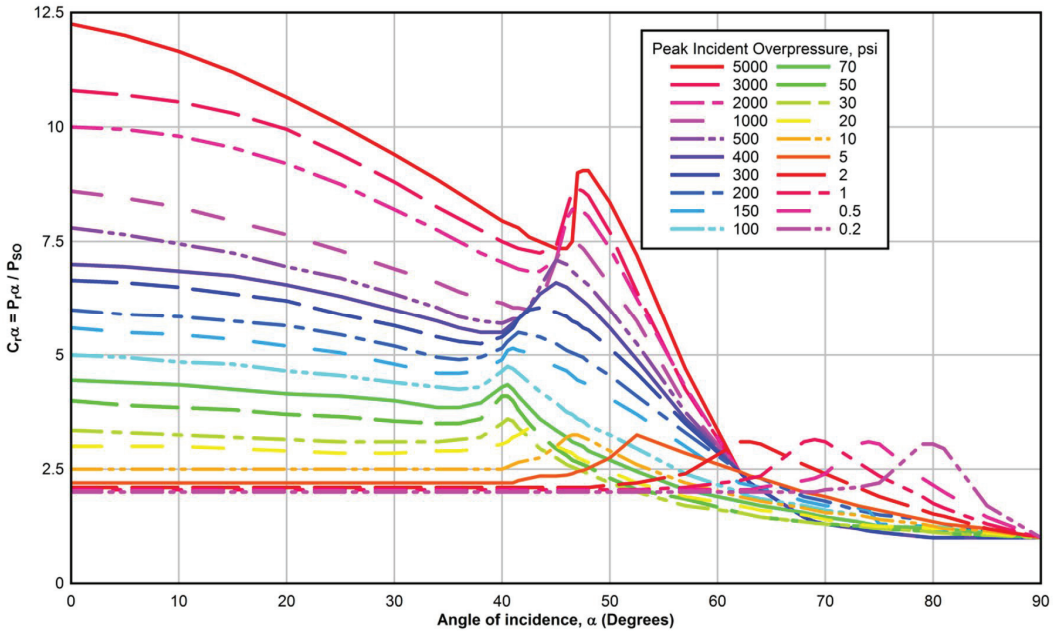

Figure 2-17: Reflected Pressure Coefficient Vs Angle of Incidence (DoD, 2008)

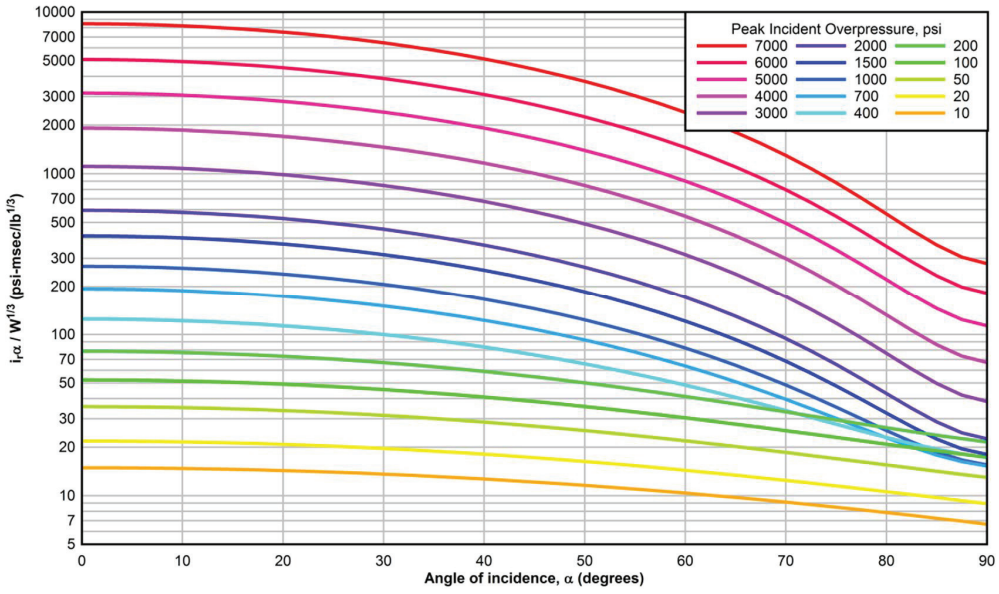

Figure 2-18: Reflected Scaled Impulse Vs Angle of Incidence (DoD, 2008)

2.4.4.3 Hydrocodes

As the blast environment is getting more complex (for instance in the case of a highway bridge located in an urban settings) higher accuracy is required. The trend nowadays is to use high-accuracy modeling tools such as hydrodynamic codes (hydrocodes in short) which are computer intensive. A hydrocode is an advanced computer program designed to perform modeling of complex, dynamic, continuum mechanics problems. In hydrocodes, a discretized mesh called a grid is used in two or three dimensions, to model the materials being evaluated. Either finite element or finite difference techniques are used, but most modern codes use finite difference modeling. Hydrocodes use equations of state (EOS) to model the hydrostatic response of materials and relate pressure, density, temperature, and internal energy of the materials.

Many different hydrocodes currently exist (e.g. AUTODYN, AIR3D, LS-DYNA), with their only common feature being the use of explicit time integration for temporal discretization. Unlike an implicit solution, explicit time integration does not require the formulation of a global stiffness matrix for each material in the model. Neither does it require the evaluation of equations of motion at the elemental or nodal level. This method is only conditionally stable, and a small time step is typically required. However, for events that occur over short periods of time, such as explosions or high-velocity impact, the small time step is an advantage.

2.4.5 Comparison of Methods for Highway Bridges

A comparative study of the different prediction methods was conducted by Ray et al. (2002) on a bridge overpass subjected to wave loads coming from an explosion below deck of a medium-size truck full of explosive. This study established that CONWEP generally overestimates the peak

reflected overpressure while underestimating the peak reflected impulse when compared to BlastX. Since the load in CONWEP was modeled as a hemispherical charge in contact above the ground, the overestimation of the pressure was somewhat expected. Estimations by CONWEP were considered unconservative since it does not take into account the multiple reflective surfaces under the bridge as BlastX does (Figure 2-19).

Comparison of BlastX with the more robust hydrocode Second Order Hydrodynamic Automatic Mesh Refinement Code (SHARMC) was undertaken. SHARMC is based on an advanced finite difference model that has been extensively refined to calculate airblast (Ray, et al., 2003). Compared to BlastX, SHAMRC predicted lower impulses and higher pressures in the vicinity of the bombs, but the reverse farther away (Figure 2-20). Ray et. al, who also analyzed the effects of clearing and charge geometry on the blast wave parameters, have concluded that clearing effects may be ignored if only a general understanding of the problem is desired and a conservative vulnerability assessment of the bridge is to be undertaken. They also concluded that for the case of the truck bomb, modelling the charge using a cylindrical element would likely produce more accurate results than the more general approach of modeling the charge as spherical. Finally, since none of the other less accurate methods could predict consistently conservative blast parameters, Ray et. al suggested that comparative studies be performed to determine the most economical and applicable methods of prediction of blast loading for a particular problem and confidently assess the design parameters.

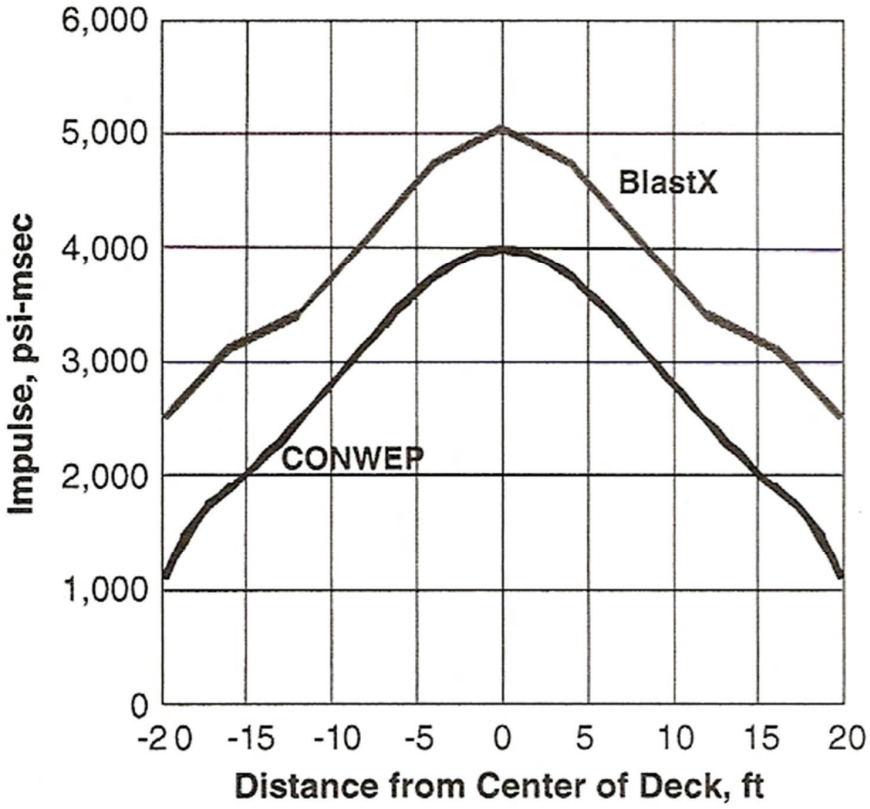

Figure 2-19: Comparison of Impulse Predicted by CONWEP and BlastX Across a 46 ft wide Bridge for Truck Bomb Located under the Deck (Ray, et al., 2003)

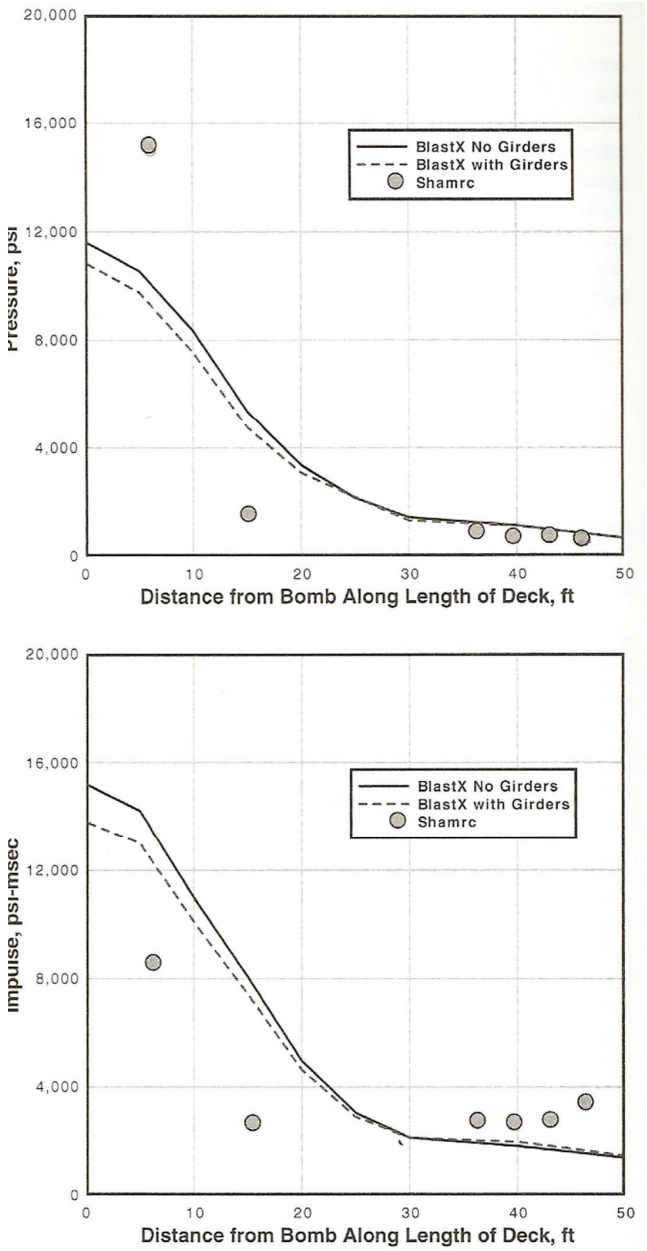

Figure 2-20: Comparison of Pressure and Impulse Predicted by BlastX and SHAMRC along the Length of the Bridge for Truck Bomb Located under the Deck (Ray, et al., 2003)

2.4.6 Blast Resistant Design Philosophy and Methods

The philosophy in blast resistant design is to guarantee life safety. As in seismic design, a level of risk must be accepted. For bridges, this means that damage is accepted for a credible blast scenario, but collapse must be avoided. Many of the analysis tools used in seismic design are also valid for blast resistant design. Since they have been discussed previously they are not repeated here. Instead a comparison of those different tools, as applied to blast analysis taken from Winget, et al. (2005), is reproduced in Table 2-6. Also the concepts of SDOF and pressure impulse, which are important in blast resistant design and assessment, are discussed here.

2.4.6.1 The Single Degree of Freedom Concept

Complexities in analyzing the dynamic response of blast-loaded structures involve the effect of high strain rates, non-linear inelastic material behavior and uncertainties of blast load calculations. Therefore, for simplified analysis, a number of assumptions related to the response of structures under blast loads are commonly made. For this purpose, a structure under blast loading is often idealized as a single degree of freedom (SDOF) elasto-plastic system and response analysis is assumed to depend on the positive duration of the blast load relative to the natural period of vibration of the structure. This leads to blast load idealization and simplifies the classification of the blast loading regimes.

Table 2-6: Comparison of Analysis Methods Used in Blast Resistant Design (Winget, et al., 2005)

	Uncoupled analysis	Coupled analysis	Static analysis/ equivalent static analysis	Dynamic analysis	SDOF analysis	MDOF analysis (including FEM)
Advantages	Much simpler to perform	Accounts for coupled effects of structural response with fluid dynamicsbehavior of an explosion load, considering time and spatial coupling	Simplified analysis procedures	Increased accuracy because it accounts for inertial effects, which can contribute significantly to stresses and strains	Reasonable accuracy for simple structures because fundamental mode dominates displacement response	Increased accuracy for more complex components because it accounts for higher-order modes or response
	Provides reasonably accurate, conservative predictions	Provides better predictions of ultimate behavior			Simplified calculations	
Disadvantages	Overestimates blast loads because it does not account for members yielding and failing	Complex models may require extensive computational resources	Inaccurate results in most cases because it only accounts for one deformation mode and does not include inertial effects	More difficult to perform analysis	Difficult to correctly model a complex structure	Difficult to perform without a computer, complex models may require several hours of computational time
		Programs often lack user-friendliness due to large number of input parameters, experience necessary to create an accurate model accounting for the correct failure modes, and difficulty in interpreting results	Difficult to conservatively determine static design load because magnitudes and locations of blast can vary, producing significantly different responses	As more modes are added beyond a certain limit, accuracy improvements will be insignificant while analysis time increases	Estimates may be very conservative, depending on geometry and contribution from higher modes	

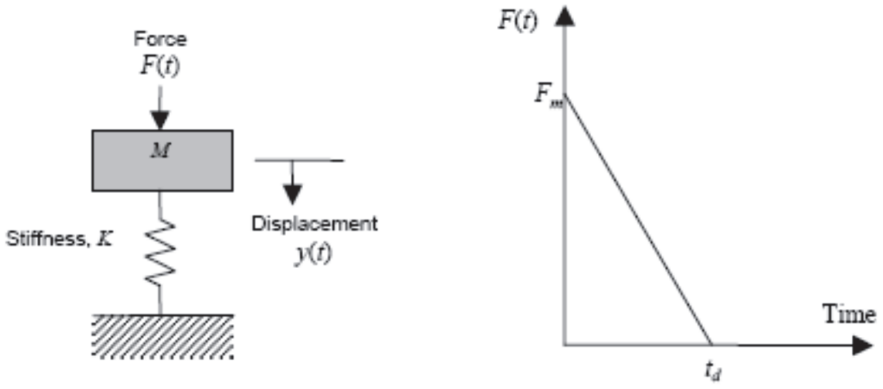

Figure 2-21: SDOF System Representation and Blast Loading Idealization

Smith and Hetherington (1994) and Mays and Smith (1995), among many, provide a good description of the method. It appears that the SDOF approach provide the simplest discretization for the transient problem. This approach replaces the actual structure by an equivalent system of one concentrated mass and one weightless spring representing the resistance of the structure against deformation. In such an equivalent system, the structural mass, M, is under the effect of an external force, $F(t)$, and the structural resistance, R, is expressed in terms of the vertical displacement, y, and the spring constant, K. The blast load is idealized as a triangular pulse having a peak force F_m and positive phase duration t_d (see Figure 2-21). The forcing function is given as:

$$F(t) = F_m\left(1 - \frac{1}{t_d}\right) \tag{2-11}$$

The blast impulse is approximated as the area under the force-time curve, and is given by

$$i = \frac{1}{2} F_m t_d \tag{2-12}$$

For the real structure, the equation of motion of the un-damped elastic SDOF system for a time ranging from 0 to the positive phase duration, t_d, is given by (Biggs, 1964) as:

$$M\ddot{x} + Kx = F(t) \tag{2-13}$$

For the equivalent system, using the subscript e to represent the equivalent system, the equation of motion can be written as:

$$M_e\ddot{x} + K_e x = F_e(t) \tag{2-14}$$

The introduction of the load factor, K_L, the mass factor, K_M, and the load mass factor K_{LM}, allow a simplification of the problem to:

$$K_{LM} M\ddot{x} + Kx = F_m(1 - t_d) \tag{2-15}$$

$$K_{LM} = \frac{K_M}{K_L} \tag{2-16}$$

$$K_M = \frac{M_e}{M} \tag{2-17}$$

$$K_L = \frac{K_e}{K} \tag{2-18}$$

Those factors are generally computed based on consideration of conservation of energy and are readily available in the literature for various types of boundary conditions. The method proceeds from there by assuming an equivalent resistance function, $R_e(y)$, which conserves the internal energy dissipation capacity of the actual structure. Assuming that the impulse delivered by the

blast load is entirely transformed into strain energy, the maximum deformation, X_M, of the system can be computed in terms of the equivalent maximum elastic deflection of the equivalent system, X_E, and the mass and the maximum internal resistance, r_u, of the actual structure as:

$$X_m = \frac{1}{2}\left(\frac{i^2}{K_{LM} M r_u} + X_E \right) \tag{2-19}$$

Furthermore, strain rate effect is integrated in the design of the structure on the resistance side by an increase of the strength of the materials through a dynamic increase factor. The value obtained for the maximum displacement is then compared against prescriptive requirements in order to ensure that the performance of the actual system is satisfactory.

2.4.6.2 Structural damage Analysis in Blast Resistant Design: Pressure-Impulse Diagram

A simple way to mathematically relate a specific structural damage level to a combination of blast pressures and impulses imposed on a particular structural element is the pressure-impulse diagram or iso-damage diagram. The bounds on the response of the target structure are characterized by a pressure (force) and a total impulse or a specific impulse. For a structure represented by a SDOF of mass M with a displacement capacity $x_{\max}$ and equivalent stiffness K_{eq}, subjected to a blast overpressure of duration t_d giving rise to a resulting force F and a resulting impulse I, the bound on pressure-induced structural damage is given by Equation (2-20):

$$\frac{2F}{Kx_{\max}}\left[\propto \frac{\text{maximum load}}{\text{maximum resistance}}\right]=1 \tag{2-20}$$

In the brackets, $\propto$ is the sign of proportionality.

On the other hand, the bound on impulse-induced structural damage is determined from Equation (2-21) :

$$\frac{Ft_d}{Kx_{\max}}\sqrt{K_{eq}M}=\frac{2I}{\left(x_{\max}\sqrt{K_{eq}M}\right)} \tag{2-21}$$

By plotting Equation (2-21) against (2-20), a non-dimensionalized pressure-impulse diagram (Figure 2-22) is formed. Such diagram can be used to assess response to a specified load. Once a maximum displacement or structural damage level is defined, this curve then indicates the combinations of loads and impulse that will cause failure. Combinations of pressure and impulse that fall to the left of and below the curve will not induce failure, while those to right and above the graph will produce structural damage in excess of the allowable limit defined by the maximum deformation, $x_{\max}$.

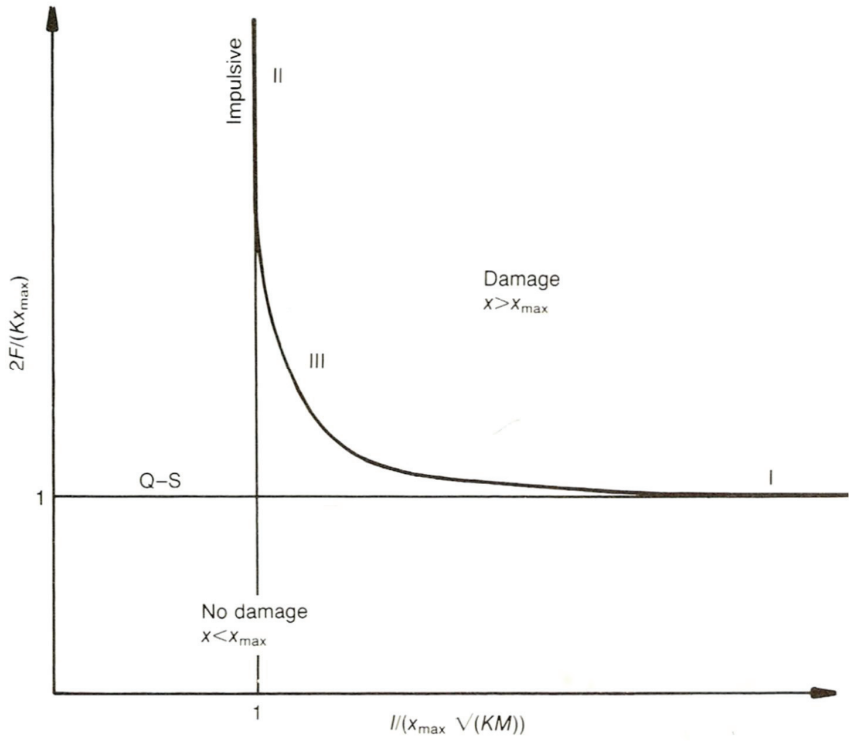

Figure 2-22: Non Dimensionalized Pressure-Impulse Diagram for SDOF Elastic System (Mays and Smith, 1995)

2.5 Seismic and Hazard Events: A Tentative Comparison

It is possible to establish similarities and differences between blast and earthquake events in terms of the salient characteristics of both hazards that are of interest in engineering application as well as of more design oriented features. Aspects like the structural damage potential of each of the hazards under study, the way in which they impose load on structures, assessment methods, and the prevalent design methods may be considered. Instances when the demands generated on structures by those hazards can be in conflict with each other, and the implications

of some seismic retrofitting schemes in the perspective of blast resistance, are also reviewed. The essence of the foregoing discussion is summarized in Table 2-7.

Both earthquake and blast release high amounts of energy. However the energy release during an earthquake is distributed over a wide area while damaging blast effects are confined to the vicinity of the explosion. Though some terrorists will be likely attracted to signature structures, a terrorist attack using exploding devices can happen anywhere, i.e. the threat posed by blast event resulting from a terrorist attack is arguably location independent. For earthquake, the zones at risk around the country are more or less well defined and more likely in specific states (e.g. California, Alaska, and Hawaii) than others.

In term of assessment, occurrence of an earthquake event is unpredictable. However, when significant information exists on the seismicity of the location where a structure is being built appropriate mitigation measures can be taken. Blasts are also highly (or in some cases) completely unpredictable, because terrorist attacks happen without warning. However, mitigation or deterrence techniques can be used to reduce the likelihood of an attack.

Epicentral distance and near source and far field considerations impact the effects of earthquake on structures along with directivity effects and source size. Structures located closer to the epicenter or particularly in the near fault zone will generally experience greater intensity of shaking. Structures located in the direction in which the earthquake waves propagate will also see a greater intensity of ground motion and will need to be designed for higher demands than another one located farther away. Furthermore, the greater the length of the fault ruptured in an earthquake event, the greater the influence it will have on structure. The same prevails for blast events as structures located near the explosion or on the path of the moving blast shock will

likely see a higher load than another one, say, located in the far field or shielded by another building. Its impacts will be more catastrophic as the bomb size increases.

Table 2-7: Similarities and Differences between Earthquakes and Blast Events

	Earthquake Event	Blast Event
Energy Release	Widespread energy release	Localized energy release
Geographic Dependence	Location-dependent	Location-independent
Site-to-Source Importance	Stronger shaking in the near fault region (or near the epicenter) Effects amplify with the fault ruptured size	Small standoff induces higher structural damage Structural damage increases with bomb size
Assessment	Predictable only probabilistically	Unpredictable
Structural damage Potential	Up to collapse	Up to collapse
Loading	Duration in seconds Vibration-type loading Load structures via ground acceleration	Duration in milliseconds Impulsive-type High overpressures applied to target structures

While both earthquakes and blast induce impulsive type of loadings on structures, some important differences remain. An earthquake can be seen as a succession of periodic pulses while a blast event will be generally characterized by a single cycle of loading. While a structure of a given period may be designed for the greatest intensity of shaking that will cause it to enter into resonance, in blast resistant design a structure components are generally designed for the impulse (area under the pressure history curve) that it will see.

While blast and seismic events are very different (beyond the fact they both release a significant amount of energy) they can have nonetheless similar effects on structures. From that similarity,

the objective of an integrated multi-hazard design for those two hazards should be to satisfactorily devise structures that can globally, or in carefully selected components, dissipate large amount of energy without collapsing or causing widespread casualties, and ideally avoiding high cost of repair or replacement for their owners.

While several design concepts and retrofitting schemes are available to help designer achieve this goal for each hazard alone (e. g. capacity design, performance based design, seismic isolation or structural hardening to name a few), there is still however some complication when considering structures that in their lifespan may be subjected to the actions of two or more hazards. The effects of each hazard alone on structures can be indeed significantly different. Thus, some design or retrofitting strategies that can reasonably be used either to design or retrofit bridges to perform well say in a seismic event can give rise to adverse effects in case of blast loading as the two events can impose conflicting demands on components and on the structure as a whole.

Relationship to system mass illustrates well the potential for conflicting demand in seismic and blast-resistant; given that seismic forces are proportional to mass, the more massive, a structure is, the higher the demand that an earthquake will impose on it. So the ideal seismic resistant structure will have as small a mass as possible and be as ductile as required to withstand safely the effects of an earthquake. However, when dealing with blast loading it is generally accepted that a more massive structure will perform better as it takes a bigger blast overpressure to move a larger mass.

Another example of conflicting demands can be found in seismic retrofitting of reinforced concrete column. One common method to increase column shear capacity and ductility in

seismic application is to use a steel jacket that is wrapped around the column to be retrofitted (Chai, et al., 1991). Steel jacketed columns, while most ductile for earthquake forces have been shown to fail in direct shear when exposed to credible blast scenario (Fujikura and Bruneau, 2008). Some insight on the expected performance of various seismically bridge components in a blast event can be found in Table 2-8.

Looking at different aspects of bridge behavior, the general seismic design approach sometimes considers the bridge superstructure as a diaphragm that transmits the lateral earthquake load to the earthquake resisting system (ERS). The ERS consist generally of the piers. Lateral bracings between the superstructure girders facilitate this behavior. In this approach the superstructure is only designed for gravity and traffic loads and is seldom checked for compliance with diaphragm behavior. By comparison blast overpressure can create significant localized loading in the out of plane direction of deck, girder web and flange, and lateral bracings. Overpressure from blast may also create loading that acts opposite the direction of gravity and traffic loading (antigravity loading).

To capture some of the complexity of the problems evoked in this section, Table 2-9 contrast the vulnerabilities of bridge components subjected to seismic and blast loadings. Repairability and cost considerations are also included in these tables on a qualitative basis.

Table 2-8: Reinforcing and Conflicting Design Aspects of Seismic Retrofit of Bridges with Blast Load Demands

Structural Components	Seismic Performance Objectives	Retrofit Options	Discussion Issues
Substructure			
Column	Supplement strengths and /or ductility in critical regions or in regions of insufficient rebar development.	Steel Jacketing over height	• Steel jacketing increases stiffness but creates plans of direct shear weaknesses at end of steel jacket at cap beam and foundation.
		Concrete Jacketing	• Improves overall shear and flexure resistance and ductility, but may also require retrofit of footing and cap beam. Direct shear may still be an issue in blast event.
		Composite Material Jacket	• Provide continuous confinement and higher strength than other options, however might still create plan of weaknesses in direct shear or may require cap beam and foundation retrofit
		Lap Splice Retrofit (Plastic Hinge Retrofit- Partial Jacketing)	• Move plan of weaknesses toward the center of the columns
Column	Increase stiffness of tall multicolumn bent	Link Beam	• Extremities of link beam can be designed to hinge and dissipate more energy • Higher mode effects can cause soft story mode of inelastic response otherwise
Cap Beams with monolithic connections	Reduce demands on cap beam	Non Hinging Link Beam	• Columns should be designed to hinge and form mechanism in seismic event, however in both blast and seismic event soft story mechanism can form due to higher mode effects
Cap Beam-Column Joint Regions	Enhance Strength	Prestress tendons	• Both positive and negative prestressing tendon s should be used to account for under the deck explosion • May be helpful against direct shear failure of cap beam
Superstructure			
Movement Joint	Restrain displacement and transfer longitudinal seismic force between frames	Seismic Restrainers	• Provide superstructure continuity which may be beneficial in under the deck explosion which places flexural demand on the superstructure
		Seat Extenders	• No benefit in blast event where a pier is destroyed
Superstructure	Increase Strength near Supports of Integral Superstructure	External Prestressing	• Increase Flexural and Shear Strength at critical sections. This increase the continuity and the local redundancy of the superstructure which may help in resisting explosion that occurs above or below the deck

Table 2-9: Failure Mechanisms and Repairability of Highway Bridge Components under Earthquake and Blast Loads

		Typical Earthquake Damage	Repairability/Cost	Blast Loads (Charge/ Description/Approximate Peak Overpressure)			Repairability/Cost
Structural Components	**Structural Elements**			• 100 lb • Package Bomb • 10000 psi	• 400 lb • Small Car • 20000 psi	• 4000 lb • Truck • 50000 psi	
Superstructure	Deck[1]	• Unseating due to unrestrained movement at expansion joints	• Very difficult to repair • Span reconstruction may be needed • Cost may be high	• Significant spalling and breaching • Punching shear failure • Significant cracks	• Localized failure • Localized separation from the girders • Significant cracks • Flexural failure	• Span failure • Shear failure • membrane failure	• Highly difficult to repair in large scale blast event (bridge reconstruction)
				• Moderate spalling and breaching • Some cracks	• Shear connectors failure/ • Localized separation from the deck • Wide negative flexural cracks	• Span failure/ uplifting • Deck separation from the girders • Shear failure • membrane failure	• Very high cost in large scale blast event
	Steel Girders Continuous Span	• Lateral torsional buckling • Diaphragm failure	• Difficult to repair (heat straightening may be needed) • Moderate cost	• Flexural failure with respect to the weak direction/ • Flexural buckling/ splice failure/ • Shear failure	• Flexural failure with respect to the weak direction • Flexural buckling • Excessive plastic hinging • Shear failure	• Flexural failure with respect to the weak direction • Flexural buckling • Shear failure • Projectile penetration • Local buckling • Splice failure • Membrane failure	• Repair cost and difficulty increases with blast event
	Steel Girders Simple Span	• Lateral torsional buckling • Diaphragm failure	• Difficult to repair (heat straightening may be needed) • Moderate cost	• Flexural failure with respect to the weak direction • Flexural buckling • Splice failure • Shear failure	• Same as above	• Same as above	• Repair cost and difficulty increases with blast event
	Concrete Diaphragms	• Shear failure	• Difficult to repair • High cost	• Moderate spalling and breaching • Some cracks	• Out of plane flexural and shear failure	• Out of plane flexural and shear failure • Direct shear failure	• Difficult to repair • High cost
	Steel Braces	• Axial buckling	• Easy to repair (brace replacement may be needed) • Low cost	• Flexural failure	• Flexural and shear failure	• Flexural and shear failure • Direct shear failure	• Easy to repair • Low cost

Connections	Fixed	• Joint shear failure	• Very difficult to repair (difficult to access) • High cost	• Shear failure	• Joint failures	• Joint failure	• Very difficult to repair (difficult to access) • High cost
	Bearings	• Overturning/fracture	• May be difficult to repair (if long span need to be lifted up to replace bearing) • High cost	• Tension failure (uplifting)	• Tension failure (uplifting) • Crushing (on deck impact after uplifting)	• Overturning/ • Tension failure • Crushing(on deck impact after uplifting)	• May be difficult to repair (if long span need to be lifted up) • High cost
	Seismic Bearings	• Overturning/fracture	• May be difficult to repair (if long span need to be lifted up) • High cost	• Tension failure (tearing of rubber laminates)	• Tension failure (tearing of rubber laminates) • Crushing (on deck impact after uplifting)	• Tension failure (tearing of rubber laminates) • Crushing (on deck impact after uplifting)	• Difficult to repair (an entire span might need to be lifted up) • High cost
Substructure	Cap Beam	• Shear failure • Insufficient ductility • Negative flexural failure	• Difficult to repair • High cost	• Damage should be minimal because of standoff	• Flexural failure (negative flexure)	• Direct shear failure at beam to column connection • Flexural failure (negative flexure)	• Repair cost and difficulty increases with blast event
	Wall Pier	• Shear failure • Flexural failure • Insufficient ductility	• Difficult to repair (pier replacement) • Very high cost	• Moderate spalling and breaching • Localized cracks in the vicinity of the bombs/flexural failure	• Localized failure • Large widespread cracks • Flexural failure	• Brisance/ direct shear/crushing/ • Shear failure • Breaching/spalling/scabbing/crushing/ • Membrane failure	• Difficult to repair (replacement) • Very high cost
	Multiple Columns Bent	• Flexural strength • Failures due to inadequate detailing • Shear failure	• Difficult to repair • High cost	• Shear failure/ • Direct shear failure	• Shear failure • Direct shear failure	• Shear failure/ • Direct shear failure • Brisance	• Repair cost and difficulty increases with blast event
	Single Column Pier	• Flexural strength • Failures due to lack of ductility/ inadequate detailing • Shear failure	• Difficult to repair (span replacement) • High cost	• Shear failure/ • Direct shear failure • P-delta failure	• Shear failure/ • Direct shear failure • Complete bridge collapse	• Shear failure/ • Direct shear failure • Brisance • Complete bridge collapse	• Span replacement is likely due to excessive • Very high cost
	CFST	• Buckling of steel shell (large D/t ratio)	• Damaged component may need replacement • Moderate cost		• Excessive rotation at base of column	• Flexural failure / • Shear failure/ • Direct shear failure	• Repair cost and difficulty increases with blast event
Foundation		• Flexural failure • Shear failure	• Very difficult to repair • Very high cost		• Cratering and breaching/ • Failure similar to scouring • Punching shear • Tension failure	• Cratering and breaching • Failure similar to scouring • Punching shear • Tension failure	• Very difficult to repair (difficult to access) • Very high cost

[1]For blast load two scenarios were considered: a contact explosion (1st row) and an under deck explosion (2nd row)

2.6 The Need for Multi-hazard Engineering

The intent of terrorist organizations to attack government and civilian infrastructures have prompted many owners, including state and federal transportation agencies, to consider blast loading in the design and retrofit of critical engineered structures. In the *Recommendations for Bridges and Tunnel Security* (2003) requested by AASHTO and sponsored jointly by FHWA, a Blue Ribbon Panel of experts from academia, professional practice and state and federal agencies observed that:

"Among the 600,000 bridges in the United States, preliminary studies indicate that there are approximately 1,000 where substantial casualties, economic disruption and other societal ramifications would result from isolated attacks."

Such attacks may be carried out using Vehicle Born Improvised Explosive Device (VBIED), like the truck bombs used in the attack of the Murrah building in the Oklahoma City bombing or in the attack observed in 2007 on a truss bridge crossing the Tigris River in Iraq (Figure 2-23).

While signature bridges may be attractive targets for terrorists because of their significance, many (ordinary) highway bridges may be as critical or even more critical because they may be at the crossroads of important commercial routes and play a key role in connecting communities, facilitating commercial exchanges and the free circulation of people between different regions. The destruction of such bridges may have overarching effects on the economy of a region as transportation infrastructures and critical commercial routes are disrupted.

Besides, for signature bridges countermeasures (such as increased inspection and surveillance) may be in place to help deter potential aggressors, detect the nature of the aggression and defend such assets from the aggressors. Since highway bridges are essentially opened structures which (for the most part) are not always closely monitored, their function becomes a key parameter of their vulnerability as they are used freely and hence can be easily targeted by terrorists.

Figure 2-23: Structural damage to Truss Bridge Due to Explosion at the Deck Level (Bridge on the Tigris River, Iraq, AFP, 2007)

As a consequence, in areas already susceptible to the effects of other extreme events, such as earthquakes, the design of new critical highway bridges should also incorporate the effects of bombings from a terrorist attack in addition to, say, seismic design requirements. Such effect may need to be assessed as well in designing mitigation measures and/or retrofit for existing

bridges. The integration of blast and seismic effects on bridges in the context of a synergistic blast and seismic design, or yet in a larger multiple hazard framework of analysis, is not easily undertaken. In reality, the situation is far more challenging as bridges can also be subjected to the actions of tsunamis waves, storm surge, vehicle/vessel collision and many other hazards.

While tsunami might be a bigger concern in coastal states like California or Alaska, devastating storm surges and flooding can happen in many other parts of the country, and, to some extent, most bridges are susceptible to structural damage caused by vehicle or vessel collisions. To have a better understanding of what is at stake statistics about bridge collapse per cause compiled by the NY State Department of Transportation for a 39 years period ranging from 1967 to 2006 (MCEER, 2008) are presented in Table 2-10. It appears clearly that the major cause of collapses is flooding followed successively by traffic overload, vessel collisions and earthquakes. This observation underscores the necessity to look beyond wind and earthquake in considering the effects of hazards in bridge engineering and design. Moreover, although events like tsunami are not included in this table, they are not irrelevant considering structural damage to bridge structures observed in the wake of the Japan Tsunami of 2011 (J_BEC, 2011).

Table 2-10: Hazard Induced Bridge Collapse from 1969-2006 (MCEER, 2008)

Hazards	Flood	Traffic Overload	Vessel Collision	Earthquake	Wind
Number of collapses	718	220	36	19	8

As for the likelihood of explosive events and bomb-related attacks in the US, Table 2-2 compiled by the Bureau of Alcohol, Tobacco and Firearms presents a list of such events for the 5 years

period covering 1993 to 1997 (Smith, 2003). This table indicates that there were 8,056 actual intentional bombings in the United States over this 5-year period. That is an average of about 1611 events per year or roughly 4 to 5 per day. They accounted for about 90% of the structural damage due to explosive events over this period and 75% of the casualties recorded. Many of these incidents go unpublicized because they only involved small amounts of explosives. These events may make local headlines, but fail to attract national attention (Smith, 2003). However, as terrorist organizations are pushing forward with their agenda, actions like the Oklahoma City bombing and the attacks on the World Trade Center (1993 and 2001) could become *modus operandi* in future terrorist attacks despite the great effort put in intelligence and monitoring of the terrorist risk at the federal level.

Complementarily, Table 2-12 presents a partial list of the number of explosive incidents by state over the same period. California alone accounted for almost 20% of the total number of explosive incidents during that 5-year period, followed by Illinois and Florida. Considering that states like Florida and California are most severely exposed to natural hazards, in particular hurricanes and earthquakes respectively, for those states, a multi-hazard engineering approach to bridge design is most relevant.

Table 2-11: Total Number of Explosive Incidents in the US by Type from 1993 to 1997 (Smith, 2003)

Type of Event	Total	Injured	Killed	Structural damage($)
Accidental Explosion	150	513	101	34,932,299
Attempted Bombings	2295	7	13	195
Attempted Incendiary Bombings	901	0	0	350
Actual Bombings	8056	2773	329	621,198,099
Actual Incendiary Bombings	2308	192	35	24,789,148
Recovered Explosives	8369	0	0	0
Stolen Explosives	426	0	0	0
TOTAL	22505	3485	478	680,880,091

The statistics in the previous tables underscore that the sole consideration of risks imposed on bridges through standalone hazard resistant design has limitation and a change in paradigm is needed when bridge exposed to multiple hazards need to be designed or retrofitted. A much more integrated multi-hazard engineering approach is desirable. One such approach is to consider all hazards the bridge may be subjected to during its lifespan and develop structural or sub-structural systems that provide sufficient protection against all. This requires that a designer possesses enough understanding of the interaction between the bridge and each hazard relevant to its design. To contribute to this understanding, some aspects of the vulnerability of bridges to multiple hazards are discussed. Because blast and earthquake actions are the focus of this study,

further information related to blast and earthquake engineering design methods are also provided.

Table 2-12: Total Number of Explosive Incidents per State 1993-1997 (Smith, 2003)

State	Total	Rank
California	4390	1
Illinois	1897	2
Florida	1729	3
Texas	1156	4
Arizona	919	5
New York	822	6
Michigan	782	7

2.7 Challenges in Multi-hazard Engineering and Design

Work done to compare the effects of multiple hazards on structural response of structures has shown how different hazards fall into different ranges in terms of response as measured in terms of amplitude and frequency (Ettouney, et al., 2005). Figure 2-24 illustrates this finding. It can be seen that little overlap exist between the hazards, which suggests the challenges in the analysis and in developing design strategies to effectively address such multiple hazard.

This little overlap between the hazards is also reflected in their effects on structures, as they can impose conflicting demands on structural components. This creates situation in which a

satisfactory design approach used to design a structure for one of the hazard can be detrimental for the same structure responding in another event.

To get around this obstacle, the designer should think globally and analyze the consequences of each design decision made. For bridges design, the information about component behavior in different hazards provided in the previous sections can be used in that sense. Here again an iterative procedure is to be used in which the design process is revised until optimum viable design compromises are found to integrate the demands of the multiple hazards considered. Those compromises should be globally sound and contribute to reduce the overall fragility of the system in multiple hazards.

In this context, multi-hazard engineering cannot be the mere consideration of demands from multiple hazards on a given structure, nor should it be about addressing demands of multiple hazards in succession independently of each other. Rather it is optimization in design by simultaneously considering the demands of multiple hazards (MCEER, 2007). This should be done through the utilization of a single structural concept with sufficient benefits for each hazard considered in the spectrum. This approach is taken throughout the rest of this work.

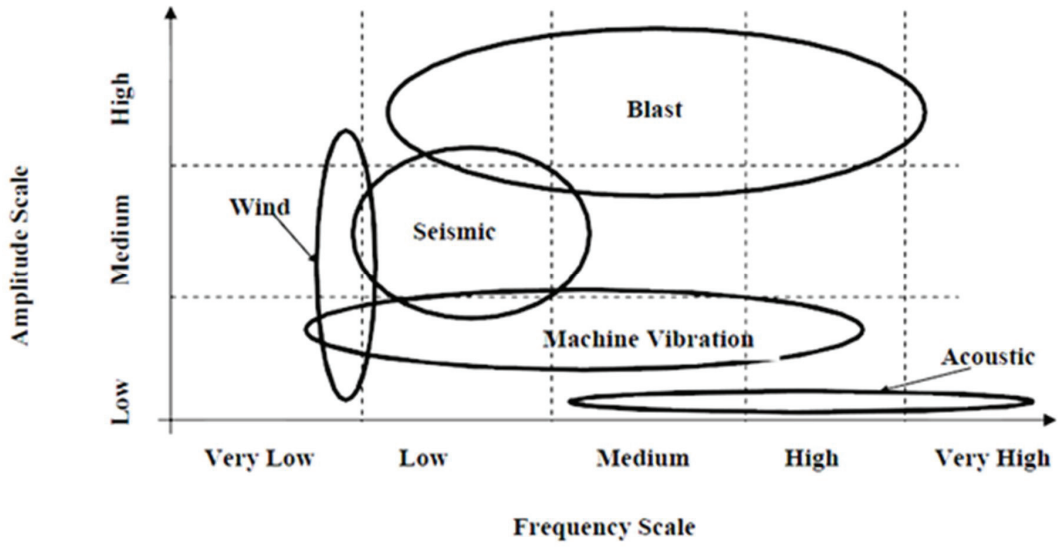

Figure 2-24: Qualitative Frequency-Amplitude Distribution for Different Hazard (Ettouney, et al., 2005)

SECTION 3

POTENTIAL OF STEEL CONCRETE STEEL SECTION FOR MULTI-HAZARD APPLICATIONS

3.1 General

While standalone blast or earthquake resistant-design approach can give satisfactory results for design of bridge components against blast or earthquake, it is however quite difficult to use either one as a broad basis for a bi-hazard design framework in which both need to be considered. This difficulty lies in the conflicting natures of the hazards that lead to low correlation not only in demands but also in responses of structures to those demands. It seems rational that a multi-hazard framework of analysis taking a holistic approach at the initial design concept stage may help anticipate conflicts in demands and responses and cope with them.

The philosophy behind this approach is that multi-hazard design should ideally seek to improve the performance of structures by promoting the development of systems capable not only to accommodate the reinforcing aspects of multiple hazards, but also able to reconcile their opposing effects. A promising and effective approach is to rely on a system in which a single concept is used to provide sufficient protection for all hazards to which a structure can be exposed in such a way that the system features accommodate consistent demands from the hazards while providing satisfactory performance for conflicting demands. Applied to engineering of bridges, this approach can be advantageous if systems that optimize responses under each specific hazard (without causing significant adverse effects for the other hazards) can be developed and implemented.

This section focuses on possible applications of the approach described above, for specific types of composite structural elements. Because of inherent structural qualities, ranging from higher strength, substantial toughness, and ductility, and because of the cost saving they can generate by permitting accelerated bridge constructions, a type of composite construction, which can be thought of as a steel-concrete-steel (SCS) "sandwich" section, is introduced and its salient characteristics are reviewed. Structural applications of this composite section are reviewed with a specific interest in its behavior under lateral load. The aim is to evaluate how such structural elements could be implemented into bridges to serve the intended multi-hazard protection purposes. As a special type of SCS, cylindrical Concrete Filled Double Skinned Tubes (CFDST), formed by two concentric steel tubes separated by concrete filler, are also reviewed in this section, and later studied and tested (Sections 5 to 9) as a substitute to reinforced concrete columns bridge piers erected in a multiple-hazards prone environment. To reduce the scope of this study, emphasis is put on the bi-hazard environment defined by earthquake loading and blast overpressures.

3.2 Steel-Concrete-Steel Sandwich Construction

Conventional bridge components of reinforced concrete or steel might not have adequate capacity and/or ductility to withstand the extreme demands imposed by various hazards, such as terrorist attack, vehicle collision, tsunami, or even earthquake (i.e., the type of multi-hazard environment considered in this study). While reinforced concrete or steel members could be hardened to resist multiple hazard demands, hardening may result in massive and heavily reinforced components that are expensive (Smith and Hetherington, 1994), prone to material

failures (breaching, cratering, scabbing), and that can generate fragments hazardous to structures, users, or other load carrying components (DoD, 2008). On the other hand, although structural elements composed of steel are not likely to be subjected to breaching (Conrath, et al., 1999), other types of material failures such as tearing, shattering and brittle failure due to fragment impacts are possible and need to be controlled (DoD, 2008). Therefore, hardening using ordinary reinforced concrete or steel components, while an acceptable solution in some instances (protective design, nuclear power plant, blast doors), is possibly not the optimal and most economical solution for multi-hazard applications in bridge engineering.

An alternative is to combine steel and concrete in a configuration that improves strength, toughness, confinement, and ductility, where the steel prevent concrete breaching and the concrete provides local stability, at no or little extra cost compared to ordinary components. One such solution is provided in steel-concrete composite materials in which the steel serves as an outside shell mechanically bonded (using studs) or not to a concrete core. By placing the steel at the periphery, it has a larger influence and its contribution to the stiffness and the strength of the composite section is optimized (Montague, 1975). Marson and Bruneau (2000) and Fujikura and Bruneau (2008), among others, have established experimentally that a composite element such as the Concrete Filled Steel Tube (CFST) has good structural characteristics under earthquake and blast loadings, can dissipate large amount of energy while maintaining its integrity and is a logical alternative to reinforced concrete bridge piers in this bi-hazard framework. However failure of this section under blast load can generate flying debris that constitute secondary hazards to other bridge structural elements or users. Considering those results, it is suggested here to build upon those two concepts to develop a bridge pier system which will retain the

characteristics of the CFST while offering improved protection in the same bi-hazard framework. This can be achieved by using a relatively new configuration of steel-concrete composite material having the potential for higher performance in multi-hazard engineering applications in bridge structures. This composite material is the Double Skin Composite Material (DSCM) or more specifically Steel-Concrete-Steel Sandwich Construction (SCS).

Two basic configurations of SCS are considered here. The first is the Double Skinned Composite Panel (DSCP) which consists of two steel-facing plates held apart by an array of transverse bar connectors welded at each end to the steel face plates with concrete filler in between (Bowerman et al., 1999). Such a construction could be used both in deck slab and pier element to resist multiple hazard effects. The second, which can be implemented in pier elements, is the Concrete Filled Double Skinned Tube (CFDST). CFDST basically consists of two concentric steel tubes with a concrete infill in between. The steel tubes can be circular hollow sections or square hollow sections, or a combination of the two. However, the cylindrical shells are likely to be preferred over the square ones as intuitively they seem to offer better confinement of the concrete, better composite action, and symmetry in geometry and structural behavior.

The most important point about this form of construction has been explained by Montague (1975, 1986) for pressure vessels: "*by separating, say, the single thickness of the conventional shell into two "flanges" spaced wide apart, the bending stiffness of the wall is increased very significantly, this also reduces the sensitivity of the shell to initial imperfections, the wall having greater resistance to the formation of circumferential lobes. In addition, the resistance to elastic instability is increased. Because both elastic instability and inelastic instability following local*

yielding is unlikely, the failure of the shell will be due to material strength failure which unlike instability is highly predictable".

Montague (1975, 1979) initially proposed the idea of steel sandwich construction for pressure vessels. While steel was usually considered as face sheets, several filler materials were investigated including epoxy resin and glass powder (Montague, 1978; Nash and Montague, 1984) and cement concrete (Goode and Fatheldin, 1980; Montague and Choo, 1981; Goode and Shukry, 1988). Because this type of sandwich cross section was believed to have high bending stiffness, significantly less instability under external pressure, lighter weight, improved fire resistance, and enhanced strength, it was forseen as a serious candidate for use in nuclear containment structures, liquid and gas retaining structures, and blast resistant shelters (Wright, et al., 1991). Moreover, in CFDST configuration, SCS was also shown to have good energy dissipation capacity and ductility (Lin and Tsai, 2001; Tao, et al., 2004; Han, et al., 2006). Also, compared to reinforced concrete, the steel skins can also act as load bearing element as well as permanent formwork. Finally, for DSCPs, the steel plates and shear connectors can be easily fabricated, without the expensive detailing required by the bending of reinforcement bars and building of reinforcement cages (Foundoukos, et al., 2007). Those overall characteristics can result in significant reduction in total construction cost as formwork and labor are the main cost drivers in reinforced concrete.

Because of all those benefits, this construction type seems suited to multi-hazard applications, where the major challenges posed by each of the hazards must be taken into account during design. To better understand its potential, the next subsection provides a brief description of the applications and structural behavior of this relatively new type of construction. This section also

presents some of the formulae that are currently used to predict the strength of different types of SCS elements.

3.3 A Brief History of SCS

Steel-Concrete-Steel Sandwich Construction was proposed for the Conway River submerged tube tunnel in the UK in 1989 (Tomlinson, et al., 1989). The system as devised is shown in Figure 3-1. Initially, the idea was to use heavily reinforced concrete panels for the construction of the tunnel, and to use a thin steel plate to provide a water barrier (Wright, et al., 1991). Eventually, contrasting with heavily reinforced concrete panel, the idea evolved toward integrating this steel into the construction by increasing its thickness and providing shear connection to the concrete (McKinley and Boswell, 2002). A solution was to use the steel plates to carry tension and compression and the concrete core for compression, whereas overlapping headed shear studs welded to the steel skins would be used to provide the necessary longitudinal and transverse shear reinforcement (Wright et al., 1991).

However, the initial concept was not implemented due to construction and financial constraints. On one hand there was difficulty associated with handling the large individual steel plates on site and the need to provide support to resist hydrostatic pressures, which would push the plates apart during concreting (Burgan, 2011). Additionally, the process used to provide the shear connection was deemed to be costly in time and labor since it would have required temporary works and welding of individual connectors (Mc Kinley and Boswell, 2002). Nonetheless, extensive experiments were carried on SCS from 1990 to 1997 as part of the “Steel-Concrete-Steel

Sandwich Construction project of the Steel Concrete Institute" and summarized in the report "Double Skin Composite Construction for Submerged Tube Tunnels" (Burgan B. , 1998).

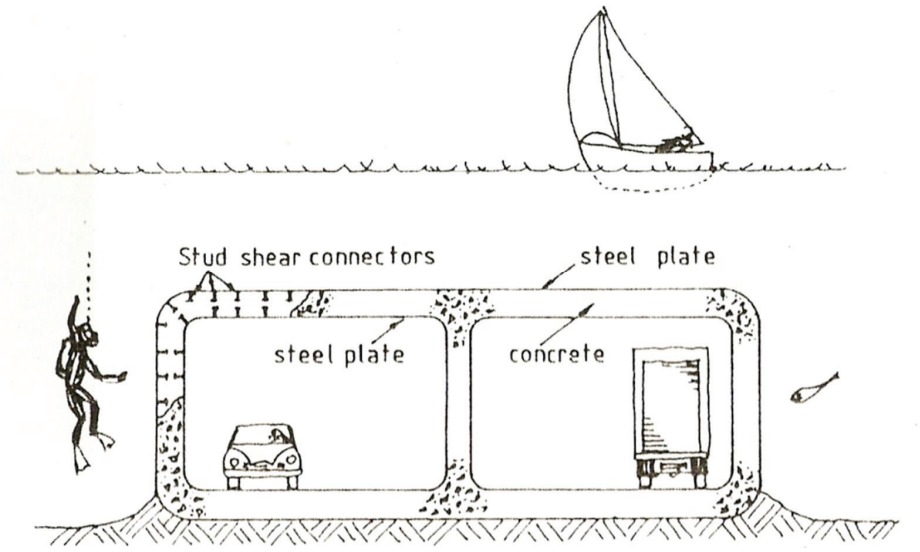

Figure 3-1: DSCP Construction in a Submerged Tube Structure (Wright et al., 1991)

An alternative to individually welding the shear connectors was later suggested in which the plates would be connected by plain bars simultaneously friction-welded at both ends (Bowerman, et al., 2002). The resulting system was developed into the Bi-Steel product, a proprietary system of British Steel (subsequently known as Corus UK, and then Tata Steel) that is manufactured in both flat and curved form and that has already been used in various projects, including protective structures, building cores, and a bridge deck (Foundoukos, et al., 2007). Figure 3-2 below shows the range of shell thicknesses, sizes, and spacings that are currently produced as Bi-Steel elements. At this time the diameter of the friction welded connectors is

fixed to 25mm (1in). The behavior of the Bi-Steel panel under various loading conditions (mostly, out-of-plane loading) has been described by Chapman et al. (2006) and is summarized here.

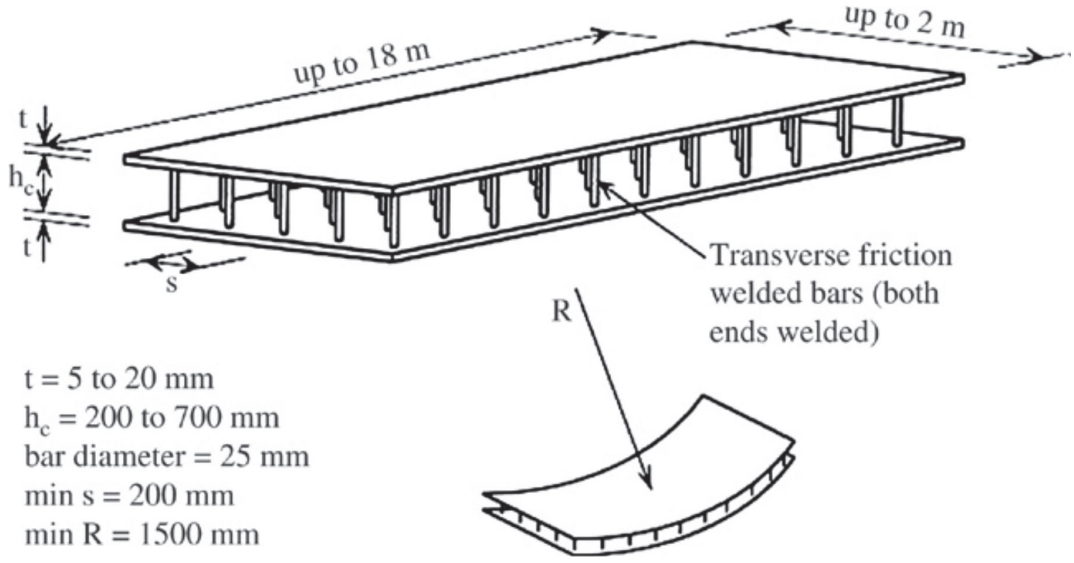

Figure 3-2: Bi-Steel Sandwich Construction (Foundoukos et al., 2007)

In Bi-Steel members with concrete infill, the friction-welded bar connectors resist longitudinal and transverse shears and serve to prevent plate buckling. Under load, these plain bar connectors are subjected to shear, tension or compression, and bending. The moment on the connectors depends on the ends fixity, which itself depends on the plate thickness and on the extent to which the connector is restrained by the concrete; tension cracks which occur at the connectors reduce the restraint and increase the moment.

Bending moment on a connector causes rotation at its ends; because the plate (between the connectors) can move away from but not towards the concrete, the rotation occurs about an axis eccentric to the center of the connector and a tensile force is produced in the connector. Also, interface slips at each end of the connector are in opposite directions, so some bar tension results from the increased distance between the ends of the connector. Depending on the plate slenderness, a tensile force may develop in the bar to prevent the separation of the compression plate from the concrete caused by that plate's tendency to buckle. The same bars can also be acting as transverse shear reinforcement.

Currently the concrete core of Bi-Steel panels does not contain longitudinal bar reinforcement. Nonetheless, as in doubly reinforced concrete sections, for out-of-plane loading, the steel plates have to resist both tensile and compressive stresses. In general, the plates in Bi-Steel members are initially deflected inwards, as a result of the welding process, but outward deflection may be caused by the pressure of the poured concrete or by bar end moments. The compression plate must be designed to prevent single or double curvature buckling. A Bi-Steel member is normally designed so that, under extreme out-of-plane overload, the tension plate would fail before the compression plate yields or buckles, and before bar failure or vertical shear failure occurs; as for reinforced concrete, the design aims to avoid non ductile failure. The buckling mode of the compression plate is determined by the relative magnitude of the orthogonal forces and the corresponding bar spacing.

3.4 Ultimate Strengths of Double Skin Composite Panels

Several quasi-static tests have been conducted on Double-Skin Composite Panels (DSCP) to establish their structural behavior. Test conducted include two and four-point bending tests by Oduyemi and Wright (1989) , Wright et al. (1991) and Roberts et al. (1995), on half scale and full scale models. Other tests on Bi-Steel have been reported by McKinley and Boswell (2002), Shanmugam et al., (2002), and Foundoukos et al., (2007).

A few dynamic tests have been conducted on DSCP by Xie and Chapman (2005) a, but these were concerned with the fatigue tensile strength of friction welded bar-plate connections embedded in concrete. Another dynamic test on DSCP by Lan et al. (2005) investigated the behavior of composite structural panels subjected to explosive loading.

Based on theoretical mechanical models or on results obtained from quasi static tests and experimental calibration, several formulae have been offered to predict the strengths of composite panels. A summary of the main equations for predicting strength for various limit states are provided below.

3.4.1 Axial Compression Strength of DSCP

No specific equation has been retrieved in the literature for the prediction of the squash load of DSCP built with overlapping shear or with friction welded studs. However, if a sufficient number of shear studs is provided to prevent plate buckling, it is conceivable for the panel to develop its full plastic axial strength before instability develops, or before failure of the studs. In such a case, the axial strength, P_u, of the panel could be estimated in the same fashion as for

reinforced concrete by considering that both the steel plates and the concrete reach their ultimate strength. If such conditions were satisfied then:

$$P_u = A_s f_y + 0.85 f_c^{'} A_c \tag{3-1}$$

In this formula, A_s is the total area of steel, A_c is the area of the concrete core, $f_c^{'}$ is the strength of the concrete used in the core, and F_y the yield strength of the steel plates.

As another limit state, global buckling of the plate could also develop, and could be calculated using the effective inertia of the composite wall (presented in a later section).

3.4.2 Moment Capacity and Flexural Stiffness of DSCP

McKinley and Boswell (2002) have developed equations for the elastic and plastic out-of-plane flexural behavior of DSCP and Bi-Steel Panels. Note that their study, which also compared Bi-Steel panels to ordinary studded panel specimen, established that the continuity of the bar connectors in the Bi-Steel panel allows this type of construction to withstand larger deformations before failure.

In the elastic range, assuming a linear distribution of the force throughout the depth of the panel and neglecting the tensile strength of the concrete, for pure bending the flexural strength can be evaluated by taking moments with respect to the center of gravity:

$$M_y = f_y b t_1 \left(\frac{z}{3} + \frac{t_1}{2} \right) \frac{z + t_1/2}{h_c - z + t_2/2} + f_y b t_2 \left(h_c - \frac{z}{3} + \frac{t_2}{2} \right) \tag{3-2}$$

I

n this equation the neutral axis (NA) location, z , is given as:

$$z = -B + \left[B^2 - 2C \right]^{\frac{1}{2}} \tag{3-3}$$

where:

$$B = m(t_1 + t_2) - t_1 \tag{3-4}$$

$$C = -\left(h_c + t_1 + t_2\right) m t_2 + \frac{1}{2}\left(m t_2^2 - m t_1^2 + t_1^2\right) \tag{3-5}$$

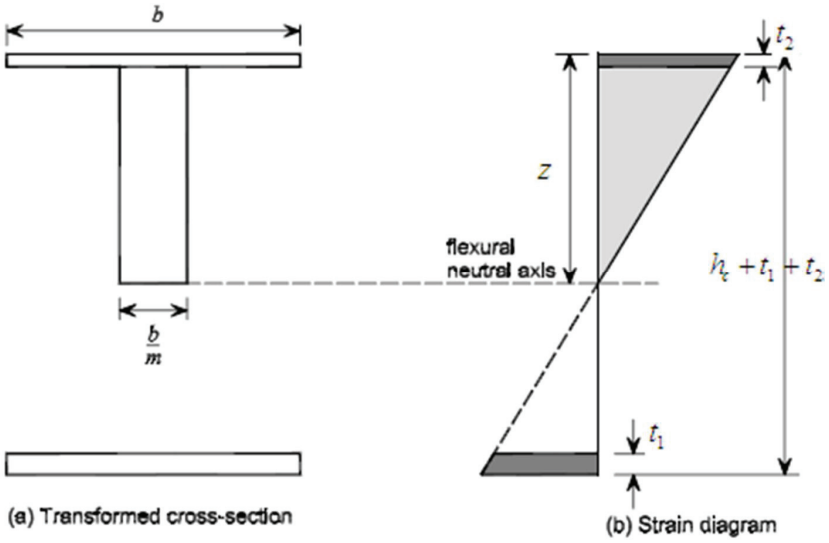

Figure 3-3: Transformed Section and Strain Diagram in Elastic Bending

(Bowerman, et al., 1999)

When the concrete core is fully cracked, the neutral axis will reach the lower surface of the plate in compression and the stress in the tension plate is at yield. In that case, the flexural strength is:

$$M_u = f_y b t_1 \left(h_c + \frac{t_1 + t_2}{2} \right) \tag{3-6}$$

In equations 3.5 and 3.6 above, t_1 represents the thickness of the compression plate, t_2 the thickness of the tension plate, h_c the height of the concrete core, and b the width of the panel. All other parameters have been defined previously except for the modular ratio, m, which is the ratio of the moduli of elasticity of the steel, E_s, and the concrete, E_c:

$$m = \frac{E_s}{E_c} \tag{3-7}$$

For flexural stiffness evaluation, a transformed section approach was used to evaluate the second moment of area of the panel. The transformed section for pure bending analysis is shown in Figure 3-3. Using this figure, the equation of the moment of inertia is calculated as:

$$I = b t_1 \left(z - \frac{t_1}{2} \right)^2 + \frac{b}{m} \frac{(z - t_1)^3}{3} + b t_2 \left(h_c + t_1 + t_2 - z - \frac{t_2}{2} \right)^2 \tag{3-8}$$

3.4.3 Combined Flexure and Axial Loads

In some instances, DSCP elements will have to withstand a combination of axial load and weak-axis bending moment. In such a case, behavior is to some extent similar to that observed for reinforced concrete members. Increasing axial loads has the effect of reducing ductility and the number and extent of cracks occurring in a DSCP component (Wright et al., 1991). This occurs

as a result of the failure becoming more a function of concrete crushing than steel yielding. Two simultaneous equations need to be solved to derive the interaction diagram relating the axial to the flexural strengths. The first one is formed by resolving the internal axial force and externally applied load acting along the element and the second is formed by resolving internal and external moments about the centroidal axis of the section (Wright et al., 1991). Theses equations are generally derived with the depth to plastic neutral axis as one of the unknowns, and either the moment capacity or axial load capacity as the other. Then the system is solved by iteration. That is, a depth to the plastic neutral axis is guessed, and then based on this guess; the ultimate section axial and bending capacities are established and checked against the applied load. The process is repeated until convergence is achieved. The full interaction diagram is generated in this fashion.

3.4.4 Shear Capacity of DSCP

An applied out-of-plane force can lead to failure in one of two modes. The first is longitudinal shear (i.e., the failure of the bar connectors to transfer the longitudinal forces from the face plates into the concrete). The second is transverse shear (i.e., the failure of the bar connectors in tension as they act as shear stirrups). Unless the transverse shear force is unusually high, the longitudinal shear mode normally governs the connector spacing (Bowerman et al., 1999). Hence, the required bar connectors spacing can be determined from the longitudinal shear and the transverse shear capacity checked for the calculated spacing.

The spacing of the connectors along the length of the panel is based on provisions similar to those applied to shear design of conventional reinforced concrete members. This means that,

theoretically, the spacing can be varied along the length of the panel such as to follow the shear distribution. For design purposes, the shear capacity Q_n of a bar connector can be determined as:

$$Q_n = 0.29\alpha d_{bar}^2 \sqrt{f_c' E_c} \le 0.8 k_L f_{ub} \frac{\pi d_{bar}^2}{4} \tag{3-9}$$

where:

f_{ub} is the ultimate tensile strength of a bar connector-normally $500MPa\left(72.5ksi\right)$

d_{bar} is the diameter of a bar connector-usually $25mm\left(1in\right)$

α is the bar connector height/diameter shape factor, taken as 1 for Bi-Steel.

Also:

$$k_L = \left(0.024t + 0.76\right)\frac{f_y}{355} \le 1 \tag{3-10}$$

and t is the thickness of the plate (generally the tension plate) closest to the critical plane in shear (plane through the end of the connector under consideration). Knowing the strength of a bar connector, the number of bar connectors required to provide the longitudinal shear resistance in given shear zones can be established.

Bar connectors can be equally spaced within shear zones, shear zones being subdivisions of the span of length , L_{vi} ,at least equal to 10% of the span length. Furthermore the spacings, s_x and s_y , of the bar connectors in a given shear zones should be such that:

$$\frac{Q_n}{s_x s_y} \ge \frac{V_L}{bL_{vi}} \tag{3-11}$$

And

$$0.64 \le \frac{s_x}{s_y} \le 1.56 \tag{3-12}$$

The longitudinal shear force, V_L, that appears in the formula above is determined from the transverse shear based on shear flow theory. It is given by:

$$V_L = V \frac{bt\overline{y}L_{vi}}{I} \tag{3-13}$$

where:

$$\overline{y} = z - \frac{t_1}{2} \tag{3-14}$$

if the longitudinal shear strength is determined in the critical plane close to the compression plate, otherwise:

$$\overline{y} = h_c + t_1 - \frac{t_2}{2} - z \tag{3-15}$$

Equation (3-15 ensures that the horizontal shear at the interface between the steel plates and the concrete core is fully transferred by the shear connectors, while equation (3-16 provides bounds to effectively control undesirable local instabilities in the plates between bar connectors.

The determination of transverse shear strength of DSCP is based on similar considerations to that adopted for reinforced concrete. While it is expected that the steel plates will contribute somewhat to the transverse shear capacity, this contribution is neglected, and the strength is computed by adding the concrete contribution V_{cn} to that V_{bn} of the bars.

$$V_n = V_{cn} + V_{bn} \tag{3-16}$$

with:

$$V_{cn} = 0.0525\left(f_c^{'}\right)^{\frac{2}{3}} \eta \left(1.2 + 40\rho\right) b h_c \le 0.45 \lambda f_c^{'} b h_c \tag{3-17}$$

$$V_{bn} = 0.9 k_T \left(\frac{\pi d_{bar}^2 f_{yb}}{4}\right)\left(\frac{b h_c}{s_x s_y}\right) \tag{3-18}$$

where:

$$\begin{cases} \eta = 1.6 - h_c \ (h_c \text{ in meters}) \\ \rho = \dfrac{t_2}{h_c} \le 0.02 \\ \lambda = 0.7 - \dfrac{f_c^{'}}{200} \ge 0.5 \\ f_c^{'} \le 40 MPa \\ k_T = 2.5\left(\dfrac{f_y}{f_{yb}}\right)\left(\dfrac{t}{d_{bar}}\right)^{1.25} \text{ with } \dfrac{t}{d_{bar}} \le 0.48 \\ f_y \le 355 MPa \end{cases} \tag{3-19}$$

3.5 Concrete Filled Double Skin Steel Tubes

A Concrete-Filled Double Skinned Steel Tubes (CFDST) is a logical extension of the steel-concrete-steel sandwich construction presented in the previous section. CFDST was studied by Montague (1975) as substitute for steel shell subjected to external pressure, by Shakir-Khalil, (1991) under monotonic lateral loading, and proposed by Wei et al. (1995) to be used in the petroleum industry in order to cope with the local and global stability concerns that often prevent steel tubes from developing their full yielding strength (API, 1989). It remains that studies on CFDST are scarce. Figure 3-4: CFDST Sectionshows a view of a CFDST cross section made of

Circular Hollow Sections (CHS) (which is one of the specimens that will be presented in later sections).

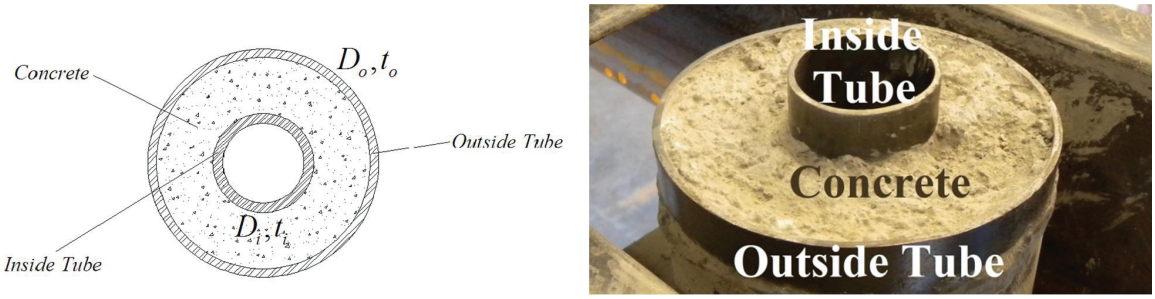

Figure 3-4: CFDST Section

As a concrete filled composite section, the structural behavior of CFDST members under load can be complex because of the interaction between the steel and the hollow concrete core. Such an observation dates back at least to Sewel's pioneering tests on concrete filled tube (Sewel, 1902), when it was observed that the ultimate axial resistance of a concrete filled tube is greater than the sum of the resistances of separately tested steel and concrete components. Further investigation by researchers such as Salani and Sims (1964) and Furlong (1968) among others established that the increase in load bearing capacity of CFSTs is mainly caused by the confining effect of the steel tube on the concrete core. Such confining effect is also expected in CFDST and is explained below.

Gardner and Jacobson (1967) observed that for CFST under axial loading, the Poisson's ratio of the concrete core is less than that of the steel shells in the initial stage of loading (a similar behavior should hold for CFDST). Consequently, under compressive loading, the radial

expansion of the steel tubes due to Poisson's effect is bigger than that of the concrete core alone (note that for CFDST, at that stage, only the inner tube would therefore engage the concrete), and no confining pressure exists yet. However, as the concrete core enters the plastic regime, its Poisson's ratio increases and cracks develop in the core. This is accompanied with an increased outward expansion of the concrete core, which eventually engages the outer tube. In CFDST, both the outer and inner steel shells would expand radially at that stage. This gives birth to bond stresses. At this stage, hoop and radial stresses develop in the steel tubes, equilibrated by stresses in the concrete. A tri-axial state of compressive stress appears at the interfaces of the tubes with the concrete core and throughout the concrete core. Because of the generally small thickness of the steel tubes, the through thickness radial stresses decrease rapidly to zero as we move from the steel-concrete interface to the outside face of a tube. So, globally, the steel tubes are considered to be in a bi-axial state of stress while the concrete core is in a tri-axial state of stress.

As the loading progresses further, the confining effect of the steel tubes on the concrete delays the propagation of cracks and increases the frictional shear stresses between cracks in the core. The overall effect is to improve the ductility of the system and delay damage; this is consistent with observation made by Johansson and Gylltoft (2002) on CFST. However, the confining effect is eventually lost when the steel tubes reach the plastic regime and flow plastically. The lateral expansion of the concrete reduces also because of aggregate interlocks and increase in shear sliding stresses. Also, any early local instability in the tubes can reduce or eliminate altogether this confining effect. In that situation, the propensity of the steel tubes to buckle is reduced by the presence of the sandwiched concrete and the outer tube will tend to buckle outward while the inner tube will indent/buckle inward (Tao el al. 2004, Han et al. 2006). By

buckling away from the concrete, the outer tube causes bond stress between the concrete and the tubes to reduce and the confining effect is lost, entraining a sudden drop in capacity and possibly failure. Consequently, those local instabilities have to be controlled by limiting the diameter-to-thickness ratio of the tubes. This would be the case for both CFST and CFDST.

3.6 Ultimate Strengths of CFDST

3.6.1 Axial Strength of CFDST

Lin and Tsai (2001) showed that a conservative estimate of the axial plastic strength of CFDST members can be established by superposing the concrete and steel strength. In that case, the full strength of the concrete $\left(f_c^{'}\right)$ is used. This estimate is closed to what AISC-LRFD specifies for computing the ultimate axial strength of concrete-filled columns, the only difference being that a reduction factor of 0.95 is applied to the nominal concrete contribution to take cracking of the concrete core into account. As such, if P_u represents the ultimate axial strength of a CFDST element, A_{so} the area of the outer tube and A_{si} the area of the inner tube, A_c the area of the concrete core and F_y the yield strength of the steel plates, then:

$$P_u = A_{so} f_y + A_{si} F_y + A_c f_c^{'} \tag{3-20}$$

3.6.2 Moment Capacity and Flexural Stiffness of CFDST

Given that no equations were found in the literature to describe the behavior of CFDST under flexural, as well as combined axial and flexural loadings, such equations have been derived and

presented in Section 7. Equation predicting the flexural stiffness of CFDST are derived and presented in Section 9.

3.6.3 Shear Capacity of CFDST

No specific method has been established in the literature for evaluation of the shear capacity of CFDST elements. Even though the confinement of the concrete core by the steel tubes is likely to improve its strength, it is however conservative to estimate the shear strength of the CFDST based of the shear capacity of the steel tubes alone, as recommended for CFST elements in AISC-LRFD 2005 (Section I, Section 16.1). Since no reinforcement is used at that time in CFDST elements, the shear capacity of the section can be based on the sum of the shear capacity of the inner and outer tube, as given per Section G, Section 16.1, of AISC-LRFD 2010 (AISC, 2010), namely:

$$V_n = \tau_{cro}\frac{A_o}{2} + \tau_{cri}\frac{A_i}{2} \tag{3-21}$$

$$\tau_{cro} = \frac{1.60E}{\sqrt{\frac{L_v}{D_o}}\left(\frac{D_o}{t_o}\right)^{\frac{5}{4}}} \geq \frac{0.78E}{\left(\frac{D_o}{t_o}\right)^{\frac{3}{2}}} \qquad \tau_{cro} \leq 0.6f_y \tag{3-22}$$

$$\tau_{cri} = \frac{1.60E}{\sqrt{\frac{L_v}{D_o}}\left(\frac{D_i}{t_i}\right)^{\frac{5}{4}}} \geq \frac{0.78E}{\left(\frac{D_i}{t_i}\right)^{\frac{3}{2}}} \qquad \tau_{cri} \leq 0.6f_y \tag{3-23}$$

where τ_{cr} represents the critical stress according to the limit states of shear yielding and shear buckling, the subscripts *i* and *o* refer respectively to the inner and outer tube, and L_v represents the distance from the points of maximum and zero shear forces.

3.7 Capacity of CFDST under Cyclic Loading

Besides having lighter weight and higher bending stiffness, CFDST have almost all of the advantages of CFT members (Tao et. al., 2004). They also have comparable cyclic performance. Experimental studies conducted by Lin and Tsai (2001) on nine beam-columns element with high slenderness ratio and variable level of axial load have established that CFDST can effectively provide strength and deformation capacity that emulates that of CFST even with diameter-to-thickness ratio in excess of the limit currently imposed by AISC (87 for grade 50 steel) on concrete filled circular steel section (ratio as high as 100-150 for the outer tubes and 90 for the inner tube were studied).

Cyclic loading tests of CFDST elements have generally demonstrated good energy dissipation capacity, as evidenced by their hysteretic response. Figure 3-5 presents predicted and experimental hysteretic loops for the CFDST elements tested by Han et. al (2006). The elements considered by Han et al. had outer tube dimensions of $D_o \times t_o(mm) = 114 \times 3$ and inner tube dimensions of $D_i \times t_i(mm) = 32 \times 3$; these were tested at axial load levels of 0.23, 0.43, and 0.63 of the ultimate axial capacity of the section. From those loops, it can be inferred that CFDST

structural elements can have good hysteretic behavior even under substantial axial load. However, Han et al. established that, for beam column under cyclic bending, an increase in the axial load level corresponds to a drop in section ductility. Note that this behavior is also a function of the cross-section diameter to thickness ratio.

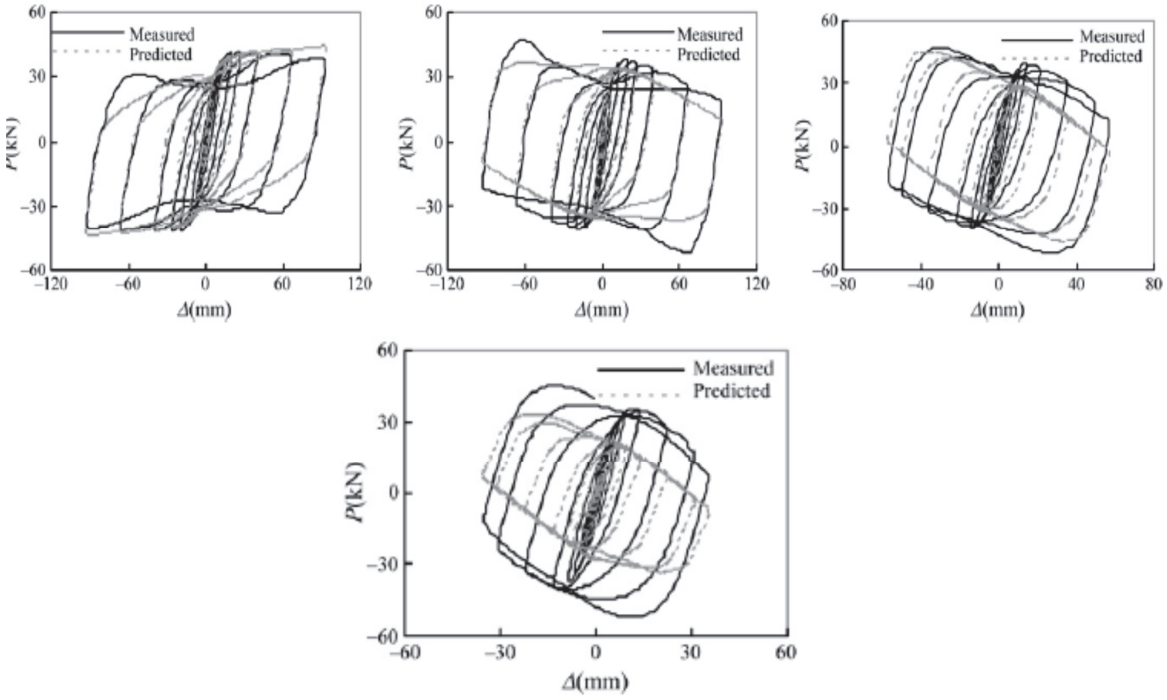

Figure 3-5: Cyclic Behavior of CFDST (Han et al., 2006)

SECTION 4

PRELIMINARY ANALYSIS OF PROPOSED MULTI-HAZARD SCS BRIDGE COLUMN PROTOTYPES

4.1 General

In the previous sections, Steel-Concrete-Steel Sandwich Construction (SCS) was reviewed as a potential bridge material for multi-hazard applications, and the main features of these types of structural systems were presented. This section explores potential uses of SCS to improve performance of bridges placed in extreme hazards environments. Since bridge substructures have often been pointed out as one of the most vulnerable components of bridges under blast loading and high impulse impact (Davis and Meyer, 1979) emphasis is put primarily on these components.

Preliminary design of proposed prototypes using double skin composite panels (DSCP) and concrete filled double skin tubes (CFDST) under earthquake and blast loading is also carried out. The results from those analyses are presented and used to assess the expected performances of the prototypes. This work served as a preliminary assessment of the possible effectiveness of a few concepts initially considered.

4.2 Multi-hazard Bridge Pier System Prototypes

Using SCS as a basic concept, several prototypes of highway bridges with different combination of substructures and superstructures have been considered. Their advantages and disadvantages are discussed below. The prototypes developed are based on a modified configuration of the

bridge in Design Example 2 of the series of seismic design examples developed for FHWA (FHWA, 1997). The bridge in this example is a three-span steel plate girder superstructure with a composite reinforced concrete deck slab. The substructure elements are seat-type abutments and wall piers. The alignment of the roadway over the bridge is straight and there is no vertical curve. The initial bridge has 25-degree skew at all four substructure elements. Plan, elevation, and cross section of the deck are presented in Figure 4-1.

In the original FHWA example, the bridge spanned a river, but for the needs of this conceptual design, it is assumed here to span a roadway. For that reason, the initial substructure height of 36ft (10.97m) was reduced to 20ft (6m). For further simplicity, the skew of the bridge is disregarded. The plan and elevation views of the bridge as modified are shown in Figure 4-2. The superstructure cross-sections remained otherwise the same.

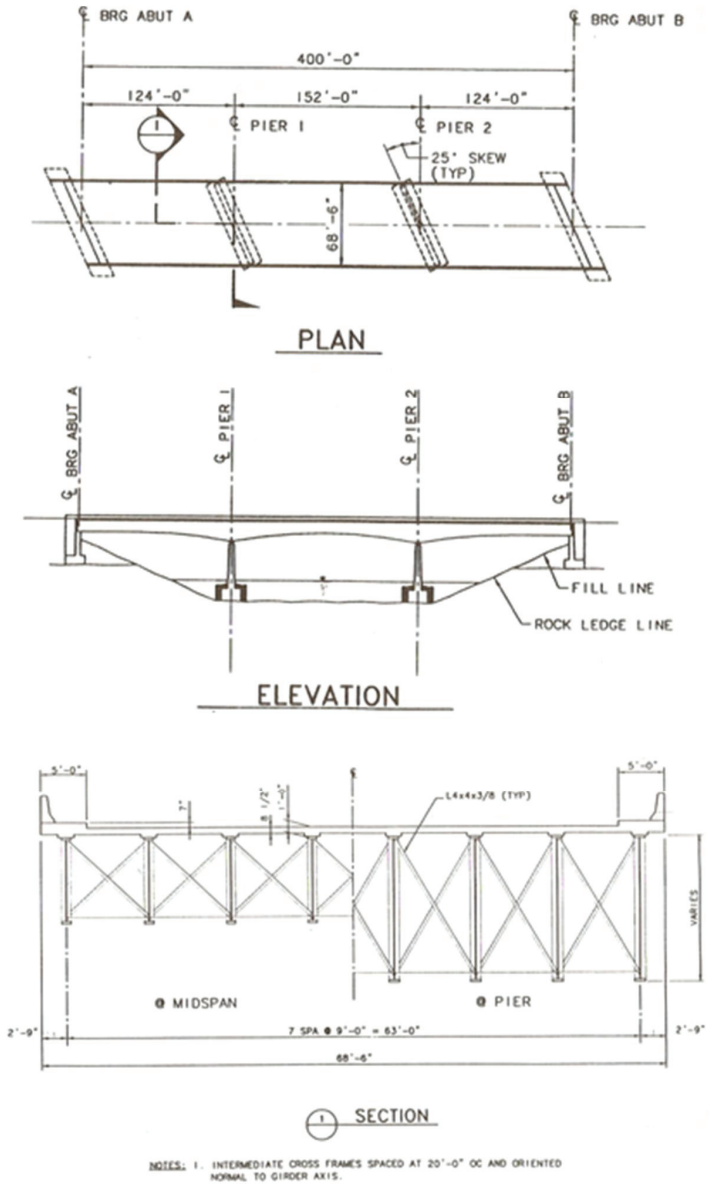

Figure 4-1: Bridge Plan, Elevation and Section (FHWA, 1997)

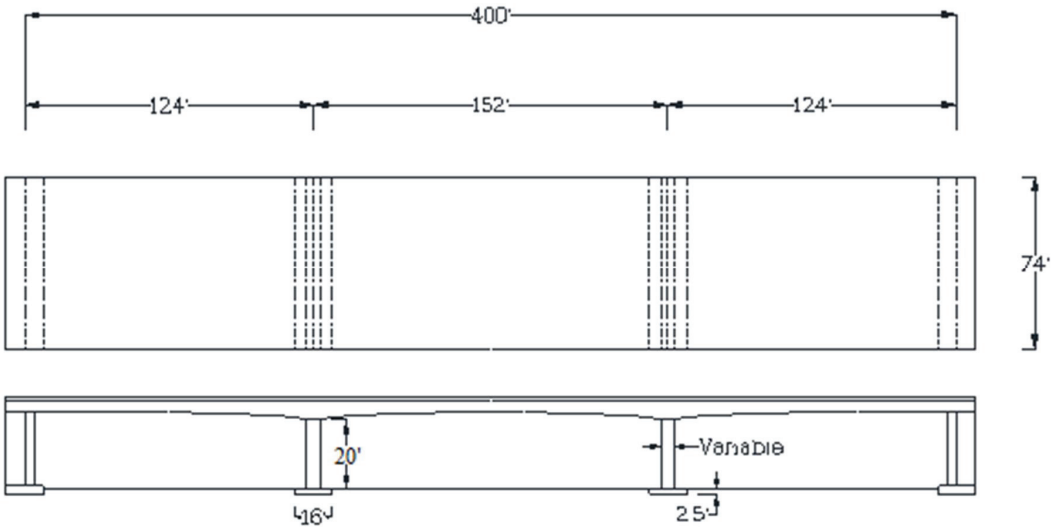

Figure 4-2: Modified Bridge Plan and Elevations

4.2.1 Prototype 1: Multi DSCP-Column Bent

As a first multi-hazard bridge pier prototype concept, dual DSCP columns (two DSCP put side to side) were considered. If single DSCP columns bent was to be used,the composite thickness each column in the bent would need to be considerably large to carry the service loads and have the required stiffness in the weak direction to prevent large deformation under earthquake loading or blast overpressure. If Bi-Steel in particular was considered for this application, the thickness of the steel shells would be out of the range available for commercial Bi-Steel panels. Moreover, using the twin configuration allows keeping the width of the panels to more reasonable dimensions. In this prototype, connection of the pier to the cap-beam and the foundation would be done using the same type of composite box beam found in Fujikura and Bruneau (2007) and described later in Section 6. Alternatively, the columns could be welded to a DSCP cap-beam and a DSCP beam foundation.

One of the shortcomings of this system as devised is the asymmetry in stiffness of the substructure. The flexural stiffness of the structure in the transverse direction which corresponds to the strong direction of the steel plates and the concrete infill can be several orders of magnitudes higher than in the longitudinal direction. For instance, for the range of available Bi-Steel panels, the estimated transverse flexural stiffness is at least one magnitude higher than that in the longitudinal direction. Overall, this situation could be detrimental to the system under earthquake loading acting in the longitudinal direction. Also, under out-of-plane blast loading or other large impulse, excessive deformation or failure of the pier may occur.

Those observations led to a second concept, which consisted in aligning some of the panels' strong direction in the transverse direction of the bridge, while the rest would have their strong axis aligned with the longitudinal direction of the bridge. This concept has several favorable implications. First, the resulting substructure offers comparable flexural stiffness in both directions, which is desirable under earthquake loads. Second, it may help control torsional response under earthquake loading. Finally, this concept would relieve the overall pressure loads on the bent in a blast event since the surface exposed to the blast wave is reduced. This arrangement would ultimately lead to a system more redundant than the initial one. Figure 4-3 shows the final configuration for Prototype 1. Figure 4-4 shows 3-D renderings of one of the DSCP in the dual DSCP columns. The concrete infill is not shown for clarity.

In terms of design implications, it is necessary to carefully control local and global buckling. Control of local buckling calls for a dense grid of stud connectors between the face plates of the DSCP, such as to keep the aspect ratio (s_x/s_y) within reasonable limits (see Section 3.3.2.3). The dual column configuration helps in control global buckling by sharing axial load between the

twin panels. However, a more systematic way of controlling global buckling would be to provide intermediate bracings that would couple the panels together and reduce the effective length of the DSCP piers in buckling. This coupling could be done so that the dual panels behave synergistically in resisting out of plane load, such as blast overpressures.

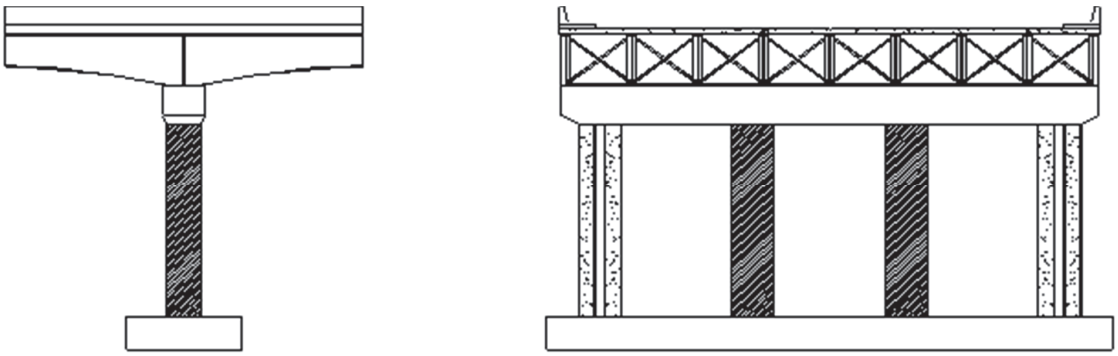

Figure 4-3: Prototype 1 Final Configuration at Pier

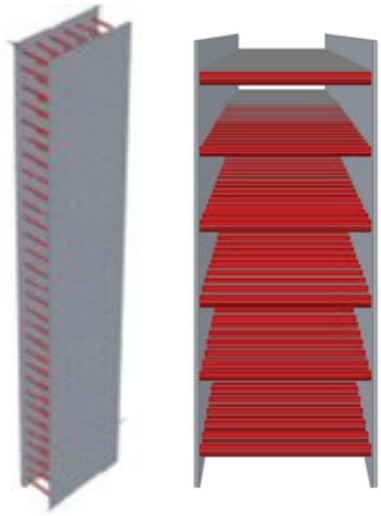

Figure 4-4: DSCP Column Dimensions and Cross Section

The composite superstructure that was used in the original design example was kept the same in this prototype. However, on a related topic, if there was a desire to prevent failure or breaching of the concrete deck or girders due to an above deck explosion (which could lead to superstructure collapse, depending on charge weight), it is noteworthy that DSCP panels could also be used as bridge deck. This solution would require ensuring that sufficient shear continuity is provided between the deck and the steel girders to also achieved composite behavior under gravity loading, which could be done by welding the steel girder to the bottom plates of the panel.

Alternatively, a perforated DSCP could also be used to serve as deck (Figure 4-5). In that case, a regular grid of small diameter holes in the DSCP would be used. The number of holes in the deck could be decided based on the amount of venting of the blast wave required to reduce the loading to a level that would prevent excessive deck damage. The diameter of the holes would also have to be chosen such that they do not interfere with normal traffic. Those holes should also be reinforced using structural pipes having the same diameter as the holes of the panels (Figure 4-6). For applications considering under-deck charges, the holes could be filled with a frangible material that would fail in case overpressure under the deck reaches a certain threshold. This would help relieve pressure and prevent uplift of the deck (to avoid transferring high tensile forces to the bearings or even to the foundation in case an integral pier cap is used). The designer would need however to make sure that the perforated deck has sufficient remaining in-plane stiffness to function as a diaphragm in an earthquake event and transfer the resulting inertia forces to the substructure.

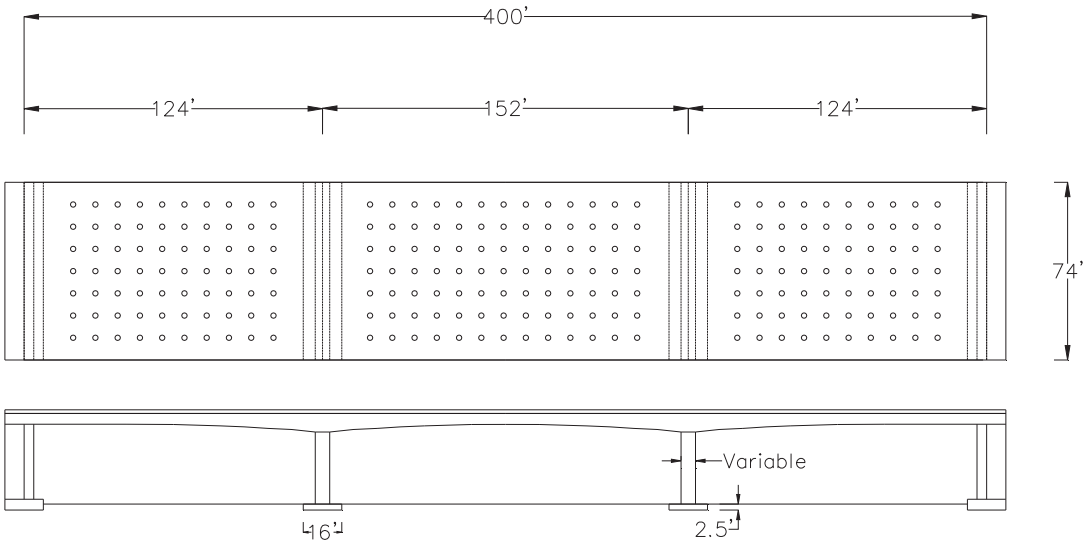

Figure 4-5: Bridge with Perforated Deck (Rolling Surface not Shown)

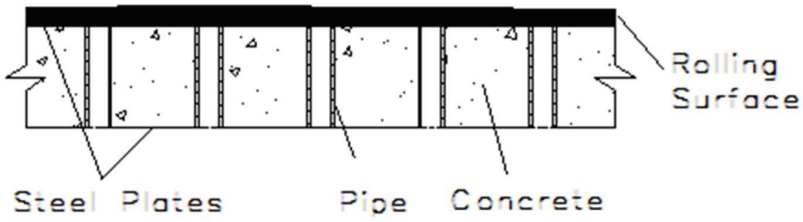

Figure 4-6: Perforated Deck Detail

4.2.2 Prototype 2: Composite Wall Pier

The Prototype 2 considered is a dual DSCP wall pier used build in similar fashion as the dual DSCP column. Such a pier could be fabricated in modules that can be assembled on site. The advantage of this concept over a reinforced concrete wall pier for instance is that it provides

continuous confinement of the concrete as well as higher strength and flexural stiffness in both directions.

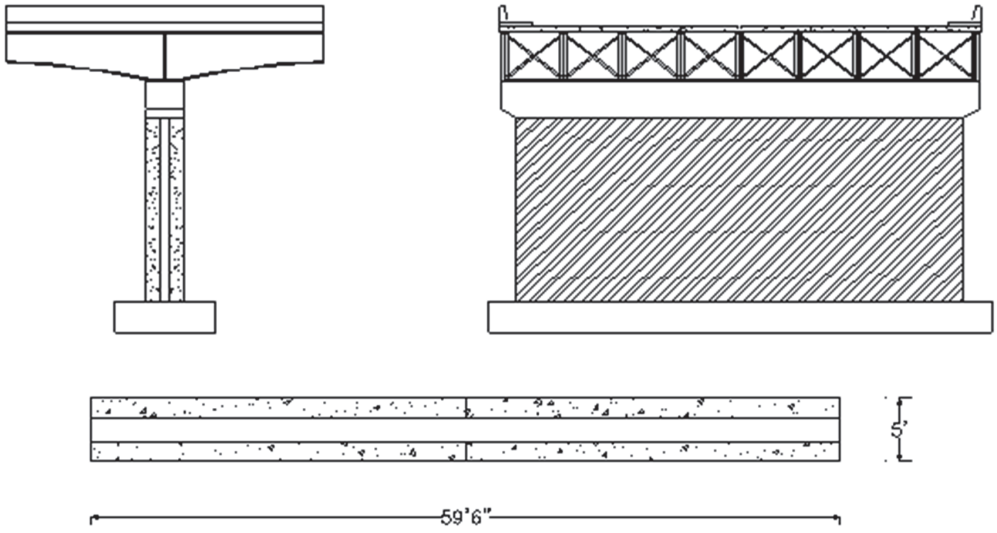

Figure 4-7: Prototype 2 Elevation and Cross Section

For that prototype, connection to the cap and the foundation can be done using composite steel-concrete cap-beam and footings. However, the amount of welding required can become important if the bridge cross section is of sizable dimension. Figure 4-7 presents a cross section view of the system at a pier whereas Figure 4-8 shows a rendering of the wall.

An anticipated deficiency of this system is that in a blast event the exposed area of the substructure would be significant and the pressure build-up would be rather large. As a consequence, significant shear load would be transferred to the foundation, which would then need to be sizeable. Clearing of blast load will also be difficult and result in even higher

reflected overpressures on the wall face in blast event. The blast environment would also become more complex and more difficult to model for that arrangement.

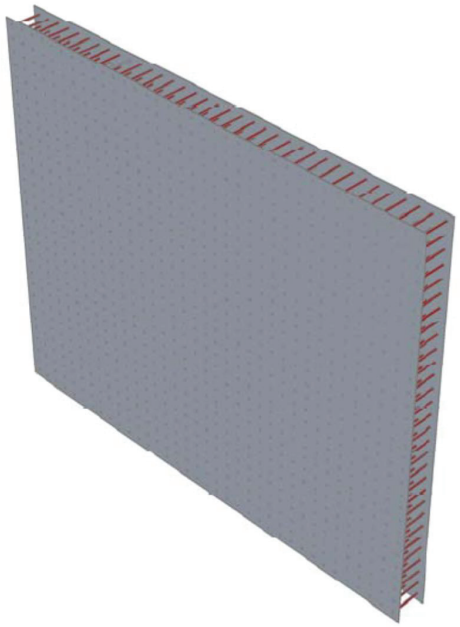

Figure 4-8: Prototype 2 Wall Pier 3-D Rendering

4.2.3 Prototype 3: Multi CFDST-Column Bent

Using CFDST as columns for the piers of Prototype 3 was then considered. This concept offers several advantages. By acting synergistically, the tubes and the concrete core gives higher and consistent flexural strength and stiffness in all direction to the bent, which provide more balanced resistance to earthquake loading and help control deformations of the bridge. The confinement of the concrete core by the tubes improves the overall ductility of the system. This would be an important feature in resisting earthquake and blast loads where large energy dissipation capacity is required. Being stiff, the system has a low-propensity to global instability,

even for cases of CFDST built with steel tubes having high diameter-to-thickness ratios. This feature is desirable to control secondary effects (P-δ and P-Δ) and limit permanent deformations of the system. The resulting pier system and section of the CFDST columns is shown in Figure 4-9 and Figure 4-10, respectively.

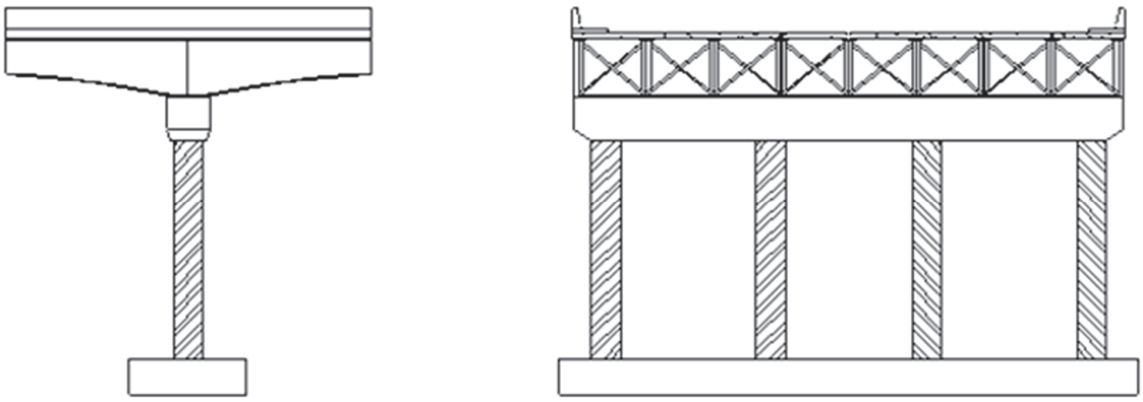

Figure 4-9: Prototype 3

Figure 4-10: Column Section of Prototype 3

4.3 Seismic Loading

The 2007 AASHTO LRFD Provisions were used to establish the seismic load for which the all the prototypes previously presented will be designed. It was assumed that the prototypes bridges were to be built in site class D, at a location for which the mapped spectral accelerations at 1 sec and in the short period range are respectively $S_1=0.5g$ and $S_s=1.5g$, with corresponding site modification factors $F_v=1.3$ and $F_a=1.0$. Those values were used to establish the response spectrum for the maximum credible earthquake at the given site (as described in Section 3.4 of these Provisions). The MCE response spectrum corresponding to those criteria is shown in Figure 4-11. The design response spectrum was directly taken as the MCE spectrum without any reduction. The shaking at the site is representative of a strong earthquake; this choice was

deliberate as the idea was to investigate if the given prototypes could perform satisfactorily under high demands.

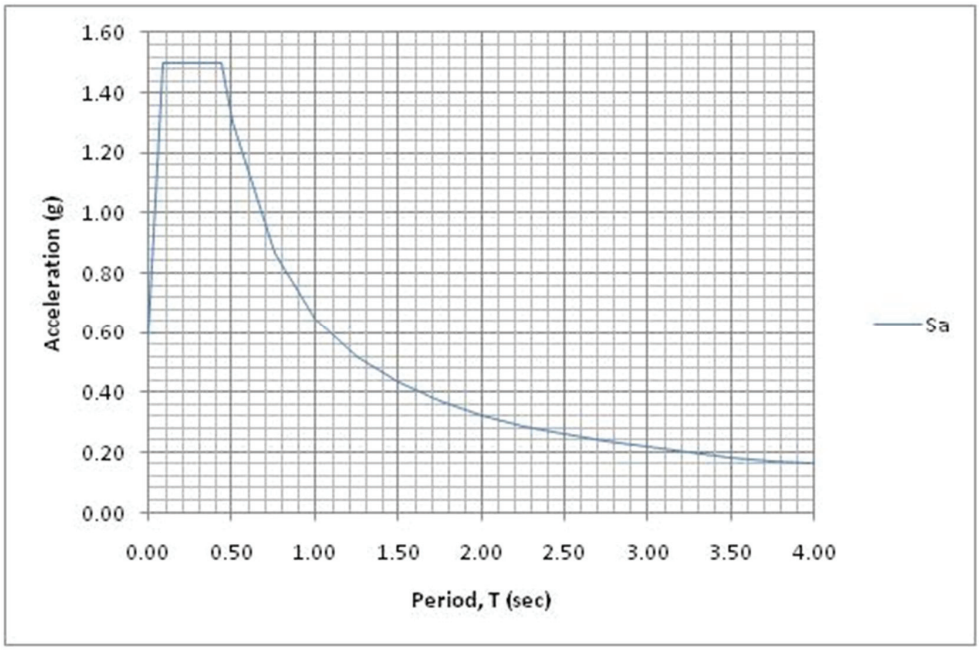

Figure 4-11: MCE Response Spectrum for Prototypes Analysis and Design

4.4 Blast Scenario

No specific code provisions exist to determine the maximum credible terrorist threat that can be placed on a bridge during its life time. This lack can be partly explained by the fact that is difficult to assess the annual rate of occurrence of a blast event caused by a terrorist attack because it depends on socio-political considerations that cannot be modeled as an engineering problem. Nonetheless, looking at the history of terrorist attacks, it can be inferred that three credible course of attacks are possible for bridges of the type considered here. The first consists of a small size bombs (suitcase bomb) at close standoff. The purpose in such an attack would be

to bring down a main load bearing element (pier), in the hope that the destruction of this element could trigger a progressive collapse of the structure. The second consist of a car bomb, of sufficient size to cause widespread damage in a close range attack. Here again, the likely target would be bridge piers. The third is a truck bomb (similar to the one used in the Oklahoma City bombing). Catastrophic damages would be expected for ordinary highway bridges under that blast scenario.

However, for the purposes of this study, a scenario in which a Vehicle Borne Improvised Explosive Device (VBIED) is detonated under the bridge was used. Charge weights consistent with this scenario were used for the analysis. It was assumed that the explosion occurred under the deck near one of the piers. This scenario is schematically represented in Figure 4-12. Following Fujikura et al. (2007), the standoff distance X_p was fixed based on typical highway bridges geometry and the height of burst was established by considering the geometry of a typical sedan car.

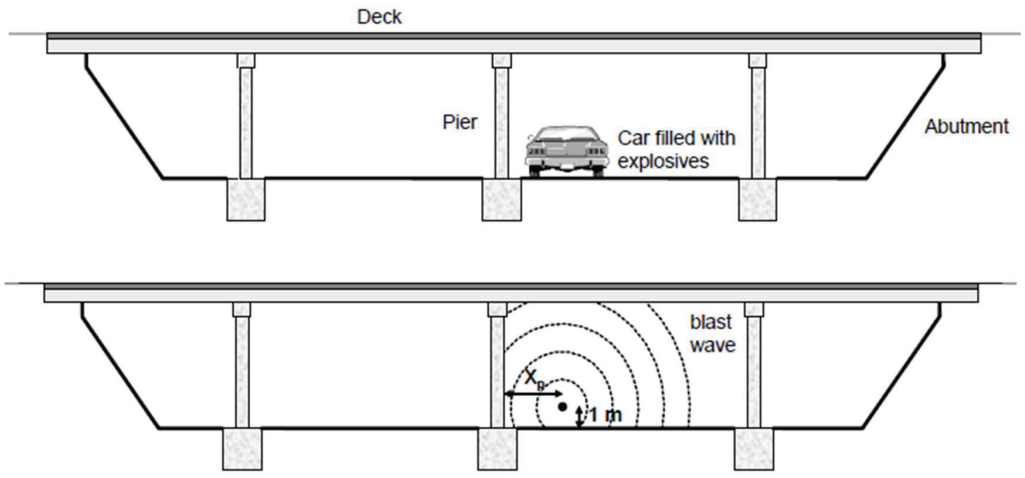

Figure 4-12: Schematics of the Car Bomb Scenario (after Fujikura et al., 2007)

4.5 Seismic Analysis and Design Procedures

For seismic analysis and design purposes, behavior of the bridge under earthquake loading was first considered. In the longitudinal direction, it was assumed that the sliding bearings used at the abutments only allow the bridge to expand and contract freely under the effects of thermal loads. In the transverse direction, girder stops are provided as failsafe mechanisms. Longitudinally, the abutments also provide a failsafe mechanism to prevent the span from dropping off. Based on those considerations the longitudinal and transverse behaviors of the bridge under seismic loading are as shown in Figure 4-13.

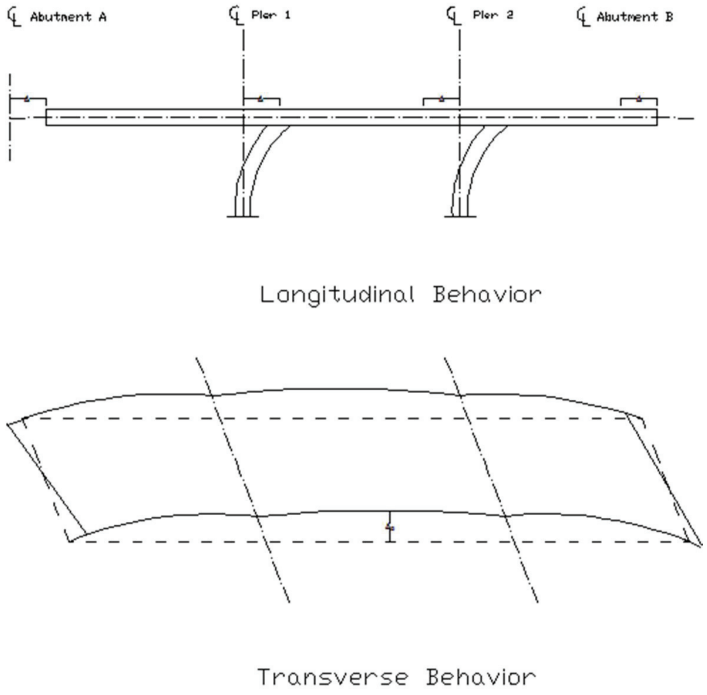

Figure 4-13: Seismic Behavior of the Bridge

Furthermore, for simplicity, it was assumed that in the longitudinal direction, the connection between the pier and the superstructure is simple while in the transverse direction it was assumed fixed, the rigidity being provided in that case by a cap-beam.

In the longitudinal direction, the bridge was analyzed as a generalized SDOF for which the stiffness is provided by the piers and the mass by the superstructure. For a pier element (column or wall) of height, H, and bending stiffness, $(EI)_e$, the lateral stiffness is given by:

$$k_c = \frac{\alpha (EI)_e}{H^3} \tag{4-1}$$

where α is equal to 12 in the fixed-fixed condition and 3 in the fixed-pinned condition. The total stiffness, K_L, of the bridge in that case is dependent upon the number, n, of elements in the piers in the longitudinal direction or:

$$K_L = nk_c \tag{4-2}$$

The total mass, M, of the superstructure is found in the previously referred FHWA design example and is equal to:

$$M = 5540 kip \tag{4-3}$$

As a consequence, the natural period, T, of the bridge in the longitudinal direction can be estimated as:

$$T = 2\pi\sqrt{\frac{M}{K_L}} \tag{4-4}$$

The displacement response, $S_D(T)$, of the bridge if the pier were to remain elastic would be given by:

$$S_D(T) = \frac{T^2 S_A(T)}{4\pi^2} \tag{4-5}$$

where S_A is the corresponding ordinate of the design response spectrum (in that case the MCE's).

The elastic lateral capacity, V_e, of each pier component is given as:

$$V_e = \gamma \frac{M_p}{H} \tag{4-6}$$

where $\gamma = 1$ for a component in a fixed-pinned condition and $\gamma = 2$ otherwise. Also, M_p, is the plastic moment capacity of each column in the pier.

The corresponding displacement capacity of each component is then given as:

$$\Delta_y = \frac{V_e}{k_c} \tag{4-7}$$

Based on the expected seismic behavior in the transverse direction, the deck can be modeled as a flexural member pinned as its ends and intermediately restrained by the pier-bents modeled by a spring of stiffness K_P that depends on the number, *m,* of components per bent (Figure 4-14). K_P can be evaluated as:

$$K_P = mk_c \tag{4-8}$$

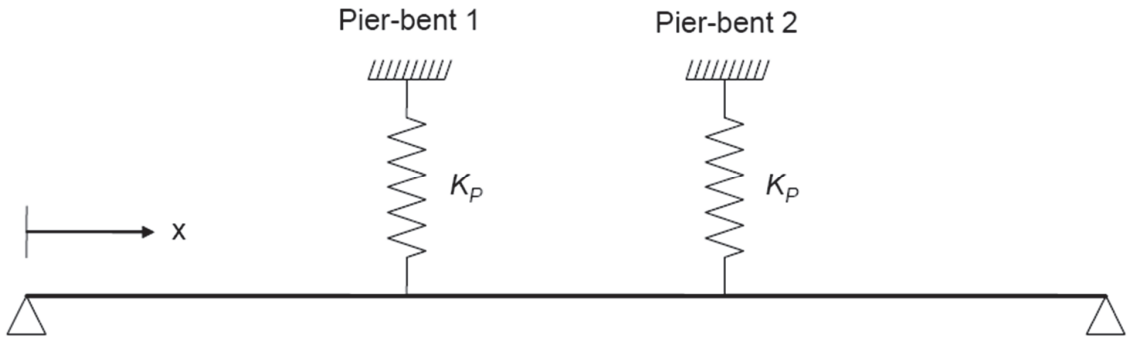

Figure 4-14: Equivalent System for Seismic Analysis in the Transverse Direction

To simplify the analysis even further, it was assumed that the deformed shape of the bridge in the transverse direction under earthquake loading at a position, *x*, along the length, *L*, of the bridge (Figure 4-14) is given by:

$$\varphi(x) = \sin\left(\frac{\pi x}{L}\right) \tag{4-9}$$

Neglecting the contribution of the masses of the piers, a generalized mass, m_e, for the system based on the superstructure was calculated, assuming that superstructure mass is distributed over its length. With a distributed mass $m(x) = m_D$, the generalized mass becomes:

$$m_e = \int_0^L m(x)\left[\varphi(x)\right]^2 dx = \frac{m_D L}{2} = \frac{M}{2} = 2770 kip \tag{4-10}$$

Also a generalized stiffness, k_e, including the superstructure rigidity can be defined as:

$$k_e = \frac{\pi^4 E_S I_D}{2L^3} + K_P\left[\varphi(x_1)\right]^2 + K_P\left[\varphi(x_2)\right]^2 \tag{4-11}$$

where E_s is the elastic modulus of concrete and I_D is the inertia about the vertical axis of the deck expressed as equivalent steel properties, since the superstructure is a composite of steel and

concrete. For the given superstructure, the steel modulus was taken as $E_s = 29000\frac{kip}{in^2}$ and the average equivalent inertia in equivalent steel calculated as $I_D = 2511.1 ft^4$. Also x_1, x_2 are the location ordinates of the piers along the length of the bridge for the origin shown on Figure 4-14. Using the equivalent mass and stiffness, the natural period of the bridge in the transverse direction can be estimated as:

$$T = 2\pi\sqrt{\frac{m_e}{k_e}} \tag{4-12}$$

Using the design response spectrum presented in Figure 4-11, the spectral acceleration S_A can be obatined and the corresponding spectral displacement demand computed using the same equation as for the longitudinal direction. The displacement demand on any pier bent of the bridge can then be estimated as:

$$\Delta_u = \Gamma S_D \varphi(x_1) = \Gamma S_D \varphi(x_2) \tag{4-13}$$

The equality follows because the bridge is symmetric. The participation factor, Γ, is computed as:

$$\Gamma = \frac{\int_0^L m(x)\varphi(x)dx}{m_e} = \frac{4}{\pi} = 1.273 \tag{4-14}$$

For design purposes, it was assumed that the criteria established by Marson and Bruneau for CFT element is applicable to CFDST component. In other words, it was assumed that a CFDST element can develop its full plastic moment capacity whenever the axial load P applied to this element is limited to:

$$P \le \left(1 - \frac{P_{ro} - P_{rc}}{P_{rc}}\right) P_r \tag{4-15}$$

Otherwise, the P-M interaction would need to be considered, with:

$$\frac{P}{P_r} + \frac{P_{ro} - P_{rc}}{P_{rc}} \frac{M}{M_p} \le 1 \tag{4-16}$$

and the additional requirement that:

$$\frac{M}{M_p} \le 1 \tag{4-17}$$

In the previous equations, for a given CFDST component, P_{ro} represents its reduced axial capacity, P_{rc} is the contribution of the concrete to its axial strength, and P_r is its nominal compressive strength (Euler buckling strength).

Furthermore it was assumed that no local instability occurs before the element develops its full moment capacity. To insure this, shear studs connectors are assumed to be used at a reasonable spacing in the DSCP Panel to limit the aspect ratio of the components to within acceptable values (for which those components are deemed compact). For CFDST, the approach consisted in providing diameter to-thickness ratios less than (or marginally exceeding) the limits provided in the AISC provisions for concrete filled sections.

4.6 Blast Analysis and Design Procedures

The blast analysis and design followed the method suggested by Fujikura and Bruneau (2007) for blast resistant analysis and design of CFT columns. Since most bridge structure components respond in the impulsive regime, Fujikura and Bruneau suggested a simplified analysis that

couples an impulse momentum approach and a SDOF analysis. The flow chart below summarizes the main steps of this approach, which are described below and commented in the context of this study.

Step 1 of this procedure calls for the determination of blast scenario, which is generally established through a risk assessment procedure. For the purpose of this study, 3 blast scenarios were analyzed to cover a wide range of possible attacks.

Step 2 consists in establishing the corresponding external loading, using the following three sub-steps that consists in:

(1) Calculating the distribution of peak impulse, $i(z)$, and peak pressure, $p(z)$, along the column height using one of the commonly used blast prediction tools

(2) Selecting a plastic deformation shape for the column, $\delta(z)$, assuming that the maximum deformation occurs at the blast height, and assuming a rigid plastic material behavior. For the blast analysis presented here, the deformed shape used in analysis is dependent on the height of burst, x, the position, z, along the column and the height, H, of the component. It can be generally expressed as.

$$\delta(z) = \begin{cases} \dfrac{z}{x} & \text{for } 0 \le z < x \\ \dfrac{H-z}{H-x} & \text{for } x \le z \le H \end{cases} \tag{4-18}$$

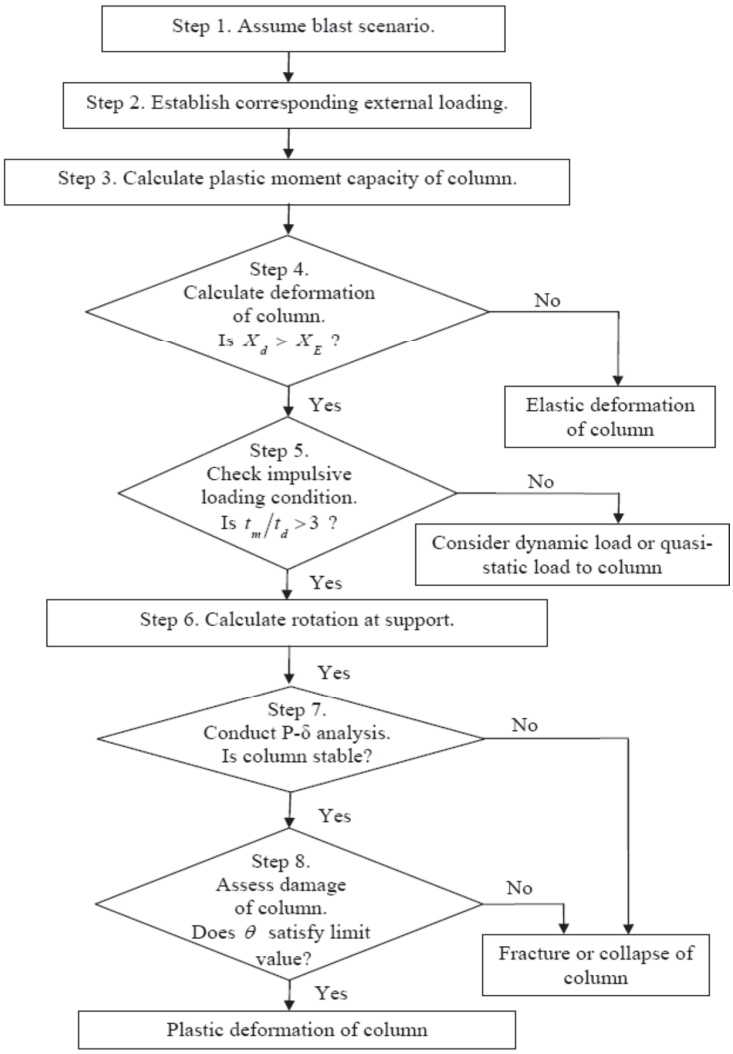

Figure 4-15: Flow Chart for Blast Resistant Design of CFST Columns

(3) Calculating the equivalent loading- peak equivalent pressure, $p_{eq}(z)$, and peak equivalent impulse $i_{eq}(z)$- by:

$$p_{eq}(z) = \frac{\int_0^H p(z)\delta(z)dz}{\int_0^H \delta(z)dz} \tag{4-19}$$

$$i_{eq}(z) = \frac{\int_0^H i(z)\delta(z)dz}{\int_0^H \delta(z)dz} \tag{4-20}$$

Step 3 consists in the computation of the plastic moment capacity of the column cross section. The methods presented in Section 3 for the computation of the strength of double-skin composite construction were used to carry out this computation.

Step 4 is the computation of the deformation demand on the element. This step is one of the most critical one and includes several sub-steps including:

(1) The computation of the equivalent flexural stiffness, $(EI)_{eff}$

(2) The evaluation of the equivalent elastic stiffness, K_E.

(3) The selection of the load mass factor, K_{LM}.

(4) The determination of the mass per unit length of the component, m.

(5) The computation of the ultimate resistance per unit length, r_u,

(6) The computation of the elastic deflection at yielding, X_E by:

$$X_E = \frac{r_u}{K_E} \tag{4-21}$$

(7) The calculation of the effective impulse per unit length, I_{eq}, by:

$$I_{eq} = \beta D i_{eq} \tag{4-22}$$

In the above equation, $\beta = 1$ if no reduction in pressure due to clearing is expected on the component. This is likely the case for a rectangular panel of significant size, like a wall pier. However for circular cross-section, Fujikura et al (2007) recommended a value of 0.45.

(8) The computation of the maximum elastic deformation, X_m, by:

$$X_m = \frac{1}{2}\left(\frac{I_{eq}^2}{K_{LM} m r_u} + X_E \right) \tag{4-23}$$

Step 5 of the method is one of the several checks that the method calls for. Focus here is to verify the initial assumption that the loading was impulsive. In this check, t_d is the duration of the blast load, and t_m the time at which the component reaches its maximum deformation, respectively given by:

$$t_m = \frac{I_{eq}}{r_u} \tag{4-24}$$

$$t_d = 2\frac{i_{eq}}{p_{eq}} \tag{4-25}$$

Steps 6 to 8 are additional checks to ensure that the deformation of each component is within acceptable values and that it is stable under gravity load in its final deformed configuration. Because not much information is available on the plastic rotation capacity of double skin composite construction, it was believed conservative here to use, as a preliminary estimate, the maximum rotation of 0.07 radians reported by Marson and Bruneau (2000) for CFST.

4.7 Seismic Analysis Results

Seismic analyses on the three different prototypes considered were carried out. In all cases, nominal material strength of 50ksi was used for all plates and tubes, together with a concrete strength of 4 ksi.

4.7.1 Prototype 1: Multi- DSCP Column Bent

Two configurations of panels were considered in this preliminary analysis. In one, the axes of the twin panels steel faces were oriented along the transverse direction of the bridge. In the other case, the panels were oriented as showed on Figure 4-3.

In the first configuration, panel widths of 30in (450mm) to 48 in (1200mm) where considered. The thickness of the concrete core and hence of each composite column was also varied. The analysis was done considering 1/2 in thick plates. Results in the longitudinal direction show that the ductility demand is extremely high; failure of the system as designed is likely in this configuration. In fact, considering the aforementioned expected rotation capacity at the base of a DSCP to be on the order of 0.07 radians, the corresponding maximum deformation capacity of the system in the longitudinal direction would be around 16.8in (420mm), which is well below the calculated deformations, S_d, in Table 4-1 for the longitudinal direction. Increasing the composite column thickness as a way to increase stiffness does not provide any significant improvement. Conversely, Table 4-2 shows that in the transverse direction the ductility demand is within reasonable limits. In both directions, however, resistance to the applied loadings is not an issue. So the system lacks ductility in its out-of-plane direction, but not strength.

For the second configuration, the arrangement of the panels was as discussed at the end of Section 4.2.1. Analysis in the longitudinal bridge direction showed significant improvement in terms of ductility demand compared to the previous one (Table 4-3). In this configuration, better distribution of stiffness in each direction is achieved.

Table 4-1: Preliminary Seismic Analysis in the Longitudinal Direction

b[in]	t[in]	h_c[in]	$(EI)_e$ [kip-in^2]	k_c [kip/in]	T[sec]	S_d[in]	Δ_y[in]	S_d/Δ_y
48	1/2	12	8.276E+07	5.32	5.15	32.69	0.65	50.11
42	1/2	16	1.148E+08	7.38	4.38	27.75	0.54	51.10
36	1/2	20	1.470E+08	9.45	3.87	24.53	0.45	54.29
30	1/2	24	1.733E+08	11.15	3.56	22.59	0.38	59.20

Table 4-2: Preliminary Seismic Analysis in the Transverse Direction

b[in]	t[in]	h_c[in]	$(EI)_e$ [kip-in^2]	k_c [kip/in]	T[sec]	S_d[in]	Δ_y[in]	S_d/Δ_y
48	1/2	12	4.02E+08	103.52	0.55	3.99	1.99	2.01
42	1/2	16	2.90E+08	74.59	0.57	4.35	2.21	1.87
36	1/2	20	1.94E+08	49.90	0.59	4.72	2.53	1.77
30	1/2	24	1.18E+08	30.41	0.62	5.05	2.97	1.62

Table 4-3: Analysis in the Longitudinal Direction for the Second Configuration

b[in]	t[in]	h_c[in]	$(EI)_e$ [kip-in^2]	k_c [kip/in]	T[sec]	S_d[in]	Δ_y[in]	S_d/Δ_y
48	1/2	12	4.02E+08	103.52	1.17	7.41	1.99	3.73
42	1/2	16	2.90E+08	74.59	1.38	8.73	2.21	3.94
36	1/2	20	1.94E+08	49.90	1.68	10.68	2.53	4.22
30	1/2	24	1.18E+08	30.41	2.16	13.68	2.97	4.60

4.7.2 Prototype 2: Composite Wall Pier

Designs with plates up to ½ in (12.7mm) thick were considered in the longitudinal direction (Table 4-4). Composite wall thickness of 12 in (300mm) to 24 in (600m) was considered for that plate thickness. However, even for such a thick plate, the ductility demand (S_d /Δ_y) in the longitudinal direction was rather high, being well above 12. As the width (*b*) of the wall was increased, the ductility demand reduced, but only slowly. This means that the design is not particularly sensitive to increase in the width of the section; consequently, an increase in plate thickness (*t*) or concrete core thickness (h_c) would be required. As anticipated this system is significantly stiff in the transverse direction and its ductility demand low (Table 4-5). Failure of such a system would more likely be caused by large ductility demands in the longitudinal direction.

Table 4-4: Preliminary Seismic Analysis in the Longitudinal Direction

b[in]	t[in]	h_c[in]	$(EI)_e$ [kip-in^2]	k_c [kip/in]	T[sec]	S_d[in]	Δ_y[in]	S_d/Δ_y
648	1/2	12	1.12E+09	71.84	1.40	8.90	0.65	13.64
648	1/2	16	1.77E+09	113.93	1.11	7.07	0.54	13.01
648	1/2	20	2.65E+09	170.14	0.91	5.78	0.45	12.80
648	1/2	24	3.74E+09	240.75	0.77	4.86	0.38	12.74

Table 4-5: Preliminary Seismic Analysis in the Transverse Direction

b[in]	t[in]	h_c[in]	$(EI)_e$ [kip-in^2]	k_c [kip/in]	T[sec]	S_d[in]	Δ_y[in]	S_d/Δ_y
648	1/16	10	9.90E+11	254694.45	0.02	0.003	0.15	0.02
648	3/16	10	1.07E+12	273932.65	0.02	0.003	0.14	0.02
648	4/16	10	1.13E+12	291004.31	0.02	0.003	0.14	0.02
648	5/16	10	1.19E+12	306453.22	0.02	0.003	0.14	0.02

4.7.3 Prototype 3: Multi CFDST Column Bent

For the CFDST column bent, diameter (D_o) of the outside tube was based on typical reinforced concrete column dimensions found in highway bridges. The diameter (D_i) of the inner tubes was chosen to achieve a void ratio (χ) making the design reasonably economical. Since not much was known yet about the system behavior of CFDST at this point, it was judged conservative to keep the void ratio to under 75%.

The ductility demands obtained after analysis in the longitudinal direction (Table 4-6) were found to remain well acceptable limits. Such limits were established first based on the fact that Lin and Tsai (2003) showed CFDST columns to have at least as good flexural ductility as CFST columns, and on the maximum CFST rotation capacity of 0.07 radians reported by Marson and Bruneau for cantilevered columns. This corresponds to maximum lateral displacement of 16.8in (426.7mm) for a 20ft high bridge. This indicates that CFDST Sections 1, 13 and 14 listed in the table would be over this limit, while 4 and 5 are close to the point of incipient failure. All other sections in that table would be acceptable.

The ductility demands in the transverse direction for most of the sections are well below those in the longitudinal direction (Table 4-7). If fact, for that direction, ductility demands were over unity (meaning inelastic response) for only 6 of the 14 CFDST columns in this pier prototype. Because of the similitude between the CFDST columns used in this prototype and CFST columns, it was deemed useful to compare the results obtained here with those that would have been obtained if CFST columns were used instead (Table 4-8 and Table 4-9). This comparison revealed that predicted behaviors of the CFDST columns in the longitudinal and transverse directions were fairly similar to CFST columns with comparable strengths.

Table 4-6: Preliminary Seismic Analysis in the Longitudinal Direction

CFDST	D_o[in]	D_i[in]	t_o[in]	t_i[in]	χ	M_p [kip-ft]	$(EI)_e$ [kip-in^2]	k_c [kip/in]	T[sec]	S_d[in]	Δ_y[in]	S_d/Δ_y
1	24	8	5/16	7/16	0.33	1115.95	8.99E+07	19.52	2.69	17.12	2.86	5.99
2	32	8	7/16	1/2	0.25	2590.90	2.84E+08	61.71	1.51	9.63	2.10	4.59
3	32	20	7/16	3/8	0.63	2991.78	3.09E+08	67.15	1.45	9.23	2.23	4.14
4	24	8	1/2	5/16	0.33	1537.72	1.16E+08	25.20	2.37	15.07	3.05	4.94
5	24	10	5/16	1/2	0.42	1210.57	9.36E+07	20.31	2.64	16.78	2.98	5.63
6	26.5	10	9/16	7/16	0.38	2180.15	1.78E+08	38.53	1.92	12.19	2.83	4.31
7	32	16	5/16	1/2	0.50	2401.94	2.61E+08	56.62	1.58	10.05	2.12	4.74
8	24	10	1/2	1/2	0.42	1675.02	1.21E+08	26.24	2.32	14.77	3.19	4.63
9	26.5	10	1/2	1/2	0.38	2023.55	1.67E+08	36.15	1.98	12.58	2.80	4.50
10	32	16	3/4	1/2	0.50	2861.67	4.12E+08	89.30	1.26	8.00	2.43	3.30
11	32	20	3/4	1/2	0.63	2861.67	4.17E+08	90.54	1.25	7.95	2.53	3.14
12	36	24	1/2	1/2	0.67	4598.94	5.18E+08	112.45	1.12	7.13	2.04	3.49
13	24	18	1/4	1/4	0.75	1107.28	8.65E+07	18.77	2.74	17.46	2.95	5.92
14	18	12	1/4	1/4	0.67	574.87	3.24E+07	7.03	4.48	28.53	4.09	6.98

Table 4-7: Preliminary Seismic Analysis in the Transverse Direction

CFDST	D_o[in]	D_i[in]	t_o[in]	t_i[in]	χ	M_p [kip-ft]	$(EI)_e$ [kip-in^2]	k_e [kip/in]	T[sec]	S_d[in]	Δ_y[in]	S_d/Δ_y
1	24	8	5/16	7/16	0.33	1115.95	8.99E+07	78.08	0.37	2.13	1.43	1.49
2	32	8	7/16	1/2	0.25	2590.90	2.84E+08	246.82	0.22	0.76	1.05	0.72
3	32	20	7/16	3/8	0.63	2991.78	3.09E+08	268.61	0.21	0.70	1.11	0.63
4	24	8	1/2	5/16	0.33	1537.72	1.16E+08	100.78	0.33	1.71	1.53	1.12
5	24	10	5/16	1/2	0.42	1210.57	9.36E+07	81.24	0.37	2.06	1.49	1.38
6	26.5	10	9/16	7/16	0.38	2180.15	1.78E+08	154.12	0.28	1.17	1.41	0.83
7	32	16	5/16	1/2	0.50	2401.94	2.61E+08	226.48	0.23	0.82	1.06	0.78
8	24	10	1/2	1/2	0.42	1675.02	1.21E+08	104.95	0.33	1.65	1.60	1.04
9	26.5	10	1/2	1/2	0.38	2023.55	1.67E+08	144.60	0.28	1.24	1.40	0.89
10	32	16	3/4	1/2	0.50	2861.67	4.12E+08	357.21	0.19	0.53	1.21	0.44
11	32	20	3/4	1/2	0.63	2861.67	4.17E+08	362.14	0.18	0.53	1.27	0.42
12	36	24	1/2	1/2	0.67	4598.94	5.18E+08	449.79	0.17	0.43	1.02	0.42
13	24	18	1/4	1/4	0.75	1107.28	8.65E+07	75.08	0.38	2.20	1.47	1.49
14	18	12	1/4	1/4	0.67	574.87	3.24E+07	28.11	0.54	3.64	2.04	1.78

Table 4-8: Preliminary Seismic Analysis in the Longitudinal Direction for CFST

CFST	D_o[in]	t[in]	M_p [kip-ft]	$(EI)_e$ [kip-in^2]	k_c [kip/in]	T[sec]	S_d[in]	Δ_y[in]	S_d/Δ_y
1	24	5/16	917.99	8.51E+07	18.47	2.77	17.60	2.49	7.08
2	32	7/16	2275.07	2.76E+08	59.97	1.54	9.77	1.90	5.15
3	24	1/2	1410.05	1.12E+08	24.39	2.41	15.32	2.89	5.30
4	26.5	9/16	1930.924	1.69E+08	36.68	1.96	12.49	2.63	4.74
5	32	5/16	1673.16	2.32E+08	50.24	1.68	10.67	1.67	6.41
6	26.5	1/2	1733.80	1.57E+08	34.08	2.04	12.96	2.54	5.09
7	32	3/4	2861.67	3.83E+08	83.05	1.30	8.30	1.72	4.82
8	36	1/2	3286.19	4.47E+08	96.92	1.21	7.68	1.70	4.53
9	24	1/4	748.76	7.56E+07	16.42	2.93	18.67	2.28	8.19
10	18	1/4	410.77	2.79E+07	6.06	4.83	30.73	3.39	9.06

Table 4-9: Preliminary Seismic Analysis in the Transverse Direction of CFST

CFST	D_o[in]	t[in]	M_p [kip-ft]	$(EI)_e$ [kip-in^2]	k_c [kip/in]	T[sec]	S_d[in]	Δ_y[in]	S_d/Δ_y
1	24	5/16	917.99	8.51E+07	73.88	0.38	2.23	1.24	1.79
2	32	7/16	2275.07	2.76E+08	239.90	0.22	0.78	0.95	0.82
3	24	1/2	1410.05	1.12E+08	97.54	0.34	1.76	1.45	1.22
4	26.5	9/16	1930.924	1.69E+08	146.70	0.28	1.23	1.32	0.93
5	32	5/16	1673.16	2.32E+08	200.98	0.24	0.92	0.83	1.10
6	26.5	1/2	1733.80	1.57E+08	136.34	0.29	1.31	1.27	1.03
7	32	3/4	2861.67	3.83E+08	332.22	0.19	0.57	0.86	0.66
8	36	1/2	3286.19	4.47E+08	387.68	0.18	0.49	0.85	0.58
9	24	1/4	748.76	7.56E+07	65.67	0.40	2.45	1.14	2.15
10	18	1/4	410.77	2.79E+07	24.23	0.57	3.81	1.70	2.25

4.7.4 Blast Analysis Results

Since prototypes 1 and 2 failed to provide satisfactory results under seismic loading in the longitudinal direction, they were not investigated further for blast loading. Prototype 3 has been analyzed for blast loading under the credible blast scenario described in Section 4.4. For this scenario the charge weight is designated by W_p. The actual charge value is not listed here as it is widely accepted that, for research involving blast load, the charge load be not disclosed to limit the availability of this information for ill-intentioned individuals. Two other analyses for charge weights of $0.5W_p$ and $2.5W_p$ were also performed. Results are shown in Table 4-10 to Table 4-12. Analysis of the ratio of the time of maximum response to the duration of the blast showed that impulsive loading regime as assumed for the analysis prevailed.

For the credible blast scenario (Table 4-11), preliminary analyses predict that all CFDST section designed for seismic loading would also perform well under the credible blast scenario. Considering that CFSTs were found to be able to develop (safe) plastic section rotation at support of up to 0.2 rad, similarities between CFST and CFDST would also warrant the assumption that the later can develop as large a support rotation. For the given blast scenario this would correspond to a lateral deformation capacity of up to 8in (200mm). Under this assumption all specimens are predicted to behave satisfactorily under the credible blast scenario. As the charge weight is increased up to $2.5W_p$ to push the designed sections to failure (Table 4-12) specimens 1, 13 and 14 which were predicted to fail under the MCE would also fail under the considered credible blast scenario. Also specimen 4 and 5 which under seismic loading was close to the point of incipient failure (Table 4-6) failed under that scenario. All other specimens, as for the seismic load case, would still perform satisfactorily. These indicates, that even when the later

CFDST sections were not explicitly designed for blast loading, blast protection would still be achieved (bundling effects) and vice versa.

Table 4-10: Preliminary Blast Analysis (Charge Weight 0.5W_p lbs @4ft)

CFDST	$(EI)_e$ [kip-in^2]	p_{eq} [psi]	i_{eq} [psi-ms]	X_e[in]	X_m[in]	M_p [kip-ft]	t_d (ms)	t_m (ms)	t_m/t_d
1	9.08E+07	7353	2146	3.11E-03	0.68	917.99	0.58	3.85	6.59
2	2.99E+08	7160	2128	2.19E-03	0.28	2275.07	0.59	2.19	3.68
3	2.45E+08	7160	2128	3.09E-03	0.33	1410.05	0.59	1.90	3.19
4	1.15E+08	7353	2146	3.38E-03	0.47	1930.924	0.58	2.79	4.78
5	8.72E+07	7353	2146	3.52E-03	0.64	1673.16	0.58	3.55	6.07
6	1.70E+08	7297	2140	3.24E-03	0.33	1733.80	0.59	2.17	3.70
7	2.32E+08	7160	2128	2.62E-03	0.36	2861.67	0.59	2.36	3.97
8	1.11E+08	7353	2146	3.83E-03	0.44	3286.19	0.58	2.56	4.39
9	1.59E+08	7297	2140	3.22E-03	0.36	748.76	0.59	2.34	3.98
10	3.64E+08	7160	2128	1.99E-03	0.27	410.77	0.59	1.98	3.34
11	3.28E+08	7160	2128	2.21E-03	0.30	917.99	0.59	1.98	3.34
12	3.62E+08	7049	2117	3.22E-03	0.22	2275.07	0.60	1.38	2.30
13	5.32E+07	7353	2146	5.27E-03	1.18	1410.05	0.58	3.88	6.64
14	2.26E+07	7460	2150	6.43E-03	1.79	1930.924	0.58	5.61	9.73

Table 4-11: Preliminary Blast Analysis (Charge Weight W_p lbs @4ft)

CFDST	$(EI)_e$ [kip-in^2]	p_{eq} [psi]	i_{eq} [psi-ms]	X_e[in]	X_m [in]	M_p [kip-ft]	t_d (ms)	t_m (ms)	t_m/t_d
1	9.08E+07	12150	3952	3.11E-03	2.30	917.99	0.65	7.08	10.89
2	2.99E+08	11850	3913	2.19E-03	0.95	2275.07	0.66	4.03	6.10
3	2.45E+08	11850	3913	3.09E-03	1.10	1410.05	0.66	3.49	5.28
4	1.15E+08	12150	3952	3.38E-03	1.60	1930.924	0.65	5.14	7.90
5	8.72E+07	12150	3952	3.52E-03	2.18	1673.16	0.65	6.53	10.04
6	1.70E+08	12070	3937	3.24E-03	1.12	1733.80	0.65	3.99	6.11
7	2.32E+08	11850	3913	2.62E-03	1.21	2861.67	0.66	4.34	6.58
8	1.11E+08	12150	3952	3.83E-03	1.48	3286.19	0.65	4.72	7.25
9	1.59E+08	12070	3937	3.22E-03	1.22	748.76	0.65	4.30	6.59
10	3.64E+08	11850	3913	1.99E-03	0.90	410.77	0.66	3.65	5.52
11	3.28E+08	11850	3913	2.21E-03	1.01	917.99	0.66	3.65	5.52
12	3.62E+08	11710	3892	3.22E-03	0.74	2275.07	0.66	2.54	3.82
13	5.32E+07	12150	3952	5.27E-03	3.98	1410.05	0.65	7.14	10.97
14	2.26E+07	12300	3965	6.43E-03	6.09	1930.924	0.64	10.35	16.05

Table 4-12: Preliminary Blast Analysis (Charge Weight 2.5 W_p lbs @4ft)

CFDST	$(EI)_e$ [kip-in^2]	p_{eq} [psi]	i_{eq} [psi-ms]	X_e[in]	X_m [in]	M_p [kip-ft]	t_d (ms)	t_m (ms)	t_m/t_d
1	9.08E+07	19060	9092	3.11E-03	12.19	917.99	0.95	16.29	17.08
2	2.99E+08	18730	8985	2.19E-03	5.01	2275.07	0.96	9.25	9.64
3	2.45E+08	18730	8985	3.09E-03	5.82	1410.05	0.96	8.01	8.35
4	1.15E+08	19060	9092	3.38E-03	8.47	1930.924	0.95	11.83	12.39
5	8.72E+07	19060	9092	3.52E-03	11.54	1673.16	0.95	15.02	15.74
6	1.70E+08	18950	9051	3.24E-03	5.93	1733.80	0.96	9.17	9.60
7	2.32E+08	18730	8985	2.62E-03	6.39	2861.67	0.96	9.98	10.40
8	1.11E+08	19060	9092	3.83E-03	7.81	3286.19	0.95	10.86	11.38
9	1.59E+08	18950	9051	3.22E-03	6.45	748.76	0.96	9.88	10.34
10	3.64E+08	18730	8985	1.99E-03	4.73	410.77	0.96	8.37	8.73
11	3.28E+08	18730	8985	2.21E-03	5.30	917.99	0.96	8.37	8.73
12	3.62E+08	18850	8931	3.22E-03	3.86	2275.07	0.95	5.83	6.15
13	5.32E+07	19060	9092	5.27E-03	21.05	1410.05	0.95	16.42	17.21
14	2.26E+07	19210	9131	6.43E-03	32.31	1930.924	0.95	23.83	25.06

SECTION 5

FINITE ELEMENT ANALYSIS OF CONCRETE FILLED AND CONCRETE FILLED DOUBLE SKIN TUBES

5.1 General

This section investigates the effectiveness of advanced finite element to replicate and predict the multi-hazard performance of cylindrical Concrete Filled Steel Tube (CFST) and Concrete Filled Double Skinned Tube (CFDST) sections used as bridge piers. The primary focus is on seismic cyclic inelastic resistance and performance in close range blast loading. This focus on multi-hazard performance is motivated by the emerging philosophy in bridge engineering that favors cost-effective systems that can provide sufficient performance against each hazard for bridges erected in environments where they can be exposed to multiple hazards.

The finite element package LS-DYNA is used to carry out this multi-hazard analysis. This section presents a brief overview of the CFDST concept and its attributes, followed by the results of analyses conducted to reproduce the experimental behavior obtained for CFSTs under loadings similar to what can occur in earthquake and blast hazards respectively (Marson and Bruneau, 2000; Fujikura and Bruneau, 2007). This step is necessary to verify and validate the LS-DYNA models used to carry the complex inelastic analysis this entails. Following that step, CFDST sections with various diameter-to-thickness ratios and having approximately the same areas of steel and concrete as the cross-sections used in those previous studies are modeled in LS-DYNA to assess their performance in that bi-hazard framework

5.2 CFDST: Description and Summary of Features

Cylindrical Concrete Filled Double Skinned Tube (CFDST thereafter) is a type of steel-concrete-steel "sandwich" section formed by two concentric steel tubes separated by a concrete filler, as shown in Figure 5-1. That configuration seeks to draw upon the benefits in strength, toughness and stiffness derived for steel-sandwich construction by placing the steel at the periphery of a filler material (as described, for example, in Montague 1975).

Due to the cylindrical shape of this sandwich construction, a void exists in its center. This allows the resulting cross section to concentrate materials where needed for optimal performance; the outside skin at the periphery of the section provides strength and stiffness, the inside skin enhances ductility, and the concrete in between provides strength as well as local and overall stability to the system. Also, because of the obvious similarities with concrete-filled tubes (CFSTs), the concrete core is expected to be confined by the tubes and provides, in return, support to the tube skins against local buckling. That synergy between the tubes and the core in resisting load is expected to result in a section with good structural and energy dissipation qualities. Furthermore, for the same structural strength, CFDSTs use fewer materials; hence have a lesser mass, which is desirable in an earthquake. They also result in slimmer columns with lesser surface to be exposed to blast overpressures, which is again desirable.

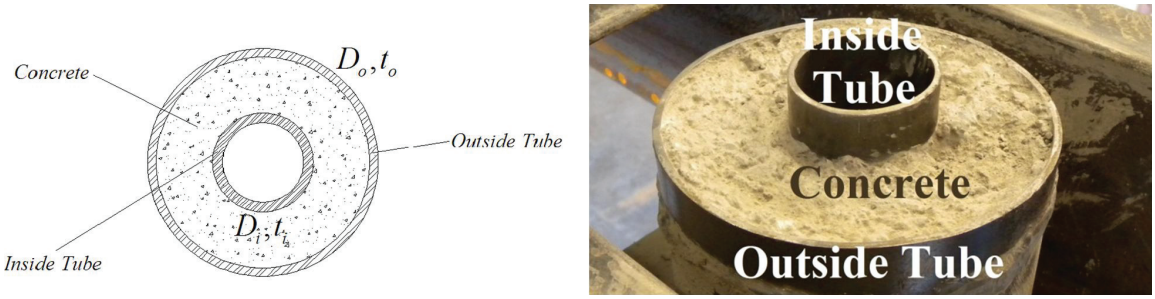

Figure 5-1: Concrete Filled Double Skin Tube

Overall, a more redundant section results, as three layers of materials have to fail before complete failure. Also since the concrete is encased between the two steel tubes, it is confined and held by the steel profiles from which it cannot easily split away even if the ultimate concrete strength is reached. This helps conserve the integrity of the core and the stability of the section even when the core is submitted to shock load that are known to provoke mechanical failures such as scabbing and spalling in applications in which reinforced concrete members are subjected to blast load.

The geometry of the section is particularly suited for blast applications as it favors evasion of the blast pressure. In fact, since the section is round, standoffs and angles of incidence increase as the pressure wave moves around the circumference of the section. This results in a drop in reflected pressures along the exposed surface of a CFDST column and a subsequent reduction in impulse. Also the cylindrical shape and the smoothness of the section means that it has a lower drag coefficient which helps keep dynamic and stagnation pressures at lower levels than on other flat surface and reduce the time duration of the pressure loading.

When no mechanical means such as shear studs are used to create composite action between steel and concrete, tests by Lu and Kennedy (1994) on square concrete filled tube have established that the load transfer from steel tube to concrete for this construction is solely by friction and adhesion. Since no sudden increase in strains or drop in the moment curvature curve of concrete filled tube specimens was observed during tests, they concluded that no slippage or loss of bond occurred during testing. This emphasizes the significance of the binding action arising from longitudinal curvature. Further tests conducted by Kilpatrick and Rangan (1997) on non-compact circular tubes filled with high strength concrete under 3- or 4-point bending showed that the bond between concrete and the steel tube has little effect on the strength of CFST under flexure. Therefore, perfect bond between concrete and steel tube is assumed for CFST under flexure. Again, because of the obvious similarities between CFST and CFDST, and because no mechanical shear connectors is used at the time in CFDST, comparable behavior is expected of CFDST.

5.3 Finite Element Analysis of CFSTs and CFDSTs

Baseline studies were carried out on CFDST using advanced finite elements methods. In these studies, CFDSTs were designed to use the same amount of materials as the concrete-filled steel tubes (CFST) specimens previously tested by Marson and Bruneau (2000) and Bruneau and Fujikura (2007). Because of the highly non-linear behaviors anticipated in analyzing CFSTs and CFDSTs in this multi-hazard framework, the advanced finite element analysis package LS-DYNA was chosen as an analysis tool. Both the implicit and the explicit solvers in LS-DYNA were used.

5.3.1 Specimens Selection

The CFST specimens selected for this analysis are found in the works by Marson and Bruneau and Fujikura and Bruneau mentioned earlier. The former tested four specimens of concrete-filled tubes with various diameters (D), thickness (t), steel and concrete strengths (F_y and $f_c^{'}$) but with constant height (H) under cyclic displacement combined to various levels of axial loads (P). The later conducted blast experiments on ten quarter scale models of concrete-filled tube pier-columns with various charge weights (W) at variable heights (Z) and scaled distances ($X/W^{1/3}$) with respect to the specimens.

Table 5-1 and Table 5-2 show some of the specimens studied by those authors and their respective characteristics and loadings. In Table 5-2, the scaled distances are expressed as multiples of the smallest scaled distance, x, considered in this section. The finite element study described in this section concerns only specimen CFST 64 and tests 5, 7 and 10 showed in Table 5-1 and Table 5-2 because they cover adequately the range of inelastic behavior observed during those experimental works.

Table 5-1: CFSTs tested by Marson and Bruneau (2000)

CFST	H (mm)	D (mm)	t (mm)	$f_c^{'}$ (MPa)	F_y (MPa)	P (kN)
64	2200	406.4	5.5	37	442	1000
34	2200	323.9	7.5	40	415	1920
42	2200	406.4	9.5	35	505	1920
51	2200	323.9	5.5	35	405	1600

Table 5-2: Specimens tested by Fujikura and Bruneau (2007)

TESTS	H (mm)	D (mm)	t (mm)	$f_c^{'}$ (MPa)	F_y (MPa)	Z (mm)	$X/W^{1/3}$ (m/kg$^{1/3}$)
5	1500	127.0	3.0	43.4	254	750	$2.27\,x$
7	1500	101.6	3.1	43.2	357	250	$1.00\,x$
10	1500	127.0	2.8	43.4	254	250	$1.43\,x$

The CFDST specimens studied were derived from the CFSTs selected earlier in such a way that they use approximately the same amount of material resulting in section with nearly identical cost. Their void ratio (χ) and their compactness ratios (D_o/t_o and D_i/t_i) are varied so as to cover a wide range of possible combinations. Table 5-3 and Table 5-4 show the different CFDST components obtained in that fashion for the two types of analysis performed. For the CFDST specimens the numbers in the first column of those tables represent in that order the depth-to-thickness ratios for the inside and outside tubes and the void ratio which is defined as the ratio of the radius of the inner tube to the radius of the outer tube which is an indirect measure of the amount of concrete used in the section. To reduce the scope of the analysis in this section, only the loading from tests 5 and 10 are considered for blast analysis of the CFDSTs.

Table 5-3: CFDSTs derived for pushover and cyclic analysis

CFDST	H (mm)	D_i (mm)	D_o (mm)	t_i (mm)	t_o (mm)	$f_c^{'}$ (MPa)	F_y (MPa)
9_132_24	2200	101.6	419.1	11.11	3.18	37	442
16_88_24	2200	101.6	419.1	6.35	4.76	37	442
64_88_24	2200	101.6	419.1	1.59	4.76	37	442
110_184_60	2200	302.5	506.0	2.75	2.75	37	442
166_113_50	2200	228.6	463.6	1.38	4.13	37	442

Table 5-4: CFDSTs derived for blast analysis

CFDST	Loading	H (mm)	D_i (mm)	D_o (mm)	t_i (mm)	t_o (mm)	$f_c^{'}$ (MPa)	F_y (MPa)
16_88_36	5	1500	50.8	139.7	3.18	1.59	43.4	254
16_88_36	10	1500	50.8	139.7	3.18	1.59	43.4	254

5.3.2 Finite Element Package

Because of the highly non-linear behaviors anticipated in analyzing CFSTs and CFDSTs in this bi-hazard framework, the advanced finite element analysis package LS-DYNA is chosen as an analysis tool. Both the implicit and the explicit solvers in LS-DYNA are used. The implicit solver in LS-DYNA is an incremental-iterative numerical algorithm based on Newton and quasi-Newton methods of analysis and is adapted to solve both linear and non-linear static, quasi-static and dynamic problems with low frequency content that may involve contact, strain rate and material and geometric non-linearities.

For implicit dynamic analysis, the Newmark method is used for integration of the equation of motion. The characteristics of this solver are well discussed elsewhere (LSTC, 2014). The

implicit solver was selected to carry-out cyclic pushover analysis of the sections studied and replicate and predict the behaviors of CFSTs and CFDSTs under seismic loading. On the other hand, the explicit solver in LS-DYNA which is built around the central difference scheme is adopted to solve the equation of motion that describes the transient problem in the blast analysis. This solver is mostly suited to situations involving high frequency short duration impulsive loading, high strain-rate, contact and geometric and material non-linearities (LSTC, 2014) which are all present in this study. LS-DYNA also offers the unique feature of coupling implicit and explicit analysis in any order that fits the problem to be solved (for an application see Rust and Schweizerhof, 2003).

5.3.3 Geometry

To model the steel tubes in both CFSTs and CFDSTs, fully integrated 4-noded shell elements are used whereas 8-noded tetrahedron solid elements with reduced integration and hourglass control for the concrete core are deemed appropriate to capture with sufficient accuracy the behavior of the core under blast load. In cyclic loading, it has been found that better accuracy is achieved by using fully integrated solid elements; however, this induces a penalty in term of computation time. Figure 5-2 below shows screenshots of the CFST models. Satisfactory convergence was obtained when any element dimension did not exceed $0.5cm$.

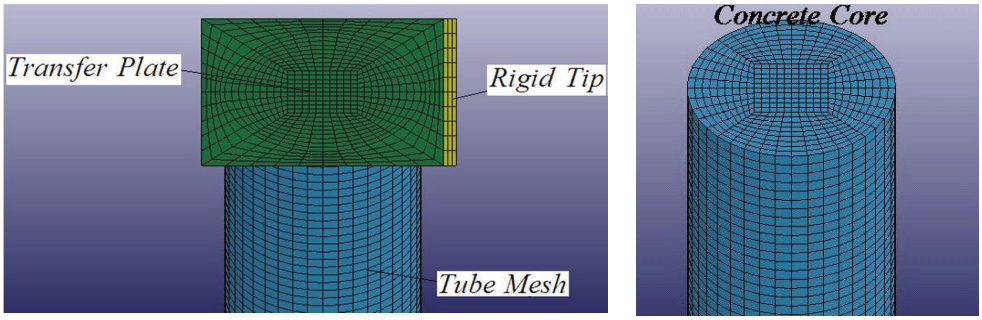

Figure 5-2: Details of the CFST models

5.3.4 Material Constitutive Models

For the CFSTs, the steel stress-strain curves are available from the experiments by Fujikura and Bruneau; however partial curves only are available from the study by Marson and Bruneau. When the full curves are available they are directly input in the material model considered for the steel, for the partial curves it is assumed that the yield stress is maintained until failure. Two Von-Mises based plasticity material models respectively coded in LS-DYNA as Material 24 (LSTC, 2014) and Material 153 (Huang and Mahin, 2008) are used to model the steel tube.

In material 24, damage is considered intrinsically using ultimate strain as failure criterion. On the other hand Material 153 was developed specifically to reproduce low-cycle fatigue as observed in steel material. Both models can capture strain hardening effects if desired. In material 24, strain rate effect is accounted for using the Cowper-Symonds model which scales the yield stress by a factor which varies with the actual strain rate (LSTC, 2014). Material 153 does not consider strain rate effects since it was not developed for that purpose. Thus, Material 24 is used for unidirectional pushover analysis or blast analysis in which failure is likely to be attained when

the composite section reach an ultimate deformation limit state whereas Material 153 is judged more adapted to the cyclic analysis in which failure is due to low-cycle fatigue.

For the concrete core, the model opted for was Mat72 REL3 in LS-DYNA whose formulation is based upon the William-Warnke three-invariant plasticity concrete material model (Malvar and Simons 1996). This model uses three shear failure surfaces to represent the behavior of the concrete material. It can account not only for confinement of the core, but also for strain-rate effects. The model considers both shear and volumetric damage in the concrete. However, an erosion algorithm available in LS-DYNA has to be appended to the concrete model as an option to physically display damage.

5.3.5 Considerations of Bond and Friction

For CFSTs, no slip was visible afterwards at the interface between the steel tube and the concrete core in the experimental works reported. As explained in Section 5.2, it can be assumed that perfect bond exists between the tube and the core. Thus, in the CFST models corresponding nodes on the contact surface between the steel tube and the concrete core are simply constrained to each other.

5.3.6 Boundary Conditions, Imperfections and Damping Considerations

Fully fixed conditions are assumed to allow progressive hinging at the fixed ends of the specimens. Although the tubes were embedded in composite foundations in both sets of experiments mentioned, no embedment length is considered in the LS-DYNA models under seismic and blast loading

Geometric imperfections are introduced into the models for pushover and cyclic analysis. They are, however, deemed of little influence over the response of the components under blast loads. Although other methods exist, geometric imperfections are introduced in this section by specifying a harmonic perturbation to a portion of the model (Rust and Schweizerhof, 2003).

Damping is considered only for blast analysis. A global value of 1% of critical is added to the model solely to make sure that models that have reached their maximum deformation without completely fracturing can return to a deformed equilibrium position in the free vibration phase that follows the attainment of maximum deformation.

5.3.7 Loading

For pushover and cyclic analysis, a plate whose meshes coincide with the meshes of the tubes and the concrete core is used as a transfer element at the top of each specimen. The plate is terminated by a rigid tip to which the displacement history is applied for pushover and cyclic analysis as shown in Figure 5-2. Pushover and cyclic analysis are done using a displacement control approach. For the pushover analysis a constant velocity is applied at the rigid tip whereas for the cyclic analysis a modified displacement history- based on the ATC-24 protocol- provides the loading. For all inelastic excursions in this displacement history only two full cycles are considered compared to the three cycles considered for inelastic excursions up to 3% percent drift in ATC-24.

Blast overpressures are applied to the models using the Airblast function in LS-DYNA which is an implementation of the airblast pressure data available in ConWep, a collection of conventional weapons effects calculations from the equations and curves of the US Army

technical manual TM 5-855-1. Because the Airblast function in LS-DYNA is unable to take into account the effects of shadowing or the reduction in pressure that may result because of the shape of a finite target, appropriate reduction factors are applied to the pressure histories obtained from LS-DYNA so that the resulting peak impulse output by the software matched the peak reflected impulse predicted by Fujikura and Bruneau for the tests using the blast overpressure generation program BEL and the correction method presented by Fujikura and Bruneau to account for the reduction in impulse due do the roundness of the section.

5.4 Multi-hazard Finite Element Analysis Results of CFST

5.4.1 Cyclic Pushover Test Analysis Results for CFST

LS-DYNA implicit is the solver chosen for the cyclic analysis of CFST64. Besides mesh refinement, displacement and energy tolerances of 1% are imposed for adequate convergence. Those tolerances could be lower but the significant increase in computation time recorded would not justify the marginal improvement in accuracy that would result. The cyclic pushover result for CFST64 in LS-DYNA is shown in Figure 5-3 below.

The ranges for strength and drift are well captured. However the pinching in the hysteresis loops observed during the test is not well reproduced. This pinching is influenced by the progressive buckling of the steel tube and the crushing in the compression zone of the concrete core. This inaccuracy might be traced back to the fact that the finite element model was not a faithful reproduction of the entire experiment, notably, as mentioned earlier, to reduce computation time the full displacement history of the test was not applied. This might explain why the pinching in

the model is further delayed as the number of inelastic cycles necessary to take the specimen close to its fatigue limit was not applied.

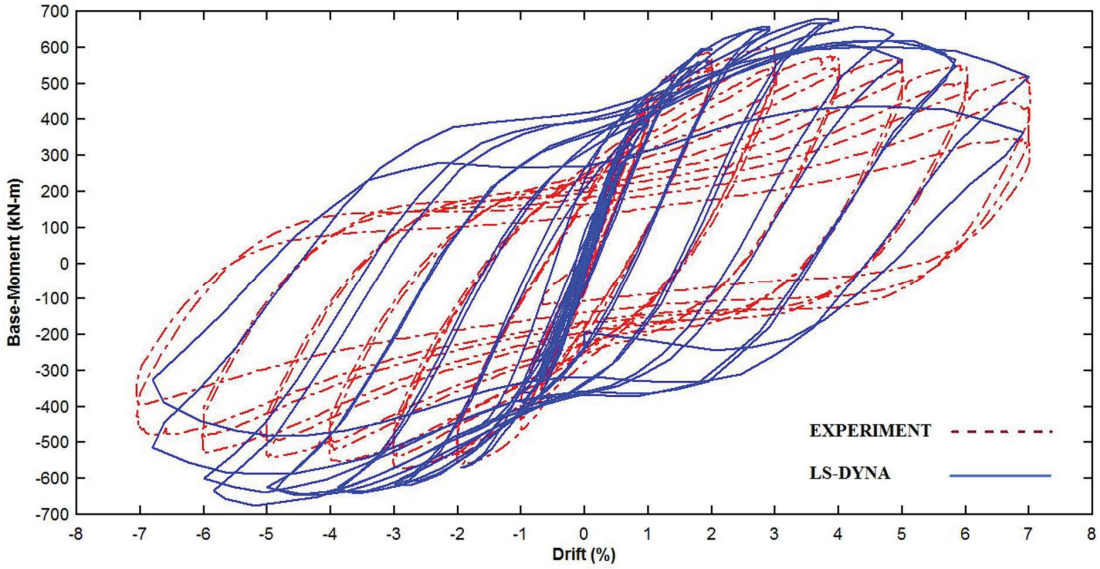

Figure 5-3: Cyclic Pushover Hysteresis Loop for CFST64

5.4.2 Blast Test Analysis Results for CFSTs

After mesh refinement, analysis of CFST for blast loading using the explicit solver in LS-DYNA converged with adequate accuracy and captured exactly the ductile sequence of limit states (yielding-plastification-fracture) experimentally observed under blast loading. Figure 5-4 respectively shows plastic deformation as measured in Test 5 and test 10. In particular, the angles of rotation from the finite element model match the ones measured after the tests. The displacement fields match also the ones measured in the tests (Figure 5-4). In test 10 the partial fracture of the shell and the concrete core is well captured.

In Figure 5-5, the finite element model captured the fracture observed for the specimen of test 7. It can be seen that the bottom part of the specimen blows away as seen in the test while the columns fracture at its top and its base.

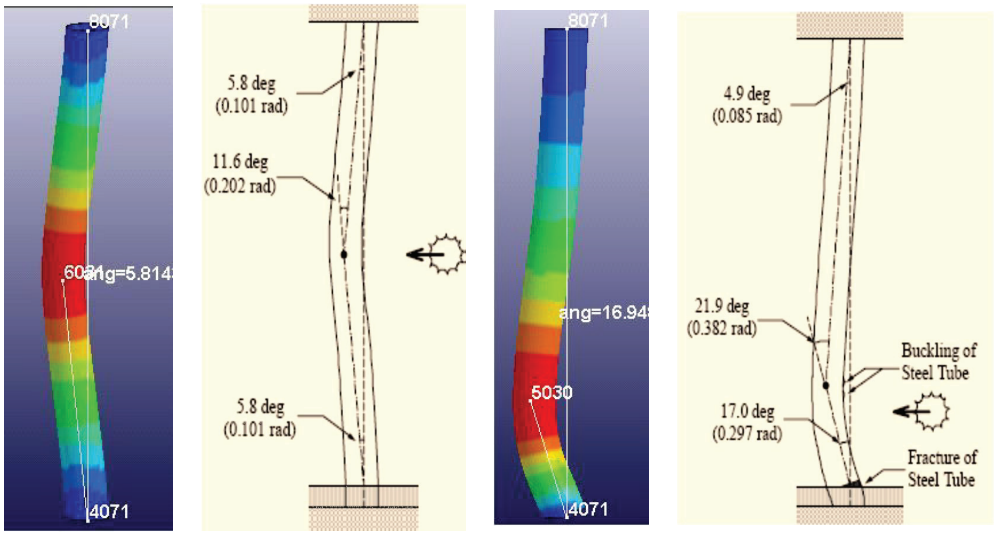

(a) (b)

Figure 5-4: (a) Plastic deformation in test 5, (b) Partial shell fracture in test 10

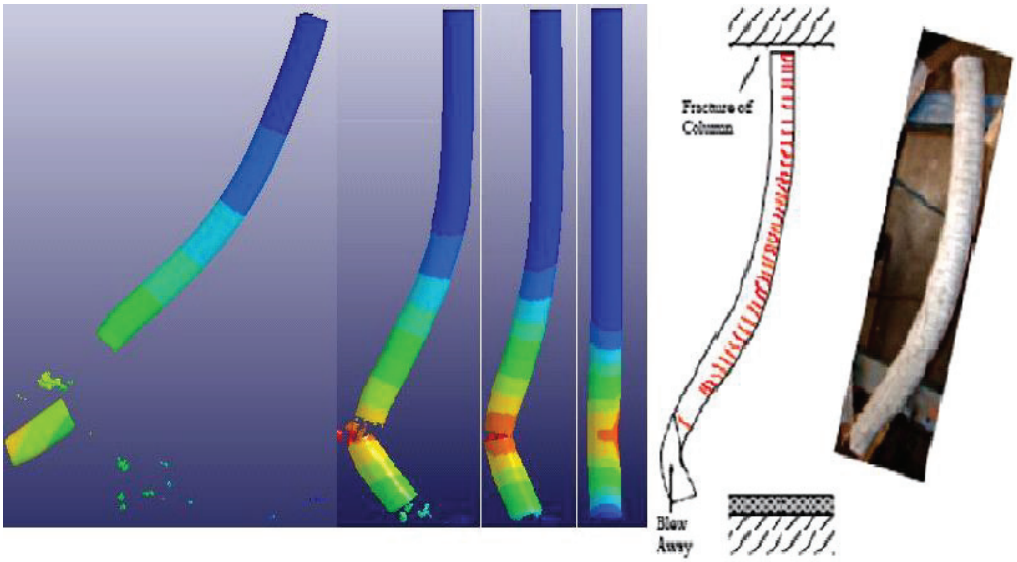

Figure 5-5: Fracture of the Specimen in test 7

5.5 Multi-hazard Finite Element Analysis Results of CFDST

5.5.1 Pushover Analysis Results for CFDSTs

Pushover analysis are performed on the specimens derived from CFST64 using elastoplastic assumption for the steel with the yield stress and modulus elasticity set as measured in the experimental work by Marson and Bruneau. Those pushover analyses were used to determine the parameters affecting the strength and ductility of CFDST and to guide the selections of the specimens for blast analysis considering both pushover and blast analysis can bring a section to a critical deformed state. The implicit-explicit switch in LS-DYNA is used here to avoid convergence problem in the buckling-post buckling analysis of the sections studied. The model as built was able to capture the behavior of the section until failure (the different components of a CFDST section at failure are shown in Figure 5-6). It is worth nothing that at failure the

concrete core shows a buckle lobe that follows the deformation of the outside tube and hence plastic deformation of the core which may cause the concrete core to "flow" was captured by the model.

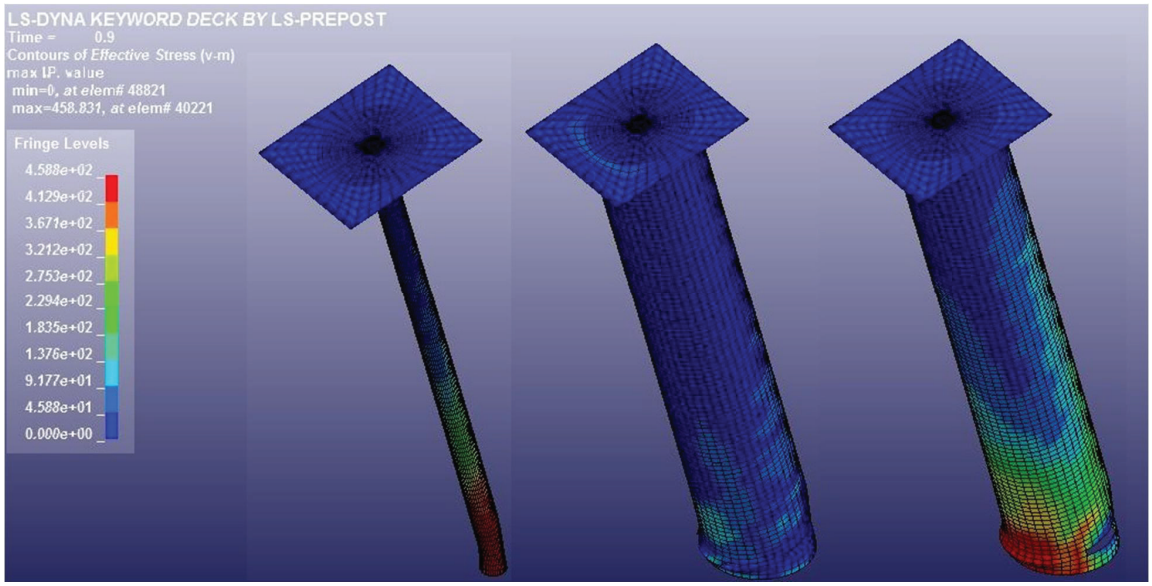

Figure 5-6: CFDSTs Components at Failure

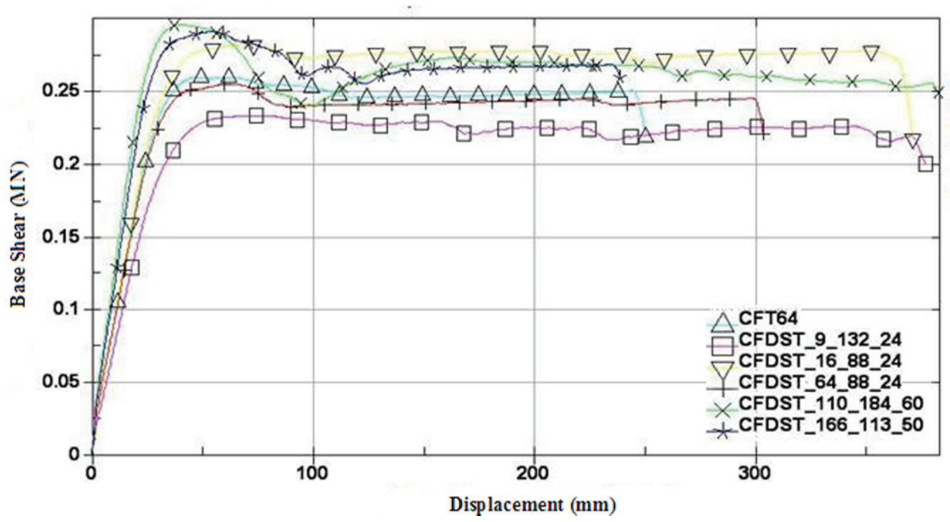

Figure 5-7: Pushover results for the selected CFSTs and CFDSTs

In Figure 5-7 the main results of the pushover analysis for all the section selected are presented. Several conclusions for the optimal geometry of CFDST can be drawn. One is more compact inner and outer tubes result in sections less susceptible to post-peak buckling, more ductile and capable to maintain their ultimate strength over a longer yield plateau (see curve for CFDST16_88_24 and CFDST64_88_24). Another is that the compactness of the inner tube seems to control the ductility of the section overall as section with more compact inner tube fail at larger drift. The pushover analysis also shows that, even for high depth-to-thickness ratios for the outside tubes, the CFDSTs are able to maintain their strength over a range of deformations comparable or even superior to that observed for the CFSTs. For large values of depth-to-thickness ratio of the outside tube a marked post peak drop is observed in the pushover curve, which can be attributed to buckling, nevertheless the post-buckling behavior remains ductile afterwards. This suggests good confinement of the core by the steel tubes as discussed next.

5.5.2 Composite Action in CFST and CFDST

To understand some of the added values (concrete confinement by the tube namely) of the layered configuration of a CFDST cross section, a series of comparisons between steel tubes, CFST and CFDST were undertaken. In those analyses, similar models to the ones described for CFST or CFDST were subjected to pushover loading. However, the concrete core was removed. In other words for CFST the cylindrical steel wrapped around the concrete was analyzed whereas for CFDST the section was reduced to the two concentric tubes sharing the loading plate at the top so they can be loaded simultaneously. For CFDST, the analysis went one step closer. Each tube component of the section was analyzed under pushover loading and the results summed. Separate analysis of the concrete core to obtain its strength and add it to the steel strength could have been useful, but it was not undertaken because it was judged that compared to the strength from the tubes, its contribution to the sum would have been minimal.

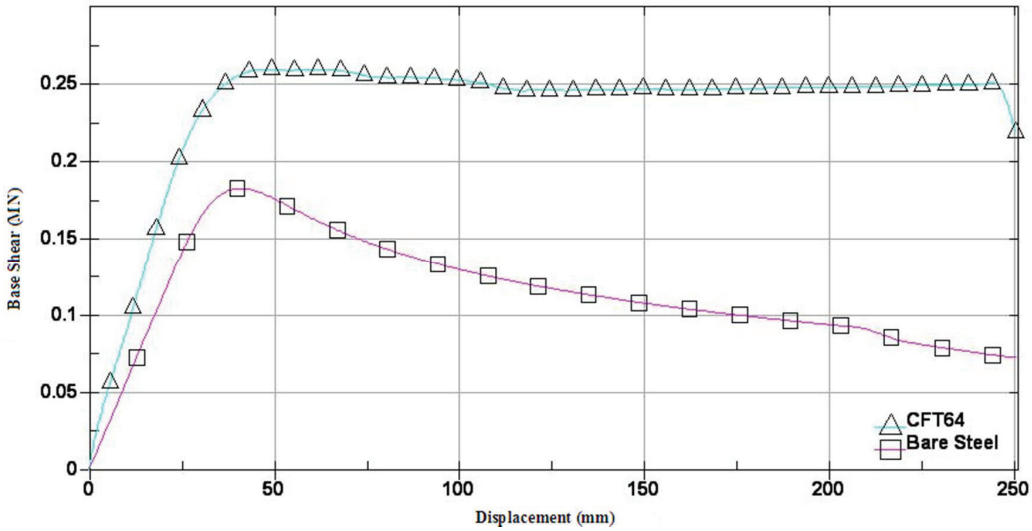

Figure 5-8: Effect of Composite Action in CFST

After analysis, it was realized that peak strengths for both bare steel components and the concrete filled-tubes were reached for similar displacements but different strengths (Figure 5-8 and Figure 5-9); the difference in strength between the tubes and the analyzed section is due to the composite action between the tubes and the concrete. Because of this synergy, CFST and CFDST were able to exhibit a ductile post-peak behavior despite local buckling of their tubes whereas for the isolated tube components strength degradation occur rapidly once the peak strength was reached. This can be traced back to the fact that, in the composite sections presence of the concrete core delays the progression of buckling of the tubes (see time stamp in Figure 5-10, the fringe plot is for Von Mises Stress).

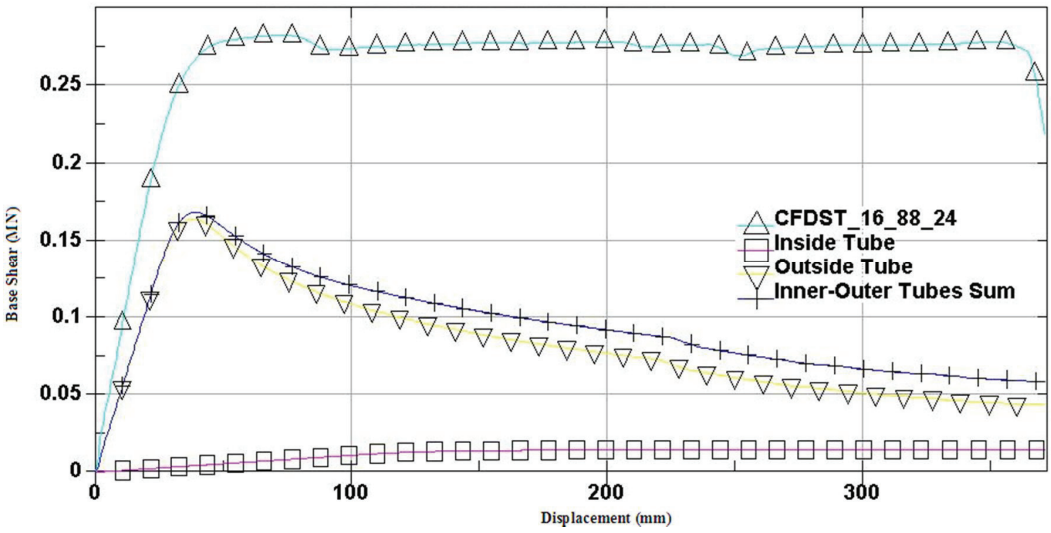

Figure 5-9: Effect of Composite Action in CFDST

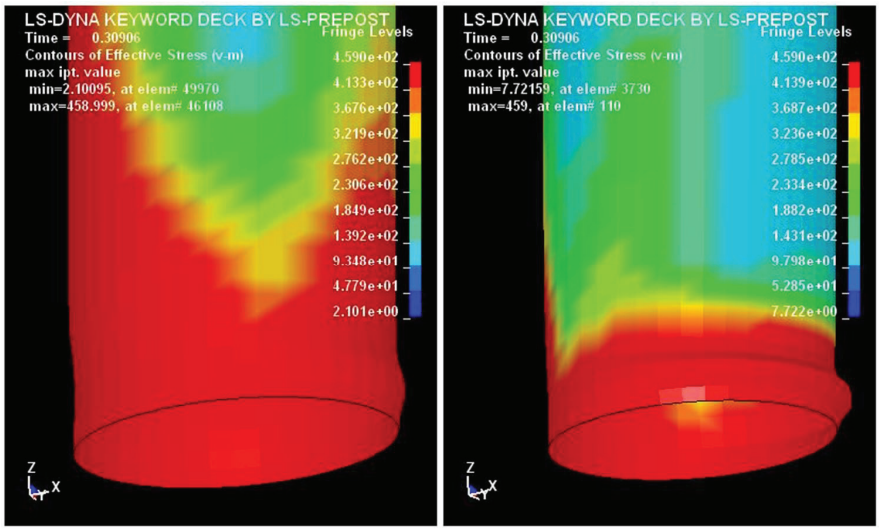

Figure 5-10: Amplitude of Buckling in the Outside Tube for CFDST vs Steel Tube Only

At the same time that the core supports the tubes, the steel tubes also confine the core so damage that can impair the strength of the section in the early stage of loading is avoided. For CFDST,

the confining effect is in general more important compared to CFST because of the triaxial state of stress that develops in the concrete due to the confining effects of the 2 tubes. In Figure 5-11 and Figure 5-12, the maximum confining effect in the concrete core as observed for CFST and CFDST is reported. As seen, similar confining stresses are reached in the core as predicted by the program; for CFDST the peak reached is maintained over a longer plateau. This explains why at similar strength and with (relatively) similar outside tube compactness[1], CFDST sections can be more ductile.

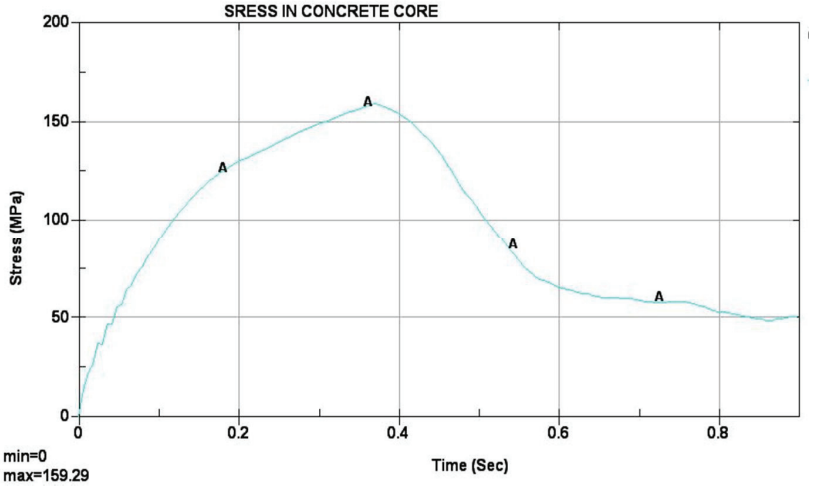

Figure 5-11: Peak Stress in the Concrete Core of CFST Section

[1] The compactness is 64 for the CFST and 88 for the CFDST. Per the seismic provision for steel structures of AISC the tube from the CFST should be capable of exhibiting highly ductile behavior whereas for the CFDST, based on the outside tube, the compactness would be only sufficient to exhibit moderately ductile behavior.

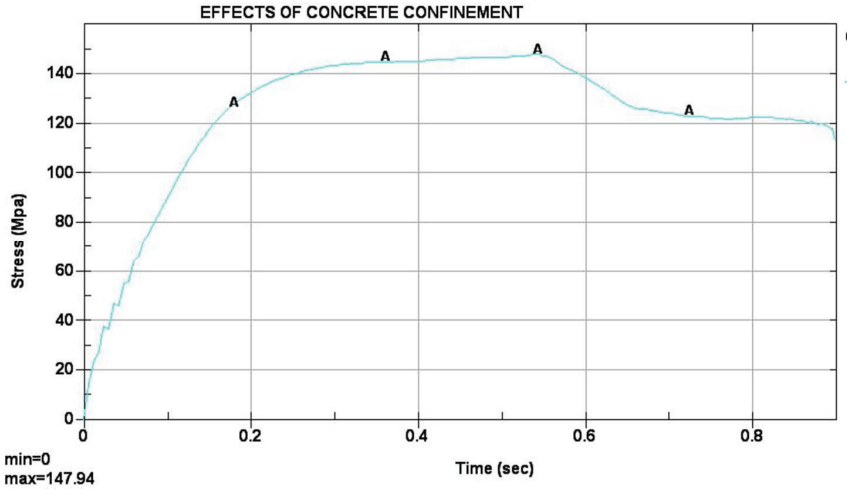

Figure 5-12: Peak Stress in the Concrete Core of a CFDST Section

5.5.3 Cyclic Analysis Result of CFDST

The results of the previous pushover analysis guided the selection of the CFDSTs shown on Table 4 for blast analysis and the selection of a candidate CFDST for cyclic pushover (CFDST16_88_24). So sections with low compactness ratios (less than the AISC limit of $0.15E/F_y$ for hollow steel tube, where E is the modulus of elasticity of the tube) are chosen, which incidentally keeps the void ratio to reasonable levels (less than 40%).

Under cyclic load, the CFDST candidate analysis conducted with LS-DYNA implicit yields comparable hysteresis behavior to that observed for CFST64 as shown in Figure 5-13. The ranges for both strength and displacement are similar. The CFDST specimen shows ductile post peak behavior with slow strength degradation which would be beneficial in resisting earthquake loading for a pier element with a CFDST cross section.

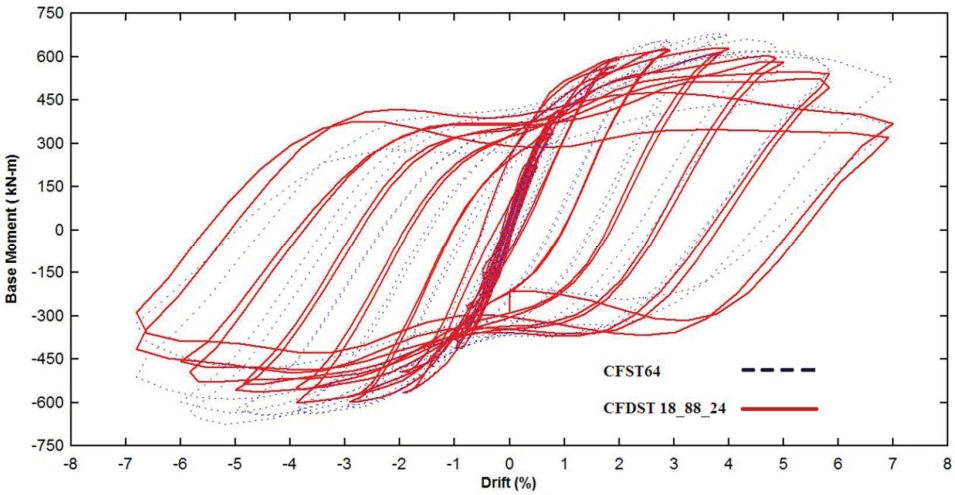

Figure 5-13: Hysteresis Loop for Cyclic Analysis of CFDST_18_88_24

5.5.4 Blast Analysis Results for CFSTs

Analysis for blast load reveal that for the same scaled distances the CFDSTs fare better than the corresponding CFSTs. Reductions in displacement as high as 25% are achieved which corroborates the initial findings of the pushover analysis that, using the same amount of material, CFDSTs can be made at least as strong and ductile as CFSTs.

Figure 5-14 shows comparison of the displacement histories of both types of section for tests 5 and 10. The actual results from the experiments are shown within the figure for comparison purpose. Figure 5-15 shows two different views at maximum deformation for each CFDST specimen; one of those views outlines both the core and the tubes. In Figure 5-15 b), no failure is visible for the CFDST which further demonstrates better performance compared to the corresponding CFST of test 10.

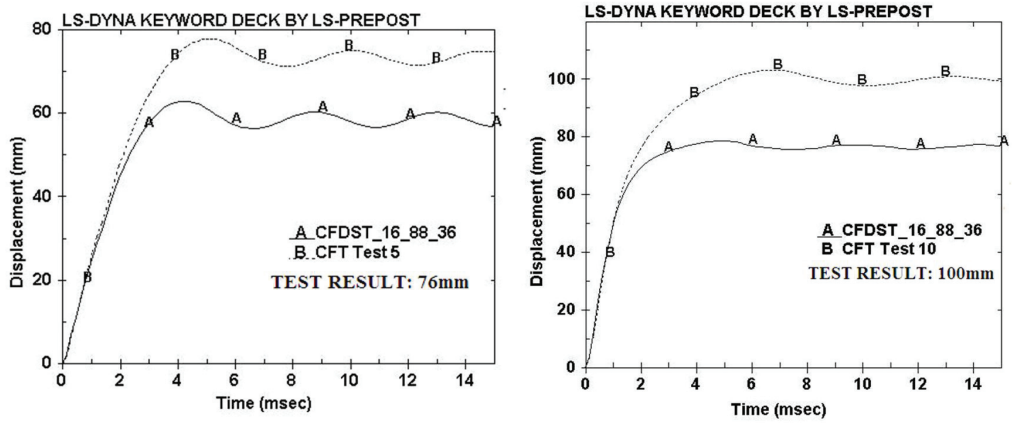

Figure 5-14: Comparison of Displacement Histories

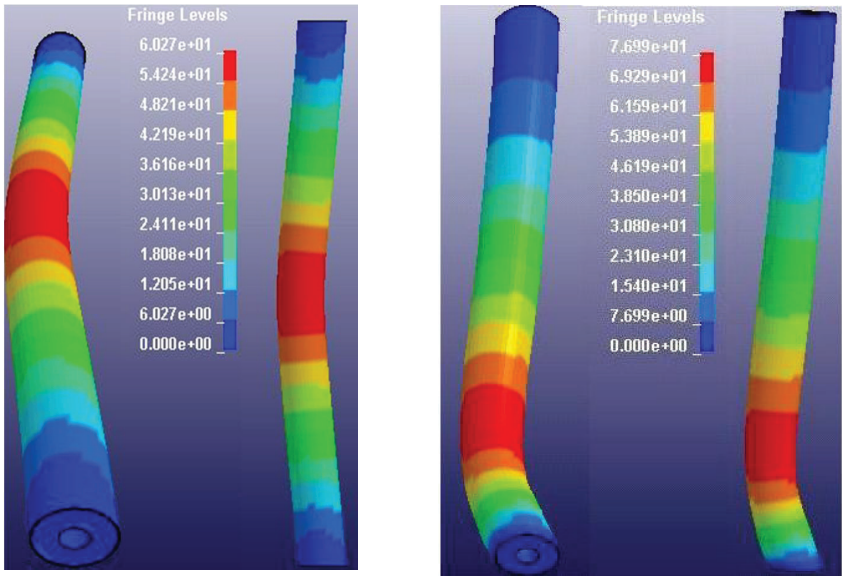

(a) (b)

Figure 5-15: Pespective and Fringe Plot for (a) Test 5 and (b) Test 10

5.6 Summary

Finite element analysis of concrete-filled tubes conducted with LS-DYNA show acceptable correlations with experimental results obtained for CFSTs under seismic and blast loading and predicts rather good performance for CFDSTs in the same conditions. However, further refinement of the finite element analysis under seismic loading might be needed to improve correlation with tests data with respect to pinching of the hysteretic curves.

In general, CFDSTs emulate CFSTs in terms of capacity to dissipate energy and, similarly, exhibits ductile behavior under load. CFDSTs can presumably reach higher deformation limit than CFSTs, however this needs to be experimentally validated to come up with safe deformation limits for seismic and blast analysis.

SECTION 6

PERFORMANCE OF CONCRETE FILLED DOUBLE SKIN TUBES UNDER CYCLIC LOADING

6.1 General

This section and the following present the details of experimental and analytical programs aimed at validating the performance of concrete filled double skinned tubes (CFDST) and modified steel jacketed columns (MSJC) for the bi-hazard framework defined earlier. A series of experiments carried out to characterize the behavior of CFDST under cyclic loading are the focus of this section, performance of CFDST and MSJC under blast loading will be discussed later in Sections 8 and 9.

Five (5) quarter scale column specimens, with geometric and section parameters representative of different arrangements of the tube shells and consistent with the conditions expected in full-scale applications, were instrumented and submitted to cyclic loading. The main objective of this test series was to evaluate experimentally the behavior of CFDST in terms of ductility and resistance to low-cycle fatigue, which are both critical for the survivability of bridge substructures. More specifically, this test series was designed and implemented to yield information that would help characterize the hysteretic behavior of CFDSTs, derive optimal parameters-with respect to strength, ductility and economy for CFDSTs construction and validate the models developed later for the analysis and design of CFDST sections.

With respect to the organization of this section, a description of the design process of the specimens and the salient features of the experimental setup are presented first. A discussion of

the different steps in the design of the experimental and instrumentation setup follows. Items such as sizing of the base connection, design of the interface between the loading actuator and the specimen, and selection and positioning of the different instruments on the specimens are presented. Finally, global observations made during testing are reported at the end of the section, along with comparison of behavior among the specimens.

6.2 Specimen Design

Design of the specimens was based on the analytical studies of different multi-hazard full-scale substructure candidates presented in the previous section. The specimens selected for this test series are simply quarter scale of the full scale CFDST designed as part of those studies. Those specimens meet the compactness limits set by AISC Seismic Provisions-AISC 341-10 (AISC, 2010) to achieve ductile behavior for concrete filled composite section. The decision to comply with those limits stemmed from the fact CFDSTs are essentially concrete filled section quite similar to CFST and, arguably, should be subjected to the same compactness limits. If this holds true, CFDSTs meeting those requirements should, accordingly and like their CFDSTs counterparts, develop the strength and ductility demands expected of them under earthquake loading. For the current research, this line of reasoning resulted in sections that combine inside and outside tubes with different compactness and corresponding expected ductility capacities as defined by the AISC Seismic Provisions (AISC-341-10).

6.2.1 Geometry of the Specimens

The limiting width-to-thickness ratios for compression elements for moderately ductile and highly ductile members contained in AISC 341-10 for filled composite members served as guide in establishing the geometry of the set of specimens. Table 6-1 summarizes those limiting diameter-to-thickness ratios for round concrete-filled steel composite sections in flexure. The limiting diameter-to-thickness ratio corresponding to the steel material used for the CFDST of this test series (ASTM A513 Type 2 tubes with yield strength $F_y = 32ksi$ and a modulus of elasticity $E = 29000ksi$) are directly calculated in this table. It was decided that all specimens should have highly compact inside tubes (see Table 6-2 for limiting diameter to thickness ratio required by the AISC Specification for Structural Steel Buildings-AISC 360-10 (AISC, 2010)) to ensure highly ductile behavior as this would be relatively easy to accomplish in bridge prototypes. In the perspective of seismic design, however, specimens S1, S2 and S5 would only have outside tube compactness deemed sufficient to develop moderate levels of ductility whereas all other specimens would develop high level of ductility.

Table 6-1: Limiting Width-to-Thickness Ratios for Compression Elements for Moderately Ductile and Highly Ductile Members, AISC 341-10

Description of the Element	Width-Thickness Ratio	Limiting Width-Thickness Ratio	
		λ_{hd} Highly Ductile	λ_{md} Moderately Ductile
Round Filled Composite	$\frac{D}{t}$	$\frac{0.076E}{f_y} = 68.9^*$	$\frac{0.15E}{f_y} = 135.9^*$

* For $F_y = 32ksi$ and $E = 29000ksi$

Table 6-2: Limiting Width-to-Thickness Ratios for Compression Steel Elements in Composite Members Subject to Flexure, AISC 360-10

Description of the Element	Width-Thickness Ratio	Limiting Width-Thickness Ratio		
		λ_{pd} Compact/Non Compact	λ_r Non Compact/Slender	Maximum Permitted
Round Filled Composite	$\frac{D}{t}$	$\frac{0.09E}{f_y} = 81.6^*$	$\frac{0.31E}{f_y} = 280.9^*$	$\frac{0.31E}{f_y} = 280.9^*$

* For $F_y = 32ksi$ and $E = 29000ksi$

The main geometric features of the specimens, labeled S1 to S5, and the ductility levels expected based on the inner and the outer tube compactness for each are presented in Table 6-3. In Table 6-3, the numbers used in the first column to designate the specimens (e.g. 17-72-33) represent in that order the depth-to-thickness ratios for the inside and outside tubes rounded to the nearest

integer (i.e. 17 and 72) and the void ratio in percentage (i.e. 33%). The second column gives information on the cantilever height (H) for each specimen; all specimens, but specimen S3, have the same height. The other parameters contained in this table are the diameter of the outside tube (D_o), the diameter of the inner tube (D_i), the thicknesses of the inner (t_i) and the outer tube (t_o), the diameter-to-thickness ratios for the inner $\left(\frac{D_i}{t_i}\right)$ and the outer tube $\left(\frac{D_o}{t_o}\right)$, and the void ratio $\left(\chi = \frac{D_i}{Do}\right)$.

Table 6-3: Cyclic Pushover Test Specimens

Designation	Specimen	H (in)	D_i (in)	D_o (in)	t_i (in)	t_o (in)	$\frac{D_i}{t_i}$	$\frac{D_o}{t_0}$	χ	Ductility Designation	
										Inside Tube	Outside Tube
17_72_33	S1	67.25	2	6	0.116	0.083	17.24	72.29	0.33	HD	MD
16_70_25	S2	67.25	2	8	0.123	0.114	16.26	70.18	0.25	HD	MD
22_50_38	S3	71.25	2.5	6.625	0.114	0.133	21.93	49.81	0.38	HD	HD
26_48_33	S4	67.25	2	6	0.076	0.117	26.32	48.00	0.33	HD	HD
56_70_63	S5	67.25	5	8	0.09	0.114	55.56	70.18	0.63	HD	MD

Note that specimen S1 and S4 have the same outside and inside tube diameters but the thicknesses of their outside and inside tubes are swapped to produce two section configurations with the same void ratio but different overall expected ductility (the outside tube of S1 is MD while that of S4 is HD). Note also that specimens S2 and S5 were chosen with outside tube that are identical but with inside tube diameters leading to section respectively having small and large void ratio (0.25 versus 0.63), yet having similar ductility designation (see Table 6-3).

Specimen S4 was chosen to fall somewhat in the middle of the spectrum of void ratios considered for the specimens. For a visual reference, scaled drawings of the different specimens that were tested are provided in Figure 6-1.

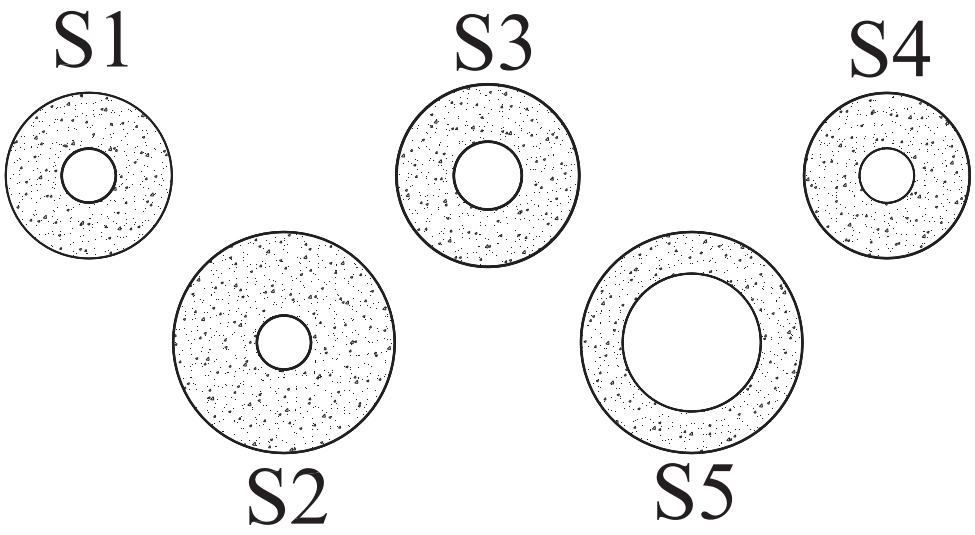

Figure 6-1: Selected Cross Sections

6.2.2 Materials

The tubes used to build the test specimens were electric resistance welded tubes. Those products are available in cold rolled strip (16 gauge and lighter), and hot rolled strip (0.083" wall and heavier). The steel used in their manufacturing complies with ASTM A513 type 1 or 2. Those tubes nominally have yield strength of 32 ksi, tensile strength of 45 ksi, and 15% minimum elongation at failure. The experimentally measured stress-strain curves for those specimens are provided in Figure 6-2 and Figure 6-3 for coupons obtained from extra lengths that were cut

from each tube before the tests. Pieces of those extra lengths of tube were flattened first and coupons were machined from them. Doing so, those coupons may have been cold-worked which may explain why not all of them reached the minimum required elongation at failure. It is also worth noting that no defined yield plateau was obtained for any of the tested coupons and consequently the 0.2% proof stress was used as the nominal yield strength of the section for all purpose.

All threaded rods used in that experiment program to connect the specimens to a strong beam or to connect a transfer stud to the specimens (see Section 6.3) were of ASTM A193 grade B7 steel. The specified nominal yield strength of the rods was 105ksi, their tensile strength 125 ksi, and their minimum elongation at failure 16%. For the stub-connection, nuts were welded to one of the extremities of the rods and the resulting piece was used as concrete anchors. A reduction factor of 10% on the strength those threaded rods was assumed to take into account the fact that the stress area for a threaded rod is based on the minor diameter (valley) of the threaded section and consequently failure of the rod with may occur at lower strength than the nominal.

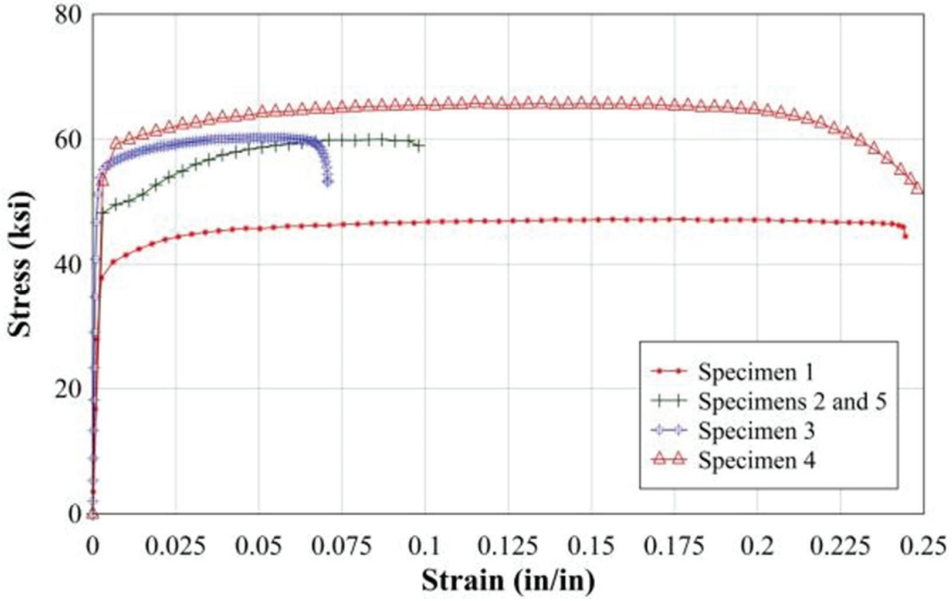

Figure 6-2: Stress Strain Curve for Outside Tube Steel Materials

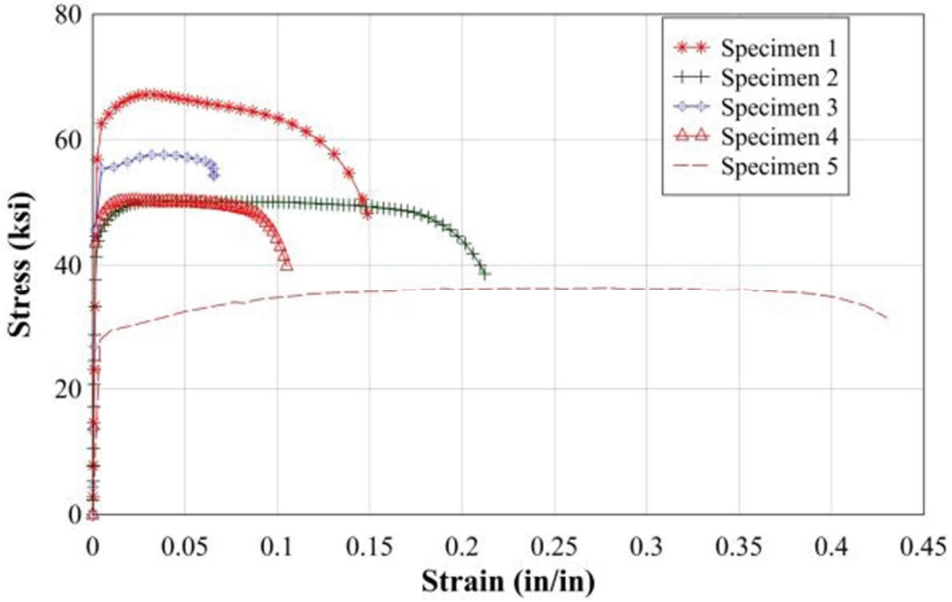

Figure 6-3: Stress Strain Curve for Inside Tube Steel Materials

For the channels and steel used to build the fixed base connection of the composite column as well as the top plate on which the transfer element rests (see Section 6.3), ASTM A36 structural steel was specified. The theoretical yield strength of that steel is 36ksi and its ultimate tensile strength of the order of 58ksi. The minimum elongation at rupture for this steel is specified as 20% minimum.

Because the regions between the tubes that were to be filled with concrete, at quarter scale, would be rather congested, a concrete with high workability was judged necessary to accelerate construction and cope with the risk of segregation of the concrete and the needs for compaction.

Because of its high workability, self-placing concrete with an average compressive stress of 5.0 ksi, maximum aggregate size of ½ of inch and a spread during the slump test between 18 and 30 inches was specified for this application. Concrete cylinders were cast during the construction and tested 42 days after the pour. The average cylinder strength obtained was 5.4 ksi with a standard deviation of 0.1ksi. Using the following relationships proposed by ACI Committee 211 (ACI, 1992) to predict the compressive strength $f'_{c(t)}$ at age t (in days) knowing the compressive strength at 28 days $f'_{c(28)}$, the compressive strength of the concrete on the day of the test was estimated for each specimen.

$$f'_{c(t)} = f'_{c(28)} \frac{t}{4 + .85t} \tag{6-1}$$

The results are presented in Table 6-4 ; the difference between the expected concrete strength at the age of the test and the average strength obtained from the cylinders was not significant (5% at most), hence the average cylinder strength was used in all subsequent calculations.

Table 6-4: Concrete Strength at Age of Test

Designation	Specimen	t (days)	$f'_{c(42)}$ (ksi)	$f'_{c(t)}$ (ksi)
17_72_33	S1	71	5.4	5.63
16_70_25	S2	74	5.4	5.65
22_50_38	S3	91	5.4	5.71
26_48_33	S4	70	5.4	5.63
56_70_63	S5	75	5.4	5.65

6.2.3 Calculated Section Strengths

Since all specimens were made of compact tube elements, it was expected that they would reach their full nominal plastic strength $\left(M_p\right)$. The nominal plastic strength of each of the specimens was calculated using the equations derived later in Section 7 It was assumed that the steel components have fully plastified (reaching the nominal yield strength F_y) and that the concrete in the compression zone has reached its full strength $\left(f'_c\right)$ although the concrete in the tensile region has cracked. Since the equations developed earlier are based on the plastic stress distribution method (AISC 360-10), considering the full strength of the concrete in the section is a small departure from the AISC Provisions which permits to use only 95% of the strength of the concrete for round filled tube. The assumption that supports this choice is that the tubes in CFDST provide enhanced confinement to the concrete compared to round-filled tube

Because the method exposed above does not take materials overstrength nor concrete confinement into account, maximum feasible flexural strengths $\left(M_{pos}\right)$ for all the specimens were also determined using the plastic stress distribution method but assuming, on one hand, an

expected yield strength for the steel tubes 25% higher than the nominal yield and a strain hardening overstrength factor of 1.25. On the other hand, on the concrete side, a factor of 1.25 was applied to the nominal strength to account for an expected compressive strength higher than the specified value in the plastic hinge region and 1.25 for possible confinement effect in the specimen (for sake of capacity design).

The shears (V_p) and (V_{prob}) corresponding respectively to lateral load when the nominal plastic and the expected flexural strengths are reached were also evaluated to facilitate rapid comparison to the values observed during testing. Calculated values for the above parameters are provided in Table 6-5.

Table 6-5: Calculated Specimens Strengths

Designation	Specimen	F_{yo} (ksi)	F_{yi} (ksi)	f_c' (ksi)	M_p (kip-in)	V_p (kip)	M_{pos} (kip-in)	V_{pos} (kip)
17_72_33	S1	40.00	61.30	5.4	207.46	3.08	324.2	4.8
16_70_25	S2	49.62	45.20	5.4	514.98	7.66	804.7	12.0
22_50_38	S3	56.00	51.04	5.4	446.09	6.26	697.0	9.8
26_48_33	S4	57.40	46.98	5.4	314.61	4.68	491.6	7.3
56_70_63	S5	49.62	28.6	5.4	532.50	7.92	832.0	12.4

6.3 Description of the Experimental Setup

The column specimens were all cantilever having a built-up steel component at their base to provide a mean to connect the specimen to the top flange of a W14x211 strong beam. The strong beam is attached to the strong floor of the laboratory and one of its extremities is welded to an A-shaped reaction frame. The actuator used to apply the loading to the specimens was also

connected to the A-frame as shown on Figure 6-4. The overall dimensions of the conceptual setup are also shown on that figure.

Each built-up component was made of 2 structural MC 12×31 channels whose flanges were facing outward and whose webs were spaced 10 in apart (Figure 6-6). Two 16*in*x16*in* square steel plates with their edges aligned with the edge-lines of the channels were fillet-welded to all free sides of the bottom and top flanges of the channels to form a box section. The channels were $16.5\,in$ long and the plates 5/16 in thick; these dimensions were established using capacity design principles as explained later. A 1/4 *in* recess was left between the longer side of the flanges and the extremity of the plates to allow welding. The resulting box section was $13.25\,in$ in height, $16.5\,in$ in length, $16.5\,in$-wide top and bottom and $10\,in$-wide at mid-height (Figure 6-5).

Slightly oversized holes were drilled through the plates and the flanges of the channels of this built-up member and 6 grade B7 high resistance threaded rods (3 on either side of the box section, 1¼ in in diameter and 24 in long) were placed through those holes and tightened in place using two nuts per rod. One nut was placed at the extremity of each rod at the top of the box section while the other one was located at the other extremity underneath the top flange of the strong beam as shown on Figure 6-5.

An impact wrench was used to tighten each nut until no turn of the nut was possible. The length for those rods was chosen so that they can moved up and down their hole and be rapidly adjusted if any adverse effect (e.g. crushing) on the threads was detected during the test. This connection had to provide sufficient fixity at the top of the composite base so that the specimen would

behave as a cantilever. The fixed end of that cantilever would ideally be located at the top of the box section and shear and moment would be transferred at this location to the strong beam.

To inhibit any risk of instability in the flanges of the channels during tightening of the threaded rods and testing under lateral loading, the two rods at the extremity of the base were inserted into tube studs having 2 in diameter and ¼ in wall thickness. Also since they had to contribute in stabilizing the flanges of the channels, the length of the tube studs were such that they can tightly fit in the space between the flanges of the channels on either side of the composite box section as seen on Figure 6-14.

The top of each specimen itself was also connected to a cap plate located at its top. A $^{3}/_{16}$ inch steel plate to which arrays of 4 through-thicknesses ½ in anchor rods had been previously welded served as cap plate at the top of each specimen. The rods of this assembly were embedded, at one end, 16*in* deep in the concrete of the cross section during the pour, and extended 2 in above the cap plate. The purpose of this extension was to facilitate connection of the top of the specimen to a rigid built-up I-section. This rigid element was 11*in* deep, 10*in* wide and 10*in* long (see Figure 6-5).Once the concrete was cured, the cap plate assembly was welded of each specimen was welded to the outside tube.

To reduce the time and the work needed to fix the test specimens in place, the same rigid element was used for all the 5 tests. Because the space between the concentric tubes of each specimen to be tested was different, two different holes patterns (as shown on Figure 6-5) were drilled in the top rigid member. The rods of the cap-plate were welded in patterns (Figure 6-13) matching one holes pattern or the other depending on the geometry of the cross section such that the rods are centered on the concrete core.

The threaded rods welded to and extending above the cap plate were tightened to the rigid transfer element at the top of the specimen. Finally, this rigid member was connected to one of the swivels of an MTS actuator using a 1–in back plate welded to its flanges and its web. The other swivel of the MTS actuator was connected to the A- frame so that, ideally, its axis is perpendicular to the vertical axis of any specimen under load.

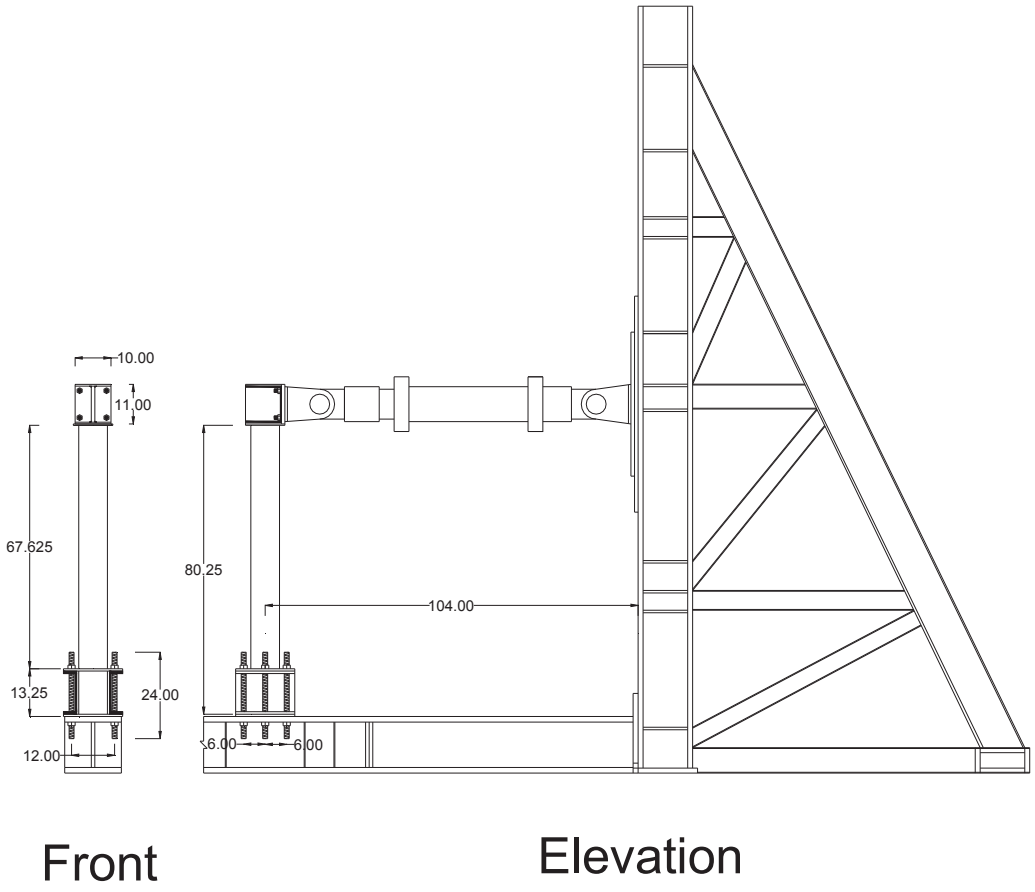

Figure 6-4: Experimental Setup [Units Shown in inches, 1in=25.4mm]

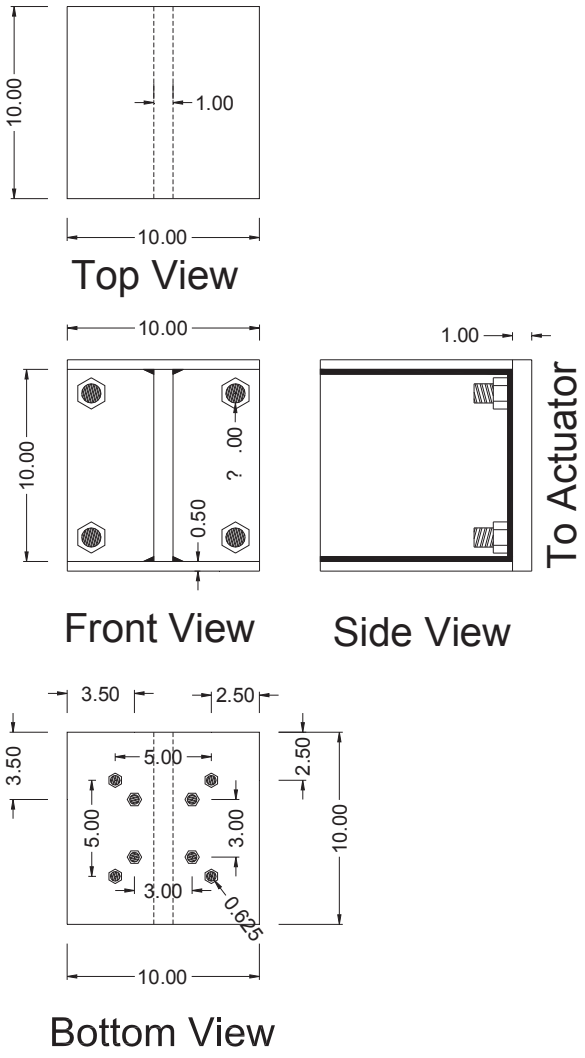

Figure 6-5: Rigid Transfer Element Details [Units Shown in inches, 1in=25.4mm]

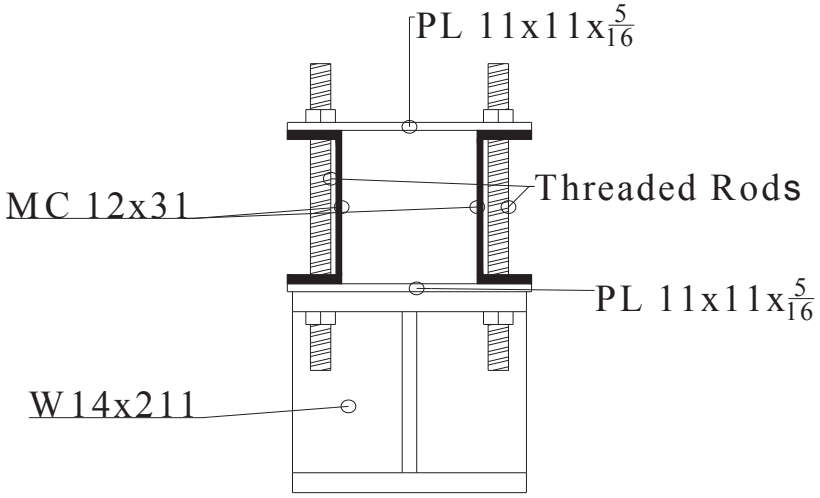

Figure 6-6: Composite Box Section and Connection Details

6.4 Design of the Experimental Setup

6.4.1 Assumptions

This section describes the experimental setup along the load path, from the point of application of the actuator loading up to the mechanism connected to the strong floor. A complete free body diagram showing the assumed load transfer mechanism is shown on Figure 6-7. On this diagram, it is assumed that the actuator loading is transferred to the connection at the top of the specimen via a rigid transfer element. This connection distributes the load from the actuator to the full composite section rather than to one of its materials because the cap plate is welded to the tube and the threaded rods connecting the transfer element to the specimen are embedded in the concrete and welded to the top plate.

The load applied to the specimen at its top is then transferred (through the specimen) to the composite box section at its base by bending and shear $\left(M_{pos}, V_{pos}\right)$ such that the point of maximum moment over the height of the assembly occurs just above the top plate of the box connection.

First the column specimen transfers the shear load to the top plate of the composite box by bearing against the tube-to-plate welded connection; shear and bending stresses result from this action in the plane of the plate which are transferred to the top flanges of the channels through the welds connecting the two components. Those stresses are estimated and used to size the top plate.

For bending, the moment transferred by the specimen is equilibrated by equal and opposite forces that develop in the top and bottom flanges of the C-channels to create a couple. So the bending moment transferred by the specimen is used directly to size the channels.

To avoid slip and rocking of the base connection, the rods that tie the composite box down to the top of the C-channels must prevent slip at the interface between the box section and the strong beam. So the box-to-strong beam connection is designed as slip critical. Because of the limited amount of materials involved in this experiment, design of the setup was carried out only for the strongest specimen and extended to all other specimens.

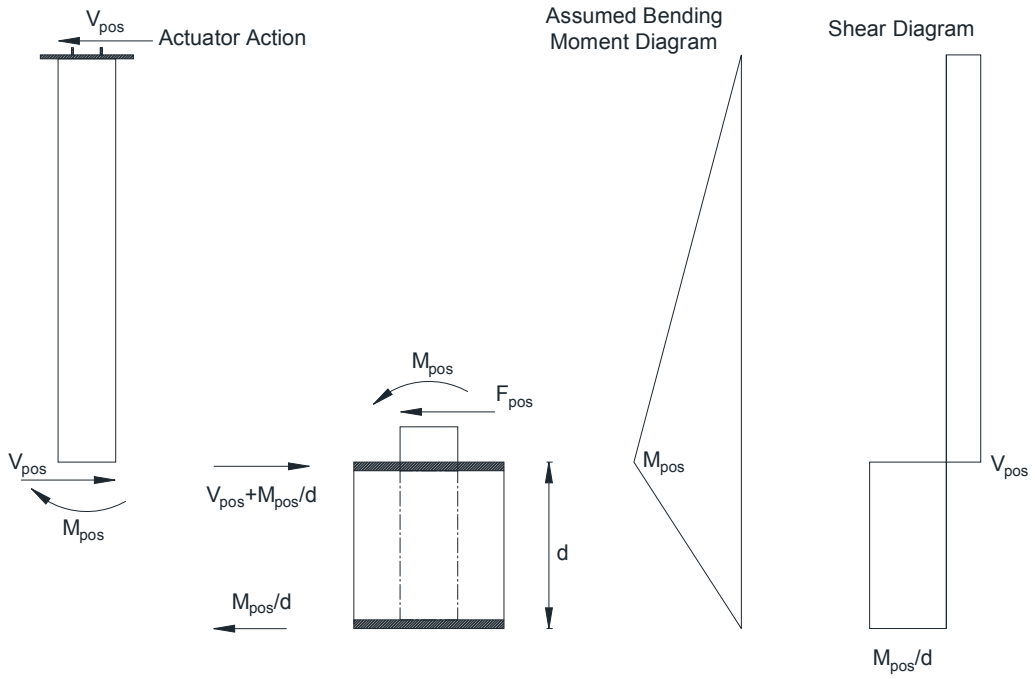

Figure 6-7: Load Transmission (only showing forces on column)

6.4.2 Selection of the Transfer Element

The transfer element played the role of a spacer and served as an extension of the actuator end; as such, it needed to be axially rigid, so as not to deform under the load applied by the actuator,

and transfer that load. This was achieved by oversizing its flanges and web; this built-up member was made by welding 1-in thick web plates to ½-in thick flange plates.

6.4.3 Cap Plate

The cap plate of the specimen was chosen so that it could transfer the maximum expected actuator load without exceeding its in-plane shear strength. Being welded to the outside tube only, it was assumed that the plate was loaded around its perimeter by stresses of magnitude:

$$f = \frac{V_{pos}}{\pi D_0 t_{cp}} \leq \phi_p F_{vp} \tag{6-2}$$

where:

D_0 is the diameter of the outside tube

ϕ_p is strength reduction factor taken as 0.9 for both bending and shear in this case

V_{pos} is the maximum expected loading coming from the actuator given by:

$$V_{pos} = \frac{M_{pos}}{H} \tag{6-3}$$

H is the cantilever height of the specimen

F_{vp} is the shear strength of the plates (taken as $0.6F_{yp} = \frac{3}{5}F_{yp}$)

F_{yp} is the yield strength of the plates (taken as 36 ksi)

t_{cp} is the thickness of the cap plate

Rearranging Equation (6-2) yields the required thickness of the plate as:

$$t_{cp} = \frac{V_{pos}}{\pi D_o \phi_p F_{vp}} = \frac{5M_{pos}}{3\pi D_o \phi_p F_{yp} H} \tag{6-4}$$

Once the thickness of the cap plate was determined, the final plate dimensions were chosen to be that of a square whose side is equal to the diameter of the tube plus an overhang. Based on the diameter ($8in$) of the largest tube of the specimen, the plate width was set to $12in$, effectively giving an overhang of 2in on all sides of the tube to allow easy welding of the plate to the external tube of the specimens.

6.4.4 Threaded Rods of the Cap Plate

As mentioned before, 4 threaded rods connecting the transfer element to the specimen via the cap plate were used to introduce load to the specimen. Hex nuts were welded at the end of the rods that were embedded in the concrete to create a headed anchor. The effective length of embedment $\left(h_{eff}\right)$ of that built-up anchor was $16in$. Because the construction of this anchor was similar to that of cast in place headed anchor bolts (Figure 6-8), its design was based on the provisions for anchors of Appendix D of ACI 318-11 (ACI, 2011).

For design, it was assumed that this anchor was simultaneously loaded in tension and in shear. The tensile force to each anchor came from bolt pretension resulting from tightening the visible extremities of the rods to the transfer element. Shear load $\left(V_{pos}\right)$ applied to the group of anchors came from the actuator load estimated for design as the shear associated with the maximum

possible flexural strength of the specimens $\left(M_{pos}\right)$. This shear was assumed to be distributed equally between the rods.

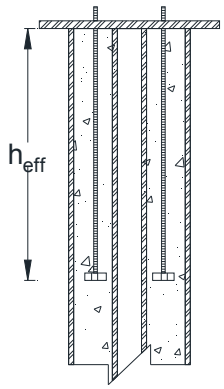

Figure 6-8: Cast in Place Threaded Rod Anchor

The interaction of tension and shear on anchors is treated in section D.7 of ACI-318. According to that section, if both $N_{ua} \geq 0.2\phi N_n$ and $V_{ua} \geq 0.2\phi V_n$, then interaction should be considered using Equation (6-5):

$$\frac{N_{ua}}{\phi N_n} + \frac{V_{ua}}{\phi V_n} \leq 1.2 \tag{6-5}$$

In this equation:

N_{ua} is the ultimate tensile load applied to an anchor or a group of anchors

ϕN_n is the tensile strength of an anchor or a group of anchors

V_{ua} is the ultimate shear load applied to an anchor or a group of anchors

ϕV_n is the shear strength of an anchor or a group of anchors

Four generic checks are needed to obtain ϕN_n (Figure 6-9). Three design checks are necessary to obtain ϕV_n (Figure 6-10). The objectives of those checks are to prevent failure of the anchors and safeguard against brittle failure modes such as concrete blowout or concrete break out. The values of the reduction factors, ϕ, for each type of failure mode can be found in section D.4.4 of ACI 318-11. For the current design, the anchors were contained within the confines of the tubes and, while still checked (for completeness), failure of the anchor resulting from brittle behavior of the concrete was unlikely. Based on this design, threaded rods design ½ in in diameter were found to provide adequate resistance for the load to transfer and the assumed embedment length.

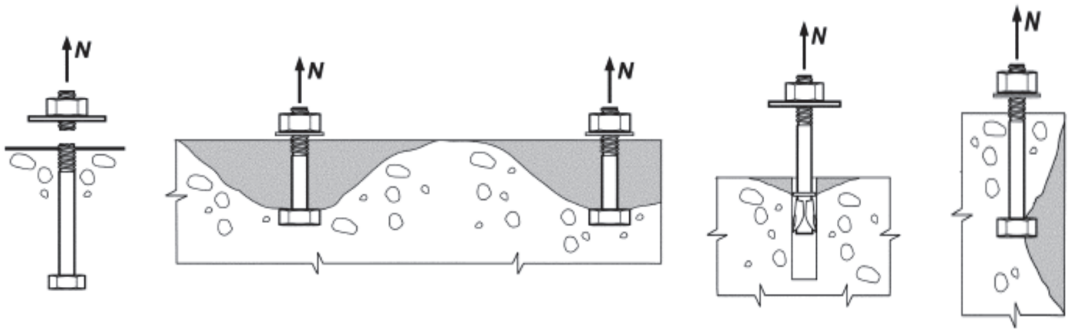

Figure 6-9: Generic Design Checks for Anchor Bolts in Tension (after ACI 318-11)

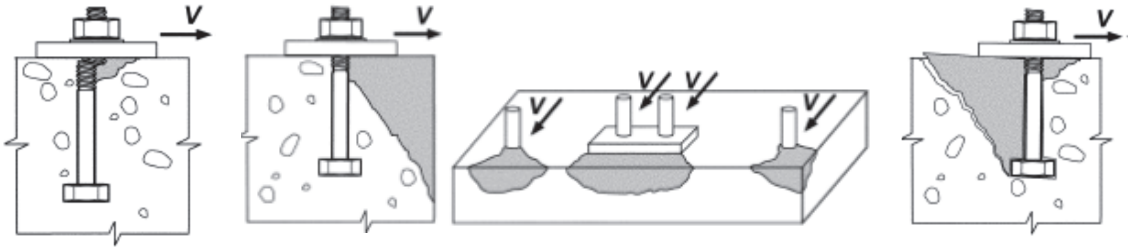

Steel Failure Concrete Breakout Concrete Pryout

Figure 6-10: Generic Design Checks for Anchor Bolts in Shear (after ACI 318-11)

6.4.5 Cap Plate-to-Specimen Weld Connection

Since connections to the transfer beam should not yield or fail, it was decided that designing the circular weld connecting the specimen to the cap plate for the full expected transferred load $\left(V_{pos}\right)$ would provide a desirable protection against connection failure. For design purpose, it was assumed that the load carried by the full length of the circular weld and uniformly distributed over its length was:

$$w_u = \frac{V_{pos}}{\pi D_0} \tag{6-6}$$

The unit resistance of the circular weld was estimated as:

$$\phi R_n = 2\int_0^{\frac{\pi}{2}} \phi\left(0.707w\right) F_w D_o d\theta \tag{6-7}$$

where:

ϕ is the load resistance factor for weld taken as 0.75

w is the thickness of the weld thickness

F_w is the nominal resistance of the weld calculated as:

$$F_w = 0.60F_{EXX}\left(1+0.5\sin^{1.5}\theta\right) \tag{6-8}$$

F_{EXX} is the resistance of the electrodes assumed equals to 70ksi

θ is the angle that sustain the circular arc of weld, for a circular weld $\theta = 2\pi$

Using this procedure, the minimum weld thickness of $1/8$ in recommended in AISC J2.4 was found to be adequate for all specimens. The base metal was checked against shear failure and the design was satisfactory.

6.4.6 Box Connection Design

No yielding of the elements used to connect the specimen to the foundation beam was allowed. In other words, the base needed to be stronger than the specimens. In that perspective, the channels that were part of the box section used at the base were capacity-designed. The selection of the structural channels was done assuming that they carried the maximum expected plastic moment of the specimen (factored to account for strain hardening). The required combined section modulus (S) of the channels was determined as function of the yield strength of the channels ($F_{yc} = 36ksi$):

$$S = \frac{M_{pos}}{F_{yc}} \tag{6-9}$$

The channels were also checked against flange local bending action, web yielding, web crippling and web compression buckling.

Some of the dimensions of the composite box section were constrained by the existing conditions in the testing area. For instance the width of the top and bottom plate of this built-up section could be at most equal to the width of the top flange of the strong beam (16*in*); no significant overhang was allowed for those plates and advantage was taken of the existing holes in the flange of the strong beam to achieve connections. Selection of the plates' thickness and length was based on an analysis of the state of stress in the plane of the plate. The main equations for that analysis were adapted from Bruneau and Fujikura (2007), where a similar analysis can be found.

Considering transmission of bearing stress between the specimen and the plate to be uniformly distributed over the perimeter of the outside tube, the minimum thickness $\left(t_p\right)$ required to limit shear stress in the plate and for the plate to transfer the bearing loads to the channels was obtained from:

$$\frac{F_p}{\pi t_p D_o} = \phi_p F_{vp} \tag{6-10}$$

Equation (6-10) can be resolved into:

$$t_p = \frac{V_{pos}}{\pi D_o \phi_p F_{yp}} + \frac{5M_{pos}}{3\pi D_o \phi_p F_{yp} d} \tag{6-11}$$

with:

$$F_p = F_{pos} + \frac{M_{pos}}{d} \tag{6-12}$$

In Equations (6-10) to (6-12) :

M_{pos} is the maximum feasible strength of the specimen

D_o is the outside diameter of the specimen

ϕ_p is the strength reduction factor taken as 0.9

d is the depth of the channels

F_{yp} is the yield strength of the plates (taken as 36 ksi)

F_{vp} is the shear strength of the plates (taken as $0.6F_{yp}$)

In addition, assuming that the plate is simply supported at its welded edges and loaded by the resultant of the bearing stress$\left(F_p\right)$, to keep elastic the average shear in the plates for the case of beam-action, the length $\left(l_p\right)$ of the plate was obtained from:

$$F_{vp}\phi_p = \frac{3\left(V_{edge}\right)}{2A_s} = \frac{3\left(\frac{F_p}{2}\right)}{2t_p l_p} \tag{6-13}$$

Substituting all variables that have previously been defined into Equation (6-13) leads to:

$$l_p = \frac{5F_{pos}}{4t_p F_{yp}\phi_p} + \frac{5M_{pos}}{4t_p F_{yp}\phi_p d} \tag{6-14}$$

Finally, the maximum bending stress in the plate under in-plane beam-type loading was not allowed to exceed $\phi_p F_{yp}$. The bending stress in the plate was calculated using mechanics as:

$$\sigma_{\max} = \frac{m_{\max}\left(l_p/2\right)}{I_P} \leq \phi_p F_{yp} \tag{6-15}$$

where I_P is the inertia of the plate considering the presence of the hole (to accommodate the outside tube in its middle), and given by:

$$I_P = \frac{1}{12} t_p \left(l_p^3 - D_o^3 \right) \tag{6-16}$$

$M_{\max}$ is the maximum moment that can develop in the "beam-plate" loaded by the resultant of the bearing stress $\left(F_p \right)$ and given by:

$$m_{\max} = 0.25 F_p b_p = 0.25 b_p \left(V_{pos} + \frac{M_{pos}}{d} \right) \tag{6-17}$$

Combining Equations (6-15) to (6-17) gives Equation (6-18), which can be solved for l_p :

$$\left(\phi_p F_{yp} t_p d \right) l_p^3 - 1.5 \left(V_{pos} d + M_{pos} \right) b_p l_p - \left(\phi_p F_{yp} t_p d \right) D_0^3 = 0 \tag{6-18}$$

where b_p is the width of the plate and all other parameters have been previously defined.

However, contrary to the case in Bruneau and Fujikura, here the plates were not embedded in concrete and were therefore not supported out-of-plane. As a result, in the current set-up, it was necessary to safeguard against out-of-plane buckling of the plate. For this purpose, the top plate was assumed simply supported on two parallel edges and loaded perpendicularly to its free edges; for such boundary conditions, the critical buckling stress in the plate can be estimated as (Timoshenko and Gere, 1961):

$$\sigma_{cr} = k \frac{\pi^2}{12} \frac{E}{1 - \nu^2} \left(\frac{t_p}{b_p} \right)^2 \tag{6-19}$$

where E is the modulus of elasticity of steel (29000ksi) and ν is the Poisson's ratio of steel (0.3)

k is a buckling coefficient which depends of the aspect ratio $\left(\frac{l_p}{b_p}\right)$ of the plate. For an aspect ratio equal to unity, it can be conservatively taken as 2.

6.4.7 Threaded Rods at the Base

The diameter of the threaded rods connecting the specimen to the foundation beam was constrained to $1.25in$ to fit existing holes in the top flange of the foundation beam. The rods were designed to transfer the maximum expected shear and the pretension in the bolts to the strong beam as a slip critical connection. AISC J.3 provisions for bolted connection were followed. In particular, the effects of combined tension and shear (AISC J.3.7 and J.3.9) were both checked.

6.4.8 Consideration of Accidental Eccentricity

Since no lateral bracing was provided for the test specimen, the effects of accidental eccentricity were evaluated. A 5% eccentricity in the applied actuator load was assumed. The existence of eccentricity would cause eccentric shear to be transferred to the rods in the transfer zone, which would result in an increase in their demands. Eccentricity would also cause biaxial bending in the composite box section, in the floor beam and a subsequent amplification of the efforts in the connections. All checks were performed and the potential effects of eccentricity were found to have insignificant effects on the setup.

6.5 Construction of the Specimens and Experimental setup

The first step in constructing the specimens consisted of pre-punching holes with the appropriate diameter in all the plates to be used. The foundation box was assembled by clamping in place its top and bottom plate to the flanges of the channels and welding them in the desired position. Figure 6-11 shows a box beam and the fully constructed base detail; the layout for the positioning of the tubes is visible on the bottom plate of the picture on the left.

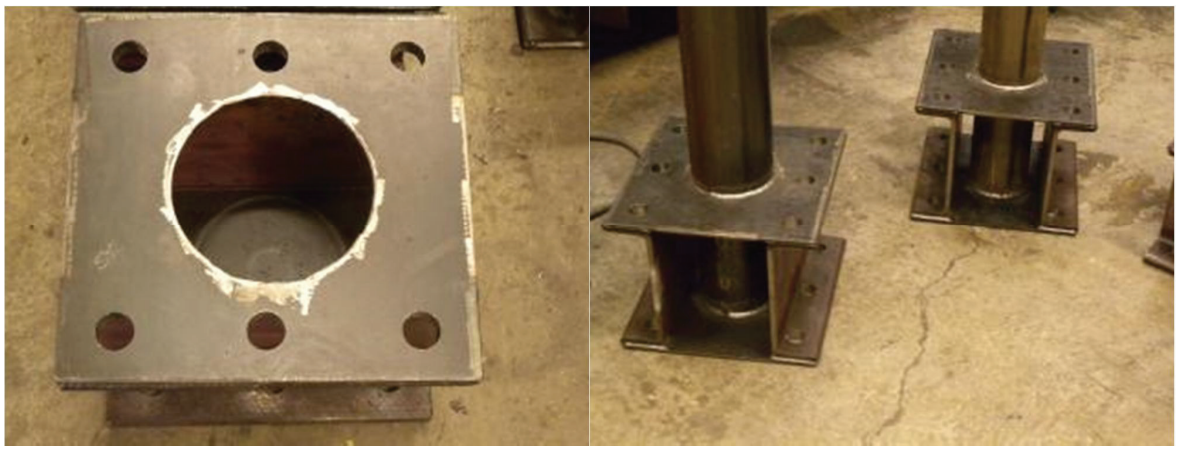

Figure 6-11: Composite Box Base

In the top plate of each base component, a circular hole centered on the plate, and whose diameter is oversized by ⅛ in with respect to the diameter of the outside tube of any given specimen, was precut (Figure 6-11). This is to allow the inner tube and the outside tube of the specimen to be respectively slid into that hole, put in contact with and centered on the base plate,

and finally fillet-welded to that plate as shown on Figure 6-12. Once this was done, the ⅛ in gap between the edge of the top plate hole and the outside tube of the specimen was filled with a fillet weld that joined the outside tubes and the top plate of the box section.

An alternate starting point was considered during the construction of the specimen which, instead of assembling the box foundation first, consisted of welding respectively the inner and the outer tubes to the base plate of the composite box section, adding the channels on the side, and then sliding the top plate of the base over the outer tube. The two methods of construction were compared, and it was realized that the first approach offered a better construction sequence and was more suited to shop construction.

Using magnetic levels, it was carefully verified that the columns were plumb at every subsequent stage of the construction. Maintaining the spacing between the concentric tubes uniform all around and all over the height of the column specimen was critical. Small diameter rebar with length matching the projected thickness of the core region were welded between the inside and outside tubes to hold them in place and obtain the desired spacing thickness. Self-consolidating concrete was then poured in between the tubes.

Figure 6-12: Tubes and Base Section Assembly

Right after concreting, the cap plate (Figure 6-13) was placed on top of each specimen, with its anchors embedded in the concrete. The edges of the cap plate had to be parallel to the edges of the base box to ensure that no significant load eccentricity was applied to the specimen. To further safeguard against such eccentricity, two sets of rod patterns matching the layout of the anchor rods in the cap plate were pre-drilled into the bottom flange of the transfer beam. These

patterns were drilled such that the axes of the (rigid) transfer element matched with the axis of the cap plate. The final step of the construction was to weld the cap plate to the top of the specimen, which was done a week after pouring.

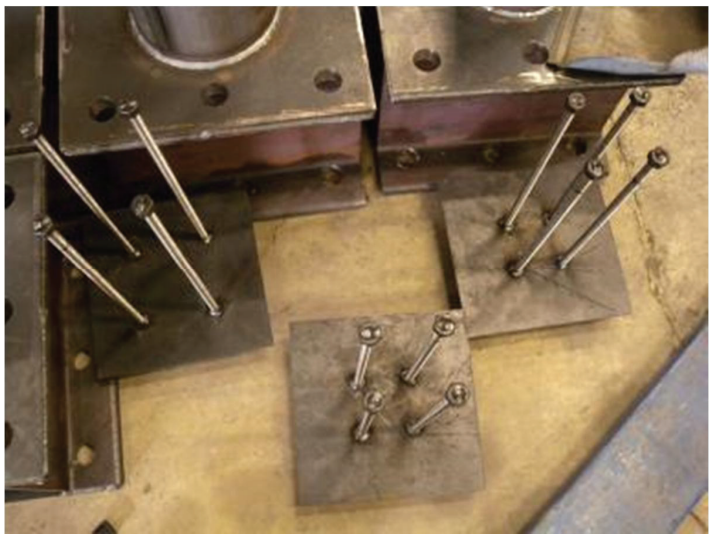

Figure 6-13: Cap Plates, showing different anchor spacing patterns

6.6 Instrumentation

The instrumentation for this test program was designed to capture response parameters essential in establishing the main structural characteristics of the specimens for comparison with theoretical values. The parameters of interest in that case were displacement response, strength, and overall deformation (deformation and strain distributions at the cross section level). In

addition, strain deformations were also collected as they were helpful to detect instances of yielding, plastic excursions, and overall strain distribution over the portion of the specimen comprised in the box beam region. Overall deformation response of the specimens could help characterize ductility and hysteretic behavior of such sections.

Because of the significance of this last parameter, redundancies were necessary to get enough confidence in the main measurements. Three different measurements of specimen deformations were taken. One came directly from the displacement transducer in the actuator, another one from a set of string displacement potentiometers (string pots) connected to an external reference point, and the last one from a Krypton Dynamic Measurement Machine (model K600 by Nikon Metrology). Figure 6-14 shows a close up view of the specimens where the locations of some of the instruments are indicated. All three sets of equipment were connected to the input channels of two data acquisition systems: a digital system entirely dedicated to the Krypton Dynamic Measurement Machine and an analog system with recording channels for the string pots and the actuator. Drawings with precise locations of instruments are presented in the following sections.

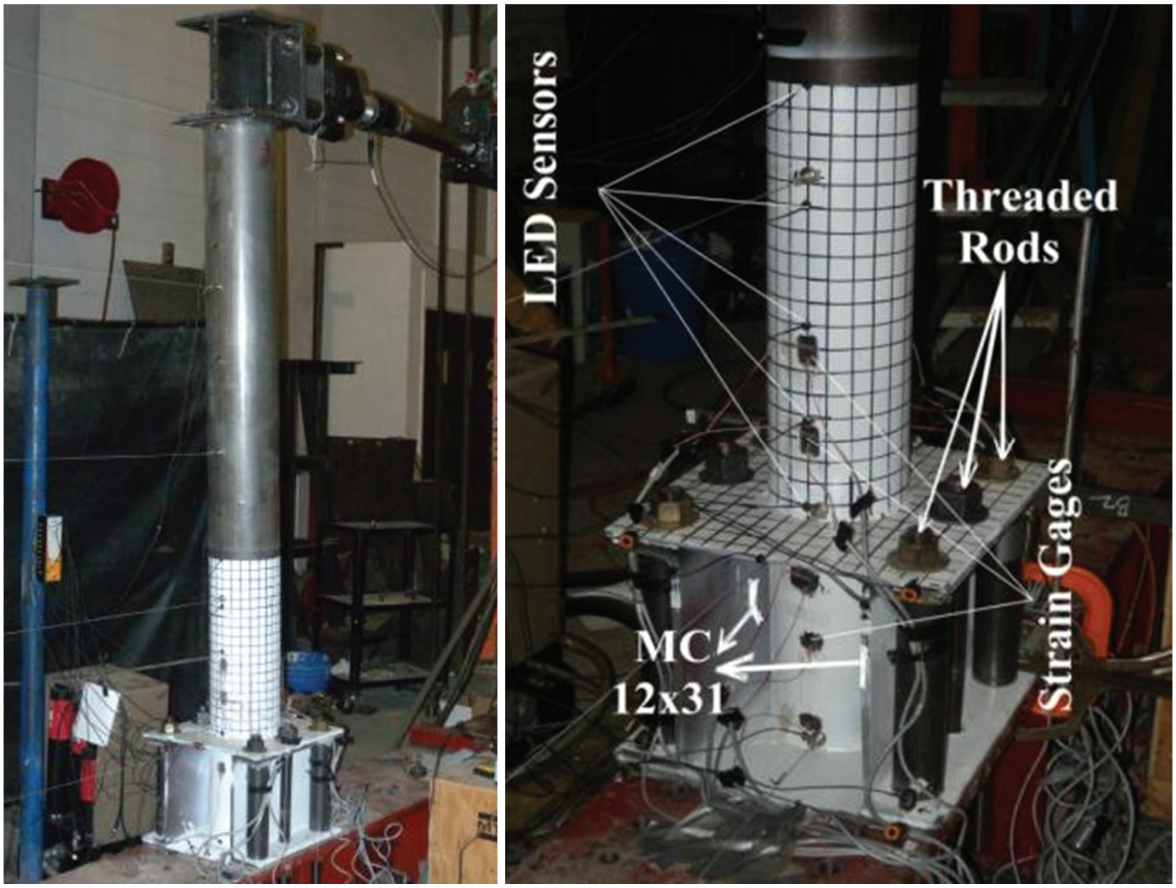

Figure 6-14: Global View and Close Up Showing Partial Instrumentation of a Specimen

6.6.1 Strain gages

Strain gages were placed in the longitudinal and circumferential directions to capture strain distribution over the base of each specimen. They were located in the expected plastic region of the cantilever, its elastic region, as well as in the hypothesized elastic to plastic transition region. Strain gages were also placed below the point at which maximum moment is expected, to check how far down plastic strain would spread below this point. All strain gages used were CAE-06-

125-UW-120 gages from VGP/Micro Measurement. Specimen S3 which was tested first was instrumented with eight (8) strain gages; the number of gages was increased to twelve (12) starting with the second test, then to sixteen (16) with the last test to determine with more accuracy the transition zone between the plastic to elastic regions of a specimen. Figure 6-15 shows the strain gage layout for the specimens, the strain gages numbered 1,3,5,7,9,11 and 13 to 16 were all placed vertically.

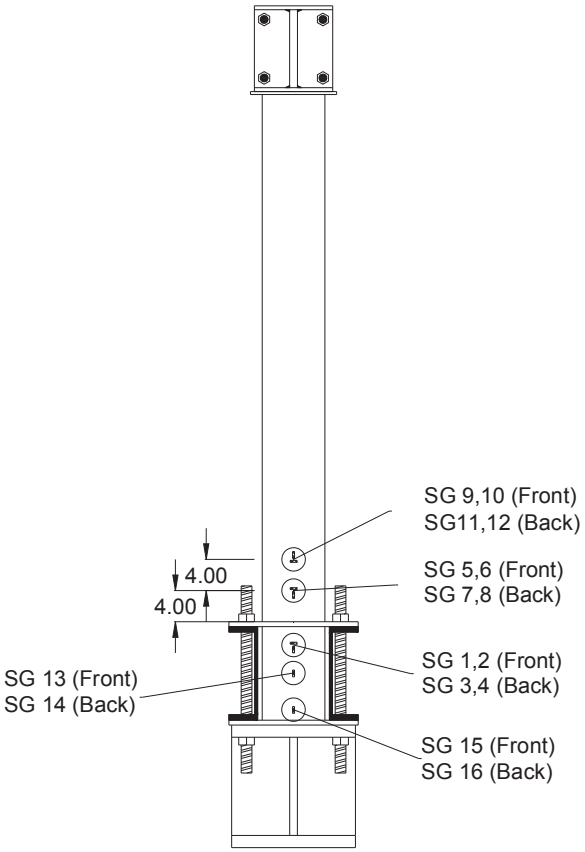

Figure 6-15: Strain Gage Layout [Units Shown in inches, 1in=25.4mm]

6.6.2 Linear Potentiometers

A MTS 244.31 actuator provided the loading for this test. This actuator has capacity rating of 25kips and a stroke of ±12in. This actuator is instrumented with integrally mounted displacement transducers and load cells which record both the displacement and the load applied to the specimen at each stage of an experiment. Although this actuator records displacement data, the

displacement output may be affected by small shift in the test setup, deformation in the load transfer region or by the flexibility of the frame to which the actuator is mounted to. This output cannot be used without proper corrections. Since it is difficult to accurately measure such small disturbances, those data are seconded by more accurate measures coming, in that case, from other linear displacement potentiometers.

A total of six (6) linear displacement potentiometers (string pots) labeled SP1 to SP6 were used on the test specimens. The locations of the string pots on the specimen are shown on Figure 6-16. The distribution was similar for the other specimen; the string pot labeled SP6 was added just above the weld connecting the CFDST specimen to the bottom plate of the composite base section. This was done to monitor possible horizontal slippage at the interface between the setup and the top flange of the foundation beam.

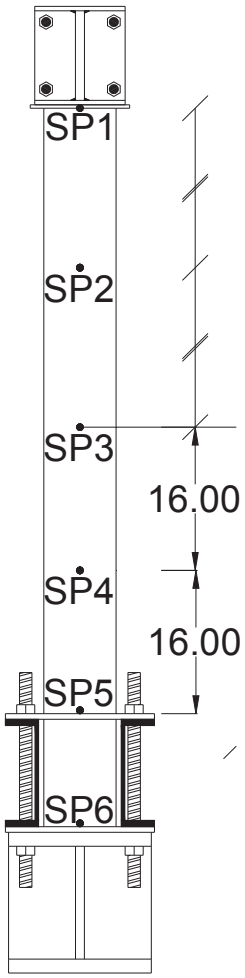

Figure 6-16: Typical String Pots Layout [Units Shown in inches, 1in=25.4mm]

6.6.3 Krypton Dynamic Measurement Machine

Each specimen was equipped with a comprehensive set of Light Emitting Diodes (LED) to produce measurements with respect to six (6) degrees of freedom (three in rotation and three in

translations). This was particularly important since no lateral bracing was provided to the specimen and it was then necessary to measure possible out of plane deformation. This was also necessary if the effect of the flexibility of the box connection, if significant, was to be considered in the measurement.

The number of LED sensors (Figure 6-17) was varied from one test to another to monitor point on the setup whose displacements could become a factor affecting the global behavior of the specimens and to be able, if necessary, to correct the data accordingly. The positions of the LED sensors on the specimen were continuously recorded by the K600 camera system. To increase accuracy, the camera was positioned as far back as feasible from the specimen so all LEDs could fit into its field-of-view without significant loss in accuracy.

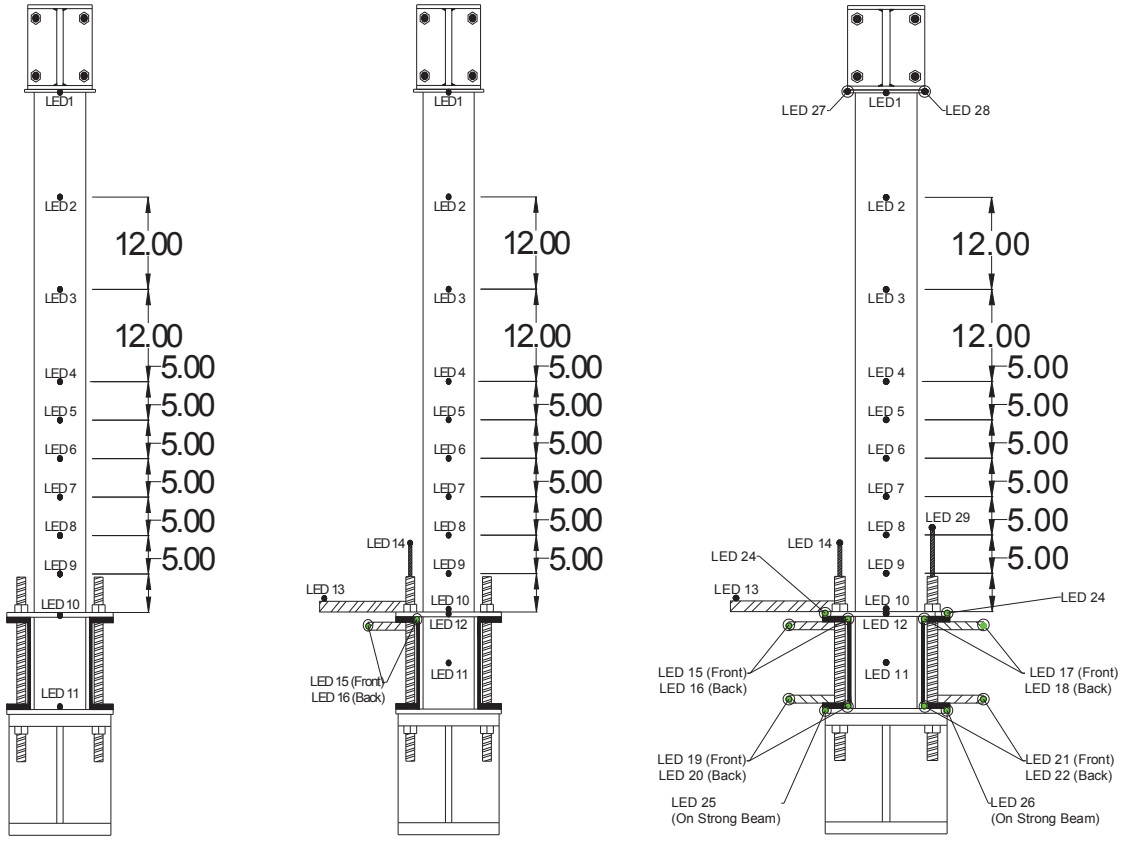

Test 1 and 2 Test 3 and 4 Test 5

Figure 6-17: LED Layout [Units Shown in inches, 1in=25.4mm]

6.7 Experimental Protocol

During the experiment the specimens were submitted to a cyclic pushover test during which each specimen was subjected to cyclic displacements of progressively increasing amplitudes, up to failure. The basic loading protocol adopted for this step is shown on Figure 6-18. At each specified displacement, the specimen was subjected to at least three cycles. Each specimen

underwent a total of at least 30 cycles, the total number of cycles applied before failure varying depending on each specimen's ductility. All tests were conducted in displacement-control mode. The main advantage of such an approach is that each specimen could be closely monitored to capture yielding, buckling and initiation of failure in the ultimate conditions.

In the initial stage of loading, the increments in displacement were smaller in order to capture each specimen's 1st yielding so to use the yield amplitude to define the subsequent cycles (as the loading protocol is in terms of multiples of the yield displacement). Once the yield displacement was determined the full loading displacement history was followed. Since CFDSTs are tested in this context to ascertain their potential for use as bridge column, which sustain relatively modest axial load (less than 10% of its axial strength), no axial force was applied to the columns. Only the lateral displacement history presented for the test protocol was applied at the top of the specimens.

To facilitate the visualization of local deformation in the specimens, the base of all specimens were coated with white wash (except S4 which already had a dark metal finish) and a grid was drawn over the base of the specimen.

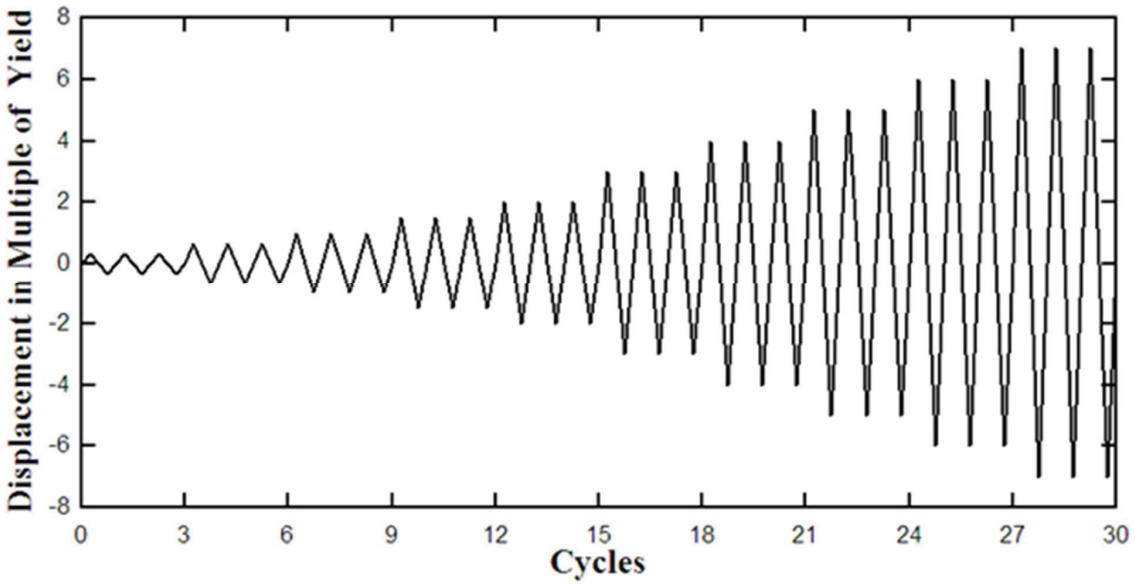

Figure 6-18: Cyclic Pushover Test Loading Protocol

6.8 Experimental Results

This section reports on the behavior of the specimens as observed during the test. Events such as yielding, buckling, and maximum capacity for each specimen are presented. Hysteresis behavior of each specimen is also reported. The displacement history of the specimen during the test was recorded by both the actuator, a string pot labeled SP1, and LEDs. Note that SP1 provided a more accurate measurement of the tip displacement of the specimen than the actuator (which also recorded deformations of the reaction frame). Also, contrary to LEDs, the sampling rate of SP1 matched that of the force from the actuator, making it easier to use the two to create the hysteresis loop of each specimen.

The connections devices at the top and bottom of the specimens did not show any evidence of yielding or instability. The weld and the bolted connections survived the test without damage. During the tests, however, a marginal amount of slip was observed at the base of the composite box for some of the specimens.

6.8.1 Test 1: Specimen S4

Specimen S4 (CFDST 26_48_33) had a measured outside tube thickness of 0.117*in* and inside tube thickness of 0.076*in*; both tubes were compact and highly ductile. The measured outside diameters of the specimen were 6*in* for the outside tube and 2*in* for the inner tube. The percentage of void in the specimen was 33%. When the specimen was cycled at stroke amplitudes of 2*in*, it was observed that the load displacement curve departed from a straight line at an actuator stroke of 1.5*in*. The displacement measured by the linear potentiometer at this time was 0.90*in,* which corresponds to a drift of 1.3%. When yielding occurred; the applied force was 2.75*kips*. Based on the deformation measured by the linear potentiometer, the corresponding stiffness was 2.12*kip/in*. The specimen did not reached its maximum lateral strength of 4.12*kips* (moment strength of 277.1 *kip-in*) until a drift of 6.65%.

When the drift was 4.3%, a buckling wave started to grow on the actuator side of the specimen. The lateral strength of the specimen at the time was 3.65*kips*; on load reversal, a similar bulge appeared on the other side. Those buckling waves observed at 4.3% drift kept growing on the outside tube from a cycle to cycle. At a drift of 7.8%, they reached a peak length of about 1in, with peak amplitude of 3/4*in* on the most compressed side of the specimen. At this stage the bulges grew to encompass about half of the circumference of the outside tube (Figure 6-19).

When the drift reached 7.8%, the actuator ran out of stroke on one side. It was decided to keep cycling the specimen at unequal displacement amplitudes. The amplitude of the displacement on the actuator side kept increasing, while it remained fixed at maximum amplitude of 7.8% drift in the other direction. On the 3rd cycle at a drift of 13% on the actuator side, localized necking in the buckled region on the outside tube was noticeable in the steel. A crack appeared in that region during the next cycles (at 15% drift), followed by a nearly 50% drop in strength. Pulverized concrete spilled out of the crack (Figure 6-20). It was decided to continue the test to see if the inside tube would easily fracture. After 3 cycles at 15% drift on the actuator side, the inner tube had not ruptured; the test was stopped when the drop in strength was about 80% of the maximum value reached during the test. This is equal to the strength (51*kip-in*) of the composite section formed by the concrete and the inner tube acting as a dowel. This also means that the outside tube, while not participating in the resistance of the section per se, was still confining the concrete core.

.

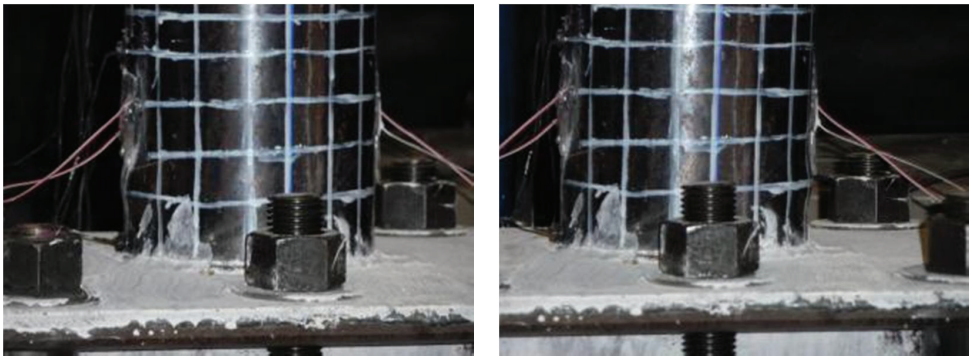

a) b)

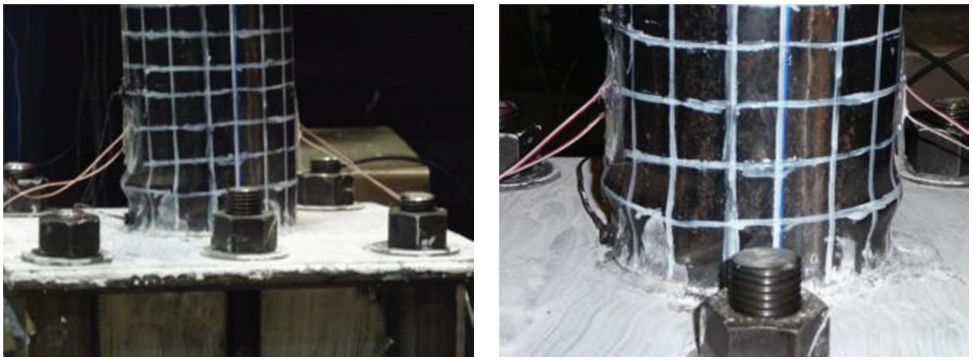

c) d)

Figure 6-19:Buckling Progression of S4

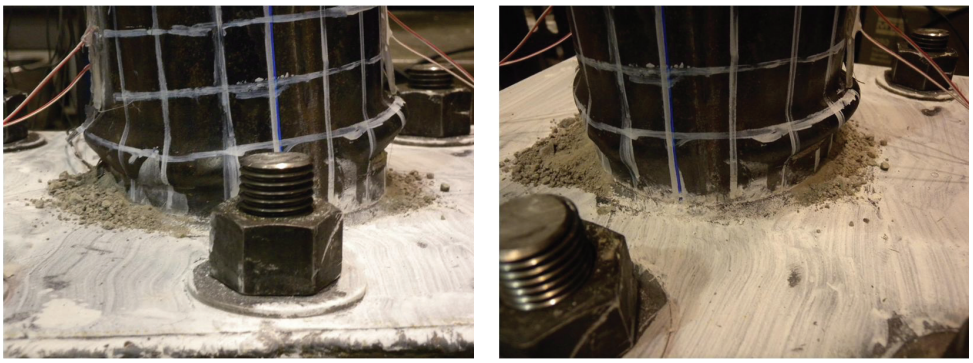

Figure 6-20: Failure of S4

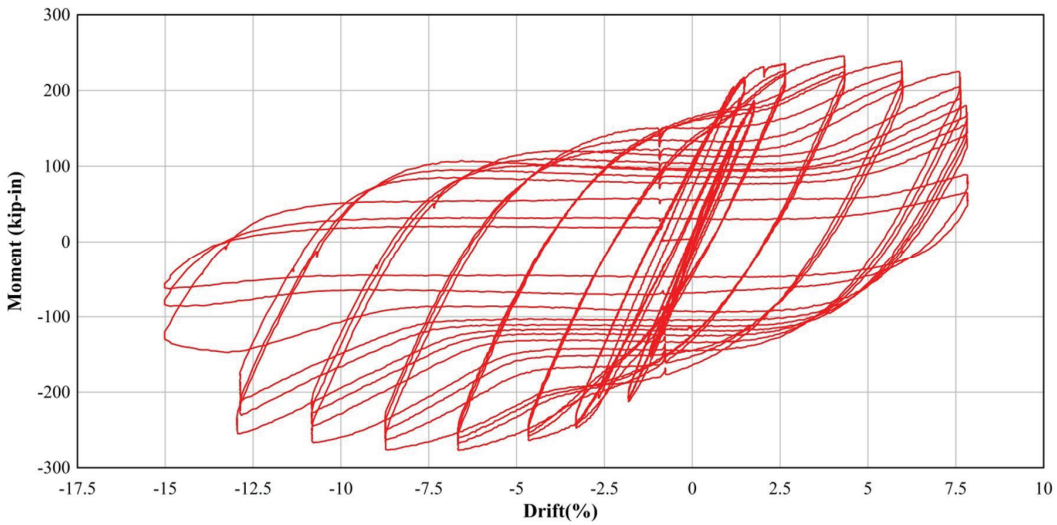

Figure 6-21: Hysteresis Loop for Specimen S4

6.8.2 Test 2: Specimen S1

The tubes thicknesses for Specimen S1 (CFDST 17_72_33) were 0.115*in* and 0.082 *in* for the inside and outside tubes, respectively, and its void ratio was 33%. To prevent the actuator from running out of stroke in one direction, as in the previous case, a spacer was added between the specimen and the reaction Frame to allow developing the full travel length of the actuator in both directions. Departure from elastic behavior was observed for the specimen at a stroke of 1.5*in*, which corresponded to a measured deformation of the specimen of 0.9*in* (1.3% drift). The strength at yield was 1.78*kips* and the apparent lateral stiffness 1.98*kip/in*.

A visible local buckle started to grow on the side opposite the actuator when the specimen was cycled at 3.8% drift. This buckle was located 2*in* from the top plate of the base connection; its wave length was about 0.5*in* and its amplitude 3/4*in* (Figure 6-22). The occurrence of buckling in the specimen was directly followed by pinching in the force-displacement curve. By a drift of 5.4%, the buckling wave was fully formed. At the same time, the specimen reached its maximum

strength of 3.23*kips* (moment strength of 217.2*kip-in*) (Figure 6-24). The full hysteresis loop for the specimen is shown in Figure 6-25.

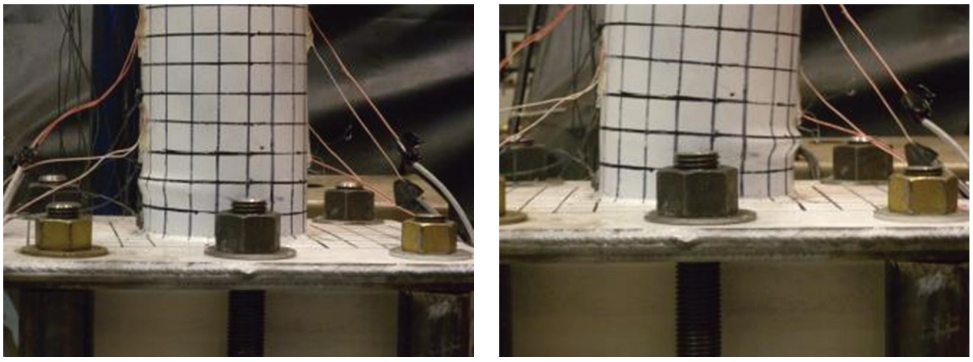

Figure 6-22: First Buckling of Specimen 1

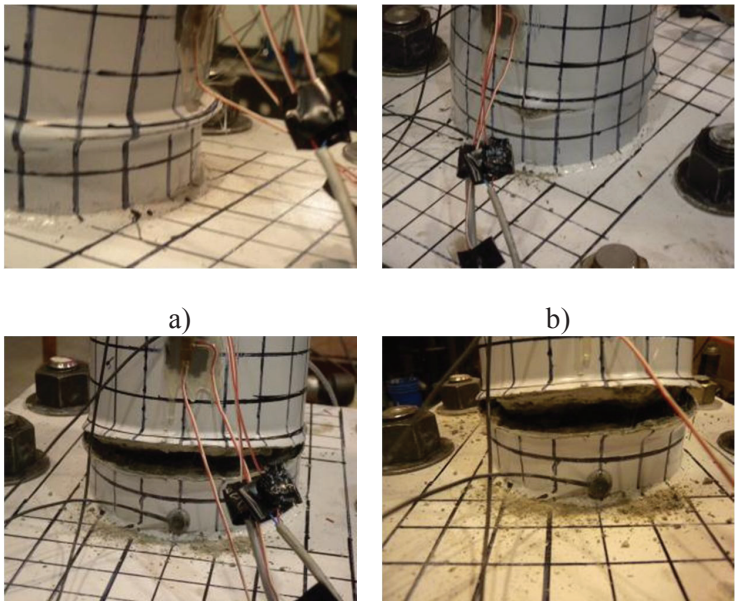

a) b)

c) d)

Figure 6-23: Progression of Failure in S1

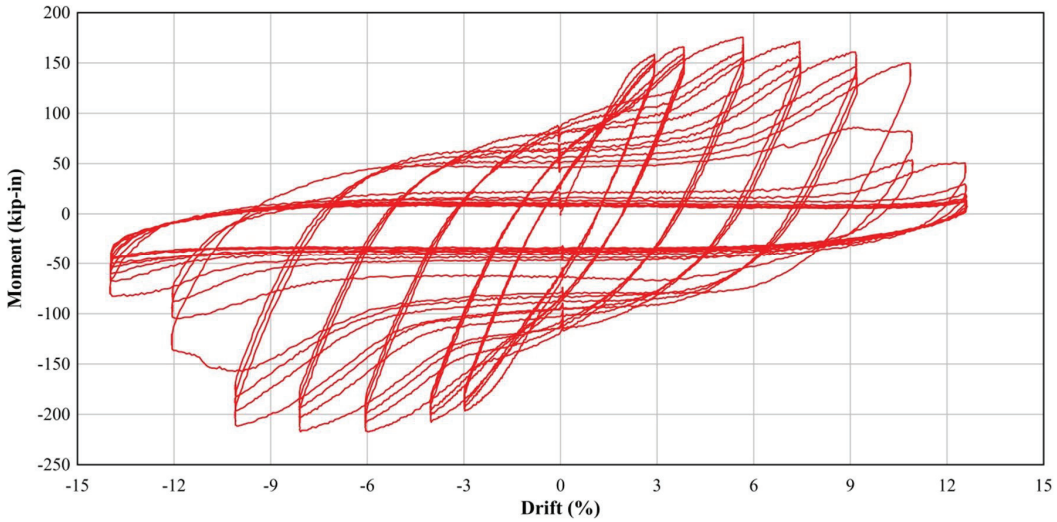

Figure 6-24: Hysteresis Loop for Specimen S1

By 7.3% drift, a crack on the buckling wave on the side opposite the actuator became visible (Figure 6-23). This was directly followed by another crack on the actuator side of the specimen when the load was reversed, which corresponded to a 33% reduction in strength. As the crack was growing, the specimen gradually lost strength. Fracture of the specimen occurred during the same cycle (Figure 6-23) and pulverized concrete came out of the crack.

As the specimen was further cycled, the hysteresis loop of the specimen stabilized to a residual loop. The residual loop was not symmetric; the average of the negative and positive peak forces was 28.5*kip-in*, which is close to the capacity of the inner tube (28.4*kip-in*).

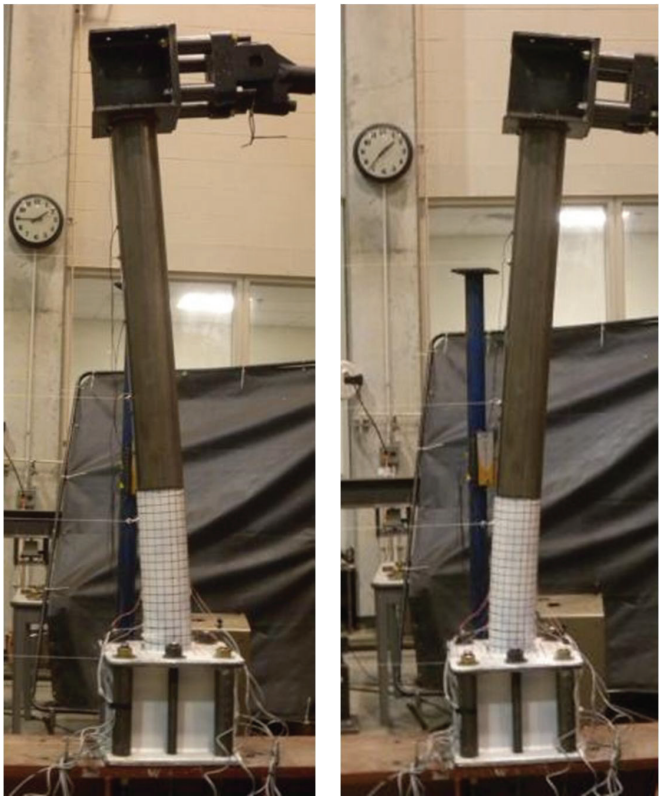

Figure 6-25: Specimen S1 at 5.4% Drift

6.8.3 Test 3: Specimen S2

Specimen S2 (16_70_25) had the lowest void ratio of all the tested specimens (25%) but its concrete core was the thickest (3in). The measured outside diameters of its tubes were respectively 8*in* and 2*in* and their thicknesses 0.112*in* and 0.115*in*. Some changes were made to the instrumentation of this specimen as discussed previously; beyond those, the test proceeded as for S1. Yielding occurred at a stroke of 1.5*in*; the corresponding potentiometer measurement was 0.9*in*, the yield force 5.85*kips,* and the apparent stiffness 6.5*kip/in*. Although some pinching in

the hysteric curve was already visible in the force-displacement at drift of 5.7%, the first buckling wave did not really form until the specimen reached its peak lateral strength of 9.44*kips* (moment capacity of 634.84*kip-in*), at a drift of 8.4% on the side opposite the actuator (Figure 6-26 and Figure 6-27). From there, the buckle grew to final amplitude of about 1*in* at 11% drift; its wave length was about the same (Figure 6-28).

Failure progression in the specimen is illustrated in Figure 6-29. Necking of the steel toward the fixed base of the specimen was detected on the tension side during the first cycle at 13.6% drift. On load reversal, a crack formed suddenly in the previously compressed side. The strength of the specimen was reduced by about a third. The specimen was cycled at that amplitude to assess the residual strength provided by the inner tube as done in the previous tests. The average residual moment strength (25*kip-in*) was about equal to the inner tube capacity (22.24*kip-in*).

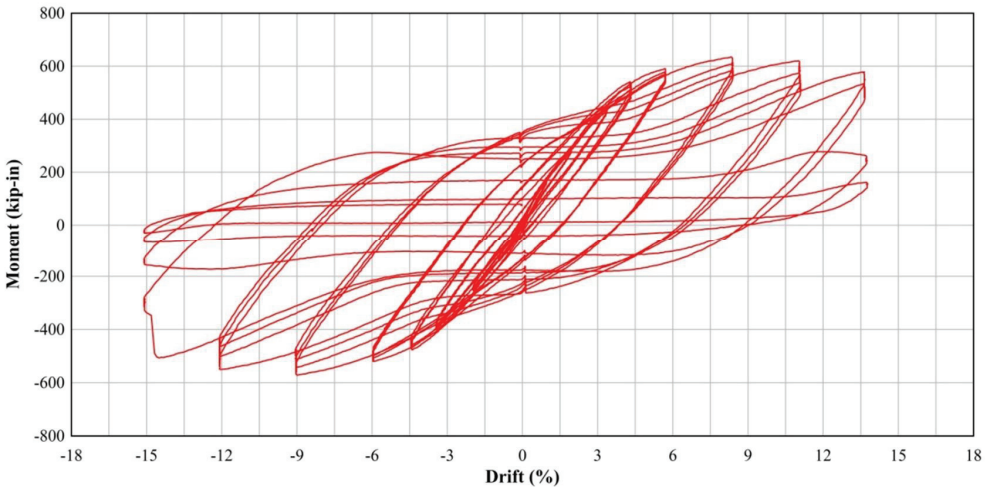

Figure 6-26: Hysteresis Loop for Specimen S2

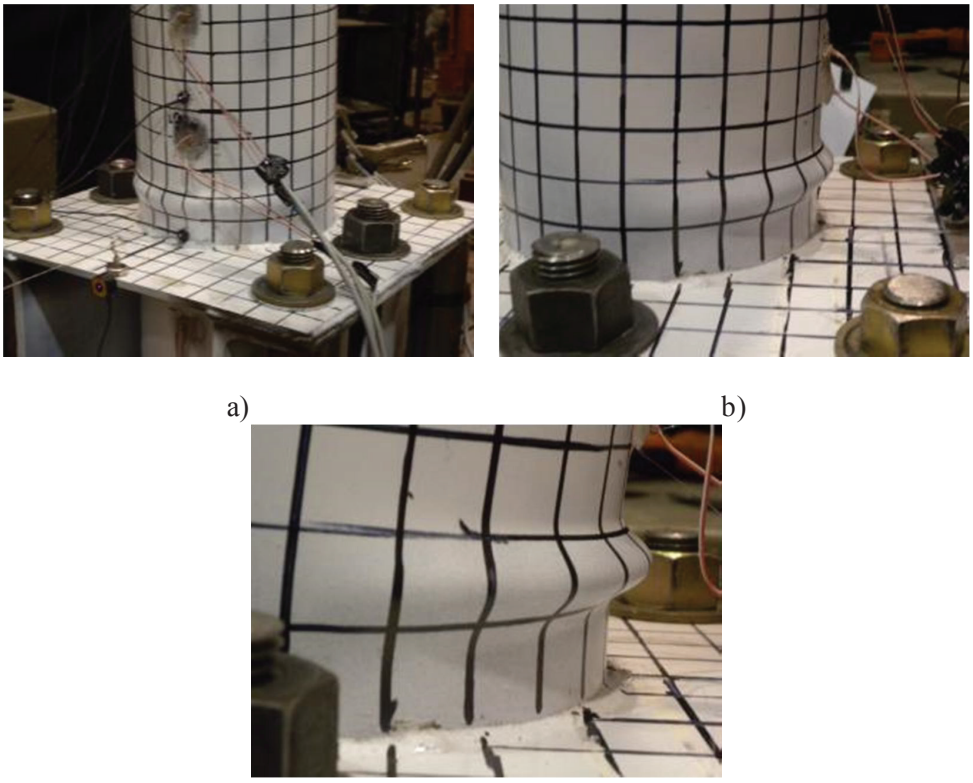

a) b)

c)

Figure 6-27: Buckling Progression in Specimen 2

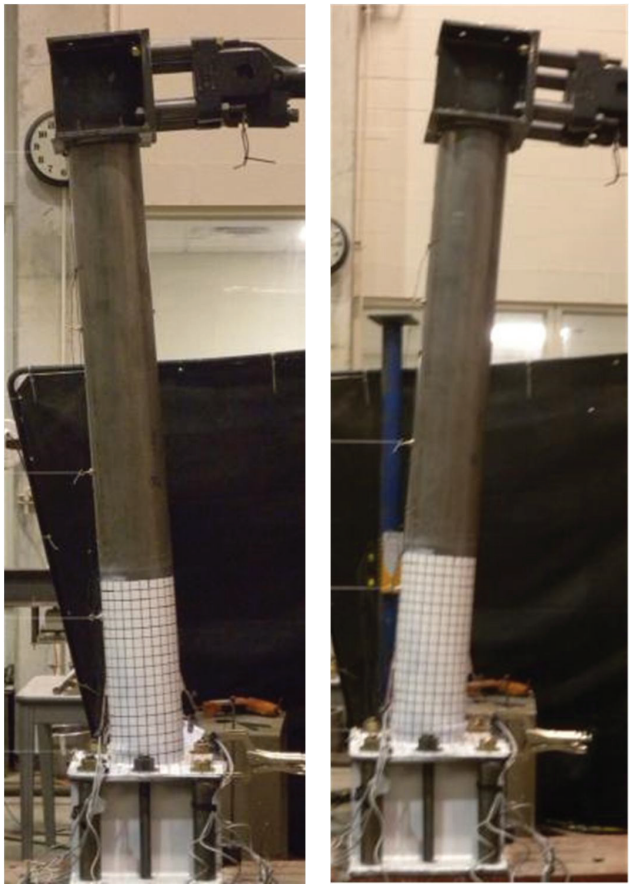

Figure 6-28: Specimen at 5.7% Drift

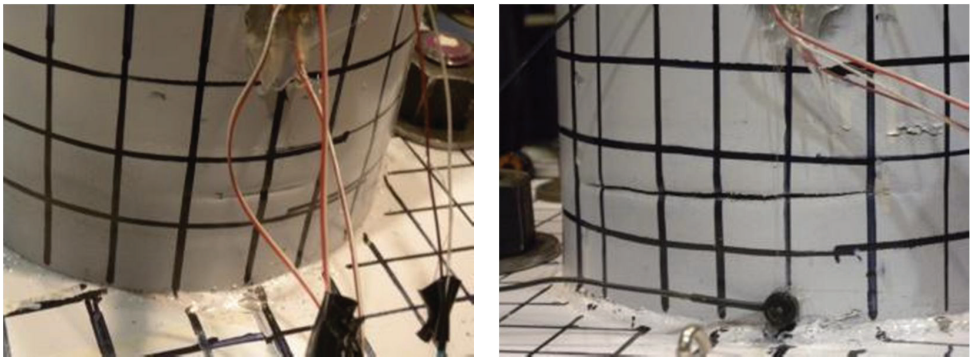

a) b)

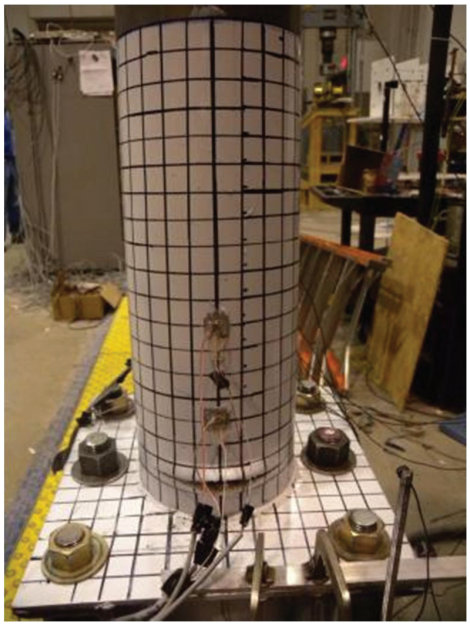

c)

Figure 6-29: Failure Progression in S2

6.8.4 Test 4: Specimen S5

Specimen S5 (CFDST 56_70_63) had similar strength to S2, but conversely to S2, its void ratio was the largest and its concrete core the thinnest of all the tubes. The outside diameters of its tubes were respectively 8*in* and 5*in*, with corresponding measured thicknesses of 0.114*in* and 0.09*in*. The force displacement response for this specimen is shown on Figure 6-30.

Yielding of the specimen occurred at the same stroke of 1.5*in* (0.9*in* specimen displacement or 1.3% drift) for an applied force of 7*kips*, which resulted in an apparent stiffness of 7.8*kip/in*. The lateral strength of the specimen reached a maximum of 10.3*kips* (moment strength of 692.7*kip-in*). Buckling happened at a drift of 5.7% (Figure 6-31). The maximum strength was also reached at this drift, as consistently observed for the other specimen.

On the side opposite to the buckle, the coating applied to the specimen started to flake, indicating that S5 was further yielding. At 7.4% drift, a buckle "bulge" grew to encompass the entire diameter of the specimen (lower right picture in Figure 6-31); the crest of that bulge was about 0.75in over a wave-length of 1in. Flaking of the coating intensified as a sign of further plastification.

Fracture in the buckled region was visible during the cycles at 9.1% drift. Progression of deformation of the base of the specimen until failure is shown in Figure 6-32, similarly to the behavior observed for all the specimens. Figure 6-33 shows the specimen at maximum deformation before rupture. At rupture, the residual strength of the specimen was about 80kip-*in*, which is higher than the resistance of the inner tube by itself (64.35*kip-in*). This suggests that some concrete was still contributing to that residual strength; as a matter of fact, the specimen

was not cycled up to the point beyond fracture after which stable residual loop could be observed (as in the other specimens).

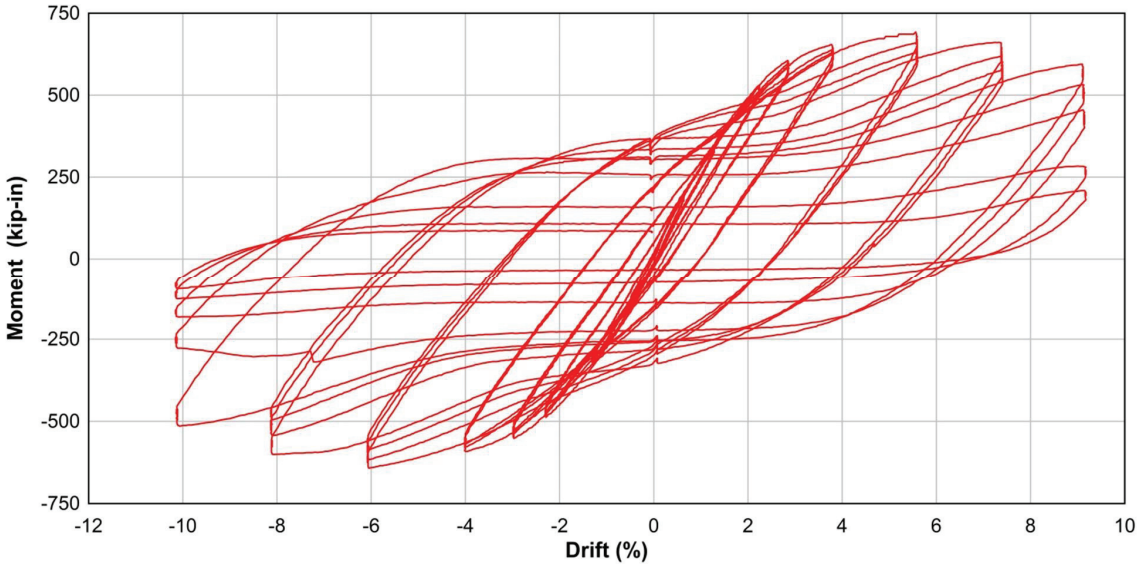

Figure 6-30: Hysteresis Loop for Specimen S5

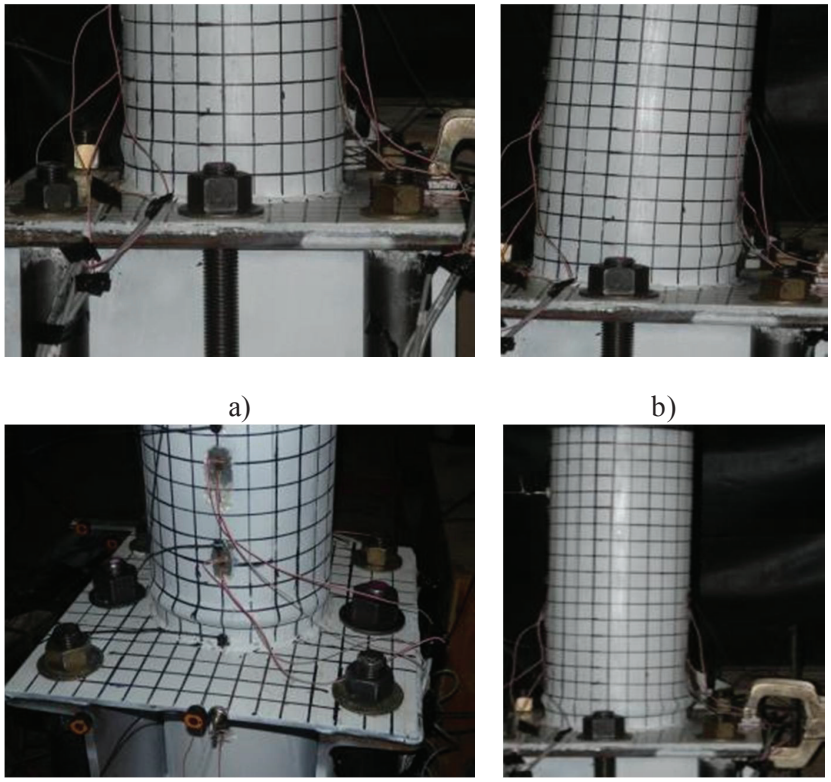

a) b)

c) d)

Figure 6-31: Progression of Buckling in S5

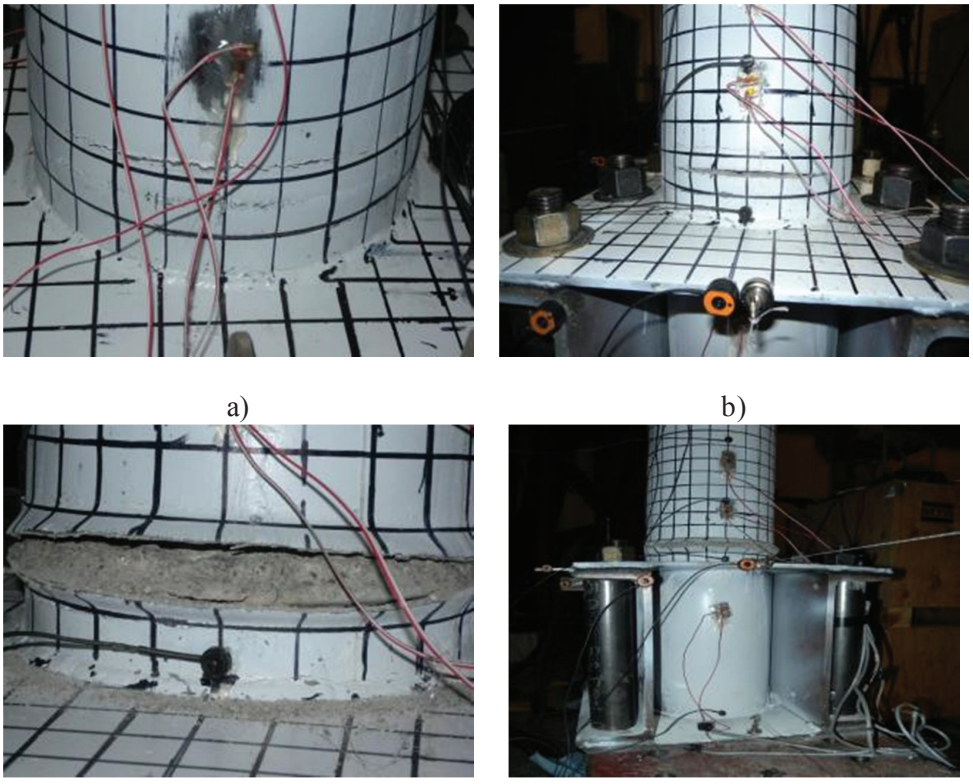

a) b)

c) d)

Figure 6-32: Progression of Rupture in S5

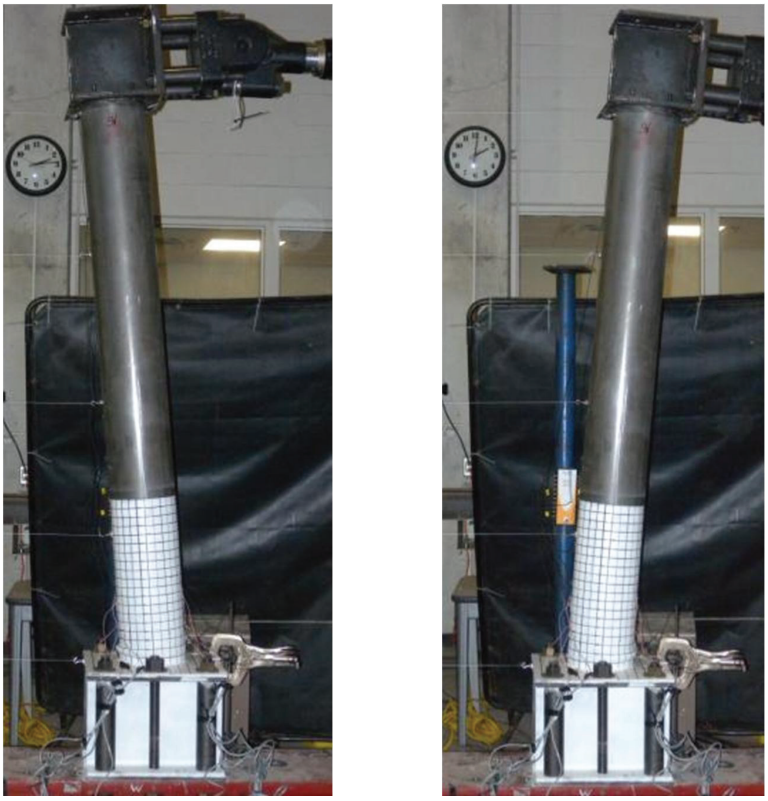

Figure 6-33: Specimen S5 at Maximum Deformation Before Failure

6.8.5 Test 5: Specimen S3

Both the inner and the outer tubes of S3 (respectively of diameter 2.5*in* and 6.625*in*) were considered highly ductile and combined for an estimated void ratio of 38%. Specimen S3 was 4*in* longer than all other specimen tested. Yielding of the specimen was observed around 1.3% drift (0.9*in* measured by the potentiometer). At yield, the lateral strength of the specimen was 3.8*kips* and its apparent stiffness 4.2 *kip/in*.

S3 did not show any sign of local buckling until a drift of 8.1%. First visible evidence of local buckling occurred when the specimen attained its peak lateral strength of 7.3*kips,* with

corresponding moment strength of 517.3 *kips-in* (see the hysteresis loop in Figure 6-34 and deformed shape in Figure 6-37), which is consistent with the previous observations. The buckling wave spanned the full diameter of the specimen; its amplitude was 0.5*in* and its wavelength 1*in* (Figure 6-35).

The strength of the specimen degraded significantly when the drift reached 12.2%, when the specimen suddenly lost 50% of its strength. This drastic reduction in strength was due to crack initiation in the buckled region (Figure 6-36), at the apex of the buckling wave.

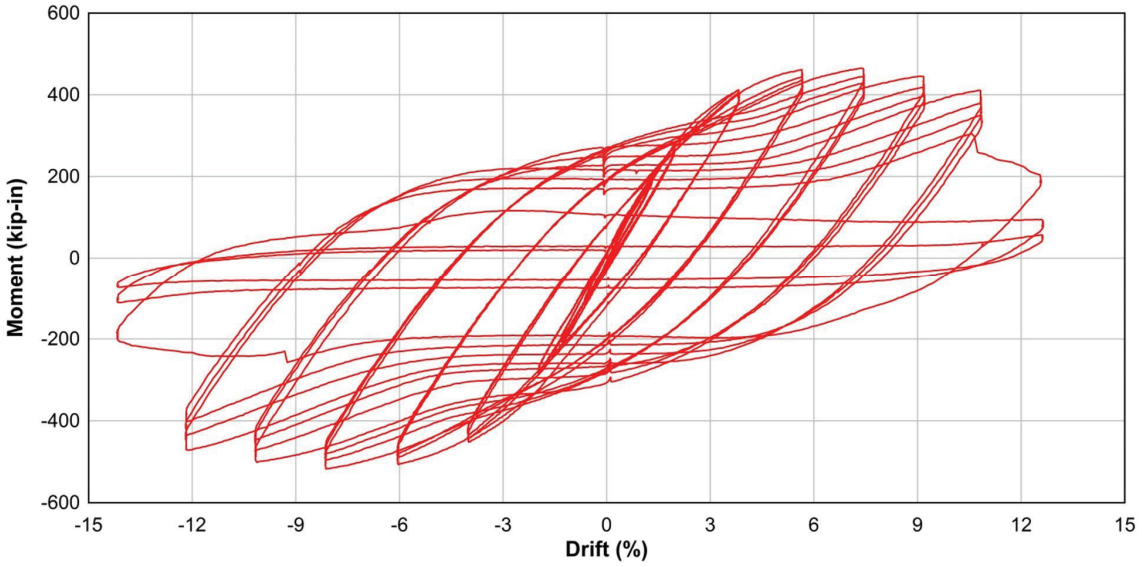

Figure 6-34: Hysteresis Loop for S3

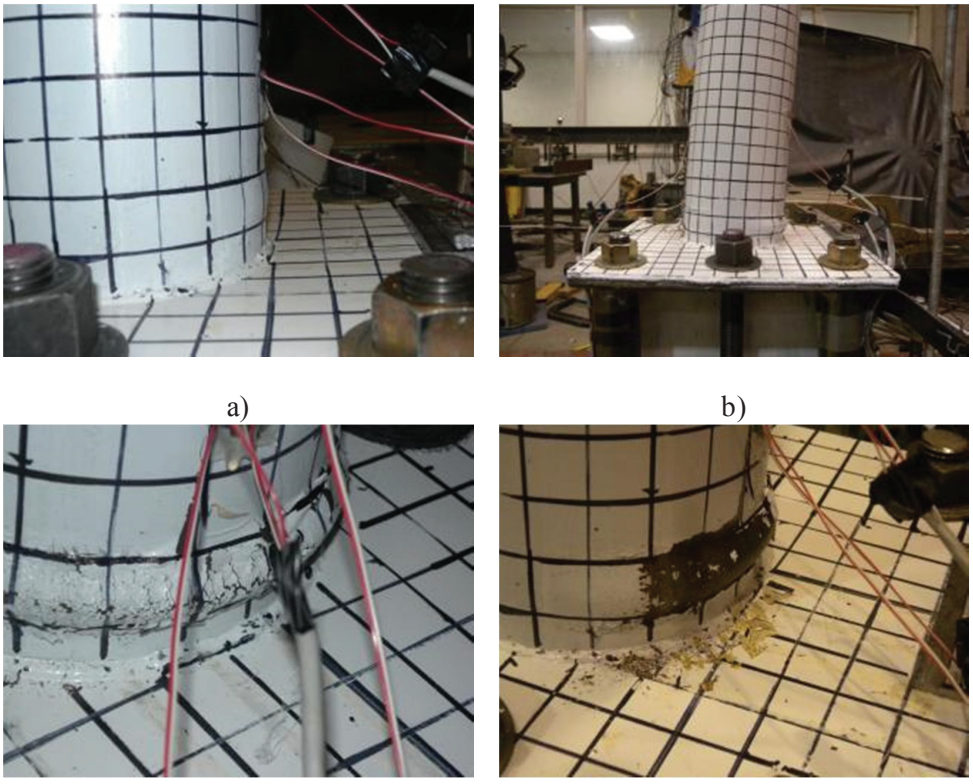

a) b)

c) d)

Figure 6-35: Progression of Buckling in S3

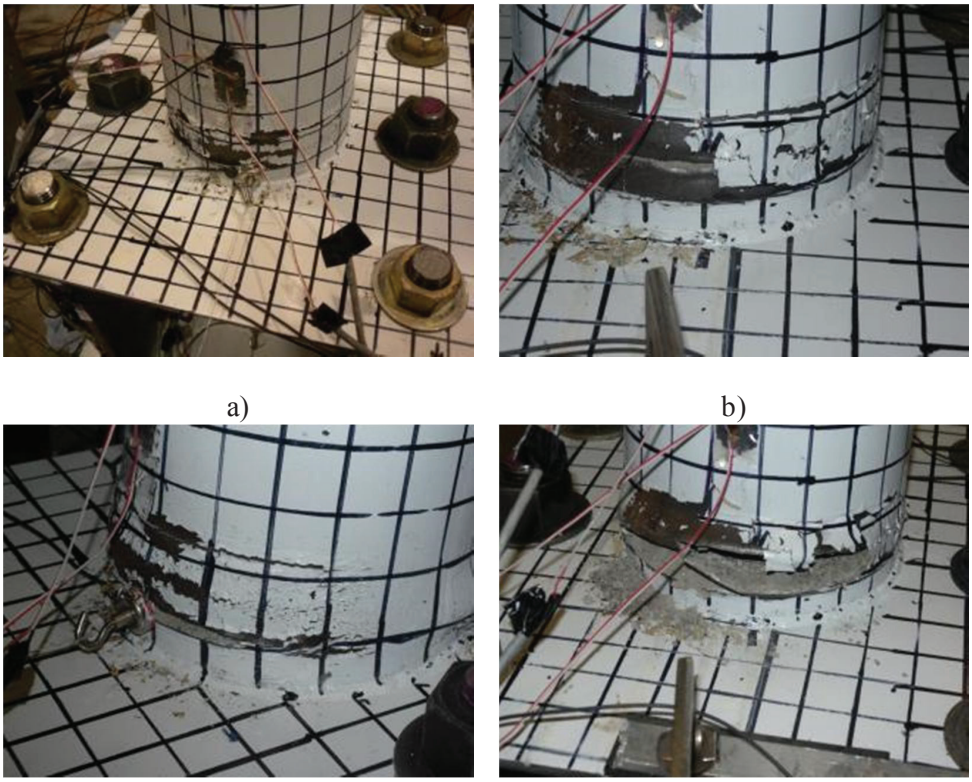

a) b)

c) d)

Figure 6-36: Progression of Failure in S3

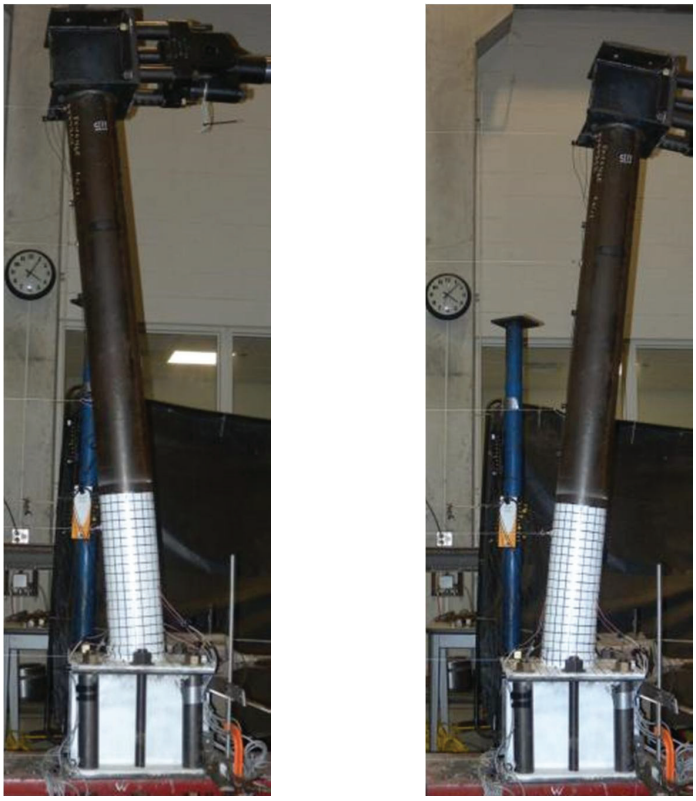

Figure 6-37: Specimen S3 at Maximum Deformation (8.1% Drift)

6.9 Considerations of Base Slip and Connection Flexibility

In the experimental program reported in this section, LED sensors and Linear Potentiometers were placed on the specimens to track the movements and deformations of the specimens and their immediate attachments. Because neither the connection at the base of the specimen nor the strong beam nor the reaction frame were truly rigid, the deformations measured for the specimens with respect to the assumed point of fixity at the level of the top plate of the box connection had to account for the slip, rigid body motion, or deformations of the connecting

elements (including the strong beam or the reaction frame itself). This section describes some of these measured effects and their significance.

6.9.1 Specimens S4 and S1

To account for the translation and rotation of the box connection for the specimens S4 and S1, readings from the String Pots 1 (see Figure 6-17), 10, and 11 were aggregated. LEDs 10 and 11 were used to evaluate the translation of the strong beam-(assuming that the base of the specimen moved in unison with it) and the translation of the top of the box connection, both of which to be subtracted from the recorded overall deformations of the specimen. Examples of such corrections follow.

Designating the readings of String Pot 1 and the LEDs along the strong beam axis as u_{1x}, u_{10x} and u_{11x}, the displacement u_x at the top of the specimen is first modified as:

$$u_{x1} = u_{1x} - \left(u_{10x} - u_{11x}\right) \tag{6-20}$$

For the same specimens, rotation of the box beam is accounted for by considering the readings along the vertical axis of the specimens. Using similar notations:

$$\theta_{y1} = \frac{\left(u_{10z} - u_{11z}\right)}{L_B} \tag{6-21}$$

In Equation (6-21), $L_B = 16in$ is the length of the box connection at the base of the specimen. From those considerations the drift reached by specimens S4 and S1 can be calculated as:

$$\delta = \frac{u_{x1}}{H} - \theta_{y1} \tag{6-22}$$

The cantilevered height (H) of the specimen, measured from the top plate of the base connection to the top of the column's cap plate is used to calculate the drift.

The additional displacement due to deformation of the strong beam and translation of the box connection is shown on Figure 6-38 for S4, which is stronger than S1. As can be seen from this graph the maximum additional deformation due to the flexibility of this specimen was about $2.9\text{x}10^{-2}in$. Compared to the deformation at maximum strength of S1 ($3.63in$), this effect would be marginal (less than 1% of reduction in deformation). The drift corresponding to this deformation (5.4%) would be virtually unchanged. The same held true when the maximum drift reached by the specimen (7.8%) was considered for analysis.

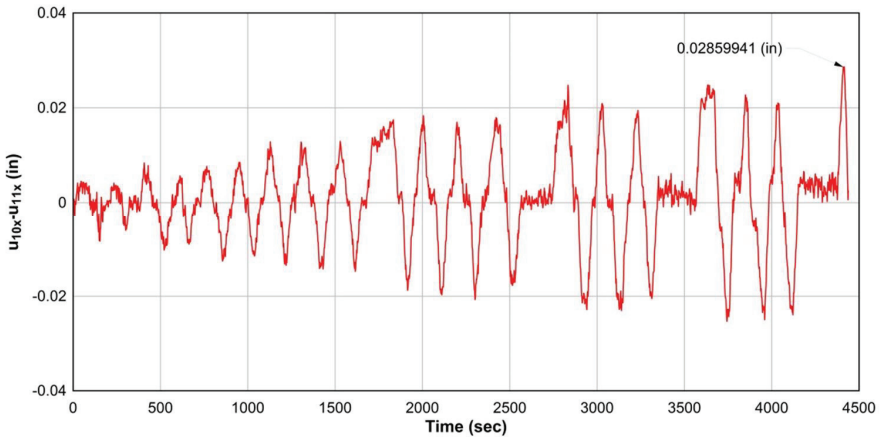

Figure 6-38: Deformation at the Base of Specimen S4

The additional drift added to the specimen due to rotation of the box connection is shown in Figure 6-39 for S4. At its maximum, it was of the order of 0.002*rad;* removing this rotation from the maximum recorded drift of 7.8% gives a corrected maximum drift of 7.6%. This correction of less than 5% is, for all practical purposes, insignificant

Because S4 was stronger than S1, larger slips and deformation at the base of the connection box of S4 were expected. Because the two specimens failed at similar drift, the impact of base slip and flexibility on S1 was even less significant than that reported above for S4.

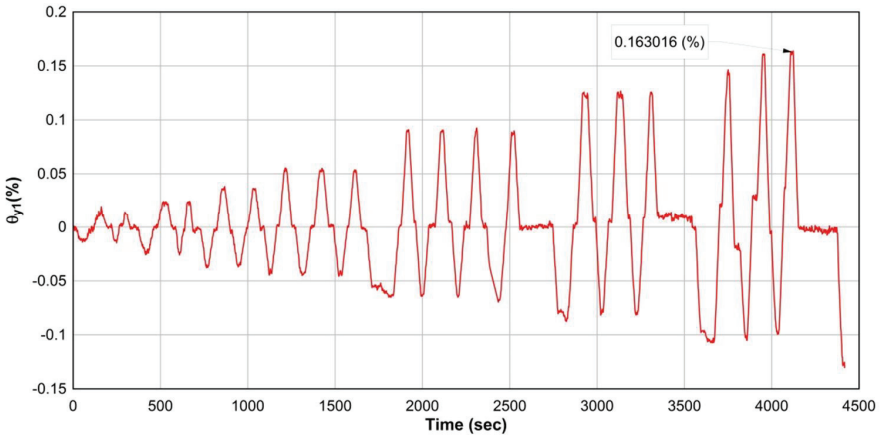

Figure 6-39: Rotation at the Base of Specimen S4

6.9.2 Specimens S2 and S5

More instruments were added for the test on specimen S5. LED 12, added at the front end of the box connection top plate, together with LED 13, mounted on an extension attached to the back end of the box connection, recorded movements of this plate. The addition of LEDs 12 to 14,

installed during test on S5, also helped account for deformations of the strong beam. Finally LEDs 15 and 16 were positioned on the top left side of the channels to account for their contribution to the overall deformation of the specimen. LED12, 13, 15 and 16 were used to give supplemental results, but random spikes made the measurements from 12 and 13 unusable. Because of their location LED10, 15 and 16 were expected to record similar movements if the box connection behaved as a rigid element. From Figure 6-40, it can be seen that this was indeed the case, although LED16 recorded the largest deformation at that location.

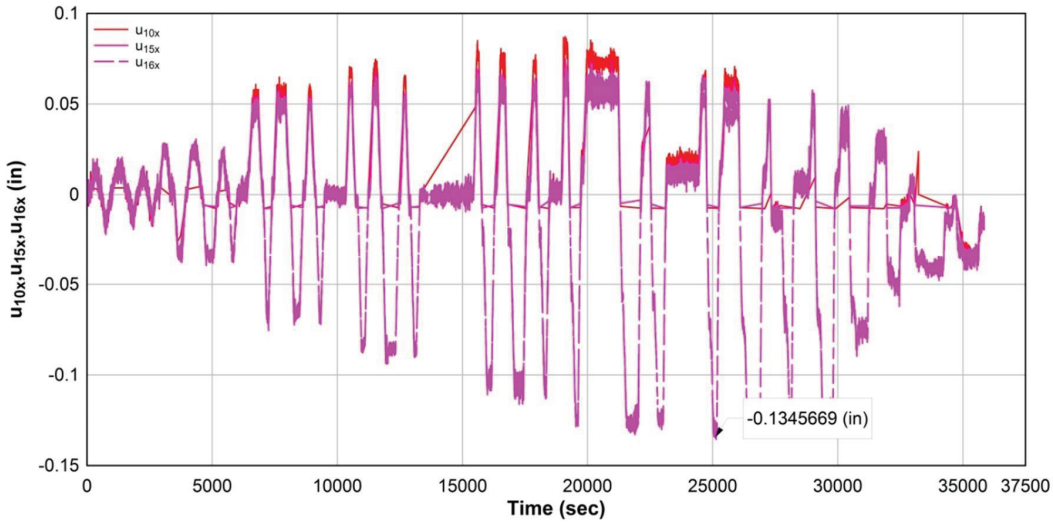

Figure 6-40: Axial Displacement History at the Top of the Box Connection of Specimen S5

Deformation of the strong beam reported by LED14 also contained too many random spikes to be reliable (see left side of Figure 6-41). An attempt was made to remove those spikes using the

graphing software DPlot (Hyde, 2013) but the resulting data still proved to be unusable (right side of Figure 6-41).

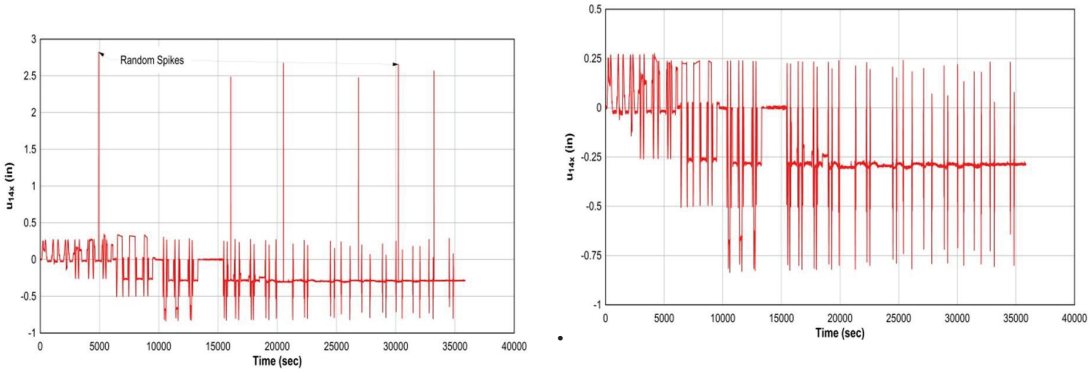

Figure 6-41: Axial Deformation History of the Strong Beam Specimen S5

As a proxy to estimate deformation of the strong beam, the string pot labeled SP6 on Figure 6-16 was used. Consequently the correction on the displacement for S2 and S5 was taken as:

$$u_{x1} = u_{1x} - \left(u_{16x} - u_{x6}\right) \tag{6-23}$$

The maximum axial deformation at the base of the specimen (Figure 6-42) was calculated as $0.128in$. As for the previous case, this deformation had little consequence on the measured maximum deformation of S5 (6.1in at failure for a drift of 9.1%).

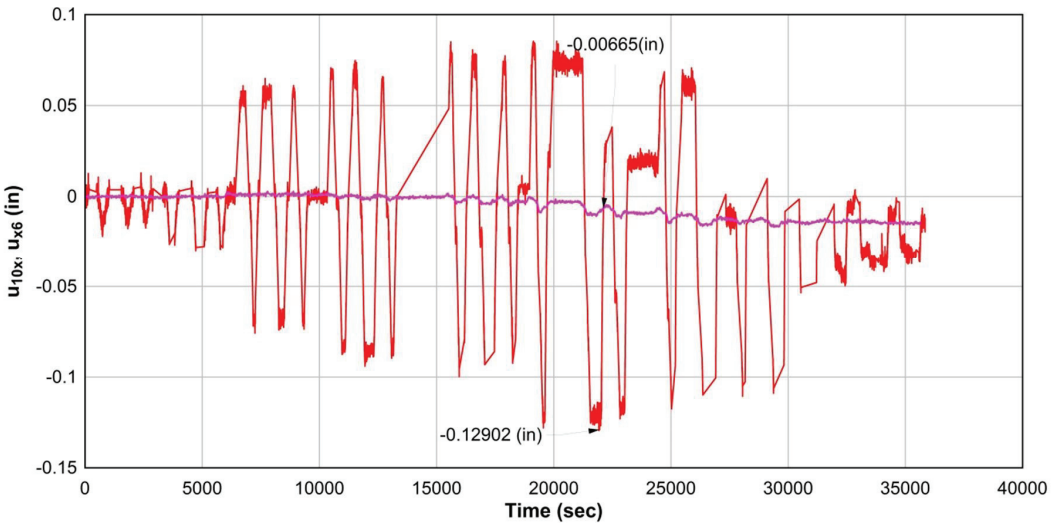

Figure 6-42: Axial Deformation History of the Strong Beam

Since the measurement from LED14 did not yield reliable data, the rotation at the base of the box connection was conservatively estimated based on the reading from LED16 as:

$$\theta_{y1} = \frac{u_{16z}}{L_B} \tag{6-24}$$

From Figure 6-43, the maximum rotation of the box connection was calculated to be 0.0045radian. Such a rotation contributed little to the drift reached by S2 (13.6%) and S5 (9.1%).

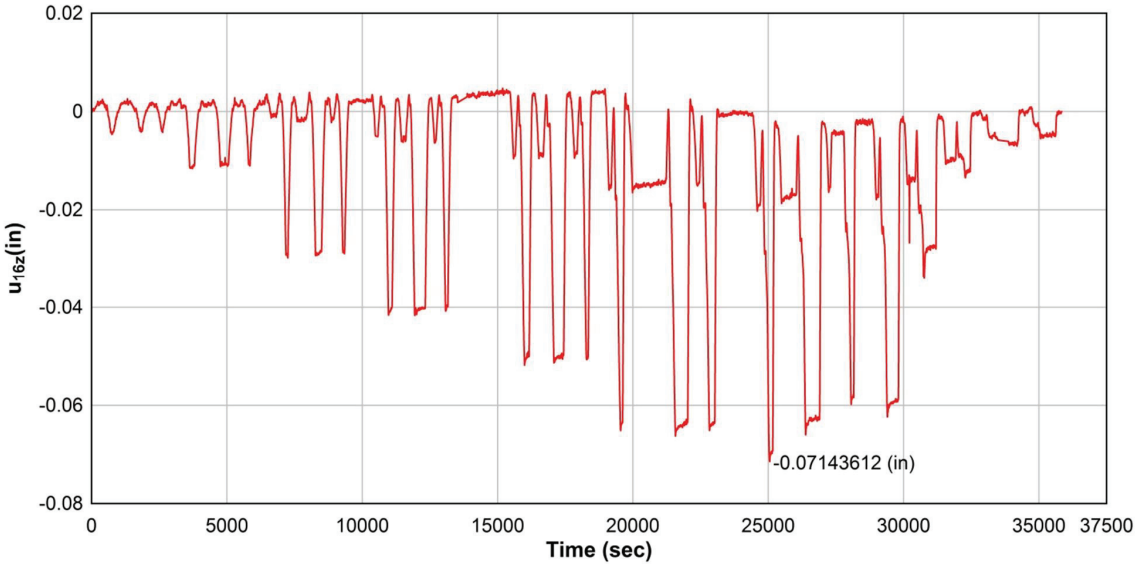

Figure 6-43: Vertical Displacement History of the Box Connection

6.9.3 Specimens S3

Ulterior modifications to the instrumentation included the addition of LEDs 25, 26 and 29 on the strong beam. Those were placed to complement the readings for LED14, so that a better understanding of the deformations of the strong beam during the test could be obtained. LEDs 15 and 16, initially placed on the C-channel of the connections, were also supplemented with LEDs 17 through 22. Finally, LEDS 23 and 24 were directly placed on the connection top plate. LEDs 10, 13, 15, 16, 17, 18, 23, and 24, because of their location at the top of the box connection, were expected to give similar measurements (Figure 6-44). Being at the base of the box beam, similarities in measurement were also expected of LEDs 19, 20, 21, 22, 25 and 26. LED 29 mounted on a rigid extension connected to the strong beam on the back of the box connection was expected to indicate yielding.

The maximum recorded deformation at the top of the box beam was 0.102*in*; the maximum deformation at the base of the box connection was similarly obtained to be 0.015*in*. So the maximum correction to the lateral deformation of the specimen was 0.087*in*. Subtracted from the maximum deformation of 8.7*in* of S3, this translation of the connection box only affected the performance of S3 marginally.

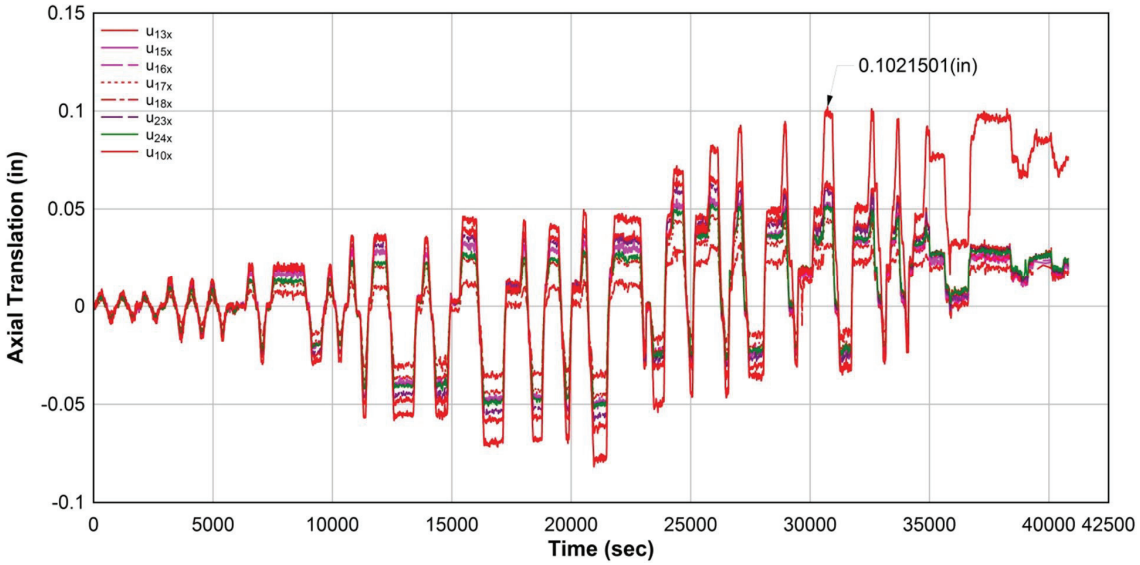

Figure 6-44: Axial Displacement History of the Top of the Box Connection for S3

The vertical deformation of the strong beam was recorded at the front and at the back. At the back, its maximum amplitude was 0.008in; at the front, it was -0.01in. Over the length of the box beam, this created a rotation of 0.001125rad calculated with (Figure 6-45 and Figure 6-46):

$$\theta_{y1} = \frac{(u_{14z} - u_{26z})}{L_B} \tag{6-25}$$

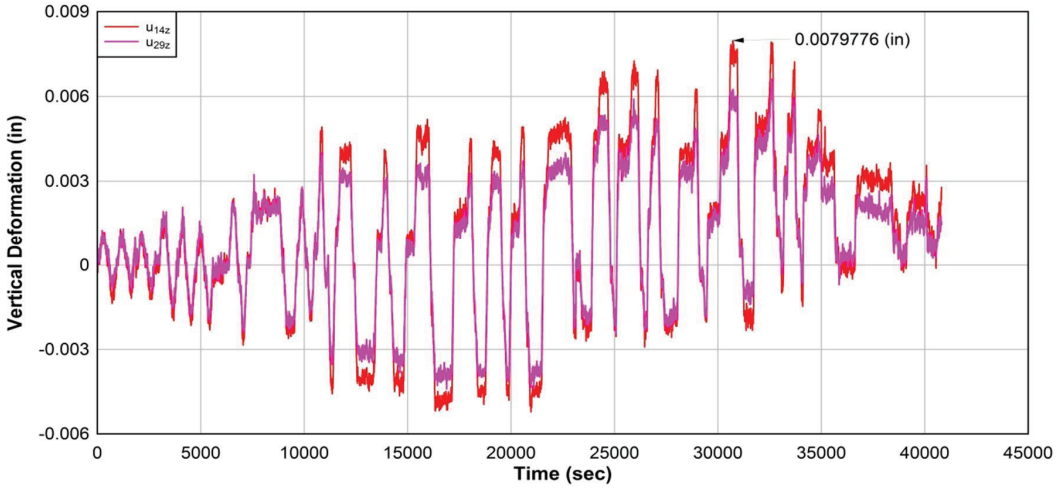

Figure 6-45: Vertical Displacement History of the Back of the Box Connection for S3

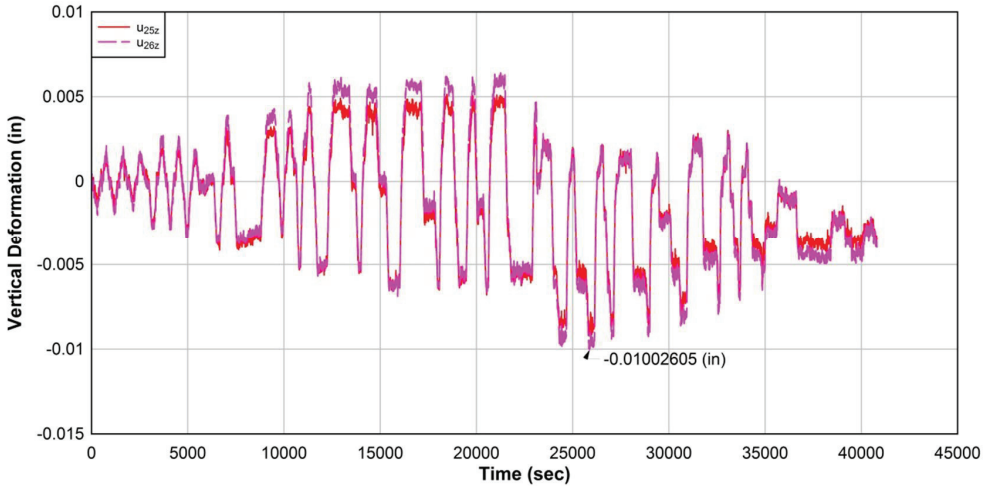

Figure 6-46: Vertical Displacement History of the Front of the Box Connection for S3

Based on the previous analysis and because the construction of the box connection of all the specimens was similar, determination of rotation for S3 was not carried out. Specimen S5 was stronger than S3, hence the rotation of the box connection of S3 was expected to be far less than that measured for S5 (0.0045rad). Since S3 reached a maximum drift of 12.2%, the effect of the box connection rotation on the performance of S3 was marginal.

6.9.4 Out-of-Plane Flexibility

Out-of-plane flexibility of the box connection during the test was not found to have unintended effects on the specimens. Out of plane deviation of the box connection was on average 10 times smaller (or the order of 0.015in at a maximum) than the measured in plane movements. The small rotations introduced in the specimens for such small values of out-of-plane movement were negligible and without significant effects on the behavior of the specimens.

6.10 Summary

All the specimens that were part of this quasi-static test program, conducted to assess the seismic resistance of CFDSTs, exhibited ductile behavior up to failure. For all specimens, irrespective of void ratio, yielding of the section preceded buckling of the outside tube; this was expected as all the tubes were compact. Yielding of the specimens did not occur until the actuator applied a displacement of 1.5*in* to the specimen, corresponding to a drift of 1.3%. Local buckling of the outside tube wasn't observed until well beyond 4% drift. Failure of all the sections happened

generally beyond 7%, even when compactness of the outside tube only meet the AISC 341-10 requirements for moderately ductile behavior.

Once a specimen reached its peak strength, no substantial reduction in strength was observed for the specimens prior to development of fracture in the outside tube. Also, the loss in effective stiffness (ratio of peak strength to applied displacement at any given cycle) for all specimens was gradual. Although pinching of the hysteresis curve proportional to the severity of local buckling happened during the test, the curve was stable, showing that the energy dissipation capacity of this specimen would have been fairly reliable under earthquake excitations.

Specimens S2 and S5 had similar strength, but the void ratio of S5 was more than twice that of S2. Both used moderately ductile tubes on the inside. Both specimens reached similar deformation and strength level; however the residual hysteresis for S5 showed higher strength due to the fact that the inner tube of S5 had higher strength than S2. This is not insignificant, since with CFDST higher void ratio is associated with cost-saving. Thus, while being cheaper than S2, S5 would ideally offer better protection under cyclic loading.

Some slippage was observed at the interface between the box section and the strong beam, as well as some vertical movements of the box connection. Those movements as observed were due to the flexibility of the flange of the strong beam but their effects of the performance of the specimen were marginal.

SECTION 7

DESIGN EQUATION FOR CFDST SUBJECTED TO CYCLIC INELASTIC LOADING

7.1 General

In this section, design equations for CDST sections are derived to characterize the capacities of CFDST at yield and in plastic conditions. Comparisons are then undertaken to the data obtained during the tests described in this research and to other data available in the literature to establish how well design equations can help predict behavior of such components.

7.2 Capacity of CFDST under Loading

The equations used here to predict the strength of a CFDST section under loading depends on the location of the section's neutral axis (NA). The neutral axis can cross the inner tube or be located above or below the inner tube (Figure 7-1 and Figure 7-2). Different strengths are achieved for each case; consequently, each case is considered separately when deriving equations for the yield and in the plastic moments. Equations for the yield moment are presented for the cases when the neutral axis is above the center of gravity (for compression above the center of gravity), whereas equations for the plastic moment are presented for all possible locations of the neutral axis. Note that the yield moment results are provided here for completeness (for cases of low axial forces), but insufficient experimental data is available to assess their accuracy. Focus in this Section is on the plastic moment, as this is more relevant in the current context, and because these equations can be readily compared against experimental data.

Since a CFDST can be seen as generalized case of CFST, equations for CFST can be derived directly for the equations proposed herein assuming that a CFST is a specific case of a CFDST with zero void.

7.2.1 Strength at first Yield of Concrete Filled Double Skinned Tubes

7.2.1.1 Neutral Axis above the Inner Tube

The strength of a CFDST at first yield can be estimated assuming full composite action between the tubes and the concrete core, and a linear elastic stress distribution in the composite section with the maximum concrete stress limited to $0.7 f_c'$ and the maximum steel stress limited to F_y as specified in section I.3 of AISC360-10 for filled composite section. It is also assumed that the wall thicknesses of the tubes are small compared to their diameters.

Knowing the yield stress $\left(F_{yo}\right)$ acting on the extreme tension fiber of the outside tube, using similar triangles in Figure 7-1, the stress distribution, $\sigma_o\left(y\right)$, in that tube at any point, y, over the height of the sections can be obtained as:

$$\sigma_o\left(y\right)=\frac{\left(y-h_{ny}\right)}{R_o+h_{ny}}F_{yo} \tag{7-1}$$

where h_{ny} is the height of the neutral axis with respect to the geometric center of the section and R_o is the radius of the inner tube. All other parameters have already been defined within this section.

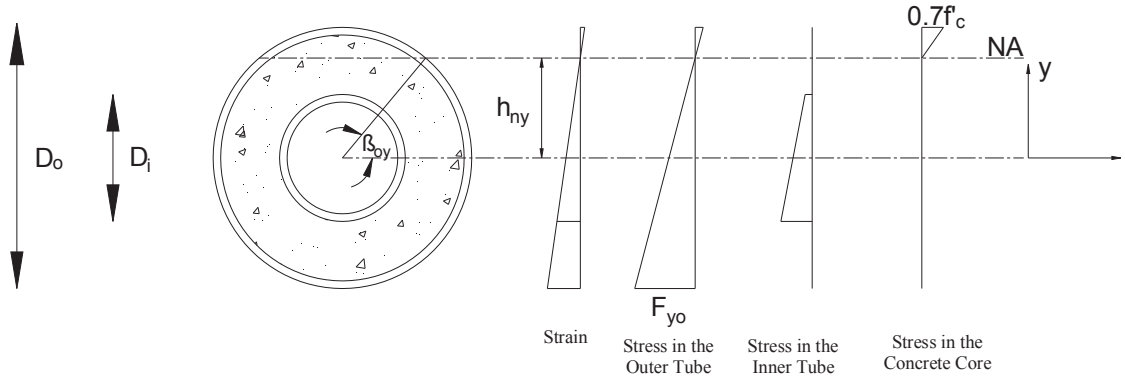

Figure 7-1: Stress Distribution at Yield, NA Above Inner Tube

If the moduli of elasticity of the inner tube $\left(E_i\right)$ and the outer tube $\left(E_o\right)$ differ (although that is usually not the case), the stress distribution over the inner tube is related to the stress over the outside tube by strain compatibility such that:

$$\sigma_i\left(y\right)=\frac{R_i+h_{ny}}{R_o+h_{ny}}\frac{E_i}{E_o}\sigma_o\left(y\right) \tag{7-2}$$

Furthermore, assuming that no tensile stress develops in the concrete core, by similar triangles in Figure 7-1, the linear elastic compressive stress distribution in the concrete can be approximated as:

$$\sigma_c\left(y\right)=\frac{\left(y-h_{ny}\right)}{R_o-h_{ny}}0.7f_c^{'} \tag{7-3}$$

When the neutral axis lies above the inner tube (Figure 7-1), a relation for the neutral axis can be written based on the geometry of the section:

$$h_{ny}=R_o\sin\beta_{oy} \tag{7-4}$$

For a yield neutral axis located above the inner tube, it is possible to calculate the corresponding moment and axial load at first yield from basic principles. These are computed by integrating the stress over the different regions of the cross-section. The axial load, equal to the resultant force obtained summing the compressive and tensile forces, is given by:

$$P_y = \int_A \sigma(y)dA = \int_{A_o} \sigma_o(y)dA_o + \int_{A_i} \sigma_i(y)dA_i + \int_{A_c} \sigma_c(y)dA_c \tag{7-5}$$

whereas, the yield moment is calculated as:

$$M_y = \int_A \sigma(y)ydA = \int_{A_o} \sigma_o(y)\,ydA_o + \int_{A_i} \sigma_i(y)ydA_i + \int_{A_c} \sigma_c(y)ydA_c \tag{7-6}$$

where A_o, A_i and A_{conc} are respectively the domains comprised by the area of the outer tube, the area of the inner tube and the area of the concrete core effective in resisting load (area between the NA and the outer tube).

For a neutral axis above the inner tube, the parameters to carry out the integrations in Equations (7-5) and (7-6) are:

$dA_o = R_o t_o d\beta$, differential area from the outer tube;

$dA_i = R_i t d\beta$, differential area from the inner tube

$dA_c = B(y)dy = (2R_o \cos\beta)(R_o \cos\beta d\beta) = 2R_o^2 \cos^2(\beta)d\beta$, differential area from the core

$y = R_o \sin\beta$ or $y = R_i \sin\beta$ depending on whether the integration is on the outer or inner tube.

Substituting those parameters into equations (7-5) and (7-6) , the axial force and moment at yield are obtained as:

$$P_y = -\frac{2\pi \sin\beta_o}{1+\sin\beta_o}\left(R_o t_o + \frac{E_i}{E_o} R_i t_i\right) F_{yo} + \frac{1.4\cos\beta_o\left(2+\sin^2\beta_o\right) - 2.1\left(\pi - 2\beta_o\right)\sin\beta_o}{6\left(1+\sin\beta_o\right)} R_o^2 f_c^{'} \tag{7-7}$$

$$M_y = -\frac{\pi}{1+\sin\beta_o}\left(R_o^2 t_o + \chi \frac{E_i}{E_o} R_i^2 t_i\right) F_{yo} - \frac{0.7\sin 2\beta_o\left(2\cos^2\beta_o + 3\right) + 2.1\left(\pi - 2\beta_o\right)}{12\left(1+\sin\beta_o\right)} R_o^3 f_c^{'} \tag{7-8}$$

For the case of pure flexure, the location of the neutral axis can be determined either from Equation (7-7) or by using a transformed cross section approach. The cross section is transformed to an equivalent concrete section by using the modular ratio $n = \frac{E_s}{E_c}$, where for normal strength concrete of unit weight w_c , the short term elastic modulus is taken as (ACI, 2011):

$$E_c = 33\left(w_c\right)^{1.5}\sqrt{f_c^{'}}\, psi \tag{7-9}$$

In uniaxial bending, under elastic stress assumptions, the moment of area of the compression zone is equal to the moment area of the tension zone. Neglecting the concrete in the tension zone in Figure 7-1, and using the modular ratio:

$$nA_{sco}\left(y_{sco} - h_y\right) + A_{co}\left(y_{co} - h_y\right) = nA_{sto}\left(y_{sto} + h_y\right) + n\left(A_{sti} + A_{sci}\right)h_y \tag{7-10}$$

with:

$$A_{scoy} = \left(\pi - 2\beta_{oy}\right) R_o t_o \tag{7-11}$$

$$A_{coy} = R_o^2 \left[\left(\frac{\pi}{2} - \beta_{oy} \right) - \sin \beta_{oy} \cos \beta_{oy} \right] \tag{7-12}$$

$$A_{stoy} = \left(\pi + 2\beta_{oy}\right) R_o t_o \tag{7-13}$$

$$A_{stiy} = \left(\pi + 2\beta_{iy}\right) R_i t_i \tag{7-14}$$

$$y_{stiy} = \frac{2R_o \cos \beta_{iy}}{\left(\pi + 2\beta_{iy}\right)} \tag{7-15}$$

$$y_{scoy} = \frac{2R_o \cos \beta_{oy}}{\left(\pi - 2\beta_{oy}\right)} \tag{7-16}$$

$$y_{stoy} = \frac{2R_o \cos \beta_{oy}}{\left(\pi + 2\beta_{oy}\right)} \tag{7-17}$$

$$y_{co} = \frac{2R_o}{3} \frac{\cos^3 \beta_{oy}}{\left(\frac{\pi}{2} - \beta_{oy} \right) - \sin \beta_{oy} \cos \beta_{oy}} \tag{7-18}$$

Substituting Equations (7-11) to (7-18) into (7-10) and making the necessary reductions yields:

$$h_{ny} = \frac{\frac{2R_o^3}{3} \cos^3 \beta_{oy}}{2n\pi R_o t_o + R_o^2 \left[\left(\frac{\pi}{2} - \beta_{oy} \right) - \sin \beta_{oy} \cos \beta_{oy} \right] + 2\pi n R_i t_i} \tag{7-19}$$

The above equation can be solved along with Equation (7-4) to obtain an estimate of h_{ny} using mathematical software such as Mathcad. For expediency, an estimate of h_{ny} can also be obtained, realizing that at yield, the neutral axis will still be close to the geometric center of the section and consequently:

$$\sin\beta_{oy} \approx \beta_{oy} \tag{7-20}$$

$$\cos\beta_{oy} \approx 1 \tag{7-21}$$

It follows then from Equations (7-4) and (7-19):

$$h_{ny} = R_o\beta_{oy} \tag{7-22}$$

$$h_{ny} = \frac{\frac{2R_o^3}{3}}{2n\pi R_o t_o + R_o^2\left[\left(\frac{\pi}{2} - \beta_{oy}\right) - \beta_{oy}\right] + 2\pi n R_i t_i} \tag{7-23}$$

From the combination of Equations (7-22) and (7-23) follows the second order equation in β_{oy} which is simpler to solve for an estimate of the location of the neutral axis:

$$3R_o^3\beta_{oy}^2 - 3n\pi R_o\left(R_o t_o + R_i t_i + \frac{\pi}{2}R_o^2\right)\beta_{oy} + R_o^3 = 0 \tag{7-24}$$

7.2.1.2 Neutral Axis across the Inner Tube

In the case of a neutral axis lying across the inner tube (Figure 7-2), for linear stress distributions in the different component of the section, Equations (7-2) and (7-3) still apply. Integration of the

stresses over the height of the section as in Section 7.2.1.1 can also be carried out. However, the equations for the axial and moment capacities at yield are now written as:

$$P_y = \int_A \sigma(y)dA = \int_{A_o} \sigma_o(y)dA_o + \int_{A_i} \sigma_i(y)dA_i + \int_{A_{co}} \sigma_c(y)dA_{co} - \int_{A_{ci}} \sigma_c(y)dA_{ci} \tag{7-25}$$

$$M_y = \int_A \sigma(y)ydA = \int_{A_o} \sigma_o(y)ydA_o + \int_{A_i} \sigma_i(y)ydA_i + \int_{A_{co}} \sigma_c(y)ydA_{co} - \int_{A_{ci}} \sigma_c(y)ydA_{ci} \tag{7-26}$$

where:

$dA_{co} = 2R_o^2 \cos^2(\beta)d\beta$ is a differential area from the domain delimited by the NA and the outer tube,

$dA_{ci} = 2R_i^2 \cos^2(\beta)d\beta$ is a differential area from the domain delimited by the NA and the inner tube,

$h_{ny} = R_o \sin\beta_{oy} = R_i \sin\beta_{iy}$ is the location of the NA

All other parameters in Equations (7-25) and have been defined in. Carrying the integrations lead to the following equations:

$$\begin{aligned} P_y = & -\frac{2\pi \sin\beta_o}{1+\sin\beta_o}\left(R_o t_o + \frac{E_i}{E_o} R_i t_i\right) F_{yo} \\ & + \frac{1.4\cos\beta_o\left(2+\sin^2\beta_o\right) - 1.4\cos\beta_i\left(2+\sin^2\beta_i\right) - 2.1\left(\pi - 2\beta_o\right)\sin\beta_o + 2.1\left(\pi - 2\beta_i\right)\sin\beta_i}{6\left(1+\sin\beta_o\right)} R_o^2 f_c' \end{aligned} \tag{7-27}$$

$$M_y = -\frac{\pi}{1+\sin\beta_o}\left(R_o^2 t_o + \chi\frac{E_i}{E_o}R_i^2 t_i\right)F_{yo} - \frac{0.7\sin 2\beta_o\left(2\cos^2\beta_o+3\right)+2.1\left(\pi-2\beta_o\right)}{12\left(1+\sin\beta_o\right)}R_o^3 f_c^{'} + \frac{0.7\sin 2\beta_i\left(2\cos^2\beta_i+3\right)+2.1\left(\pi-2\beta_i\right)}{12\left(1+\sin\beta_o\right)}\chi R_i^3 f_c^{'} \tag{7-28}$$

Again, for the case of pure flexure a transformed cross section can be used and the following equations are obtained to locate the neutral axis:

$$nA_{sco}\left(y_{sco}-h_y\right)+nA_{sci}\left(y_{sci}-h_y\right)+A_{co}\left(y_{co}-h_y\right)-A_{ci}\left(y_{ci}-h_y\right) = nA_{sto}\left(y_{sto}+h_y\right)+nA_{sti}\left(y_{sti}+h_y\right) \tag{7-29}$$

$$h_{ny} = R_o\sin\beta_{oy} = R_i\sin\beta_{iy} \tag{7-30}$$

with:

$$A_{sci} = \left(\pi-2\beta_{iy}\right)R_i t_i \tag{7-31}$$

$$A_{ci} = R_i^2\left[\left(\frac{\pi}{2}-\beta_{iy}\right)-\sin\beta_{iy}\cos\beta_{iy}\right] \tag{7-32}$$

$$y_{sciy} = \frac{2R_i\cos\beta_{iy}}{\left(\pi-2\beta_{iy}\right)} \tag{7-33}$$

$$y_{ciy} = \frac{2R_i}{3}\frac{\cos^3\beta_{iy}}{\left(\frac{\pi}{2}-\beta_i\right)-\sin\beta_{iy}\cos\beta_{iy}} \tag{7-34}$$

All other parameters having been previously defined, algebraic substitutions and simplifications similar to those performed for the previous case lead to:

$$h_y = \frac{\frac{2}{3}\left(R_o^3 \cos^3 \beta_o - R_i^3 \cos^3 \beta_i\right)}{2n\pi R_o t_o + 2\pi n R_i t_i + R_o^2\left[\left(\frac{\pi}{2} - \beta_o\right) - \sin \beta_o \cos \beta_o\right] + R_i^2\left[\left(\frac{\pi}{2} - \beta_i\right) - \sin \beta_i \cos \beta_i\right]} \tag{7-35}$$

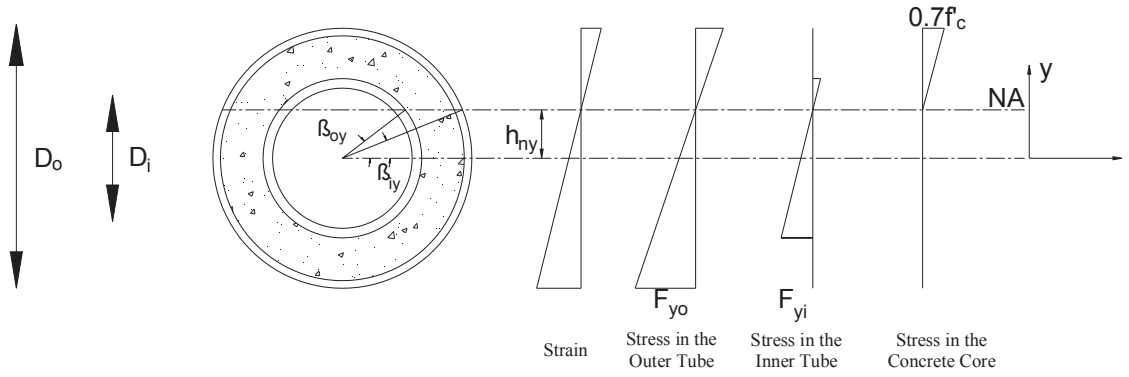

Figure 7-2: Stress Distribution at Yield, NA Crossing Inner Tube

Simplifications can also be introduced here to obtain approximate equations that define the location of the neutral axis, namely:

$$\sin \beta_o \approx \beta_o \tag{7-36}$$

$$\cos \beta_o \approx 1 \tag{7-37}$$

$$\sin \beta_i \approx \beta_i \tag{7-38}$$

$$\cos \beta_i \approx 1 \tag{7-39}$$

Substituting those equations into (7-35) leads to the two quadratic equations in β_i and β_o which can be used in Equation (7-30) to obtain an estimate of the location of the neutral axis:

$$6\left(R_o+R_i\right)R_o^2\beta_o^2-3\left[2n\pi\left(R_ot_o+R_it_i\right)+\frac{\pi}{2}\left(R_o^2+R_i^2\right)\right]R_o\beta_o+2\left(R_o^3-R_i^3\right)=0 \tag{7-40}$$

$$6\left(R_o+R_i\right)R_i^2\beta_i^2-3\left[2n\pi\left(R_ot_o+R_it_i\right)+\frac{\pi}{2}\left(R_o^2+R_i^2\right)\right]R_i\beta_i+2\left(R_o^3-R_i^3\right)=0 \tag{7-41}$$

7.2.1.3 Yield Strength of CFST

Treating CFST as a specific case of a CFDST with zero void, equations to locate the NA of CFST at yield as well a nominal capacities at yield can be obtained by neglecting the terms related to the inner tube in the equations derived in Section 7.2.1.1 or 7.2.1.2. Based on that observation, equations for the nominal axial force and moment strengths at yield can be obtained respectively from Equation (7-7) or (7-27) and Equation (7-8) or (7-28):

$$P_y=-\frac{2\pi\sin\beta_o}{1+\sin\beta_o}R_ot_oF_{yo}+\frac{1.4\cos\beta_o\left(2+\sin^2\beta_o\right)-2.1\left(\pi-2\beta_o\right)\sin\beta_o}{6\left(1+\sin\beta_o\right)}R_o^2f_c^{'} \tag{7-42}$$

$$M_y=-\frac{\pi}{1+\sin\beta_o}R_o^2t_oF_{yo}-\frac{0.7\sin2\beta_o\left(2\cos^2\beta_o+3\right)+2.1\left(\pi-2\beta_o\right)}{12\left(1+\sin\beta_o\right)}R_o^3f_c^{'} \tag{7-43}$$

In the same way, location of the NA of a CFST in pure flexure at yield can be obtained either from Equation (7-23) or Equation (7-35) :

$$h_y = \frac{2}{3}\frac{R_o^3 \cos^3 \beta_o}{2n\pi R_o t_o + R_o^2\left[\left(\frac{\pi}{2} - \beta_o\right) - \sin\beta_o \cos\beta_o\right]} \tag{7-44}$$

Approximate equation for the NA can also be obtained either from Equation (7-24) or Equation (7-40):

$$3R_o^3\beta_o^2 - 3n\pi R_o\left(R_o t_o + \frac{\pi}{2}R_o^2\right)\beta_o + R_o^3 = 0 \tag{7-45}$$

7.2.2 Nominal Plastic Strength

To calculate the plastic strength of a CFDST section, it can be assumed that both tubes have fully plastified and the concrete in compression has reached and sustained it crushing strength whereas full composite action is still maintained. This approach is similar to the one adopted for CFST and that yielded results in good agreement with prior CFST experiments (Bruneau and Marson, 2004). As for the yield strength calculations presented in the previous section, equations must be derived depending on whether the plastic neutral axis (PNA) is located across, above or below the inner tube and the stress distribution as showed on Figure 7-3 to Figure 7-6.

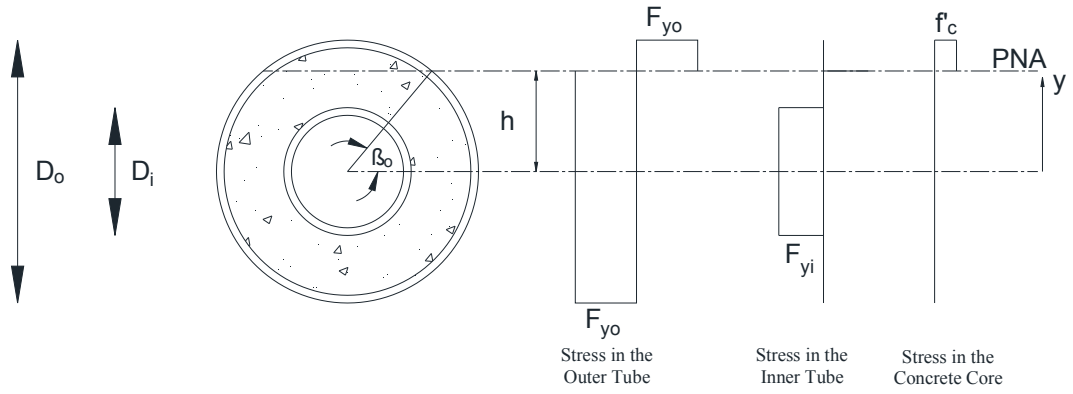

Figure 7-3: Stress Distribution in Plastic Conditions, PNA Above Inner Tube

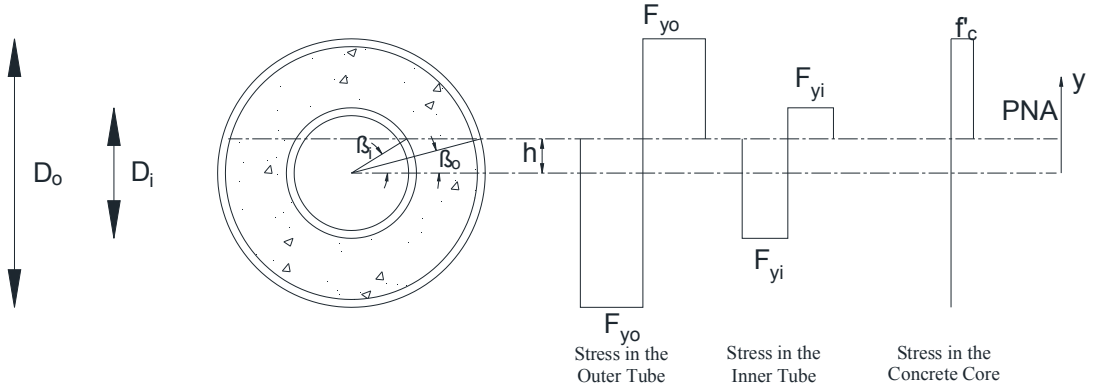

Figure 7-4: Stress Distribution in Plastic Conditions, PNA Across Inner Tube

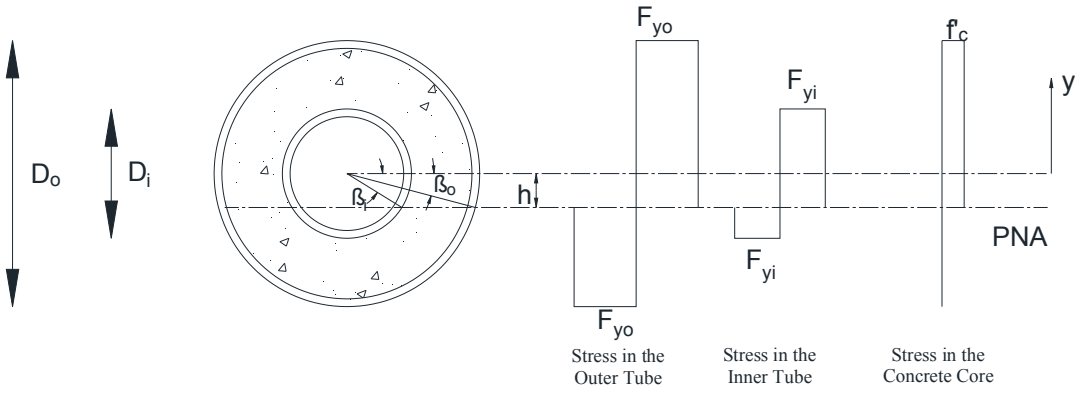

Figure 7-5: Stress Distribution in Plastic Conditions, PNA Across Inner Tube

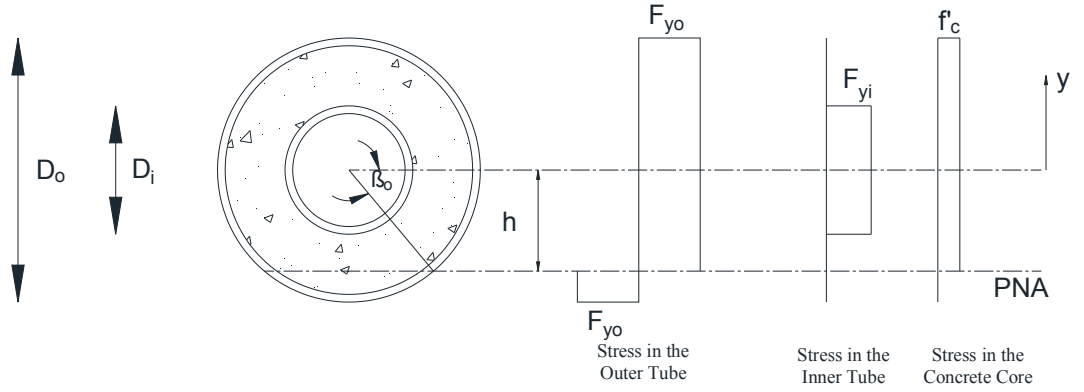

Figure 7-6: Stress Distribution in Plastic Conditions, PNA Below Inner Tube

7.2.2.1 Neutral Axis above the Inner Tube

When the neutral axis is located above the inner tube, the resultant of the compressive and tensile forces maintaining the sections in equilibrium are as follow:

$$C_{ro} = \left(\pi - 2\beta_o\right) R_o t_0 F_{yo} \tag{7-46}$$

$$C_r^{'} = \left[\left(\frac{\pi}{2} - \beta_o\right)R_o^2 - \frac{1}{2}R_o^2 \sin\left(2\beta_o\right)\right] f_c^{'} \tag{7-47}$$

$$T_{ri} = 2\pi R_i t_i F_{yi} \tag{7-48}$$

$$T_{ro} = \left(\pi + 2\beta_o\right) R_o t_o F_{yo} \tag{7-49}$$

where, C_{ro} is the resultant compressive force acting on the outer tube, $C_r^{'}$ is the resultant compressive force in the concrete, T_i is the resultant tensile force on the inner tube, and T_{ro}, is the resultant tensile force acting on the outer tube. The corresponding points of application for the above-defined forces with respect to the geometric center of the section respectively are:

$$y_{sco} = \frac{2R_o Cos\beta_o}{\left(\pi - 2\beta_o\right)} \tag{7-50}$$

$$y_c = \frac{2R_o}{3}\frac{Cos^3\beta_o}{\left(\frac{\pi}{2} - \beta_o\right) - \frac{1}{2}\sin\left(2\beta_o\right)} \tag{7-51}$$

$$y_{sti} = 0 \tag{7-52}$$

$$y_{sto} = \frac{2R_o Cos\beta_o}{\left(\pi + 2\beta_o\right)} \tag{7-53}$$

where

y_{sco} is the point of application of the resultant compressive force acting on the outer tube

y_c is the point of application of the resultant compressive force in the concrete <define

y_{sti} is the point of application of the resultant tensile force on the inner tube

y_{sto} is the point of application of the resultant tensile force acting on above the outer tube .

With those parameters, the resultant axial and flexural capacities of the section are defined as:

$$P = \left(C_{ro} + C_r^{'}\right) - \left(T_{ri} + T_{ro}\right) \tag{7-54}$$

$$M_p = C_{ro} y_{sco} + C_r^{'} y_c + T_{ri} y_{sti} + T_{ro} y_{sto} \tag{7-55}$$

Carrying out the necessary calculations leads to the following equations:

$$P = \left(\frac{\pi}{2} - \beta_o - \frac{1}{2}\sin 2\beta_o\right) R_o^2 f_c^{'} - 4\beta_o R_o t_o F_{yo} - 2\pi R_i t_i F_{yi} \tag{7-56}$$

$$M_p = \frac{2}{3} R_o^3 \cos^3 \beta_o f_c^{'} + 4R_o^2 \cos\beta_o t_o F_{yo} \tag{7-57}$$

The location of the neutral axis for the case of pure flexure on the section is obtained by setting the axial force in the above equations to zero, leading to the mixed equation in β_o.

$$\left(4R_o t_o F_{yo} + R_o^2 f_c^{'}\right)\beta_o + \frac{1}{2} R_o^2 f_c^{'} \sin 2\beta_o + \left(2\pi R_i t_i F_{yi} - \frac{\pi}{2} R_o^2 f_c^{'}\right) = 0 \tag{7-58}$$

This equation can be solved in Mathcad. Alternatively, a conservative estimate can be obtained using the approximation:

$$\sin\beta_o \approx \beta_o \tag{7-59}$$

$$\cos\beta_o \approx 1 \tag{7-60}$$

which results in the equation in β_o:

$$\beta_o = \frac{\pi R_o^2 f_c^{'} - 4\pi R_i t_i F_{yi}}{8R_o t_o F_{yo} + 4R_o^2 f_c^{'}} \tag{7-61}$$

Where:

$$\sin^{-1}\left(\frac{R_i}{R_o}\right) < \beta_o \le \frac{\pi}{2} \tag{7-62}$$

The location of the plastic neutral axis (h) can then be calculated using the geometry of the section as:

$$h = R_o \sin\beta_o \tag{7-63}$$

7.2.2.2 Neutral Axis across the Inner Tube and above the Centroid of the Section

For a neutral axis located across the inner tube, the equations for the forces acting on the cross section and their corresponding points of application are:

$$C_{ro} = (\pi - 2\beta_o) R_o t_0 F_{yo} \tag{7-64}$$

$$C_{ri} = (\pi - 2\beta_i) R_i t_i F_{yi} \tag{7-65}$$

$$C_r' = \left[\left(\frac{\pi}{2} - \beta_o\right) R_o^2 - \left(\frac{\pi}{2} - \beta_i\right) R_i^2 - \frac{1}{2} R_o^2 \sin(2\beta_o) + \frac{1}{2} R_i^2 \sin(2\beta_i)\right] f_c' \tag{7-66}$$

$$T_{ro} = (\pi + 2\beta_o) R_o t_o F_{yo} \tag{7-67}$$

$$T_{ri} = (\pi + 2\beta_i) R_i t_i F_{yi} \tag{7-68}$$

$$y_{sco} = \frac{2R_o Cos\beta_o}{(\pi - 2\beta_o)} \tag{7-69}$$

$$y_{sci} = \frac{2R_i Cos\beta_i}{(\pi - 2\beta_i)} \tag{7-70}$$

$$y_c = \frac{2R_o}{3} \frac{Cos^3\beta_o}{\left(\frac{\pi}{2} - \beta_o\right) - \frac{1}{2}\sin(2\beta_o)} \tag{7-71}$$

$$y_{sto} = \frac{2R_o Cos\beta_o}{(\pi + 2\beta_o)} \tag{7-72}$$

$$y_{sto} = \frac{2R_i Cos\beta_i}{(\pi + 2\beta_i)} \tag{7-73}$$

The axial force and moment acting on the cross-section in this configuration are:

$$P_u = \left(C_{ro} + C_{ro} + C_r^{'}\right) - \left(T_{ri} + T_{ro}\right) \tag{7-74}$$

$$M_u = C_{ro} y_{sco} + C_{ri} y_{sci} + C_r^{'} y_c + T_{ri} y_{sti} + T_{ro} y_{sto} \tag{7-75}$$

After all substitutions and algebraic manipulations have been carried out, the following equations are obtained:

$$P = \left[\left(\frac{\pi}{2} - \beta_o - \frac{1}{2}\sin\beta_o\right)R_o^2 - \left(\frac{\pi}{2} - \beta_i - \frac{1}{2}\sin\beta_i\right)R_i^2\right] f_c^{'} - 4\beta_o R_o t_o F_{yo} - 4\beta_i R_i t_i F_{yi} \tag{7-76}$$

$$M_p = \frac{2}{3}\left(R_o^3 \cos^3 \beta_o - R_i^3 \cos^3 \beta_i\right) f_c^{'} + 4\left(R_o^2 \cos \beta_o t_o F_{yo} + R_i^2 \cos \beta_i t_i F_{yi}\right) \tag{7-77}$$

As before, the location of the neutral axis for the pure flexure condition can be solved for by setting P_u to zero. The following equations in β_o and β_i are obtained:

$$\left(4R_o t_o F_{yo} + R_o^2 f_c^{'}\right)\beta_o + \left(4R_i t_i F_{yi} - R_i^2 f_c^{'}\right)\beta_i + \left(\frac{1}{2}R_o^2 \sin 2\beta_o - \frac{1}{2}R_i^2 \sin 2\beta_i\right) f_c^{'} - \left(\frac{\pi}{2}R_o^2 f_c^{'} - \frac{\pi}{2}R_i^2 f_c^{'}\right) = 0 \tag{7-78}$$

$$h = R_o \sin \beta_o = R_i \sin \beta_i \tag{7-79}$$

The following approximations are then introduced along with Equations (7-56) and (7-57) :

$$\sin \beta_i \approx \beta_i \tag{7-80}$$

$$\cos \beta_o \approx 1 \tag{7-81}$$

Using those approximations estimate of the location of the plastic neutral axis can be obtained from Equation (7-79) with:

$$\beta_o = \frac{\pi\left(R_o^2 - R_i^2\right) f_c^{'}}{4R_o\left[2\left(t_o F_{yo} + t_i F_{yi}\right) + \left(R_o - R_i\right) f_c^{'}\right]} \tag{7-82}$$

$$\beta_i = \frac{\pi\left(R_o^2 - R_i^2\right) f_c^{'}}{4R_i\left[2\left(t_o F_{yo} + t_i F_{yi}\right) + \left(R_o - R_i\right) f_c^{'}\right]} \tag{7-83}$$

In that case:

$$0 \le \beta_o \le \sin^{-1}\left(\frac{R_i}{R_o}\right) \tag{7-84}$$

7.2.2.3 Neutral Axis across the Inner Tube and below the Centroid of the Section

As a CFDST section is further stressed in compression (increasing axial load), its plastic neutral axis can move below the geometric centroid of the section while still crossing the inner tube. The additional part of the section that is now in compression compared to the previous case contributes to increase the axial capacity of the section; however, it does not lead to any increase in moment capacity compared to the case when the neutral axis is located at the same distance from the center of gravity but above the centroid, and across the inner tube. In this case the equations that describe the strength of the section are:

$$P = \pi\left(R_o^2 - R_i^2\right) f_c^{'} - \left[\left(\frac{\pi}{2} + \beta_o + \frac{1}{2}\sin\beta_o\right)R_o^2 - \left(\frac{\pi}{2} + \beta_i + \frac{1}{2}\sin\beta_i\right)R_i^2\right] f_c^{'} - 4\beta_o R_o t_o F_{yo} - 4\beta_i R_i t_i F_{yi} \tag{7-85}$$

$$M_p = \frac{2}{3}\left(R_o^3\cos^3\beta_o - R_i^3\cos^3\beta_i\right) f_c^{'} + 4\left(R_o^2\cos\beta_o t_o F_{yo} + R_i^2\cos\beta_i t_i F_{yi}\right) \tag{7-86}$$

The same equation that describes the location of the neutral axis in the previous case can be used but one should bear in mind that the neutral axis is now located symmetrically with respect to geometric centroid. Consequently, the angle (β_o) under which the neutral axis cut the outer tube is negative and such that:

$$-\sin^{-1}\left(\frac{R_i}{R_o}\right) \le \beta_o < 0 \tag{7-87}$$

7.2.2.4 Neutral Axis below the Inner Tube

For a neutral axis below the inner tube, the same increase in axial strength will be observed, however the moment capacity will still not change compared to the case when the neutral axis is located at the same distance but above the center of gravity, as the additional part of the section that is now stressed does not contribute any increase in moment capacity. So the equations to describe that situation can be directly derived from the case where the neutral axis is located above the inner tube to be:

$$P = \pi\left(R_o^2 - R_i^2\right) f_c^{'} - \left[\left(\frac{\pi}{2} + \beta_o + \frac{1}{2}\sin 2\beta_o\right) R_o^2 f_c^{'} + 4\beta_o R_o t_o F_{yo} - 2\pi R_i t_i F_{yi}\right] \tag{7-88}$$

$$M_u = \frac{2}{3} R_o^3 \cos^3 \beta_o f_c^{'} + 4R_o^2 \cos\beta_o t_o F_{yo} \tag{7-89}$$

with:

$$-\frac{\pi}{2} \le \beta_o < -\sin^{-1}\left(\frac{R_i}{R_o}\right) \tag{7-90}$$

7.2.2.5 Plastic Strength of CFST

Note that (as was done for the yield moment case) the equations derived above for the plastic strength of CFDST can be used to obtain the plastic strength (axial force and moment) of a concrete filled steel tube (CFST) sections. This is done by ignoring the contribution of the inner

tube in the above equations. This results in the following equations for the case when the neutral axis is located above the geometric center of the section:

$$P = \left(\frac{\pi}{2} - \beta_o - \frac{1}{2} \sin 2\beta_o \right) R_o^2 f_c^{'} - 4\beta_o R_o t_o F_{yo} \tag{7-91}$$

$$M_p = \frac{2}{3} R_o^3 \cos^3 \beta_o f_c^{'} + 4R_o^2 \cos \beta_o t_o F_{yo} \tag{7-92}$$

with:

$$0 < \beta_o \leq \frac{\pi}{2} \tag{7-93}$$

Correspondingly, an estimate for the location of the neutral axis can be obtained as:

$$h = R_o \sin \beta_o \tag{7-94}$$

with:

$$\beta_o = \frac{\pi R_o^2 f_c^{'}}{8R_o t_o F_{yo} + 4R_o^2 f_c^{'}} \tag{7-95}$$

Similarly, equations to estimate the strength of the section when the neutral axis is located below the geometric center of the section can be obtained:

$$P = \pi R_o^2 f_c^{'} - \left[\left(\frac{\pi}{2} + \beta_o + \frac{1}{2} \sin 2\beta_o \right) R_o^2 f_c^{'} + 4\beta_o R_o t_o F_{yo} \right] \tag{7-96}$$

$$M_p = \frac{2}{3} R_o^3 \cos^3 \beta_o f_c^{'} + 4R_o^2 \cos \beta_o t_o F_{yo} \tag{7-97}$$

With:

$$-\frac{\pi}{2} < \beta_o \leq 0 \tag{7-98}$$

7.2.2.6 Application to the Test Specimens

In this section, comparison between the exact equations and their approximate counterparts are undertaken for the specimens tested. The properties of the specimens were discussed in the previous section and are reproduced in Table 6-3 and

Table 7-3. A summary of the calculations are tabulated in Table 7-1. The results referring to the approximate values appear with the subscript "approx".

Table 7-1: Calculated Section Neutral Axis and Strengths

Specimen	h (in)	h_approx (in)	Error (%)	M_P (kip-in)	M_{P_approx} (kip-in)	Error (%)
S1	0.93	0.88	-5.4%	207.456	205.127	-1.1%
S2	1.543	1.494	-3.2%	514.981	519.743	0.9%
S3	0.992	0.937	-5.5%	446.091	444.284	-0.4%
S4	0.97	0.883	-9.0%	314.609	312.202	-0.8%
S5	1.607	1.559	-3.0%	532.50	529.051	-0.6%

From those results, it can be seen that the error between the approximate equations and the exact ones are small (or the order of 1% or less for the moment). Best match is obtained when the neutral axis crosses the inner tube (i.e., specimens S1, S3, S4, S5), with the moments predicted by the approximate equations being conservative. The accuracy of the approximate equation is also seen to increase as the void ratio is increased when comparing with groups of specimens having similar neutral axis characteristics (in this case, this being those for which the neutral axis

crosses the neutral axis, for example). However, note that here, the neutral axis is above the neutral axis only for Specimen S2, which is incidentally the specimen with the lowest void ratio (25%).

7.2.3 Plastic Interaction Diagram

Under combined axial and flexural loads, the reduction in moment capacity for various axial loading conditions is best expressed in terms of an interaction diagram that relates the axial force to the bending moment. For CFDST, the relationships previously derived provide the equations that can be used to develop the cross-section interaction curve. Since those equations are directly related to the angles β_o and β_i which are themselves related to the location of the neutral axis, a full interaction diagram can be generated by varying the position of the neutral axis from the situation in which the section sustains pure tensile action (neutral axis at the upper edge of the section) to the one where the section sustains pure compression (neutral axis at the lowest edge of the section), as typically done to construct interaction diagrams. Mathematically this corresponds to varying β_o from $-\frac{\pi}{2}$ to $\frac{\pi}{2}$. Using Equations (7-56), (7-57), (7-76), (7-77), (7-85), (7-86), (7-87) and (7-88) and applying the correct bounds lead to a set of equations that fully described the interaction diagram.

When $R_i < h \le R_0$ or $\sin^{-1}\left(\frac{R_i}{R_o}\right) < \beta_o \le \frac{\pi}{2}$

$$P = \left(\frac{\pi}{2} - \beta_o - \frac{1}{2}\sin 2\beta_o\right) R_o^2 f_c^{'} - 4\beta_o R_o t_o F_{yo} - 2\pi R_i t_i F_{yi} \tag{7-99}$$

$$M_p = \frac{2}{3} R_o^3 \cos^3 \beta_o f_c^{'} + 4R_o^2 \cos \beta_o t_o F_{yo} \tag{7-100}$$

When $0 \le h \le R_i$ or $0 \le \beta_o \le \sin^{-1}\left(\frac{R_i}{R_o}\right)$

$$P = \left[\left(\frac{\pi}{2} - \beta_o - \frac{1}{2}\sin 2\beta_o\right) R_o^2 - \left(\frac{\pi}{2} - \beta_i - \frac{1}{2}\sin 2\beta_i\right) R_i^2\right] f_c^{'} - 4\beta_o R_o t_o F_{yo} - 4\beta_i R_i t_i F_{yi} \tag{7-101}$$

$$M_p = \frac{2}{3}\left(R_o^3 \cos^3 \beta_o - R_i^3 \cos^3 \beta_i\right) f_c^{'} + 4\left(R_o^2 \cos \beta_o t_o F_{yo} + R_i^2 \cos \beta_i t_i F_{yi}\right) \tag{7-102}$$

When $-R_i \le h < 0$ or $-\sin^{-1}\left(\frac{R_i}{R_o}\right) \le \beta_o < 0$

$$P = \pi\left(R_o^2 - R_i^2\right) f_c^{'} - \left[\left(\frac{\pi}{2} + \beta_o + \frac{1}{2}\sin\beta_o\right) R_o^2 - \left(\frac{\pi}{2} + \beta_i + \frac{1}{2}\sin\beta_i\right) R_i^2\right] f_c^{'} - 4\beta_o R_o t_o F_{yo} - 4\beta_i R_i t_i F_{yi} \tag{7-103}$$

$$M_p = \frac{2}{3}\left(R_o^3 \cos^3 \beta_o - R_i^3 \cos^3 \beta_i\right) f_c^{'} + 4\left(R_o^2 \cos \beta_o t_o F_{yo} + R_i^2 \cos \beta_i t_i F_{yi}\right) \tag{7-104}$$

When $-R_0 \le h < -R_i$ or $-\frac{\pi}{2} \le \beta_o < -\sin^{-1}\left(\frac{R_i}{R_o}\right)$

$$P = \pi\left(R_o^2 - R_i^2\right) f_c^{'} - \left[\left(\frac{\pi}{2} + \beta_o + \frac{1}{2}\sin 2\beta_o\right) R_o^2 f_c^{'} + 4\beta_o R_o t_o F_{yo} - 2\pi R_i t_i F_{yi}\right] \tag{7-105}$$

$$M_p = \frac{2}{3} R_o^3 \cos^3 \beta_o f_c^{'} + 4R_o^2 \cos \beta_o t_o F_{yo} \tag{7-106}$$

This process can be programmed in a spreadsheet or mathematical software such as Matchcad to obtain a full interaction diagram for a CFDST section or CFST section (ignoring terms related to inner tube).

7.2.4 Approximate Interaction Curve

7.2.4.1 Polygonal Fit

As an alternative, an approximate interaction diagram can be developed by taking advantage of the symmetry of the section. This method initially explained by Roik and Bermann (1989), is applied here to the symmetrically layered section of the CFDST. In this method the interaction diagram is approximated by a polygon (Figure 7-7). The vertices of this polygon are designated as A, B, C, and D. At point A the section is in pure compression. Point B corresponds to the section being in pure bending. At Point C, the moment capacity is the same at B, however axial loads are also present. At point D the maximum moment capacity of the section under axial loading is reached.

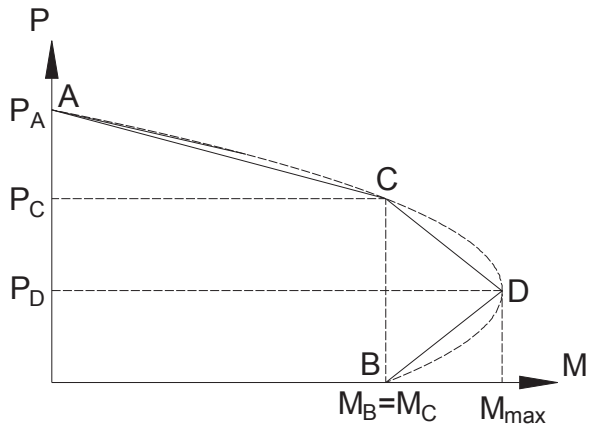

Figure 7-7: Polygonal Approximation of the Interaction Diagram

Point A is obtained by setting the neutral axis at the lower edge of the section. Hence $\beta_o = \beta_i = -\frac{\pi}{2}$ and a state of pure compression is represented (Figure 7-8). In this state the section does not resist any bending moment. Provided that no instability develops at the cross section level, the axial force it can sustain will be the sum of the compressive strengths of the concrete core and the steel tubes so that:

$$P_A = \pi\left(R_o^2 - R_i^2\right) f_c^{'} + 2\pi R_o t_o F_{yo} + 2\pi R_i t_i F_{yi} \tag{7-107}$$

$$M_A = 0 \tag{7-108}$$

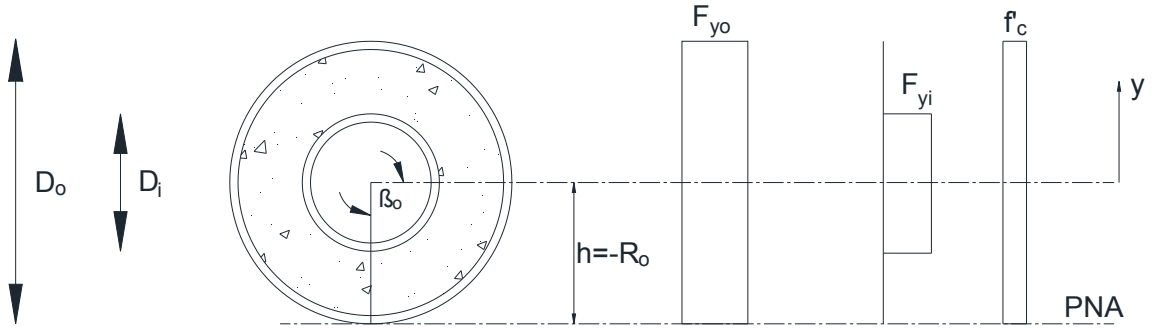

Figure 7-8: Stress Distribution at Point A

Point B is obtained for the pure flexure situation as described by one of the situations of Figure 7-3 or Figure 7-4. Based on the hypothesized location of the neutral axis (across or above the inner tube), the corresponding set of equations established for pure flexure condition are used.

Point D of the interaction diagram represents the maximum moment the section can sustain in the presence of axial load. This point is obtained when the neutral axis lies exactly on the centroid of the section. In that position, assuming a perfectly plastic stress distribution over each component of the section that participates in the strength calculation, it can be seen that the resultant of the stresses in the steel tubes is zero. This is because the upper halves of the inner tube and the outer tube are in compression, whereas their corresponding lower halves are in tension. As a consequence, the resultants of the compressive and tensile stresses compensate each other. Once this has been established, by simple inspection, the axial load the section can sustain in that condition is half of the compressive strength of the concrete core (with the general assumption that the concrete in tension does not contribute to the internal resistance of the section).

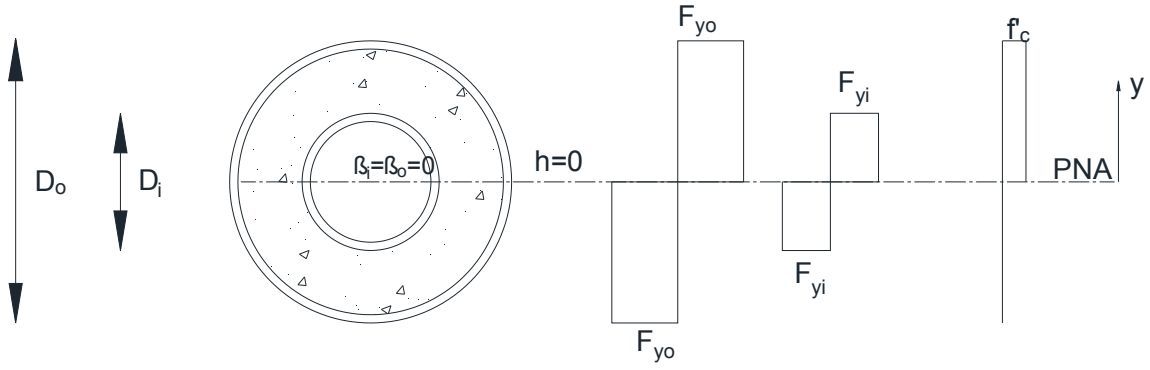

Figure 7-9: Stress Distribution at Point D

This can be further proved by inspecting Equation (7-77). This equation reaches a maximum when $\beta_o = 0$, and consequently $\beta_i = 0$, such that the absolute maximum moment under axial load is obtained when the neutral axis is aligned with the horizontal center line of the section. In this condition the maximum moment is then:

$$M_D = M_{\max} = \frac{2}{3}\left(R_o^3 - R_i^3\right) f_c^{'} + 4\left(R_o^2 t_o F_{yo} + R_i^2 t_i F_{yi}\right) \tag{7-109}$$

with a corresponding axial force:

$$P_D = \frac{\pi}{2}\left(R_o^2 - R_i^2\right) f_c^{'} \tag{7-110}$$

At point C, the stress distribution is similar to what has been shown in Figure 7-5 and Figure **7-6**. Point C is symmetric to point B with respect to point D, in that the moment capacity at C is the same as at B. Consequently, the neutral axis of the section at point C is symmetric to that for the case at point B (with respect to the geometric center of the section). This is logical because although the compressed area has increased, thus increasing the axial capacity of the section, this increase does not affect the parts of the stress distribution used to compute the moment capacity when compared to point B. Furthermore, the axial force that the section can sustain in this condition has doubled though from that corresponding to the situation at point D:

$$P_C = \pi\left(R_o^2 - R_i^2\right) f_c^{'} \tag{7-111}$$

$$M_C = M_B \tag{7-112}$$

7.2.4.2 Parabolic Fit

A parabolic fit can also be used for the moment interaction curve since its vertex (point of maximum moment) and the intercept with the moment axis (the moment in pure flexure) are known. Writing the equation of a parabola for which the vertex and an intercept are known yields:

$$M = a\left(P - P_D\right)^2 + M_{\max} \tag{7-113}$$

where a is a parameter that can be determined based on the fact that the plastic moment is known, and (P,M) are the points that described the interaction diagram.

When the section is in pure flexure, it can then be written:

$$M_P = a\left(0 - P_D\right)^2 + M_{\max} \tag{7-114}$$

Thus:

$$a = \frac{M_P - M_{\max}}{P_D^2} \tag{7-115}$$

Consequently:

$$M = \frac{M_P - M_{\max}}{P_D^2}\left(P - P_D\right)^2 + M_{\max} \tag{7-116}$$

After rearranging Equation (7-116), the approximate closed form solution to the interaction diagram is obtained:

$$\frac{M - M_{\max}}{M_P - M_{\max}} = \left(\frac{P - P_D}{P_D}\right)^2 \tag{7-117}$$

It is worth noting that the same equation will hold for CFST. Also, since the moment intercept was used to fit the interaction diagram by a parabola, the strength of the section under pure axial

load may not be correctly estimated. It is suggested that when this parabolic fit is used for design, the diagram be capped by the maximum axial load so that:

$$P \le P_{\max} \tag{7-118}$$

7.2.4.3 Preliminary Design of CFDST and CFST Sections for Earthquake Loading

Equation (7-116) is an important result which can be used for the preliminary design CFDST or CFST sections. Knowing the set of forces $\left(P_u, M_u\right)$ acting on a cross-section, the designer can, for given material properties, select the optimum section to resist those forces by setting:

$$P_u \le P_D \tag{7-119}$$

$$M_u \le M_{\max} = M_D \tag{7-120}$$

Strength reduction factors of unity are assumed here for expediency, but the same equation could be rewritten considering such reduction factors. In the ultimate conditions, it follows from Equations (7-119) and (7-120) that:

$$P_D = \frac{\pi}{2}\left(R_o^2 - R_i^2\right) f_c^{'} \tag{7-121}$$

$$M_D = \frac{2}{3}\left(R_o^3 - R_i^3\right) f_c^{'} + 4\left(R_o^2 t_o F_{yo} + R_i^2 t_i F_{yi}\right) \tag{7-122}$$

At this stage, the designer can assume a thicknesses for the inner and outer tube and solve Equations (7-121) and (7-122) for the unknown radii. Alternatively, it is possible to start by fixing the void ratio and the compactness of the outside tube. Once this is done, since the section's void ratio is a constant of proportionality between the radii of the inner tube and the outer tube for CFDST, Equations (7-121) and (7-122) are effectively reduced to one unknown. For seismic applications, a large void ratio may be desired to maximize the strength per weight ratio and achieve better economy, but for multi-hazard applications, a moderate void ratio and more stringent tube compactness may be more appropriate.

For CFST, the inner tube radius is neglected and Equations (7-121) and (7-122) become:

$$P_u = \frac{\pi}{2} R_o^2 f_c^{'} \tag{7-123}$$

$$M_u = \frac{2}{3} R_o^3 f_c^{'} + 4 R_o^2 t_o F_{yo} \tag{7-124}$$

The radius of the tube is then obtained directly from Equation (7-123) and its thickness subsequently from (7-124). The final design may need to take into account code limits on compactness of the section.

It is understood that the above design approach is helpful in obtaining preliminary sizes and that some iterations will allow to optimize the cross-section properties for specific combinations of flexure and axial loads.

7.2.4.4 Applications to the Tests Specimens

To validate the equations derived above, interaction diagrams for the test specimens have been derived using the different methods and compared. As can be seen from Figure 7-10 to Figure **7-14**, the approximate methods yield results that compare well with the exact method. As mentioned before, the parabolic fit deviates from the exact curves for sections subjected to high axial load and low bending moments, as a consequence of the approach taken in developing this approximation.

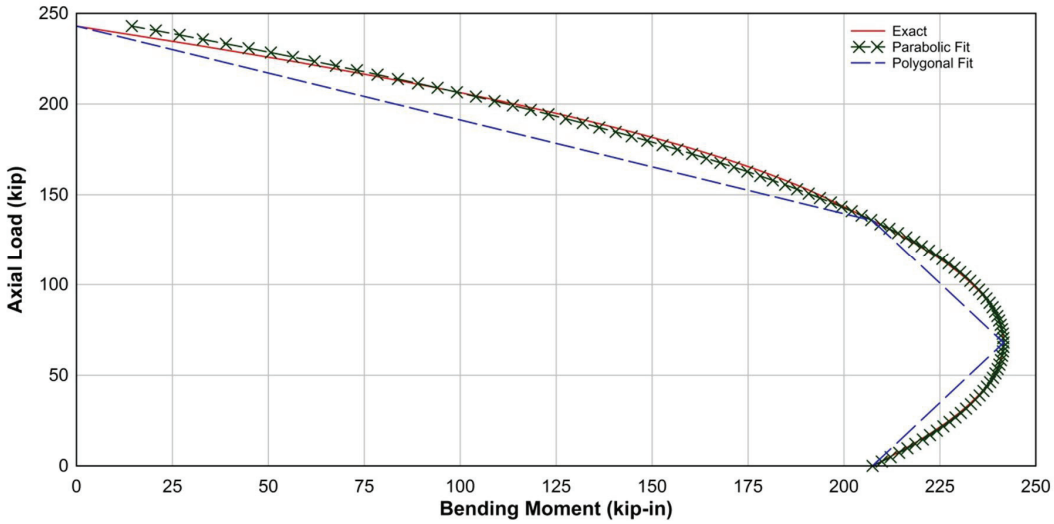

Figure 7-10: Interaction Diagram for Specimen S1

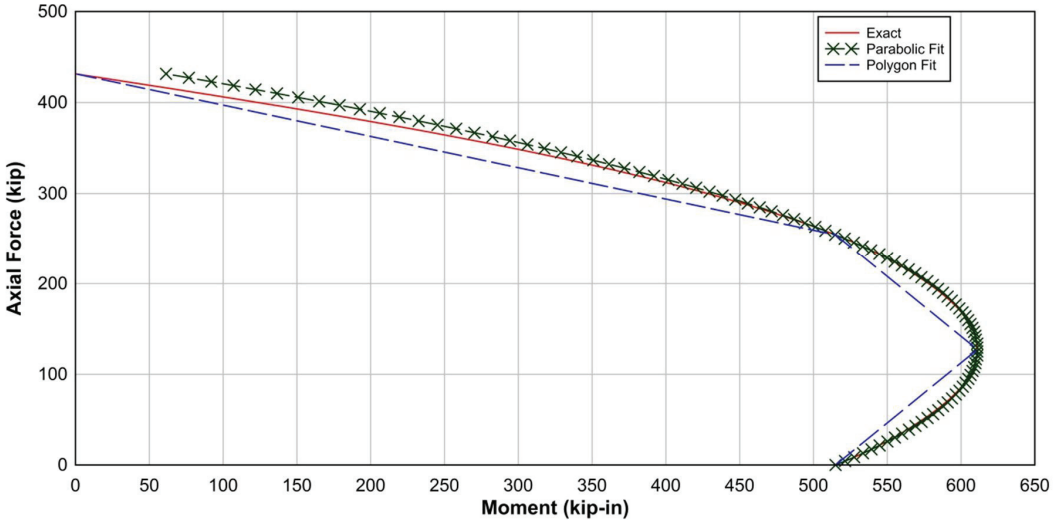

Figure 7-11: Interaction Diagram for Specimen S2

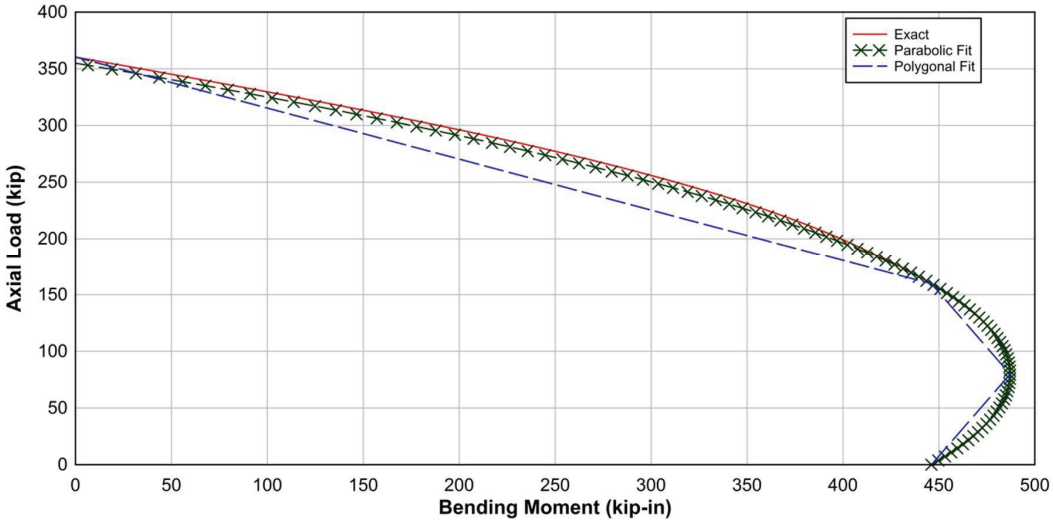

Figure 7-12: Interaction Diagram for Specimen S3

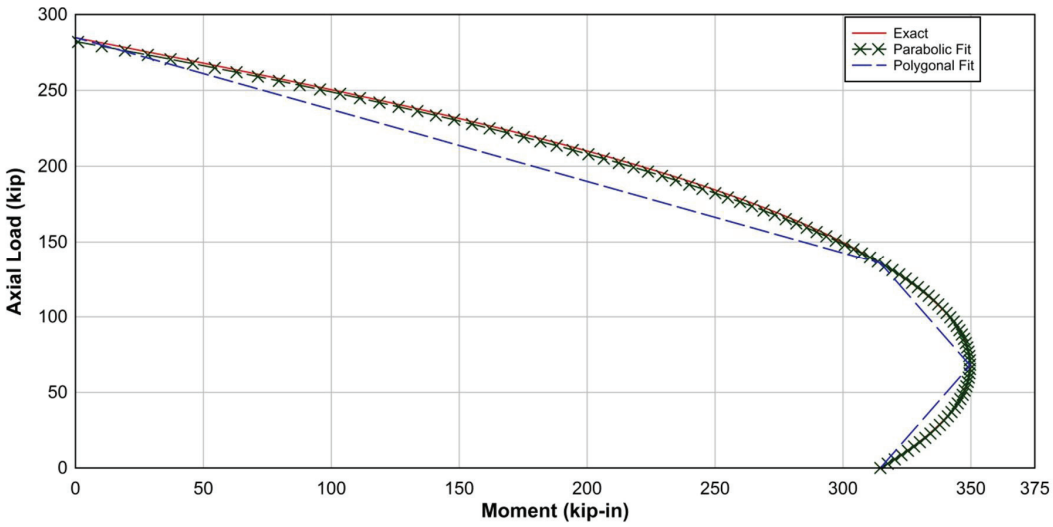

Figure 7-13: Interaction Diagram for Specimen S4

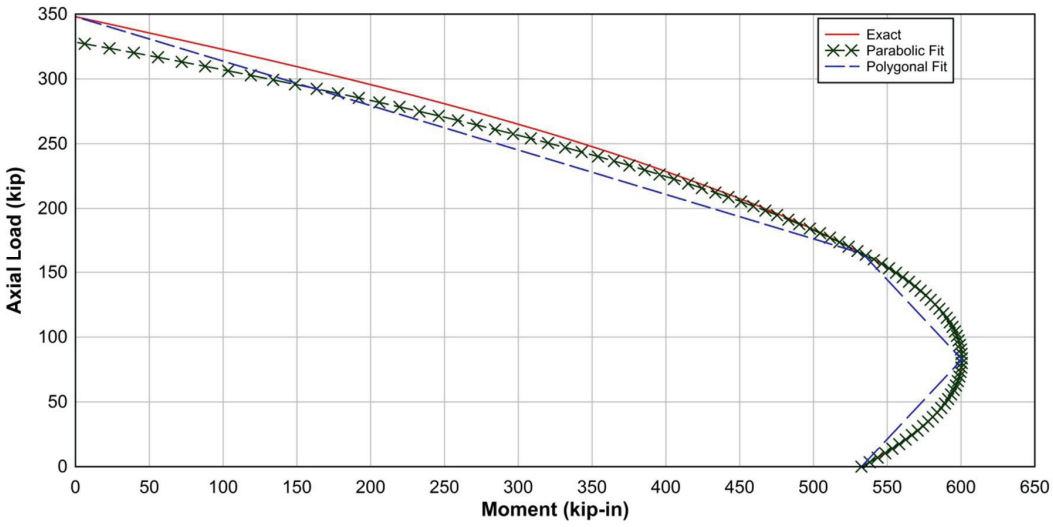

Figure 7-14: Interaction Diagram for Specimen S5

7.3 Correlation with Test Data

As mentioned before, tests on the flexural behavior of cylindrical CFDST are scarce. Nonetheless, the limited test data available in the literature is used below to validate the design equations derived in this section. CFDST in pure bending are considered in Section 7.3.1, followed by CFDST in combined axial and flexure in Section 7.3.2.

7.3.1 Pure Bending

The geometry and mechanical properties of the trdy specimens are listed in Table 7-2 and

(references are added for specimens tested by others). Predicted strength $\left(M_p\right)$) is compared to the maximum experimentally developed strength $\left(M_{p\_\exp}\right)$. Out-of-curiosity, predicted values of the plastic moment are calculated using both the yield stress (as normally done), and the ultimate stress obtained from material testing for each specimen (as an upper bound – although not accounting for possible increased concrete strength due to confinement). The corresponding resulting values are reported in Table 7-3 as $M_p\left(F_y\right)$ and $M_p\left(F_u\right)$.

Table 7-2: Specimens Geometry

Reference	Specimen	H (in)	D_i (in)	D_o (in)	t_i (in)	t_o (in)	$\frac{D_i}{t_i}$	$\frac{D_o}{t_0}$	χ
	S1	67.25	2	6	0.116	0.083	17.24	72.29	0.33
	S2	67.25	2	8	0.123	0.114	16.26	70.18	0.25
	S3	71.25	2.5	6.625	0.114	0.133	21.93	49.81	0.38
	S4	67.25	2	6	0.076	0.117	26.32	48.00	0.33
	S5	67.25	5	8	0.090	0.114	55.56	70.18	0.63
Lin and Tsai (2001)	DS-06-4-2	43.3	7.1	11.8	0.079	0.157	90	100	0.60
Lin and Tsai (2001)	DS-06-2-2	43.3	7.1	11.8	0.079	0.079	90	150	0.60

Table 7-3: Specimens Properties

Ref.	Specimen	F_{yo} (ksi)	F_{yi} (ksi)	F_{uo} (ksi)	F_{ui} (ksi)	f_c' (ksi)	M_{u_exp} (kip-in)
	S1	40.00	61.30	47.25	67.23	5.4	302.63
	S2	49.62	45.20	60.00	50.30	5.4	634.84
	S3	56.00	51.04	60.30	57.66	5.4	463.13
	S4	57.40	46.98	65.76	50.32	5.4	245.46
	S5	49.62	28.6	60.00	36.40	5.4	699.40
Lin and Tsai	DS-06-4-2	43.05	44.27	NA	NA	3.96	1619.69
Lin and Tsai	DS-06-2-2	44.27	44.27	NA	NA	4.08	1097.49

The correlation between the predicted and the observed strengths is generally good. As gathered from the comparison results in Table 7-3 and Figure 7-15 to Figure **7-19**, the predicted strengths are on the conservative side when the yield strength of the tubes are used for the calculation, with predictions equal, on average, to 90% of the maximum experimentally obtained strength (although, for two specimens, predictions exceeded the experimental values for reasons that could not be identified) . It is also observed that the ultimate strength of the section does not

consistently yield conservative (or unconservative) results, and are therefore no longer to be considered beyond this point. .

The results obtained here confirm that all specimens tested in the current research program, or reported in the literature, have been able to develop their plastic capacity during tests, even when compactness of the outside tube was as high as 150 (although it should not be inferred from this that they necessarily exhibited similar cyclic behavior).

Table 7-4: Specimens Strength Comparison

Ref.	Specimen	M_{p_exp} (kip-in)	$M_p(F_y)$ (kip-in)	$\frac{M_p(F_y)}{M_{p\_exp}}$	$M_p(F_u)$ (kip-in)	$\frac{M_p(F_u)}{M_{p\_exp}}$
	S1	198.39	207.456	1.05	234.11	1.18
	S2	634.84	514.981	0.81	601.538	0.95
	S3	463.13	446.091	0.86	478.186	0.92
	S4	245.46	314.609	1.14	353.107	1.27
	S5	699.40	532.50	0.77	634.50	0.92
Lin and Tsai	DS-06-4-2	1619.69	1385	0.86	NA	
Lin and Tsai	DS-06-2-2	1097.49	893.948	0.81	NA	
			Average	0.90		1.05

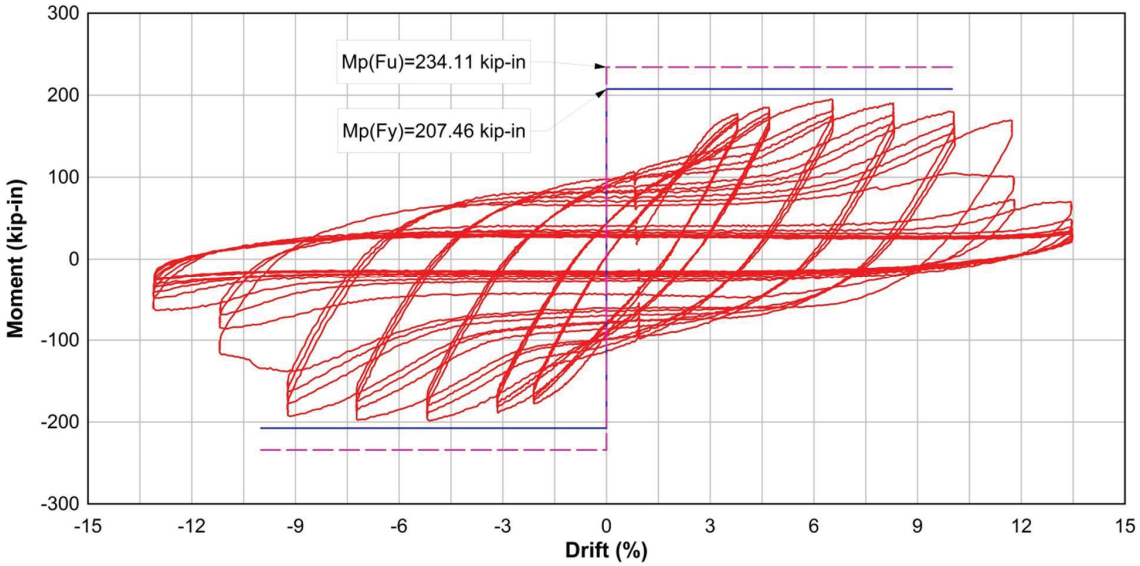

Figure 7-15: Comparison Between Predicted and Obtained Strength for S1

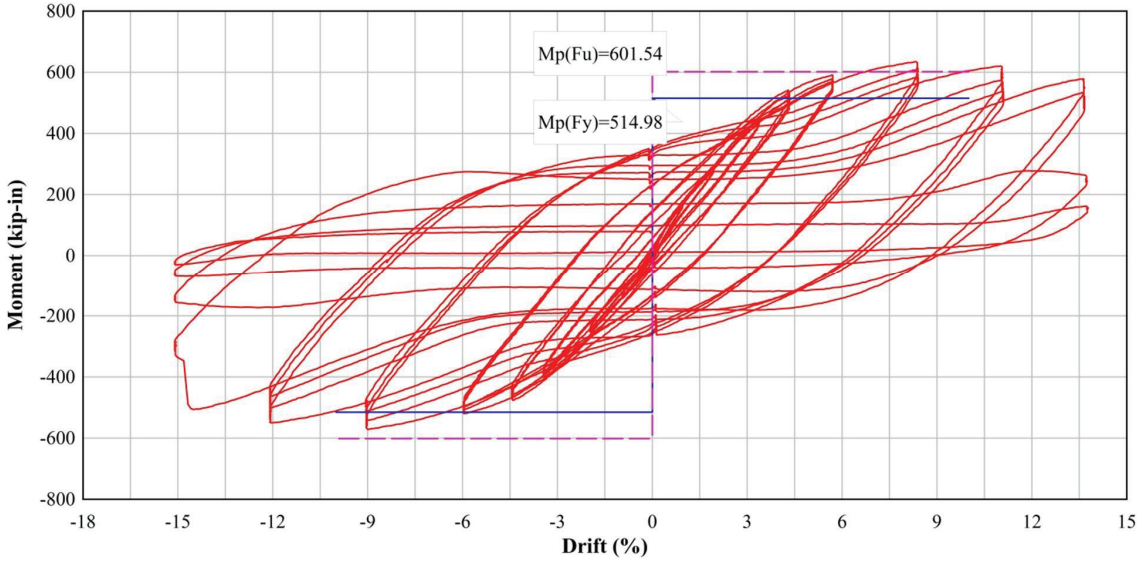

Figure 7-16: Comparison Between Predicted and Obtained Strength for S2

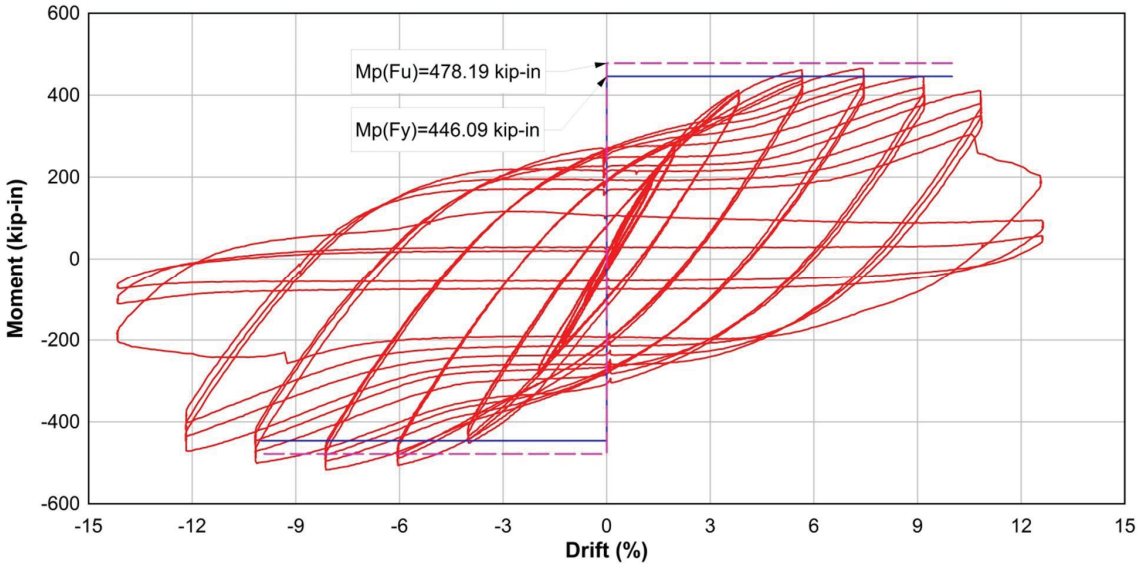

Figure 7-17: Comparison Between Predicted and Obtained Strength for S3

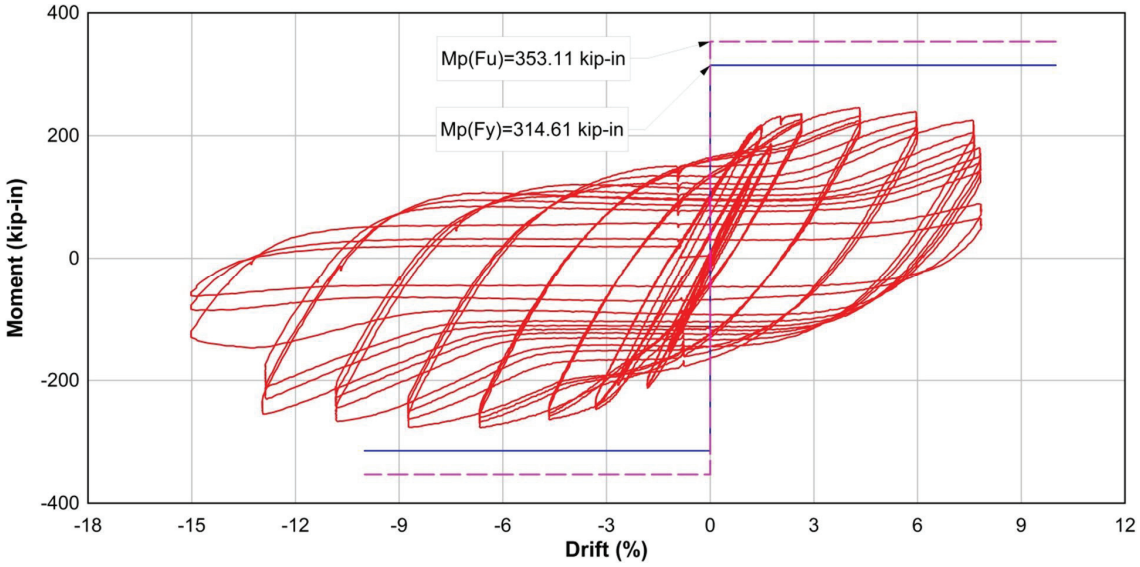

Figure 7-18: Comparison Between Predicted and Obtained Strength for S4

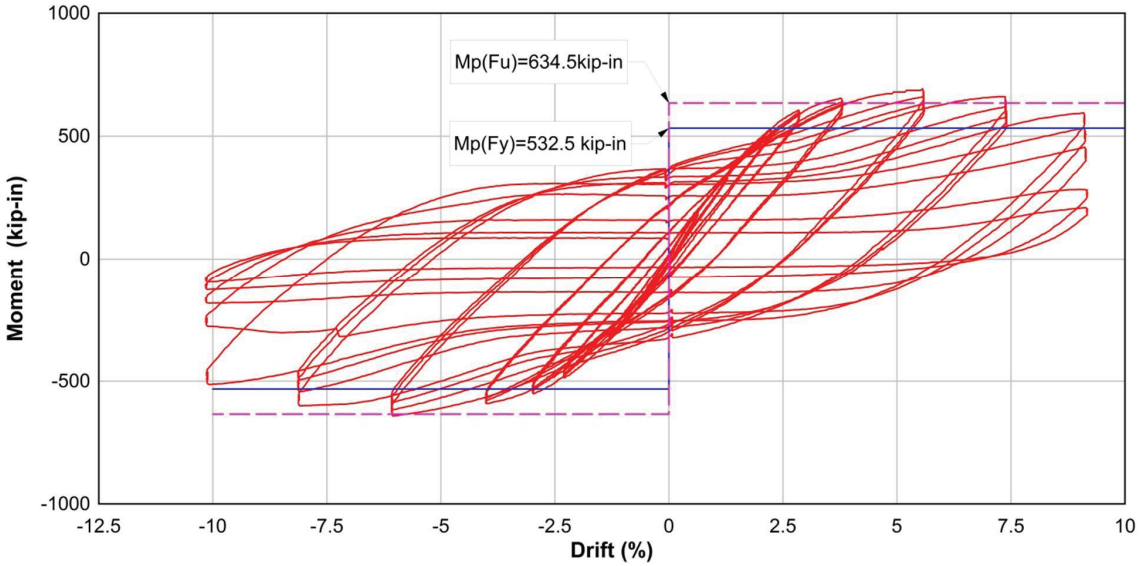

Figure 7-19: Comparison Between Predicted and Obtained Strength for S5

7.3.2 Combined Axial and Bending Case

The test series in this current research did not consider the combined effects of axial load and bending moment on the CFDST tested. Hence, test data on the strength of cylindrical CFDST subjected to such loading condition were retrieved from the literature; Results from Shakir Khalil, (1991), Lin and Tsai (2001) and Han et al. (2006) are used here to assess the effectiveness of the interaction diagram equations developed in prior sections.

For each test series, the reported properties of the specimens and the data collected are summarized. Using those properties, families of interaction diagrams are derived following the procedures described in Section 7.2.3. The couples (P_{exp}, M_{exp}) that characterize the failure of the specimen are placed on those interaction curve for comparison. Here, predicted bending moment strength corresponding to the applied axial load (P_{exp}) is calculated using Equation (7-117).

7.3.2.1 Shakir-Khalil (1991)

Shakir-Khalil tested 6 beam-column specimens having geometry and properties reported in Table 7-5 . All inner and outer tubes of the specimens tested were made from the same steel sheet. Micro-concrete was poured between the tubes as filler. All specimens were tested monotonically and bending moment was introduced by applying an axial load with an eccentricity at each end of the specimen. For some specimens, the eccentricities (e_1, e_2) at each end of the specimen were identical, whereas for others they differed. Although the author only reported the ultimate axial load on the specimens, enough data on the properties of the specimens, the loading, and the deformation under maximum load (δ_{max}) were available to allow calculating the ultimate flexural strength developed simultaneously to the applied axial load. Results are shown in Figure 7-20, along with the corresponding interaction diagrams developed per the above equations.

Table 7-5: Specimens Geometry and Mechanical Properties

*Spec.	H (in)	D_i (in)	D_o (in)	t_i (in)	t_o (in)	$\frac{D_i}{t_i}$	$\frac{D_o}{t_o}$	χ	e_1 (in)	e_2 (in)	δ_{max} (in)	$F_{yo} = F_{yi}$ (ksi)	f_c' (ksi	P_{exp} (kip)	M_{exp} (kip-in)
SKB1	144.88	6.81	7.36	0.041	0.078	166	94.4	0.93	0.39	0.39	1.18	28.43	6.4	76.4	120.4
SKB2	144.88	6.81	7.36	0.041	0.078	166	94.4	0.93	0.98	0.98	0.79	31.33	6.4	66.1	117.1
SKB3	144.88	6.81	7.36	0.041	0.078	166	94.4	0.93	2.95	2.95	1.97	30.46	7.0	66.1	198.1
SKB4	144.88	6.81	7.36	0.041	0.078	166	94.4	0.93	5.91	5.91	2.26	29.73	6.2	26.8	218.5
SKB5	144.88	6.81	7.36	0.041	0.078	166	94.4	0.93	2.95	0.98	1.18	30.02	6.3	50.6	209.1
SKB6	144.88	6.81	7.36	0.041	0.078	166	94.4	0.93	5.91	2.95	1.38	31.47	6.4	36.2	263.7

*SK was added to the labelling of the specimens reported to avoid confusion with other specimen tested in this research

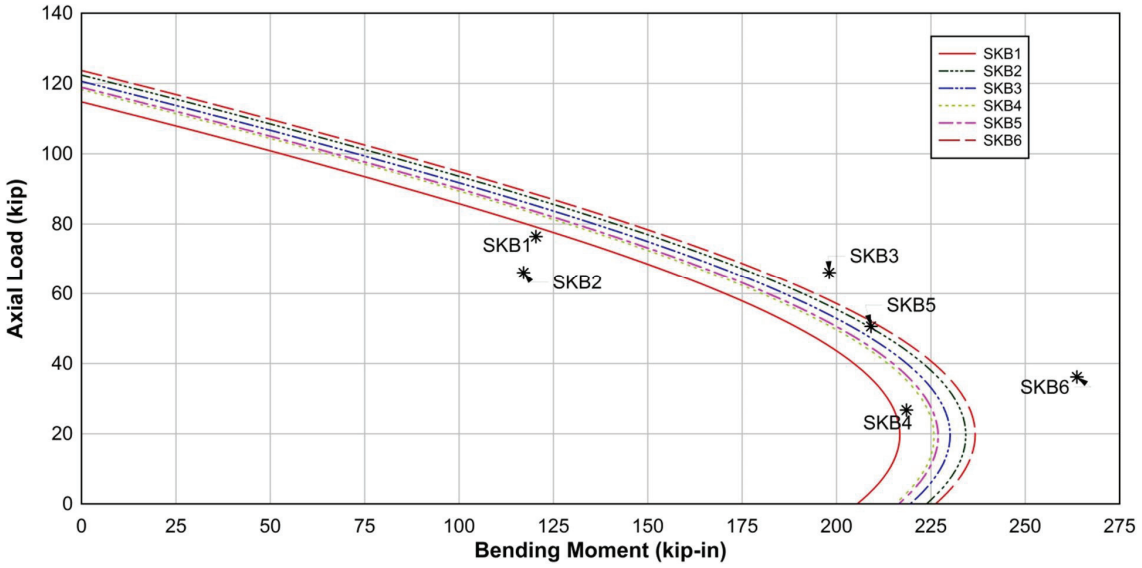

Figure 7-20: Comparison between Predicted and Obtained Strength for SK Series

Table 7-6: Moment Prediction for SK Series Using Equation (7-117)

Spec.	P_D (kip)	M_p (kip-in)	M_{max} (kip-in)	P_{exp} (kip)	M_{calc} (kip-in)	M_{exp} (kip-in)	$\frac{M_{calc}}{M_{exp}}$
SKB1	76.4	205.46	216.747	76.4	122.15	120.4	1.01
SKB2	66.1	223.14	233.576	66.1	174.64	117.1	1.49
SKB3	66.1	221.84	234.295	66.1	180.29	198.1	0.91
SKB4	26.8	215.75	226.227	26.8	224.67	218.5	1.03
SKB5	50.6	216.80	227.514	50.6	200.65	209.1	0.96
SKB6	36.2	226.22	236.726	36.2	229.49	263.7	0.87
						Average	1.05

With one exception, SKB2 (Figure 7-20), good agreement was generally obtained between the prediction and the observed bending moment. No specific reason for this deviation could be inferred from the information available. Ultimate strength of the specimen was, in general, conservatively predicted.

7.3.2.2 Lin and Tsai (2002)

Lin and Tsai (2002) also tested specimens under combined axial and flexural loading, with three levels of axial loads (corresponding to 25%, 40%, and 70% and the nominal axial capacity of each specimen). Data for those specimens are reported in Table 7-7, along with strength prediction by the above equations. The specimens with a level of axial load of 25% were tested under cyclic lateral loading. Ultimate strength of the specimens for the level of loading reported is again predicted with reasonable accuracy, and conservatively (Figure 7-21).

Table 7-7: Moment Prediction for DS Series Using Equation (7-117)

*Spec.	P_D (kip)	M_p (kip-in)	M_{max} (kip-in)	P_{exp} (kip)	M_{calc} (kip-in)	M_{exp} (kip-in)	$\frac{M_{calc}}{M_{exp}}$
DS-06-4-2-25	138.14	1384.9	1541.49	109.0	1541.22	1699.3	0.91
DS-06-2-2-25	138.14	890.42	1087.36	132.4	1078.60	1221.4	0.88
DS-06-4-2-40	138.14	1384.9	1541.49	174.5	1496.96	1672.8	0.89
DS-06-2-2-40	138.14	890.42	1087.36	211.8	1073.71	1203.7	0.89
DS-06-4-2-70	138.14	1384.9	1541.49	305.3	1097.94	1079.8	1.02
DS-06-2-2-70	138.14	890.42	1087.36	370.6	798.96	947	0.84
						Average	0.91

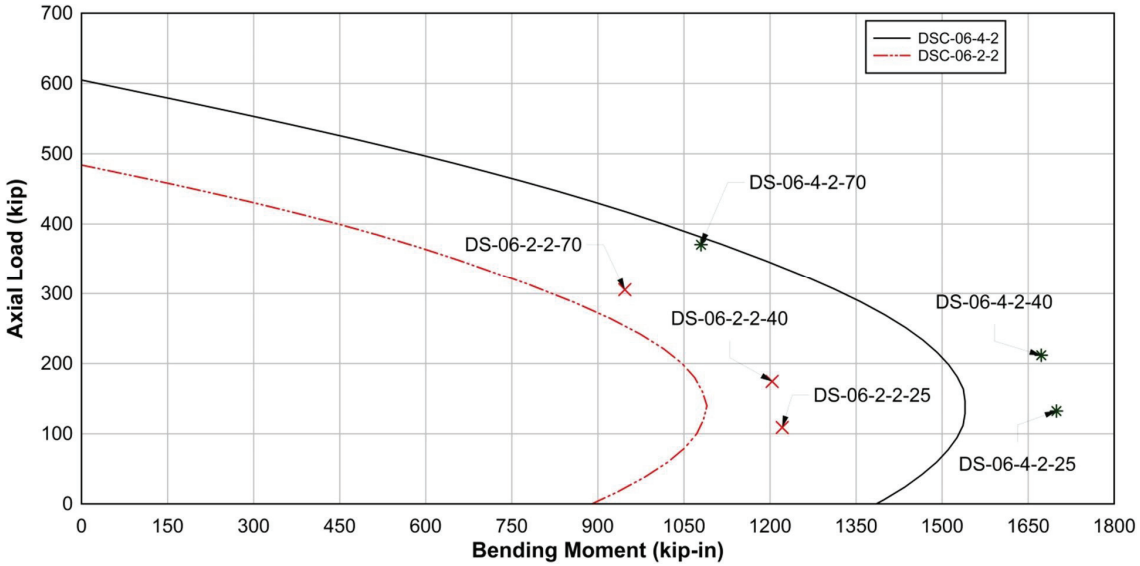

Figure 7-21: Comparison between Predicted and Obtained Strength for SKB Series

7.3.2.3 Han et al. (2006)

Han et al. (2006) tested 8 beam-column cylindrical CFDST specimens subjected to cyclic loading (Table 7-8). Axial load corresponding to 0%, 21%, 42%, and 64% of the nominal axial strength of the sections were applied concentrically on the specimens. The experimentally obtained strengths reported by the authors did not take into account second order effects coming from the application of the axial loading. To account for second order moment, the lateral deformations (δ_{max}) of the specimens at peak strength are multiplied by the applied axial loads. Consequently, in Table 7-9 , comparisons to the strength directly reported by Han et al. and the "corrected" strength that takes into account the second order effect are reported. When second order effects are considered better agreement (Figure 7-23) is obtained with the calculated strengths compared to the case where they are ignored (Figure 7-22).

Table 7-8: Specimens Geometry and Mechanical Properties

Spec.	H (in)	D_i (in)	D_o (in)	t_i (in)	t_o (in)	$\frac{D_i}{t_i}$	$\frac{D_o}{t_o}$	χ	F_{yo} (ksi)	F_{yi} (ksi)	f_c' (ksi
cc2-1	59.06	4.50	1.25	0.118	0.118	10.7	38	0.30	44.7	61.25	5.64
cc2-2	59.06	4.50	1.25	0.118	0.118	10.7	38	0.30	44.7	61.25	5.64
cc2-3	59.06	4.50	1.25	0.118	0.118	10.7	38	0.30	44.7	61.25	5.64
cc2-4	59.06	4.50	1.25	0.118	0.118	10.7	38	0.30	44.7	61.25	5.64
cc3-1	59.06	4.50	1.25	0.118	0.118	19.3	38	0.54	44.7	54.32	5.64
cc3-2	59.06	4.50	1.25	0.118	0.118	19.3	38	0.54	44.7	54.32	5.64
cc3-3	59.06	4.50	1.25	0.118	0.118	19.3	38	0.54	44.7	54.32	5.64
cc3-4	59.06	4.50	1.25	0.118	0.118	19.3	38	0.54	44.7	54.32	5.64

Table 7-9: Moment Prediction for Han et al. Test Series Using Equation (7-117)

*Spec.	P_D (kip)	M_p (kip-in)	M_{max} (kip-in)	P_{exp} (kip)	δ_{max} (in)	M_{calc} (kip-in)	$^{*}M_{exp}$ (kip-in)	$^{**}M_{exp}$ (kip-in)	$\frac{M_{calc}}{^{*}M_{exp}}$	$\frac{M_{calc}}{^{**}M_{exp}}$
cc2-1	41.11	147.50	159.33	0.00	0.79	147.50	134.76	134.76	1.09	1.09
cc2-2	41.11	147.50	159.33	34.43	0.79	159.02	125.13	152.22	1.27	1.04
cc2-3	41.11	147.50	159.33	68.85	0.55	153.94	128.78	166.70	1.20	0.92
cc2-4	41.11	147.50	159.33	103.28	0.47	132.27	117.83	166.58	1.12	0.79
cc3-1	33.08	172.26	180.91	0.00	1.14	172.26	152.02	152.02	1.13	1.13
cc3-2	33.08	172.26	180.91	32.40	0.87	180.91	154.34	182.38	1.17	0.99
cc3-3	33.08	172.26	180.91	64.80	0.43	172.95	140.07	168.11	1.23	1.03
cc3-4	33.08	172.26	180.91	97.20	0.43	148.40	103.89	145.95	1.43	1.02
								Average	1.21	1.00

*Second order effect not accounted for
**Second order Effect considered

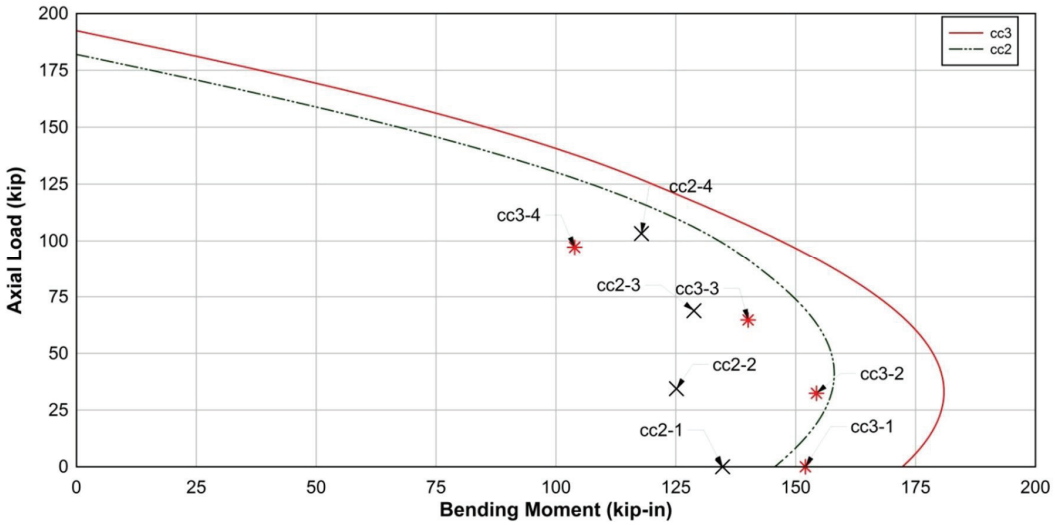

Figure 7-22: Comparison between Predicted and Reported Strength for Han et al. Series

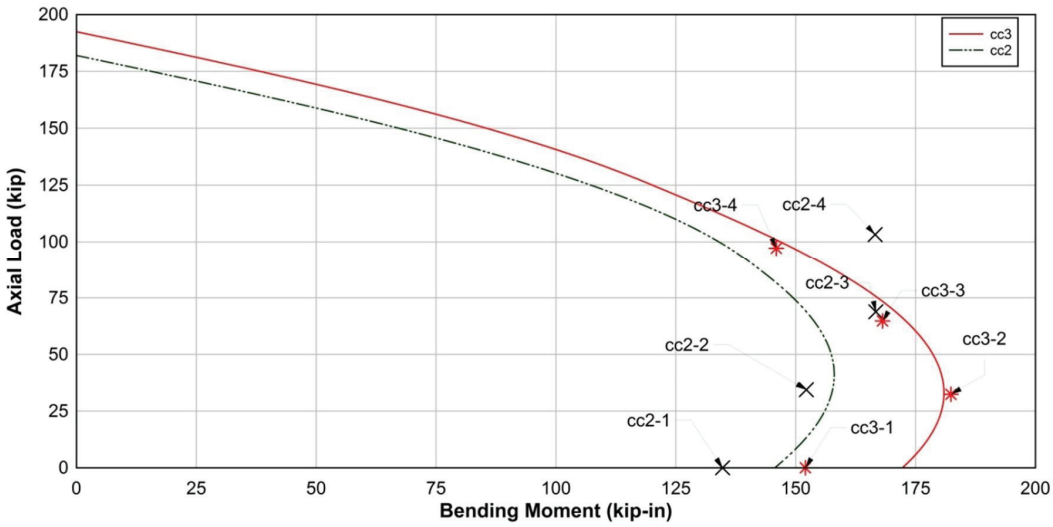

Figure 7-23: Comparison between Predicted and Corrected Strength for Han et al. Series

7.4 Summary

In this section, equations to predict the flexural strength of CFDST have been derived, together with interaction diagrams for flexure-axial interaction. Exact and approximate design equations were proposed, and both were found to give conservative results when compared to data collected in this research or available from the literature. More specifically:

1) Conservative estimates of the flexural strength was obtained for combination of large void ratio (up to 93%) and high compactness ratios for the inner and outer tube when compared to data from the literature (up to 94.4 and 166, respectively)..
2) Conservative estimates were also obtained when large axial loads (up to 70% of the nominal axial capacity of the section) were applied.

Finally, a simple equation was proposed for the preliminary design of CFDST (and CFST) subjected to a combination of axial load and bending moment.

SECTION 8

PERFORMANCE OF CONCRETE FILLED DOUBLE SKIN TUBES AND MODIFIED STEEL JACKECTED COLUMNS UNDER BLAST LOADING

8.1 General

A test program was conducted to investigate the blast worthiness of CFDST and MSJC. A total of 12 quarter-scale CFDST column specimens grouped into 3 bents of 4 columns each, and another bent made of 4 quarter-scale MSJC columns, were tested. Two 4-column CFDST bents were tested at the University at Buffalo's outdoor Experimental Campus for Large Infrastructure Protection, Sustainability and Enhancement (ECLIPSE), whereas another 4-column bent was tested later at the Big Black Testing Site of the US Army's Engineer Research and Development Center (ERDC) in Vicksburg, Mississippi. In parallel to the CFDST experiments at ERDC, tests were also carried out on the quarter-scale MSJC column bent. A total of 17 blast tests were carried on the CFDST bents while another 7 tests were conducted on the MSJC bent. Note that when referring to total number of CFDST specimens in this report, this number implicitly comprises one CFST specimen included for comparison with results of previous studies.

This section discusses the two test series separately, in subsequent sections, each organized as follows. For each series, the test setup and the design of the specimens are briefly presented, along with a description of their construction. Then, instrumentation scheme for each test is discussed and the rationale for using any given instrument explained. This is followed by a description of the testing protocol. Each section ends on observations and measurements made

after the tests. The section itself ends with a summary of the main observations made during both series of tests.

8.2 The ECLIPSE Test Series

In the ECLIPSE series, the main emphasis was on confirming performance – predicted by simplified analysis and finite element models of CFDST analyzed in LS-DYNA – and assessing experimentally how it is affected by various design and geometric parameters (larger vs. smaller void, tube compactness with respect to specified limits for highly ductile vs. moderately ductile behavior, etc.).

8.2.1 Specimens, Materials and Section Properties

Of the 8 specimens tested as part of this series, five were CFDSTs similar in cross section to the columns subjected to cyclic testing as described in Section 6, and one was a CFST with a specified outside tube diameter of 152mm (6 in). The other two were CFDSTs; of those two one had the smallest void ratio (25%) of all the specimens tested and the other one (50% void) was selected to complete the spectrum of void ratios which varied from 25% to 63%. The selection process was otherwise similar to the seismic test series. Table 8-1 summarizes the main geometric and section features of the specimens. The notation used in Table 8-1 for the specimen names is consistent with that used in Section 5, except that the prefix B is used instead of S to designate the specimens of this blast test series.

Table 8-1: ECLIPSE Tests Specimens

	Specimen	Column Designation	H (mm)	D_i (mm)	D_o (mm)	t_i (mm)	t_o (mm)	Void Ratio	Ductility	
									Inside Tube	Outside Tube
Bent 1	17_72_33	B1	1500	50.80	152.4	2.9464	2.1082	0.33	HD	MD
	16_70_25	B3	1500	50.80	203.2	3.1242	2.8956	0.25	HD	MD
	56_70_63	B7	1500	127	203.2	2.2860	2.8956	0.63	HD	MD
	26_48_33	B5	1500	50.80	152.4	1.9304	3.1750	0.33	HD	HD
Bent 2	20_73_42	B2	1500	63.50	152.4	3.1750	2.0828	0.42	HD	MD
	22_50_38	B4	1500	63.5	168.3	2.8956	3.3782	0.38	HD	HD
	33_94_50	B6	1500	101.6	203.2	3.0480	2.1590	0.50	HD	MD
	-	B8	1500	-	152.4	-	3.0480	0	-	HD

Highly (HD) or moderately ductile (MD) tubes as per the AISC Seismic Provisions were used in the construction of all the specimens. All tube materials were ASTM A513 Type 2 steel with nominal yield strength of 32ksi and modulus of elasticity of 29000*ksi*, as described in Section 6.2.2 for the seismic test series. The stress-strain curves for all the specimens are presented on Figure 8-1 and Figure 8-2 for the inner tubes and the outer tubes of the specimens respectively.

The concreting of the seismic and blast specimens occurred at the same time. The concrete used in all specimens was a ready mix, self-compacting, accelerated cure concrete with a specified strength of 5ksi. Fiber-reinforced concrete was used to cast the foundation and the cap beams.

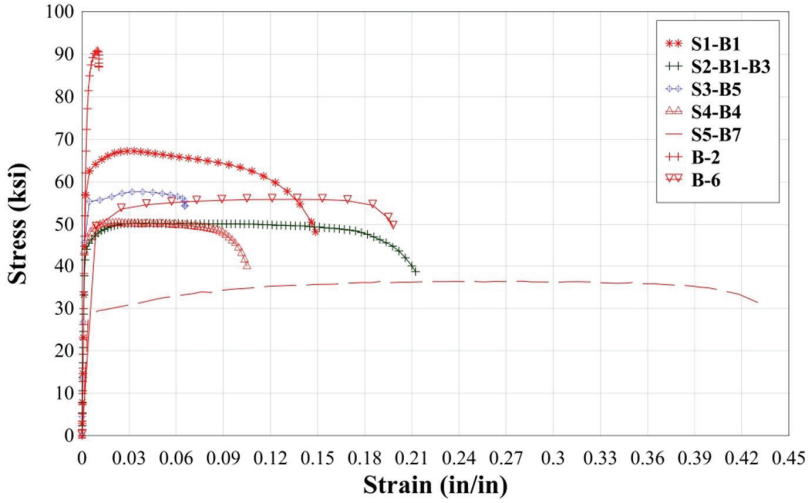

Figure 8-1: Stress Strain Curves for the Steel of the Inner Tubes of the Specimens

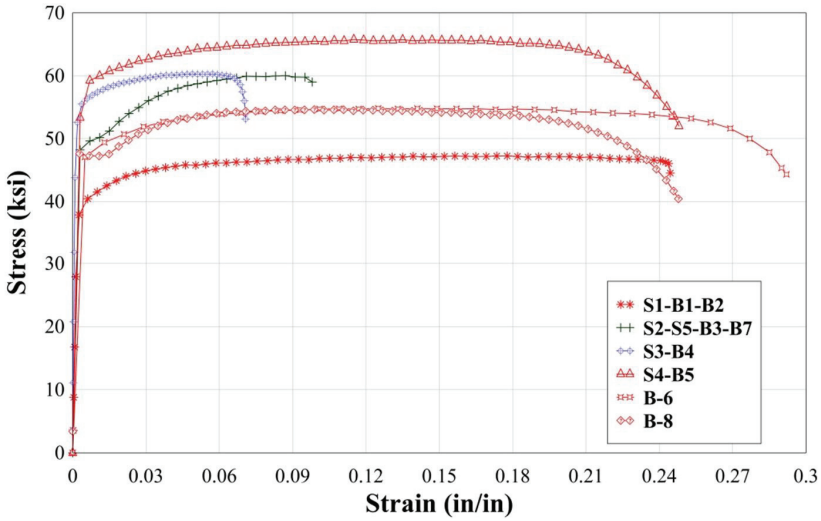

Figure 8-2: Stress Strain Curves for the Steel of the Outer Tubes of the Specimens

8.2.2 Description of the Experimental Setup

The test setup in the ECLIPSE series was similar to the one found in the work by Fujikura and Bruneau mentioned earlier. Concrete encased built-up steel sections were used as cap and

foundation beams of each multi-column bent. The built-up steel sections were similar to the box sections described for the seismic test but spanned the entire length of the bent. For design purposes, the cap beam was made stronger than the foundation beam. This is because, as discussed later, the design of the cap beam was controlled by blast overpressures whereas the foundation beam was designed for the capacity of the strongest specimen attached to it.

Each bent contained 4 equally spaced columns. Since the test procedure called for the columns to be tested in turn, the spacing between the columns was selected such that, when any column was being tested, the neighboring columns would remain elastic. It was found that a spacing of about 1270mm (50 in) on center for the columns of each bent would amply suffice for that purpose.

A reaction frame connected to the cap-beam of each bent served to provide lateral support and simulate the boundary conditions and rigidity that the deck of a bridge would have provided at the top of the beams if it was present. Figure 8-3 and Figure 8-4 show front elevation and top views of the reaction frame while Figure 8-5 shows the experimental setup as-built. The foundation of the reaction frame was directly cast in place in concrete cylinders embedded 3 feet into the ground.

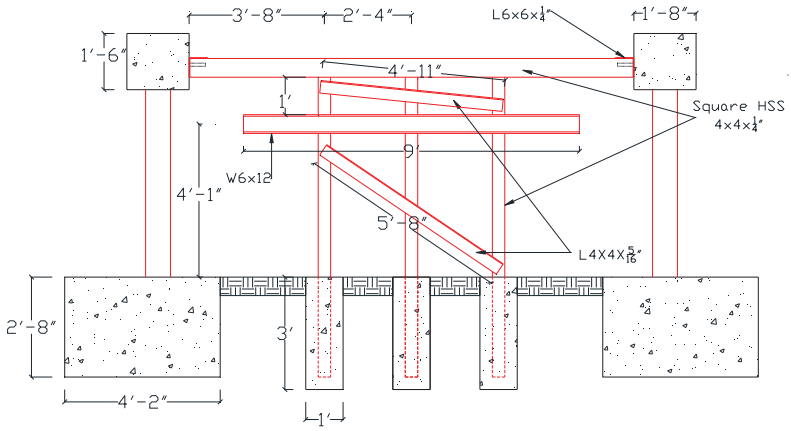

Figure 8-3: Reaction Frame Elevation and Attached Bents

[Units Shown in Feet and Inches, 1in=25.4mm]

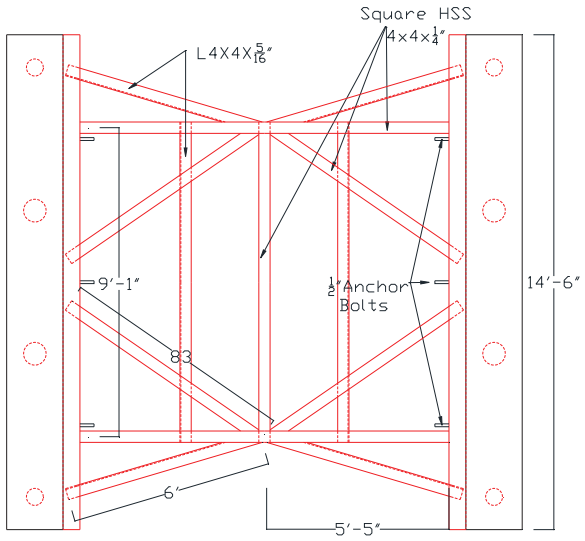

Figure 8-4: Top view of the Reaction Frame and Neighboring Bents

[Units Shown in Feet and Inches, 1in=25.4mm]

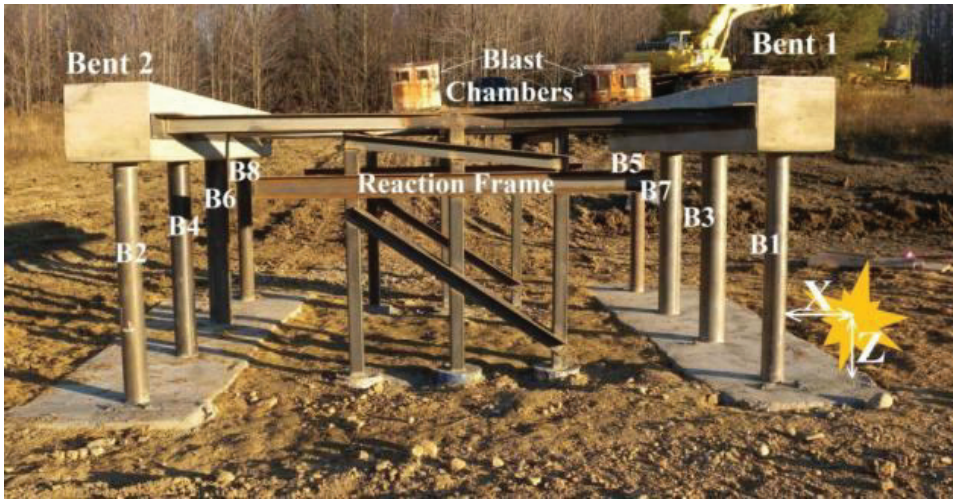

Figure 8-5: Reaction Frame and Bents as Built

8.2.3 Design of the Specimens

8.2.3.1 Design of the Cap-Beam

The cap beam was to remain elastic so it could survive throughout the tests without strength impairing damage. Initial considerations led to conclude that the design of the cap-beam would be controlled by the expected overpressures it would see during the tests rather than by capacity design (as would have been the case for earthquake loading). Estimate of the distribution of overpressures seen by the cap-beam was obtained using the program BEL (USACE-ERDC, 2004) for the position of the charge which would induce the highest overpressures on the cap-beam. This position corresponded incidentally with the position of the charge for which the standoff to a targeted column was the smallest. In such a scenario blast overpressures would be applied to the underside of the cap-beam and each portion of the cap beam spanning between the columns would behave as a beam with built-in supports.

The design of the cap beam was based on an equivalent SDOF approach. For simplicity it was assumed that both the steel and the concrete contributed to the mass and the stiffness of the system whereas the strength was only coming from the steel. Blast overpressures in the upward direction were assumed to be uniformly distributed and calculated using equivalent pressure and impulse obtained respectively as:

$$p_{eq} = \frac{\int_o^l p(x)\delta(x)dx}{\int_o^l \delta(x)dx} \tag{8-1}$$

$$i_{eq} = \frac{\int_o^H i(x)\delta(x)dx}{\int_o^H \delta(x)dx} \tag{8-2}$$

where $p(x)$ and $i(x)$ are respectively taken as the distributions of peak overpressures and impulses on the centerline of the span of the cap beam under consideration as obtained from BEL, x is a generalized coordinate defined along the length of the target span of the cap-beam, and L the span length taken as 1270mm (50in). Also, $\delta(x)$ is an elastic shape function based on the deformed shape of a uniformly loaded beam with built-in supports given by:

$$\delta(x) = 16\frac{x^2}{L^4}(L-x)^2 \tag{8-3}$$

As expected this shape function is unity at mid-span where the maximum deformation is expected for this model and gives values of zero at the extremities of the beam.

The maximum elastic deformation of the cap-beam was estimated by equating the energy transferred by the blast impulse to the elastic strain energy of the SDOF to give:

$$X_E = \frac{\left(\beta\, i_{eq}\right)^2}{K_{LM}\, m\, r_u} \tag{8-4}$$

where β is a (shape) factor accounting for the reduction in impulse seen by the cap-beam because of its shape (β is taken in as 0.80 in the analysis), $K_{LM} = 0.77$ is the load mass factor (Biggs, 1965), m is the mass per unit length of the composite beam and r_u is the ultimate strength of the cap-beam, which in the SDOF model is a function of the flexural strength $\left(M_p\right)$ of the cap-beam and is given by:

$$R_u = \frac{12 M_p}{L^2} \tag{8-5}$$

The flexural strength of the cap-beam is based, in this model, only on the capacity of the C-channels. This is a quite conservative assumption, but it guarantees that the strength of the cap-beam is not exceeded even if the concrete is damaged during testing. The sizing of the channels of the cap-beam is itself an iterative procedure; a starting point for this iteration was to consider the channel sizes predicted by capacity design and to increase the size of the section as needed to meet the above demands.

8.2.3.2 Design of the Foundation Beam

The sizing of the foundation beam was capacity driven. For simplicity, the foundation of each bent was sized for the ultimate capacity of the strongest CFDST specimen that was attached to it. The process is similar to the sizing of the base of the seismic test specimen presented in Section 5. Since the C-channels of the foundation beam were embedded in concrete, unlike the seismic test setup, its plates did not need to be designed against buckling; this resulted in thinner plate

components. The dimensions of the different components of the cap and foundation beams are shown on Figure 8-6.

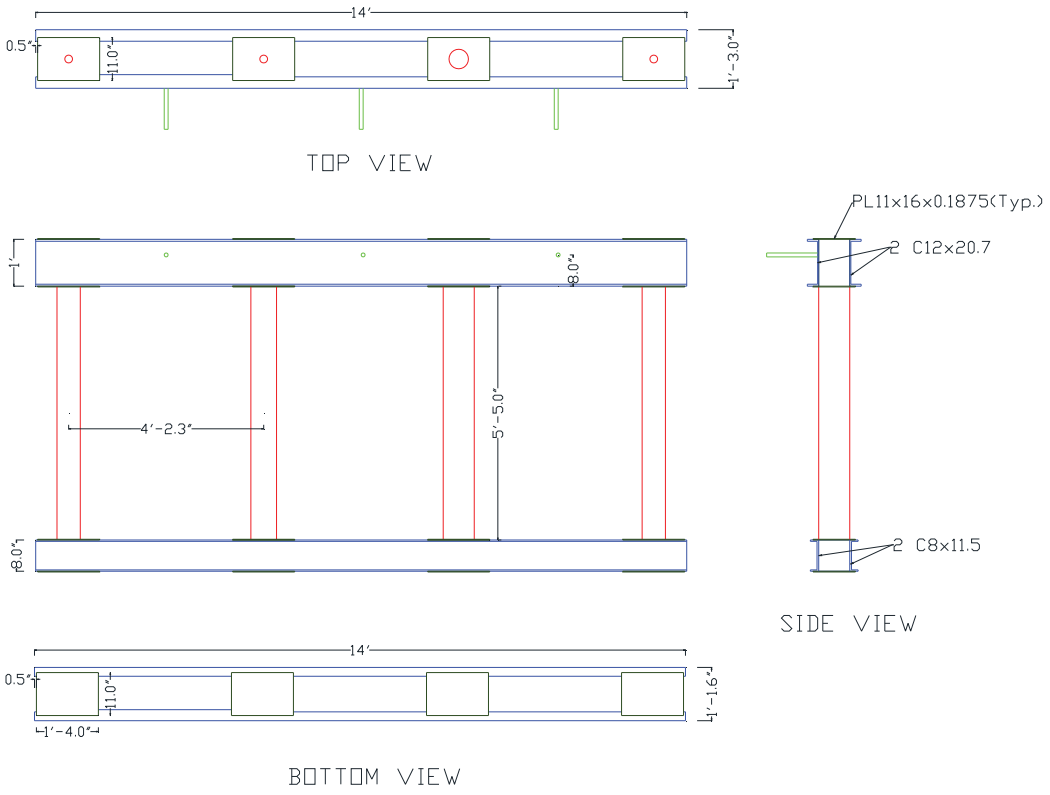

Figure 8-6: Final Design of the Steel Components of the Cap and Foundation Beams

[Units Shown in feet and inches, 1in=25.4mm]

8.2.4 Construction of the Specimens

The construction of the CFDST bents was relatively straightforward. The bent was built upside down since the cap beam built-up steel section was heavier than that of the foundation. The construction of the bents included the following steps:

Step 1) Construction of the Cap and Foundation Box Girders

The cap and the foundation box girders were built-up steel sections formed by two (2) C-channels and eight (8) rectangular steel plates. Four of those plates were welded to the top flange of the channels at the emplacement of the CFDST and 4 corresponding plates were welded to the bottom flanges of the channels at the same location. The construction of the cap beam for the ECLIPSE series was globally similar to that of the base of the seismic specimens, the only difference being that the channels extended the full length of the bent (Figure 8-7).

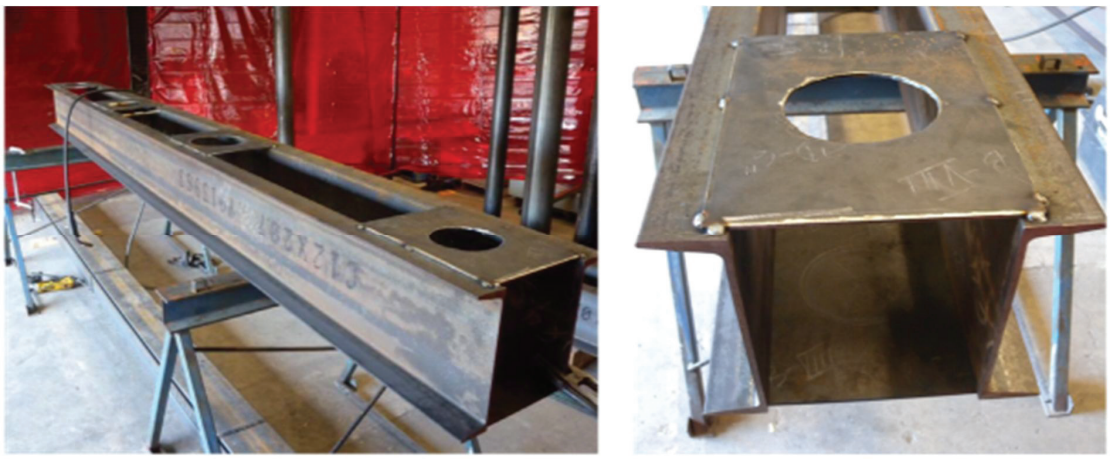

Figure 8-7: Cap-Beam and Plates to C-Channel Connections in the Cap Beam

The construction of the foundation beam was similar, but only the top plates were welded at this stage. The bottom plate in which a hole was bored to allow insertion and welding of the inner tube was connected in the last stage of the construction (Figure 8-8).

Step 2) Welding of the Inner Tube to the Base Plate of the Foundation Beam

The next step in the construction process was the welding of the inner tube to the top plate of the cap beam (Figure 8-9). The inner tube was cut 25.4mm (1in) longer than the outer tube to facilitate its placement inside the hole of the foundation bottom plate and its subsequent welding to that plate.

Step 3) Welding of the Outer Tubes to the Plates of the Foundation Beam

This step is illustrated in Figure 8-10. The outside tubes were positioned first in the holes of the bottom plates of the cap-beam using magnetic levels to insure that they were plumb. Then, the tubes were tack-welded to the bottom and top plates of the foundation beam to keep them in position. The tubes were finally fillet-welded all around to both plates in their final position.

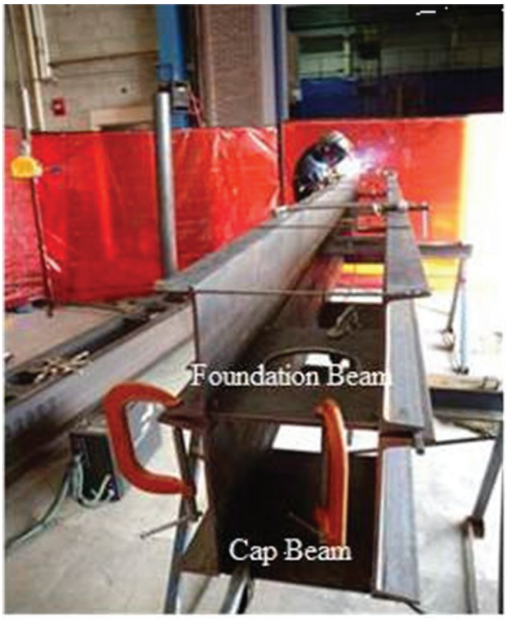

Figure 8-8: Cap and Foundation Beams Shown Superposed

Step 4) Foundation Beam to Tube Assemblage

In this step, the pre-assembled foundation box was positioned at the proper location along the top of the base of the outer tube and welded such that the bottom of the tube was flushed with the bottom flanges of the channels (Figure 8-11).

Step 5) Concreting

Once the steel skeletons of both bents were completed, the next step was to pour concrete in the annular regions between the tubes. Figure 8-12 and Figure 8-13 show respectively the annular region and the concreting of the tubes. The bents were inclined during that step. The concrete

used was self-consolidating; since self-consolidating concrete requires little compaction to be put in place, an external vibrator applied to the outer tube to help it flow in place.

Step 6) Foundation Beam Bottom Plate Welding

After concrete was poured in the CFDST columns, and after 7 days to allow some concrete curing and prevent the head imparted by welding to the CFDST to create water build-up inside the CFDST (by evaporation and condensation of the water in unset concrete), the bottom plates of the foundation beam were welded to the flanges of the C-channels and the extension of the inner tubes (Figure 8-14; in that figure the specimen is shown upside down as it was built) to seal the concrete inside the annular region.

Figure 8-9: Inner Tube to Cap Beam Top Plate Welding

Figure 8-10: Outer Tube to Cap Beam Plates Connection

Figure 8-11: Assembly of the Foundation Beam to the Tubes

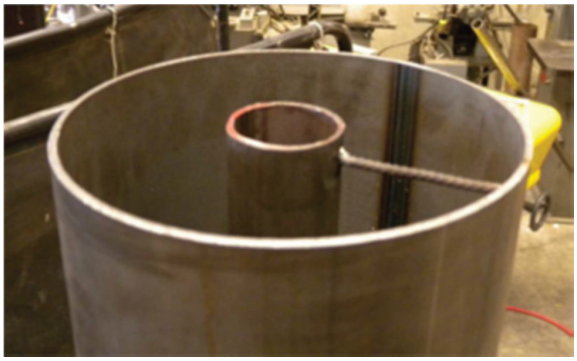

Figure 8-12: Region between the Tubes

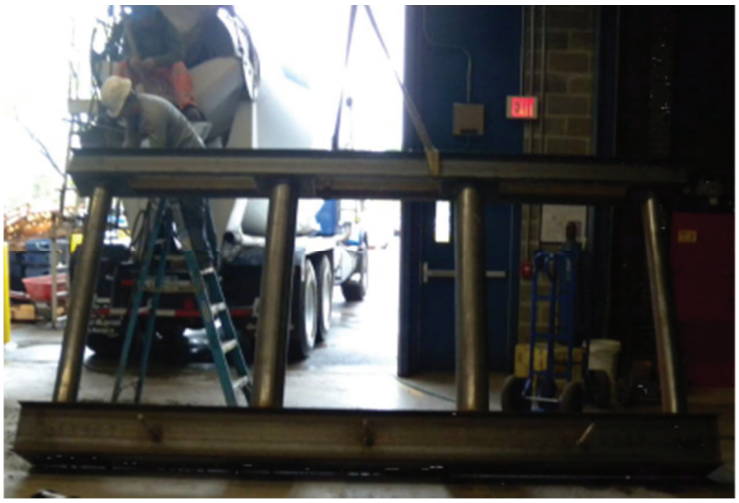

Figure 8-13: Concreting of the CFDST Columns

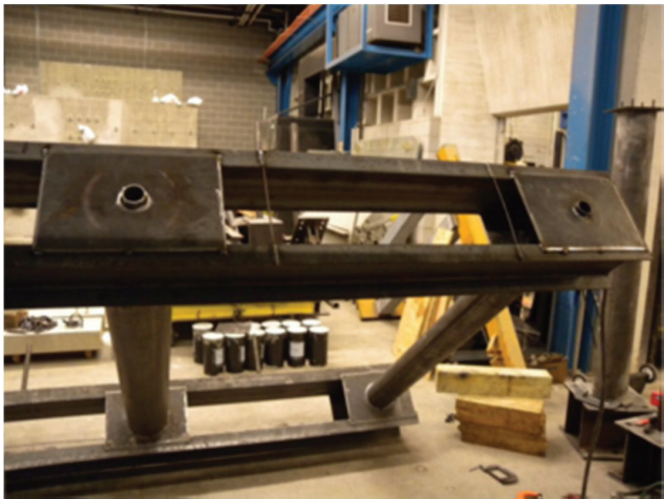

Figure 8-14: Bottom Plates to Foundation Beam Connection

8.2.5 Instrumentation

Because of issues related to survivability of instruments in the fireball, the instrumentation of the specimen for this first round of tests was kept simple. The overall instrumentation consisted of two accelerometers, two Quartz free-field ICP blast pressure pencil probes, 1 thermometer and a high speed camera. Accelerometers and probes were connected to a portable signal conditioner to capture the output from those instruments.

The accelerometers were used for pre-shot forced vibration tests on some of the specimens with the purpose of obtaining a vibratory signal whose modes would be extracted to establish correlations, if any, between frequencies measured for the specimens and estimations obtained from analytical and numerical methods. The accelerometers were positioned at about 250mm (10in) from the bottom face of the cap-beam (Figure 8-15). This would, ideally, be the mirror location, with respect to the center of the specimen, of the position of the center of the explosive

charge defined in the experimental protocol. The idea was to excite the same mode(s) that the explosive charge would excite if the specimen was responding elastically.

Free-field measurements of the blast overpressures were obtained using the pressure probes. It was decided to use the same charge for all the tests but to vary only the standoffs to adjust the explosive yield. The probes were placed at specified ranges from the center of burst of the explosives to help determine, based on pressures recorded at similar standoffs, how consistent the weights of the charges detonated were and, for the sake of analysis, how valid were the models used to predict the loading on the specimen.

The ECLIPSE tests occurred in relatively cold temperatures. To determine afterward if the ambient temperature had any adverse effects on the behavior observed for the specimens or on the yield of the charges, the ambient temperatures were recorded on the first day of the tests for the first 3 tests. The average recorded temperatures during those tests were 48.3^{o}F on the side of the specimen facing the explosive and 49.3^{o}F on the opposite side. The temperatures recorded for the first day of test were deemed to affect neither the behavior of the specimen (no brittle steel failure) nor the yield of the explosive (no misfire nor partial burn nor inconsistency in the overpressures recorded); it was decided to stop taking temperature measurements after the third test on that day.

On the second day of the ECLIPSE tests series, however, the average temperature on the test site dropped to 33^{o}F. Such temperature could adversely affect the ductility of steel (if per code standard its notch toughness falls below 15lb-ft at 40^{o}F) and specifically so for the range of strain rate expected (greater than 0.30 s^{-1} for blast load in the high pressure ranges as per UFC 3-340-02). However, specific information on how low temperatures affect the ductility of ASTM A513

steel pipes specifically is not readily available. Although notch toughness is not related to yield strength (Bruneau, et al., 2011) similarity between the nominal yield strength (32ksi) and the minimum elongation at failure (15%) of ASTM A513 to the yield (36ksi) and minimum elongation at failure (20%) of ASTM A36 could be used to prudently advance that the average temperature during the test would not affect the ductility of the tubes. As reported in the literature, A36 steel generally exceeds the minimum code requirement for notch toughness resistance for the temperature measured during the test. If the similarity evoked does hold true, it is expected that ASTM A513 would also surpass the minimum code requirement.

Figure 8-15: Specimen Instrumented with Accelerometers

8.2.6 Experimental Approach

A total of 12 charges were detonated during a two-day testing period. Of those tests, 8 were done on the pristine specimens and 4 were retests. Nitromethane with 10% Diethylenetriamine (DETA) sensitizer was used to prepare all charges. The use of nitromethane for those tests was based on the observation that, as a solvent in various industrial applications, nitromethane can, despite the best efforts to control circulation of explosive substance, still be accessible to terrorists. One prime example of the use of nitromethane in an explosive compound was in the terrorist attack on the Murrah Building in the Oklahoma City bombing of 1995.

At its purest state nitromethane is an insensitive explosive with a velocity of detonation of 6400 m/s (21000 ft/s). The addition of a sensitizer to this organic compound creates a high explosive more energetic than TNT (TNT equivalent 1.14). In ambient conditions, nitromethane is in liquid state; cylinder shapes were thus used as containers for the explosives of the tests. All 12 cylindrical charges had the same weight and were center detonated at a height of burst (HOB) of 254 mm (10in) with respect to the top of the cover concrete of the footing of any bent being tested.

The columns were tested in sequence, one column at the time. For the first 8 tests, a hammer test preceded the blast test. To record the oscillations of a specimen, it was instrumented with two piezoelectric accelerometers, as shown on Figure 8-15, and put into free vibration by giving an impulse with the hammer on the opposite face. The vibratory signals captured for each test specimen were subsequently filtered and processed to extract their main frequencies which in that case corresponds with the frequencies of the specimen itself. The results of the forced

vibration tests are discussed in Section 9 where correlations between the measured frequencies and simple hand calculations are used in the context of determining an expression to help predict the flexural stiffness of CFDST.

The charge weight was chosen to be consistent with a design threat based on a scenario in which a Vehicle Borne Improvised Explosive Device (VBIED) is detonated near a column of the corresponding full scale bridge. The weight of the charge was then scaled for the need of the test using the Hopkinson-Cranz scaling law (pressure scaling) to obtain similar overpressures to the full scale situations. Each charge was weighed to verify that the proper amount was detonated each time. Since it was deemed that uncertainty may exist with respect to the standoffs achievable with a VBIED in such an attack scenario[2], the standoffs for the scaled explosive were varied to reflect this situation. Varying the standoff resulted in variations in the distribution of the overpressures and the impulses seen by the specimens and, thus, allowed to simulate different loading conditions.

Three principal objectives were defined for the blast tests. The first objective was to create plastic deformations in the specimens to ascertain how they deform globally and locally under blast loading. The second objective was to induce the maximum feasible deformation without compromising stability of the column specimens under axial load. Finally, the third objective

[2] This uncertainty is due to the fact that in such a scenario, although some assumptions can be made with respect to the shape of the explosive, there is, however, no definitive answer as of where the center of the charge itself would ultimately lie. To avoid detection, a terrorist might opt to carry a charge in the trunk of a vehicle instead of trying to conceal the charge in the rear seats. Yet, to maximize explosive yield and inflict more damage, he may elect to fill both locations with explosive. Each of those cases would result in different loadings and may affect the overpressures on the target.

was to bring the specimen to the point of incipient collapse to determine the likely failure mechanism.

The first 4 shots serve the purpose of the first objective of the tests; the columns of Bent 2 in Figure 8-5 were tested for that sequence. The objective of the next 4 shots was to bring the column specimens of Bent 1 closer to the ultimate conditions of deformation. Finally, the last 4 shots were retests on the specimens of Bent 2 to bring them to failure; more specifically, the aim was to induce fracture of the outside shell of the CFDST.

Table 8-2 presents the test matrix and summarizes the objectives for the ECLIPSE test series. In this table the charge weight and the explosive locations are expressed in terms of W and x, respectively the charge weight and the smallest measured scaled distance $\left(X/W^{1/3}\right)$ of the tests. As a reminder the scale distance itself $\left(x = X/W^{1/3}\right)$ is obtained from the charge weight and the standoff (X) which for each test is measured from the face of the corresponding column to the geometric center of the explosive. The values of W and x are not disclosed and kept confidential for security purposes, as commonly done for this type of experiments.

Table 8-2: Test Matrix for the ECLIPSE Test Series

Test	Charge	Scaled Distance $X/W^{1/3}$	Column Tested	Test Objective
1	W	1.71 *x*	**B8**	**Plastic Deformation**
2	W	1.29 *x*	**B2**	
3	W	1.43 *x*	**B4**	
4	W	2.29 *x*	**B6**	
5	W	1.29 *x*	**B7**	**Maximum Feasible Deformation**
6	W	1.29 *x*	**B5**	
7	W	1.29 *x*	**B1**	
8	W	1.00 *x*	**B3**	
9	W	1.00 *x*	**B8**	**Outside Shell Fracture**
10	W	1.29 *x*	**B2**	
11	W	1.07 *x*	**B6**	
12	W	1.07 *x*	**B4**	

8.2.7 Experimental Observations

The main observations of the test are reported in this section. Cross-section deformation (denting/caving) was an important deformation mechanism for CFDSTs subjected to overpressures from near contact explosion; global deformations are thus reported in two different formats. For sections that were not dented, maximum lateral bending deformation and the associated rotations at three locations (top, bottom and point of maximum deformation) are reported. For dented sections, the maximum lateral deformation and cross section deformations

are reported. The maximum lateral deformation in that case includes the dent depth and needs to be corrected for denting so rotation due to bending only can be calculated; this is done later.

8.2.7.1 Test 1: Specimen B8

Specimen B8 was a CFST whose purpose was to provide a point of comparison with previous tests reported on CFST and to CFDST of similar strength. B8 had a measured average outside diameter of 150.6mm (5.93in) and a measured wall thickness of 0.120in (nominal 0.125in); this resulted in compactness in compliance with the limit for highly ductile members (per AISC 341). The scaled distance for this first test on B8 was $1.71\lambda x$ .The charge was suspended such that its center was located at 254mm (10 in) from the ground.

Figure 8-16: Distribution of Deformation along the Height of Specimen B8

The maximum deformation measured for this test occurred at a height of 406.4mm (16in) from the top of the foundation and was about 25.4mm (1in). This corresponds respectively to overall rotations of 0.063 rad at the base of the specimen and 0.024 rad at the top of the specimen, resulting in a 0.087 rad in-span rotation.

A sense for the global distribution of deformations along the height of B8 can be gathered from Figure 8-16 whereas Figure 8-17 shows a crude measurement of the maximum deformation of B8 using a ruler. No damage was recorded to the cap beam, however, a crater formed in the concrete of the foundation beam.

Figure 8-17: Measurement of the Maximum Deformation of Specimen B8

8.2.7.2 Test 2: Specimen B2

Specimen B2 had a void ratio of 38%; the diameter-to-thickness ratios of the inner and outer shells were such that they can respectively exhibit highly ductile and moderately ductile

behaviors as per AISC 341. In comparison to B8, B2 had a lower expected strength. Consequently it was tested at a scaled distance of $2.29x$. It is worth noting that, starting with this test, the cylindrical charge was put in place by seating it on top of a styrofoam pad. This positioning offered more stability and less interaction with the ambient wind compared to the first method.

The maximum measured plastic deformation (Figure 8-18) for this test was 19mm (¾ in) measured at 254mm (10in) from the base of the specimen. The corresponding calculated rotations at the bottom and the top of that specimen were respectively 0.075 rad and 0.016 rad. The in span rotation necessary to achieve those rotations at the top and the bottom is 0.091rad.

A localized dent 12.5mm (½ in) deep and 75mm (3in) wide formed in Specimen B2 at 12 in from the ground on its right side (Figure 8-19). Because of the location of the dent (not in the area where the overpressures on the specimen would be the highest), and because no rupture of the inner tube was found after opening the specimen, it was guessed that this dent was likely caused by a void in the concrete core that may have resulted from insufficient compaction at that location (but this presumption could not be verified). Other than that, at the cross section level, the pre and post-shot measurements at the location of the maximum deformation were not significantly different and for all purpose, it can be considered that no significant deformation at the cross section was observed.

Figure 8-18: Deformation of Specimen B2 After the Test

Figure 8-19: Dent in Specimen B2

8.2.7.3 Test 3: Specimen B4

The inner and outer tubes of B4 were chosen to have highly ductile behavior; the nominal void ratio in B4 was 42%. The scaled distance for this test was $1.43x$. A maximum deformation of 17.5mm (11⁄16 in) for specimen B4 was observed at 254mm (10in) from the ground. A view of the deformations near the base of the column is shown in Figure 8-20.The angles of rotations at the base and the top of specimen B4 were calculated to be 0.069 rad and 0.014 rad. These combined for an in-span rotation of 0.083 rad.

Figure 8-20: Deformation of Specimen B4 after the Test

The cross section of B4 maintained its integrity during the test. This further pointed toward the hypothesis that the dent observed in B2 was due to the existence of some defect in the concrete.

A crater formed after removal of some of the cover concrete of the footing and a crack extending diagonally from the column was visible underneath the cap-beam (Figure 8-21).

Figure 8-21: Crack in the Cap Beam in the Vicinity of B4

8.2.7.4 Test 4: Specimen B6

Designed with tubes expected to have highly ductile behavior (inner tube) and moderately ductile behavior (outer tube) specimen B6 had also the smallest void ratio (25%) of all the specimens tested. B6 had similar predicted strength to B4. The scaled distance for the test on B6 was set at $2.29x$. At the end of the test, the maximum measured deformation of B6 was 12.5mm (½ in) at 254mm (10in) from the ground which corresponded to a base rotation of 0.05 rad and a top rotation of 0.01 rad (see Figure 8-22). The in-span rotation for that case was 0.06rad. The cross section of specimen B6 remained circular; no significant deformation was observed between the pre and post-shot measurements of the cross section.

Figure 8-22: Distribution of Deformation near the Base of B6

8.2.7.5 Test 5: Specimen B7

Specimen B7 had comparable strength to B3, the strongest specimen, but had the biggest void ratio and the thinnest composite wall at 37.5mm (1.5in) of all the specimens. Both inner and outer tubes of B7 were expected to exhibit highly ductile behavior. B7 was tested at a scaled distance of $1.29x$.

After the test, local denting of the cross sections of the specimen was observed over a region extending approximately 460mm (18in) from the base of the specimen (Figure 8-24). This is incidentally about twice the height of burst. The valley of the dent was the maximum at a height of 254mm (10in) from the top of the foundation. The profile of the dent was measured and its main dimensions are reported in Table 8-3.

The total lateral deformation of the specimen (including denting) at the same location corresponded to the maximum observed deformation of the test and was measured to be 116mm ($4.56in$). A crack 97mm (3.8in) long and 12.5mm (0.50in) wide was also observed in the outside tube at 17in from the base of the specimen (Figure 8-23).

After removal of the concrete of the foundation, further observations and measurements on the specimen were done. In particular, another crack was noted at the junction between the specimen and the top plate of the foundation beam. Also, the dented region extended all the way down to that junction. After the outside tubes were split opened and the concrete core removed, no failure of the inner tube was noted.

Table 8-3: Cross Sections Deformations of B7

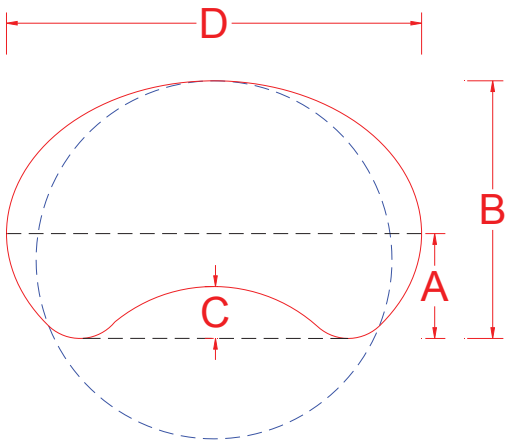

H (in)	A(in)	B (in)	C (in)	D(in)
18	NA	5¼	NA	8¾
14	NA	5	⅞	9
12	NA	5	1	9
10	NA	4¾	⅜	NA
8	NA	4¾	¾	8⅞
6	NA	4 9/16	⅝	8⅞
4	NA	4¾	¼	NA
2	NA	5½	0	NA

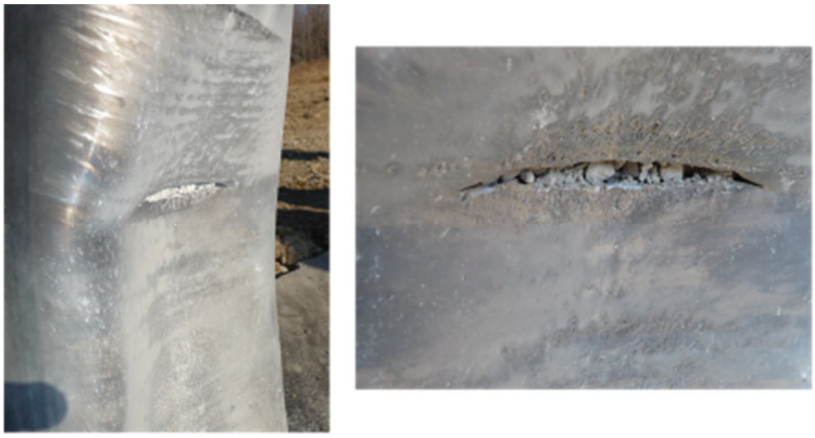

Figure 8-23: Crack in Specimen B7

Figure 8-24: Overview of the Deformations of Specimen B7

Figure 8-25: Crack in the Outside Tube at the Specimen to Foundation Beam Connection

Figure 8-26: Final Deformed Shape of Specimen B7

8.2.7.6 Test 6: Specimen B5

Highly ductile behavior was expected for both tubes that composed specimen B5. The overall void ratio for this specimen was 33%. The thickness of the composite wall for this specimen was 50mm (2 in). The scaled distance of the explosive charge for B5 was $1.29x$; a view of the blast fireball of this test is shown on Figure 8-27. After the test, B5 had a maximum residual deformation of 76mm (3in), at 254mm (10in) from the ground. Some flattening of the face of the specimen exposed to the blast was noted (Figure 8-28), the overall section at that location deformed into an oval shape with small and big axes measures of 132mm (5.2 in) and 165mm (6.5in) respectively. This specimen with part of the foundation beam and part of the cap-beam still connected to it was retrieved after the test; on closer inspection no other deformation or adverse effects besides the ones reported were observed.

Figure 8-27: View of the Blast Fireball of the Test on Specimen B5

Figure 8-28: Diagonal View of the Front of Specimen B5

Table 8-4: Cross Sections Deformations of Specimen B5

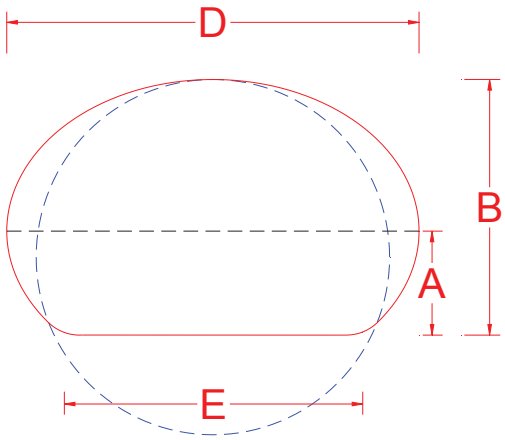

H (in)	A(in)	B (in)	D(in)	E(in)
20	NA	5 7/8	6 1/8	3.9
16	NA	5½	6¼	3.9
12	NA	5¼	6½	3.9
8	NA	5¼	6½	3.9
4	NA	5 7/8	6¼	3.9
2	NA	NA	NA	3.9

8.2.7.7 Test 7: Specimen B1

Similar to B5, B1 had a void ratio of 33% but its inner tube was chosen to have a highly ductile behavior under load while the behavior would be moderately ductile for the outside tube. This specimen was conceived such that the thicknesses of the tubes used to fabricate B5 were swapped while the diameters of the tubes were kept the same. The predicted strengths of the specimen differed by less than 10%. However, this specimen was expected to be more flexible. Because of that similarity in strength, the standoff was kept the same as for B5. At the end of the test a permanent deformation of 111mm (4.4in) was measured at the location of maximum deformation which was in that case located at 305mm (12in) from the base (Figure 8-29). As for specimen B5, the front face of the specimen flattened into an oval shape with measured axis of 124mm (4.9in) and 165mm (6.5in) in the region of maximum deformation (Figure 8-30). It is

worth noting-because of the similarities between the two specimens-that those deformations are fairly similar to the ones recorded for B5.

The front face of the specimen looked wrinkled also in the flattened area and at least 5 visible lobes formed over that face. After removal of the cover concrete of the base, a fracture at the connection of the specimen to the top plate of the foundation beam became apparent. This fracture combined to the partial removal of the cover concrete of the foundation near the base of the specimen may have contributed to the measured deformation.

Figure 8-29: View of the Global Deformation of Specimen B1

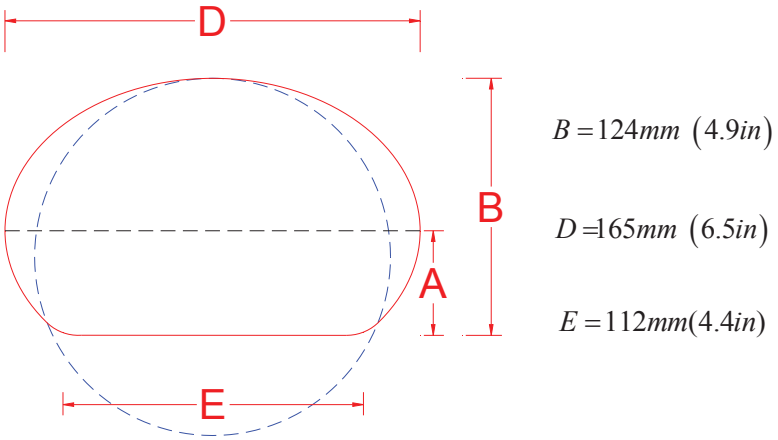

Figure 8-30: Deformation of the Cross Section of Specimen B1

Figure 8-31: Final Deformed Shape of Specimen B1

8.2.7.8 Test 8: Specimen B3

Specimen B3 had the second largest void ratio (50%) after B7 and was also the strongest. The scaled distance for the charge detonated in front of this specimen was $1.00x$; the closest of all the series. The maximum deformation of B3 was 73mm (2.88in) measured at a height of 305mm (12in) from the top of the footing.

Figure 8-32 shows a view of the specimen after it had been removed from the test setup. After the test, a flattened region (Figure 8-33) could be clearly distinguished but it was not as pronounced as in B7. A buckling lobe formed within that region in the front face of B3 at 18 in from the top of the foundation. The minimum and maximum depths of the section in the flattened region were respectively 178mm (7.0in) and 221mm (8.7in). The width of the flattened region was 96.3mm (3.8in) as illustrated on Figure 8-33 and Figure 8-34 .

Figure 8-32: Final Deformed Shape of Specimen B3

Figure 8-33: Flattening of the Front Face of Specimen B3

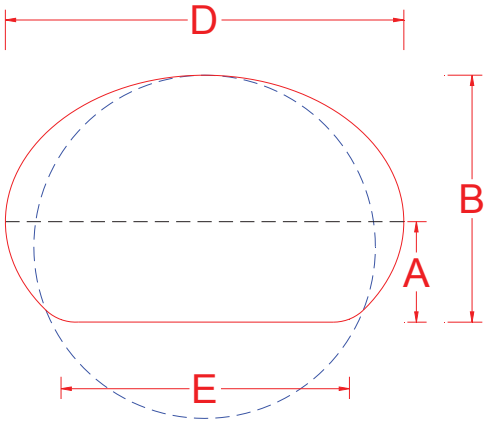

$B = 178mm\ (7.0in)$

$D = 221mm(8.7in)$

$E = 112mm(4.4in)$

Figure 8-34: Deformation of the Cross Section of Specimen B3

8.2.7.9 Test 9: Specimen B8

Specimen B8 was retested at a scaled distance of $1.00x$. A piece about 12in long sheared off the base of the specimen (Figure 8-35) whereas the rest was torn out from the underside plate of the cap-beam at the location it was attached (Figure 8-36 and Figure 8-37). The piece from the base flew away from the initial location of the specimen and was found about 30m (100 ft) away from

the test setup. Its location was also offset from the test setup. The offset angle was estimated to be 30 degrees. Note that, the same failure mode was observed by Fujikura and Bruneau in their previous tests on CFST. The rest of the specimen was found on the ground.

Figure 8-35: Torn Base of Specimen B8

Figure 8-36: Failure of Specimen B8

Figure 8-37: Tear of Specimen B8 from the Cap Beam

8.2.7.10 Test 10: Specimen B2

Specimen B2 was retested at a closer scaled distance ($1.29x$) than the first time. After the second test, the concrete covers of the cap and foundation beam in the vicinity of B2 were removed. The overall deformation of the test including the residual deformation from the

previous test was 133mm (5.25in) and happened at 380mm (15 in) from the top of the foundation beam. Important denting of the section accompanied this deformation. The final deformed shape of specimen B2 is shown on Figure 8-38. The maximum cross section deformations over the dented area is reported in Figure 8-40.

Fracture of the outside tube occurred (Figure 8-39), but as mentioned in the test objective this was expected. It is worth nothing though that the inside tube did not fracture. In this design, the inner tube provided a dowel action that prevented the specimen from being blown away (as happed to the previous specimen) in spite of the fracture of the outside tube.

Figure 8-38: Final Deformed Shape of Specimen B2

Figure 8-39: Fracture at the Base of Specimen B2

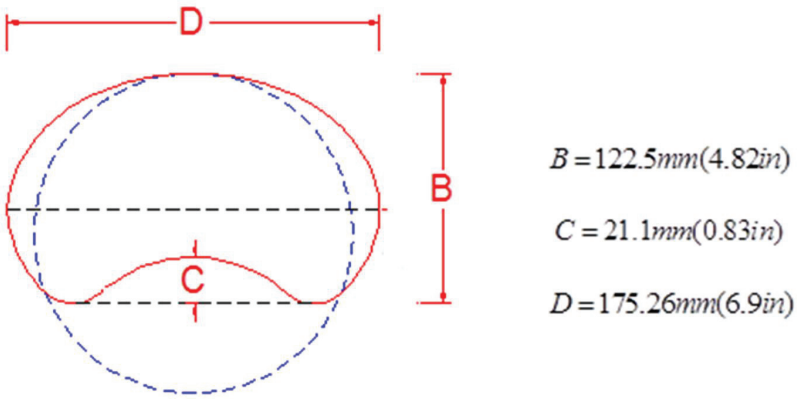

Figure 8-40: Maximum Cross Sections Deformations of Specimen B2

8.2.7.11 Test 11: Specimen B6

The second test on specimen B6 was done at a scaled distance of $1.07x$. An important indentation was observed in B6 after the test. The maximum final deformation of B6 was 175mm (6.88in) at 356mm (14in) from the top of the foundation. This represented an additional 162.5mm (6.38in) of deformation. The final deformed shape of the specimen is shown in Figure 8-41. The cross section was also severely dented as seen on Figure 8-42 and Figure 8-43. As

expected fracture of the outside shell of the specimen occurred, however the inner shell was crushed but not fractured.

Figure 8-41: Final Deformation of Specimen B6

Figure 8-42: Denting and Fracture of Specimen B6

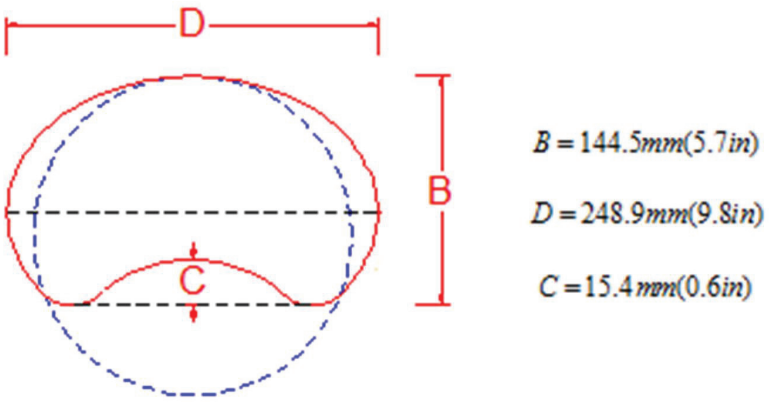

Figure 8-43: Maximum Cross Deformation of Specimen B6

8.2.7.12 Test 12: Specimen B4

The second test on specimen B4 was done at a scaled distance of $1.07x$. The maximum deformation of B4 was measured to be 127mm (5in) at a height of 356mm (14in) over the top of the footing. An indentation was visible in the tube over most of the region extending about 510mm (20in) from the top of the foundation. The indentation was the deepest at the point at which the maximum lateral deformation of the element was measured. The average minor and major axes of the deformed cross section at the location of maximum lateral deformation for B4 measured respectively 130mm (5.12in) and 191mm (7.50in). Fracture of the outside shell of B4 occurred above the weld connecting the specimen to the top of the embedded foundation beam.

Figure 8-44: Final Deformed Shape of Specimen B4

8.3 The ERDC Test Series

For near contact explosion, as defined later, important cross section deformation were observed during the ECLIPSE test series for specimens with large void ratios. The observed local mechanism of deformation was complex. Since, as established before, CFDSTs are also more economical when built with larger voids, an attempt to understand the parameters that possibly controls this behavior was well worth investigating. Because the void needed to be kept large, some of the specimens with the largest voids from the ECLIPSE series were modified such that more compact (thicker) outside tubes were used. While it was recognized that more factors (e.g. compactness of the inner tube, thickness of the concrete core, strengths of the tubes and the concrete) could affect the observed local deformation, the premise for this test was that increasing the compactness of the outside tube would be significant in controlling denting. The

two sections with the largest void ratios from the ECLIPSE series were thus modified to have depth-to-thickness ratios of their outside tubes such that they met the AISC 341 requirements for highly ductile members.

A second objective of the ERDC tests on CFDST was to gather complementary data on specimen with moderate void ratio (which could still offer reasonable cost saving), while also trying to reproduce some of the results obtained on such specimens at ECLIPSE (for validation purposes). Therefore, two specimens similar to B2 and B4 were built and incorporated in this test series.

While investigation of the blast worthiness of CFDSTs as structural solutions for new bridges continued during this test series, it was recognized that some essential bridges in the USA may need upgrading to reduce their vulnerability against multiple hazards. Hence, innovative, yet economical, structural solutions able to provide protection against multiple hazards to existing bridge columns need to be developed. As a third objective of the series, a concept was tested as a solution to extend to blast loading the protection against earthquake already provided by steel jacketing to reinforced concrete bridge column.

Furthermore, for both the ECLIPSE and the ERDC test series, the standoffs were small and almost all the tests in those series could be considered to fall in the "near-contact" category (defined here as equivalent to scaled distance less than $0.5\frac{ft}{lb^{1/3}}$). For these ranges, the processes of formation of the blast wave is complex and the uncertainty on the loading seen by the specimens is high, most specifically because it is difficult to get instruments to survive long enough in the blast fireball to yield accurate measurements. Whereas empirical and

phenomenological models are not considered robust enough to predict peak loading in that range with sufficient accuracy, more robust first principle models, thought to provide good correlations with expected loading, have been routinely used to predict blast loading. Very few measures exist, however, to corroborate such correlations. Based on this observation, as a final objective of the test series, the instrumentation scheme for the tests was conceived to collect data that could, at least indirectly, help getting a better sense of the loading seen by the specimens tested in the fireball.

Note that the construction sequence for the CFDST was the same as for the ECLIPSE series. For the ERDC series the construction sequence for the MSJC is described in Section 8.3.1.

8.3.1 Specimens, Materials and Section Properties

The CFDST specimens tested as part of the ERDC test series are presented in Table 8-5. ASTM A53 Grade B pipes with a minimum yield of 245MPa (35ksi) and a minimum elongation at failure of 35% were substituted to the A513 steel tubes used in the ECLIPSE series in their construction (see Figure 8-45 and Figure 8-46 for stress-strain curves). Self-consolidating concrete with strength of 35 MPa (5ksi) was cast in place to form the core. Concrete with a minimum expected strength of 28MPa (4ksi) was used to cast the cap-beam.

The specifications for the materials of the steel jacketed columns (SJC) were similar to what is reported by Bruneau and Fujikura. The steel plate used for the jacket was a cold-rolled commercial steel sheet complying with ASTM 1008 CS. Typically this steel has yield strength between 140 and 280 MPa (20 and 40 ksi) and an elongation at failure of 30% minimum in 50mm (2in). For the quarter scale model of this experimental series, the thickness of the steel

jacket was specified to be 1.2mm (Gage 18 plate with a thickness of 0.048in). The corresponding stress-strain curve for this specimen is given in Figure 8-47.

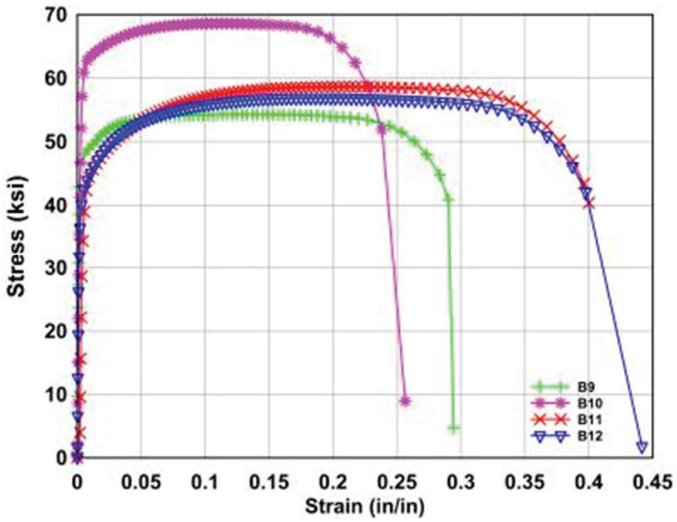

Figure 8-45: Stress Strain Curves for the Steel of the Inner Tubes of the Specimens

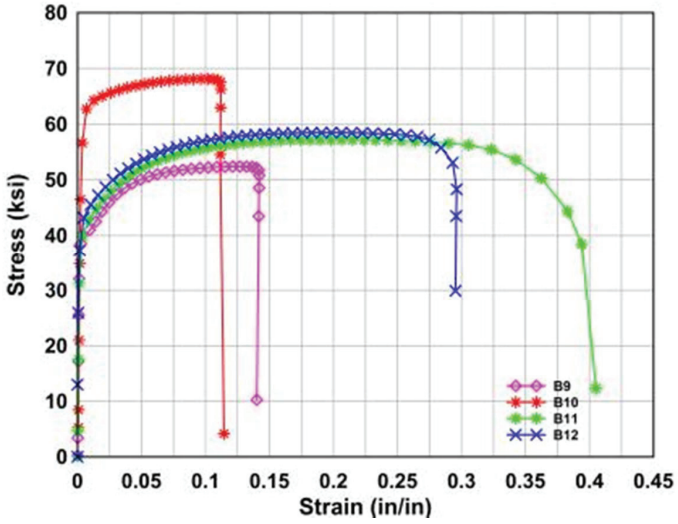

Figure 8-46: Stress Strain Curves for the Steel of the Outer Tubes of the Specimens

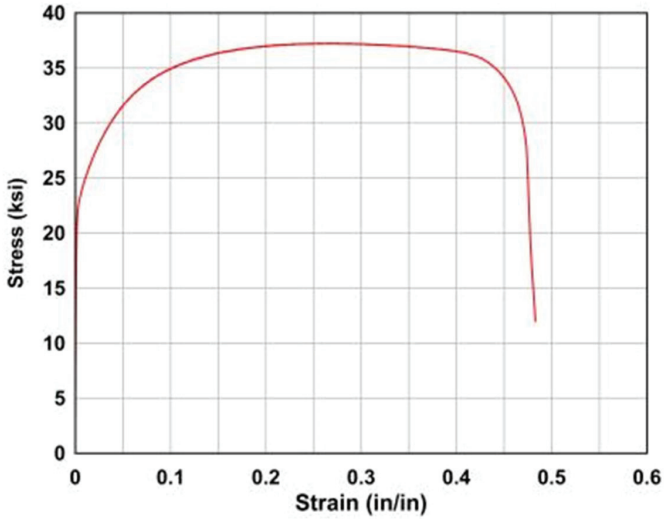

Figure 8-47: Stress Strain Curves for the Steel Jacketed Columns

The MSJC specimens tested during the ERDC series are presented in Table 8-6. D3 and D1 deformed steel wires were used for the construction of the jacketed columns. D3 wires served as

flexural reinforcement and D1 wires as spiral (shear) reinforcement. The average diameter of a D3 wire is 4.95mm (0.195in) and its average area 19.35mm2 (0.03in2); for the D1 wire those properties are 2.87mm (0.113in) and 6.45 (0.01 in2), respectively. Mechanical properties of deformed wires are different from rebar'; they were thus annealed to confer them similar properties to rebar. During the annealing process, the wires were placed in a vacuum furnace and heated to 1135^{o}F for 12 hours overnight for two nights consecutively. The resulting average stress-strain curve obtained for the wires after this process is presented in Figure 8-48.

.

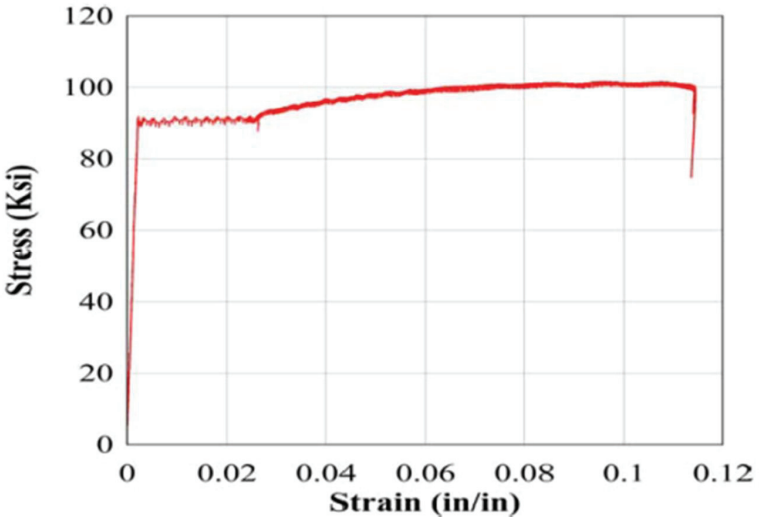

Figure 8-48: Stress Strain Curve for D-3

The structural steel collars placed around the gaps at the top and bottom of the jacketed columns to help increase the shear strength locally were made by welding an A53 steel tube of 216 mm (8.5 in) diameter and 8mm (5/16 in) thick to a 9.5mm A36 steel plate. This assembly was then tied to the adjacent elements (cap beam and footing) with concrete anchors. The concrete

anchors had similar properties to the one used for the seismic tests. They were 19.05mm (3/4 in) in diameter. A non-stick interface between the collar and the column was created using Rulon tape to allow only smooth contact between the collar and the jacketed column thus increasing only shear strength while leaving flexural strength of the column virtually unchanged as normally intended in steel jacketing. The details of the construction of the collar can be seen on Figure 8-49.

Table 8-5: ERDC CFDST Tests Specimens

	Specimen	Column Designation	H (mm)	D_i (mm)	D_o (mm)	t_i (mm)	t_o (mm)	Void Ratio	Ductility	
									Inside Tube	Outside Tube
Bent 1	21_50_42	B9	1500	63.5	151.5	3.0480	3.0480	0.42	HD	HD
	21_51_38	B10	1500	63.5	165.3	3.0226	3.2512	0.38	HD	HD
	30_41_50	B11	1500	101.0	201.5	3.3528	4.9022	0.50	HD	HD
	40_42_62	B12	1500	124.6	201.4	3.1496	4.8006	0.62	HD	HD

Table 8-6: ERDC MSJC Tests Specimens

	Specimen	Column Designation	H (mm)	D (mm)	t (mm)	Height of Collar (mm)	
						Top	Bottom
Bent 2	1	MSJC1	1500	63.5	3.0480	-	50
	2	MSJC2	1500	63.5	3.2512	100	100
	3	MSJC3	1500	101.0	4.9022	50	50
	4	MSJC4	1500	124.6	4.8006	50	50

Figure 8-49: Steel Collar: Components (Left and Middle) and Construction (Right)

8.3.2 Design of the Experimental Setups

The experimental setup used for the ERDC test series was similar to the one used for the ECLIPSE tests. The design approach of the CFDSFs was identical to that used for the ECLIPSE test series, so this section focuses mainly on the design of the proposed MSJC retrofit concept. For the MSJC, the cap and the foundation beams were the same as those reported in Fujikura and

Bruneau (2007, 2008), except that for the cap and foundation beams, #2 rebars were used instead of D2 and D1 deformed wires as the primary reinforcement.

8.3.2.1 Design of the MSJC Base Retrofit

For design of the base retrofit of the MSJC, it was assumed that the collar and the steel jacketed column were fully decoupled. In that case, the SJC would resist moment at the base of the specimen and the collar would supply the shear strength needed to prevent direct shear failure. The thickness of the collar was thus calculated assuming that the shear associated with the flexural capacity of the SJC was to be resisted by the effective area in shear of the collar, such that:

$$f_{vc} = \frac{2V_{pr}}{A_{c\_eff}} \tag{8-6}$$

where:

f_{vc} is the shear strength of the collar, taken as $0.6F_{yc}$ (F_{yc} being the yield strength of the collar)

V_{pr} is the strength reached when the SJC develops its flexural capacity, calculated using the bending moment diagram shown in Figure 8-50:

$$V_{pr} = \frac{M_{pc} + M_{pnc}}{h_b} \tag{8-7}$$

where M_{pc} is the moment strength of the SJC calculated based on the assumption that the reinforced concrete column and the steel jacket behave compositely, M_{pnc} is the strength of the reinforced concrete column (flexural resistance of the system at the gap that exists at the base or

at the top of a SJC), and h_b is the height of the center of the charge with respect to the base of the SJC (Figure 8-50).

Furthermore, A_{c_eff} is the area of the collar effective in shear, which depends on the diameter of the collar (d_c) and its thickness (t_c), and calculated as:

$$A_{c\_eff} = 2d_c t_c \tag{8-8}$$

Substituting Equations (8-7) and (8-8) into (8-6) and solving for t_c leads to:

$$t_c = \frac{2\left(M_{pc} + M_{pnc}\right)}{2d_c h_b f_{vc}} = \frac{3\left(M_{pc} + M_{pnc}\right)}{5d_c h_b F_{yc}} \tag{8-9}$$

The inner diameter of the collar (d_{ci}) can be used instead of d_c in Equation (8-9) to obtain an estimate of its required thickness. The inner diameter of the collar is determined by allowing a gap of 1/8in between the SJC and the collar (Figure 8-51):

$$d_{ci} = D + 2 \times \frac{1}{8} in \tag{8-10}$$

where D is the diameter of the steel jacketed column.

Once an estimate of the thickness was obtained, it was revised accordingly to take into account the true diameter of the collar.

Since two pieces of tubes were welded together to form the collar, it was expected that under load, the seam at the weld would be put in tension by hoop stresses. To prevent the weld from splitting, it was designed conservatively assuming that the magnitude of the hoop stress (σ_θ) in the collar was:

$$\sigma_\theta = \frac{V_{pr}}{t_c h_c} \tag{8-11}$$

In another words, the required resistance per unit length of the weld (i.e., dividing the total required strength of the weld by the weld length, L_w) was defined as:

$$\frac{R_n}{L_w} = \sigma_\theta t_c = \frac{V_{pr}}{h_c} \tag{8-12}$$

Given that the length of the weld must be equal to the height of the collar (for practical reasons), the required unfactored resistance of the weld was therefore:

$$R_n = V_{pr} \tag{8-13}$$

The height of the collar was determined considering two scenarios. One in which partial contact develops at the top of the collar between the collar and the SJC, and another where full contact between the SJC and the collar was assumed. For the deformations of the SJC and the collar to be compatible for both cases, a hinge may need to form at the base of the collar. With that assumption, the height of the collar in the first scenario, for a point load applied at the top of the collar, becomes:

$$h_c = \frac{M_{cr}}{V_{pr}} \tag{8-14}$$

where M_{cr} is the reduced moment capacity of the collar calculated using a reduced thickness(t_{rc}) that considers the fact that part of the section is used to resist the shear V_u:

$$M_{cr} = \frac{d_c^3 - \left(d_c - 2t_{rc}\right)^3}{6} F_{yc} \tag{8-15}$$

with:

$$t_{rc} = t_c \left[1 - \left(\frac{2V_{pr}}{V_{cp}} - 1 \right)^2 \right] \tag{8-16}$$

where V_{cp} is the theoretical plastic shear capacity of the tube calculated considering that the full cross section of the collar is effective in shear.

In the second scenario, when full contact exists between the collar and the SJC, it is assumed that the shear transferred by the SJC as a uniformly distributed load over the height of the collar, and consequently the height of the collar is equal to twice the value predicted by Equation (8-14) and given by:

$$h_c = \frac{2M_{cr}}{V_{pr}} \tag{8-17}$$

Collar heights resulting from both scenarios were considered for the tests. However, after the tests, as will be presented in later sections, it was observed that full contact between the SJC and the collar was never achieved. Consequently, it is suggested that for sizing of the collar, Equation (8-14) alone be used to estimate the height.

Once the dimensions of the collar were determined, the next step in the design was to size the threaded bolts used as concrete anchors at the base of the specimen. The preliminary design of these anchors was done using Appendix D of ACI318-11. It was assumed for design that the shear resisted by the collar was transmitted to and equally shared by the bolts. Once a tentative bolt diameter was found, the effects of tension-shear interaction were checked per Appendix D (see Section 6) with the tension acting on the bolt set equal to the pretension needed to tighten it in place.

Sizing of the base plate of the collar was accomplished using the assumed plastic mechanism shown in Figure 8-52. That mechanism considered that the lip of the plate developed a yield line tangent to the bolt (*B*) of the array that is the most exposed to the blast wave. It was also assumed that this would happen when the resultant of the force acting on the lip of the base plate is equal to the pretension (T_b) in the bolt (Figure 8-52). Note that while yielding of the plate was allowed, failure of the anchors bolts was not.

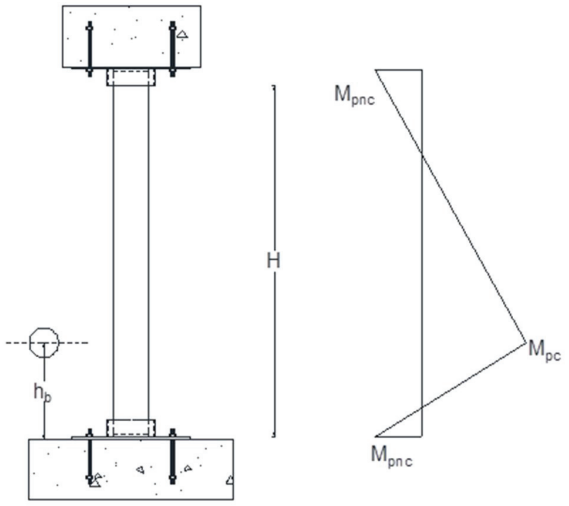

Figure 8-50: Plastic Moment Distribution for MSCJ

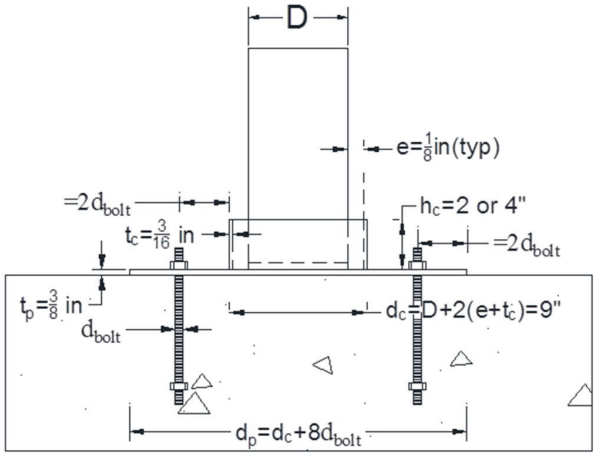

Figure 8-51: Key for the Design of the Base of MSJC (Not To Scale)

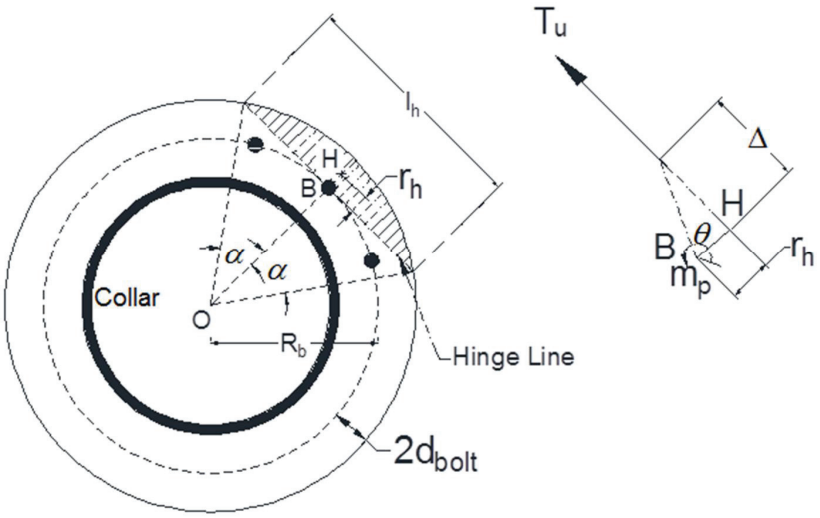

Figure 8-52: Key for the Design of the Base of MSJC

The resultant of the applied force on the base plate was assumed to act at the center of gravity (*H*) of the shaded area in Figure 8-50. Using simple plastic theory, the work done by the external

forces on the lip of the base plate can be equated to the internal work done by the unit plastic moment capacity (m_p) of the base plate on the yield line of length l_h . Using the notation shown in the figure, this is expressed as:

$$T_u \Delta = m_p l_h \theta \tag{8-18}$$

From the geometry of the plastic mechanism shown in Figure 8-52, a relation between Δ and θ is obtained:

$$\Delta = \theta r_h \tag{8-19}$$

The unit plastic moment for the plate is:

$$m_p = \frac{t_p^2}{4} F_{yp} \tag{8-20}$$

By substituting Equations (8-19) and (8-20) into (8-18), the thickness of the plate can be shown to be:

$$t_p = \sqrt{\frac{4 T_b r_h}{\phi F_{yp} l_h}} \tag{8-21}$$

(where a reduction factor $\phi = 0.9$ was added to multiply the yield strength of the plate for design purposes). Also based on the geometry of the mechanism:

$$r_h = \frac{4R \sin^3(\alpha)}{3(2\alpha - \sin 2\alpha)} - R\cos\alpha \tag{8-22}$$

$$l_h = 2R \sin\alpha \tag{8-23}$$

$$\alpha = \cos^{-1}\left(\frac{R_b}{R}\right) \tag{8-24}$$

The top of a SJC may also fail in direct shear under blast load. It was therefore decided to also test some MJSC specimens having a collar at their top. Design of the top collar was done similarly to the design of the bottom one, with the only difference that a square top plate was used and that the estimated demand at the top of the specimens was smaller than at their base. Consequently, the bolts at the top of the specimen were smaller. The demand for which the bolts at the top were designed, for a MSJC of height H, were determined by considering the bending moment diagram in Figure 8-50, such that:

$$V_{prt} = \frac{M_{pc} + M_{pnc}}{H - h_b} \tag{8-25}$$

The rest of the design procedure is otherwise similar to that followed for the bottom collar.

The final design of the retrofit called for a collar having a 9*in* outside diameter and a wall thickness 3/16*in*. A 3/8" base plate was found to be adequate, together with 9-$\phi\frac{3}{4}in$ threaded bolts embedded 6*in* into the foundation. Similar dimensions were used for the top collar, except that 9-$\phi\frac{1}{4}in$ were used (with a similar embedment in the cap beam).

8.3.3 Instrumentation

The instrumentation scheme for the ERDC test series was designed to collect more information than in the previous test series. To obtain information on the peak velocity of the specimen during its response and estimate the impulse seen, a series of shorting pins were used; their description and the data collected are presented in Section 9. The shorting pins were mounted on a plexiglas box and positioned such that the centerline of the box assembly was aligned with the

center of the explosive (10*in* from the top of the foundation). When the shorting pins were shorted during the test, the time at which contact between the pins and the specimen occurred for each individual pin was recorded using a data acquisition system.

Overpressures were measured for all tests using a pencil pressure probe (Figure 8-53) placed at a fixed standoff of $94X$. Attempts were also made to collect acceleration histories at the back of the specimens at two different elevations using shock accelerometers of respective capacities 200,000 *g*'s and 60,000 *g*'s. However this attempt did not yield satisfactory results; the capacities of the accelerometers were exceeded during the tests. Strain gages were installed on the inside surface of the outside tube of the larger sections to collect strain histories in the regions of the specimens that were to remain elastic. Those gages, installed during the construction of the specimen were not responsive when received at the test site, and consequently no data could be collected from them.

Figure 8-53: Pressure Probe and Supporting Mount

8.3.4 Experimental Observations on the CFDST

Five tests were carried on the CFDST bent. As before, the standoffs were varied to simulate different loading conditions and cover a spectrum of credible treats; the charge weight remained unchanged during the tests. It was expected that, the response of the CFDST specimens would be a combination of denting at the cross section level and bending at the global level. To provide a better sense of the deformation of the centerline of the specimen, a line parallel to the axis of the specimen was drawn on the left and right sides of the specimen. Measurements on the specimens were taken both on its front side and its right side (using the drawn line).

8.3.4.1 Test 13: Specimen B9

The purpose of the test on B9 was to provide additional data on the behavior under blast of CFDST falling near the median for the range of void ratios tested. The same charge weight and the same scaled distance as in test 10 on specimen B2 were maintained. Conversely to specimen B2, only one test was performed on B9. B9 was instrumented with 3 shorting pins on the back (Figure 8-54 and Figure 8-55). The maximum measured deformation on the front side of the specimen was 4.50in and occurred at a height of 12in from the top of the foundation. Although more accurate measurements were made using a digital Vernier caliper, Figure 8-56 shows a picture of had hoc measurement made on the specimen using two measuring tapes. The maximum deformation of the specimen measured from the right side at the same height was 3.96in. A buckle lobe formed toward the top of the dented regions at a height of 14in from the

top of the foundation. The height of the lobe was about 1/8in. Visible striations were noted above and below this lobe.

As previously observed, a region extending approximately 18 in from the top of the foundation was dented (Figure 8-56), the depth of the indentation reached its peak at the point where the maximum lateral deformation of the specimen was measured. Table 8-7 presents the on-site measurements of the cross section deformations. The initially circular cross-section (bisymmetric) deformed in that region into an axisymmetric section. Outside that region the specimen deformed in bending but did not change shape.

Besides the crater that formed in the foundation, several longitudinal cracks appeared at the underside of the cap-beam. This behavior of the cap-beam was not observed during the ECLIPSE test and was likely due to the fact that ordinary concrete was used in the cap-beams in the ERDC test series (recall that fiber reinforced concrete was used to construct the cap-beam in the ECLIPSE tests).

Figure 8-54: Base of Specimen B9 Showing Shorting Pin Mount

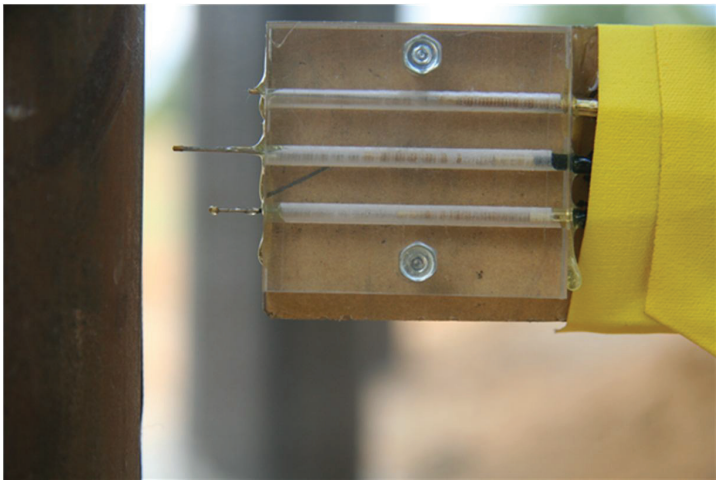

Figure 8-55: Shorting Pins Assembly Specimen B9

Table 8-7: Cross Sections Deformations in Specimen B9

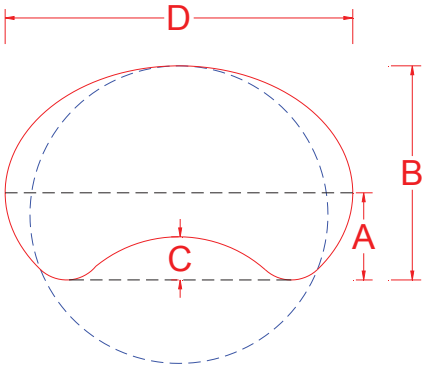

H (in)	A(in)	B (in)	C (in)	D(in)
20	NA	NA	0	6¼
18	2½	5¼	0	6½
16	2⅜	5	1/16	6 5/8
14	2⅛	4¾	⅛	6 13/16
12	2	4¾	7/16	6 13/16
10	2⅛	4 9/16	½	6 7/8
8	2	4¾	⅜	6 7/8
6	2	5	¼	6¾
4	2¼	5¼	1/16	6¾
2	NA	NA	0	6¾

Figure 8-56: Observed Deformation of Specimen B9

8.3.4.2 Test 14: Specimen B10

Both tubes of specimen B10 were designated as highly ductile and the specimen had a void ratio of 42%. The scaled distance for this test was$1.29x$. Figure 8-57 shows the location and the

arrangement of the shorting pins used with specimen B10. The same trend in response was observed with a combination of denting and bending of the specimen. The dented region was similar to that observed for the previous specimen. The indentation on that specimen was less pronounced than in B9 and B2 although the void was slightly bigger (42% versus 38%). Recall that both tubes of B10 were highly ductile, whereas only the inner tube of B2 was highly ductile.

Figure 8-57: Shorting Pins Arrangement on Specimen B10

The maximum measured deformation of specimen B10 was 3in at a height of 10in from the top of the foundation. As observed throughout the test series the resulting cross sections in the dented region after deformation are fairly axisymmetric. A lobe formed between a height of 14 and 15*in* above the foundation top. This lobe did not appear to be due to buckling of the outside tube of the specimen but to a denivelation in the dented region.

Cracks extending the full length of the cap beam were visible on its underside (Figure 8-58). The pattern observed was more likely due to debonding of the concrete from the embedded steel channel than from bending deformation.

Figure 8-58: Longitudinal Crack Underneath the Cap Beam

Table 8-8: Cross Sections Deformations of Specimen B10

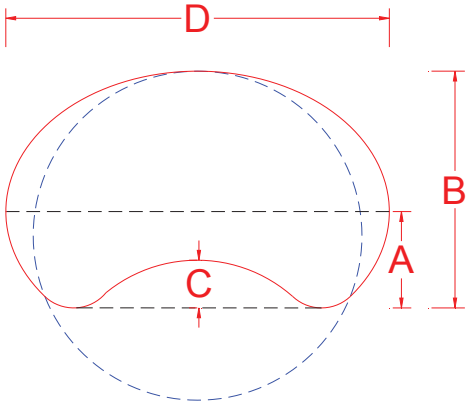

H (in)	B (in)	C (in)	D(in)
18	6	0	6½
16	5 3/4	0	6½
14	5 4/8	1/8	6 5/8
12	5 3/8	5/16	7 3/8
10	5 3/8	5/16	7 3/8
8	5½	¼	7 3/8
6	5½	1/8	7¼
4	5¾	0	7¼
2	6	0	7¼

8.3.4.3 Test 15: Specimen B11

Specimen B11 had a void ratio of 50%. The same nominal tubes diameters as B6 were used; the thickness of the outer tube was increased, however, to seek to improve ductility of the specimen overall. B6 was tested respectively at scaled distances of $2.29x$ and $1.07x$, it was decided to test B11 at a scaled distance which was the average of those two values ($1.71x$).

After the test, moderate flattening of the front face of the specimen was observed. The maximum measured lateral deformation from this first test was 1.48in at a height of 10in. The shape of the cross section after deformation is illustrated in Figure 8-59.

.

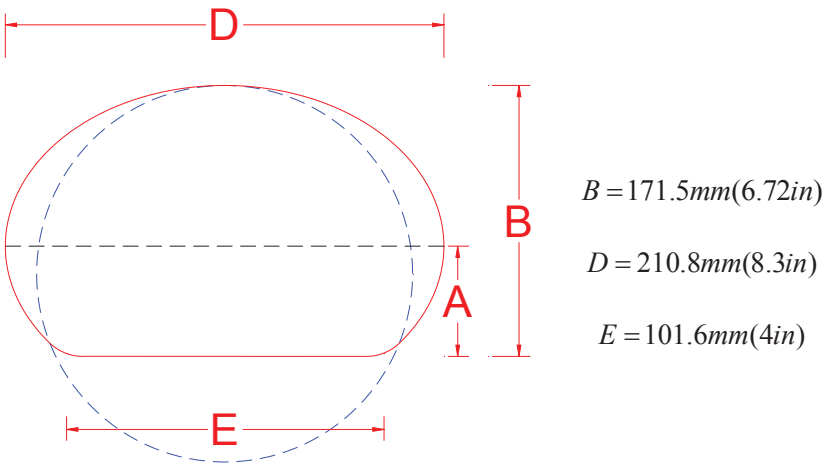

Figure 8-59: Deformation of the Cross Section of Specimen B11

8.3.4.4 Test 16: Specimen B11

This is a retest of B11; the same charge was used but placed closer (scaled distance of $1.43x$) to the already deformed target than in the previous test on the undeformed specimen No shorting pins were used in that test, only overpressures were recorded. Because the cover concrete of the underside of the cap-beam was entirely removed in the previous test, specimen B11 became 2in longer. The cumulative deformation after the second test reached a maximum of 4.70in at 10in over the top of the foundation. Denting and bending of the specimen was once again observed. The profile of the deformed cross-section is reported on Table 8-9.

Table 8-9: Cross Sections Deformations of Specimen B11 after the Second Test

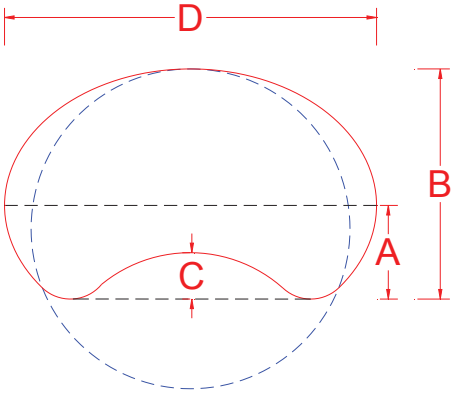

H (in)	B (in)	C (in)	D(in)
18	5¼	0	6¾
16	5	0	6½
14	5	⅛	6½
12	4¾	5/16	6 5/8
10	4¾	5/16	7 3/8
8	4 9/16	¼	7 3/8
6	4¾	⅛	7 3/8
4	5½	0	7¼

8.3.4.5 Test 17: Specimen B12

B12 was a modified version of B7 whose outside tube was made thicker to obtain a more compact tube, and eventually a section more resilient to caving. The scaled distance from specimen B12 to the charge was fixed at $1.29x$. B12 deformed a full 5.0in including denting at the cross section level. Denting of the specimen was rather important; the reduction in diameter was as much as 38%. Relevant measures of the deformations of the specimen are shown on Table 8-10.After this test, only the concrete core between the steel channels and the concrete connected to the reaction frame remained in the cap-beam. The concrete directly exposed to the blast overpressures was completely debonded from the embedded channels.

Table 8-10: Cross Sections Deformations of B12 after Test

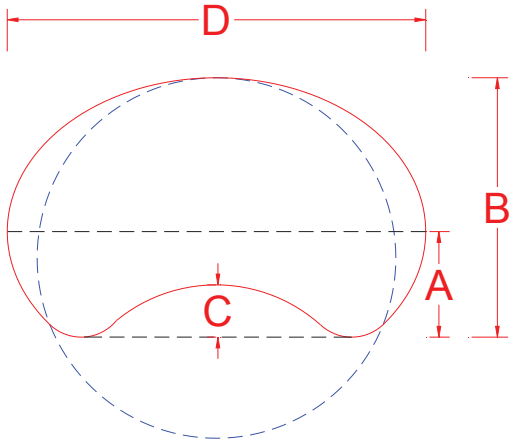

H (in)	C (in)
18	1/8
16	1/2
14	3/4
12	1
10	1
8	1
6	7/8
4	3/4
0	1/8

8.3.5 Experimental Observations on the MSJC

This test series was designed to provide direct comparison to the experiments conducted by Bruneau and Fujikura on SJC (2011), by using virtually identical specimens, except for the fact that the specimens in the present test series were retrofitted by the addition of 2in or 4in wide cylindrical collar at the base of the specimen and/or at their top, to increase their direct shear strength. This retrofit strategy was intended to prevent the direct shear failures observed by Bruneau and Fujikura during their blast test on SJC.

Accelerometers were placed respectively at 10in from the top of the foundation beam and 20in from the underside of the cap-beam. However, the acceleration recorded by the specimen were well over the capacities of the accelerometers used, as the recorded data was consistently

clipped; for that reason, use of those instruments was stopped after the first specimens, as no useful data could be collected.

Free field measurements were taken using a pencil pressure probe; a post-test shot showing the pressure probe which has been rotated by the blast wind pressure is shown on Figure 8-60. Following this observation, sandbags were placed on the base of the probe to keep it in place during the blast tests.

Figure 8-60: Pressure Probe After Test 1 on Specimen MSJC1

8.3.5.1 Test 1: Specimen MSJC1

The charge weight and the scaled distance ($3x$) were negligibly smaller than on specimen SJC1 reported by Bruneau and Fujikura (2011). After the test, the specimen deformed to a maximum of 1/8 in at a height of 12in. No direct shear failure was observed at the base of the specimen as reported in the previous study. This seems to point to the effectiveness of the collar in enhancing direct shear resistance. Some deformation was observed in the collar but it didn't affect the capacity of MSCJ1 to resist the blast load. In fact, the same specimen was retested twice to push it to its limit of resistance. Upon close inspection of the specimen after those tests, horizontal crack was found at the top of the column, suggesting initiation of a direct shear failure at that location (Figure 8-62). This is consistent with observation made during the Fujikura and Bruneau test and with the results presented in Section 5.

Specimen MSJC1 was instrumented with 2 shock accelerometers on its backside (Figure 8-61). Based on the data collected, the shock accelerometers located near the foundation experienced accelerations exceeding its range; it also got dislodged from its mount. The accelerometer installed higher up the specimen also saturated. Given that both accelerometers reached their maximum output capacity and data was clipped at that point, it can be inferred that the acceleration of the specimen exceeded $200000g$ at the height of burst (HOB) and $60000g$ near its top end (those values were the peak acceleration capacities of the accelerometers at those locations).

A shorting pin assembly consisting of 5 pins was also added on the back-side of the specimen. Of the 5 shorting pins, only 2 shorted because the deformation of MSJC1 was not enough to cause its back side to touch all the pins. Since the pins were spaced at 1/8in increment with the

longest one nearly touching the back of MSJC1, this means that the specimen deformed more than the measured residual deformation and that elastic rebound occurred.

Figure 8-61: Shock Accelerometers on Specimen MSJC1

Figure 8-62: Crack at the Top of Specimen MSJC1

Figure 8-63: Deformation of Collar after Test 1 on Specimen MSJC1

Figure 8-64: Deformation of Specimen SJC1

8.3.5.2 Test 2: Specimen MSJC4

Specimen MSJC4 was similar to the previous specimen, except that, because direct shear failure was anticipated at the top of the specimen, to prevent such failure, a collar was also provided at that location (in addition to the one used at the bottom). The scaled distance for the specimen

was reduced to $1.29x$ for that test. The instrumentation was simpler and consisted of the pressure probe and the 200kg shock accelerometer which was mounted at 20in from the underside of the cap-beam, in a second attempt to record acceleration at that location (i.e., using the higher capacity accelerometer at a location of expected lower accelerations).

During the blast, the steel jacket was torn along its seam. As a consequence, the concrete column became exposed, and several rebars and spiral reinforcement fractured near the base of the specimen. The observed "unzipping" of the seam was attributed to failure of its weld. The confinement provided by the steel jacket being lost, and the reinforced concrete column inside the jacket being not ductile, the column lost its capacity to carry load.

Notable deformations and failure at the weld connections of the collar were observed both in the front and in the back of the column. This led to believe that the front rim of the collar saw important overpressures, whereas excessive deformation of the specimen generated important hoop stress in the back rim.

Figure 8-65: Bottom (Left) and Top (Right) Collars of Specimen MSJC4

Figure 8-66: Accelerometer of the Back Side of Specimen MSJC4

Figure 8-67: Global View and Close-up of the Base of MSJC4 After the Test

8.3.5.3 Test 3: Specimen MSJC1

Since MSJC1 survived the first shot with minimal damage, a second test at closer range ($2.57x$) was done on this specimen. An assembly with 5 shorting pins was placed on the backside of MSJC1 for this retest. A pressure probe placed in front of the specimen was used to measure overpressures at some standoff from the specimen. Figure 8-68 shows the placement of the shorting pins and the pressure probe for that test.

Measurements taken after the test showed that the specimen deformed to $0.42in$ from its initial deformation of 1/8 in. This represents about $5/16in$ increase in deformation from the previous test. Besides a few notches and pits observed on the outside steel jacket, no significant

deformation of the cross section of the specimen was noted. The front face of the collar deformed inward (Figure 8-70) likely under the action of the overpressure seen at that location. Fracture of both weld connections of the collar was noted. Since the specimen was bearing in the back on the collar, hoop stress might have developed in the collar leading to that fracture.

The crack in the concrete core that appeared at the top of MSJC1 after the first test widened (Figure 8-73); however, no failure of the rebars was noted. MSJC1 could have still continued to carry load despite those two successive tests. MSJCS1 was therefore tested at third time, as described in a later section.

Figure 8-68: View of Specimen MSJC1 Showing the Shorting Pins Arrangement in the Back and the Pressure Probe in the Front

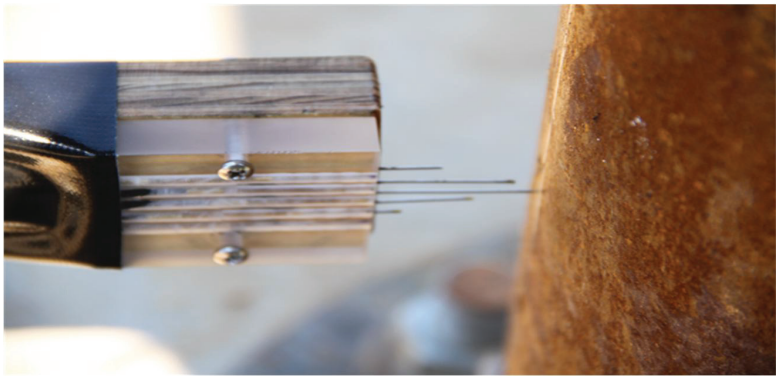

Figure 8-69: Close Up View of the Pin Assembly on Specimen MSJC1

Figure 8-70: Inward Deformation of the Collar in the Front of Specimen MSJC1

Figure 8-71: Crack in the Collar of MSJC1 at Weld Connection

Figure 8-72: Collar Deformations Measured Using the Depth Probe of a Vernier Caliper

Figure 8-73: Widening of the Pre-existing Crack at the Top of Specimen MSJC1

8.3.5.4 Test 4: Specimen MSJC3

The construction of MSJC3 was identical to MSJC4, the only difference being the fact that a Rulon tape was present at the interface between the steel jacket and the collar in MSJC4; this detail was not present in MSJC3. MSJC3 was first tested at a scaled distance of $2.14x$. The shorting pin assembly for this consisted of 5 pins (Figure 8-75). Only 4 of the five pins were deformed after the test (Figure 8-75).

Deformation of the collar at the front and the back of the specimen was noted. A tear at the junction of the two halves of the collar at the base was also observed, possibly due to hoop stress in the collar exceeding the capacity of the weld. The lip of the base plate of this collar deformed upward (maybe due to blast overpressure being entering a small gap existing between that plate and the top of the foundation). The top collar on the other hand did not suffer any visible damage.

MSJC3 did not deform much under load (Figure 8-74). The maximum permanent deformation over the height of the specimen was 0.60in at a height of 18 in (0.03 radians). Measurement of the diameters of the specimen at the HOB showed that some marginal deformation in cross section occurred, but there was no significant ovalization of the section per se.

Figure 8-74: Post-shot View of MSJC3 Showing Lip Deformation

Figure 8-75: Pre and Post-shot View of the Shorting Pin Assembly on the Back of Specimen MSJC3

8.3.5.5 Test 5: Specimen MSJC2

MSJC3 had 4-in collars top and bottom (Figure 8-76) and was tested only once. The length of the longer collar was established assuming that load transmitted from the specimen to the collar would result in the latter failing in flexure while following the rotation at the base of the specimen. The scaled distance ($1.57x$) was fixed such that direct comparison could be made with MSJC1 and MSJC3 which were also tested at that scaled distance and had 2-in collars.

To enhance the resolution with which the velocity history at the back of the specimen was captured, the number of shorting pins in the assembly was increased to 10. The pins were divided between two blocks of 5 pins (Figure 8-77). All the pins were shorted at the end of the test (Figure 8-78).

Post-blast measurements on MSJC2 showed that the specimen deformed up to $2.13in$ at a height of 14in. This corresponds approximately to 0.15rad of rotation at the base of the specimen.

Splitting and opening of the collar in the back of the specimen was observed as a consequence of this important rotation demand (Figure 8-79). Several buckling lobes (Figure 8-80) developed on the front face of the specimen. The jacketed column and the collar came into contact near the top, as evidenced by a mark on the steel jacket matching the location of the collar (Figure 8-81).

Figure 8-76: View of the Collars of Specimen Specimen MSJC2

Figure 8-77: Shorting Pins on the Back of Specimen MSJC2

Figure 8-78: Post-Shot View of the Pin Assembly on Specimen MSJC2

Figure 8-79: Post-shot Failure of the Collar on Specimen MSJC2

Figure 8-80: Post-Shot Views of on Specimen MSJC2

Figure 8-81: Evidence of Contact Between on Specimen MSJC2 and its Collar

8.3.5.6 Test 6: Specimen MSJC1

The damage to the collar of MSJC1 from its previous tests was repaired before this third test. The lip of the tear was reinforced with a ¼ in thick piece of steel and welded (Figure 8-82). The scaled distance between the charge and the target was set at $1.57x$. An assembly of ten shorting pins was placed on the back side of this specimen (Figure 8-83).

After the test, several additional buckling waves developed on the front face of MSJC1 and failure of the seam was visible (Figure 8-85). The repaired collar did not suffer any damage. During its deformation, the steel jacket came into contact with the collar (Figure 8-84). The additional deformation demand on the specimen from this test caused the steel jacket to slip over the internal face of the collar on the side exposed to the blast. The back side of the collar rotated and deformed but did not fail. The lip of the base plate exposed to the blast deformed upward causing some of the threaded rod in front of the blast to rotate (Figure 8-85).

The overall mechanism of deformation at the base of the specimen possibly occurred in the following sequence. First, the front side of the collar came into contact with the steel jacket; as

the specimen deformed, the local contact forces on the front side were not enough to prevent slipping between the collar and the jacket. In the meantime on the back side, the deforming specimen bore against the back side of the collar, pushing it out and causing it to deform. Contact followed by slip on the front side, as evidenced by tearing of the Rulon tape (Figure 8-86), whereas in the backside, after bearing against the collar a clear deformation mark was left on the steel jacket.

The crack visible at the top of the specimen from the first test widened further exposing the reinforcement of the column. On inspection none of the rebars were severed. From about ½ in deformation from the two previous tests, MSJC1 deformed an additional 2.40in. This deformation was measured at a height of 16in; this corresponds to 0.15 radians of additional rotation. The final rotation at the end of the test was 0.18 radians.

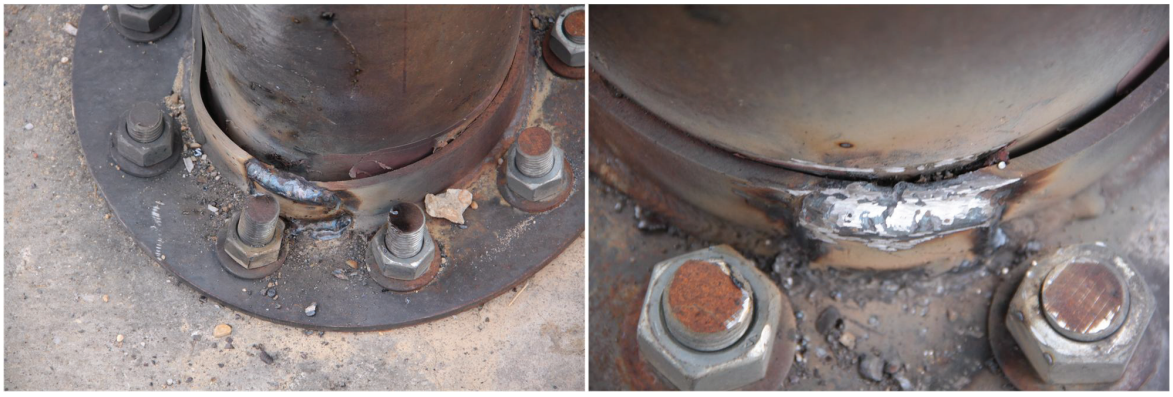

Figure 8-82: Repair to the Collar of on Specimen MSJC1

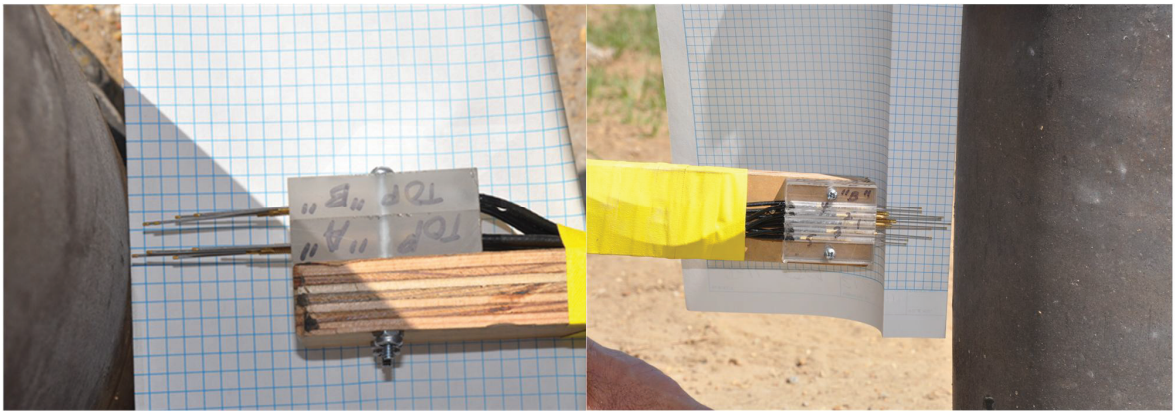

Figure 8-83: Pin Assembly on the Back of Specimen MSJC1

Figure 8-84: Mark on the Steel Jacket Resulting From Bearing on the Collar

Figure 8-85: Seam Failure of Specimen MSJC1and Base Deformation

Figure 8-86: Damage to the Rulon Tape and Slip of Specimen MSJC1 over the Collar

Figure 8-87: Widening of the Crack at the Top of Specimen MSJC1

8.3.5.7 Test 7: Specimen MSJC3

After repairing the collar of MSJC3 (Figure 8-88) to restore its resistance, the specimen was re-tested. Note that some of the front nuts of the base plate were found to be slightly loose after the prior tests; since the lip of the base plate deformed upward, this deformation may have generated some uplift force in the bolts causing the nuts to slightly disengage from their threads. Therefore, the nuts were re-tightened prior to the second test (Figure 8-89). The shorting pin arrangement on the back of MSJC3 consisted of 10 pins mounted on two blocks (Figure 8-90). The scaled distance was maintained at $1.57x$.

The final maximum deformation of MSJC3 was identical to MSJC1 (2.40in at a height of 16in, 0.18radian at the base). The additional deformation from the 1st test and the second in that case was 1.80in. Several buckling waves developed in the front face of MSCJ3 (Figure 8-91). Contrarily to observations on MSJC1, the seam of MSJC3 survived the test. For comparison, note that MSJC3 was tested twice (at scaled distances of $2.14x$ and $1.57x$) and that MSJC1 was tested three times (at scaled distances of $3.00x$, $2.57x$ and $1.57x$).

Plastic deformations (Figure 8-92) in the bottom collar did not cause failure at the weld connection as observed in the first test. Slip between the collar and the steel jacket was observed in mostly the same fashion as in the last test on MSJC1 (upper left picture in Figure 8-92). The top collar remained undamaged and virtually undeformed (Figure 8-93).

Figure 8-88: Repair of the Bottom Collar Fracture of Specimen MSJC3

Figure 8-89: Loose Bolt Being Retightened on Specimen MSJC3

Figure 8-90: Shorting Pin Arrangement for MSJC3

Figure 8-91: Deformation of Specimen MSJC3

Figure 8-92: State of the Bottom Collar after the Test

Figure 8-93: State of the Top Collar after the Test

8.3.6 Internal Deformations

Further processing of the CFDST sections was carried out to observe their response at the cross section level. The specimens from both the ECLIPSE and the ERDC tests were split open to

expose their concrete core and determine the state of the internal tube. On opening, it was generally observed that the face of the concrete core exposed to the blast was severely deformed or crushed and that the concrete flowed significantly in trying to follow the deformation of the cross section (Figure 8-94).

Figure 8-94: Concrete Core of CFDST after Opening

On the upper part of the specimen, horizontal flexural cracks were generally visible, in the region were the concrete was on the tension side of the specimen under bending. The extent of the cracked region from one specimen to the other was fairly identical.

Figure 8-95: Crack Pattern in the Upper Part Specimens B5 (Left), B6 (Middle) and B1 (Right)

In the dented region, the deformation of the cross section varied. Deformation of the cross section was directly linked to the state of the inner tube, the void ratio (hence the thickness of the composite wall) and certainly to the loading seen by the specimen (Figure 8-96). The less compact the inner tube, the more deformable the section was, and the more severe the cross section indentation. At the center of the dented region (section facing directly the charge) the deformation of the cross section was generally severe for large void ratio (50% and more) and inner tube with compactness well over 20. For those sections, the inner tubes generally folded into themselves. For moderate void ratios (38% to 42%), the inner tube was more compact and would deform but not crush. This is evidenced by B2 which was tested twice and for which the inner tube did not completely collapse. For low void ratio (33% or less), the behavior of the inner tube seems to be affected by the compactness of the tube. For instance for specimen B5 which

was tested once, the compactness of the inner tube was 26 and the inner tube collapsed into itself. The impact of void ratio on deformation of the specimen can be inferred from Figure 8-97, which shows the specimens ordered according to their void ratio (increasing, left to right, from low void ratios to high ones). As the void ratio increased, deformations of the cross sections also increased. Incidentally, note that if the specimens were to be classed in order of increasing compactness of their inner tubes, they would have been presented in the same order shown on Figure 8-97 and the same trend in deformation would be observed.

Moving away from the center of the dented region toward the top or the bottom of the column, deformations of the inner tube decrease significantly. The decrease is particularly important for specimen with low void ratio. There is a clear reduction for specimen with large void ratio but it is not as significant.

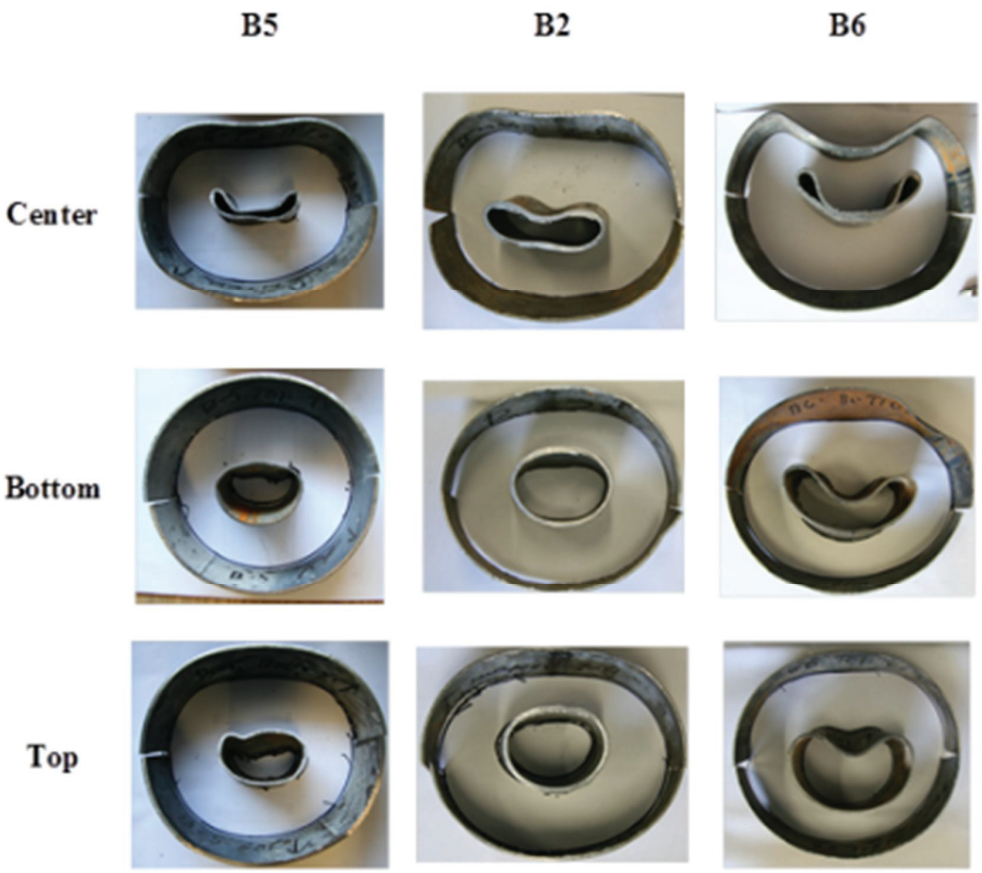

Figure 8-96: Sample of Cross Section Deformation in the Dented Region

Figure 8-97: Overall Deformation of the Specimens from the ECLIPSE Test

SECTION 9

SIMPLIFIED ANALYSIS OF CFDST AND MSJC UNDER BLAST LOADING

9.1 General

The purpose of this section is three-fold. First, in Section 9.2, the data collected during the ECLIPSE and the ERDC tests are analyzed to respectively establish the dynamic characteristics (frequency, damping) of CFDST and determine the peak impulse imparted to the specimens. Then, because of the significance of local indentation in the deformation process of CFDST subjected to blast overpressures, an analytical attempt is made to predict the depth and the extent of that indentation. Finally, simplified methods are developed to predict the global deformation of CFDST loaded by blast overpressures. For CFDST the global deformation includes the contributions of both bending and denting.

9.2 Correlation of Vibration Characteristics of CFDST to Hammer Tests Results

During the Eclipse tests, all, but one, of the specimens were instrumented with 2 accelerometers located toward the top of the specimen at the same distance with respect to the cap-beam that the center of the charge is to the foundation beam. A hammer test was then conducted to determine the acceleration of the specimen for the mode excited. Raw acceleration histories were then obtained filtered and their main frequencies extracted using the power spectrum approach (see sample for B1 shown in Figure 5-2 to Figure 9-3).

Transforming the problem to a single degree of freedom analysis of a uniformly loaded beam, the principal frequency of the mode was calculated under the assumption that the bending stiffness of the specimen is the sum of the respective stiffness of the steel tubes and the concrete core (appropriately reduced by the factor *k* to take cracking of the core in the elastic range into account):

$$EI = EI_{steel} + kEI_{concrete} \tag{9-1}$$

For the mode excited, the equivalent elastic stiffness is based on the UFC-3-340-02 equations for single degree of freedom and given by:

$$K_{eq} = \frac{384EI}{L^4} \tag{9-2}$$

Recalling that the load –mass factor for a single degree of freedom responding in the elastic range is $K_{LM} = 0.77$, the frequency of a beam of unit mass, *m*, treated as a single degree of freedom is given by:

$$F = \frac{1}{2\pi}\sqrt{\frac{K_{eq}}{K_{LM}m}} \tag{9-3}$$

Table 5-4Table 9-1 summarizes the calculation for the specimens. Of the results for the specimens, 6 are in good agreement with the experimentally obtained frequencies and one, B4, seems to underestimate the experimentally obtained frequency by more than 50%. The experimental value should however be taken with caution as it does not seem to follow the trend

observed for the other measurements. On average however, the frequency was overestimated by only 1% for $k = 0.85$.

Looking at Equation (9-3), two main sources of uncertainties would be the mass of the specimen, which can be fairly well evaluated, and the equivalent stiffness of the specimen which depends itself on the bending stiffness. Despite the limited data set used, Equation (9-1) can be seen as a good estimate of the bending stiffness of CFDST.

Table 9-1: Experimental versus Calculated Frequencies for CFDST

Specimen	EI (kip-in^2)	K_{eq} (lb/in/in)	m (lb-sec2/in2)	F (Hz)	$F_{\exp}$ (Hz)	$\frac{F}{F_{\exp}}$
B1	374896.74	11108.05	0.00698	228.76	187	1.22
B3	1225049.88	36297.77	0.0126	307.58	278	1.11
B7	1012815.91	30009.36	0.00939	324.30	304	1.07
B5	459793.69	13623.52	0.00721	249.36	217	1.15
B2	358846.56	10632.49	0.00676	227.44	219	1.04
B6	976303.98	28927.53	0.01067	298.66	289	1.03
B4	659457.14	19539.47	0.00872	271.49	603	0.45
					Average	1.01

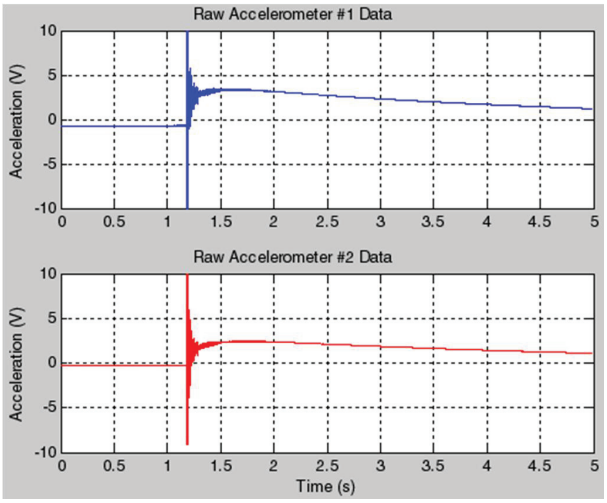

Figure 9-1: Raw Acceleration History for Specimen B1

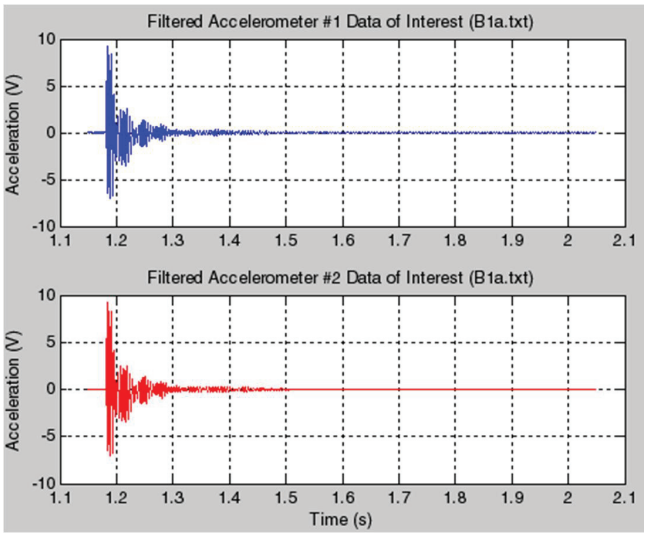

Figure 9-2: Filtered Acceleration History for Specimen B1

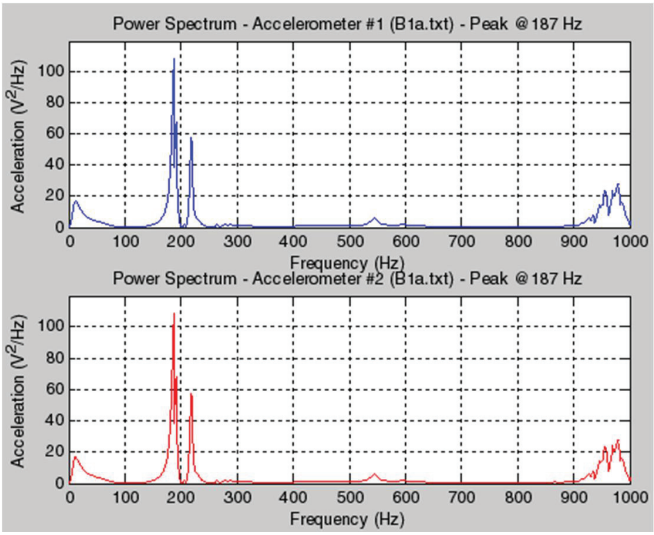

Figure 9-3: Main Frequency of Specimen B1

9.3 Characterization of Blast Loading Applied to CFDST and MSJC using Shorting Pins

9.3.1 Methodology

In the ERDC test series, assemblages of shorting pins having their center of gravity located at the same height as the center of the detonated charge were used on the back face of a few specimens. As a specimen is deforming under blast overpressure, the pins touch the specimen and the current in the pin is "short-circuited" (i.e. the pins are "shorted"). The number of pins that are shorted depends on the magnitude of the deformation, hence on the impulse imparted to the specimen. As the pins are shorted, the time at which the back face of the specimen contacts the extremity of each pin is recorded. The distance between the back face of the specimen and the extremities of the multiple pins used are preset. Knowing those spacing and the time of arrival of the back face of the specimen at the pin tips, a portion of the velocity history of the back face

of the specimen can then be determined. Knowing the velocity history on the back face of a specimen, an estimate of the resultant impulse at the height of burst can then be established. This approach is valid provided that the cross section of the specimen maintains its shape. For a deforming cross-section, each point of the cross-section will be moving at a specific velocity and the estimate of the impulse will be somewhat affected.

If the spacing between the extremities of pins 1 to *n* and the back face of the specimen at rest are respectively designated by $x_1, x_2, ..., x_i, ..., x_n$, and the corresponding times at which contact with the pins occurs are $\tau_1, \tau_2, ..., \tau_i, ..., \tau_n$, then, the velocities v_i at which the back face of the specimen travels from the extremity of pin i to that of pin $i+1$ can be obtained using:

$$v_i = \frac{x_{i+1} - x_i}{\tau_{i+1} - \tau_i} \ , \ 1 \le i \le n \tag{9-4}$$

where n is the number of pins. The velocity history at the back face of the specimen is given by the pairs (τ_i, v_i). If we assume that the velocity history so calculated represents the velocity of the back of the specimen at the same height as the center of the charge (which is where the pins are located), the resultant impulse per unit length seen by that section can be estimated as the product of the mass of the section (mass per unit length of the specimen) and the velocity so calculated. The impulse per unit area, i_i, normally reported by software like BEL is obtained by dividing the impulse per unit length, I_i, by the breadth or the diameter (D) of the section exposed to the blast.

$$I_i = mv_i,\ 1 \le i \le n \tag{9-5}$$

$$i_i = \frac{I_i}{D},\ 1 \le i \le n \tag{9-6}$$

9.3.2 Application to the ERDC Test Series

It was found that, with less than 10 pins, the velocity history at the back of a specimen was truncated, and no estimate of the peak or the deceleration of the specimen afterwards could be obtained for those cases. The CFDST specimens, all instrumented with a 5-pin assembly, fall in that category. For specimens instrumented with 10 pins, Figure 9-4 illustrates a typical pin assemblage on the back face of the element. The 10 pins were split between two blocks (A and B) of 5 pins each, allowing to calculate 10 data points of the velocity history on the back face of the specimen. The distance between the tip of each pin and the back face of the specimen were calculated and the time of contact between the back face of the specimen and each pin was read from the data collected for the pins. The times of arrival for all specimens instrumented with the 10-pin assemblies are reported on Table 9-2. The velocities and impulses calculated per the equations from the previous section are also showed.

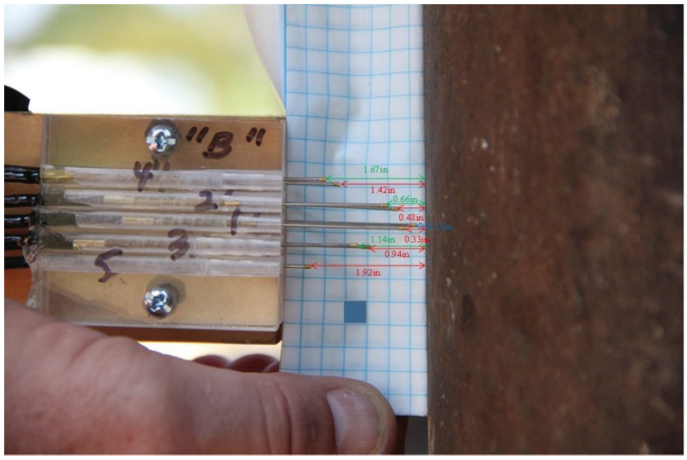

Figure 9-4: Shorting Pin Assembly on the Back of MSJC2 (Block A is Hidden behind B)

Table 9-2: Velocity and impulse Histories Calculation for MSJC Specimens

MSJC1				MSJC2				MSJC3			
$x_i(mm)$	$\tau_i(\sec)$	$v_i\left(m/s\right)$	I_i $(MPa-m\sec)$	$x_i(mm)$	$\tau_i(\sec)$	$v_i\left(m/s\right)$	I_i $(MPa-m\sec)$	$x_i(mm)$	$\tau_i(\sec)$	$v_i\left(m/s\right)$	I_i $(MPa-m\sec)$
1.83	2.95E-04	6.21E+00	2.24	4.32	2.22E-04	1.94E+01	7.00	2.16	2.68E-04	8.08E+00	2.91
4.76	3.98E-04	2.85E+01	10.25	8.38	3.28E-04	3.86E+01	13.92	5.20	3.59E-04	3.33E+01	12.00
5.86	4.04E-04	1.83E+02	66.00	12.19	3.36E-04	4.48E+02	161.52	8.23	3.91E-04	9.47E+01	34.13
8.43	4.49E-04	5.70E+01	20.53	16.76	4.29E-04	4.92E+01	17.71	10.39	4.58E-04	3.23E+01	11.64
12.09	5.67E-04	3.10E+01	11.19	23.88	5.35E-04	6.71E+01	24.18	14.29	5.95E-04	2.84E+01	10.25
17.22	6.52E-04	6.03E+01	21.74	28.96	6.15E-04	6.35E+01	22.88	17.75	6.11E-04	2.16E+02	78.00
17.95	8.44E-04	3.82E+00	1.38	36.07	7.23E-04	6.59E+01	23.73	21.65	7.99E-04	2.07E+01	7.47
18.68	8.68E-04	3.05E+01	11.00	42.42	8.56E-04	4.77E+01	17.20	22.08	8.12E-04	3.33E+01	12.00
26.74	9.65E-04	8.31E+01	29.94	48.77	9.68E-04	5.67E+01	20.43	28.58	1.11E-03	2.22E+01	7.99

9.4 Plastic Analysis of CFDST Section Subjected to Localized Blast Impulse

9.4.1 Observed Mechanism of Deformation of CFDST Cross Section

The mechanism of indentation of CFDST under blast loading is a dynamic process that goes through several steps. Depending of the depth of the dent, three main observations can be made with respect to the final deformed shape of the cross section. For low to moderate indentation, the cross section deformed in such a way that 3 circular sandwich arcs and a flatten regions facing the blast source are formed. Those 4 sections of the mechanism are articulated at 4 plastic hinge segments located along AA', BB', CC' and DD' as shown on Figure 9-5. These hinges are not stationary, they are dynamic hinges. They move so that the flattened region lengthens while the radius of the longer arc section increases and the radii of the smaller arcs diminish. For this type of deformation, the concrete is lightly damaged and still confined, thus still contributing to the overall resistance of the section. Deformation consistent with this description was observed for specimen B1 of the test series.

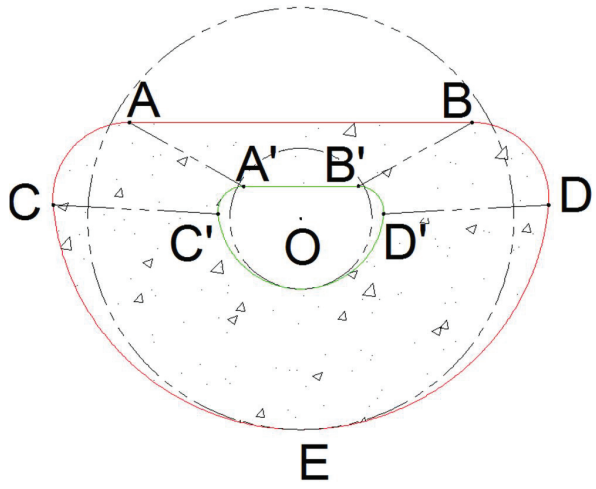

Figure 9-5: CFDST Cross Section Deformation for Moderate Indentation

For severe indentation, an additional local hinge may form in the flattened region of the inner tube along with the initial four other hinge lines (which have moved) while the flattened region grows but remains flat in the outer tube (Figure 9-6). The contribution of the concrete exposed to the blast is negligible in this case; the concrete is crushed and lost its competency. This type of deformation was observed for specimen B2 and B5 upon removing the outside tube and observing the state of the concrete core.

Furthermore, when the indentation exceeds the radius of the inner tube by more than 50% or for moderate to large void ratio, crushing of the inner tube may ensue accompanied by hinging of the flattened region of the outer tube resulting in a case of extreme indentation of the section (Figure 9-7). The concrete facing the blast is typically pulverized in this case as observed from the test data. This type of deformation was observed for specimens B4, B6 and B7.

Because of the limited data set of this series of experiment, it is difficult to provide bounds on the dent depth for which the types of deformation described previously hold. Further experiments might be needed to set those limits.

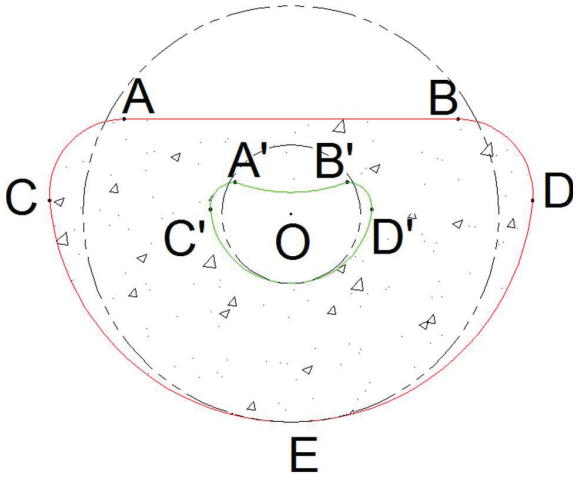

Figure 9-6: CFDST Cross Section Deformation for Severe Indentation

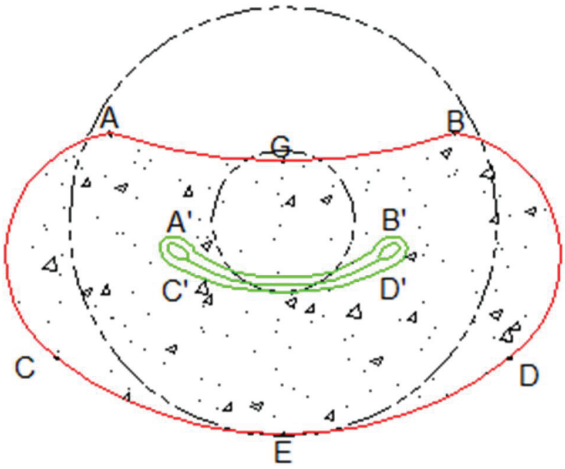

Figure 9-7: CFDST Cross Section Deformation for Extreme Indentation

9.4.2 Geometry of the Mechanism of Deformation of CFDST

Mathematical relations can be established to approximate the geometry of the deformed cross section. This can be done by tracking the different stages of deformation under load, starting with the initial hinging of the cross section all the way through crushing of the inner tube.

9.4.2.1 Hinge Formation in CFDST Cross Section

For this section, an analysis presented by Owens and Symonds (1955) for the deformation of thin rings under dynamic loading is adapted to consider the case of a CFDST ring. It is assumed that all materials involved are elastoplastic. Under this assumption, the effect of the externally applied blast loading can be replaced by an equivalent crushing force that grows up to its maximal value and remains constant afterwards. This force is equilibrated by the inertia forces related to the uniform acceleration, *f*, that develops in the cross section under the impulse imparted. Its effect is to create bending of the composite wall without extension in the circumferential direction. For reason of symmetry, half of the section only is considered. By writing the equations of force equilibrium with respect to the principal axes and the equilibrium of moment with respect to point O shown on Figure 9-8, Equations (9-7) and (9-8) follow. An additional relationship, Equation (9-9) is obtained by taking the moment with respect to a section located under an angle θ_o (see right insert of Figure 9-8):

$$P = 2\pi \left(R_o + R_i\right) m_s f + 2\pi \times \frac{1}{2}\left(R_o + R_i\right) m_c f \tag{9-7}$$

$$2N_o \times \frac{1}{2}(R_o + R_i) = \int_0^{\pi} m_s R_o f R_o d\theta \sin\theta + \int_0^{\pi} m_s R_i f R_i d\theta \sin\theta + \int_0^{\pi} m_c \frac{1}{2}(R_o + R_i) f d\theta \frac{1}{2}(R_o + R_i)\sin\theta \tag{9-8}$$

$$\begin{aligned} M_{\theta_o} = M - N_o \times \frac{1}{2}(R_o + R_i)(1 - \cos\theta_o) + P \times \frac{1}{2}(R_o + R_i)\sin\theta_o \\ - \int_0^{\pi} m_s R_o f \left[\frac{1}{2}(R_o + R_i)\sin\theta_o - R_o \sin\theta\right] d\theta \\ - \int_0^{\pi} m_s R_i f \left[\frac{1}{2}(R_o + R_i)\sin\theta_o - R_i \sin\theta\right] d\theta \\ - \int_0^{\pi} m_c \times \frac{1}{2}(R_o + R_i) f \times \frac{1}{2}(R_o + R_i)\left[\sin\theta_o - \sin\theta\right] d\theta \end{aligned} \tag{9-9}$$

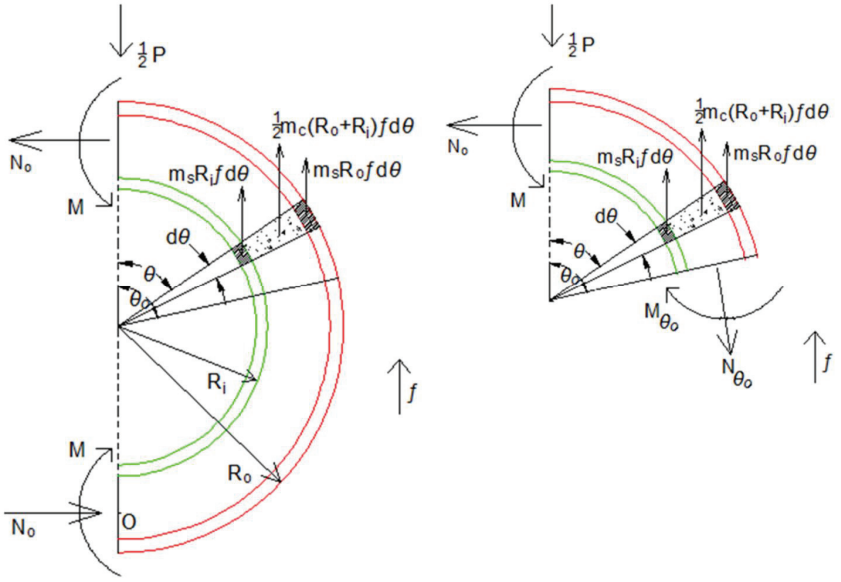

Figure 9-8: Dynamic Equilibrium of a Half CFDST Ring

After carrying out the integral and making some arrangements those equations reduce to:

$$P = 2\pi \overline{R} m f \tag{9-10}$$

$$N_o = \frac{\overline{M}}{\overline{R}} f \tag{9-11}$$

$$M_{\theta_o} = M + \overline{R} \sin\theta_o \left(\frac{1}{2} P - m \overline{R} \theta_o f \right) \tag{9-12}$$

where the following substitutions have been made:

$\overline{R} = \frac{1}{2}(R_o + R_i)$: the average radius of the composite section

$m = 2m_s + m_c$: the total mass per unit length of the element

$\overline{M} = m_s \left(R_o^2 + R_i^2 \right) + m_c \overline{R}^2$: the moment of inertia of the composite section

The principal variables in these equations are:

θ_o: the angle of the mechanism

f: the acceleration of the cross section

M_{θ_o}: resultant of the internal moment at a section located under an angle θ_o

N_o: the horizontal component of the resultant of the internal forces at point O

P: the equivalent crushing force

M : the resultant internal moment at point O

m_s is the mass per unit length of the steel tubes

m_c is the mass per unit length of the concrete core

Those three equations are significant in defining response. For instance, knowing the acceleration of the cross section at peak loading, Equations (9-10) and (9-11) can be used to

estimate the crushing and the axial forces acting on the cross section. The results obtained in Section 9.3 can then be used to estimate the acceleration of the specimen around that peak. Also, Equation (9-12) being a function of θ_o, it can be sought whether a maximum is reached for a given θ_o. Taking the derivative of Equation (9-12) the following relationship is obtained:

$$\frac{\partial M_{\theta_o}}{\partial \theta_o} = \frac{1}{2} P \overline{R} \cos\theta_o - m \overline{R}^2 f \left(\theta_o \cos\theta_o + \sin\theta_o\right) \tag{9-13}$$

By substituting Equations (9-10) and (9-11) into Equation (9-13) and equating the result to zero, a condition on θ_o is obtained.

$$\tan\theta_o = \pi - \theta_o \tag{9-14}$$

It then follows that, over the range of interest:

$$\begin{cases} \theta_{o1} = 1.113 \text{rad } (63.8 \text{deg}) \\ \theta_{o2} = \pi \end{cases} \tag{9-15}$$

This is the angles under which the first hinges form in the cross section. For reason of symmetry hinges will also form under the following angles:

$$\begin{cases} \theta_{o3} = 0 \\ \theta_{o4} = -1.113 \text{rad } (-63.8 \text{deg}) \end{cases} \tag{9-16}$$

In summary (up to this point), 4 segments with plastic hinges at their ends need to form for the cross-section indentation process to begin. Once those hinges have formed, indentation of the cross section will initiate and 4 rigid composite arcs will form. Those hinges are not stationary; once they have formed, they start moving. The bottom hinge vanishes however as it is merely needed to allow the indentation process to initiate. As the dent depth grows, the two intermediate

hinges move outwardly such that θ_o theoretically grows from 1.113 to π. During its movement, the top hinge splits (divides in two) rolls (becoming a so-called "rolling hinge") and creates a flattened region. The lengths of the plateaux of that region are the same for the inner and the outer tube initially. At some point, the plateau of the inner tube will reach a maximum and deformation will continue only if a hinge segment forms in the center of both the inner and the outer tubes leading to sagging of the plateaux.

9.4.2.2 Mathematical Model

Before the flattened region reaches a maximum in the tubes, the equations that describe the geometry of the deformed shape of the cross section are:

$$\delta = 2R_o - R_{o1}\left(1+\cos\theta\right) - R_{o2}\left(1-\cos\theta\right) \tag{9-17}$$

$$R_{o1}(\pi-\theta) + R_{o2}\theta + \left(R_{o1} - R_{o2}\right)\sin\theta = \pi R_o \tag{9-18}$$

$$\delta = 2R_i - R_{i1}\left(1+\cos\theta\right) - R_{i2}\left(1-\cos\theta\right) \tag{9-19}$$

$$R_{i1}(\pi-\theta) + R_{i2}\theta + \left(R_{i1} - R_{i2}\right)\sin\theta = \pi R_i \tag{9-20}$$

All parameters are depicted on Figure 9-9 and as before the indices '*o*' and '*i*' refer to the outer and the inner tube respectively. Compatibility of deformation at the cross-section level requires that the deformation of the inner and the outer are identical and equal to δ. This is expressed by Equations (9-17) and (9-19). Furthermore, the relative deformations of the tubes are related to each other by the void ratio, χ, such that:

$$\frac{\delta}{2R_i} = \frac{1}{\chi}\frac{\delta}{2R_o} \tag{9-21}$$

Equations (9-18) and (9-20) on the other hand express that the deformation of the tubes is inextensible in the circumferential direction. Knowing the depth of the dent in each tube, an additional equation is needed to fully capture the kinematic of the deformation. A relationship between the dent depth and the angle of the mechanism can be deducted. As θ varies from θ_o to to π, the dent depth δ varies from zero to twice the radius of the inner tube which, because of the construction of the cross section, can crush entirely while the presence of the concrete limit the deformation of the outer tube even after the inner tube has completely collapsed. Assuming a linear relationship between θ_o and δ, it follows that:

$$\frac{\delta}{2R_i} = \frac{\theta - \theta_o}{\pi - \theta_o}, \tag{9-22}$$

$$\frac{\delta}{2R_o} = \chi\frac{\theta - \theta_o}{\pi - \theta_o} \tag{9-23}$$

Equations (9-17) to (9-23) can be solved to lead to geometric relationships between the radii of the rigid arcs and θ:

$$\frac{R_{o1}}{R_o} = \frac{(\theta - \sin\theta)\left[(\pi - \theta_o) - \chi(\theta - \theta_o)\right] - \pi(\pi - \theta_o)\sin^2\left(\frac{\theta}{2}\right)}{\left(\theta - \sin\theta - \pi\sin^2\left(\frac{\theta}{2}\right)\right)(\pi - \theta_o)} \tag{9-24}$$

$$\frac{R_{o2}}{R_o} = \frac{(\theta - \sin\theta - \pi)\left[(\pi - \theta_o) - \chi(\theta - \theta_o)\right] + \pi(\pi - \theta_o)\cos^2\left(\frac{\theta}{2}\right)}{\left(\theta - \sin\theta - \pi\sin^2\left(\frac{\theta}{2}\right)\right)(\pi - \theta_o)} \tag{9-25}$$

$$\frac{R_{i1}}{R_i} = \frac{(\theta - \sin\theta)(\pi - \theta) - \pi(\pi - \theta_o)\sin^2\left(\frac{\theta}{2}\right)}{\left(\theta - \sin\theta - \pi\sin^2\left(\frac{\theta}{2}\right)\right)(\pi - \theta_o)} \tag{9-26}$$

$$\frac{R_{i2}}{R_i} = \frac{(\theta - \sin\theta - \pi)(\pi - \theta) + \pi(\pi - \theta_o)\cos^2\left(\frac{\theta}{2}\right)}{\left(\theta - \sin\theta - \pi\sin^2\left(\frac{\theta}{2}\right)\right)(\pi - \theta_o)} \tag{9-27}$$

Equations (9-24) to (9-27) verify the conditions of inextensibility imposed on the tubes. They also establish a key result for the mechanism of deformation, namely:

$$R_{o1} - R_{i1} = R_o - R_i \tag{9-28}$$

$$R_{o2} - R_{i2} = R_o - R_i \tag{9-29}$$

These results mean that up until the tubes sag, the concrete core maintain is thickness. Once sagging initiates, the geometry of the mechanism changes. For simplicity, it will be assumed that sagging of the plateaux in both tubes occur at the same time.

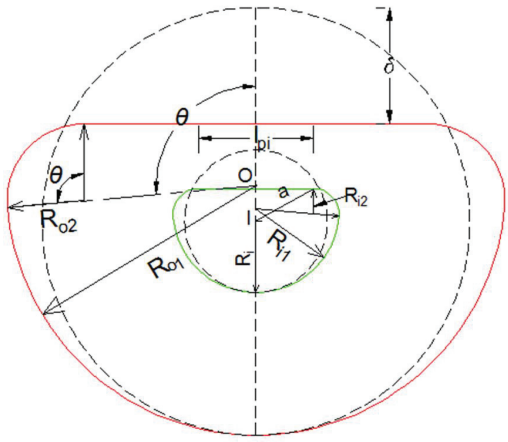

Figure 9-9: Initial Geometry of the Mechanism

An estimation of the dent depth for which the plateau reached a maximum can be obtained by looking at the deflection pattern of the inner dented tube (Figure 9-9). From geometrical consideration, a relation between the dent and the plateau length, l_{pi}, can be written.

$$\delta = R_i - \sqrt{a^2 - \left(\frac{l_{p_i}}{2}\right)^2} \tag{9-30}$$

From which follows an equation for the plateau length:

$$l_{pi}(\delta) = 2\sqrt{(a - R_i + \delta)(R_i + a - \delta)} \tag{9-31}$$

The latter expression reaches a maximum (for a assumed constant) when:

$$\delta = \delta_{pi} = R_i \tag{9-32}$$

The angle of the mechanism at which the plateau reach a maximum and snap through initiates in the inner tube can also be estimated from Equation (9-22):

$$\theta_{pi} = \frac{\pi + \theta_o}{2} = 121.9\,\text{deg} \tag{9-33}$$

From the geometry of the mechanism estimates of the length of the plateaux for the inner and the outer tube are:

$$l_{pi\_\max} = 2(R_{i1} - R_{i2})\sin\theta_{pi} \tag{9-34}$$

$$l_{po} = 2(R_{o1} - R_{o2})\sin\theta_{pi} = l_{pi\_\max} \tag{9-35}$$

Any deformation in excess of R_i is assumed to cause sagging in the plateaux of the tubes. The concrete is heavily damaged in this phase of deformation, and any bond with the outer tube is lost. The damaged concrete is accelerating against the inner tube, and further deformation of the inner tube occurs. At this stage compatibility of deformation between the tubes is no longer

maintained as they no longer deform in unison. To obtain an approximate solution to the problem it is assumed, in the following sections, that the previous equations still hold for this phase as it is difficult to derive a closed form solution that would provide more rigorous description of the deformed shape of the cross section.

9.4.3 Estimation of the reduced Moment Capacity of Dented CFDST Section

Once the geometry of the section has been established, the reduced moment capacity can be calculated. Calculations of the reduced moment section capacity can be carried out using an "exact" approach or a simplified approach. In the exact approach, the geometry of the mechanism described in the previous sections would be used to estimate the reduced moment capacity. For the simplified approach a substitute section is used to calculate the reduced moment strength.

9.4.3.1 Exact Approach

For the exact approach, it is assumed that the section has fully plastified and that the concrete participates in the resistance up to the point at which the plateau has reached a maximum. Using mechanic of materials principles the moment resistance of the cross section can be evaluated as:

$$M_R(\delta) = \int_{Area} F_y y dA \tag{9-36}$$

However, this calculation is not easily performed as a closed-form expression for the neutral axis location is difficult to determine. As a consequence an approximate treatment of the problem using substitute section is proposed.

9.4.3.2 Simplified Approach

For the simplified approach a square cross section is used as a substitute for the CFDST cross section. It is assumed that all materials are elastoplastic. The substitute cross section is chosen such that both tubes are inextensible in their circumferential direction and have the same thicknesses as the CFDST tubes. The dimensions of the square tubes of the substitute section should then be:

$$4a_o t_o = \pi D_o t_o \tag{9-37}$$

$$4a_i t_i = \pi D_i t_i \tag{9-38}$$

which leads to:

$$a_o = \frac{\pi D_o}{4} \tag{9-39}$$

$$a_i = \frac{\pi D_i}{4} \tag{9-40}$$

It is assumed that the deformation in the substitute cross section is compatible with the deformation in the real section and deformation of the substitute cross section does not cause any extension of the perimeter of the tubes. As a consequence for a lateral dent of magnitude δ, the substitute cross section deformed into a rectangle of dimensions $a_i - \delta$ and $a_i + \delta$. This is only an approximation of the true mechanism of deformation.

Plastic analysis principles are applied to the equivalent cross section to compute estimates of the reduced moment capacity of the cross section. Because of the configuration of the section, the plastic neutral axis can be located either across the inner tube or above the inner tube. When the plastic neutral axis is located across the inner tube, the equations describing the reduced moment capacity are as followed:

$$y_p = \frac{\left(a_0^2 - a_i^2\right) f_c^{'}}{8\left(f_{yo}t_o + f_{yi}t_i\right) + 2\left(a_o - a_i\right) f_c^{'}} \le \frac{a_i - \delta}{2} \tag{9-41}$$

$$\begin{aligned} M_R(\delta) = &\left[\left(a_o^2 - \delta^2\right) + \frac{1}{2}\left(a_o - \delta\right)^2 - 2y_p^2\right] f_{yo}t_o + \left[\left(a_i^2 - \delta^2\right) + \frac{1}{2}\left(a_i - \delta\right)^2 - 2y_p^2\right] f_{yi}t_i \\ &+ \left(a_o - a_i\right)\left[\left(\frac{a_o - \delta}{2}\right)^2 - y_p^2\right] f_c^{'} \end{aligned} \tag{9-42}$$

In the case the neutral axis is located above the inner tube, those equations are respectively:

$$y_p = \frac{\left(a_0^2 - \delta^2\right) f_c^{'}}{8 f_{yo}t_o + 2\left(a_o + \delta\right) f_c^{'}} > \frac{a_i - \delta}{2} \tag{9-43}$$

$$M_R(\delta) = \frac{1}{2}\left(a_o - \delta\right)\left(3a_o + \delta\right) f_{yo}t_o + \frac{1}{2}\left(a_i - \delta\right)\left(3a_i + \delta\right) f_{yi}t_i + \frac{1}{8}\left(a_o + \delta\right)\left[\left(a_o - \delta\right)^2 - 4y_p^2\right] f_c^{'} \tag{9-44}$$

The neutral axis of the substitute section for each case was calculated using an approach similar to the one described in Section 7 for the determination of the neutral axis of bisymmetric section. It is worth noting that Equation (9-41) is independent of the dent depth δ. In reality Equations (9-41) to (9-44) complete each other. Equation (9-41) can be used as a starting point. For each value of δ, the plastic neutral axis is first assumed located across the inner substitute tube. If the result is within the range of application given, the reduced plastic moment corresponding to each value of δ is calculated using Equation (9-42). Otherwise, Equations (9-43) and (9-44) are used.

9.4.3.3 Application to the ECLIPSE and ERDC Tests

Equations (9-41) to (9-44) were used to calculate the residual strength of the CFDST specimens used in the ECLIPSE and ERDC tests. The properties of the sections tested are presented in Table 9-3. In the two columns next to the last in this table, the plastic moment capacity calculated using an exact approach for non-dented section is tabulated along with the plastic

moment calculated using Equations (9-41) to (9-44) and $\delta = 0$. The agreement between the simplified formula and the exact value when the dent depth is zero is good. On average the simplified formula underestimates the moment capacity of the section, which is conservative.

On the other hands, the reduced moment capacities in function of denting in the specimens were calculated using the simplified formula. Sample results are presented on Figure 9-10 to Figure 9-15. From the results it can be seen that the relationship between the reduced moment capacity and the dent depth is approximately linear. A solid line represents this relationship on each figure. Two other dotted lines represent respectively a linear fit for the reduced moment capacity of the specimen and an estimate of the reduced moment capacity provided by Equation (9-45).

$$M_R = M_p\left(1-\frac{\delta}{R_o}\right) = M_p\left(1-\chi\frac{\delta}{R_i}\right) \quad \delta \le 2R_i \tag{9-45}$$

where the reduced moment is designated by M_R, the plastic moment by M_p and χ is the void ratio. All other parameters have been previously defined.

Equation (9-45) is a lower bound of the reduced moment capacity of the dented sections. Although this equation looks very conservative for the specimens presented, the contribution of the concrete was however considered in the derivation of the reduced moment capacity. Because the concrete is likely to be damaged, its contribution to the strength of the section should be negligible, for large denting.

Because caving in excess the diameter of the inner tube would be impossible to achieve, a limit on δ is imposed in Equation (9-45). In reality, once $\delta = 2R_i$ is reached, the moment capacity has to reach a minimum value and should not be reduced any further since the section is transformed into a (crush) concrete filled (deformed) tube which cannot caved in further.

Table 9-3: Properties of the Specimen Tested

	f_c (MPa)	f_{yo} (MPa)	f_{yi} (MPa)	t_o (mm)	t_i (mm)	D_o (mm)	D_i (mm)	M_{exact} (kN-M)	M(kN-m)	Ratio
B1	37.23	275.65	307.23	2.11	2.95	152.40	50.80	26.51	23.02	0.87
B3	37.23	330.95	307.23	2.90	3.12	203.20	50.80	67.99	61.00	0.90
B7	37.23	330.95	220.63	2.90	2.29	203.20	127.00	71.72	62.08	0.87
B5	37.23	379.21	379.21	3.18	1.93	152.40	50.80	43.62	40.51	0.93
B2	37.23	275.65	558.48	2.08	3.18	152.40	63.50	33.19	30.96	0.93
B4	37.23	368.87	325.50	3.38	2.90	168.28	63.50	57.91	54.48	0.94
B6	37.23	321.09	315.99	2.16	3.05	203.20	101.60	62.26	55.17	0.89
B9	37.23	396.17	406.51	4.76	3.05	203.20	127.00	46.22	43.03	0.93
B10	37.23	470.50	483.64	3.38	2.90	168.28	63.50	72.91	68.56	0.94
B11	37.23	389.28	405.34	4.76	3.18	203.20	101.60	127.97	116.90	0.91
B12	37.23	396.17	406.51	4.76	3.05	203.20	127.00	136.08	122.00	0.90
									Average	**0.91**
									Deviation	**0.03**

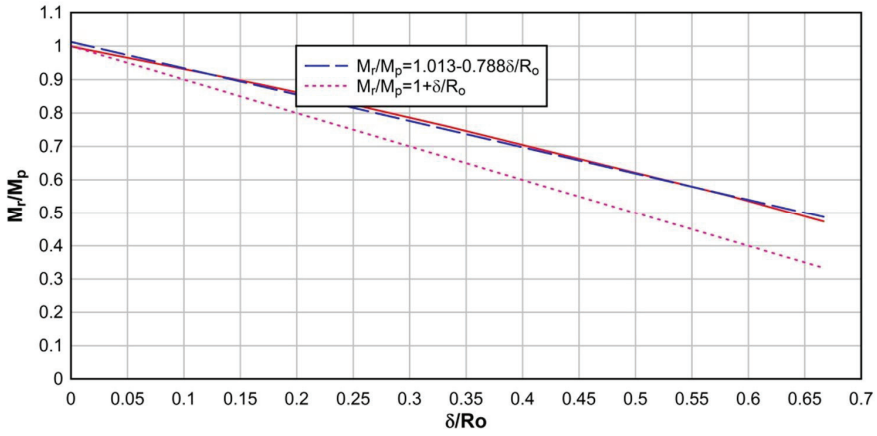

Figure 9-10: Reduced Moment Capacity in Function of Denting of Specimen B1

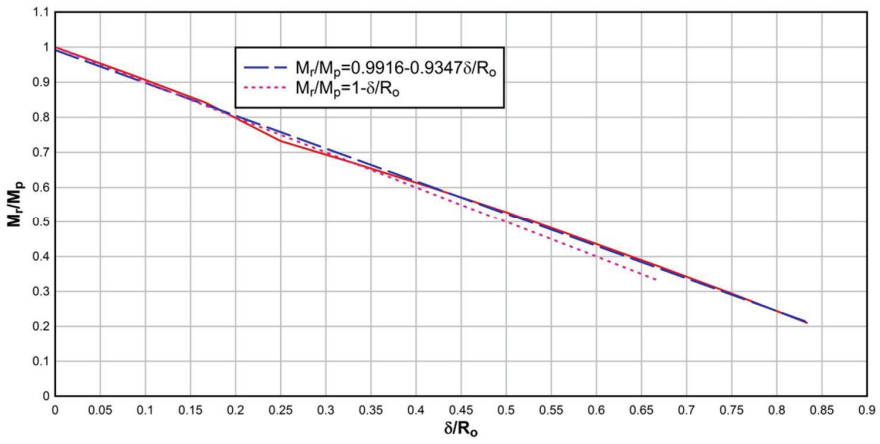

Figure 9-11: Reduced Moment Capacity in Function of Denting of Specimen B2

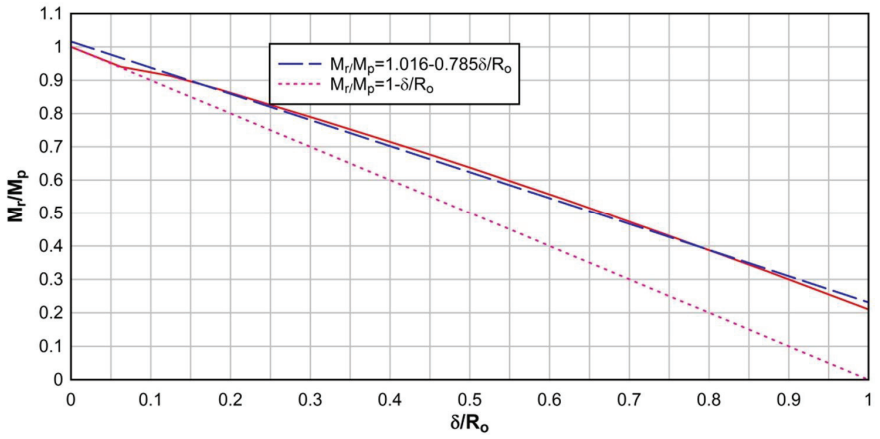

Figure 9-12: Reduced Moment Capacity in Function of Denting of Specimen B6

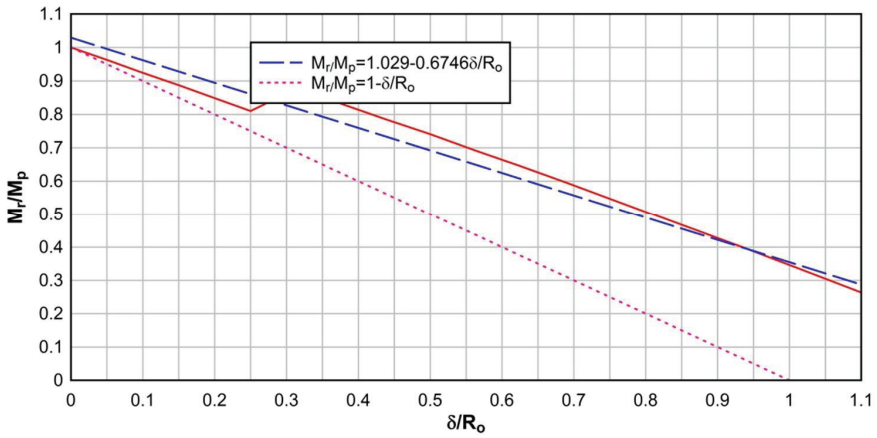

Figure 9-13: Reduced Moment Capacity in Function of Denting of Specimen B7

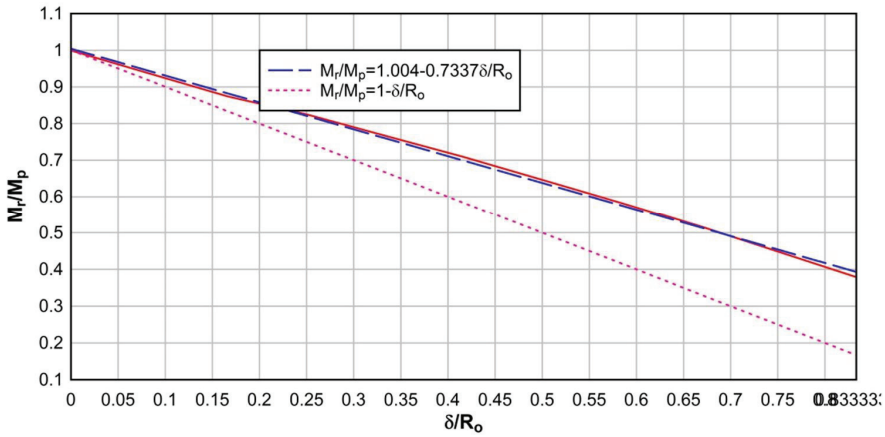

Figure 9-14: Reduced Moment Capacity in Function of Denting of Specimen B9

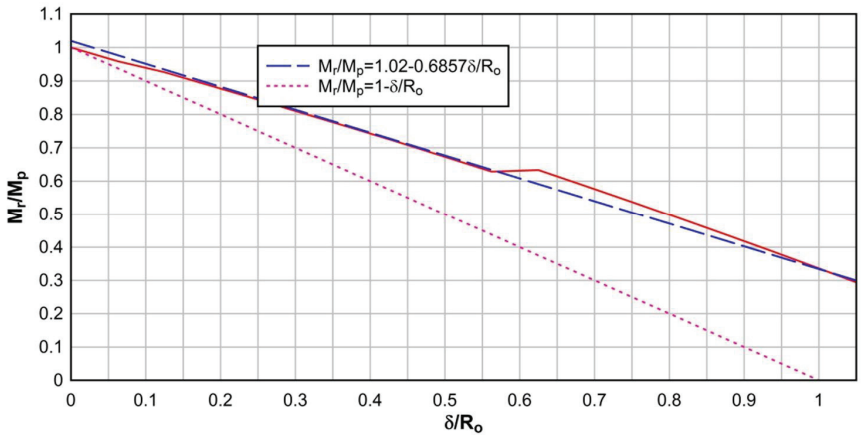

Figure 9-15: Reduced Moment Capacity in Function of Denting of Specimen B12

9.5 Simplified Approach to Predict Denting of CFDST under Impulsive Loading

An approximate equation to estimate the maximum depth and the extent of the dent in CFDST subjected to a highly localized impulsive blast loading can be obtained by making a few simplifying assumptions and comparing the energy imparted by the blast to the internal work done over the section of the dented region effective in absorbing the energy transferred. Note that for the case of close-range blast loading, as considered in this research, the energy imparted is impulsive and several orders of magnitude larger than the work done by other externally applied forces (e.g. gravity, braking load from the superstructure) on the deforming and yielding target. Therefore these local forces are ignored in the analysis.

For CFDST, the input energy is dissipated by a combination of two inelastic processes involving crushing of the cross-section, and membrane action in the collapsing surfaces of the inner and outer cylindrical tubes. During those processes, internal work is produced to dissipate the input

energy; the components of this work coming from the crushing of the composite cross-section and the collapsing of the tubes need to be evaluated in deriving an approximate equation for the maximum depth of the dent.

The process of denting of CFDST under impulsive loading is a complex dynamic problem similar to the denting of metal tubes under impact loading. A treatment for denting of metal tubes subjected to impulsive (impact and blast) loading was previously proposed by Wierzbicki and Hoo Fatt (1993). The rates of input and dissipated energy were considered by those authors in the formulation of the problem and efforts were made to track the history of deformation and solve the true dynamic problem involved in denting of tubes under impulsive loading. For CFDST, the final state of deformation is of interest; hence certain aspects of the aforementioned treatment as related to the determination of the internal energy of deformation of the cross section and the equivalent axial force have been adapted for the present study. On the other hand, the definition and derivation of the equivalent crushing force as introduced in this section, as well as the derivation of the input energy and the final dent equations are new proposed analytical formulations to investigate the denting problem.

9.5.1 Input Energy

The energy imparted by a blast impulse to the dented region of a CFDST is purely kinetic and can be estimated by summing the elementary energies transferred to each of the differential elements of the region directly located under the impulse. Along the original undeformed cylindrical surface, each differential element of mass dm and length dz is sustained by a central

angle $d\theta$ (see Figure 9-16). The area of the differential element exposed to the impulse is dA. The kinetic energy, dK, imparted to the exposed area dA of this differential element is:

$$dK = \frac{i^2(z,\theta)(dA)^2}{2dm} = \frac{\pi i^2(z,\theta)\left(R_o d\theta dz\right)^2}{2\pi\left[\gamma_s\left(R_o t_o + R_i t_i\right) + \gamma_c \frac{\left(R_o + R_i\right)}{2}\left(R_o - R_i\right)\right] d\theta dz} \tag{9-46}$$

where $i(z,\theta)$ is the impulse acting on the differential element and an expression for dm has been substituted in the denominator considering the specific density of steel and concrete, γ_s and γ_c, respectively. Both the denominator and the numerator have been multiplied by π for reason that will become evident shortly. Recognizing that 2π times the expression between brackets in the denominator is equal to the mass per unit length, m, of the CFDST, Equation (9-46) simplifies to:

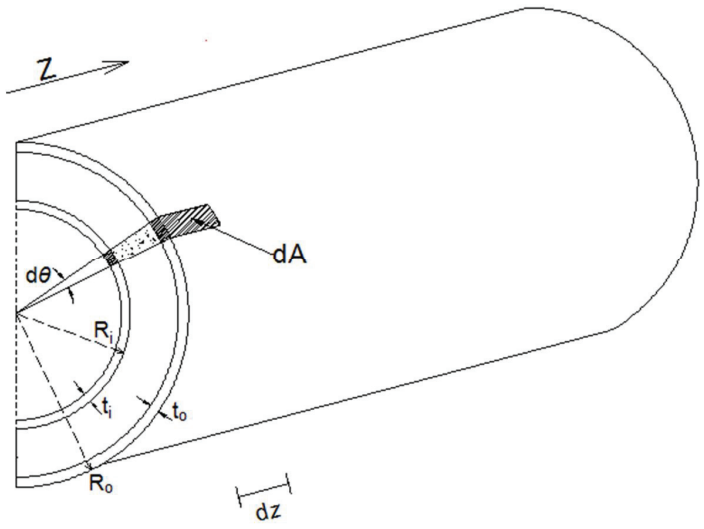

Figure 9-16: Differential Element Used in Deriving the Kinetic Energy

$$dK = \frac{i^2(z,\theta)(dA)^2}{2dm} = \frac{\pi R_o^2 i^2(z,\theta)}{m} d\theta dz \tag{9-47}$$

Because the impulse from blast overpressure is generally a function of both the angle of incidence and the standoff with respect to the target, it is assumed here that its distribution over the target area can be written using independent shape functions in terms of two coordinates (z,θ), which can be related to the angle of incidence and the standoff. Using that approach, it is possible to write:

$$i(z,\theta) = i_0 f(z) g(\theta) \tag{9-48}$$

where i_0 is the peak impulse applied to the CFDST, $f(z)$ is a shape function that describes the distribution of the impulse along the length of the CFDST while $g(\theta)$ is a shape function describing the distribution of the impulse along the circumferential direction of the CFDST as shown on Figure 9-17.

Following the treatment proposed for metal tubes by Wiersbicki and Hoo Fatt, those shape functions are assumed to have a fixed shape but variable amplitudes along the length of the specimen and the circumferential direction respectively. The reflected impulse is postulated to be acting on the centerline of the column and distributed as shown on Figure 9-17; its distribution over the diameter of the column is also represented by a cosine function. The shape functions that represent the situations are respectively defined as:

$$\begin{cases} f(z) = \cos^2\left(\dfrac{\pi z}{l}\right), -\dfrac{l}{2} \le z \le \dfrac{l}{2} \\ f(z) = 0 \qquad\qquad \text{elsewhere} \end{cases} \tag{9-49}$$

$$\begin{cases} g(\theta) = \cos^2\left(\dfrac{\pi\theta}{2\alpha_o}\right), -\alpha_o \le \theta \le \alpha_o \\ g(\theta) = 0 \quad \text{elsewhere} \end{cases} \tag{9-50}$$

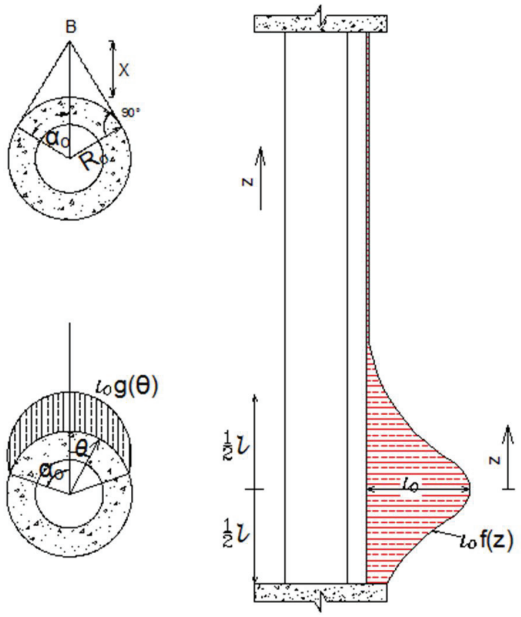

Figure 9-17: Assumed Peak Impulse Distribution over a CFDST Column

where l is the extent of the dented region along the length of the specimen as shown in Figure 9-17. The equations used for those shape functions indicate the peak reflected pulse reduces sharply as one move away from the source along the circumference of the outside tube, as expressed by $g(\theta)$. The choice of $f(z)$ is obvious because of the initial assumption made. The

choice of $g(\theta)$ can be justified by the fact that close range blast loadings are considered in this research and while relatively large reflected impulse will prevail on the face of the specimen, there exists a region on the exposed circumference where reflection of the blast wave no longer occurs and consequently the peak reflected impulses are null. This region is illustrated on Figure 9-4. For a blast source *B* located at a standoff *X* the angle α_o whose supplement $(\pi - \alpha_o)$ subscribes this region is given by:

$$\cos\alpha_o = \frac{R_o}{R_o + X} \tag{9-51}$$

Other expressions could be used for the shape functions, but the one used here, while simple, offers a satisfactory representation of the problem for the current purpose.

A closed form expression for the input energy can then be obtained by integrating Equation (9-47) over the region defined by the extent of the dent and the circumferential distribution of the pulse:

$$K = \int_{-l/2}^{l/2}\int_{-\alpha_o}^{\alpha_o} dK = \int_{-l/2}^{l/2}\int_{-\alpha_o}^{\alpha_o} \frac{\pi R_o^2 i_o^2}{m} f^2(z) g^2(\theta) d\theta dz \tag{9-52}$$

$$K = \frac{3\pi\alpha_o R_o^2 i_o^2 l}{4m} = \frac{3\pi\alpha_o D_o^2 i_o^2 l}{16m} \tag{9-53}$$

9.5.2 Internal Energy of Deformation in the Dented Region

For this analysis, a CFDST is considered as formed by an ensemble of juxtaposed elastic perfectly plastic rings and longitudinal composite steel-concrete-steel beams, of unit width, simply supported by the rings all around their circumference. In this simplified model, the rings

and the beams are bound through compatibility of deformations, and it is assumed that a state of perfect bond exist between the steel and the concrete core. Under load, the beams deform and elongate whereas the rings crush; the combination of both deformation results in a dented region. If it is assumed that the crushing of the rings is not accompanied by any extension of the composite ring in the circumferential direction but only by bending of the ring wall, the work W_{int} done in the composite wall can be written as:

$$W_{\text{int}} = \int_{-l/2}^{l/2}\int_{-\pi}^{\pi} \left| M_{pw}\psi_{\theta\theta}(z,\theta) \right| \bar{R} d\theta dz + \frac{1}{2}\int_{-l/2}^{l/2}\int_{-\pi}^{\pi} \left| \left(N_{pwi}R_i + N_{pwo}R_o \right) w_z(z,\theta) w_z(z,\theta) \right| d\theta dz \tag{9-54}$$

In this expression, the first term on the right represents the energy dissipated in crushing of the composite wall. This term results from the work done by the moment capacity of the wall on the curvature of the wall. The second term on the right is the expression of the work done by the unit tensile axial capacity of the tubes (the tensile capacity of the concrete is ignored) working on the corresponding membrane (stretching) action in the surface of the tubes. It is evaluated using formulation from large deformation theory in which both the axial and the shear contribution to the total axial deformation are ignored. In the above expression, and corresponding to the values shown in the illustrative diagrams (Figure 9-19 and Figure 9-20)

M_{pw} is the unit moment capacity of the composite wall treated as a sandwich section,

N_{pwi} is the unit tensile capacity of the inner tube,

N_{pwo} is the unit tensile capacity of the outer tube,

$\psi_{\theta\theta}(z,\theta) = \dfrac{\partial^2 w(z,\theta)}{\partial\theta^2}$ is the curvature distribution over the circumference of a unit composite ring at a specified location z along the length of the CFDST, it is a function of both the axial

coordinate z along the length of the CFDST and the circumferential coordinate θ along its circumference,

$w_z(z,\theta)=\dfrac{\delta w(z,\theta)}{\delta z}$ is the rotation distribution over the circumference of a unit composite ring located at a distance z from the assumed origin over the length of the CFDST, as shown in Figure 9-18-note that $w(z,0)$ correspond to the maximum local deformation which we want to estimate,

$w(z,\theta)$ is the final position on the deformed section of a point initially located under an angle, θ, at a location, z, over the length of the CFDST column

l is used to fix the extent of the dented region effective in dissipating the input energy and is taken in that analysis to correspond to the wave length of the applied pulse (see Figure 9-17)

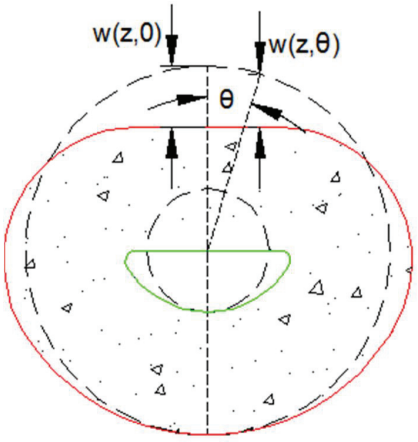

Figure 9-18: Definitions of $w(z,\theta)$ and $w(z,0)$

Under the assumption that the rings are made of elastic perfectly plastic materials, and treating each ring as an isolated element, the work done during the crushing of the ring can be approximated by the work done by an equivalent crushing force applied to the ring. For any given ring, this force can be interpreted as a single load applied at the point of the ring that undergoes the maximum deformation (see Figure 9-18). Under this assumption, the first term in Equation (9-54) would become:

$$\int_{-l/2}^{l/2}\int_{-\pi}^{\pi}\left|M_{pw}\varphi_{\theta\theta}(z,\theta)\right|\overline{R}d\theta dz=\int_{-l/2}^{l/2}P_{eq}w(z,0)\,dz \tag{9-55}$$

where the following substitution has been made:

$$\int_{-\pi}^{\pi}\left|M_{pw}\varphi_{\theta\theta}(z,\theta)\right|\overline{R}d\theta=P_{eq}w(z,0) \tag{9-56}$$

P_{eq} is the equivalent crushing resistance of any given ring due to bending, and, $w(z,0)=\delta_o$ is the maximum local deformation of a ring located at a distance z from the origin. Using this equation, the expression for the contribution of crushing of the composite ring to the internal work is greatly simplified. Once the characteristic crushing force is known, this component of the internal work can be obtained from Equation (9-55). This force is estimated later.

Using a similar approach, the contribution of the membrane action to the work done by crushing of the rings in the dented region can also be simplified by introducing an equivalent axial force $\left(N_{eq}\right)$ such that:

$$\int_{-l/2}^{l/2}\int_{-\pi}^{\pi}\left|\left(N_{pwi}R_i+N_{pwo}R_o\right)w_z(z,\theta)\,w_z(z,\theta)\right|d\theta dz=\int_{-l/2}^{l/2}N_{eq}w_z(z,0)\,w_z(z,0)dz \tag{9-57}$$

In Equation (9-57), the membrane energy is estimated using a lumped approach similar to the one used for the crushing energy by making the following substitution:

$$\int_{-\pi}^{\pi} \left| \left(N_{pwi} R_i + N_{pwo} R_o \right) w_z(z,\theta)\, w_z(z,\theta) \right| d\theta = N_{eq}\, w_z(z,0)\, w_z(z,0) \tag{9-58}$$

As before, once the equivalent axial force is evaluated, the membrane energy can be readily obtained using Equation (9-57). This equivalent axial force is calculated in the two following sections.

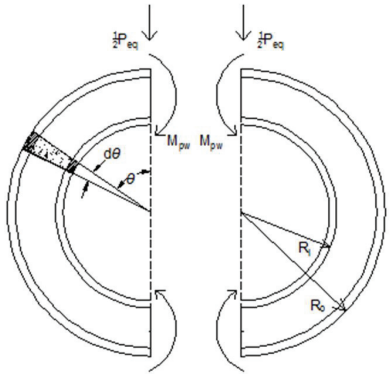

Figure 9-19: Correspondence Between P_{eq} and M_{pw}

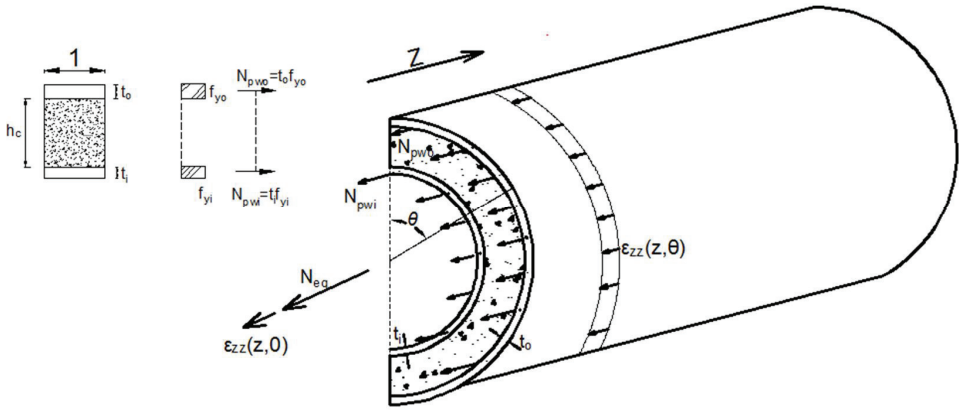

Figure 9-20: Correspondence Between N_{eq}, N_{pwi} and N_{pwo}

9.5.3 Equivalent Crushing Force

An estimate of the crushing resistance of the section can be obtained using a substitute section. The substitute section is chosen such that the resistance of its composite wall is identical to that of the true section. In that case:

$$a_o = D_o = 2R_o \tag{9-59}$$

$$a_i = D_i = 2R_i \tag{9-60}$$

The crushing strength can be evaluated by plastic analysis of the upper half of the substitute section. Because of the conditions of the problem (the bottom of the mechanism is not fully constrained horizontally), it is expected that the mechanism at collapse will be caused by joint rotations. When the lateral resistance of the section is reached, it deforms into the plastic mechanism shown on Figure 9-21. Equating external to internal works for the mechanism shown yield the following results for the collapse load:

$$P_{eq} = r_{crush} = \frac{8M_{pw}}{\bar{R}} \tag{9-61}$$

M_{pw} m_p being the unit moment capacity of the composite wall of both the CFDST and the substitute section.

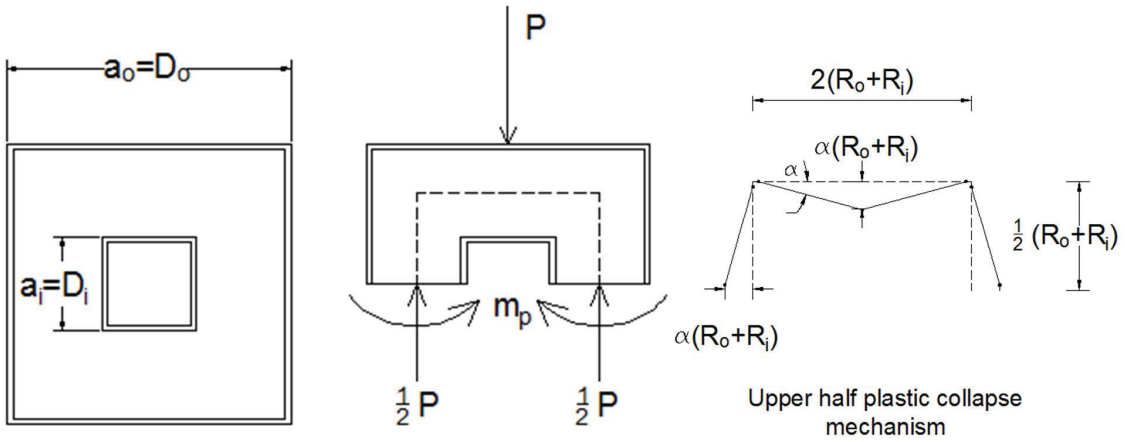

Figure 9-21: Equivalent Section Plastic Analysis

In determining M_{pw} the contribution of the concrete to the bending resistance of the wall is considered. Two cases need to be considered depending on the relative thicknesses on the tubes. For $f_{yo}t_o \geq f_{yi}t_i$, Figure 9-22 illustrates the situation, the equation giving the location of the plastic neutral axis, y_p and the unit bending resistance of the wall are respectively:

$$y_p = \frac{(2t_c + t_o) f_{yo} - f_{yi}t_i}{2f_{yo}}, \qquad f_{yo}t_o \geq f_{yi}t_i \tag{9-62}$$

$$M_{pw} = \frac{1}{2}\left(2y_p + t_i\right)t_i f_{yi} + \frac{1}{2}\left(2y_p + 2t_c + t_o\right)t_o f_{yo} \tag{9-63}$$

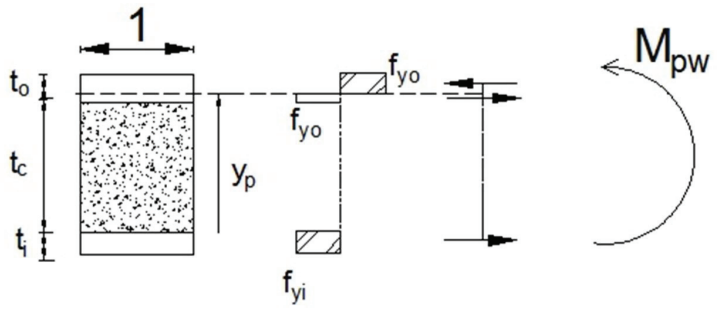

Figure 9-22: Stress Distribution in the Wall at Ultimate Capacity

Otherwise, based on Figure 9-23, the equations giving the unit bending resistance of the walls are:

$$y_p = t_c + \frac{f_{yo}t_o - f_{yi}t_i}{f_c^{'}}, \qquad f_{yo}t_o \le f_{yi}t_i \tag{9-64}$$

$$M_{pw} = \left(t_c + \frac{t_o + t_i}{2}\right)t_i f_{yi} + \frac{1}{2}\left(t_c - y_p + t_o\right)\left(t_c - y_p\right)f_c^{'} \tag{9-65}$$

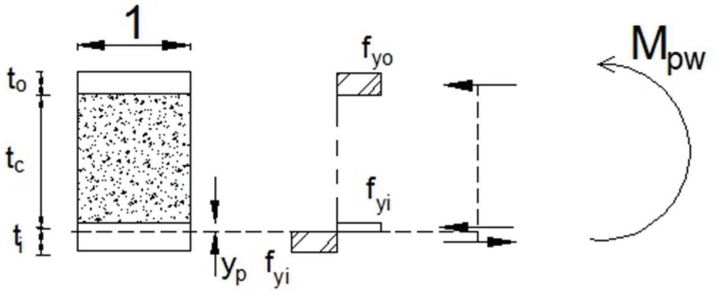

Figure 9-23: Stress Distribution in the Wall at Ultimate Capacity

Another estimate of the crushing resistance was sought out by considering the simple case of a thick composite ring subjected to a case of uniformly distributed hydrostatic pressure, p. Free-body diagrams of such ring components are shown in Figure 9-24. Because the composite wall of the ring is thick, equilibrium of the ring core must be expressed via the Lame's equations, whereas for the thinner ring shell simple equilibrium may be used. It is assumed that both shells have yielded and a uniform state of stress exists through their thicknesses (this is likely to be the case because the thickness of the tubes is small with respect to their diameter). Although the state of stress in the concrete core cannot be exactly determined; it can be assumed that, at the interface between the core and the inner tube, the ultimate strength of the concrete core is reached before collapse of the composite ring. This is also likely to be the case given that, in the Lame formulation, the principal stresses (circumferential and shear) are maximum on the inner face of a thick ring.

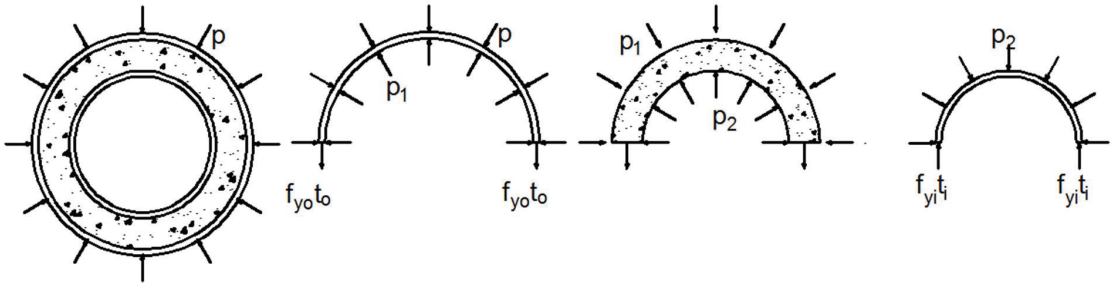

Figure 9-24: Free Body Diagrams of the Composite Wall Components

Writing the equilibrium of the inner tube gives:

$$p_2 = \frac{2t_i f_{yi}}{D_i} \tag{9-66}$$

Likewise, equilibrium of the outer tube leads to:

$$p = \frac{2t_o f_{yo}}{D_o} + p_1 \tag{9-67}$$

Using Lame's formula on the interface between the concrete core and the inner tube, gives:

$$\sigma_c = \frac{2p_1 d_1^2 - p_2\left(d_1^2 + d_2^2\right)}{d_1^2 - d_2^2} \tag{9-68}$$

Combining those equations leads to the following expression:

$$p = 2\frac{t_o f_{yo}}{D_o} + \frac{t_i f_{yi}}{D_i}\frac{\left(d_1^2 + d_2^2\right)}{d_1^2} + \frac{1}{2}\sigma_c \frac{\left(d_1^2 - d_2^2\right)}{d_1^2} \tag{9-69}$$

where, in the above four equations:

p is the characteristic collapse pressure of the CFDST (the hydrostatic pressure causing collapse of the composite thick ring),

p_1 is the radial pressure at the outside skin-core interface,

p_2 is the radial pressure at the inside skin-core interface,

t_o is the thickness of the outside tube,

t_i is the thickness of the inside tube,

f_{yo} is the minimum static yield stress of the outside tube in the circumferential direction,

f_{yi} is the minimum static yield stress of the inside tube in the circumferential direction,

D_o is the average diameter of the outside tube,

D_i is the average diameter of the inside tube,

d_1 is the outside diameter of the concrete core,

d_2 is the inside diameter of the concrete core,

σ_c is the stress at the inner face of the concrete core when both tubes have yielded circumferentially, taken here as equal to the 28-day compressive strength of the concrete $f_c^{'}$

The equivalent crushing resistance of the ring under hydrostatic loading can then be evaluated as:

$$P_{eq} = pD_o \tag{9-70}$$

This approach however was deemed more appropriate for a case where uniform pressure would prevail over the circumference of the CFDST and did not yield satisfactory results for the case at hand and has not been used thereafter.

9.5.4 Equivalent Axial Force

Estimation of the equivalent axial force requires the use of a hypothesized deformation field. As for the definition of the input energy, shape functions are used to characterize the deformation field which is written as:

$$w(z,\theta) = i(z)k(\theta)w(0,0) \tag{9-71}$$

where $i(z)$ and $k(\theta)$ are defined below, and $w(0,0)$ is the maximum dent of the cross-section.

$$i(z) = \cos^2 \frac{\pi z}{l} \tag{9-72}$$

$$\begin{cases} k(\theta) = 1 & -\frac{\pi}{2} \le z \le \frac{\pi}{2} \\ k(\theta) = 0 & elsewhere \end{cases} \tag{9-73}$$

Using these shape functions:

$$w(z,\theta) = \delta_0 \cos^2 \frac{\pi z}{l} \quad -\frac{l}{2} \le z \le \frac{l}{2},\ -\frac{\pi}{2} \le \theta \le \frac{\pi}{2} \tag{9-74}$$

Using this expression, Equation (9-58) is rewritten as:

$$\int_{-\pi/2}^{\pi/2} \left| \left(N_{pwi} R_i + N_{pwo} R_o \right) w_z(z,\theta)\, w_z(z,\theta) \right| d\theta = N_{eq} \left(\frac{2\pi}{l} \sin \frac{\pi z}{l} \cos \frac{\pi z}{l} \delta_0 \right)^2 \tag{9-75}$$

Introducing Equation (9-74) in Equation (9-75) and integrating lead to:

$$\left(N_{pwi} R_i + N_{pwo} R_o \right) \left(\frac{2\pi}{l} \sin \frac{\pi z}{l} \cos \frac{\pi z}{l} \delta_0 \right)^2 2 \int_{-\pi/2}^{0} d\theta = N_{eq} \left(\frac{2\pi}{l} \sin \frac{\pi z}{l} \cos \frac{\pi z}{l} \delta_0 \right)^2 \tag{9-76}$$

Hence:

$$N_{eq} = \pi \left(N_{pwi} R_i + N_{pwo} R_o \right) = \frac{\pi}{2} \left(N_{pwi} D_i + N_{pwo} D_o \right) \tag{9-77}$$

where:

$$\begin{cases} N_{pwi} = F_{yi} t_i \\ N_{pwo} = F_{yo} t_o \end{cases} \tag{9-78}$$

As for the crushing energy, substitution of Equation (9-74) and Equation (9-77) in Equation (9-57) leads to the simplified expression:

$$\int_{-l/2}^{l/2} N_{eq} w_x(z,0)\, w_x(z,0) dz = N_{eq} \frac{\pi^2}{2l} \delta_0^2 = \left(F_{yi} t_i R_i + F_{yo} t_o R_o \right) \frac{\pi^3}{2l} \delta_0^2 \tag{9-79}$$

9.5.5 Estimates of the Internal and Kinetic Energies

Using the results from Sections 9.5.3, the internal energy due to bending in the wall Equation (9-55) is further reduced to:

$$\int_{-l/2}^{l/2} P_{eq} w(z,0)\, dz = \frac{1}{2} P_{eq} l \delta_0 \tag{9-80}$$

Equation (9-80) can serve to estimate the dynamic bending energy of the composite ring with due considerations of strain rate effects. This is done by substituting the dynamic values of steel yield stress f_{dyo} and f_{dyi} for the outer and inner tubes respectively and concrete compressive strength ($f_{dc}^{'}$) to their static values in the expression of P_{eq} .

Now, combining Equations (9-80) and (9-79), the total internal energy in the dented region is given by:

$$W_{\text{int}}(l) = \frac{1}{2} P_{eq} l \delta_0 + \frac{1}{4} N_{eq} \frac{\pi^2}{l} \delta_0^2 \tag{9-81}$$

It can be assumed that during the deformation process, the CFDST element will deform in such a way that the internal energy is minimized and only a portion of the dented region is truly effective in dissipating the input energy. Equating the first derivative with respect to l of Equation (9-81) to zero gives:

$$\frac{\delta W_{\text{int}}(l)}{\delta l} = \frac{1}{2} P_{eq} \delta_0 - N_{eq} \frac{\pi^2}{4l^2} \delta_0^2 = 0 \tag{9-82}$$

which leads to a minimum at:

$$l_{\min} = \sqrt{\frac{N_{eq} \pi^2 \delta_0}{2 P_{eq}}} \tag{9-83}$$

Substituting $l_{\min}$ back into Equation (9-81) gives a simpler, yet dimensionally consistent, expression for the internal energy:

$$W_{\text{int}} = \pi \sqrt{\frac{N_{eq} P_{eq}}{2}} \delta_0^{3/2} \tag{9-84}$$

Similarly, a simplified expression for the kinetic energy can be obtained using Equation (9-53):

$$K = \frac{3\pi \alpha_o R_o^2 i_o^2}{4m} \sqrt{\frac{N_{eq} \pi^2 \delta_0}{2P_{eq}}} \tag{9-85}$$

9.5.5.1 Maximum Depth of the Dent: Application to the ECLIPSE and ERDC Tests

The final expressions for the kinetic and internal energies established, the dent depth can be estimated by equating the kinetic energy to the internal energy. This leads to the following expression for the dent depth:

$$\delta_0 = \frac{3\pi \alpha_o R_o^2 i_o^2}{4mP_{eq}} = \frac{3\pi \alpha_o D_o^2 i_o^2}{16mP_{eq}} \tag{9-86}$$

As expected the dent depth is inversely proportional to the collapse resistance of the CFDST and to its mass per unit length.

9.5.5.2 Application to the ECLIPSE and ERDC Tests

These equations were used to estimate the dent expected in the specimen during the tests. The principal results are presented in Table 9-4. Although variations exist between the calculated values and the experimentally observed values, the predictions are generally on the conservative

side. The denting depth is overestimated for about half of the specimens by more than 50% (see next to the last column in Table 9-4). For some of those specimens (B6, B7) for which the predicted dent is in excess of the inner tube diameter, fracture had occurred in the dented region. For the other half, the prediction and the measurement are generally in good agreement. If the former are considered outliers and are removed from the observations, the dent depth is predicted within 25% accuracy from specimen to specimen, and with 1% accuracy on average (see last column in Table 9-4).

Note that the formula over-predicts the dent depth on average more for specimen with lower void ratio and thicker composite wall (e.g. B1, B3, and B5). The predictions improve considerably for specimens with medium to high void ratios, with the exception of specimens for which fracture at the cross section level has been observed (e.g. B3, B6).

Table 9-4: Dent Depth Calculation for the Specimens Tested

	M_{pw}(kN-m/m)	i_o (MPa-msec)	*Peq (kN/m)* EQ (8-6)	δ_o (mm)	δ_{exp} (mm)	Ratio1	Ratio2
B1	87.45	54.28	1.38E+04	80.27	27.94	2.87	
B2*	120.41	34.47	1.79E+04	63.98	51.04	1.25	1.25
B3	219.96	46.64	2.77E+04	80.81	22.69	3.56	
B4*	185.45	48.15	2.57E+04	73.53	46.42	1.58	
B5	145.61	52.23	2.29E+04	46.63	22.35	2.09	
B6*	60.75	48.15	6.38E+03	309.46	73.66	4.20	
B7	85.52	45.28	8.30E+03	168.13	111	1.51	
B9	66.94	47.51	7.03E+03	48.05	49.21	0.98	0.98
B10	201.13	48.15	2.81+04	29	36.58	0.79	0.79
B11	158.03	48.15	1.67+04	29.19	32.51	0.90	0.90
B12	123.32	45.28	1.21E+04	99.78	90.25	1.11	1.11
					Average	1.90	1.01
					Deviation	1.06	0.29

*Second test on the specimen

The fact that the simplified method didn't consistently give accurate results but generally conservative ones is likely a consequence a simplifying assumption made in deriving the dent equation, where the cross-section was considered to be a thin ring. The thickness of the CFDST "ring" of concrete and steel provides a shear strength and stiffness against denting deformation that has been neglected in the above equations. This can be particularly significant for CFDST sections having smaller void ratios, for which the thickness of the composite ring can be significant, resulting in greater errors between measured denting values and predictions assuming thin ring theory. While the composite strength of the composite ring was considered in deriving the internal (bending and membrane) energy of the deforming cross section, the energy from shear may also be as significant (short beam theory). This may be further investigated in future research.

9.5.6 Extent of the Dent

The extent of the dent can also be estimated by determining the impulse (i_e) for which the response of a composite ring is purely elastic. In that case any axial deformation is ignored and the strain energy is due to the maximum lateral force working over the elastic deformation (δ_e):

$$E_s = \frac{1}{2} P_{eq} \delta_e \tag{9-87}$$

The energy transferred to a ring can be shown to be:

$$K = \frac{\pi \alpha_o R_o^2 i_e^2}{m} \tag{9-88}$$

The elastic deformation (δ_e) can be estimated using the expression developed by Timoshenko and Gere (1962) for a ring compressed between two opposite point loads acting along a same diameter:

$$\delta_e = \frac{P_{eq} \overline{R}^3}{4 E_w I_w} \frac{\pi^2 - 8}{\pi} \tag{9-89}$$

Where the ring is assumed fully composite with an average diameter $\overline{R}$ given by:

$$\overline{R} = \frac{1}{2}\left(R_o + R_i\right) \tag{9-90}$$

The bending stiffness $E_w I_w$ of the wall is estimated by summing the bending stiffness of its component:

$$E_w I_w = (EI)_s + (EI)_c \tag{9-91}$$

where $(EI)_s$ and $(EI)_c$ are respectively the bending stiffnesses of the steel shells and the concrete core. Therefore:

$$(EI)_s = \frac{E_s\left(R_o - R_i\right)^2\left(t_o + t_i\right) + 2\left(R_o - R_i\right)\left(t_o^2 + t_i^2\right)}{4\left(1-\mu_s^2\right)} \tag{9-92}$$

$$(EI)_c = \frac{E_c\left(R_o - R_i\right)^3}{12\left(1-\mu_c^2\right)} \tag{9-93}$$

By equating the strain energy to the kinetic energy, the impulse for which no dent forms in the CFDST wall is such that:

$$i_e = \sqrt{\frac{2mP_{eq}\delta_e}{\pi\alpha_o D_o^2}} \tag{9-94}$$

The distribution of impulse over the length of a target element can be obtained from the prediction of software such as BEL. The impulse predicted by Equation (9-94) can then be compared to that distribution to determine the point at which the impulse on the element falls below i_e. The extent of the dented region is twice the vertical distance between the center of the charge and the point at which the impulse on the element falls below i_e.

9.6 Response of CFDST Column Subjected to Blast Loading

9.6.1 Resistance Deflection Function and Maximum Response

The total lateral deformation of CFDST column can be seen as made of two components, one due to bending and the other one due to denting. Assuming that, the two processes occur simultaneously, but can be decoupled, the total lateral deformation of a CFDST under blast loading can be written as:

$$X_u = X_m + \delta_o \tag{9-95}$$

For load which does not induce denting of the cross-section, the cross section will be able to develop its maximum strength and the global mechanism of deformation of the column will be similar to what has been observed for CFST under blast loading. As a consequence the resistance deflection function can be built assuming that the full plastic capacity of the sections develops at the hinge location. It can be shown that the lateral ultimate resistance of the column, r_u, under blast load is a direct function of the moment capacity of the cross section. The resistance-deflection (Figure 9-25) in that case can be approximated by a bilinear relation with an initial elastic range and a plateau at yield. The corresponding maximum deformation can be estimated using the impulse equation for impulsive loading and the appropriate shape factor reduction as found in Fujikura and Bruneau (2007):

$$X_m = \frac{1}{2}\left[\frac{I_{eq}^2}{K_{LM} m r_u} + X_E\right] \tag{9-96}$$

$$I_{eq} = \beta D_o i_{eq} \tag{9-97}$$

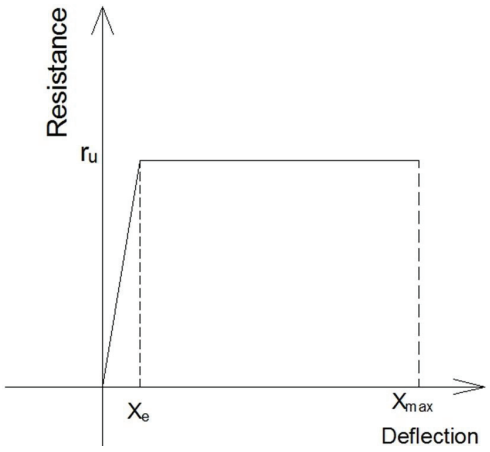

Figure 9-25: Resistance Deflection Function for CFDST without Denting

As the column deforms in the plastic range, a three-hinge mechanism forms and the maximum lateral resistance, r_u, of the column can be determined based on SDOF treatment. For the configuration of the ECLIPSE and the ERDC tests, it can be shown that this resistance as a function of the plastic moment capacity, M_p, and the length L of the CFDST is calculated as:

$$r_u = \frac{28.8 M_p}{L^2} \tag{9-98}$$

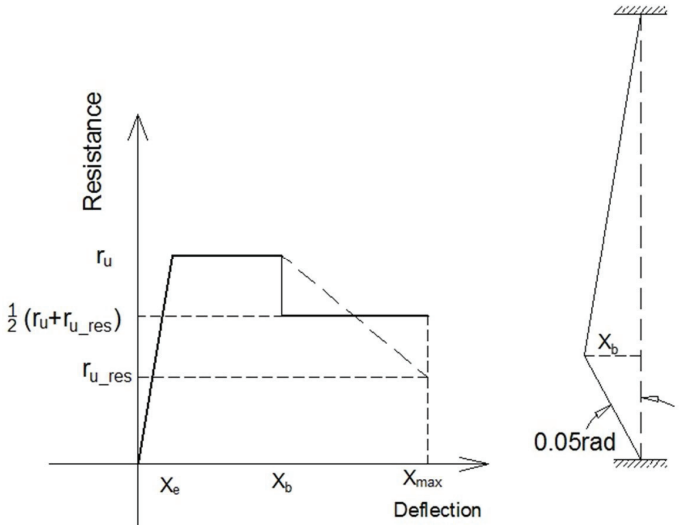

Figure 9-26: Resistance Deflection Function for CFDST Considering Denting

Passed a threshold, deformation of the specimen can no longer take place without cross section denting. At this point the lateral resistance of the tube diminishes until it reaches a residual value, r_{u_res} which is a function both of the reduced moment capacity and the plastic moment capacity. If we assume that the decrease in strength is progressive a possible resistance deflection function for denting at the local level is given by Figure 9-26, in which the dashed

sloping line represents the reduction in bending resistance due to denting. The reduced lateral resistance is a function of the reduced capacity of the dented section. Using a three hinged mechanism, as shown in the insert of Figure 9-26 and assuming that a dented CFDST column maintains its full capacity at the top while a reduced moment capacities exist at the height of burst (HOB) and at the base of the column and are designated by M_{r1} and M_{r2}, it can be shown using plastic analysis that the residual resistance is:

$$r_{u\_res} = \frac{12M_p + 72M_{r1} + 60M_{r2}}{5L^2} \tag{9-99}$$

Substituting the result obtained in Section 9.4.3.2 and taking $M_{r1} = M_{r2}$, Equation (9-99) becomes:

$$r_{u\_res} = \frac{M_p}{5L^2}\left(144 - 132\frac{\delta}{R_o}\right) = r_u - \frac{132M_p}{5L^2}\frac{\delta}{R_o} \tag{9-100}$$

It can be verified that when denting is not expected, Equation (9-100) reduces to Equation (9-98). The transition between the maximum resistance and the residual resistance of the section must be defined for the resistance deflection to be fully characterized. Based on the results obtained for CFDST which during test deformed without denting and reached support rotation slightly above 0.05rad, it was decided to use the lateral deformation corresponding to this rotation as a transition point as illustrated in the right insert of Figure 9-26.

The sloping dotted line of the resistance deflection function showed on Figure 9-26 can be replaced by a solid straight line invoking equal energy. In that case an intermediate resistance r_{u1}

which is the average of the residual resistance and the plastic resistance of the section can be defined as in Equation (9-101).

$$r_{u1} = \frac{1}{2}\left(r_u + r_{u\_res}\right) \tag{9-101}$$

With the later result, the total deformation, X_m, of CFDST columns for which indentation is expected, can be calculated by equating the impulse (kinetic) energy to the energy of deformation of the system.

$$\frac{I_{eq}^2}{2K_{LM}m} = \frac{1}{2}r_u X_E + r_u\left(X_b - X_E\right) + r_{u1}\left(X_m - X_b\right) \tag{9-102}$$

Solving for X_m yields:

$$X_m = \frac{I_{eq}^2}{2K_{LM}mr_{u1}} - \frac{r_u}{r_{u1}}\left(X_b - \frac{1}{2}X_E\right) + X_b \tag{9-103}$$

where:

$$X_E = \frac{r_u}{K_{eq}} \tag{9-104}$$

Equation (9-103) reduces to (9-96) when denting of the section is not expected.

9.6.2 Application to the ECLIPSE and ERDC Tests

The equations derived in this section were used to estimate deformation for the specimens tested. When no denting of a specimen was observed experimentally, either Equation (9-96) or (9-103) were used to determine the global deformation assuming the dent depth is zero and using a shape factor of 0.45. When denting was of interest, only Equation (9-103) was used. Elastic rebound was considered in calculating the bending deformation for undented section, whereas,

for the dented specimen, it was considered negligible as the elastic stiffness of a dented section would be severely reduced, thus diminishing its capacity to rebound.

Table 9-5 presents the results for sections for which no dent was visible after the tests. The agreement for the usual value of the shape factor is not good. However, if rebound is ignored and the maximum deformation (X_m) is estimated using Equation (9-96), the agreement improved. One possible explanation for this behavior is that due the shock load, deformation of the inner tube may have occurred (this could not be observed because the specimens in question were tested a second time). If this was the case, then rebound of the specimen may have been significantly smaller than the one predicted by the elastic deformation or negligible altogether.

Table 9-5: Deformation Calculation for Undented Specimens

	M_p (kN-m/m)	i_{eq} (MPa-msec)	β	r_u (kN/m)	X_e (mm)	X_m (mm)	X_m- X_e (mm)	X_{exp} (mm)
B2	33.19	8.93	0.45	411.59	11.84	17.78	**5.94**	**21.00**
B4	60.439	10.12	0.45	749.44	10.84	22.30	**11.46**	**17.50**
B6	64.55	7.94	0.45	800.35	8.74	11.17	**2.43**	**12.50**

In Table 9-6, calculations of the deformation due to bending (X_m) and global deformation (X_u) for each specimen have been carried out. When all data points are included, the total deformation of the specimen seems conservatively estimated. However, the results from B6 and B7 for which cross section fracture has been observed need to be interpreted with caution. If those two data points are excluded from the data set, a clearer picture emerges. From the last column in Table 9-6, it can be seen that, on average, aggregating the predictions for the dent and the maximum bending deformation will yield satisfactory estimate of the overall deformation of a specimen.

Table 9-6: Deformation Calculation for Dented Specimens

	M_p (kN-m)	i_{eq} (MPa-msec)	β	δ_o (mm)	r_u (kN/m)	r_{u_res} (kN/m)	X_e (mm)	X_m (mm)	X_u (mm) $\delta_{o+} X_m$	X_{exp} (mm)	Ratio1	Ratio2
B1	27.36	12.42	0.45	**80.27**	339.22	287.39	10.135	**49.83**	**130.1**	111	1.17	1.17
B2*	33.19	12.42	0.45	**63.98**	411.59	168.98	11.84	**37.93**	**101.91**	112	0.91	0.91
B3	69.82	8.76	0.45	**80.81**	865.8	234.54	8.2	**19.276**	**89.01**	73	1.22	1.22
B4*	72.91	12.42	0.45	**73.53**	749.44	144.72	10.17	**24.41**	**97.94**	109	0.90	0.90
B5	43.95	12.42	0.45	**46.63**	545	239.26	11.31	**23.85**	**70.48**	76	0.93	0.93
B6*	64.54	13.67	0.45	**309.46**	800.35	0	9.64	**147.66**	**457.12**	162.5	2.81	-
B7	71.72	10.69	0.45	**168.13**	895.33	0	7.224	**19.6**	**187.73**	116	1.62	-
B9	38.1	10.95	0.45	**62.74**	472.38	113.636	9.57	**29.62**	**92.36**	114.3	0.81	0.81
B10	63.81	10.94	0.45	**36.87**	791.282	467.7	12.2	**18.18**	**55.05**	76.2	0.72	0.72
B11	88.57	9.18	0.45	**28.21**	1098.24	816.324	6.06	**14.2**	**36.46**	37.59	0.97	0.97
B12	97.17	10.69	0.45	**99.78**	1204.94	110.5	6.43	**10.08**	**109.86**	127	0.87	0.87
										Average	1.17	0.94
										Deviation	0.55	0.14

*Corrected for residual deformation from previous tests

9.7 Summary

This section considered different aspects of the behavior of CFDST and MSJC columns under blast loading. The vibration characteristics of CFDST subjected to hammer test were derived and compared against estimates of those properties, showing good correlation between the experimentally measured values and their theoretical estimates. Also, using shorting pin assemblies, a methodology to determine the load imposed on the specimens by blast loading during experiments was presented.

Equations were also derived to approximate the geometry of dented CFDST sections. However, because of the complexity of the deformation at the cross section level of CFDST exposed to blast loading, closed form equations to calculate the reduced capacity of those sections could not

be directly derived using this approximate geometry. As a proxy, a substitute section approach was used to establish approximately how denting of the cross section affects its flexural capacity. Because of the importance of denting in the deformation process of CFDST, a closed form solution to predict denting at the cross section level was presented. Conservative estimates were generally obtained, particularly for section with thick composite wall and low void ratio (possibly because shear stiffness and strength of the cross section was neglected).

Finally, by aggregating the deformation at the local level (dent) and the global bending deformation of the dented column, good estimates of the overall specimen deformation could be obtained.

SECTION 10

CONCLUSIONS

10.1 Summary

A proposed paradigm to protect bridges exposed to multiple hazards calls for a system approach in which one structural concept combines features that provide sufficient performance against each design basis hazard. Steel-concrete-steel "sandwich" construction (SCS) possesses many qualities making them suitable to multiple hazard protection applications. Concrete-filled double skin tubes (CFDST) and modified steel jacketed (MSJC) bridge columns are two such concepts proposed in this research. Both were considered as candidate multi-hazard systems for bridge applications.

For new bridge construction, performance of CFDST in a bi-hazard framework of analysis consisting of earthquake and blast loading was investigated (as an alternative to reinforced concrete or CFST columns). For existing non-ductile bridge reinforced concrete columns presenting deficiencies under earthquake loading (lack of ductility and shear resistance) that have been steel jacketed as a prior seismic retrofit but that still lack the direct shear resistance needed to resist blast loading, MSJC were proposed to effectively correct the observed deficiencies without altering the intended flexural behavior.

Numerical analysis, cyclic tests, and blast tests conducted as part of the research reported here showed that CFDSTs (as a type of sandwich construction) possess structural features that warrant their consideration as multi-hazard bridge pier columns. In particular, CFDSTs possess good energy dissipation capacity, are ductile under both earthquake and blast loads, and preserve their strength up to failure. When emphasis is on seismic and blast resistant design, the resulting

composite section is lighter than a reinforced concrete section of comparable strength and results in slimmer yet more ductile columns. The reduction in mass is desirable for seismic application whereas the slimmer column translates into lesser surface to be exposed to blast overpressures. In blast resistance design, local denting of CFDST section was observed as an additional energy dissipation mechanism.

Experimental work on MSCJ showed that the addition of an anchored collar around the top and the base of the jacket can be an effective strategy. Large flexural deformations were achievable during blast test of the MSCJ, and direct shear failure was prevented. One instance of a weld "unzipping" failure was observed however at the seam on one of the specimen, due to what is believed to be faulty fabrication.

Collecting data in the fireball during blast loading has long been a challenge. In this research, the use of shorting pins has permitted the measurement of specimen velocity, from which blast impulse history has been derived.

Analytical solutions for CFDST subjected to static, cyclic and inelastic loading have been developed and compared against experimental data gathered in the literature and generated in this research. Design equations for sizing CFDST and CFST under combination of loadings have also been derived.

Solutions for the reduced moment capacity of dented CFDST have been developed to facilitate plastic analysis and prediction of deformation during blast events. Equations to predict denting of CFDST section have also been proposed with results correlating particularly well for CFDST with large void ratio. For MSJC, design equations for sizing the collars and its connections were derived using plastic analysis and available procedures for cast-in place anchors.

10.2 Conclusions

CFDST and MSJC bridge column have been investigated as promising multi-hazard resistant concepts for new and existing columns respectively. Multi-hazard bridge piers built using such columns were analyzed, built, and tested at quarter scale under quasi-static and dynamic loading. Some key findings of this research program are as follows:

1. CFDST do provide enhanced protection against blast and earthquake loading. In cyclic tests, the energy dissipation capacity of CFDST was shown to be excellent and stable. In near contact blast tests, CFDST specimens were able to sustain the maximum credible blast scenario without adverse reduction in strength. For extreme blast events, local denting of CFDST and failure of the outside tube were observed. In such situations, the presence of the inner tube in CFDST serves as a dowel that effectively prevents direct shear failure of the section. This is an important improvement compared to CFST tested for the same blast scenario.
2. One multi-hazard benefit of CFDST is that blast resistance can be obtained, even if just designed for seismic resistance ("bundling" benefit), and vice-versa.
3. Advanced non-linear finite element models can reproduce fairly well the behavior of CFST and CFDST under cyclic and blast loading.
4. Under cyclic loading, it was shown that cantilevered CFDST columns with moderately ductile outer tube and highly ductile inner tube could reach plastic rotation well above 7% drift (0.07 rad approximately), which is similar to what has been established for CFST. However, when both the outside and the inner tubes were highly ductile, section

rotation of up to 0.12 rads were achievable at the base of the specimen, meaning deformation twice as large were reached at the point of maximum deformation.

5. Under blast loading, section rotations of CFDST of 0.05 rad were observed without local denting. Denting accompanied by section rotation of up to 0.239 rad was achieved if fracture of a moderately ductile outside tube was not observed (specimen B3). For highly ductile outer tubes, denting of the section could lead to average rotation at the base in excess of 0.40 rad (average of specimen B9, B10, B11 and B12) without any fracture.
6. In MSJC, providing SJC with collar both at the top and the bottom effectively changes the failure mechanism of SJC under blast loading from brittle direct shear failure to ductile flexural failure. While in previous tests. SJC would typically fail in direct shear, section flexural rotation of up to 0.18 rad was obtained at the base of MSJC.
7. Design equations for CFDST in flexure or in combined flexure and axial loading produced conservative estimates even when slender sections were considered. Furthermore a simple equation was established for preliminary sizing of CFDST under combined flexure and axial loading.
8. The proposed design equations for denting, and denting combined with bending of CFDST, are conservative on average. In particular, correlation of the denting equation for CFDST with large void ratio (40% or above) was excellent, while for lower void ratio the correlation was poor, but giving conservative predictions. This is because the proposed formulation does not take shear stiffness into account.

10.3 Recommendations for Further Studies

As interest on multi-hazard design grows, CFST and CFDST are increasingly appealing solutions. As a consequence, advancing knowledge on their behavior under different regimes of loading is key to their adoption in multi-hazard applications. The following items are suggested possible further research on these structural systems:

1. Modeling of blast structure interaction for CFDST and MSJC subjected to blast loading is needed to help optimize design parameters for both systems.
2. Investigation of alternative instrumentation techniques to quantify real-time dynamic response of bridge piers under blast and impulsive loading is needed.
3. Investigation of the importance of scale effect on the performance of CFDST and MSCJ is desirable, and could be addressed by conducting ½-scale or full scale tests on both systems. In particular, for larger scale CFDST, the composite wall is expected to be stronger. Since the current research has related denting to the resistance of the composite wall of CFDST, and because the charge weight has been scaled to yield similar pressure and impulse as for the full scale situation, dent depth is not expecting to scale up accordingly.
4. Investigation of the effectiveness of adding passive infill material such as sand or other materials in the void of CFDST is an option worth considering to prevent cross-section distortion at extremely close scaled distances and improve energy dissipation capacity.
5. Additional blast tests are desirable on CFDST and dowel reinforced CFST to investigate resistance to contact charges as well as shear resistance at footing when column rotation capability is exceeded.

6. Research could investigate CFST columns with self-centering capacity added by prestressing the inner core and introducing hinge types support at the extremities for multi-hazard applications.
7. Future research investigations could also investigate the effectiveness of Engineered Cementitious Concrete (ECC) (a.k.a. “bendable concrete” or “ultra-high performance fiber reinforced concrete”) for enhanced ductile concrete plastic flow in CFST and CFDST.

SECTION 11

REFERENCES

AASHTO. (2010). *AASHTO LRFD Bridge Design Specifications* (5th ed.). Washinton, DC: AASHTO.

ACI. (1992). *Standard Practice for Selecting Proportions for Normal, Heavyweight, and Mass Concrete*. Detroit, MI: American Concrete Insitute.

ACI. (2011). *Building Code Requirements for Structural Concrete and Commentary*. Detroit, MI: American Concrete Institute.

AISC. (2010). *Seismic Provisions for Structural Steel Buildings*. Chicago, IL: AMERICAN INSTITUTE OF STEEL CONSTRUCTION.

AISC. (2010). *Specification for Structural Steel Buildings*. Chicago, IL: American Institute of Steel Construction.

API. (1989). *Draft Recommended Practice for Planning, Designing and Constructing Fixed Offshore Platforms- Load and Resistance Factor Design*. Washington, D.C: American Petroleum Institute.

ASCE. (1999). *Structural Design for Physical Security*. Reston, VA: Task Committee on Structural Design for Physical Security of the Structural Engineering Institute of ASCE.

ASCE. (2010). *Design of Blast-Resistant Buildings in Petrochemical Facilities* (2nd ed.). Reston, VA: Task Committee on Blast-Resistant Design of the Petrochemical Committee of the Energy Division of ASCE.

ASCE/JSCE. (2011). *Tohoku Tsunami Survey*.

Baker, W., Cox, P., Westine, P., Kulesz, J., & Strehlow, R. (1983). *Explosion hazards and evaluation*. New York, NY: Elsevier Scientific Publishing Company.

Biggs, J. M. (1964). *Introduction to Structural Dynamics*. New York: McGraw-Hill.

Bowerman, H., Coyle, N., & Chapman, J. C. (2002). An Innovative Steel/Concrete Construction System. *Structural Engineering, 80*(20), 33-38.

Bowerman, H., Gough, M., & King, C. (1999). *Bi-Steel Design and Construction Guide*. London,UK: British Steel Ltd.

Brode, H. (1955). Numerical solutions of spherical blast waves. *J. Applied Phys, 26*, 766-766.

Bruneau, M., Uang, C. M., & Sabelli, R. (2011). *Ductile Design of Steel Structures* (2nd ed.). New York, NY: McGraw-Hill Professional.

Bulson, P. (2003). *Explosive Loading of Engineering Structures: A history of research and a review of recent developments*. Taylor & Francis e-Library.

Burgan, B. (1998). *Double Skin Composite Construction for Submerged Tube Tunnels*. Berkshire, UK: The Steel Construction Institute.

Burgan, B. A. (2011). A Concrete History. *Nuclear Engineering International*.

Chai, Y., Priestley, M., & Seible, F. (1991). Seismic Retrofit of Circular Bridge Columns for Enhanced Flexural Performance. *ACI Structural Journal, 88,*(5), 572-484.

Chen, W., & Duan, L. (1999). *Bridge Engineering Handbook*. Boca Raton, FL: CRC Press.

Conrath, E., Krauthammer, T., Marchand, K., & Mlakar, P. (1999). *Structural Design for Physical Security: State of the Practice*. Reston, VA: ASCE.

Cormie, D., Mays, G., & Smith, P. (2009). *Blast effects on buildings* (2nd ed.). London, UK: Thomas Telford.

Cranz, C. (1926). *Lehburg der Ballistik.* Berlin: Springer.

Davis, K. L., & Meyer, J. (1979). *Vulnerability of Bridge Piers to Conventional Munitions.* Vickbursg, MS: Structures Laboratory US Army Engineer Waterways Experiment Station.

DoD. (2008). *Structures to Resist the Effects of Accidental Explosions (UFC-3-340-02).* Washington, DC: Unified Facilities Criteria Program.

Dusenberry, D. (2010). *Handbook for Blast Resistant Design of Buildings.* Hoboken, NY: John Wiley and Sons, Inc.

Ettouney, M., Alampalli, S., & Agrawal, A. (2005). Theory of multihazards in bridge engineering. *New York City Bridge Conf., Bridge Engineer Association.* New York.

FEMA. (2004). Design Guide for Improving School Safety in Earthquakes, Floods, and High Winds. FEMA.

FHWA. (1997). *Seismic Design of Bridges - Design Example No. 2: Three-Span Continuous Steel Girder Bridge.* Washington, DC: Federal Highway Administration.

FHWA. (2003). *Recommendations for Bridges and Tunnel Security* . Washington, DC: Prepared by the Blue Ribbon Panel on Bridge and Tunnel Security.

FHWA. (2006). *Seismic Retrofitting Manual for Highway Structures: Part 1-Bridges.* McLean, VA: FHWA.

Foundoukos, N., Xie, M., & Chapman, J. (2007). Fatigue Tests on Steel–Concrete–Steel Sandwich Components and Beams. *Journal of Constructional Steel Research, 63*(7), 922–940.

Fujikura, S., & Bruneau, M. (2008). *Experimental and Analytical Investigation of Blast Performance of Seismically Resistant Bridge Piers.* Amherst,NY: MCEER.

Fujikura, S., Bruneau, M., & Lopez-Garcia, D. (2007). *Experimental Investigation of Blast Performance of Seismically Resistant Concrete-Filled Steel Tube Bridge Piers.* Buffalo, NY: MCEER.

Furlong, R. (1968). Design of Steel-Encased Concrete Beams Columns. *Journal of the Structural Division, 94*(1), 267–281.

Gardner, N. J., & Jacobson, E. R. (1967). Structural Behavior of Concrete Filled Steel Tubes. *Journal of the American Concrete Institute, 64*(11), 404-413.

Glasstone, S., & Dolan, P. (1977). *The Effects of nuclear weapons.* U.S. Government Publication.

Goode, C. D., & Fatheldin, Y. T. (1980). Sandwich Cylinders (Steel-Concrete-Steel) Subjected to External Pressure. *ACI Journal, 77*(2), 109-115.

Goode, C. D., Montague, P., & Nash, T. (1996). Large Reinforced Concrete Cylinders under External Pressure. *Proceedings of the Institution of Civil Engineers, 116*(2), 163- 173.

Goode, C., & Shukry, M. (1988). Effect of Damage on Composite Cylinders Subjected to External Pressure. *Structural Journal, 85*(4), 405-413.

Han, L. H., H., H., Tao, Z., & Zhao, X. (2006). Concrete-Filled Double Skin Steel Tubular (CFDST) Beam–Columns Subjected to Cyclic Bending. *Engineering Structures, 28*(12), 1698–1714.

Hopkinson, B. (1915). British Ordnance Board Minutes 13565.

Huang, Y., & Mahin, S. (2008). A Cyclic Damaged Plasticity Model: Implementation and Applications. Dearborn, Michigan: 10th International LS-DYNA User's Conference.

Hyde, D. (2013). DPlot Graph Software. Vicksburg, Mississippi: HydeSoft Computing.

J_BEC. (2011). *Damage to Highway Bridges Caused by the 2011 Tohoku-Oki Earthquake.* JAPAN BRIDGE ENGINEERING CENTER.

Johansson, M., & And Gylltoft, K. (2002). Mechanical Behaviour of Circular Steel-Concrete Composite Stub Columns. *Journal of Structural Engineering, 128*(8), 1073-1081.

Kilpatrick, A. E., & Rangan, B. V. (1997). *Tests on high-strength composite concrete columns.* Perth, Australia: Curtin University of Technology.

Krauthammer, T. (2008). *Modern Protective Structures.* Boca Raton, FL: CRC Press.

Lan, S., Lok, T. S., & L., H. (2005). Composite structural panels subjected to explosive loading. *Construction and Building Materials, 19*(5), 387–395.

Lin, M. L., & Tsai, K. C. (2001). Behavior of Double-Skinned Composite Steel Tubular Columns Subjected to Combined Axial and Flexural Loads. Pusan, Korea: First International Conference on Steel and Composite Structures.

LSTC. (2014). *LS-DYNA Keywords User's Manual.* Livermore, CA: Livermore Software Technology Corporation.

Lu, Y., & Kennedy, D. (1994). Flexural Behaviour of Concrete filled Hollow Structural Sections. *Canadian Journal of Civil Engineering, 21*(1), 111-130.

Malvar, J. L., & Simons, D. (1996). Concrete Material Modeling in Explicit Computations. Glendale, CA.: Karagozian and Case .

Marsh, M. L., Mayes, R. L., & Friedland, I. M. (2001). *Recommanded LRFD Guidelines for the Seismic Design of Highway Bridges*. Retrieved March 1, 2014, from http://www.abam.com/sites/default/files/tech-papers/tp-RecommendedLRFDGuidelines.pdf

Marson, J., & Bruneau, M. (2000). *Cyclic Testing of Concrete-Filled Circular Steel Tube Bridge Columns Having Encased Fixed Base Detail.* Ottawa, Canada: Department of Civil Engineering, University of Ottawa.

Mays, G., & Smith, P. (1995). *Blast effects on buildings* (1st ed.). London, UK: Thomas Telford.

MCEER. (2007). *Leading Experts Present Emerging Developments in Multi-Hazard Engineering at AEI-MCEER Symposium*. Retrieved March 1, 2014, from http://mceer.buffalo.edu/meetings/AEI/default.asp

MCEER. (2008). *Damage to Engineered Bridges from Wind, Storm Surge and Debris in the Wake of Hurricane Katrina.*

MCEER. (2008). *Design of Highway Bridges Against Extreme Hazard Events: Issues, Principles and Approaches.* Buffalo,NY: MCEER.

McKinley, B., & Boswell, L. (2002). Behaviour of Double Skin Composite Construction. *Journal of Constructional Steel Research, 58*, 1347–1359.

Mills, C. A. (1987). The design of concrete structure to resist explosions and weapon effects. Edinburgh, UK: Proceedings of the 1st Intl. Conf. On concrete for hazard protections.

Montague, P. (1975). Simple Composite Construction for Cylindrical Shells Subjected to External Pressure. *Journal of Mechanical Engineering Science, 17*(2), 105-113.

Montague, P. (1978). The experimental behavior of double-skinned, composite, circular cylindrical shells under external pressure. *Mech. Engrg. Sci., 20*(1), 21-34.

Montague, P. (1979). The theoretical behavior of steel-concrete circular cylindrical shells subjected to external pressure. *Proc., Insf. of Civ Engrg., 67*, 483-499.

Montague, P. (1986). Composite vessels for deepwater operation: the influence of shell strength and severe damage. *Proc., Insf. of Civ. Engrs., 81*(6), 191-219.

Montague, P., & Choo, S. (1981). Double-Skin Construction Of Large Pressure Vessels For Sub-Sea Systems. Houston, TX: Offshore Technology Conference.

Nash, T., & Montague, P. (1984). The strength-instability interaction of double-skinned composite circular shells under external pressure. *Proc., Insf. of Mech. Engrs., 16*, 293-301.

Newmark, N., & Hansen, R. (1961). *Design of blast resistant structures, Shock and Vibration Handbook* (3rd ed.). New York, NY: McGraw-Hill.

Oduyemi, T., & Wright, H. (1989). An experimental investigation into the behaviour of double-skin sandwich beams. *Journal of Constructional Steel Research, 14*(3), 197-220.

Owens, R. H., & Symonds, P. S. (1954). *Plastic Deformations of a Free Ring under Concentrated Dynamic Loading*. Providence, RI: Brown University.

Priestley, M. J., Seible, F., & Calvi, G. M. (1996). *Seismic Design and Retrofit of Bridges*. New York: Wiley.

Ray, J., Armstrong, B., & Slawson T. R. (2003). Airblast Environment Beneath a Bridge Overpass. *Transportation Research Record: Journal of the Transportation Research Board, 1827*(Highway Pavements and Structures Maintenance and Security), 63-68.

Roik, K., & Bermann, R. (1989). *Eurocode No.4: Composite columns*. University of Bochum.

Rust, W., & Schweizerhof, K. (2003). Finite Element Limit Load Analysis of Thin-Walled Structures by ANSYS (Implicit), LS-DYNA (Explicit) and in Combination. *Thin-Walled Structures, 41*(2-3), 227-244.

Salani, H. R., & Sims, J. R. (1964). Behavior of Mortar Filled Steel Tubes in Compression. *Journal of American Concrete Institute, 61*(10), 1271–1283.

Sewel, J. S. (1902). Columns for buildings. *Engineering News, 48*(17), 36–39.

Shakir-Khalil, H. (1991). Composite Columns of Double-Skinned Shells. *Journal of Constructional Steel Research, 19*(2), 133-152.

Shanmugam, N., Kumar, G., & Thevendran, V. (2002). Finite element modeling of double skin composite slabs. *Finite Elements in Analysis and Design, 38*(7), 579–599.

Smith, J. (2003). *Anti-Terrorism: Criteria, Tools & Technology*. Retrieved May 1, 2014, from http://www.protectiveglazing.org/resources/Anti-Terrorism%20-%20Criteria,%20Tools%20and%20Technology.pdf

Smith, P., & Hetherington, J. (1994). *Blast and Ballistic Loading of Structures*. Oxford, UK: Butterworth Heinemann.

Tao, Z., Han, L. H., & Zhao, X. L. (2004). Behaviour of concrete-filled double skin (CHS inner and CHS outer) steel tubular stub columns and beam–columns. *Journal of Constructional Steel Research, 60*(8), 1129–58.

Tomlinson, M., Tomlinson, A., Chapman, M., Jefferson, A., & H.D., W. (1989). Shell Composite Construction for Shallow Draft Immersed Tube Tunnels. Manchester, UK: Proceedings of the ICE international conference on immersed tube tunnel techniques.

USDA. (1986). *TM 5-855-1: Fundamentals of Protective Design for Conventional Weapons.* Washington, DC: US Department of the Army, Navy, and Air Force.

USDA. (1990). *TM1300: The Design of Structures to Resist the Effects of Accidental Explosions.* Washington, DC: US Department of the Army, Navy, and Air Force.

Wei, S., Mau, S. T., Vipulanandan, C., & Mantrala, S. K. (1995). Performance of new sandwich tube under axial loading: experiment. *Journal of Structural Engineering, 121*(12), 1806–14.

Weidlinger, P. (1994). Civilian Structures: Taking the Defensive. *Civil Engineering, 64*(11), 48-50.

Wierzbicki, T., & Hoo Fatt, M. S. (1993). Damage assessment of cylinders due to impact and explosive loading. *International Journal of Impact Engineering, 13*(2), 215-241.

Winget, D. G., Marchand, K. A., & Williamson, E. (2005). Analysis and Design of Critical Bridges Subjected to Blast Loads. *Journal of Structural Engineering, 131*(8), 1243-1255.

Wright, H. D., Oduyemi, T. O., & Evans, H. R. (1991). The Experimental Behaviour of Double Skin Composite Elements. *J. Constructional Steel Research, 19*, 97-110.

Xie, M., & Chapman, J. (2005). Static and fatigue tensile strength of friction-welded bar–plate connections embedded in concrete. *Journal of Constructional Steel Research, 61*(5), 651–73.

MCEER Technical Reports

MCEER publishes technical reports on a variety of subjects written by authors funded through MCEER. These reports are available from both MCEER Publications and the National Technical Information Service (NTIS). Requests for reports should be directed to MCEER Publications, MCEER, University at Buffalo, State University of New York, 133A Ketter Hall, Buffalo, New York 14260. Reports can also be requested through NTIS, P.O. Box 1425, Springfield, Virginia 22151. NTIS accession numbers are shown in parenthesis, if available.

NCEER-87-0001 "First-Year Program in Research, Education and Technology Transfer," 3/5/87, (PB88-134275, A04, MF-A01).

NCEER-87-0002 "Experimental Evaluation of Instantaneous Optimal Algorithms for Structural Control," by R.C. Lin, T.T. Soong and A.M. Reinhorn, 4/20/87, (PB88-134341, A04, MF-A01).

NCEER-87-0003 "Experimentation Using the Earthquake Simulation Facilities at University at Buffalo," by A.M. Reinhorn and R.L. Ketter, not available.

NCEER-87-0004 "The System Characteristics and Performance of a Shaking Table," by J.S. Hwang, K.C. Chang and G.C. Lee, 6/1/87, (PB88-134259, A03, MF-A01). This report is available only through NTIS (see address given above).

NCEER-87-0005 "A Finite Element Formulation for Nonlinear Viscoplastic Material Using a Q Model," by O. Gyebi and G. Dasgupta, 11/2/87, (PB88-213764, A08, MF-A01).

NCEER-87-0006 "Symbolic Manipulation Program (SMP) - Algebraic Codes for Two and Three Dimensional Finite Element Formulations," by X. Lee and G. Dasgupta, 11/9/87, (PB88-218522, A05, MF-A01).

NCEER-87-0007 "Instantaneous Optimal Control Laws for Tall Buildings Under Seismic Excitations," by J.N. Yang, A. Akbarpour and P. Ghaemmaghami, 6/10/87, (PB88-134333, A06, MF-A01). This report is only available through NTIS (see address given above).

NCEER-87-0008 "IDARC: Inelastic Damage Analysis of Reinforced Concrete Frame - Shear-Wall Structures," by Y.J. Park, A.M. Reinhorn and S.K. Kunnath, 7/20/87, (PB88-134325, A09, MF-A01). This report is only available through NTIS (see address given above).

NCEER-87-0009 "Liquefaction Potential for New York State: A Preliminary Report on Sites in Manhattan and Buffalo," by M. Budhu, V. Vijayakumar, R.F. Giese and L. Baumgras, 8/31/87, (PB88-163704, A03, MF-A01). This report is available only through NTIS (see address given above).

NCEER-87-0010 "Vertical and Torsional Vibration of Foundations in Inhomogeneous Media," by A.S. Veletsos and K.W. Dotson, 6/1/87, (PB88-134291, A03, MF-A01). This report is only available through NTIS (see address given above).

NCEER-87-0011 "Seismic Probabilistic Risk Assessment and Seismic Margins Studies for Nuclear Power Plants," by Howard H.M. Hwang, 6/15/87, (PB88-134267, A03, MF-A01). This report is only available through NTIS (see address given above).

NCEER-87-0012 "Parametric Studies of Frequency Response of Secondary Systems Under Ground-Acceleration Excitations," by Y. Yong and Y.K. Lin, 6/10/87, (PB88-134309, A03, MF-A01). This report is only available through NTIS (see address given above).

NCEER-87-0013 "Frequency Response of Secondary Systems Under Seismic Excitation," by J.A. HoLung, J. Cai and Y.K. Lin, 7/31/87, (PB88-134317, A05, MF-A01). This report is only available through NTIS (see address given above).

NCEER-87-0014 "Modelling Earthquake Ground Motions in Seismically Active Regions Using Parametric Time Series Methods," by G.W. Ellis and A.S. Cakmak, 8/25/87, (PB88-134283, A08, MF-A01). This report is only available through NTIS (see address given above).

NCEER-87-0015 "Detection and Assessment of Seismic Structural Damage," by E. DiPasquale and A.S. Cakmak, 8/25/87, (PB88-163712, A05, MF-A01). This report is only available through NTIS (see address given above).

NCEER-87-0016 "Pipeline Experiment at Parkfield, California," by J. Isenberg and E. Richardson, 9/15/87, (PB88-163720, A03, MF-A01). This report is available only through NTIS (see address given above).

NCEER-87-0017 "Digital Simulation of Seismic Ground Motion," by M. Shinozuka, G. Deodatis and T. Harada, 8/31/87, (PB88-155197, A04, MF-A01). This report is available only through NTIS (see address given above).

NCEER-87-0018 "Practical Considerations for Structural Control: System Uncertainty, System Time Delay and Truncation of Small Control Forces," J.N. Yang and A. Akbarpour, 8/10/87, (PB88-163738, A08, MF-A01). This report is only available through NTIS (see address given above).

NCEER-87-0019 "Modal Analysis of Nonclassically Damped Structural Systems Using Canonical Transformation," by J.N. Yang, S. Sarkani and F.X. Long, 9/27/87, (PB88-187851, A04, MF-A01).

NCEER-87-0020 "A Nonstationary Solution in Random Vibration Theory," by J.R. Red-Horse and P.D. Spanos, 11/3/87, (PB88-163746, A03, MF-A01).

NCEER-87-0021 "Horizontal Impedances for Radially Inhomogeneous Viscoelastic Soil Layers," by A.S. Veletsos and K.W. Dotson, 10/15/87, (PB88-150859, A04, MF-A01).

NCEER-87-0022 "Seismic Damage Assessment of Reinforced Concrete Members," by Y.S. Chung, C. Meyer and M. Shinozuka, 10/9/87, (PB88-150867, A05, MF-A01). This report is available only through NTIS (see address given above).

NCEER-87-0023 "Active Structural Control in Civil Engineering," by T.T. Soong, 11/11/87, (PB88-187778, A03, MF-A01).

NCEER-87-0024 "Vertical and Torsional Impedances for Radially Inhomogeneous Viscoelastic Soil Layers," by K.W. Dotson and A.S. Veletsos, 12/87, (PB88-187786, A03, MF-A01).

NCEER-87-0025 "Proceedings from the Symposium on Seismic Hazards, Ground Motions, Soil-Liquefaction and Engineering Practice in Eastern North America," October 20-22, 1987, edited by K.H. Jacob, 12/87, (PB88-188115, A23, MF-A01). This report is available only through NTIS (see address given above).

NCEER-87-0026 "Report on the Whittier-Narrows, California, Earthquake of October 1, 1987," by J. Pantelic and A. Reinhorn, 11/87, (PB88-187752, A03, MF-A01). This report is available only through NTIS (see address given above).

NCEER-87-0027 "Design of a Modular Program for Transient Nonlinear Analysis of Large 3-D Building Structures," by S. Srivastav and J.F. Abel, 12/30/87, (PB88-187950, A05, MF-A01). This report is only available through NTIS (see address given above).

NCEER-87-0028 "Second-Year Program in Research, Education and Technology Transfer," 3/8/88, (PB88-219480, A04, MF-A01).

NCEER-88-0001 "Workshop on Seismic Computer Analysis and Design of Buildings With Interactive Graphics," by W. McGuire, J.F. Abel and C.H. Conley, 1/18/88, (PB88-187760, A03, MF-A01). This report is only available through NTIS (see address given above).

NCEER-88-0002 "Optimal Control of Nonlinear Flexible Structures," by J.N. Yang, F.X. Long and D. Wong, 1/22/88, (PB88-213772, A06, MF-A01).

NCEER-88-0003 "Substructuring Techniques in the Time Domain for Primary-Secondary Structural Systems," by G.D. Manolis and G. Juhn, 2/10/88, (PB88-213780, A04, MF-A01).

NCEER-88-0004 "Iterative Seismic Analysis of Primary-Secondary Systems," by A. Singhal, L.D. Lutes and P.D. Spanos, 2/23/88, (PB88-213798, A04, MF-A01).

NCEER-88-0005 "Stochastic Finite Element Expansion for Random Media," by P.D. Spanos and R. Ghanem, 3/14/88, (PB88-213806, A03, MF-A01).

NCEER-88-0006 "Combining Structural Optimization and Structural Control," by F.Y. Cheng and C.P. Pantelides, 1/10/88, (PB88-213814, A05, MF-A01).

NCEER-88-0007 "Seismic Performance Assessment of Code-Designed Structures," by H.H-M. Hwang, J-W. Jaw and H-J. Shau, 3/20/88, (PB88-219423, A04, MF-A01). This report is only available through NTIS (see address given above).

NCEER-88-0008 "Reliability Analysis of Code-Designed Structures Under Natural Hazards," by H.H-M. Hwang, H. Ushiba and M. Shinozuka, 2/29/88, (PB88-229471, A07, MF-A01). This report is only available through NTIS (see address given above).

NCEER-88-0009 "Seismic Fragility Analysis of Shear Wall Structures," by J-W Jaw and H.H-M. Hwang, 4/30/88, (PB89-102867, A04, MF-A01).

NCEER-88-0010 "Base Isolation of a Multi-Story Building Under a Harmonic Ground Motion - A Comparison of Performances of Various Systems," by F-G Fan, G. Ahmadi and I.G. Tadjbakhsh, 5/18/88, (PB89-122238, A06, MF-A01). This report is only available through NTIS (see address given above).

NCEER-88-0011 "Seismic Floor Response Spectra for a Combined System by Green's Functions," by F.M. Lavelle, L.A. Bergman and P.D. Spanos, 5/1/88, (PB89-102875, A03, MF-A01).

NCEER-88-0012 "A New Solution Technique for Randomly Excited Hysteretic Structures," by G.Q. Cai and Y.K. Lin, 5/16/88, (PB89-102883, A03, MF-A01).

NCEER-88-0013 "A Study of Radiation Damping and Soil-Structure Interaction Effects in the Centrifuge," by K. Weissman, supervised by J.H. Prevost, 5/24/88, (PB89-144703, A06, MF-A01).

NCEER-88-0014 "Parameter Identification and Implementation of a Kinematic Plasticity Model for Frictional Soils," by J.H. Prevost and D.V. Griffiths, not available.

NCEER-88-0015 "Two- and Three- Dimensional Dynamic Finite Element Analyses of the Long Valley Dam," by D.V. Griffiths and J.H. Prevost, 6/17/88, (PB89-144711, A04, MF-A01).

NCEER-88-0016 "Damage Assessment of Reinforced Concrete Structures in Eastern United States," by A.M. Reinhorn, M.J. Seidel, S.K. Kunnath and Y.J. Park, 6/15/88, (PB89-122220, A04, MF-A01). This report is only available through NTIS (see address given above).

NCEER-88-0017 "Dynamic Compliance of Vertically Loaded Strip Foundations in Multilayered Viscoelastic Soils," by S. Ahmad and A.S.M. Israil, 6/17/88, (PB89-102891, A04, MF-A01).

NCEER-88-0018 "An Experimental Study of Seismic Structural Response With Added Viscoelastic Dampers," by R.C. Lin, Z. Liang, T.T. Soong and R.H. Zhang, 6/30/88, (PB89-122212, A05, MF-A01). This report is available only through NTIS (see address given above).

NCEER-88-0019 "Experimental Investigation of Primary - Secondary System Interaction," by G.D. Manolis, G. Juhn and A.M. Reinhorn, 5/27/88, (PB89-122204, A04, MF-A01).

NCEER-88-0020 "A Response Spectrum Approach For Analysis of Nonclassically Damped Structures," by J.N. Yang, S. Sarkani and F.X. Long, 4/22/88, (PB89-102909, A04, MF-A01).

NCEER-88-0021 "Seismic Interaction of Structures and Soils: Stochastic Approach," by A.S. Veletsos and A.M. Prasad, 7/21/88, (PB89-122196, A04, MF-A01). This report is only available through NTIS (see address given above).

NCEER-88-0022 "Identification of the Serviceability Limit State and Detection of Seismic Structural Damage," by E. DiPasquale and A.S. Cakmak, 6/15/88, (PB89-122188, A05, MF-A01). This report is available only through NTIS (see address given above).

NCEER-88-0023 "Multi-Hazard Risk Analysis: Case of a Simple Offshore Structure," by B.K. Bhartia and E.H. Vanmarcke, 7/21/88, (PB89-145213, A05, MF-A01).

NCEER-88-0024 "Automated Seismic Design of Reinforced Concrete Buildings," by Y.S. Chung, C. Meyer and M. Shinozuka, 7/5/88, (PB89-122170, A06, MF-A01). This report is available only through NTIS (see address given above).

NCEER-88-0025 "Experimental Study of Active Control of MDOF Structures Under Seismic Excitations," by L.L. Chung, R.C. Lin, T.T. Soong and A.M. Reinhorn, 7/10/88, (PB89-122600, A04, MF-A01).

NCEER-88-0026 "Earthquake Simulation Tests of a Low-Rise Metal Structure," by J.S. Hwang, K.C. Chang, G.C. Lee and R.L. Ketter, 8/1/88, (PB89-102917, A04, MF-A01).

NCEER-88-0027 "Systems Study of Urban Response and Reconstruction Due to Catastrophic Earthquakes," by F. Kozin and H.K. Zhou, 9/22/88, (PB90-162348, A04, MF-A01).

NCEER-88-0028 "Seismic Fragility Analysis of Plane Frame Structures," by H.H-M. Hwang and Y.K. Low, 7/31/88, (PB89-131445, A06, MF-A01).

NCEER-88-0029 "Response Analysis of Stochastic Structures," by A. Kardara, C. Bucher and M. Shinozuka, 9/22/88, (PB89-174429, A04, MF-A01).

NCEER-88-0030 "Nonnormal Accelerations Due to Yielding in a Primary Structure," by D.C.K. Chen and L.D. Lutes, 9/19/88, (PB89-131437, A04, MF-A01).

NCEER-88-0031 "Design Approaches for Soil-Structure Interaction," by A.S. Veletsos, A.M. Prasad and Y. Tang, 12/30/88, (PB89-174437, A03, MF-A01). This report is available only through NTIS (see address given above).

NCEER-88-0032 "A Re-evaluation of Design Spectra for Seismic Damage Control," by C.J. Turkstra and A.G. Tallin, 11/7/88, (PB89-145221, A05, MF-A01).

NCEER-88-0033 "The Behavior and Design of Noncontact Lap Splices Subjected to Repeated Inelastic Tensile Loading," by V.E. Sagan, P. Gergely and R.N. White, 12/8/88, (PB89-163737, A08, MF-A01).

NCEER-88-0034 "Seismic Response of Pile Foundations," by S.M. Mamoon, P.K. Banerjee and S. Ahmad, 11/1/88, (PB89-145239, A04, MF-A01).

NCEER-88-0035 "Modeling of R/C Building Structures With Flexible Floor Diaphragms (IDARC2)," by A.M. Reinhorn, S.K. Kunnath and N. Panahshahi, 9/7/88, (PB89-207153, A07, MF-A01).

NCEER-88-0036 "Solution of the Dam-Reservoir Interaction Problem Using a Combination of FEM, BEM with Particular Integrals, Modal Analysis, and Substructuring," by C-S. Tsai, G.C. Lee and R.L. Ketter, 12/31/88, (PB89-207146, A04, MF-A01).

NCEER-88-0037 "Optimal Placement of Actuators for Structural Control," by F.Y. Cheng and C.P. Pantelides, 8/15/88, (PB89-162846, A05, MF-A01).

NCEER-88-0038 "Teflon Bearings in Aseismic Base Isolation: Experimental Studies and Mathematical Modeling," by A. Mokha, M.C. Constantinou and A.M. Reinhorn, 12/5/88, (PB89-218457, A10, MF-A01). This report is available only through NTIS (see address given above).

NCEER-88-0039 "Seismic Behavior of Flat Slab High-Rise Buildings in the New York City Area," by P. Weidlinger and M. Ettouney, 10/15/88, (PB90-145681, A04, MF-A01).

NCEER-88-0040 "Evaluation of the Earthquake Resistance of Existing Buildings in New York City," by P. Weidlinger and M. Ettouney, 10/15/88, not available.

NCEER-88-0041 "Small-Scale Modeling Techniques for Reinforced Concrete Structures Subjected to Seismic Loads," by W. Kim, A. El-Attar and R.N. White, 11/22/88, (PB89-189625, A05, MF-A01).

NCEER-88-0042 "Modeling Strong Ground Motion from Multiple Event Earthquakes," by G.W. Ellis and A.S. Cakmak, 10/15/88, (PB89-174445, A03, MF-A01).

NCEER-88-0043 "Nonstationary Models of Seismic Ground Acceleration," by M. Grigoriu, S.E. Ruiz and E. Rosenblueth, 7/15/88, (PB89-189617, A04, MF-A01).

NCEER-88-0044 "SARCF User's Guide: Seismic Analysis of Reinforced Concrete Frames," by Y.S. Chung, C. Meyer and M. Shinozuka, 11/9/88, (PB89-174452, A08, MF-A01).

NCEER-88-0045 "First Expert Panel Meeting on Disaster Research and Planning," edited by J. Pantelic and J. Stoyle, 9/15/88, (PB89-174460, A05, MF-A01).

NCEER-88-0046 "Preliminary Studies of the Effect of Degrading Infill Walls on the Nonlinear Seismic Response of Steel Frames," by C.Z. Chrysostomou, P. Gergely and J.F. Abel, 12/19/88, (PB89-208383, A05, MF-A01).

NCEER-88-0047 "Reinforced Concrete Frame Component Testing Facility - Design, Construction, Instrumentation and Operation," by S.P. Pessiki, C. Conley, T. Bond, P. Gergely and R.N. White, 12/16/88, (PB89-174478, A04, MF-A01).

NCEER-89-0001 "Effects of Protective Cushion and Soil Compliancy on the Response of Equipment Within a Seismically Excited Building," by J.A. HoLung, 2/16/89, (PB89-207179, A04, MF-A01).

NCEER-89-0002 "Statistical Evaluation of Response Modification Factors for Reinforced Concrete Structures," by H.H-M. Hwang and J-W. Jaw, 2/17/89, (PB89-207187, A05, MF-A01).

NCEER-89-0003 "Hysteretic Columns Under Random Excitation," by G-Q. Cai and Y.K. Lin, 1/9/89, (PB89-196513, A03, MF-A01).

NCEER-89-0004 "Experimental Study of `Elephant Foot Bulge' Instability of Thin-Walled Metal Tanks," by Z-H. Jia and R.L. Ketter, 2/22/89, (PB89-207195, A03, MF-A01).

NCEER-89-0005 "Experiment on Performance of Buried Pipelines Across San Andreas Fault," by J. Isenberg, E. Richardson and T.D. O'Rourke, 3/10/89, (PB89-218440, A04, MF-A01). This report is available only through NTIS (see address given above).

NCEER-89-0006 "A Knowledge-Based Approach to Structural Design of Earthquake-Resistant Buildings," by M. Subramani, P. Gergely, C.H. Conley, J.F. Abel and A.H. Zaghw, 1/15/89, (PB89-218465, A06, MF-A01).

NCEER-89-0007 "Liquefaction Hazards and Their Effects on Buried Pipelines," by T.D. O'Rourke and P.A. Lane, 2/1/89, (PB89-218481, A09, MF-A01).

NCEER-89-0008 "Fundamentals of System Identification in Structural Dynamics," by H. Imai, C-B. Yun, O. Maruyama and M. Shinozuka, 1/26/89, (PB89-207211, A04, MF-A01).

NCEER-89-0009 "Effects of the 1985 Michoacan Earthquake on Water Systems and Other Buried Lifelines in Mexico," by A.G. Ayala and M.J. O'Rourke, 3/8/89, (PB89-207229, A06, MF-A01).

NCEER-89-R010 "NCEER Bibliography of Earthquake Education Materials," by K.E.K. Ross, Second Revision, 9/1/89, (PB90-125352, A05, MF-A01). This report is replaced by NCEER-92-0018.

NCEER-89-0011 "Inelastic Three-Dimensional Response Analysis of Reinforced Concrete Building Structures (IDARC-3D), Part I - Modeling," by S.K. Kunnath and A.M. Reinhorn, 4/17/89, (PB90-114612, A07, MF-A01). This report is available only through NTIS (see address given above).

NCEER-89-0012 "Recommended Modifications to ATC-14," by C.D. Poland and J.O. Malley, 4/12/89, (PB90-108648, A15, MF-A01).

NCEER-89-0013 "Repair and Strengthening of Beam-to-Column Connections Subjected to Earthquake Loading," by M. Corazao and A.J. Durrani, 2/28/89, (PB90-109885, A06, MF-A01).

NCEER-89-0014 "Program EXKAL2 for Identification of Structural Dynamic Systems," by O. Maruyama, C-B. Yun, M. Hoshiya and M. Shinozuka, 5/19/89, (PB90-109877, A09, MF-A01).

NCEER-89-0015 "Response of Frames With Bolted Semi-Rigid Connections, Part I - Experimental Study and Analytical Predictions," by P.J. DiCorso, A.M. Reinhorn, J.R. Dickerson, J.B. Radziminski and W.L. Harper, 6/1/89, not available.

NCEER-89-0016 "ARMA Monte Carlo Simulation in Probabilistic Structural Analysis," by P.D. Spanos and M.P. Mignolet, 7/10/89, (PB90-109893, A03, MF-A01).

NCEER-89-P017 "Preliminary Proceedings from the Conference on Disaster Preparedness - The Place of Earthquake Education in Our Schools," Edited by K.E.K. Ross, 6/23/89, (PB90-108606, A03, MF-A01).

NCEER-89-0017 "Proceedings from the Conference on Disaster Preparedness - The Place of Earthquake Education in Our Schools," Edited by K.E.K. Ross, 12/31/89, (PB90-207895, A012, MF-A02). This report is available only through NTIS (see address given above).

NCEER-89-0018 "Multidimensional Models of Hysteretic Material Behavior for Vibration Analysis of Shape Memory Energy Absorbing Devices, by E.J. Graesser and F.A. Cozzarelli, 6/7/89, (PB90-164146, A04, MF-A01).

NCEER-89-0019 "Nonlinear Dynamic Analysis of Three-Dimensional Base Isolated Structures (3D-BASIS)," by S. Nagarajaiah, A.M. Reinhorn and M.C. Constantinou, 8/3/89, (PB90-161936, A06, MF-A01). This report has been replaced by NCEER-93-0011.

NCEER-89-0020 "Structural Control Considering Time-Rate of Control Forces and Control Rate Constraints," by F.Y. Cheng and C.P. Pantelides, 8/3/89, (PB90-120445, A04, MF-A01).

NCEER-89-0021 "Subsurface Conditions of Memphis and Shelby County," by K.W. Ng, T-S. Chang and H-H.M. Hwang, 7/26/89, (PB90-120437, A03, MF-A01).

NCEER-89-0022 "Seismic Wave Propagation Effects on Straight Jointed Buried Pipelines," by K. Elhmadi and M.J. O'Rourke, 8/24/89, (PB90-162322, A10, MF-A02).

NCEER-89-0023 "Workshop on Serviceability Analysis of Water Delivery Systems," edited by M. Grigoriu, 3/6/89, (PB90-127424, A03, MF-A01).

NCEER-89-0024 "Shaking Table Study of a 1/5 Scale Steel Frame Composed of Tapered Members," by K.C. Chang, J.S. Hwang and G.C. Lee, 9/18/89, (PB90-160169, A04, MF-A01).

NCEER-89-0025 "DYNA1D: A Computer Program for Nonlinear Seismic Site Response Analysis - Technical Documentation," by Jean H. Prevost, 9/14/89, (PB90-161944, A07, MF-A01). This report is available only through NTIS (see address given above).

NCEER-89-0026 "1:4 Scale Model Studies of Active Tendon Systems and Active Mass Dampers for Aseismic Protection," by A.M. Reinhorn, T.T. Soong, R.C. Lin, Y.P. Yang, Y. Fukao, H. Abe and M. Nakai, 9/15/89, (PB90-173246, A10, MF-A02). This report is available only through NTIS (see address given above).

NCEER-89-0027 "Scattering of Waves by Inclusions in a Nonhomogeneous Elastic Half Space Solved by Boundary Element Methods," by P.K. Hadley, A. Askar and A.S. Cakmak, 6/15/89, (PB90-145699, A07, MF-A01).

NCEER-89-0028 "Statistical Evaluation of Deflection Amplification Factors for Reinforced Concrete Structures," by H.H.M. Hwang, J-W. Jaw and A.L. Ch'ng, 8/31/89, (PB90-164633, A05, MF-A01).

NCEER-89-0029 "Bedrock Accelerations in Memphis Area Due to Large New Madrid Earthquakes," by H.H.M. Hwang, C.H.S. Chen and G. Yu, 11/7/89, (PB90-162330, A04, MF-A01).

NCEER-89-0030 "Seismic Behavior and Response Sensitivity of Secondary Structural Systems," by Y.Q. Chen and T.T. Soong, 10/23/89, (PB90-164658, A08, MF-A01).

NCEER-89-0031 "Random Vibration and Reliability Analysis of Primary-Secondary Structural Systems," by Y. Ibrahim, M. Grigoriu and T.T. Soong, 11/10/89, (PB90-161951, A04, MF-A01).

NCEER-89-0032 "Proceedings from the Second U.S. - Japan Workshop on Liquefaction, Large Ground Deformation and Their Effects on Lifelines, September 26-29, 1989," Edited by T.D. O'Rourke and M. Hamada, 12/1/89, (PB90-209388, A22, MF-A03).

NCEER-89-0033 "Deterministic Model for Seismic Damage Evaluation of Reinforced Concrete Structures," by J.M. Bracci, A.M. Reinhorn, J.B. Mander and S.K. Kunnath, 9/27/89, (PB91-108803, A06, MF-A01).

NCEER-89-0034 "On the Relation Between Local and Global Damage Indices," by E. DiPasquale and A.S. Cakmak, 8/15/89, (PB90-173865, A05, MF-A01).

NCEER-89-0035 "Cyclic Undrained Behavior of Nonplastic and Low Plasticity Silts," by A.J. Walker and H.E. Stewart, 7/26/89, (PB90-183518, A10, MF-A01).

NCEER-89-0036 "Liquefaction Potential of Surficial Deposits in the City of Buffalo, New York," by M. Budhu, R. Giese and L. Baumgrass, 1/17/89, (PB90-208455, A04, MF-A01).

NCEER-89-0037 "A Deterministic Assessment of Effects of Ground Motion Incoherence," by A.S. Veletsos and Y. Tang, 7/15/89, (PB90-164294, A03, MF-A01).

NCEER-89-0038 "Workshop on Ground Motion Parameters for Seismic Hazard Mapping," July 17-18, 1989, edited by R.V. Whitman, 12/1/89, (PB90-173923, A04, MF-A01).

NCEER-89-0039 "Seismic Effects on Elevated Transit Lines of the New York City Transit Authority," by C.J. Costantino, C.A. Miller and E. Heymsfield, 12/26/89, (PB90-207887, A06, MF-A01).

NCEER-89-0040 "Centrifugal Modeling of Dynamic Soil-Structure Interaction," by K. Weissman, Supervised by J.H. Prevost, 5/10/89, (PB90-207879, A07, MF-A01).

NCEER-89-0041 "Linearized Identification of Buildings With Cores for Seismic Vulnerability Assessment," by I-K. Ho and A.E. Aktan, 11/1/89, (PB90-251943, A07, MF-A01).

NCEER-90-0001 "Geotechnical and Lifeline Aspects of the October 17, 1989 Loma Prieta Earthquake in San Francisco," by T.D. O'Rourke, H.E. Stewart, F.T. Blackburn and T.S. Dickerman, 1/90, (PB90-208596, A05, MF-A01).

NCEER-90-0002 "Nonnormal Secondary Response Due to Yielding in a Primary Structure," by D.C.K. Chen and L.D. Lutes, 2/28/90, (PB90-251976, A07, MF-A01).

NCEER-90-0003 "Earthquake Education Materials for Grades K-12," by K.E.K. Ross, 4/16/90, (PB91-251984, A05, MF-A05). This report has been replaced by NCEER-92-0018.

NCEER-90-0004 "Catalog of Strong Motion Stations in Eastern North America," by R.W. Busby, 4/3/90, (PB90-251984, A05, MF-A01).

NCEER-90-0005 "NCEER Strong-Motion Data Base: A User Manual for the GeoBase Release (Version 1.0 for the Sun3)," by P. Friberg and K. Jacob, 3/31/90 (PB90-258062, A04, MF-A01).

NCEER-90-0006 "Seismic Hazard Along a Crude Oil Pipeline in the Event of an 1811-1812 Type New Madrid Earthquake," by H.H.M. Hwang and C-H.S. Chen, 4/16/90, (PB90-258054, A04, MF-A01).

NCEER-90-0007 "Site-Specific Response Spectra for Memphis Sheahan Pumping Station," by H.H.M. Hwang and C.S. Lee, 5/15/90, (PB91-108811, A05, MF-A01).

NCEER-90-0008 "Pilot Study on Seismic Vulnerability of Crude Oil Transmission Systems," by T. Ariman, R. Dobry, M. Grigoriu, F. Kozin, M. O'Rourke, T. O'Rourke and M. Shinozuka, 5/25/90, (PB91-108837, A06, MF-A01).

NCEER-90-0009 "A Program to Generate Site Dependent Time Histories: EQGEN," by G.W. Ellis, M. Srinivasan and A.S. Cakmak, 1/30/90, (PB91-108829, A04, MF-A01).

NCEER-90-0010 "Active Isolation for Seismic Protection of Operating Rooms," by M.E. Talbott, Supervised by M. Shinozuka, 6/8/9, (PB91-110205, A05, MF-A01).

NCEER-90-0011 "Program LINEARID for Identification of Linear Structural Dynamic Systems," by C-B. Yun and M. Shinozuka, 6/25/90, (PB91-110312, A08, MF-A01).

NCEER-90-0012 "Two-Dimensional Two-Phase Elasto-Plastic Seismic Response of Earth Dams," by A.N. Yiagos, Supervised by J.H. Prevost, 6/20/90, (PB91-110197, A13, MF-A02).

NCEER-90-0013 "Secondary Systems in Base-Isolated Structures: Experimental Investigation, Stochastic Response and Stochastic Sensitivity," by G.D. Manolis, G. Juhn, M.C. Constantinou and A.M. Reinhorn, 7/1/90, (PB91-110320, A08, MF-A01).

NCEER-90-0014 "Seismic Behavior of Lightly-Reinforced Concrete Column and Beam-Column Joint Details," by S.P. Pessiki, C.H. Conley, P. Gergely and R.N. White, 8/22/90, (PB91-108795, A11, MF-A02).

NCEER-90-0015 "Two Hybrid Control Systems for Building Structures Under Strong Earthquakes," by J.N. Yang and A. Danielians, 6/29/90, (PB91-125393, A04, MF-A01).

NCEER-90-0016 "Instantaneous Optimal Control with Acceleration and Velocity Feedback," by J.N. Yang and Z. Li, 6/29/90, (PB91-125401, A03, MF-A01).

NCEER-90-0017 "Reconnaissance Report on the Northern Iran Earthquake of June 21, 1990," by M. Mehrain, 10/4/90, (PB91-125377, A03, MF-A01).

NCEER-90-0018 "Evaluation of Liquefaction Potential in Memphis and Shelby County," by T.S. Chang, P.S. Tang, C.S. Lee and H. Hwang, 8/10/90, (PB91-125427, A09, MF-A01).

NCEER-90-0019 "Experimental and Analytical Study of a Combined Sliding Disc Bearing and Helical Steel Spring Isolation System," by M.C. Constantinou, A.S. Mokha and A.M. Reinhorn, 10/4/90, (PB91-125385, A06, MF-A01). This report is available only through NTIS (see address given above).

NCEER-90-0020 "Experimental Study and Analytical Prediction of Earthquake Response of a Sliding Isolation System with a Spherical Surface," by A.S. Mokha, M.C. Constantinou and A.M. Reinhorn, 10/11/90, (PB91-125419, A05, MF-A01).

NCEER-90-0021 "Dynamic Interaction Factors for Floating Pile Groups," by G. Gazetas, K. Fan, A. Kaynia and E. Kausel, 9/10/90, (PB91-170381, A05, MF-A01).

NCEER-90-0022 "Evaluation of Seismic Damage Indices for Reinforced Concrete Structures," by S. Rodriguez-Gomez and A.S. Cakmak, 9/30/90, PB91-171322, A06, MF-A01).

NCEER-90-0023 "Study of Site Response at a Selected Memphis Site," by H. Desai, S. Ahmad, E.S. Gazetas and M.R. Oh, 10/11/90, (PB91-196857, A03, MF-A01).

NCEER-90-0024 "A User's Guide to Strongmo: Version 1.0 of NCEER's Strong-Motion Data Access Tool for PCs and Terminals," by P.A. Friberg and C.A.T. Susch, 11/15/90, (PB91-171272, A03, MF-A01).

NCEER-90-0025 "A Three-Dimensional Analytical Study of Spatial Variability of Seismic Ground Motions," by L-L. Hong and A.H.-S. Ang, 10/30/90, (PB91-170399, A09, MF-A01).

NCEER-90-0026 "MUMOID User's Guide - A Program for the Identification of Modal Parameters," by S. Rodriguez-Gomez and E. DiPasquale, 9/30/90, (PB91-171298, A04, MF-A01).

NCEER-90-0027 "SARCF-II User's Guide - Seismic Analysis of Reinforced Concrete Frames," by S. Rodriguez-Gomez, Y.S. Chung and C. Meyer, 9/30/90, (PB91-171280, A05, MF-A01).

NCEER-90-0028 "Viscous Dampers: Testing, Modeling and Application in Vibration and Seismic Isolation," by N. Makris and M.C. Constantinou, 12/20/90 (PB91-190561, A06, MF-A01).

NCEER-90-0029 "Soil Effects on Earthquake Ground Motions in the Memphis Area," by H. Hwang, C.S. Lee, K.W. Ng and T.S. Chang, 8/2/90, (PB91-190751, A05, MF-A01).

NCEER-91-0001 "Proceedings from the Third Japan-U.S. Workshop on Earthquake Resistant Design of Lifeline Facilities and Countermeasures for Soil Liquefaction, December 17-19, 1990," edited by T.D. O'Rourke and M. Hamada, 2/1/91, (PB91-179259, A99, MF-A04).

NCEER-91-0002 "Physical Space Solutions of Non-Proportionally Damped Systems," by M. Tong, Z. Liang and G.C. Lee, 1/15/91, (PB91-179242, A04, MF-A01).

NCEER-91-0003 "Seismic Response of Single Piles and Pile Groups," by K. Fan and G. Gazetas, 1/10/91, (PB92-174994, A04, MF-A01).

NCEER-91-0004 "Damping of Structures: Part 1 - Theory of Complex Damping," by Z. Liang and G. Lee, 10/10/91, (PB92-197235, A12, MF-A03).

NCEER-91-0005 "3D-BASIS - Nonlinear Dynamic Analysis of Three Dimensional Base Isolated Structures: Part II," by S. Nagarajaiah, A.M. Reinhorn and M.C. Constantinou, 2/28/91, (PB91-190553, A07, MF-A01). This report has been replaced by NCEER-93-0011.

NCEER-91-0006 "A Multidimensional Hysteretic Model for Plasticity Deforming Metals in Energy Absorbing Devices," by E.J. Graesser and F.A. Cozzarelli, 4/9/91, (PB92-108364, A04, MF-A01).

NCEER-91-0007 "A Framework for Customizable Knowledge-Based Expert Systems with an Application to a KBES for Evaluating the Seismic Resistance of Existing Buildings," by E.G. Ibarra-Anaya and S.J. Fenves, 4/9/91, (PB91-210930, A08, MF-A01).

NCEER-91-0008 "Nonlinear Analysis of Steel Frames with Semi-Rigid Connections Using the Capacity Spectrum Method," by G.G. Deierlein, S-H. Hsieh, Y-J. Shen and J.F. Abel, 7/2/91, (PB92-113828, A05, MF-A01).

NCEER-91-0009 "Earthquake Education Materials for Grades K-12," by K.E.K. Ross, 4/30/91, (PB91-212142, A06, MF-A01). This report has been replaced by NCEER-92-0018.

NCEER-91-0010 "Phase Wave Velocities and Displacement Phase Differences in a Harmonically Oscillating Pile," by N. Makris and G. Gazetas, 7/8/91, (PB92-108356, A04, MF-A01).

NCEER-91-0011 "Dynamic Characteristics of a Full-Size Five-Story Steel Structure and a 2/5 Scale Model," by K.C. Chang, G.C. Yao, G.C. Lee, D.S. Hao and Y.C. Yeh," 7/2/91, (PB93-116648, A06, MF-A02).

NCEER-91-0012 "Seismic Response of a 2/5 Scale Steel Structure with Added Viscoelastic Dampers," by K.C. Chang, T.T. Soong, S-T. Oh and M.L. Lai, 5/17/91, (PB92-110816, A05, MF-A01).

NCEER-91-0013 "Earthquake Response of Retaining Walls; Full-Scale Testing and Computational Modeling," by S. Alampalli and A-W.M. Elgamal, 6/20/91, not available.

NCEER-91-0014 "3D-BASIS-M: Nonlinear Dynamic Analysis of Multiple Building Base Isolated Structures," by P.C. Tsopelas, S. Nagarajaiah, M.C. Constantinou and A.M. Reinhorn, 5/28/91, (PB92-113885, A09, MF-A02).

NCEER-91-0015 "Evaluation of SEAOC Design Requirements for Sliding Isolated Structures," by D. Theodossiou and M.C. Constantinou, 6/10/91, (PB92-114602, A11, MF-A03).

NCEER-91-0016 "Closed-Loop Modal Testing of a 27-Story Reinforced Concrete Flat Plate-Core Building," by H.R. Somaprasad, T. Toksoy, H. Yoshiyuki and A.E. Aktan, 7/15/91, (PB92-129980, A07, MF-A02).

NCEER-91-0017 "Shake Table Test of a 1/6 Scale Two-Story Lightly Reinforced Concrete Building," by A.G. El-Attar, R.N. White and P. Gergely, 2/28/91, (PB92-222447, A06, MF-A02).

NCEER-91-0018 "Shake Table Test of a 1/8 Scale Three-Story Lightly Reinforced Concrete Building," by A.G. El-Attar, R.N. White and P. Gergely, 2/28/91, (PB93-116630, A08, MF-A02).

NCEER-91-0019 "Transfer Functions for Rigid Rectangular Foundations," by A.S. Veletsos, A.M. Prasad and W.H. Wu, 7/31/91, not available.

NCEER-91-0020 "Hybrid Control of Seismic-Excited Nonlinear and Inelastic Structural Systems," by J.N. Yang, Z. Li and A. Danielians, 8/1/91, (PB92-143171, A06, MF-A02).

NCEER-91-0021 "The NCEER-91 Earthquake Catalog: Improved Intensity-Based Magnitudes and Recurrence Relations for U.S. Earthquakes East of New Madrid," by L. Seeber and J.G. Armbruster, 8/28/91, (PB92-176742, A06, MF-A02).

NCEER-91-0022 "Proceedings from the Implementation of Earthquake Planning and Education in Schools: The Need for Change - The Roles of the Changemakers," by K.E.K. Ross and F. Winslow, 7/23/91, (PB92-129998, A12, MF-A03).

NCEER-91-0023 "A Study of Reliability-Based Criteria for Seismic Design of Reinforced Concrete Frame Buildings," by H.H.M. Hwang and H-M. Hsu, 8/10/91, (PB92-140235, A09, MF-A02).

NCEER-91-0024 "Experimental Verification of a Number of Structural System Identification Algorithms," by R.G. Ghanem, H. Gavin and M. Shinozuka, 9/18/91, (PB92-176577, A18, MF-A04).

NCEER-91-0025 "Probabilistic Evaluation of Liquefaction Potential," by H.H.M. Hwang and C.S. Lee," 11/25/91, (PB92-143429, A05, MF-A01).

NCEER-91-0026 "Instantaneous Optimal Control for Linear, Nonlinear and Hysteretic Structures - Stable Controllers," by J.N. Yang and Z. Li, 11/15/91, (PB92-163807, A04, MF-A01).

NCEER-91-0027 "Experimental and Theoretical Study of a Sliding Isolation System for Bridges," by M.C. Constantinou, A. Kartoum, A.M. Reinhorn and P. Bradford, 11/15/91, (PB92-176973, A10, MF-A03).

NCEER-92-0001 "Case Studies of Liquefaction and Lifeline Performance During Past Earthquakes, Volume 1: Japanese Case Studies," Edited by M. Hamada and T. O'Rourke, 2/17/92, (PB92-197243, A18, MF-A04).

NCEER-92-0002 "Case Studies of Liquefaction and Lifeline Performance During Past Earthquakes, Volume 2: United States Case Studies," Edited by T. O'Rourke and M. Hamada, 2/17/92, (PB92-197250, A20, MF-A04).

NCEER-92-0003 "Issues in Earthquake Education," Edited by K. Ross, 2/3/92, (PB92-222389, A07, MF-A02).

NCEER-92-0004 "Proceedings from the First U.S. - Japan Workshop on Earthquake Protective Systems for Bridges," Edited by I.G. Buckle, 2/4/92, (PB94-142239, A99, MF-A06).

NCEER-92-0005 "Seismic Ground Motion from a Haskell-Type Source in a Multiple-Layered Half-Space," A.P. Theoharis, G. Deodatis and M. Shinozuka, 1/2/92, not available.

NCEER-92-0006 "Proceedings from the Site Effects Workshop," Edited by R. Whitman, 2/29/92, (PB92-197201, A04, MF-A01).

NCEER-92-0007 "Engineering Evaluation of Permanent Ground Deformations Due to Seismically-Induced Liquefaction," by M.H. Baziar, R. Dobry and A-W.M. Elgamal, 3/24/92, (PB92-222421, A13, MF-A03).

NCEER-92-0008 "A Procedure for the Seismic Evaluation of Buildings in the Central and Eastern United States," by C.D. Poland and J.O. Malley, 4/2/92, (PB92-222439, A20, MF-A04).

NCEER-92-0009 "Experimental and Analytical Study of a Hybrid Isolation System Using Friction Controllable Sliding Bearings," by M.Q. Feng, S. Fujii and M. Shinozuka, 5/15/92, (PB93-150282, A06, MF-A02).

NCEER-92-0010 "Seismic Resistance of Slab-Column Connections in Existing Non-Ductile Flat-Plate Buildings," by A.J. Durrani and Y. Du, 5/18/92, (PB93-116812, A06, MF-A02).

NCEER-92-0011 "The Hysteretic and Dynamic Behavior of Brick Masonry Walls Upgraded by Ferrocement Coatings Under Cyclic Loading and Strong Simulated Ground Motion," by H. Lee and S.P. Prawel, 5/11/92, not available.

NCEER-92-0012 "Study of Wire Rope Systems for Seismic Protection of Equipment in Buildings," by G.F. Demetriades, M.C. Constantinou and A.M. Reinhorn, 5/20/92, (PB93-116655, A08, MF-A02).

NCEER-92-0013 "Shape Memory Structural Dampers: Material Properties, Design and Seismic Testing," by P.R. Witting and F.A. Cozzarelli, 5/26/92, (PB93-116663, A05, MF-A01).

NCEER-92-0014 "Longitudinal Permanent Ground Deformation Effects on Buried Continuous Pipelines," by M.J. O'Rourke, and C. Nordberg, 6/15/92, (PB93-116671, A08, MF-A02).

NCEER-92-0015 "A Simulation Method for Stationary Gaussian Random Functions Based on the Sampling Theorem," by M. Grigoriu and S. Balopoulou, 6/11/92, (PB93-127496, A05, MF-A01).

NCEER-92-0016 "Gravity-Load-Designed Reinforced Concrete Buildings: Seismic Evaluation of Existing Construction and Detailing Strategies for Improved Seismic Resistance," by G.W. Hoffmann, S.K. Kunnath, A.M. Reinhorn and J.B. Mander, 7/15/92, (PB94-142007, A08, MF-A02).

NCEER-92-0017 "Observations on Water System and Pipeline Performance in the Limón Area of Costa Rica Due to the April 22, 1991 Earthquake," by M. O'Rourke and D. Ballantyne, 6/30/92, (PB93-126811, A06, MF-A02).

NCEER-92-0018 "Fourth Edition of Earthquake Education Materials for Grades K-12," Edited by K.E.K. Ross, 8/10/92, (PB93-114023, A07, MF-A02).

NCEER-92-0019 "Proceedings from the Fourth Japan-U.S. Workshop on Earthquake Resistant Design of Lifeline Facilities and Countermeasures for Soil Liquefaction," Edited by M. Hamada and T.D. O'Rourke, 8/12/92, (PB93-163939, A99, MF-E11).

NCEER-92-0020 "Active Bracing System: A Full Scale Implementation of Active Control," by A.M. Reinhorn, T.T. Soong, R.C. Lin, M.A. Riley, Y.P. Wang, S. Aizawa and M. Higashino, 8/14/92, (PB93-127512, A06, MF-A02).

NCEER-92-0021 "Empirical Analysis of Horizontal Ground Displacement Generated by Liquefaction-Induced Lateral Spreads," by S.F. Bartlett and T.L. Youd, 8/17/92, (PB93-188241, A06, MF-A02).

NCEER-92-0022 "IDARC Version 3.0: Inelastic Damage Analysis of Reinforced Concrete Structures," by S.K. Kunnath, A.M. Reinhorn and R.F. Lobo, 8/31/92, (PB93-227502, A07, MF-A02).

NCEER-92-0023 "A Semi-Empirical Analysis of Strong-Motion Peaks in Terms of Seismic Source, Propagation Path and Local Site Conditions, by M. Kamiyama, M.J. O'Rourke and R. Flores-Berrones, 9/9/92, (PB93-150266, A08, MF-A02).

NCEER-92-0024 "Seismic Behavior of Reinforced Concrete Frame Structures with Nonductile Details, Part I: Summary of Experimental Findings of Full Scale Beam-Column Joint Tests," by A. Beres, R.N. White and P. Gergely, 9/30/92, (PB93-227783, A05, MF-A01).

NCEER-92-0025 "Experimental Results of Repaired and Retrofitted Beam-Column Joint Tests in Lightly Reinforced Concrete Frame Buildings," by A. Beres, S. El-Borgi, R.N. White and P. Gergely, 10/29/92, (PB93-227791, A05, MF-A01).

NCEER-92-0026 "A Generalization of Optimal Control Theory: Linear and Nonlinear Structures," by J.N. Yang, Z. Li and S. Vongchavalitkul, 11/2/92, (PB93-188621, A05, MF-A01).

NCEER-92-0027 "Seismic Resistance of Reinforced Concrete Frame Structures Designed Only for Gravity Loads: Part I - Design and Properties of a One-Third Scale Model Structure," by J.M. Bracci, A.M. Reinhorn and J.B. Mander, 12/1/92, (PB94-104502, A08, MF-A02).

NCEER-92-0028 "Seismic Resistance of Reinforced Concrete Frame Structures Designed Only for Gravity Loads: Part II - Experimental Performance of Subassemblages," by L.E. Aycardi, J.B. Mander and A.M. Reinhorn, 12/1/92, (PB94-104510, A08, MF-A02).

NCEER-92-0029 "Seismic Resistance of Reinforced Concrete Frame Structures Designed Only for Gravity Loads: Part III - Experimental Performance and Analytical Study of a Structural Model," by J.M. Bracci, A.M. Reinhorn and J.B. Mander, 12/1/92, (PB93-227528, A09, MF-A01).

NCEER-92-0030 "Evaluation of Seismic Retrofit of Reinforced Concrete Frame Structures: Part I - Experimental Performance of Retrofitted Subassemblages," by D. Choudhuri, J.B. Mander and A.M. Reinhorn, 12/8/92, (PB93-198307, A07, MF-A02).

NCEER-92-0031 "Evaluation of Seismic Retrofit of Reinforced Concrete Frame Structures: Part II - Experimental Performance and Analytical Study of a Retrofitted Structural Model," by J.M. Bracci, A.M. Reinhorn and J.B. Mander, 12/8/92, (PB93-198315, A09, MF-A03).

NCEER-92-0032 "Experimental and Analytical Investigation of Seismic Response of Structures with Supplemental Fluid Viscous Dampers," by M.C. Constantinou and M.D. Symans, 12/21/92, (PB93-191435, A10, MF-A03). This report is available only through NTIS (see address given above).

NCEER-92-0033 "Reconnaissance Report on the Cairo, Egypt Earthquake of October 12, 1992," by M. Khater, 12/23/92, (PB93-188621, A03, MF-A01).

NCEER-92-0034 "Low-Level Dynamic Characteristics of Four Tall Flat-Plate Buildings in New York City," by H. Gavin, S. Yuan, J. Grossman, E. Pekelis and K. Jacob, 12/28/92, (PB93-188217, A07, MF-A02).

NCEER-93-0001 "An Experimental Study on the Seismic Performance of Brick-Infilled Steel Frames With and Without Retrofit," by J.B. Mander, B. Nair, K. Wojtkowski and J. Ma, 1/29/93, (PB93-227510, A07, MF-A02).

NCEER-93-0002 "Social Accounting for Disaster Preparedness and Recovery Planning," by S. Cole, E. Pantoja and V. Razak, 2/22/93, (PB94-142114, A12, MF-A03).

NCEER-93-0003 "Assessment of 1991 NEHRP Provisions for Nonstructural Components and Recommended Revisions," by T.T. Soong, G. Chen, Z. Wu, R-H. Zhang and M. Grigoriu, 3/1/93, (PB93-188639, A06, MF-A02).

NCEER-93-0004 "Evaluation of Static and Response Spectrum Analysis Procedures of SEAOC/UBC for Seismic Isolated Structures," by C.W. Winters and M.C. Constantinou, 3/23/93, (PB93-198299, A10, MF-A03).

NCEER-93-0005 "Earthquakes in the Northeast - Are We Ignoring the Hazard? A Workshop on Earthquake Science and Safety for Educators," edited by K.E.K. Ross, 4/2/93, (PB94-103066, A09, MF-A02).

NCEER-93-0006 "Inelastic Response of Reinforced Concrete Structures with Viscoelastic Braces," by R.F. Lobo, J.M. Bracci, K.L. Shen, A.M. Reinhorn and T.T. Soong, 4/5/93, (PB93-227486, A05, MF-A02).

NCEER-93-0007 "Seismic Testing of Installation Methods for Computers and Data Processing Equipment," by K. Kosar, T.T. Soong, K.L. Shen, J.A. HoLung and Y.K. Lin, 4/12/93, (PB93-198299, A07, MF-A02).

NCEER-93-0008 "Retrofit of Reinforced Concrete Frames Using Added Dampers," by A. Reinhorn, M. Constantinou and C. Li, not available.

NCEER-93-0009 "Seismic Behavior and Design Guidelines for Steel Frame Structures with Added Viscoelastic Dampers," by K.C. Chang, M.L. Lai, T.T. Soong, D.S. Hao and Y.C. Yeh, 5/1/93, (PB94-141959, A07, MF-A02).

NCEER-93-0010 "Seismic Performance of Shear-Critical Reinforced Concrete Bridge Piers," by J.B. Mander, S.M. Waheed, M.T.A. Chaudhary and S.S. Chen, 5/12/93, (PB93-227494, A08, MF-A02).

NCEER-93-0011 "3D-BASIS-TABS: Computer Program for Nonlinear Dynamic Analysis of Three Dimensional Base Isolated Structures," by S. Nagarajaiah, C. Li, A.M. Reinhorn and M.C. Constantinou, 8/2/93, (PB94-141819, A09, MF-A02).

NCEER-93-0012 "Effects of Hydrocarbon Spills from an Oil Pipeline Break on Ground Water," by O.J. Helweg and H.H.M. Hwang, 8/3/93, (PB94-141942, A06, MF-A02).

NCEER-93-0013 "Simplified Procedures for Seismic Design of Nonstructural Components and Assessment of Current Code Provisions," by M.P. Singh, L.E. Suarez, E.E. Matheu and G.O. Maldonado, 8/4/93, (PB94-141827, A09, MF-A02).

NCEER-93-0014 "An Energy Approach to Seismic Analysis and Design of Secondary Systems," by G. Chen and T.T. Soong, 8/6/93, (PB94-142767, A11, MF-A03).

NCEER-93-0015 "Proceedings from School Sites: Becoming Prepared for Earthquakes - Commemorating the Third Anniversary of the Loma Prieta Earthquake," Edited by F.E. Winslow and K.E.K. Ross, 8/16/93, (PB94-154275, A16, MF-A02).

NCEER-93-0016 "Reconnaissance Report of Damage to Historic Monuments in Cairo, Egypt Following the October 12, 1992 Dahshur Earthquake," by D. Sykora, D. Look, G. Croci, E. Karaesmen and E. Karaesmen, 8/19/93, (PB94-142221, A08, MF-A02).

NCEER-93-0017 "The Island of Guam Earthquake of August 8, 1993," by S.W. Swan and S.K. Harris, 9/30/93, (PB94-141843, A04, MF-A01).

NCEER-93-0018 "Engineering Aspects of the October 12, 1992 Egyptian Earthquake," by A.W. Elgamal, M. Amer, K. Adalier and A. Abul-Fadl, 10/7/93, (PB94-141983, A05, MF-A01).

NCEER-93-0019 "Development of an Earthquake Motion Simulator and its Application in Dynamic Centrifuge Testing," by I. Krstelj, Supervised by J.H. Prevost, 10/23/93, (PB94-181773, A-10, MF-A03).

NCEER-93-0020 "NCEER-Taisei Corporation Research Program on Sliding Seismic Isolation Systems for Bridges: Experimental and Analytical Study of a Friction Pendulum System (FPS)," by M.C. Constantinou, P. Tsopelas, Y-S. Kim and S. Okamoto, 11/1/93, (PB94-142775, A08, MF-A02).

NCEER-93-0021 "Finite Element Modeling of Elastomeric Seismic Isolation Bearings," by L.J. Billings, Supervised by R. Shepherd, 11/8/93, not available.

NCEER-93-0022 "Seismic Vulnerability of Equipment in Critical Facilities: Life-Safety and Operational Consequences," by K. Porter, G.S. Johnson, M.M. Zadeh, C. Scawthorn and S. Eder, 11/24/93, (PB94-181765, A16, MF-A03).

NCEER-93-0023 "Hokkaido Nansei-oki, Japan Earthquake of July 12, 1993, by P.I. Yanev and C.R. Scawthorn, 12/23/93, (PB94-181500, A07, MF-A01).

NCEER-94-0001 "An Evaluation of Seismic Serviceability of Water Supply Networks with Application to the San Francisco Auxiliary Water Supply System," by I. Markov, Supervised by M. Grigoriu and T. O'Rourke, 1/21/94, (PB94-204013, A07, MF-A02).

NCEER-94-0002 "NCEER-Taisei Corporation Research Program on Sliding Seismic Isolation Systems for Bridges: Experimental and Analytical Study of Systems Consisting of Sliding Bearings, Rubber Restoring Force Devices and Fluid Dampers," Volumes I and II, by P. Tsopelas, S. Okamoto, M.C. Constantinou, D. Ozaki and S. Fujii, 2/4/94, (PB94-181740, A09, MF-A02 and PB94-181757, A12, MF-A03).

NCEER-94-0003 "A Markov Model for Local and Global Damage Indices in Seismic Analysis," by S. Rahman and M. Grigoriu, 2/18/94, (PB94-206000, A12, MF-A03).

NCEER-94-0004 "Proceedings from the NCEER Workshop on Seismic Response of Masonry Infills," edited by D.P. Abrams, 3/1/94, (PB94-180783, A07, MF-A02).

NCEER-94-0005 "The Northridge, California Earthquake of January 17, 1994: General Reconnaissance Report," edited by J.D. Goltz, 3/11/94, (PB94-193943, A10, MF-A03).

NCEER-94-0006 "Seismic Energy Based Fatigue Damage Analysis of Bridge Columns: Part I - Evaluation of Seismic Capacity," by G.A. Chang and J.B. Mander, 3/14/94, (PB94-219185, A11, MF-A03).

NCEER-94-0007 "Seismic Isolation of Multi-Story Frame Structures Using Spherical Sliding Isolation Systems," by T.M. Al-Hussaini, V.A. Zayas and M.C. Constantinou, 3/17/94, (PB94-193745, A09, MF-A02).

NCEER-94-0008 "The Northridge, California Earthquake of January 17, 1994: Performance of Highway Bridges," edited by I.G. Buckle, 3/24/94, (PB94-193851, A06, MF-A02).

NCEER-94-0009 "Proceedings of the Third U.S.-Japan Workshop on Earthquake Protective Systems for Bridges," edited by I.G. Buckle and I. Friedland, 3/31/94, (PB94-195815, A99, MF-A06).

NCEER-94-0010 "3D-BASIS-ME: Computer Program for Nonlinear Dynamic Analysis of Seismically Isolated Single and Multiple Structures and Liquid Storage Tanks," by P.C. Tsopelas, M.C. Constantinou and A.M. Reinhorn, 4/12/94, (PB94-204922, A09, MF-A02).

NCEER-94-0011 "The Northridge, California Earthquake of January 17, 1994: Performance of Gas Transmission Pipelines," by T.D. O'Rourke and M.C. Palmer, 5/16/94, (PB94-204989, A05, MF-A01).

NCEER-94-0012 "Feasibility Study of Replacement Procedures and Earthquake Performance Related to Gas Transmission Pipelines," by T.D. O'Rourke and M.C. Palmer, 5/25/94, (PB94-206638, A09, MF-A02).

NCEER-94-0013 "Seismic Energy Based Fatigue Damage Analysis of Bridge Columns: Part II - Evaluation of Seismic Demand," by G.A. Chang and J.B. Mander, 6/1/94, (PB95-18106, A08, MF-A02).

NCEER-94-0014 "NCEER-Taisei Corporation Research Program on Sliding Seismic Isolation Systems for Bridges: Experimental and Analytical Study of a System Consisting of Sliding Bearings and Fluid Restoring Force/Damping Devices," by P. Tsopelas and M.C. Constantinou, 6/13/94, (PB94-219144, A10, MF-A03).

NCEER-94-0015 "Generation of Hazard-Consistent Fragility Curves for Seismic Loss Estimation Studies," by H. Hwang and J-R. Huo, 6/14/94, (PB95-181996, A09, MF-A02).

NCEER-94-0016 "Seismic Study of Building Frames with Added Energy-Absorbing Devices," by W.S. Pong, C.S. Tsai and G.C. Lee, 6/20/94, (PB94-219136, A10, A03).

NCEER-94-0017 "Sliding Mode Control for Seismic-Excited Linear and Nonlinear Civil Engineering Structures," by J. Yang, J. Wu, A. Agrawal and Z. Li, 6/21/94, (PB95-138483, A06, MF-A02).

NCEER-94-0018 "3D-BASIS-TABS Version 2.0: Computer Program for Nonlinear Dynamic Analysis of Three Dimensional Base Isolated Structures," by A.M. Reinhorn, S. Nagarajaiah, M.C. Constantinou, P. Tsopelas and R. Li, 6/22/94, (PB95-182176, A08, MF-A02).

NCEER-94-0019 "Proceedings of the International Workshop on Civil Infrastructure Systems: Application of Intelligent Systems and Advanced Materials on Bridge Systems," Edited by G.C. Lee and K.C. Chang, 7/18/94, (PB95-252474, A20, MF-A04).

NCEER-94-0020 "Study of Seismic Isolation Systems for Computer Floors," by V. Lambrou and M.C. Constantinou, 7/19/94, (PB95-138533, A10, MF-A03).

NCEER-94-0021 "Proceedings of the U.S.-Italian Workshop on Guidelines for Seismic Evaluation and Rehabilitation of Unreinforced Masonry Buildings," Edited by D.P. Abrams and G.M. Calvi, 7/20/94, (PB95-138749, A13, MF-A03).

NCEER-94-0022 "NCEER-Taisei Corporation Research Program on Sliding Seismic Isolation Systems for Bridges: Experimental and Analytical Study of a System Consisting of Lubricated PTFE Sliding Bearings and Mild Steel Dampers," by P. Tsopelas and M.C. Constantinou, 7/22/94, (PB95-182184, A08, MF-A02).

NCEER-94-0023 “Development of Reliability-Based Design Criteria for Buildings Under Seismic Load,” by Y.K. Wen, H. Hwang and M. Shinozuka, 8/1/94, (PB95-211934, A08, MF-A02).

NCEER-94-0024 “Experimental Verification of Acceleration Feedback Control Strategies for an Active Tendon System,” by S.J. Dyke, B.F. Spencer, Jr., P. Quast, M.K. Sain, D.C. Kaspari, Jr. and T.T. Soong, 8/29/94, (PB95-212320, A05, MF-A01).

NCEER-94-0025 “Seismic Retrofitting Manual for Highway Bridges,” Edited by I.G. Buckle and I.F. Friedland, published by the Federal Highway Administration (PB95-212676, A15, MF-A03).

NCEER-94-0026 “Proceedings from the Fifth U.S.-Japan Workshop on Earthquake Resistant Design of Lifeline Facilities and Countermeasures Against Soil Liquefaction,” Edited by T.D. O’Rourke and M. Hamada, 11/7/94, (PB95-220802, A99, MF-E08).

NCEER-95-0001 "Experimental and Analytical Investigation of Seismic Retrofit of Structures with Supplemental Damping: Part 1 - Fluid Viscous Damping Devices," by A.M. Reinhorn, C. Li and M.C. Constantinou, 1/3/95, (PB95-266599, A09, MF-A02).

NCEER-95-0002 "Experimental and Analytical Study of Low-Cycle Fatigue Behavior of Semi-Rigid Top-And-Seat Angle Connections," by G. Pekcan, J.B. Mander and S.S. Chen, 1/5/95, (PB95-220042, A07, MF-A02).

NCEER-95-0003 "NCEER-ATC Joint Study on Fragility of Buildings," by T. Anagnos, C. Rojahn and A.S. Kiremidjian, 1/20/95, (PB95-220026, A06, MF-A02).

NCEER-95-0004 "Nonlinear Control Algorithms for Peak Response Reduction," by Z. Wu, T.T. Soong, V. Gattulli and R.C. Lin, 2/16/95, (PB95-220349, A05, MF-A01).

NCEER-95-0005 "Pipeline Replacement Feasibility Study: A Methodology for Minimizing Seismic and Corrosion Risks to Underground Natural Gas Pipelines," by R.T. Eguchi, H.A. Seligson and D.G. Honegger, 3/2/95, (PB95-252326, A06, MF-A02).

NCEER-95-0006 "Evaluation of Seismic Performance of an 11-Story Frame Building During the 1994 Northridge Earthquake," by F. Naeim, R. DiSulio, K. Benuska, A. Reinhorn and C. Li, not available.

NCEER-95-0007 "Prioritization of Bridges for Seismic Retrofitting," by N. Basöz and A.S. Kiremidjian, 4/24/95, (PB95-252300, A08, MF-A02).

NCEER-95-0008 "Method for Developing Motion Damage Relationships for Reinforced Concrete Frames," by A. Singhal and A.S. Kiremidjian, 5/11/95, (PB95-266607, A06, MF-A02).

NCEER-95-0009 "Experimental and Analytical Investigation of Seismic Retrofit of Structures with Supplemental Damping: Part II - Friction Devices," by C. Li and A.M. Reinhorn, 7/6/95, (PB96-128087, A11, MF-A03).

NCEER-95-0010 "Experimental Performance and Analytical Study of a Non-Ductile Reinforced Concrete Frame Structure Retrofitted with Elastomeric Spring Dampers," by G. Pekcan, J.B. Mander and S.S. Chen, 7/14/95, (PB96-137161, A08, MF-A02).

NCEER-95-0011 "Development and Experimental Study of Semi-Active Fluid Damping Devices for Seismic Protection of Structures," by M.D. Symans and M.C. Constantinou, 8/3/95, (PB96-136940, A23, MF-A04).

NCEER-95-0012 "Real-Time Structural Parameter Modification (RSPM): Development of Innervated Structures," by Z. Liang, M. Tong and G.C. Lee, 4/11/95, (PB96-137153, A06, MF-A01).

NCEER-95-0013 "Experimental and Analytical Investigation of Seismic Retrofit of Structures with Supplemental Damping: Part III - Viscous Damping Walls," by A.M. Reinhorn and C. Li, 10/1/95, (PB96-176409, A11, MF-A03).

NCEER-95-0014 "Seismic Fragility Analysis of Equipment and Structures in a Memphis Electric Substation," by J-R. Huo and H.H.M. Hwang, 8/10/95, (PB96-128087, A09, MF-A02).

NCEER-95-0015 "The Hanshin-Awaji Earthquake of January 17, 1995: Performance of Lifelines," Edited by M. Shinozuka, 11/3/95, (PB96-176383, A15, MF-A03).

NCEER-95-0016 "Highway Culvert Performance During Earthquakes," by T.L. Youd and C.J. Beckman, available as NCEER-96-0015.

NCEER-95-0017 "The Hanshin-Awaji Earthquake of January 17, 1995: Performance of Highway Bridges," Edited by I.G. Buckle, 12/1/95, not available.

NCEER-95-0018 "Modeling of Masonry Infill Panels for Structural Analysis," by A.M. Reinhorn, A. Madan, R.E. Valles, Y. Reichmann and J.B. Mander, 12/8/95, (PB97-110886, MF-A01, A06).

NCEER-95-0019 "Optimal Polynomial Control for Linear and Nonlinear Structures," by A.K. Agrawal and J.N. Yang, 12/11/95, (PB96-168737, A07, MF-A02).

NCEER-95-0020 "Retrofit of Non-Ductile Reinforced Concrete Frames Using Friction Dampers," by R.S. Rao, P. Gergely and R.N. White, 12/22/95, (PB97-133508, A10, MF-A02).

NCEER-95-0021 "Parametric Results for Seismic Response of Pile-Supported Bridge Bents," by G. Mylonakis, A. Nikolaou and G. Gazetas, 12/22/95, (PB97-100242, A12, MF-A03).

NCEER-95-0022 "Kinematic Bending Moments in Seismically Stressed Piles," by A. Nikolaou, G. Mylonakis and G. Gazetas, 12/23/95, (PB97-113914, MF-A03, A13).

NCEER-96-0001 "Dynamic Response of Unreinforced Masonry Buildings with Flexible Diaphragms," by A.C. Costley and D.P. Abrams," 10/10/96, (PB97-133573, MF-A03, A15).

NCEER-96-0002 "State of the Art Review: Foundations and Retaining Structures," by I. Po Lam, not available.

NCEER-96-0003 "Ductility of Rectangular Reinforced Concrete Bridge Columns with Moderate Confinement," by N. Wehbe, M. Saiidi, D. Sanders and B. Douglas, 11/7/96, (PB97-133557, A06, MF-A02).

NCEER-96-0004 "Proceedings of the Long-Span Bridge Seismic Research Workshop," edited by I.G. Buckle and I.M. Friedland, not available.

NCEER-96-0005 "Establish Representative Pier Types for Comprehensive Study: Eastern United States," by J. Kulicki and Z. Prucz, 5/28/96, (PB98-119217, A07, MF-A02).

NCEER-96-0006 "Establish Representative Pier Types for Comprehensive Study: Western United States," by R. Imbsen, R.A. Schamber and T.A. Osterkamp, 5/28/96, (PB98-118607, A07, MF-A02).

NCEER-96-0007 "Nonlinear Control Techniques for Dynamical Systems with Uncertain Parameters," by R.G. Ghanem and M.I. Bujakov, 5/27/96, (PB97-100259, A17, MF-A03).

NCEER-96-0008 "Seismic Evaluation of a 30-Year Old Non-Ductile Highway Bridge Pier and Its Retrofit," by J.B. Mander, B. Mahmoodzadegan, S. Bhadra and S.S. Chen, 5/31/96, (PB97-110902, MF-A03, A10).

NCEER-96-0009 "Seismic Performance of a Model Reinforced Concrete Bridge Pier Before and After Retrofit," by J.B. Mander, J.H. Kim and C.A. Ligozio, 5/31/96, (PB97-110910, MF-A02, A10).

NCEER-96-0010 "IDARC2D Version 4.0: A Computer Program for the Inelastic Damage Analysis of Buildings," by R.E. Valles, A.M. Reinhorn, S.K. Kunnath, C. Li and A. Madan, 6/3/96, (PB97-100234, A17, MF-A03).

NCEER-96-0011 "Estimation of the Economic Impact of Multiple Lifeline Disruption: Memphis Light, Gas and Water Division Case Study," by S.E. Chang, H.A. Seligson and R.T. Eguchi, 8/16/96, (PB97-133490, A11, MF-A03).

NCEER-96-0012 "Proceedings from the Sixth Japan-U.S. Workshop on Earthquake Resistant Design of Lifeline Facilities and Countermeasures Against Soil Liquefaction, Edited by M. Hamada and T. O'Rourke, 9/11/96, (PB97-133581, A99, MF-A06).

NCEER-96-0013 "Chemical Hazards, Mitigation and Preparedness in Areas of High Seismic Risk: A Methodology for Estimating the Risk of Post-Earthquake Hazardous Materials Release," by H.A. Seligson, R.T. Eguchi, K.J. Tierney and K. Richmond, 11/7/96, (PB97-133565, MF-A02, A08).

NCEER-96-0014 "Response of Steel Bridge Bearings to Reversed Cyclic Loading," by J.B. Mander, D-K. Kim, S.S. Chen and G.J. Premus, 11/13/96, (PB97-140735, A12, MF-A03).

NCEER-96-0015 "Highway Culvert Performance During Past Earthquakes," by T.L. Youd and C.J. Beckman, 11/25/96, (PB97-133532, A06, MF-A01).

NCEER-97-0001 "Evaluation, Prevention and Mitigation of Pounding Effects in Building Structures," by R.E. Valles and A.M. Reinhorn, 2/20/97, (PB97-159552, A14, MF-A03).

NCEER-97-0002 "Seismic Design Criteria for Bridges and Other Highway Structures," by C. Rojahn, R. Mayes, D.G. Anderson, J. Clark, J.H. Hom, R.V. Nutt and M.J. O'Rourke, 4/30/97, (PB97-194658, A06, MF-A03).

NCEER-97-0003 “Proceedings of the U.S.-Italian Workshop on Seismic Evaluation and Retrofit,” Edited by D.P. Abrams and G.M. Calvi, 3/19/97, (PB97-194666, A13, MF-A03).

NCEER-97-0004 "Investigation of Seismic Response of Buildings with Linear and Nonlinear Fluid Viscous Dampers," by A.A. Seleemah and M.C. Constantinou, 5/21/97, (PB98-109002, A15, MF-A03).

NCEER-97-0005 "Proceedings of the Workshop on Earthquake Engineering Frontiers in Transportation Facilities," edited by G.C. Lee and I.M. Friedland, 8/29/97, (PB98-128911, A25, MR-A04).

NCEER-97-0006 "Cumulative Seismic Damage of Reinforced Concrete Bridge Piers," by S.K. Kunnath, A. El-Bahy, A. Taylor and W. Stone, 9/2/97, (PB98-108814, A11, MF-A03).

NCEER-97-0007 "Structural Details to Accommodate Seismic Movements of Highway Bridges and Retaining Walls," by R.A. Imbsen, R.A. Schamber, E. Thorkildsen, A. Kartoum, B.T. Martin, T.N. Rosser and J.M. Kulicki, 9/3/97, (PB98-108996, A09, MF-A02).

NCEER-97-0008 "A Method for Earthquake Motion-Damage Relationships with Application to Reinforced Concrete Frames," by A. Singhal and A.S. Kiremidjian, 9/10/97, (PB98-108988, A13, MF-A03).

NCEER-97-0009 "Seismic Analysis and Design of Bridge Abutments Considering Sliding and Rotation," by K. Fishman and R. Richards, Jr., 9/15/97, (PB98-108897, A06, MF-A02).

NCEER-97-0010 "Proceedings of the FHWA/NCEER Workshop on the National Representation of Seismic Ground Motion for New and Existing Highway Facilities," edited by I.M. Friedland, M.S. Power and R.L. Mayes, 9/22/97, (PB98-128903, A21, MF-A04).

NCEER-97-0011 "Seismic Analysis for Design or Retrofit of Gravity Bridge Abutments," by K.L. Fishman, R. Richards, Jr. and R.C. Divito, 10/2/97, (PB98-128937, A08, MF-A02).

NCEER-97-0012 "Evaluation of Simplified Methods of Analysis for Yielding Structures," by P. Tsopelas, M.C. Constantinou, C.A. Kircher and A.S. Whittaker, 10/31/97, (PB98-128929, A10, MF-A03).

NCEER-97-0013 "Seismic Design of Bridge Columns Based on Control and Repairability of Damage," by C-T. Cheng and J.B. Mander, 12/8/97, (PB98-144249, A11, MF-A03).

NCEER-97-0014 "Seismic Resistance of Bridge Piers Based on Damage Avoidance Design," by J.B. Mander and C-T. Cheng, 12/10/97, (PB98-144223, A09, MF-A02).

NCEER-97-0015 “Seismic Response of Nominally Symmetric Systems with Strength Uncertainty,” by S. Balopoulou and M. Grigoriu, 12/23/97, (PB98-153422, A11, MF-A03).

NCEER-97-0016 “Evaluation of Seismic Retrofit Methods for Reinforced Concrete Bridge Columns,” by T.J. Wipf, F.W. Klaiber and F.M. Russo, 12/28/97, (PB98-144215, A12, MF-A03).

NCEER-97-0017 “Seismic Fragility of Existing Conventional Reinforced Concrete Highway Bridges,” by C.L. Mullen and A.S. Cakmak, 12/30/97, (PB98-153406, A08, MF-A02).

NCEER-97-0018 “Loss Asssessment of Memphis Buildings,” edited by D.P. Abrams and M. Shinozuka, 12/31/97, (PB98-144231, A13, MF-A03).

NCEER-97-0019 “Seismic Evaluation of Frames with Infill Walls Using Quasi-static Experiments,” by K.M. Mosalam, R.N. White and P. Gergely, 12/31/97, (PB98-153455, A07, MF-A02).

NCEER-97-0020 “Seismic Evaluation of Frames with Infill Walls Using Pseudo-dynamic Experiments,” by K.M. Mosalam, R.N. White and P. Gergely, 12/31/97, (PB98-153430, A07, MF-A02).

NCEER-97-0021 “Computational Strategies for Frames with Infill Walls: Discrete and Smeared Crack Analyses and Seismic Fragility,” by K.M. Mosalam, R.N. White and P. Gergely, 12/31/97, (PB98-153414, A10, MF-A02).

NCEER-97-0022 "Proceedings of the NCEER Workshop on Evaluation of Liquefaction Resistance of Soils," edited by T.L. Youd and I.M. Idriss, 12/31/97, (PB98-155617, A15, MF-A03).

MCEER-98-0001 "Extraction of Nonlinear Hysteretic Properties of Seismically Isolated Bridges from Quick-Release Field Tests," by Q. Chen, B.M. Douglas, E.M. Maragakis and I.G. Buckle, 5/26/98, (PB99-118838, A06, MF-A01).

MCEER-98-0002 "Methodologies for Evaluating the Importance of Highway Bridges," by A. Thomas, S. Eshenaur and J. Kulicki, 5/29/98, (PB99-118846, A10, MF-A02).

MCEER-98-0003 "Capacity Design of Bridge Piers and the Analysis of Overstrength," by J.B. Mander, A. Dutta and P. Goel, 6/1/98, (PB99-118853, A09, MF-A02).

MCEER-98-0004 "Evaluation of Bridge Damage Data from the Loma Prieta and Northridge, California Earthquakes," by N. Basoz and A. Kiremidjian, 6/2/98, (PB99-118861, A15, MF-A03).

MCEER-98-0005 "Screening Guide for Rapid Assessment of Liquefaction Hazard at Highway Bridge Sites," by T. L. Youd, 6/16/98, (PB99-118879, A06, not available on microfiche).

MCEER-98-0006 "Structural Steel and Steel/Concrete Interface Details for Bridges," by P. Ritchie, N. Kauhl and J. Kulicki, 7/13/98, (PB99-118945, A06, MF-A01).

MCEER-98-0007 "Capacity Design and Fatigue Analysis of Confined Concrete Columns," by A. Dutta and J.B. Mander, 7/14/98, (PB99-118960, A14, MF-A03).

MCEER-98-0008 "Proceedings of the Workshop on Performance Criteria for Telecommunication Services Under Earthquake Conditions," edited by A.J. Schiff, 7/15/98, (PB99-118952, A08, MF-A02).

MCEER-98-0009 "Fatigue Analysis of Unconfined Concrete Columns," by J.B. Mander, A. Dutta and J.H. Kim, 9/12/98, (PB99-123655, A10, MF-A02).

MCEER-98-0010 "Centrifuge Modeling of Cyclic Lateral Response of Pile-Cap Systems and Seat-Type Abutments in Dry Sands," by A.D. Gadre and R. Dobry, 10/2/98, (PB99-123606, A13, MF-A03).

MCEER-98-0011 "IDARC-BRIDGE: A Computational Platform for Seismic Damage Assessment of Bridge Structures," by A.M. Reinhorn, V. Simeonov, G. Mylonakis and Y. Reichman, 10/2/98, (PB99-162919, A15, MF-A03).

MCEER-98-0012 "Experimental Investigation of the Dynamic Response of Two Bridges Before and After Retrofitting with Elastomeric Bearings," by D.A. Wendichansky, S.S. Chen and J.B. Mander, 10/2/98, (PB99-162927, A15, MF-A03).

MCEER-98-0013 "Design Procedures for Hinge Restrainers and Hinge Sear Width for Multiple-Frame Bridges," by R. Des Roches and G.L. Fenves, 11/3/98, (PB99-140477, A13, MF-A03).

MCEER-98-0014 "Response Modification Factors for Seismically Isolated Bridges," by M.C. Constantinou and J.K. Quarshie, 11/3/98, (PB99-140485, A14, MF-A03).

MCEER-98-0015 "Proceedings of the U.S.-Italy Workshop on Seismic Protective Systems for Bridges," edited by I.M. Friedland and M.C. Constantinou, 11/3/98, (PB2000-101711, A22, MF-A04).

MCEER-98-0016 "Appropriate Seismic Reliability for Critical Equipment Systems: Recommendations Based on Regional Analysis of Financial and Life Loss," by K. Porter, C. Scawthorn, C. Taylor and N. Blais, 11/10/98, (PB99-157265, A08, MF-A02).

MCEER-98-0017 "Proceedings of the U.S. Japan Joint Seminar on Civil Infrastructure Systems Research," edited by M. Shinozuka and A. Rose, 11/12/98, (PB99-156713, A16, MF-A03).

MCEER-98-0018 "Modeling of Pile Footings and Drilled Shafts for Seismic Design," by I. PoLam, M. Kapuskar and D. Chaudhuri, 12/21/98, (PB99-157257, A09, MF-A02).

MCEER-99-0001 "Seismic Evaluation of a Masonry Infilled Reinforced Concrete Frame by Pseudodynamic Testing," by S.G. Buonopane and R.N. White, 2/16/99, (PB99-162851, A09, MF-A02).

MCEER-99-0002 "Response History Analysis of Structures with Seismic Isolation and Energy Dissipation Systems: Verification Examples for Program SAP2000," by J. Scheller and M.C. Constantinou, 2/22/99, (PB99-162869, A08, MF-A02).

MCEER-99-0003 "Experimental Study on the Seismic Design and Retrofit of Bridge Columns Including Axial Load Effects," by A. Dutta, T. Kokorina and J.B. Mander, 2/22/99, (PB99-162877, A09, MF-A02).

MCEER-99-0004 "Experimental Study of Bridge Elastomeric and Other Isolation and Energy Dissipation Systems with Emphasis on Uplift Prevention and High Velocity Near-source Seismic Excitation," by A. Kasalanati and M. C. Constantinou, 2/26/99, (PB99-162885, A12, MF-A03).

MCEER-99-0005 "Truss Modeling of Reinforced Concrete Shear-flexure Behavior," by J.H. Kim and J.B. Mander, 3/8/99, (PB99-163693, A12, MF-A03).

MCEER-99-0006 "Experimental Investigation and Computational Modeling of Seismic Response of a 1:4 Scale Model Steel Structure with a Load Balancing Supplemental Damping System," by G. Pekcan, J.B. Mander and S.S. Chen, 4/2/99, (PB99-162893, A11, MF-A03).

MCEER-99-0007 "Effect of Vertical Ground Motions on the Structural Response of Highway Bridges," by M.R. Button, C.J. Cronin and R.L. Mayes, 4/10/99, (PB2000-101411, A10, MF-A03).

MCEER-99-0008 "Seismic Reliability Assessment of Critical Facilities: A Handbook, Supporting Documentation, and Model Code Provisions," by G.S. Johnson, R.E. Sheppard, M.D. Quilici, S.J. Eder and C.R. Scawthorn, 4/12/99, (PB2000-101701, A18, MF-A04).

MCEER-99-0009 "Impact Assessment of Selected MCEER Highway Project Research on the Seismic Design of Highway Structures," by C. Rojahn, R. Mayes, D.G. Anderson, J.H. Clark, D'Appolonia Engineering, S. Gloyd and R.V. Nutt, 4/14/99, (PB99-162901, A10, MF-A02).

MCEER-99-0010 "Site Factors and Site Categories in Seismic Codes," by R. Dobry, R. Ramos and M.S. Power, 7/19/99, (PB2000-101705, A08, MF-A02).

MCEER-99-0011 "Restrainer Design Procedures for Multi-Span Simply-Supported Bridges," by M.J. Randall, M. Saiidi, E. Maragakis and T. Isakovic, 7/20/99, (PB2000-101702, A10, MF-A02).

MCEER-99-0012 "Property Modification Factors for Seismic Isolation Bearings," by M.C. Constantinou, P. Tsopelas, A. Kasalanati and E. Wolff, 7/20/99, (PB2000-103387, A11, MF-A03).

MCEER-99-0013 "Critical Seismic Issues for Existing Steel Bridges," by P. Ritchie, N. Kauhl and J. Kulicki, 7/20/99, (PB2000-101697, A09, MF-A02).

MCEER-99-0014 "Nonstructural Damage Database," by A. Kao, T.T. Soong and A. Vender, 7/24/99, (PB2000-101407, A06, MF-A01).

MCEER-99-0015 "Guide to Remedial Measures for Liquefaction Mitigation at Existing Highway Bridge Sites," by H.G. Cooke and J. K. Mitchell, 7/26/99, (PB2000-101703, A11, MF-A03).

MCEER-99-0016 "Proceedings of the MCEER Workshop on Ground Motion Methodologies for the Eastern United States," edited by N. Abrahamson and A. Becker, 8/11/99, (PB2000-103385, A07, MF-A02).

MCEER-99-0017 "Quindío, Colombia Earthquake of January 25, 1999: Reconnaissance Report," by A.P. Asfura and P.J. Flores, 10/4/99, (PB2000-106893, A06, MF-A01).

MCEER-99-0018 "Hysteretic Models for Cyclic Behavior of Deteriorating Inelastic Structures," by M.V. Sivaselvan and A.M. Reinhorn, 11/5/99, (PB2000-103386, A08, MF-A02).

MCEER-99-0019 "Proceedings of the 7th U.S.- Japan Workshop on Earthquake Resistant Design of Lifeline Facilities and Countermeasures Against Soil Liquefaction," edited by T.D. O'Rourke, J.P. Bardet and M. Hamada, 11/19/99, (PB2000-103354, A99, MF-A06).

MCEER-99-0020 "Development of Measurement Capability for Micro-Vibration Evaluations with Application to Chip Fabrication Facilities," by G.C. Lee, Z. Liang, J.W. Song, J.D. Shen and W.C. Liu, 12/1/99, (PB2000-105993, A08, MF-A02).

MCEER-99-0021 "Design and Retrofit Methodology for Building Structures with Supplemental Energy Dissipating Systems," by G. Pekcan, J.B. Mander and S.S. Chen, 12/31/99, (PB2000-105994, A11, MF-A03).

MCEER-00-0001 "The Marmara, Turkey Earthquake of August 17, 1999: Reconnaissance Report," edited by C. Scawthorn; with major contributions by M. Bruneau, R. Eguchi, T. Holzer, G. Johnson, J. Mander, J. Mitchell, W. Mitchell, A. Papageorgiou, C. Scaethorn, and G. Webb, 3/23/00, (PB2000-106200, A11, MF-A03).

MCEER-00-0002 "Proceedings of the MCEER Workshop for Seismic Hazard Mitigation of Health Care Facilities," edited by G.C. Lee, M. Ettouney, M. Grigoriu, J. Hauer and J. Nigg, 3/29/00, (PB2000-106892, A08, MF-A02).

MCEER-00-0003 "The Chi-Chi, Taiwan Earthquake of September 21, 1999: Reconnaissance Report," edited by G.C. Lee and C.H. Loh, with major contributions by G.C. Lee, M. Bruneau, I.G. Buckle, S.E. Chang, P.J. Flores, T.D. O'Rourke, M. Shinozuka, T.T. Soong, C-H. Loh, K-C. Chang, Z-J. Chen, J-S. Hwang, M-L. Lin, G-Y. Liu, K-C. Tsai, G.C. Yao and C-L. Yen, 4/30/00, (PB2001-100980, A10, MF-A02).

MCEER-00-0004 "Seismic Retrofit of End-Sway Frames of Steel Deck-Truss Bridges with a Supplemental Tendon System: Experimental and Analytical Investigation," by G. Pekcan, J.B. Mander and S.S. Chen, 7/1/00, (PB2001-100982, A10, MF-A02).

MCEER-00-0005 "Sliding Fragility of Unrestrained Equipment in Critical Facilities," by W.H. Chong and T.T. Soong, 7/5/00, (PB2001-100983, A08, MF-A02).

MCEER-00-0006 "Seismic Response of Reinforced Concrete Bridge Pier Walls in the Weak Direction," by N. Abo-Shadi, M. Saiidi and D. Sanders, 7/17/00, (PB2001-100981, A17, MF-A03).

MCEER-00-0007 "Low-Cycle Fatigue Behavior of Longitudinal Reinforcement in Reinforced Concrete Bridge Columns," by J. Brown and S.K. Kunnath, 7/23/00, (PB2001-104392, A08, MF-A02).

MCEER-00-0008 "Soil Structure Interaction of Bridges for Seismic Analysis," I. PoLam and H. Law, 9/25/00, (PB2001-105397, A08, MF-A02).

MCEER-00-0009 "Proceedings of the First MCEER Workshop on Mitigation of Earthquake Disaster by Advanced Technologies (MEDAT-1), edited by M. Shinozuka, D.J. Inman and T.D. O'Rourke, 11/10/00, (PB2001-105399, A14, MF-A03).

MCEER-00-0010 "Development and Evaluation of Simplified Procedures for Analysis and Design of Buildings with Passive Energy Dissipation Systems, Revision 01," by O.M. Ramirez, M.C. Constantinou, C.A. Kircher, A.S. Whittaker, M.W. Johnson, J.D. Gomez and C. Chrysostomou, 11/16/01, (PB2001-105523, A23, MF-A04).

MCEER-00-0011 "Dynamic Soil-Foundation-Structure Interaction Analyses of Large Caissons," by C-Y. Chang, C-M. Mok, Z-L. Wang, R. Settgast, F. Waggoner, M.A. Ketchum, H.M. Gonnermann and C-C. Chin, 12/30/00, (PB2001-104373, A07, MF-A02).

MCEER-00-0012 "Experimental Evaluation of Seismic Performance of Bridge Restrainers," by A.G. Vlassis, E.M. Maragakis and M. Saiid Saiidi, 12/30/00, (PB2001-104354, A09, MF-A02).

MCEER-00-0013 "Effect of Spatial Variation of Ground Motion on Highway Structures," by M. Shinozuka, V. Saxena and G. Deodatis, 12/31/00, (PB2001-108755, A13, MF-A03).

MCEER-00-0014 "A Risk-Based Methodology for Assessing the Seismic Performance of Highway Systems," by S.D. Werner, C.E. Taylor, J.E. Moore, II, J.S. Walton and S. Cho, 12/31/00, (PB2001-108756, A14, MF-A03).

MCEER-01-0001 "Experimental Investigation of P-Delta Effects to Collapse During Earthquakes," by D. Vian and M. Bruneau, 6/25/01, (PB2002-100534, A17, MF-A03).

MCEER-01-0002 "Proceedings of the Second MCEER Workshop on Mitigation of Earthquake Disaster by Advanced Technologies (MEDAT-2)," edited by M. Bruneau and D.J. Inman, 7/23/01, (PB2002-100434, A16, MF-A03).

MCEER-01-0003 "Sensitivity Analysis of Dynamic Systems Subjected to Seismic Loads," by C. Roth and M. Grigoriu, 9/18/01, (PB2003-100884, A12, MF-A03).

MCEER-01-0004 "Overcoming Obstacles to Implementing Earthquake Hazard Mitigation Policies: Stage 1 Report," by D.J. Alesch and W.J. Petak, 12/17/01, (PB2002-107949, A07, MF-A02).

MCEER-01-0005 "Updating Real-Time Earthquake Loss Estimates: Methods, Problems and Insights," by C.E. Taylor, S.E. Chang and R.T. Eguchi, 12/17/01, (PB2002-107948, A05, MF-A01).

MCEER-01-0006 "Experimental Investigation and Retrofit of Steel Pile Foundations and Pile Bents Under Cyclic Lateral Loadings," by A. Shama, J. Mander, B. Blabac and S. Chen, 12/31/01, (PB2002-107950, A13, MF-A03).

MCEER-02-0001 "Assessment of Performance of Bolu Viaduct in the 1999 Duzce Earthquake in Turkey" by P.C. Roussis, M.C. Constantinou, M. Erdik, E. Durukal and M. Dicleli, 5/8/02, (PB2003-100883, A08, MF-A02).

MCEER-02-0002 "Seismic Behavior of Rail Counterweight Systems of Elevators in Buildings," by M.P. Singh, Rildova and L.E. Suarez, 5/27/02. (PB2003-100882, A11, MF-A03).

MCEER-02-0003 "Development of Analysis and Design Procedures for Spread Footings," by G. Mylonakis, G. Gazetas, S. Nikolaou and A. Chauncey, 10/02/02, (PB2004-101636, A13, MF-A03, CD-A13).

MCEER-02-0004 "Bare-Earth Algorithms for Use with SAR and LIDAR Digital Elevation Models," by C.K. Huyck, R.T. Eguchi and B. Houshmand, 10/16/02, (PB2004-101637, A07, CD-A07).

MCEER-02-0005 "Review of Energy Dissipation of Compression Members in Concentrically Braced Frames," by K.Lee and M. Bruneau, 10/18/02, (PB2004-101638, A10, CD-A10).

MCEER-03-0001 "Experimental Investigation of Light-Gauge Steel Plate Shear Walls for the Seismic Retrofit of Buildings" by J. Berman and M. Bruneau, 5/2/03, (PB2004-101622, A10, MF-A03, CD-A10).

MCEER-03-0002 "Statistical Analysis of Fragility Curves," by M. Shinozuka, M.Q. Feng, H. Kim, T. Uzawa and T. Ueda, 6/16/03, (PB2004-101849, A09, CD-A09).

MCEER-03-0003 "Proceedings of the Eighth U.S.-Japan Workshop on Earthquake Resistant Design f Lifeline Facilities and Countermeasures Against Liquefaction," edited by M. Hamada, J.P. Bardet and T.D. O'Rourke, 6/30/03, (PB2004-104386, A99, CD-A99).

MCEER-03-0004 "Proceedings of the PRC-US Workshop on Seismic Analysis and Design of Special Bridges," edited by L.C. Fan and G.C. Lee, 7/15/03, (PB2004-104387, A14, CD-A14).

MCEER-03-0005 "Urban Disaster Recovery: A Framework and Simulation Model," by S.B. Miles and S.E. Chang, 7/25/03, (PB2004-104388, A07, CD-A07).

MCEER-03-0006 "Behavior of Underground Piping Joints Due to Static and Dynamic Loading," by R.D. Meis, M. Maragakis and R. Siddharthan, 11/17/03, (PB2005-102194, A13, MF-A03, CD-A00).

MCEER-04-0001 "Experimental Study of Seismic Isolation Systems with Emphasis on Secondary System Response and Verification of Accuracy of Dynamic Response History Analysis Methods," by E. Wolff and M. Constantinou, 1/16/04 (PB2005-102195, A99, MF-E08, CD-A00).

MCEER-04-0002 "Tension, Compression and Cyclic Testing of Engineered Cementitious Composite Materials," by K. Kesner and S.L. Billington, 3/1/04, (PB2005-102196, A08, CD-A08).

MCEER-04-0003 "Cyclic Testing of Braces Laterally Restrained by Steel Studs to Enhance Performance During Earthquakes," by O.C. Celik, J.W. Berman and M. Bruneau, 3/16/04, (PB2005-102197, A13, MF-A03, CD-A00).

MCEER-04-0004 "Methodologies for Post Earthquake Building Damage Detection Using SAR and Optical Remote Sensing: Application to the August 17, 1999 Marmara, Turkey Earthquake," by C.K. Huyck, B.J. Adams, S. Cho, R.T. Eguchi, B. Mansouri and B. Houshmand, 6/15/04, (PB2005-104888, A10, CD-A00).

MCEER-04-0005 "Nonlinear Structural Analysis Towards Collapse Simulation: A Dynamical Systems Approach," by M.V. Sivaselvan and A.M. Reinhorn, 6/16/04, (PB2005-104889, A11, MF-A03, CD-A00).

MCEER-04-0006 "Proceedings of the Second PRC-US Workshop on Seismic Analysis and Design of Special Bridges," edited by G.C. Lee and L.C. Fan, 6/25/04, (PB2005-104890, A16, CD-A00).

MCEER-04-0007 "Seismic Vulnerability Evaluation of Axially Loaded Steel Built-up Laced Members," by K. Lee and M. Bruneau, 6/30/04, (PB2005-104891, A16, CD-A00).

MCEER-04-0008 "Evaluation of Accuracy of Simplified Methods of Analysis and Design of Buildings with Damping Systems for Near-Fault and for Soft-Soil Seismic Motions," by E.A. Pavlou and M.C. Constantinou, 8/16/04, (PB2005-104892, A08, MF-A02, CD-A00).

MCEER-04-0009 "Assessment of Geotechnical Issues in Acute Care Facilities in California," by M. Lew, T.D. O'Rourke, R. Dobry and M. Koch, 9/15/04, (PB2005-104893, A08, CD-A00).

MCEER-04-0010 "Scissor-Jack-Damper Energy Dissipation System," by A.N. Sigaher-Boyle and M.C. Constantinou, 12/1/04 (PB2005-108221).

MCEER-04-0011 "Seismic Retrofit of Bridge Steel Truss Piers Using a Controlled Rocking Approach," by M. Pollino and M. Bruneau, 12/20/04 (PB2006-105795).

MCEER-05-0001 "Experimental and Analytical Studies of Structures Seismically Isolated with an Uplift-Restraint Isolation System," by P.C. Roussis and M.C. Constantinou, 1/10/05 (PB2005-108222).

MCEER-05-0002 "A Versatile Experimentation Model for Study of Structures Near Collapse Applied to Seismic Evaluation of Irregular Structures," by D. Kusumastuti, A.M. Reinhorn and A. Rutenberg, 3/31/05 (PB2006-101523).

MCEER-05-0003 "Proceedings of the Third PRC-US Workshop on Seismic Analysis and Design of Special Bridges," edited by L.C. Fan and G.C. Lee, 4/20/05, (PB2006-105796).

MCEER-05-0004 "Approaches for the Seismic Retrofit of Braced Steel Bridge Piers and Proof-of-Concept Testing of an Eccentrically Braced Frame with Tubular Link," by J.W. Berman and M. Bruneau, 4/21/05 (PB2006-101524).

MCEER-05-0005 "Simulation of Strong Ground Motions for Seismic Fragility Evaluation of Nonstructural Components in Hospitals," by A. Wanitkorkul and A. Filiatrault, 5/26/05 (PB2006-500027).

MCEER-05-0006 "Seismic Safety in California Hospitals: Assessing an Attempt to Accelerate the Replacement or Seismic Retrofit of Older Hospital Facilities," by D.J. Alesch, L.A. Arendt and W.J. Petak, 6/6/05 (PB2006-105794).

MCEER-05-0007 "Development of Seismic Strengthening and Retrofit Strategies for Critical Facilities Using Engineered Cementitious Composite Materials," by K. Kesner and S.L. Billington, 8/29/05 (PB2006-111701).

MCEER-05-0008 "Experimental and Analytical Studies of Base Isolation Systems for Seismic Protection of Power Transformers," by N. Murota, M.Q. Feng and G-Y. Liu, 9/30/05 (PB2006-111702).

MCEER-05-0009 "3D-BASIS-ME-MB: Computer Program for Nonlinear Dynamic Analysis of Seismically Isolated Structures," by P.C. Tsopelas, P.C. Roussis, M.C. Constantinou, R. Buchanan and A.M. Reinhorn, 10/3/05 (PB2006-111703).

MCEER-05-0010 "Steel Plate Shear Walls for Seismic Design and Retrofit of Building Structures," by D. Vian and M. Bruneau, 12/15/05 (PB2006-111704).

MCEER-05-0011 "The Performance-Based Design Paradigm," by M.J. Astrella and A. Whittaker, 12/15/05 (PB2006-111705).

MCEER-06-0001 "Seismic Fragility of Suspended Ceiling Systems," H. Badillo-Almaraz, A.S. Whittaker, A.M. Reinhorn and G.P. Cimellaro, 2/4/06 (PB2006-111706).

MCEER-06-0002 "Multi-Dimensional Fragility of Structures," by G.P. Cimellaro, A.M. Reinhorn and M. Bruneau, 3/1/06 (PB2007-106974, A09, MF-A02, CD A00).

MCEER-06-0003 "Built-Up Shear Links as Energy Dissipators for Seismic Protection of Bridges," by P. Dusicka, A.M. Itani and I.G. Buckle, 3/15/06 (PB2006-111708).

MCEER-06-0004 "Analytical Investigation of the Structural Fuse Concept," by R.E. Vargas and M. Bruneau, 3/16/06 (PB2006-111709).

MCEER-06-0005 "Experimental Investigation of the Structural Fuse Concept," by R.E. Vargas and M. Bruneau, 3/17/06 (PB2006-111710).

MCEER-06-0006 "Further Development of Tubular Eccentrically Braced Frame Links for the Seismic Retrofit of Braced Steel Truss Bridge Piers," by J.W. Berman and M. Bruneau, 3/27/06 (PB2007-105147).

MCEER-06-0007 "REDARS Validation Report," by S. Cho, C.K. Huyck, S. Ghosh and R.T. Eguchi, 8/8/06 (PB2007-106983).

MCEER-06-0008 "Review of Current NDE Technologies for Post-Earthquake Assessment of Retrofitted Bridge Columns," by J.W. Song, Z. Liang and G.C. Lee, 8/21/06 (PB2007-106984).

MCEER-06-0009 "Liquefaction Remediation in Silty Soils Using Dynamic Compaction and Stone Columns," by S. Thevanayagam, G.R. Martin, R. Nashed, T. Shenthan, T. Kanagalingam and N. Ecemis, 8/28/06 (PB2007-106985).

MCEER-06-0010 "Conceptual Design and Experimental Investigation of Polymer Matrix Composite Infill Panels for Seismic Retrofitting," by W. Jung, M. Chiewanichakorn and A.J. Aref, 9/21/06 (PB2007-106986).

MCEER-06-0011 "A Study of the Coupled Horizontal-Vertical Behavior of Elastomeric and Lead-Rubber Seismic Isolation Bearings," by G.P. Warn and A.S. Whittaker, 9/22/06 (PB2007-108679).

MCEER-06-0012 "Proceedings of the Fourth PRC-US Workshop on Seismic Analysis and Design of Special Bridges: Advancing Bridge Technologies in Research, Design, Construction and Preservation," Edited by L.C. Fan, G.C. Lee and L. Ziang, 10/12/06 (PB2007-109042).

MCEER-06-0013 "Cyclic Response and Low Cycle Fatigue Characteristics of Plate Steels," by P. Dusicka, A.M. Itani and I.G. Buckle, 11/1/06 06 (PB2007-106987).

MCEER-06-0014 "Proceedings of the Second US-Taiwan Bridge Engineering Workshop," edited by W.P. Yen, J. Shen, J-Y. Chen and M. Wang, 11/15/06 (PB2008-500041).

MCEER-06-0015 "User Manual and Technical Documentation for the REDARS^{TM} Import Wizard," by S. Cho, S. Ghosh, C.K. Huyck and S.D. Werner, 11/30/06 (PB2007-114766).

MCEER-06-0016 "Hazard Mitigation Strategy and Monitoring Technologies for Urban and Infrastructure Public Buildings: Proceedings of the China-US Workshops," edited by X.Y. Zhou, A.L. Zhang, G.C. Lee and M. Tong, 12/12/06 (PB2008-500018).

MCEER-07-0001 "Static and Kinetic Coefficients of Friction for Rigid Blocks," by C. Kafali, S. Fathali, M. Grigoriu and A.S. Whittaker, 3/20/07 (PB2007-114767).

MCEER-07-0002 "Hazard Mitigation Investment Decision Making: Organizational Response to Legislative Mandate," by L.A. Arendt, D.J. Alesch and W.J. Petak, 4/9/07 (PB2007-114768).

MCEER-07-0003 "Seismic Behavior of Bidirectional-Resistant Ductile End Diaphragms with Unbonded Braces in Straight or Skewed Steel Bridges," by O. Celik and M. Bruneau, 4/11/07 (PB2008-105141).

MCEER-07-0004 "Modeling Pile Behavior in Large Pile Groups Under Lateral Loading," by A.M. Dodds and G.R. Martin, 4/16/07(PB2008-105142).

MCEER-07-0005 "Experimental Investigation of Blast Performance of Seismically Resistant Concrete-Filled Steel Tube Bridge Piers," by S. Fujikura, M. Bruneau and D. Lopez-Garcia, 4/20/07 (PB2008-105143).

MCEER-07-0006 "Seismic Analysis of Conventional and Isolated Liquefied Natural Gas Tanks Using Mechanical Analogs," by I.P. Christovasilis and A.S. Whittaker, 5/1/07, not available.

MCEER-07-0007 "Experimental Seismic Performance Evaluation of Isolation/Restraint Systems for Mechanical Equipment – Part 1: Heavy Equipment Study," by S. Fathali and A. Filiatrault, 6/6/07 (PB2008-105144).

MCEER-07-0008 "Seismic Vulnerability of Timber Bridges and Timber Substructures," by A.A. Sharma, J.B. Mander, I.M. Friedland and D.R. Allicock, 6/7/07 (PB2008-105145).

MCEER-07-0009 "Experimental and Analytical Study of the XY-Friction Pendulum (XY-FP) Bearing for Bridge Applications," by C.C. Marin-Artieda, A.S. Whittaker and M.C. Constantinou, 6/7/07 (PB2008-105191).

MCEER-07-0010 "Proceedings of the PRC-US Earthquake Engineering Forum for Young Researchers," Edited by G.C. Lee and X.Z. Qi, 6/8/07 (PB2008-500058).

MCEER-07-0011 "Design Recommendations for Perforated Steel Plate Shear Walls," by R. Purba and M. Bruneau, 6/18/07, (PB2008-105192).

MCEER-07-0012 "Performance of Seismic Isolation Hardware Under Service and Seismic Loading," by M.C. Constantinou, A.S. Whittaker, Y. Kalpakidis, D.M. Fenz and G.P. Warn, 8/27/07, (PB2008-105193).

MCEER-07-0013 "Experimental Evaluation of the Seismic Performance of Hospital Piping Subassemblies," by E.R. Goodwin, E. Maragakis and A.M. Itani, 9/4/07, (PB2008-105194).

MCEER-07-0014 "A Simulation Model of Urban Disaster Recovery and Resilience: Implementation for the 1994 Northridge Earthquake," by S. Miles and S.E. Chang, 9/7/07, (PB2008-106426).

MCEER-07-0015 "Statistical and Mechanistic Fragility Analysis of Concrete Bridges," by M. Shinozuka, S. Banerjee and S-H. Kim, 9/10/07, (PB2008-106427).

MCEER-07-0016 "Three-Dimensional Modeling of Inelastic Buckling in Frame Structures," by M. Schachter and AM. Reinhorn, 9/13/07, (PB2008-108125).

MCEER-07-0017 "Modeling of Seismic Wave Scattering on Pile Groups and Caissons," by I. Po Lam, H. Law and C.T. Yang, 9/17/07 (PB2008-108150).

MCEER-07-0018 "Bridge Foundations: Modeling Large Pile Groups and Caissons for Seismic Design," by I. Po Lam, H. Law and G.R. Martin (Coordinating Author), 12/1/07 (PB2008-111190).

MCEER-07-0019 "Principles and Performance of Roller Seismic Isolation Bearings for Highway Bridges," by G.C. Lee, Y.C. Ou, Z. Liang, T.C. Niu and J. Song, 12/10/07 (PB2009-110466).

MCEER-07-0020 "Centrifuge Modeling of Permeability and Pinning Reinforcement Effects on Pile Response to Lateral Spreading," by L.L Gonzalez-Lagos, T. Abdoun and R. Dobry, 12/10/07 (PB2008-111191).

MCEER-07-0021 "Damage to the Highway System from the Pisco, Perú Earthquake of August 15, 2007," by J.S. O'Connor, L. Mesa and M. Nykamp, 12/10/07, (PB2008-108126).

MCEER-07-0022 "Experimental Seismic Performance Evaluation of Isolation/Restraint Systems for Mechanical Equipment – Part 2: Light Equipment Study," by S. Fathali and A. Filiatrault, 12/13/07 (PB2008-111192).

MCEER-07-0023 "Fragility Considerations in Highway Bridge Design," by M. Shinozuka, S. Banerjee and S.H. Kim, 12/14/07 (PB2008-111193).

MCEER-07-0024 "Performance Estimates for Seismically Isolated Bridges," by G.P. Warn and A.S. Whittaker, 12/30/07 (PB2008-112230).

MCEER-08-0001 "Seismic Performance of Steel Girder Bridge Superstructures with Conventional Cross Frames," by L.P. Carden, A.M. Itani and I.G. Buckle, 1/7/08, (PB2008-112231).

MCEER-08-0002 "Seismic Performance of Steel Girder Bridge Superstructures with Ductile End Cross Frames with Seismic Isolators," by L.P. Carden, A.M. Itani and I.G. Buckle, 1/7/08 (PB2008-112232).

MCEER-08-0003 "Analytical and Experimental Investigation of a Controlled Rocking Approach for Seismic Protection of Bridge Steel Truss Piers," by M. Pollino and M. Bruneau, 1/21/08 (PB2008-112233).

MCEER-08-0004 "Linking Lifeline Infrastructure Performance and Community Disaster Resilience: Models and Multi-Stakeholder Processes," by S.E. Chang, C. Pasion, K. Tatebe and R. Ahmad, 3/3/08 (PB2008-112234).

MCEER-08-0005 "Modal Analysis of Generally Damped Linear Structures Subjected to Seismic Excitations," by J. Song, Y-L. Chu, Z. Liang and G.C. Lee, 3/4/08 (PB2009-102311).

MCEER-08-0006 "System Performance Under Multi-Hazard Environments," by C. Kafali and M. Grigoriu, 3/4/08 (PB2008-112235).

MCEER-08-0007 "Mechanical Behavior of Multi-Spherical Sliding Bearings," by D.M. Fenz and M.C. Constantinou, 3/6/08 (PB2008-112236).

MCEER-08-0008 "Post-Earthquake Restoration of the Los Angeles Water Supply System," by T.H.P. Tabucchi and R.A. Davidson, 3/7/08 (PB2008-112237).

MCEER-08-0009 "Fragility Analysis of Water Supply Systems," by A. Jacobson and M. Grigoriu, 3/10/08 (PB2009-105545).

MCEER-08-0010 "Experimental Investigation of Full-Scale Two-Story Steel Plate Shear Walls with Reduced Beam Section Connections," by B. Qu, M. Bruneau, C-H. Lin and K-C. Tsai, 3/17/08 (PB2009-106368).

MCEER-08-0011 "Seismic Evaluation and Rehabilitation of Critical Components of Electrical Power Systems," S. Ersoy, B. Feizi, A. Ashrafi and M. Ala Saadeghvaziri, 3/17/08 (PB2009-105546).

MCEER-08-0012 "Seismic Behavior and Design of Boundary Frame Members of Steel Plate Shear Walls," by B. Qu and M. Bruneau, 4/26/08 . (PB2009-106744).

MCEER-08-0013 "Development and Appraisal of a Numerical Cyclic Loading Protocol for Quantifying Building System Performance," by A. Filiatrault, A. Wanitkorkul and M. Constantinou, 4/27/08 (PB2009-107906).

MCEER-08-0014 "Structural and Nonstructural Earthquake Design: The Challenge of Integrating Specialty Areas in Designing Complex, Critical Facilities," by W.J. Petak and D.J. Alesch, 4/30/08 (PB2009-107907).

MCEER-08-0015 "Seismic Performance Evaluation of Water Systems," by Y. Wang and T.D. O'Rourke, 5/5/08 (PB2009-107908).

MCEER-08-0016 "Seismic Response Modeling of Water Supply Systems," by P. Shi and T.D. O'Rourke, 5/5/08 (PB2009-107910).

MCEER-08-0017 "Numerical and Experimental Studies of Self-Centering Post-Tensioned Steel Frames," by D. Wang and A. Filiatrault, 5/12/08 (PB2009-110479).

MCEER-08-0018 "Development, Implementation and Verification of Dynamic Analysis Models for Multi-Spherical Sliding Bearings," by D.M. Fenz and M.C. Constantinou, 8/15/08 (PB2009-107911).

MCEER-08-0019 "Performance Assessment of Conventional and Base Isolated Nuclear Power Plants for Earthquake Blast Loadings," by Y.N. Huang, A.S. Whittaker and N. Luco, 10/28/08 (PB2009-107912).

MCEER-08-0020 "Remote Sensing for Resilient Multi-Hazard Disaster Response – Volume I: Introduction to Damage Assessment Methodologies," by B.J. Adams and R.T. Eguchi, 11/17/08 (PB2010-102695).

MCEER-08-0021 "Remote Sensing for Resilient Multi-Hazard Disaster Response – Volume II: Counting the Number of Collapsed Buildings Using an Object-Oriented Analysis: Case Study of the 2003 Bam Earthquake," by L. Gusella, C.K. Huyck and B.J. Adams, 11/17/08 (PB2010-100925).

MCEER-08-0022 "Remote Sensing for Resilient Multi-Hazard Disaster Response – Volume III: Multi-Sensor Image Fusion Techniques for Robust Neighborhood-Scale Urban Damage Assessment," by B.J. Adams and A. McMillan, 11/17/08 (PB2010-100926).

MCEER-08-0023 "Remote Sensing for Resilient Multi-Hazard Disaster Response – Volume IV: A Study of Multi-Temporal and Multi-Resolution SAR Imagery for Post-Katrina Flood Monitoring in New Orleans," by A. McMillan, J.G. Morley, B.J. Adams and S. Chesworth, 11/17/08 (PB2010-100927).

MCEER-08-0024 "Remote Sensing for Resilient Multi-Hazard Disaster Response – Volume V: Integration of Remote Sensing Imagery and VIEWS^{TM} Field Data for Post-Hurricane Charley Building Damage Assessment," by J.A. Womble, K. Mehta and B.J. Adams, 11/17/08 (PB2009-115532).

MCEER-08-0025 "Building Inventory Compilation for Disaster Management: Application of Remote Sensing and Statistical Modeling," by P. Sarabandi, A.S. Kiremidjian, R.T. Eguchi and B. J. Adams, 11/20/08 (PB2009-110484).

MCEER-08-0026 "New Experimental Capabilities and Loading Protocols for Seismic Qualification and Fragility Assessment of Nonstructural Systems," by R. Retamales, G. Mosqueda, A. Filiatrault and A. Reinhorn, 11/24/08 (PB2009-110485).

MCEER-08-0027 "Effects of Heating and Load History on the Behavior of Lead-Rubber Bearings," by I.V. Kalpakidis and M.C. Constantinou, 12/1/08 (PB2009-115533).

MCEER-08-0028 "Experimental and Analytical Investigation of Blast Performance of Seismically Resistant Bridge Piers," by S.Fujikura and M. Bruneau, 12/8/08 (PB2009-115534).

MCEER-08-0029 "Evolutionary Methodology for Aseismic Decision Support," by Y. Hu and G. Dargush, 12/15/08.

MCEER-08-0030 "Development of a Steel Plate Shear Wall Bridge Pier System Conceived from a Multi-Hazard Perspective," by D. Keller and M. Bruneau, 12/19/08 (PB2010-102696).

MCEER-09-0001 "Modal Analysis of Arbitrarily Damped Three-Dimensional Linear Structures Subjected to Seismic Excitations," by Y.L. Chu, J. Song and G.C. Lee, 1/31/09 (PB2010-100922).

MCEER-09-0002 "Air-Blast Effects on Structural Shapes," by G. Ballantyne, A.S. Whittaker, A.J. Aref and G.F. Dargush, 2/2/09 (PB2010-102697).

MCEER-09-0003 "Water Supply Performance During Earthquakes and Extreme Events," by A.L. Bonneau and T.D. O'Rourke, 2/16/09 (PB2010-100923).

MCEER-09-0004 "Generalized Linear (Mixed) Models of Post-Earthquake Ignitions," by R.A. Davidson, 7/20/09 (PB2010-102698).

MCEER-09-0005 "Seismic Testing of a Full-Scale Two-Story Light-Frame Wood Building: NEESWood Benchmark Test," by I.P. Christovasilis, A. Filiatrault and A. Wanitkorkul, 7/22/09 (PB2012-102401).

MCEER-09-0006 "IDARC2D Version 7.0: A Program for the Inelastic Damage Analysis of Structures," by A.M. Reinhorn, H. Roh, M. Sivaselvan, S.K. Kunnath, R.E. Valles, A. Madan, C. Li, R. Lobo and Y.J. Park, 7/28/09 (PB2010-103199).

MCEER-09-0007 "Enhancements to Hospital Resiliency: Improving Emergency Planning for and Response to Hurricanes," by D.B. Hess and L.A. Arendt, 7/30/09 (PB2010-100924).

MCEER-09-0008 "Assessment of Base-Isolated Nuclear Structures for Design and Beyond-Design Basis Earthquake Shaking," by Y.N. Huang, A.S. Whittaker, R.P. Kennedy and R.L. Mayes, 8/20/09 (PB2010-102699).

MCEER-09-0009 "Quantification of Disaster Resilience of Health Care Facilities," by G.P. Cimellaro, C. Fumo, A.M Reinhorn and M. Bruneau, 9/14/09 (PB2010-105384).

MCEER-09-0010 "Performance-Based Assessment and Design of Squat Reinforced Concrete Shear Walls," by C.K. Gulec and A.S. Whittaker, 9/15/09 (PB2010-102700).

MCEER-09-0011 "Proceedings of the Fourth US-Taiwan Bridge Engineering Workshop," edited by W.P. Yen, J.J. Shen, T.M. Lee and R.B. Zheng, 10/27/09 (PB2010-500009).

MCEER-09-0012 "Proceedings of the Special International Workshop on Seismic Connection Details for Segmental Bridge Construction," edited by W. Phillip Yen and George C. Lee, 12/21/09 (PB2012-102402).

MCEER-10-0001 "Direct Displacement Procedure for Performance-Based Seismic Design of Multistory Woodframe Structures," by W. Pang and D. Rosowsky, 4/26/10 (PB2012-102403).

MCEER-10-0002 "Simplified Direct Displacement Design of Six-Story NEESWood Capstone Building and Pre-Test Seismic Performance Assessment," by W. Pang, D. Rosowsky, J. van de Lindt and S. Pei, 5/28/10 (PB2012-102404).

MCEER-10-0003 "Integration of Seismic Protection Systems in Performance-Based Seismic Design of Woodframed Structures," by J.K. Shinde and M.D. Symans, 6/18/10 (PB2012-102405).

MCEER-10-0004 "Modeling and Seismic Evaluation of Nonstructural Components: Testing Frame for Experimental Evaluation of Suspended Ceiling Systems," by A.M. Reinhorn, K.P. Ryu and G. Maddaloni, 6/30/10 (PB2012-102406).

MCEER-10-0005 "Analytical Development and Experimental Validation of a Structural-Fuse Bridge Pier Concept," by S. El-Bahey and M. Bruneau, 10/1/10 (PB2012-102407).

MCEER-10-0006 "A Framework for Defining and Measuring Resilience at the Community Scale: The PEOPLES Resilience Framework," by C.S. Renschler, A.E. Frazier, L.A. Arendt, G.P. Cimellaro, A.M. Reinhorn and M. Bruneau, 10/8/10 (PB2012-102408).

MCEER-10-0007 "Impact of Horizontal Boundary Elements Design on Seismic Behavior of Steel Plate Shear Walls," by R. Purba and M. Bruneau, 11/14/10 (PB2012-102409).

MCEER-10-0008 "Seismic Testing of a Full-Scale Mid-Rise Building: The NEESWood Capstone Test," by S. Pei, J.W. van de Lindt, S.E. Pryor, H. Shimizu, H. Isoda and D.R. Rammer, 12/1/10 (PB2012-102410).

MCEER-10-0009 "Modeling the Effects of Detonations of High Explosives to Inform Blast-Resistant Design," by P. Sherkar, A.S. Whittaker and A.J. Aref, 12/1/10 (PB2012-102411).

MCEER-10-0010 "L'Aquila Earthquake of April 6, 2009 in Italy: Rebuilding a Resilient City to Withstand Multiple Hazards," by G.P. Cimellaro, I.P. Christovasilis, A.M. Reinhorn, A. De Stefano and T. Kirova, 12/29/10.

MCEER-11-0001 "Numerical and Experimental Investigation of the Seismic Response of Light-Frame Wood Structures," by I.P. Christovasilis and A. Filiatrault, 8/8/11 (PB2012-102412).

MCEER-11-0002 "Seismic Design and Analysis of a Precast Segmental Concrete Bridge Model," by M. Anagnostopoulou, A. Filiatrault and A. Aref, 9/15/11.

MCEER-11-0003 'Proceedings of the Workshop on Improving Earthquake Response of Substation Equipment," Edited by A.M. Reinhorn, 9/19/11 (PB2012-102413).

MCEER-11-0004 "LRFD-Based Analysis and Design Procedures for Bridge Bearings and Seismic Isolators," by M.C. Constantinou, I. Kalpakidis, A. Filiatrault and R.A. Ecker Lay, 9/26/11.

MCEER-11-0005 "Experimental Seismic Evaluation, Model Parameterization, and Effects of Cold-Formed Steel-Framed Gypsum Partition Walls on the Seismic Performance of an Essential Facility," by R. Davies, R. Retamales, G. Mosqueda and A. Filiatrault, 10/12/11.

MCEER-11-0006 "Modeling and Seismic Performance Evaluation of High Voltage Transformers and Bushings," by A.M. Reinhorn, K. Oikonomou, H. Roh, A. Schiff and L. Kempner, Jr., 10/3/11.

MCEER-11-0007 "Extreme Load Combinations: A Survey of State Bridge Engineers," by G.C. Lee, Z. Liang, J.J. Shen and J.S. O'Connor, 10/14/11.

MCEER-12-0001 "Simplified Analysis Procedures in Support of Performance Based Seismic Design," by Y.N. Huang and A.S. Whittaker.

MCEER-12-0002 "Seismic Protection of Electrical Transformer Bushing Systems by Stiffening Techniques," by M. Koliou, A. Filiatrault, A.M. Reinhorn and N. Oliveto, 6/1/12.

MCEER-12-0003 "Post-Earthquake Bridge Inspection Guidelines," by J.S. O'Connor and S. Alampalli, 6/8/12.

MCEER-12-0004 "Integrated Design Methodology for Isolated Floor Systems in Single-Degree-of-Freedom Structural Fuse Systems," by S. Cui, M. Bruneau and M.C. Constantinou, 6/13/12.

MCEER-12-0005 "Characterizing the Rotational Components of Earthquake Ground Motion," by D. Basu, A.S. Whittaker and M.C. Constantinou, 6/15/12.

MCEER-12-0006 "Bayesian Fragility for Nonstructural Systems," by C.H. Lee and M.D. Grigoriu, 9/12/12.

MCEER-12-0007 "A Numerical Model for Capturing the In-Plane Seismic Response of Interior Metal Stud Partition Walls," by R.L. Wood and T.C. Hutchinson, 9/12/12.

MCEER-12-0008 "Assessment of Floor Accelerations in Yielding Buildings," by J.D. Wieser, G. Pekcan, A.E. Zaghi, A.M. Itani and E. Maragakis, 10/5/12.

MCEER-13-0001 "Experimental Seismic Study of Pressurized Fire Sprinkler Piping Systems," by Y. Tian, A. Filiatrault and G. Mosqueda, 4/8/13.

MCEER-13-0002 "Enhancing Resource Coordination for Multi-Modal Evacuation Planning," by D.B. Hess, B.W. Conley and C.M. Farrell, 2/8/13.

MCEER-13-0003 "Seismic Response of Base Isolated Buildings Considering Pounding to Moat Walls," by A. Masroor and G. Mosqueda, 2/26/13.

MCEER-13-0004 "Seismic Response Control of Structures Using a Novel Adaptive Passive Negative Stiffness Device," by D.T.R. Pasala, A.A. Sarlis, S. Nagarajaiah, A.M. Reinhorn, M.C. Constantinou and D.P. Taylor, 6/10/13.

MCEER-13-0005 "Negative Stiffness Device for Seismic Protection of Structures," by A.A. Sarlis, D.T.R. Pasala, M.C. Constantinou, A.M. Reinhorn, S. Nagarajaiah and D.P. Taylor, 6/12/13.

MCEER-13-0006 "Emilia Earthquake of May 20, 2012 in Northern Italy: Rebuilding a Resilient Community to Withstand Multiple Hazards," by G.P. Cimellaro, M. Chiriatti, A.M. Reinhorn and L. Tirca, June 30, 2013.

MCEER-13-0007 "Precast Concrete Segmental Components and Systems for Accelerated Bridge Construction in Seismic Regions," by A.J. Aref, G.C. Lee, Y.C. Ou and P. Sideris, with contributions from K.C. Chang, S. Chen, A. Filiatrault and Y. Zhou, June 13, 2013.

MCEER-13-0008 "A Study of U.S. Bridge Failures (1980-2012)," by G.C. Lee, S.B. Mohan, C. Huang and B.N. Fard, June 15, 2013.

MCEER-13-0009 "Development of a Database Framework for Modeling Damaged Bridges," by G.C. Lee, J.C. Qi and C. Huang, June 16, 2013.

MCEER-13-0010 "Model of Triple Friction Pendulum Bearing for General Geometric and Frictional Parameters and for Uplift Conditions," by A.A. Sarlis and M.C. Constantinou, July 1, 2013.

MCEER-13-0011 "Shake Table Testing of Triple Friction Pendulum Isolators under Extreme Conditions," by A.A. Sarlis, M.C. Constantinou and A.M. Reinhorn, July 2, 2013.

MCEER-13-0012 "Theoretical Framework for the Development of MH-LRFD," by G.C. Lee (coordinating author), H.A Capers, Jr., C. Huang, J.M. Kulicki, Z. Liang, T. Murphy, J.J.D. Shen, M. Shinozuka and P.W.H. Yen, July 31, 2013.

MCEER-13-0013 "Seismic Protection of Highway Bridges with Negative Stiffness Devices," by N.K.A. Attary, M.D. Symans, S. Nagarajaiah, A.M. Reinhorn, M.C. Constantinou, A.A. Sarlis, D.T.R. Pasala, and D.P. Taylor, September 3, 2014.

MCEER-14-0001 "Simplified Seismic Collapse Capacity-Based Evaluation and Design of Frame Buildings with and without Supplemental Damping Systems," by M. Hamidia, A. Filiatrault, and A. Aref, May 19, 2014.

MCEER-14-0002 "Comprehensive Analytical Seismic Fragility of Fire Sprinkler Piping Systems," by Siavash Soroushian, Emmanuel "Manos" Maragakis, Arash E. Zaghi, Alicia Echevarria, Yuan Tian and Andre Filiatrault, August 26, 2014.

MCEER-14-0003 "Hybrid Simulation of the Seismic Response of a Steel Moment Frame Building Structure through Collapse," by M. Del Carpio Ramos, G. Mosqueda and D.G. Lignos, October 30, 2014.

MCEER-14-0004 "Blast and Seismic Resistant Concrete-Filled Double Skin Tubes and Modified Steel Jacketed Bridge Columns," by P.P. Fouche and M. Bruneau, June 30, 2015.

MCEER
EARTHQUAKE ENGINEERING TO EXTREME EVENTS
University at Buffalo, The State University of New York
133A Ketter Hall ▪ Buffalo, New York 14260-4300
Phone: (716) 645-3391 ▪ Fax: (716) 645-3399
Email: *mceer@buffalo.edu* ▪ Web: *http://mceer.buffalo.edu*
University at Buffalo *The State University of New York*

ISSN 1520-295X